15 November 2013 | $10

Science

AAAS

EDITORIAL

NEWS OF THE WEEK

NEWS & ANALYSIS

NEWS FOCUS

LETTERS

BOOKS *ET AL.*

POLICY FORUMS

PERSPECTIVES

ASSOCIATION AFFAIRS

CONTENTS continued >>

page 790

page 803

ON THE WEB THIS WEEK

>> *Science* Podcast
Listen to stories on the origin of domestic dogs, tracking adaptation over 50,000 generations, ramping up solar power with perovskites, and more.

>> Find More Online
Check out *Science* Express, our podcast, videos, daily news, our research journals, and *Science* Careers at **www.sciencemag.org**.

COVER

The Basenji represents one of the most divergent dog lineages in existence today. Genetic analyses of modern and ancient canids, including some of the oldest known dog remains, place the origin of modern dogs in Europe between 18,800 and 32,100 years ago. See pages 785 and 871.

Photo: © Barbara von Hoffmann/Alamy

DEPARTMENTS

REVIEW

RESEARCH ARTICLES

REPORTS

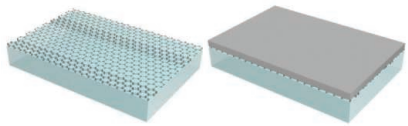

page 833

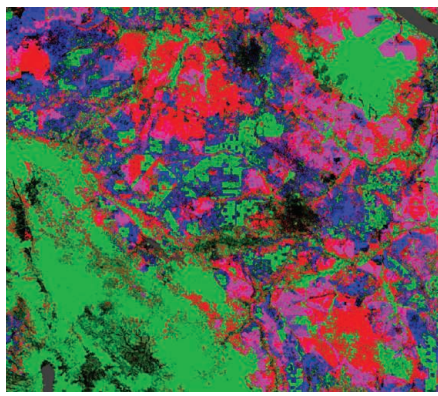

page 850

SCIENCE (ISSN 0036-8075) is published weekly on Friday, except the last week in December, by the American Association for the Advancement of Science, 1200 New York Avenue, NW, Washington, DC 20005. Periodicals Mail postage (publication No. 484460) paid at Washington, DC, and additional mailing offices. Domestic individual membership and subscription (51 issues): $149 ($74 allocated to subscription). Domestic institutional subscription (51 issues): $990; Foreign postage extra: Mexico, Caribbean (surface mail) $55; other countries (air assist delivery) $85. First class, airmail, student, and emeritus rates on request. Canadian rates with GST available upon request, GST #1254 88122. Publications Mail Agreement Number 1069624. **Printed in the U.S.A.**

Change of address: Allow 4 weeks, giving old and new addresses and 8-digit account number. **Postmaster:** Send change of address to AAAS, P.O. Box 96178, Washington, DC 20090–6178. **Single-copy sales:** $10.00 current issue, $15.00 back issue prepaid includes surface postage; bulk rates on request. **Authorization to photocopy** material for internal or personal use under circumstances not falling within the fair use provisions of the Copyright Act is granted by AAAS to libraries and other users registered with the Copyright Clearance Center (CCC) Transactional Reporting Service, provided that $30.00 per article is paid directly to CCC, 222 Rosewood Drive, Danvers, MA 01923. The identification code for *Science* is 0036-8075. *Science* is indexed in the *Reader's Guide to Periodical Literature* and in several specialized indexes.

Quick-Dry Region >>

The Sahara Desert is one of the driest places on Earth. However, 11,000 to 5000 years ago, it was a relatively lush region containing savannah grasslands and humid tropical forests. This interval, the Early Holocene African Humid Period, ended, of course, but whether the drying occurred rapidly or gradually is unclear. **Tierney and deMenocal** (p. 843, published online 10 October; see the Perspective by **Bard**) report results from the Horn of Africa that suggest that the transitions both into and out of the humid period were abrupt—occurring within centuries rather than over millennia.

Monolayer Graphene via Two Transfers

Oriented monolayers of graphene containing some bilayer regions can be formed on silicon carbide crystal surfaces, but, to be cost effective, the graphene needs to be exfoliated and transferred to other substrates so that the silicon carbide crystal can be reused. **Kim *et al.*** (p. 833, published online 31 October) used a nickel film grown to a thickness designed to impart a particular surface stress as a "handle" to exfoliate the graphene layer for transfer to a silica substrate. An additional gold layer was then used to remove the excess monolayer from the bilayer regions to create a monolayer suitable for electronics applications.

Answers from Exomes

Exome sequencing, which targets only the protein-coding regions of the genome, has the potential to identify the underlying genetic causes of rare inherited diseases. **Angulo *et al.*** (p. 866, published online 17 October; see Perspective by **Conley and Fruman**) performed exome sequencing of individuals from seven unrelated families with severe, recurrent respiratory infections. The patients carried the same mutation in the gene coding for the catalytic subunit of phosphoinositide 3-kinase δ (PI3Kδ). The mutation caused aberrant activation of this kinase, which plays a key role in immune cell signaling. Drugs inhibiting PI3Kδ are already in clinical trials for other disorders.

Forests in Flux

Forests worldwide are in a state of flux, with accelerating losses in some regions and gains in others. **Hansen *et al.*** (p. 850) examined global Landsat data at a 30-meter spatial resolution to characterize forest extent, loss, and gain from 2000 to 2012. Globally, 2.3 million square kilometers of forest were lost during the 12-year study period and 0.8 million square kilometers of new forest were gained. The tropics exhibited both the greatest losses and the greatest gains (through regrowth and plantation), with losses outstripping gains.

Long-Lived Donors

Quantum computing in materials such as silicon would simplify integration with existing electronic components; however, the coherence times of such qubits, especially at room temperature, are affected by the interaction with the busy environment of a solid. Eliminating isotopic impurities from the host material improves coherence times, as observed for qubits, based on the nuclear spin of neutral P donors in Si. **Saeedi *et al.*** (p. 830) modified this system by using charged P donors instead of neutral ones; by manipulating the states of the donors optically and using dynamical decoupling, the coherence time of the qubits was extended to 3 hours at cryogenic temperatures and 39 minutes at room temperature.

Scaling Spindle Size

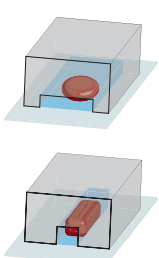

The difficulty of modulating cell size in vivo has made it hard to test hypotheses for organelle size scaling during development. To this end, **Hazel *et al.*** (p. 853) and **Good *et al.*** (p. 856) developed microfluidic systems in which cytoplasmic extracts are encapsulated in compartments with definable size. The size of mitotic spindles assembled within cell-free extracts scaled with the volume of the compartment within which the spindle assembled. The findings suggest that the diminished availability of cytoplasmic components, notably tubulin, concomitant with cell size reduction, prescribes a smaller spindle size.

Slipping the NET

One spectacular response to bacterial infection is the release of NETs (neutrophil extracellular traps) of DNA from polymorphonuclear leukocytes that immobilize the pathogens and prevent phagocytosis by macrophages. *Staphylococcus aureus* evades NETs by degrading the DNA into deoxyadenosine (dAdo). **Thammavongsa *et al.*** (p. 863) found that dAdo also promotes immune cell death, which appears to ensure the exclusion of macrophages from the center of abscesses within which the bacteria survive.

Dog Domestication

The precise details of the domestication and origins of domestic dogs are unclear. **Thalmann *et al.*** (p. 871; see the cover) analyzed complete mitochondrial genomes from present-day dogs and wolves, as well as 18 fossil canids dating from 1000 to 36,000 years ago from the Old and New Worlds. The data suggest that an ancient, now extinct, central European population of wolves was directly ancestral to domestic dogs. Furthermore, several ancient dogs may represent failed domestication events.

Stabilizing Silicon

Solar-driven water splitting has potential as an energy storage mechanism to supplement the direct conversion of sunlight to electricity. A submersed integrated device has been proposed both to absorb the light and to catalyze the reaction, but stability has been a problem. **Kenney *et al.*** (p. 836; see the Perspective by **Turner**) found that a nickel coating, thin enough to let light through, could protect a silicon absorber in the alkaline environment of a lithium/potassium borate electrolyte. The nickel also functioned as the oxidation catalyst, and the lithium ions helped to establish a protective film structure in situ.

Additional summaries

Dead Wood

Trees can be affected by a wide variety of diseases caused by insects, fungi, and other pathogens. Such diseases often make the headlines—particularly when iconic tree species are affected—for example, in the case of the ash dieback currently spreading through Europe, or the chestnut blight that devastated American chestnut trees. But what is the effect of these diseases on ecosystem services performed by trees in natural and managed ecosystems? **Boyd *et al.*** (p. 823) review the spread of tree diseases, as a result of globalization and climate change, and analyze the resulting damage to timber and fruit production, to climate regulation, and to parks and woodlands caused by tree diseases.

The pK_a of P450

Cytochrome P450 enzymes oxidize hydrocarbons through activation of oxygen at heme iron centers. However, the protein backbone has various sites (particularly tyrosine residues) that are also sensitive to oxidation, so how can the enzyme rapidly transform substrates without attacking itself? **Yosca *et al.*** (p. 825) explored the energetics of the competition between substrate and self-oxidation by measuring the pK_a of the enzyme's iron(IV)hydroxide motif. Cysteine thiolate coordination to iron in the P450 structure raised the pK_a almost to 12—rendering the iron oxo far more basic than analogous motifs in other heme environments. Correspondingly, the electronic environment for H-atom transfer from the substrate was relatively favorable, compared to electron transfer from a backbone residue.

[2+2] Asymmetrically

Catalysts in thermal reactions operate by lowering energy barriers of bound substrates, and thereby increasing the proportion of reagents that can proceed to products at a given temperature. In photochemical reactions, light provides the energy to surmount the barrier. It is therefore challenging to alter selectivity through catalysis, because the catalyst may not be bound when a given reagent absorbs the light. **Brimioulle and Bach** (p. 840) surmounted this problem in the light-induced intramolecular [2+2] cycloaddition of enones by using a catalyst that shifted the absorption wavelength of the bound substrate. The light was thus predominantly absorbed by substrate-catalyst complexes, enabling asymmetric induction by the catalyst to provide enantiomerically enriched products.

Getting the Dosage Right

As sex chromosomes evolve, they must compensate for differential gene dosage, especially in non-sex-specific genes. However, owing to the relative rarity of chromosomes that are in the process of becoming sex chromosomes, the ongoing evolutionary processes resulting in dosage compensation are unclear. **Ellison and Bachtrog** (p. 846; see the Perspective by **Chuong and Feschotte**) identified a specific transposable element involved in dosage compensation in males on the evolutionarily new neo-X chromosome of *Drosophila miranda*. A particular copy of this transposable element has been inserted at chromatin entry sites on the neo-X chromosome that favorably binds to the male-specific lethal complex, which in turn facilitates the spreading of chromatin silencing on a single chromosome to provide dosage compensation.

The Root of the Problem

The quiescent center (QC) within the root meristem plays a key role as a stem cell organizer to sustain the root stem cell niche. The QC cells execute a dual role: prevention of the differentiation of neighboring stem cells, and maintenance of the root structure by undergoing only occasional cell division. The mechanisms that account for the low QC proliferation are unclear, although the anaphase-promoting complex/cyclosome (APC/C) E3 ubiquitin ligase is known to suppress QC cell division. Through a systematic functional analysis of APC/C-copurifying proteins, **Heyman *et al.*** (p. 860) characterized a transcription factor ERF115 as a rate-limiting factor for QC cell division. ERF115 needs to be destroyed to retain QC cells in a resting state. ERF115 operates in a brassinosteroid-dependent manner and controls QC cell division through transcriptional activation of phytosulfokine signaling.

Dissecting Initiation

Ribosomes make proteins. The initiation step of protein synthesis involves initiation factors (IFs) that help to position the initiation codon of the messenger RNA (mRNA) and the initiator transfer RNA. The initiation factor eIF5B is universally conserved, and promotes recruitment of the large ribosomal subunit during the terminal

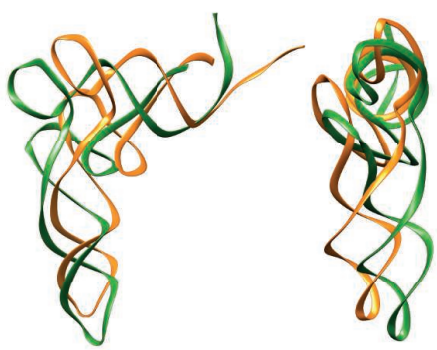

step of initiation. **Fernández *et al.*** (p. 824, published online 8 November) used cryoelectron microscopy to determine the structure of the yeast eIF5B initiation complex and provide a snapshot of the final step of eukaryotic translation initiation.

CREDIT: FERNÁNDEZ *ET AL.*

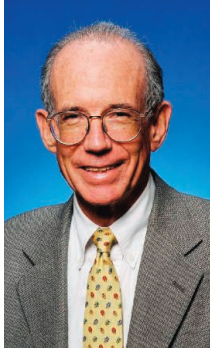

Donald Kennedy is president emeritus at Stanford University, Stanford, CA, and a former editor-in-chief of *Science*. E-mail: kennedyd@stanford.edu.

Time to Deal with Antibiotics

ANTIBIOTIC DRUGS—PENICILLIN, TETRACYCLINE, AND THEIR MORE MODERN SUCCESSORS—HAVE been critical elements in the world's efforts to sustain health and deal with human diseases. Unfortunately, the vital role of these drugs has been critically compromised by the prevalence of dangerous infections that antibiotics can no longer control, because bacteria are resistant to them. Even nations with strong health care systems, respected medical centers, and fine hospitals are experiencing a growing epidemic of infections that they now simply cannot cure. Here in the United States, such infections kill nearly 23,000 people each year, according to the Centers for Disease Control and Prevention's (CDC's) report *Antibiotic Resistance Threats in the United States, 2013*. Farming practices are largely to blame for the rise of antibiotic-resistant strains, and at last there is hope for reform.

The story is an old one. Back in 1977–1978, the U.S. Food and Drug Administration (FDA) proposed a regulation to deny the feeding of three antibiotics (penicillin, tetracycline, and chlortetracycline) to cattle to promote their growth rather than to respond to disease. As FDA commissioner at the time, I argued that the vulnerability of infectious agents to antibiotics constituted a "kind of Commons"—that is, a future health benefit shared by all members of the public. Our effort, hard fought by the livestock industry, failed to get congressional support, as the industry blamed the practice of human medicine for the resistance problem. Of course a physician may write a prescription for the wrong indication, or a patient will use more antibiotic in hope of subduing a virus. But antibiotic resistance will be solved only when we end the use (or rather, the abuse) of these agents in veterinary medicine.

Many groups interested in health issues have since pushed for more regulatory action, and in 2008 the Pew Charitable Trusts issued a report calling for an end to the use of antibiotics for nontherapeutic indications. The report made special note of the conditions under which cattle, pigs, and chickens were kept in preparation for market. These often involved crowding the animals in confined spaces with unhealthy environments, thus encouraging their keepers to guard against possible epidemics by prophylactic applications of antibiotics. That report elicited a strong reaction from the agricultural community, making its familiar claim that antibiotic resistance is all about physicians and their prescription habits. But those concerned with health policy know from the 2013 CDC report that at least 73% of the antibiotics sold in the United States are destined for veterinary use. As the Pew study emphasized, that's where the challenge of antibiotic resistance has to be met.

Now, fortunately, a new opportunity for resolution has arrived. Last month, a distinguished panel of experts assembled by the Johns Hopkins University's Center for a Livable Future concluded that the use of antibiotics in managing animal health and production has become a major public health problem. Moreover, new analyses show that there are links between antibiotic use in animals and antibiotic-resistant pathogens in humans who live near, or care for, the animals. Accordingly, the FDA issued in April 2012 a preliminary regulatory proposal to finalize "Food and Drug Administration Guidance #213." The guidance would end antibiotic use for growth promotion and "unnecessary disease prevention": i.e., prophylactic administration to animals whose health is threatened by crowding. It also would require veterinary oversight of antibiotics introduced into animal feed. Taken together, the provisions of this guidance offer a serious chance for ending the abuses that have brought about today's medical disaster of widespread antibiotic resistance. Guidance #213 makes clear the distinction between the use of antibiotics for treating sick animals and uses that are actually aimed at increasing production. It should be finalized as soon as possible.

— Donald Kennedy

10.1126/science.1248056

EDITED BY GILBERT CHIN AND MARIA CRUZ

ECOLOGY

Jet Transport

Deposits of windblown dust originating from the Sahara may have been responsible for the prehistoric condition of the Everglades, the vast area of wetlands at the southern end of the Florida peninsula. Our understanding of the history of the Everglades ecosystem and of the ecological conditions that produced and sustained it has been hampered by the extensive human transformation of the landscape, particularly in the past century. An analysis of sediments deposited over the past 4600 years provides a record of the vegetation and soil nutrient patterns and shifts in hydrology, revealing some of the processes that have hitherto remained obscure. Glaser *et al.* show that dust deposition mediated by frequent tropical storms was an important source of nutrients for the Everglades until about 2800 years ago, when a climatic shift in the tropical Atlantic and Gulf of Mexico led to weather patterns that sharply decreased the level of dust inputs and led to a drier climate and a gradual loss of soil phosphorus, carbon, and nitrogen. The vegetation concomitantly changed from a slough assemblage of aquatic and semiaquatic plants to communities of sawgrass and pine, which began to dominate as the water table fell and the nutrient levels decreased. — AMS

Proc. Natl. Acad. Sci. U.S.A. **110**, 10.1073/pnas.1222239110 (2013).

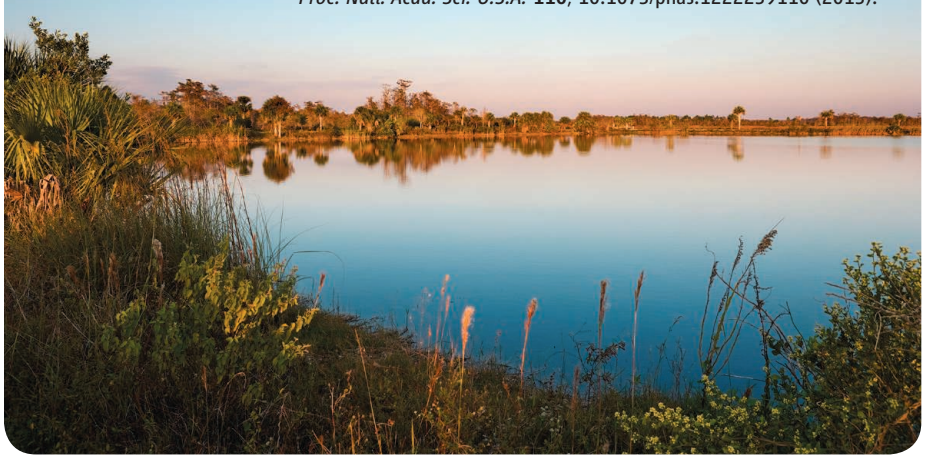

BIOCHEMISTRY

Dual Use

Protein phosphatase 2A (PP2A) is a serine/threonine phosphatase involved in many essential cellular processes. The core enzyme is a heterotrimer in which a catalytic subunit (PP2Ac) associates with a scaffold subunit A and with one of a diverse set of regulatory subunits B; the catalytic subunit must be activated for proper holoenzyme formation. Guo *et al.* have determined the structure of PP2Ac in complex with a fusion protein comprising the PP2A phosphatase activator protein (PTPA) and a mini-A subunit, and with ATPgS bound. The structure shows that both PTPA and PP2Ac interact with ATPgS and that the phosphate of ATP binds to catalytic metal ions. The authors suggest that the ATP-binding pocket is created upon complex formation and that this results in ATP hydrolysis at the PP2Ac active site, which is also where the removal of phosphates from serine/threonine occurs. Biochemical experiments suggest that ATP facilitates binding of the appropriate metal ions to PP2A and that this reduces nonspecific phosphatase removal. Coordinated regulation of both PP2Ac activity and holoenzyme formation would allow for a tight regulation of PP2A function. — VV

Cell Res. **23**, 10.1038/cr.2013.138 (2013).

MATERIALS SCIENCE

In Rare Titania Form

One route for synthesizing mesoporous and microporous inorganic materials is to use an organic material as a template, such as a surfactant or a block copolymer, but the resulting pore network can be disordered. Hall *et al.* show that the inherent microporosity of a metal-organic framework (MOF) compound can be used to template an ordered microporous form of titanium oxide. They used the MOF HKUST-1, in which copper ions linked together by benzene-1,3,5-tricarboxylate ligands create a network of 1-nm pores. The material was impregnated with a metal oxide precursor, titanium(IV) isopropoxide, and then underwent a hydrothermal treatment at 200°C for 20 hours in a water-ethanol solvent. This product was treated with acid and then hydrogen peroxide. These procedures removed almost all of the MOF framework, although some copper and residual carbon were retained. Transmission electron microscopy and x-ray diffraction studies showed that the morphology of the HKUST-1 template and the pore size of 1 nm were retained in the metal oxide. These studies also revealed that the phase of titania is brookite, which probably formed instead of the more common rutile or anatase phases because of the presence of copper ions. However, nitrogen adsorption-desorption studies revealed that disordered mesopores are present, which probably resulted from incomplete pore filling by the precursor. — PDS

J. Am. Chem. Soc. **135**, 10.1021/ja4083254 (2013).

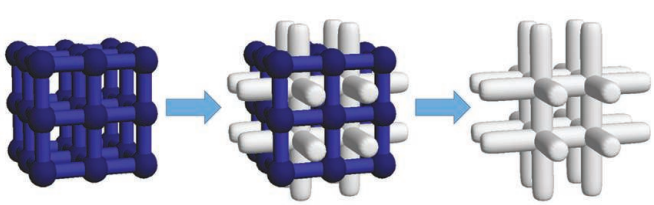

BEHAVIOR

Genetic Conformity

Fish who swim in schools find that doing so brings benefits and costs. On the positive side of the ledger, there is greater safety from predators in numbers, it's easier to find a mate, and swimming efficiency is enhanced; drawbacks include being vulnerable to fish harvesting. Comparing two populations of threespine sticklebacks—strongly schooling marine sticklebacks from Hokkaido, Japan, and benthic sticklebacks from Paxton Lake in British Columbia (a population that displays much weaker schooling inclination)—Greenwood *et al.* have identified two genomic regions that contribute to distinct dimensions of sociality. First, there is the tendency to swim with others, quantified on the basis of time spent in school, latency to enter school, and number of episodes. Second, individuals are constrained when schooling to swim in parallel to their neighbors, which was measured as relative orientation angle. Comparing the populations revealed that marine fish adopt parallel orientations more than the benthic fish. Prior work has shown that the sensory system for body

Published by AAAS

position relies on the lateral line, a peripheral mechanoreceptive system, and the authors established a genetic link between schooling position and lateral line variation. — BAP

Curr. Biol. **23**, 1884 (2013).

ENVIRONMENTAL SCIENCE

Mercury Biomagnification

In aquatic ecosystems, mercury is converted to methylmercury, which can be accumulated in top predators at levels millions of times higher than in surface waters. This biomagnification can result in toxic concentrations in fish and fish-eating species. However, mercury concentrations in fish and invertebrates differ widely between ecosystems, and it remains unclear whether biomagnification is only affected by food web processes such as growth rate and species diversity or also by physicochemical variables such as water pH, temperature, and nutrient concentrations. Lavoie *et al.* have compiled data from 69 studies of marine and freshwater ecosystems around the globe to determine the total mercury and methylmercury tropic magnification slopes, which are key indicators of the biomagnifying potential in food webs. The results show biomagnification to be highly variable among the reviewed sites. It is positively related to latitude and highest in cold, low-productivity ecosystems. A combination of variables related to temperature is likely to be responsible for the latitude effect, but the mechanism remains unclear. — JFU

Environ. Sci. Technol. 10.1021/es403103t (2013).

PHYSICS

A Superradiant Amplifier

The usual notion of laser operation involves populating an excited state of a gain medium so that there are more atoms in the excited state than there are in the ground state. This population inversion can then be stimulated to emit many photons coherently with the same wavelength. The spontaneous emission of photons from atoms is a common occurrence, but the conditions for lasing cannot always be met. Six decades ago, it was shown theoretically that an ensemble of spontaneously emitting atoms could, under the right conditions, behave collectively and emit in unison, thereby giving rise to superradiant emission. In this scenario, population inversion is not necessary. Svidzinsky *et al.* show that a driving field of infrared light illuminating the superradiant ensemble can result in the amplified emission of coherent light but at much higher frequencies. If experimentally realized, their proposed mechanism could provide a route for the generation of coherent radiation in the UV or even x-ray range of the electromagnetic spectrum. — ISO

Phys. Rev. X **3**, 041001 (2013).

CLIMATE SCIENCE

Our Rain

More intense precipitation events are expected to occur as climate warms. Warmer air holds more water vapor, relative humidity should not change as air temperatures increase, and precipitation intensity depends mostly on the availability of moisture in the atmosphere. Zhang *et al.* use updated observational data in a multimodel ensemble analysis of global climate model simulations available from the Coupled Model Intercomparison Project Phase 5 to quantify the human influence on extreme precipitation. They find that the model response to anthropogenic effects is consistent with the changes in extreme precipitation observed over land in the Northern Hemisphere and that the observed change cannot be explained by either natural internal variability or the response to natural external forcing. They estimate that the amount of rainfall over both 1- and 5-day intervals increased by between 5.2 and 5.9% between 1951 and 2005. This means that the single-day precipitation of a size expected to recur once every 20 years on average in the early 1950s has become an event that recurs every 15 years in the early 2000s and that the increased frequency is attributable to human influence. — HJS

Geophys. Res. Lett. **40**, 5252 (2013).

CREDIT: © DBURKE/ALAMY

Published by AAAS

AROUND THE WORLD

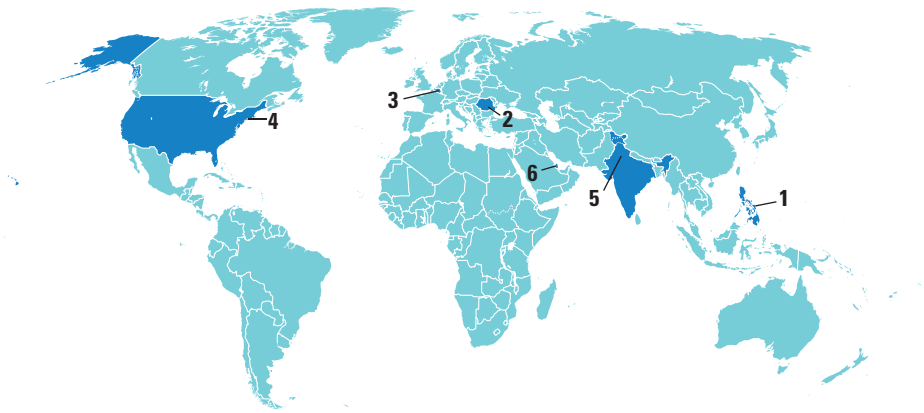

Tacloban, Philippines **1**

Supertyphoon Poses Questions for Scientists

Typhoon Haiyan, which raged across the Philippines last week packing wind speeds of up to 314 kph, is the most powerful tropical cyclone known to hit land. While Philippine authorities scramble to provide relief to survivors, scientists are pondering the storm's ferocity and seeking lessons for the future.

Geologist Jonathan Nott, of James Cook University in Cairns, Australia, notes that after starting out last week as a small storm, Haiyan underwent "very rapid intensification" on 6 and 7 November before making landfall just after 4 a.m. on 8 November.

Then it also moved "relatively quickly" across the islands. That sudden intensification left remote communities "precious little time to prepare for this event," says marine biologist Helen Yap of the University of the Philippines, Diliman. On the other hand, the storm's quick pace limited its impact. "The slower a storm system moves, the more wind damage it causes," Nott says. Hovering longer would also likely have soaked hillsides, raising the risk of landslides. Sorting out what this means for future mitigation efforts will take time, says Alfredo Mahar Lagmay, a geologist also at the University of the Philippines, Diliman. "Every disaster unfolds in a different way, and only after the disaster is over can you know its lessons," he says.

Flattened. Tacloban residents in the ruin of their house in the aftermath of supertyphoon Haiyan.

Bucharest **2**

Mining Project Plan Rejected

Controversial plans to mine one of Europe's largest gold reserves are on hold. Romania's Rosia Montana region in Transylvania has been mined since pre-Roman times, and archaeologists say the site provides unique insights into millennia of mining technology (*Science*, 9 May 2003, p. 890).

On 11 November, a parliamentary commission unanimously rejected the draft law that would have allowed a Canadian company, Gabriel Resources, to begin mining. In recent months, thousands of protesters have marched in Romania to protest the bill, primarily because of plans to create a cyanide-laced tailings lake.

The full Parliament is expected to follow the commission's recommendations, which also said the country should craft a new law to govern gold and silver mining. Gabriel Resources officials have said they would sue the Romanian government for up to $4 billion in damages if the project is blocked. Opponents of the mine want the region to be designated a UNESCO World Heritage site.

Brussels **3**

Europe Could Get New GM Maize

In 2001, the agriculture giant now called DuPont Pioneer asked for approval to grow a new genetically modified (GM) maize variety in the European Union's fields. Twelve years later, the European Commission has made a decision: On 6 November, it proposed to allow cultivation of "maize 1507." It would be the third GM crop allowed for cultivation in the European Union, where consumers and many national governments have strong reservations about genetically engineered food.

Maize 1507 is engineered to produce its own insecticide against the European corn borer, a moth whose caterpillars chew on corn ears and stalks. The European Food Safety Authority (EFSA) greenlit the variety in six reports since 2005, but environmental groups worry that maize 1507 will harm nontarget species.

Target. Maize 1507 resists the European corn borer.

Based on EFSA's advice, the European Commission issued a draft decision to authorize the crop, on which member states had to sign off. But the committee failed to reach a consensus. Pioneer fought the resulting inaction in court, and now, the commission is pressuring member states to decide. If the Council of Ministers does not muster a weighted majority to reject the crop's cultivation within 3 months, the European Commission says it will authorize it anyway.
http://scim.ag/GMmaize

Cold Spring Harbor, New York **4**

New Biology Preprint Server

A well-known research lab is throwing its weight behind an idea that some biologists say is ripe for their field: a free website that will post raw manuscripts online before they're submitted to a journal.

BioRxiv, launched this week by the nonprofit Cold Spring Harbor Laboratory (CSHL) in New York, aims to be biologists' version of arXiv, the popular physics preprint server. The goal is to speed the dissemination of research and give scientists a way to get feedback on their draft papers before they

CREDITS (TOP TO BOTTOM): KEITH WELLER/ARS/WIKIMEDIA COMMONS; ERIK DE CASTRO/REUTERS

Published by AAAS

Oldest Slime Mats

While tromping across some of the world's oldest rocks, geobiologists led by Nora Noffke of Old Dominion University in Norfolk, Virginia, discovered what looked like rolled-up mats of sand several centimeters thick encased in rock. These turned out to be the oldest known "microbially induced sedimentary structures," distinctive shapes in sedimentary rock formed by layers of now-gone slime.

All manner of microbes can live layered on the bottom of shallow waters. Such microbial layers bind sand grains to form sand-laden mats, so that when, say, a strong current rips off a bit of mat and rolls it up, the sand form can be found embedded in rock eons later. In the December issue of *Astrobiology*, the scientists report finding a fresh mat fragment on a North Carolina barrier island (right) and examples lingering in 2.9-billion-year-old rock in southern Africa (middle) and in 3.5-billion-year-old rock in Western Australia (left). No vestige of life, micro- or megascopic, older than the Australian example has been found.

are formally peer-reviewed, says John Inglis, CSHL Press executive director. Although it's not the first attempt at a biology preprint server, he says "there is a growing desire in the community for this kind of service."

Anybody can submit a paper, but "affiliate" scientists have agreed to screen submissions to "assure us that this is real science," Inglis says. "We certainly don't want the enterprise to be sunk by publishing a load of crap." The site will publish papers only in the life sciences, not medicine. **http://scim.ag/bioRxiv**

New Delhi **5**

India's Mars Mission Recovers

After an early hiccup, India's maiden mission to Mars, Mangalyaan, is back on track, according to the Indian Space Research Organisation (ISRO). Launched on 5 November from India's spaceport Sriharikota, the spacecraft has been circling Earth as ISRO steadily raises its orbit, increasing the maximum distance between the satellite and the planet before it heads to Mars in December 2013.

But on 11 November, during the fourth orbit-raising operation, the spacecraft hit a snag after an onboard rocket motor failed to respond to specific commands and tests as instructed by ground controllers, resulting in failure to reach the required velocity. To compensate for the loss, ISRO successfully carried out a supplementary burn on 12 November.

ISRO Chair K. Radhakrishnan says "the spacecraft is healthy and the orbit raising as planned went off successfully." The $100 million mission will study the martian atmosphere after it reaches the Red Planet toward the end of 2014, following a 10-month journey.

Doha **6**

Desert 'Greening' Experiment's First Results

A project to "green" desert areas with a mix of technologies—producing food, biofuel, clean water, energy, and salt—reached a milestone last week. A pilot plant in Qatar, built by the Sahara Forest Project (SFP) and supported by Qatari fertilizer companies Yara International and Qafco, produced 75 kilograms of vegetables per square meter in three crops annually, comparable to commercial farms in Europe, while consuming only sunlight and seawater.

In SFP's greenhouse, fans blow hot desert air through a honeycombed curtain with salt water trickling down it to produce cool, moist conditions suitable for growing vegetables. Some of that moisture is recaptured by condensation to provide fresh water to irrigate the plants. Similar evaporative cooling is used to grow more crops outside, such as barley and arugula, and an onsite concentrated solar power plant provides electricity for the whole facility.

That a greenhouse with just 600 square meters of growing area produced such good yields suggests that a commercial plant could do even better, says SFP chief Joakim Hauge. SFP is now engaged in studies aimed at building a 20-hectare test facility near Aqaba in Jordan. **http://scim.ag/greendesert**

Dampness does it. Using seawater to cool the air makes farming the desert feasible.

Published by AAAS

Random Sample

Sex and the Single Sand Flea

The sand flea *Tunga penetrans* spends half of its life in the ground—and the other half in a living host, such as a human foot. Infestations—widespread in South America and sub-Saharan Africa—can produce a painful condition called tungiasis that makes it difficult to walk and can lead to other infections. But the disease gets scant attention from health workers or researchers, who know relatively little about the creature's life cycle—not even where (in the ground or in a host) it has sex and fertilizes its eggs.

So when Marlene Thielecke, a Ph.D. student at Charité University Medicine in Berlin who was studying tungiasis in Madagascar, discovered that she was hosting the parasite, she let her own body become a laboratory to study the creature.

The immature female burrows into a host's skin where, over 2 weeks, it swells to up to 10 mm across. She soon begins expelling eggs, then dies after 4 to 6 weeks. The only way to get rid of the parasites is to dig them out.

Thielecke took regular photographs of her infestation. The flea grew normally, but it wasn't laying eggs. It was also oddly long-lived—it was still alive after 2 months (at which point she extracted it).

The likely explanation? The flea was never fertilized, Thielecke and her supervisor, tungiasis expert Hermann Feldmeier, concluded in a paper published this month in *Travel Medicine and Infectious Disease*. On finding the flea, Thielecke had taken precautions, wearing socks and closed shoes to ward off other fleas—including potentially fertilizing males. This suggests an answer to the long-standing puzzle of whether fleas are fertilized before or after they embed. **http://scim.ag/fleafert**

NEWSMAKERS

BP Scientist Tapped To Head ARPA-E


Williams

Physicist **Ellen Williams** is a "brilliant" pick to head the U.S. government's lead agency for transforming edgy ideas into breakthrough energy technologies, former colleagues say. President Barack Obama on 6 November announced that he would nominate Williams, chief scientist at energy giant BP and a longtime professor at the University of Maryland (UMD), College Park, to lead the Advanced Research Projects Agency-Energy (ARPA-E). If confirmed by the Senate, she would succeed Arunava Majumdar, who left the post last June after serving as ARPA-E's inaugural director for 2.5 years (*Science*, 18 May 2012, p. 787).

"[Williams] is analytically one of the most brilliant people I've ever met, and knows technology inside and out," says particle physicist Drew Baden, chair of UMD's physics department, where Williams taught from 1991 through 2009 before joining BP. And she's got the management experience to help ARPA-E get the most out of its $230 million portfolio of high-risk but potentially high-reward commercialization projects, he adds. "She's the one if you want ARPA-E to make an impact, and not just chip around the edges."

FINDINGS

Ancient Himalayan 'Big Cat' Revealed

Researchers have discovered the oldest fossil yet of the pantherine lineage, which includes tigers, jaguars, and lions. Skull and jaw fragments and teeth recovered from the Tibetan Plateau reveal a new species, similar to the snow leopard, dating back 4 million to 6 million years. The next-oldest pantherine fossils (3.8 million years) came from East Africa. "It's given us a new part of the world to look at for the evolution of the big cat lineage," says Andrew Kitchener, a mammalogist at the National Museum of Scotland in Edinburgh. Previous studies suggested that the first pantherine emerged 10 million to 11 million years ago, but likely didn't split into other species for at least 5 million years. However, the new find suggests that big cats emerged and diversified earlier and more gradually than previously thought, says vertebrate paleontologist Z. Jack Tseng of the American Museum of Natural History in New York City. Tseng and colleagues describe the new species, *Panthera blytheae*, this week in the *Proceedings of the Royal Society B*. **http://scim.ag/catfossil**

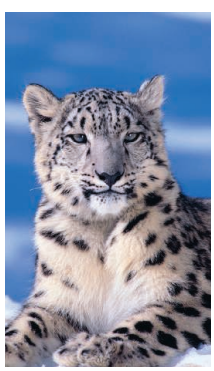

Frigid find. Extinct cat species resembled the snow leopard.

BY THE NUMBERS

70% Percent of U.S. research universities that say the sequester reduced research money for faculty and slowed ongoing research projects, according to a poll released this week.

600,000 Bat mortality from wind turbines in the contiguous United States in 2012, based on an estimate in *BioScience*.

$6 billion Cost of developing an Alzheimer's drug, which is nearly three times the industry average, finds a new report by the New York Academy of Sciences.

Science LIVE

Join us on Thursday, 21 November, at 3 p.m. EST for a live chat on cheaper, more efficient ways to **split water for solar energy storage**. **http://scim.ag/science-live**

CREDITS (TOP TO BOTTOM): EYE OF SCIENCE/SCIENCE SOURCE; THINKSTOCK; PHOTO COURTESY OF BP PLC

Published by AAAS

Don't let sleeping dogs lie. This 1000-year-old buried dog in Illinois provided DNA for dog domestication studies.

CREDIT: DEL BASTON/CENTER FOR AMERICAN ARCHAEOLOGY

ANCIENT DNA

Old Dogs Teach a New Lesson About Canine Origins

The story of dogs began thousands of years ago, when gray wolves began sidling out of the shadows and into the company of humans. There's little argument about that scenario—but plenty about when and where it took place, with the leading theories suggesting dogs were domesticated either in the Middle East or in East Asia. A study on page 871 draws on a new source of evidence, DNA from the fossils of ancient dogs and wolves, and comes to a third conclusion: Dogs originated in Europe, from a now-extinct branch of gray wolves.

The dogfight goes on. Based on the new study, "you will be hard-pressed to come up with a narrative about how dogs were not domesticated in Europe," says Greger Larson, an evolutionary biologist at the University of Durham in the United Kingdom. But some fans of the East Asia theory argue that the DNA examined, from cell organelles called mitochondria, cannot tell the whole story and that the analysis may be skewed because the ancient samples are primarily from Europe. "Critical observers will need more than mitochondrial DNA to be convinced," says Stephen O'Brien, a geneticist at St. Petersburg State University in Russia, who says he is in neither dog origin camp.

The archeological record is strewn with ancient wolf and dog remains, but researchers have had trouble piecing together canine history from the bones because it can be difficult to distinguish between those of dogs and wolves. Nor has the distribution of wolf-dog fossils, mostly found in Europe so far, clearly pointed to dogs' birthplace. While the wild ancestors of sheep and goats, for example, lived in only one small Middle Eastern region, wolves once ranged from Portugal to Siberia and throughout North America. Given that, several researchers have suggested that dogs originated more than once, in different places.

Those hunting for the first Fido have turned to the DNA of modern animals for clues. In 2002, geneticist Peter Savolainen of the Royal Institute of Technology (KTH) in Stockholm, Ya-ping Zhang at the Kunming Institute of Zoology in China, and their colleagues analyzed small pieces of mitochondrial DNA (mtDNA) from dozens of wolves and hundreds of dogs around the world. They found the greatest genetic diversity—a potential marker of a species' origin—in southern East Asia, implying that dogs were domesticated there. Their later work on the complete mitochondrial genomes and Y-chromosomes of dogs, wolves, and coyotes supported this conclusion.

But in 2010, Robert Wayne from the University of California, Los Angeles, and his colleagues analyzed 48,000 markers across the whole genomes of hundreds of dogs and gray wolves from all over the world. Dogs had more DNA sequences in common with Middle Eastern wolves than with East Asian wolves, including markers thought to be unique to animals from the Middle East. To Wayne, that suggested that dogs' ancestors came from that part of the world.

Each side has argued that the other camp failed to include the widest range of samples, skewing their results. And last year, Larson and his colleagues weighed in with an analysis suggesting that modern DNA could not settle the question, because of intermixing between dogs and wolves and between different kinds of dogs in the millennia since they were domesticated. "Only ancient DNA can help," agrees Jean-Denis Vigne, an archaeozoologist at CNRS, the French national research agency, and the National Museum of Natural History in Paris.

Wayne had already been thinking along those lines. Since the 1990s, his team had periodically gotten permission from various archaeologists to extract DNA from ancient canid remains, but lacked the ability to sequence enough genetic material to compare. By 2010, however, with evolutionary geneticist Olaf Thalmann on board as a postdoc, the group was ready to start pulling out entire mitochondrial genomes and key parts of the nuclear DNA for study.

Wayne, Thalmann (now at the University of Turku in Finland), and their team got most or all of the mitochondrial genome from 18 ancient samples, eight classified as doglike and 10 classified as wolflike, found mostly in Europe (see table, p. 786). The researchers compared the mtDNA of the samples, which ranged from 1000 to 36,000 years old, to similar sequences in modern animals: 77 dogs from a wide assortment of breeds, 49 wolves, and four coyotes. Based on sequence differences in the DNA, they built a family tree that showed the relatedness of the various samples.

The analysis yielded two surprises. First, most living dogs turned out to be more closely related to ancient wolves than to modern ones. "The [gray wolf] population that gave rise to modern dogs is most likely extinct," Thalmann says. The finding supports the results of a whole-genomes study, reported

in May at The Biology of Genomes meeting in Cold Spring Harbor, New York, in which Wayne's team also concluded that modern wolves are not dogs' direct ancestors.

The second surprise was geographic: The ancient remains most closely related to modern dogs were all European. For example, the closest wolf relative for the largest branch of modern dogs was 14,500 years old and hailed from a cave in Switzerland; ancient dogs from Germany were the closest relatives of another modern dog branch. "This provides crucial new information," says Renato Mariani-Costantini, a pathologist at the "G. d'Annunzio" University of Chieti-Pescara in Italy who had previously published a mitochondrial DNA study of five prehistoric Italian dogs that suggested a European origin of canines.

Some geneticists argue that dogs became domesticated once agriculture arose, but the new study reinforces the idea that domestication happened much earlier, among hunter-gatherers. Wayne and his colleagues calculate, based on mutation rates and observed genetic differences in their samples, that dog domestication began between 18,800 and 32,100 years ago, and that canines were well entrenched with people between 15,000 and 20,000 years ago, before humans farmed.

The researchers were unable to get suitable DNA from ancient Middle Eastern canids and had no access to ancient specimens from East Asia. That's a major flaw, says Savolainen, who remains convinced that dogs originated in southern China. "It's not really an objective study." He and others also fault the work for including just a few modern wolves from the Middle East and China but dozens from Europe. "[It is] the same as if you wanted to do a study of the origins of humans and you didn't have a single sample from Africa."

Furthermore, mtDNA, which is passed down from mother to daughter, "reflects a small part of the evolutionary history," says Chung-I Wu, an evolutionary biologist at the University of Chicago in Illinois. Given how much human migration there was early in dog domestication, Wu suspects that male dogs coming from outside Europe might have been bred with European dams, leading to the mitochondrial story Wayne and Thalmann propose, but not the correct overall picture of dog domestication. "Two parts of the genome can tell two different stories."

Wayne and Thalmann are now trying to get good nuclear sequence data from dog and wolf fossils, as are Larson and other researchers (*Science*, 1 November, p. 543). But O'Brien is not sure that more complete genomes will settle the debates, given how much dogs and wolves must have muddied the genetic waters over history by interbreeding. "Genomic archaeology has its limitations and the dogs are testing it," he says. "It may settle one day, but don't count on it."

–ELIZABETH PENNISI

ANCIENT SAMPLES STUDIED

Country	Approximate age (years)	Morphological classification
Belgium	36,000	*Doglike*
Russia	33,500	*Doglike*
Belgium	30,000	Wolflike
Alaska	28,000	Wolflike
Belgium	26,000	Wolflike
Russia	22,000	Wolflike
Alaska	21,000	Wolflike
Alaska	20,800	Wolflike
Russia	18,000	Wolflike
Russia	15,000	Doglike
Germany	14,700	Doglike
Switzerland	14,500	Wolflike
Switzerland	14,500	Wolflike
Switzerland	14,500	Wolflike
Germany	12,500	Doglike
USA	8,500	Doglike
Argentina	1,000	Doglike
USA	1,000	Doglike

Wolf or dog? Mitochondrial DNA from 18 fossils and from modern canids revealed that two considered doglike (italic) were not closely related to dogs at all.

INFECTIOUS DISEASES

Goal of Ending AIDS Gains Traction

SAN FRANCISCO, CALIFORNIA—A *Who's Who* of HIV/AIDS researchers from six continents, major funders like the Bill & Melinda Gates Foundation, public health officials, and the first person ever cured of an HIV infection gathered here last week to explore the question: "What will it take to achieve an AIDS-free world?" Tremendous headway in science over the past few years has brought this once-fanciful idea into the realm of possibility, many agreed. But talk of "ending AIDS" alarms some experts, alert to the risks of overselling that promise and underplaying the huge logistical and financial challenges.

Richard Horton, editor of *The Lancet*—which co-sponsored the unusual meeting with its sister journal *Cell*—noted that he recently spoke with an unnamed "senior AIDS person" who branded talk about an AIDS-free world as "nonsense," "irresponsible," and "dangerous," warning that it might lead to complacency. "I agree completely, it's much too soon for a victory lap," said Anthony Fauci of the National Institute of Allergy and Infectious Diseases (NIAID) in Bethesda, Maryland, who noted that last year alone saw 2.3 million new HIV infections, raising the global burden to 35.3 million people. But an AIDS-free world is not an audacious notion, Fauci said. "We have a scientific and public health basis for in fact talking about this."

Meeting participants debated what, exactly, an "AIDS-free world" means. "Everyone is talking about the 'end of AIDs,' but everyone seems to have a different perspective," Steven Deeks, a clinician at the University of California, San Francisco, told *Science*. The U.S. government has championed a goal it calls the "AIDS-free generation," in which antiretroviral (ARV) drugs completely prevent transmission to babies and allow HIV-infected people to live near-normal lifespans. Others contend that only a vaccine can end the epidemic, but this elusive goal is "at least 10 years away," said Nobelist David Baltimore of the California Institute of Technology in Pasadena.

High hopes. Dramatic progress has sparked endgame talk.

SOURCES (TOP TO BOTTOM): O. THALMANN *ET AL.*, *SCIENCE*; ADAPTED FROM WAFAA EL-SADR/COLUMBIA UNIVERSITY

ARVs certainly have made extraordinary strides. Thanks to a massive infusion of funds, the number of HIV-infected people receiving the drugs in sub-Saharan Africa has skyrocketed from 50,000 in 2002 to more than 7 million last year. A landmark study funded by NIAID showed 2 years ago (*Science*, 23 December 2011, p. 1628) that the drugs can prevent as well as treat infection; when people take ARVs as prescribed, they suppress HIV

Published by AAAS

Far out. The Alpha Magnetic Spectrometer juts from the International Space Station.

CREDIT: NASA

PARTICLE PHYSICS

Hint of Dark Matter May Be Just Cosmic Ray Debris

Suppose you thought you glimpsed Bigfoot in your yard. You might be disappointed if somebody suggested you'd actually seen a bear. You'd feel doubly let down if the bear turned out to be your neighbor. That's how some physicists may feel about a new analysis of data from an ambitious space-based experiment that seemed to show hints of dark matter.

The data come from the Alpha Magnetic Spectrometer (AMS), a $2 billion detector on the International Space Station that snares particles from space called cosmic rays. In April, AMS confirmed an apparent increase in the ratio of antielectrons (positrons) to electrons at high energies (*Science*, 12 April, p. 135). Those positrons could come from particles of dark matter—the invisible stuff whose gravity binds the galaxies—annihilating one another. Or, skeptics countered, they could flow from some nearby pulsar, a spinning neutron star.

But not even a pulsar is needed because there are no extra positrons, argue Kfir Blum and Boaz Katz of the Institute for Advanced Study in Princeton, New Jersey, and Eli Waxman of the Weizmann Institute of Science in Rehovot, Israel. Instead, they say, the positrons are all "secondary" cosmic rays produced when primary cosmic rays, such as protons from exploding stars, smack into hydrogen and helium in space.

The theorists use measurements of other secondary cosmic rays such as boron nuclei to infer how many secondary positrons could be produced at a given energy. AMS never sees more than that number, they report in a paper in press at *Physical Review Letters*. The ratio of positrons to electrons only appears to increase at high energies, they argue, because the numbers of lower energy positrons dwindle as the particles lose energy swirling in magnetic fields and colliding with photons. The energy loss shifts them to energies lower than AMS measured.

That last point is tricky. At first glance, higher energy positrons ought to drain away more rapidly than low-energy ones. But, Waxman argues, higher energy positrons could survive if they escape the galaxy's disk and its magnetic fields and photons faster than they lose energy. Igor Moskalenko, a theorist at Stanford University in Palo Alto, California, says the assumption that high-energy positrons escape so quickly could mess up modeling of other aspects of cosmic rays. Waxman says he's not worried because current models "include lots of assumptions that are not justified."

AMS researchers stick to their claim that secondary positrons alone cannot explain their data, says Andrei Kounine, an AMS team member from the Massachusetts Institute of Technology in Cambridge. But Stéphane Coutu, a cosmic ray physicist at Pennsylvania State University, University Park, cheers the new analysis. "Much too much emphasis has been placed on the dark-matter interpretation, the sexy thing," he says. "What we need now are sober second looks such as this one."

–ADRIAN CHO

so powerfully that it becomes undetectable in blood, making heterosexual transmission rare. Studies have also proven that taking ARVs works as a preventive for uninfected people at high risk—a strategy known as pre-exposure prophylaxis (PrEP). Male circumcision curbs spread, too, as do needle exchange, opiate substitution, and other "harm reduction" efforts with injecting drug users.

Two people even seem to have been cured. The first, Timothy Brown of Las Vegas, Nevada, cleared his HIV infection only after dangerous bone marrow transplantations to combat his leukemia; now, a baby may have been cured simply by starting ARVs shortly after birth (*Science*, 8 March, p. 1134).

Yet the progress has stark limits. Deeks, who treats patients at San Francisco General Hospital, noted that "we don't see AIDS anymore but we see a new version of HIV infection." Even in people taking ARVs, low levels of HIV cause chronic inflammation that hastens morbidities from non-AIDS conditions like heart disease, kidney damage, and cancers, he said.

Although proven interventions exist, all too often they don't reach the people most in need or aren't used properly. For instance, World Health Organization recommendations call for starting 25.9 million people on ARVs, but the drugs are available to fewer than half that number—and no funds exist to expand treatment. Stigma and discrimination leads many locales to ignore "key affected populations" like injecting drug users, sex workers, and men who have sex with men. People who have access to ARVs often fail to "adhere" as directed; in the United States, fewer than 25% of infected people have undetectable viral levels, and the situation is bleaker still in some poor countries. When it comes to prevention, few uninfected people have benefited from PrEP because clinicians rarely offer it and neither drugmakers nor public health campaigns vigorously promote it.

Epidemiologist Wafaa El-Sadr said we can only "treat our way out of the epidemic" if communities do more to find all infected people and then help them take their daily pills. "I don't believe anyone in this room thinks there's a silver bullet," said El-Sadr, who is running a study in the Bronx to evaluate ways to improve ARV adherence.

The meeting did not aim to draft a manifesto with action points to promote an AIDS-free world, but it did end up with a general consensus that it's "an essential aspiration," as Myron Cohen of the University of North Carolina, Chapel Hill, put it. "The cancer field has race to the cure, run for the cure, crawl for the cure, limp to the cure—there is no metaphor that the cancer field has not used," Cohen noted. "I don't say this to make fun of the field. They understand what they're doing."

–JON COHEN

Published by AAAS

GENOMICS

Initiative Aims to Minister To Mexico's Unique Genetic Heritage

MEXICO CITY—When Hernán Cortés landed on Mexico's eastern coast in 1519, he brought more than a conquering army that would soon topple the Aztec empire. He and his men also brought their genomes. In the 50,000 years or so since the European and Amerindian populations had last been in contact, their genomes had diverged in small but significant ways. A mutation here, a difference in selection pressure there, and inexorably some genetic variations became prevalent in one population and all but absent in the other. When Cortés married his indigenous translator La Malinche, their union—and many others like it—set the divergent genomes on a collision course.

Five hundred years later, the average Mexican genome contains a mixture of European, Amerindian, and African ancestry. The quest to understand the consequences of that heritage got a boost last month, when telecommunications billionaire Carlos Slim Helú announced a plan to plow $74 million into the Slim Initiative for Genomic Medicine in the Americas (SIGMA), which aims to develop diagnostic tools and medicines for diseases, including breast cancer and type 2 diabetes, that are especially prevalent in the Mexican population.

Until recently, large-scale human genome sequencing initiatives focused almost exclusively on populations of European ancestry, says Eric Lander, a geneticist and director of the Broad Institute in Cambridge, Massachusetts, which is teaming up on SIGMA with the Carlos Slim Health Institute here. That European bias makes genomic findings less relevant for people of other backgrounds. Most gene variations, or alleles, are present in all human populations, Lander explains, but their frequencies "differ a lot." What scientists learn from studying the genome of one population "may or may not apply [to] individuals of other ancestries," says Bogdan Pasaniuc, a population geneticist at the University of California, Los Angeles.

As a case in point, a study published online this week in *Nature Medicine* found that the platelets of African Americans form blood clots faster than those of white Americans when exposed to a particular clotting agent. This difference may mean that blood-thinning medications designed with the European genome in mind are not as effective for African Americans. Similar issues could be plaguing Latin Americans, leaving them underserved by the technologies that are supposed to be revolutionizing health care, says epidemiologist Miguel Betancourt, global solutions director at the Slim institute. In medicine, he says, "genomics is the language of the future." Without a comprehensive understanding of the Latin American genome and its specific risk factors, he says, Mexicans will be left behind.

That didn't sit right with Slim, whose 2013 net worth of $67.1 billion ranked him as the second richest person in the world. In 2010, his foundation provided $65 million for SIGMA's first stage, during which scientists from Mexican universities and government institutes like the National Institute of Genomic Medicine (INMEGEN) here worked with Broad to comb through the Mexican genome for disease-related alleles. The search paid off: By sequencing tumors from Mexican patients, SIGMA-funded researchers found several new genes implicated in breast cancer. They also identified new mutations associated with head and neck cancer, and brought a decadelong struggle to a satisfying conclusion by pinpointing the genetic risk factor for the devastating kidney disease MCKD1. And perhaps most significant for Mexico, the country with the world's highest rate of adult diabetes (see graph), SIGMA researchers recently uncovered the first genetic risk factor for type 2 diabetes that appears to be specific to Latin American populations. The paper detailing the variant, called SLC 16 A11, is in press at *Nature*.

The Slim institute hopes to move fast to translate these basic discoveries into clinical tools, Betancourt says: "We are very impatient here." During SIGMA's second phase, which will last until 2016, Broad will take the lead on developing drugs that target the newly identified disease pathways, while Mexican partners work on new diagnostic tools for Latin American populations. "Everyone that shares the Amerindian genome will benefit" from SIGMA, Betancourt predicts.

Genomics experts hail the effort. "I have no question the goals [of SIGMA] will be achieved," says former INMEGEN director Gerardo Jiménez, a professor of public health at Harvard University. But translating genomics insights into useful tools and practices will take much longer than the program's 3-year second phase, Jiménez says, "especially in an economy like Mexico's," in which more than half the population lives in poverty.

Socioeconomic realities also mean that Mexican scientists must "aim for the lowest possible cost" by simplifying diagnostics and treatments or by focusing on technologies that don't require refrigeration or electricity, INMEGEN director-general Xavier Soberón says. "We cannot just copy" techniques that work in other countries. Only by taking into account Mexico's present reality will scientists be able to develop tools to help the descendents of Cortés and La Malinche reckon with the history written in their genomes. **–LIZZIE WADE**

Family tree. The typical Mexican genome contains a mixture of European and Amerindian ancestry, represented by the family in this 1770 painting.

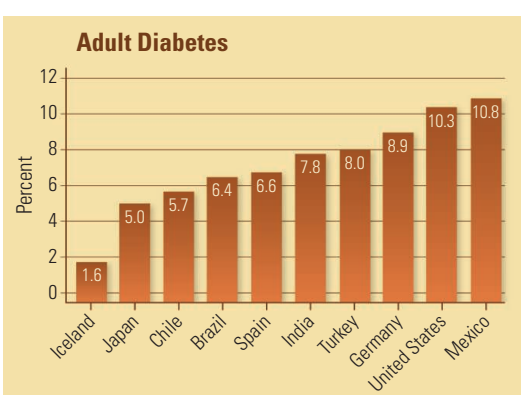

At risk. An allele discovered by SIGMA researchers may help explain why Mexico has the world's highest prevalence of adult diabetes (2010 data).

Published by AAAS

CREDIT: © IMAGEBROKER/ALAMY

Getting a grip. A study is testing whether rapamycin improves physical and mental deficits of aging.

BIOMEDICINE

A Putative Antiaging Drug Takes a Step From Mice to Men

Five years ago, rapamycin was an obscure drug with an exotic pedigree. Isolated from bacteria that live on Rapa Nui, aka Easter Island, it was used to suppress the immune system in transplant recipients and to treat some cancers. Now, rapamycin is at the center of a high-profile debate over whether it combats aging.

A 2009 finding in mice had shown that the drug increases lifespan and might delay aging, but a study earlier this year downplayed the antiaging effect. A new analysis, published online this week in *Science Translational Medicine*, defends the original claim, and the drug is being tested in a small clinical trial that may yield the first hints of whether it can slow aging in people.

In the 2009 study that put rapamycin in the news, a team that included biogerontologist Richard Miller of the University of Michigan, Ann Arbor, and geneticist David Harrison of the Jackson Laboratory in Bar Harbor, Maine, reported that the drug boosted the longevity of mice by 9% to 14%. It was the first sign that any drug could increase lifespan in a mammal (*Science*, 18 December 2009, p. 1600). In a follow-up mouse study last year, Miller, Harrison, and colleagues found that rapamycin slows tendon stiffening and liver deterioration, two markers of aging. This year, another group described benefits for heart function in older mice.

But a comprehensive cognitive and physical analysis of treated mice "is the only way to test whether some of these interventions truly affect aging," argues neuroscientist Dan Ehninger of the German Center for Neurodegenerative Diseases in Bonn. He and his colleagues measured rapamycin's power against 150 age-related changes, and the results, out in August, were disappointing for many fans of the drug. The team reported in *The Journal of Clinical Investigation* that the drug did not forestall typical age-related deficits, such as lower grip strength, reduced visual acuity, and dulled sensitivity to pain.

Rapamycin did appear to help grizzled mice in some ways, boosting their memory and their willingness to explore, for example. The team also dosed young mice, however, and found that rapamycin affected them in the same way, leading the researchers to conclude that most of the drug's benefits do not stem from slowed aging. As for why the mice live longer than normal, Ehninger and his colleagues surmise that the drug inhibits cancer through an aging-independent mechanism.

Other researchers praise the study's breadth but dispute the team's conclusions. Harrison disagrees that an antiaging effect is ruled out if rapamycin influences young and old animals similarly. "That's a misconception," he says, noting that researchers agree that calorie restriction can slow aging—yet its metabolic effects are identical in young and old animals. And in *Science Translational Medicine*, molecular biologist Matt Kaeberlein of the University of Washington, Seattle, faults the argument that rapamycin increases lifespan through cancer prevention. He and his colleagues argue that the German team didn't show that tumors killed the mice. "The only conclusion you can draw is that rapamycin has effects on at least some [healthy lifespan] measures in mice," Kaeberlein says.

Does that justify testing rapamycin in healthy people? Some researchers say no. Rapamycin leads to insulin resistance—a precursor of diabetes—in mice and humans, and transplant recipients have developed diabetes. "I'd be very hesitant to be a participant" in a clinical trial, Miller says.

But much of what scientists know about rapamycin's side effects comes from transplant patients, who typically are ill and taking several other drugs. "We don't have a huge body of evidence on its effects in a healthy older adult," says molecular biologist Toren Finkel of the National Heart, Lung, and Blood Institute in Bethesda, Maryland.

The clinical trial, run by cardiovascular physiologist and clinician Dean Kellogg of the University of Texas Health Science Center, San Antonio, and colleagues, might yield some clues. For 16 weeks, five men in their late 80s and 90s took half the dose of rapamycin that a kidney transplant patient would receive. A similar number served as the control group. The only side effect so far has been diarrhea in one of the subjects, Kellogg notes. "I've been pleasantly surprised at how innocuous this drug has been," he says.

Although the trial is continuing, the researchers have seen preliminary signs of benefits, they reported at a conference in Italy this year. Grip strength didn't improve after a course of rapamycin, but walking ability did. Beforehand, the youngest man in the experimental group, now 89, needed 17 to 18 seconds to walk 12 meters. After taking rapamycin, his time dropped to 7 to 8 seconds, Kellogg says. The men receiving rapamycin also responded more strongly to the hepatitis B vaccine than did the controls.

Kellogg believes rapamycin will eventually be used "to slow aging in geriatric patients." But molecular biologist Brian Kennedy of the Buck Institute for Research on Aging in Novato, California, says its role might be to guide researchers to safer drugs that interact with the same molecular target: a protein known as TOR, which helps coordinate nutrition, growth, and aging. One way or another, Kennedy predicts, "we will find things that have an effect on aging without the serious side effects."

–MITCH LESLIE

The Man Who Bottled Evolution

Richard Lenski's 25-year experiment in bacterial evolution shows no signs of running out of surprises about how mutation and selection shape living things

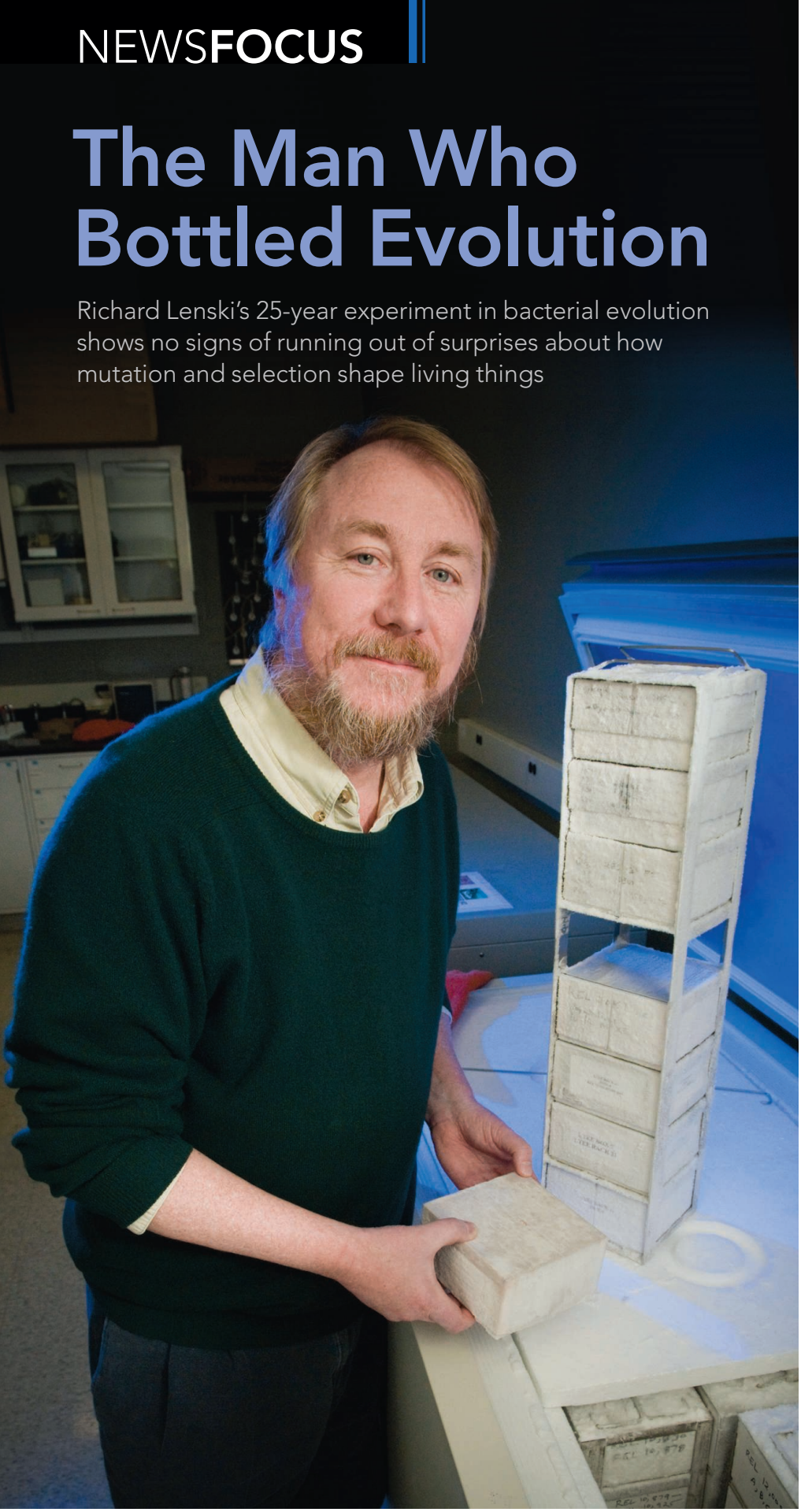

Time traveler. To turn back evolution's clock, Richard Lenski dips into his freezer.

CREDIT: G. L. KOHUTH/MICHIGAN STATE UNIVERSITY (2009)

EAST LANSING, MICHIGAN—When most biologists want to understand how evolution unfolds, they look for clues in the fossil record or the natural world. Richard Lenski simply walks across his Michigan State University lab to his freezers. There, stored in 4000 vials, are bacteria dating back to 1988. That was the year Lenski started a simple but radical experiment. He put samples of *Escherichia coli* into a sugar solution, stoppered the flasks, and waited to see what would happen. It was a study with no defined endpoint, so risky that he didn't try very hard to get outside funding for it.

After 25 years and 58,000 bacterial generations, Lenski's bacteria are still growing, mutating, and evolving. They are proving as critical to understanding the workings of evolution as classic paleontology studies such as Stephen Jay Gould's research on the pace of change in mollusks. Lenski's humble *E. coli* have shown, among other things, how multiple small mutations can prepare the ground for a major change; how new species can arise and diverge; and that Gould was mistaken when he claimed that, given a second chance, evolution would likely take a completely different course. Most recently, the colonies have demonstrated that, contrary to what many biologists thought, evolution never comes to a stop, even in an unchanging environment. The work is "an absolutely magnificent achievement," says Douglas Futuyma, an evolutionary biologist at Stony Brook University in New York.

Other researchers have done experimental evolution, setting up populations of insects, yeast, and even fish in the lab and in controlled field conditions, and subjecting the organisms to a particular environmental stress for relatively short periods. But Lenski's long-term experiment "is just orders of magnitude beyond what anyone else has done," Futuyma says.

The project's quarter-century has witnessed the rise of bioinformatics and the birth of whole-genome sequencing, and Lenski has taken advantage of both technologies to glean new insights. Generations of students have tended and analyzed the microbes, and the project sparked a memorable conflict between Lenski and creationists. Fifteen years ago, he almost abandoned it for digital models of evolution, then reconsidered—and was vindicated when his bacteria took one of their most dramatic evolutionary leaps. As

Scott Edwards, an evolutionary biologist at Harvard University, said at a June evolution meeting,* "the principles of evolution that Rich has uncovered have touched all of us and caused us to look at evolution in a new way."

Hard data

Lenski, 57, has been a MacArthur Fellow, a member of several editorial boards, and a society president; he belongs to the National Academy of Sciences and served on committees that evaluated genetically modified organisms and the investigation of the 2001 anthrax attacks. In August, he became an avid tweeter and started his own blog, Telliamed Revisited, named after an 18th century book that stressed the importance of understanding the world through observations and not religious dogma. He has collected old scientific texts and baseball statistics, although these days, he says, "my granddaughter is my current hobby."

But one thing will always capture his attention. Show up at his door with new data, and he's "like a 5-year-old at Christmas," says graduate student Michael Wiser. That hunger for hard data about evolution was what drew him to bacteria in the first place. Lenski never had a course in microbiology. As a graduate student at the University of North Carolina, Chapel Hill, he studied the ecology of ground beetles—work he found interesting but limited. "[I]t was difficult to imagine feasible experiments that would really test the scientific ideas that most excited me," he wrote in an August blog. For his postdoctoral training in 1982, he switched gears and joined the lab of Bruce Levin, one of the few researchers doing experimental evolution in microbes. They studied the interactions between bacteria and viruses called bacteriophages. But their systems were still too complex to get at the question Lenski most wanted to answer: Was Gould right about evolution's irreproducible nature, or would evolution often repeat itself if given a second chance?

So after starting his own lab at the University of California, Irvine, Lenski used some of his own money, from a National Science Foundation (NSF) Presidential Young Investigator Award, to set up a much simpler system using just bacteria. It was "like a physics experiment [where] you try to strip [out] all the complications so you can isolate the phenomenon that you want to describe," explains Lenski postdoc Noah Ribeck, a physicist.

In 1988, Lenski placed identical *E. coli* populations into 12 flasks filled with a liquid containing nutrients and 25 milligrams of glucose per liter. Every 24 hours, with constant stirring and a comfortable 37°C environment, the bacteria multiplied explosively, depleting the sugar. Each day, 1% of the bacteria were transferred to a new glucose-laden flask. Every 75 days—about 500 generations for *E. coli*—Lenski's team froze some of the bacteria for future studies and as backups should the experiment become contaminated. This protocol has continued day in and day out, weekends and holidays, virtually uninterrupted for 25 years. (The cultures were temporarily frozen during one winter break when the campus was deserted and when Lenski moved his lab from California to Michigan.)

Online
sciencemag.org
Podcast interview with Richard Lenski (http://scim.ag/pod_6160a).

Setting up the protocol and sticking with it "took a certain spirit and vision," Levin says. Early on, skeptics argued that evolution in bacteria, particularly bacteria growing in a stable, comfortable environment, wouldn't reveal much about how the process unfolds in nature. Yet, as they monitored their cultures, Lenski and his colleagues saw what looked very much like an accelerated process of evolutionary change. By using bacteria instead of a slower-growing organism, Lenski compressed time: The *E. coli* go through 6.6 generations in a day, compared with more than a year for the same number of generations in mice. In 25 years, he's seen the equivalent of a million years of evolution in humans. With that span, "you can examine a whole range of ideas that there hasn't been an opportunity to look at before," says Graham Bell, an evolutionary biologist at McGill University in Montreal, Canada.

By thawing out frozen vials from generations past, Lenski can go back in time to look at intermediate stages of evolutionary change. "It's like the perfect fossil record," says Douglas Emlen, an evolutionary biologist at the University of Montana in Missoula. "They can pinpoint exactly when [a trait] arose." And Lenski can restart the experiment with those ancestral bacteria to see if history repeats itself. "A graduate student who is 22 today can study populations that come from before they were born and use techniques that haven't existed before," says Christopher Marx, a microbiologist at Harvard University and a former Lenski postdoc.

For the first decade, things hummed along. The investigators monitored the bacteria's fitness by measuring how fast they could multiply relative to their ancestors. At first, their fitness rapidly increased, but then the improvement slowed. Over the whole experiment to date, fitness has improved by an average of 70%—meaning the most recent

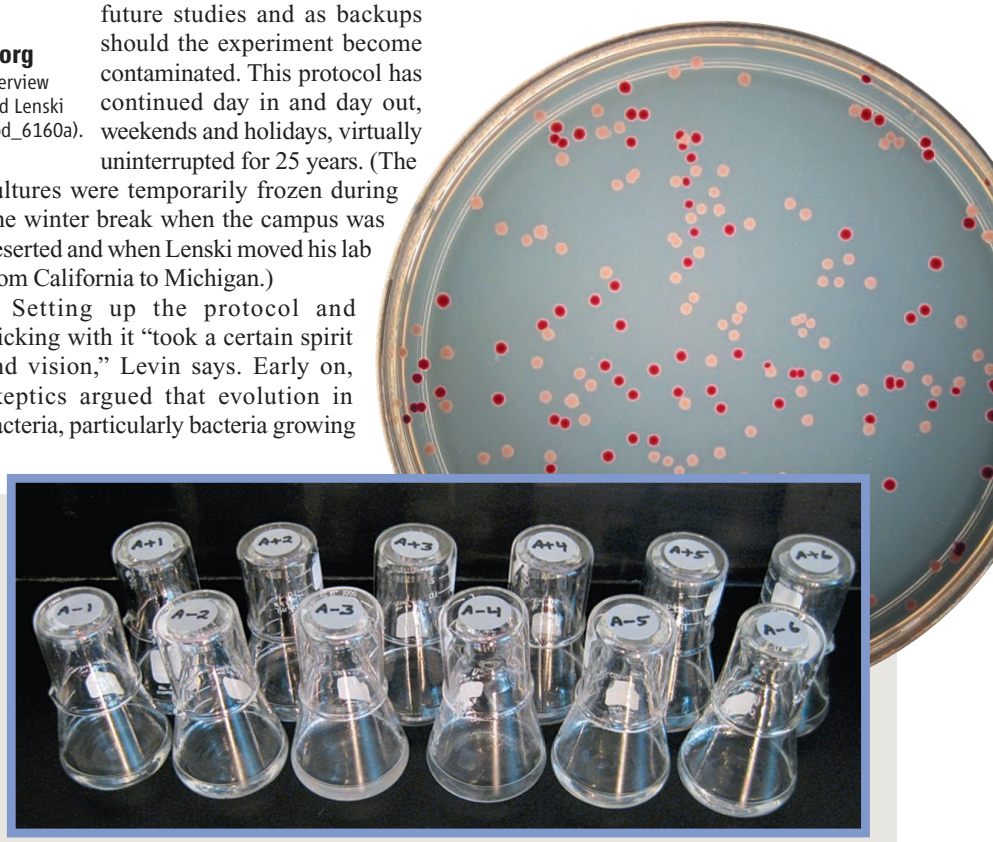

Evolution on display. A mutation led to a population boom in one of 12 cultures, turning the medium turbid (third flask from left). Investigators can compare two strains' fitness by culturing them together and then counting colonies (petri dish). One strain carries a mutation that makes its colonies red.

CREDITS: BRIAN BAER AND NEERJA HAJELA/MSU (2)

*Evolution 2013, Snowbird, Utah, 21 to 25 June.

Published by AAAS

descendants undergo 1.7 doublings in the time it took the original microbes to double once.

All 12 lines improved by about the same amount, showing that, broadly speaking, evolution is reproducible (*Science*, 25 June 1999, p. 2108). But some lines improved faster than others, and genetic analyses of the strains showed that they had taken different evolutionary paths. For example, six lines developed defects in DNA repair, and instead of dying out, began sustaining higher mutation rates than their counterparts. "Historically, which mutations arise early changes the subsequent evolution," explains Janette Boughman, an evolutionary biologist at Michigan State University. "But you really get to the same endpoint": better fitness in sugar solutions.

Other striking differences emerged among the flasks. At generation 6500, about 3 years into the experiment, two types of *E. coli* evolved in one of the flasks: one that made small colonies consisting of relatively small cells and one that made large colonies, with large cells. Lenski expected that eventually one type would take over and the other would disappear, or both would be ousted by a bacterium with an even more beneficial mutation. But to his surprise, both types have persisted, creating an ecosystem in which competition and other interactions between the colony types allowed both to be viable. "He created his own Galápagos Islands," Marx says.

Going digital

Having done so, Lenski almost gave up on the flask experiment. He had caught a glimpse of an experimental evolution system that promised to be even simpler and faster. "He's a shiny object researcher," says former student Paul Turner, now an evolutionary biologist at Yale University. "If there's something interesting to pursue, he will try to pursue it." During a squash game, a physics colleague invited Lenski to a seminar by California Institute of Technology physicist Christoph Adami. With his graduate student Charles Ofria, Adami had developed software that allowed self-replicating computer programs, aka digital organisms, to compete with one another for processing power and evolve new functions. Lenski was entranced. "One of the first data slides [Adami] put up looked like data from my long-term experiment," he recalls.

In 1998, Adami sent Lenski an advance copy of his book *Introduction to Artificial Life* (*Science*, 8 May 1998, p. 849). Lenski stayed up for 2 nights straight reading about the program and trying out simulations he had designed himself. The digital organisms replicated thousands of times faster than his microbes, and their "mutations" could be tracked in more detail. For the next 6 years, he focused as much on digital evolution as on bacteria.

In 2003, he teamed up with Ofria and Adami, both of whom are now at Michigan State, and with Robert T. Pennock, a philosopher there, to follow mutation by mutation how computer programs that initially could do no more than replicate evolved the ability to perform complex operations, such as checking whether one numerical string equals another. They found that many earlier mutations—some of them deleterious in the short term—had to accumulate before a final "enabling" mutation conferred the new trait. The work demonstrated that complex traits, such as the vertebrate eye, likely come about through a series of intermediate steps that open the way for future adaptation.

Lenski's fascination with digital life hasn't faded. In 2010, he, Ofria, and others got funding for BEACON, an NSF Center for the Study of Evolution in Action, which includes 400 investigators and students from five U.S. universities. They collaborate on studies of evolution as it occurs in both real and digital organisms.

Fortunately, he did not abandon his first love. The weekend that Lenski discovered digital organisms, he had told his wife he might shut down the long-term experiment. Only her nudging convinced him to keep it going—and in January 2003, the value of doing so became clear, when the bacteria served up yet another surprise. "Digital organisms have the advantage that you can get complete information about pretty much all aspects of an experiment," Lenski explains. "The bacteria, though, are a lot more complex and so they have a lot more

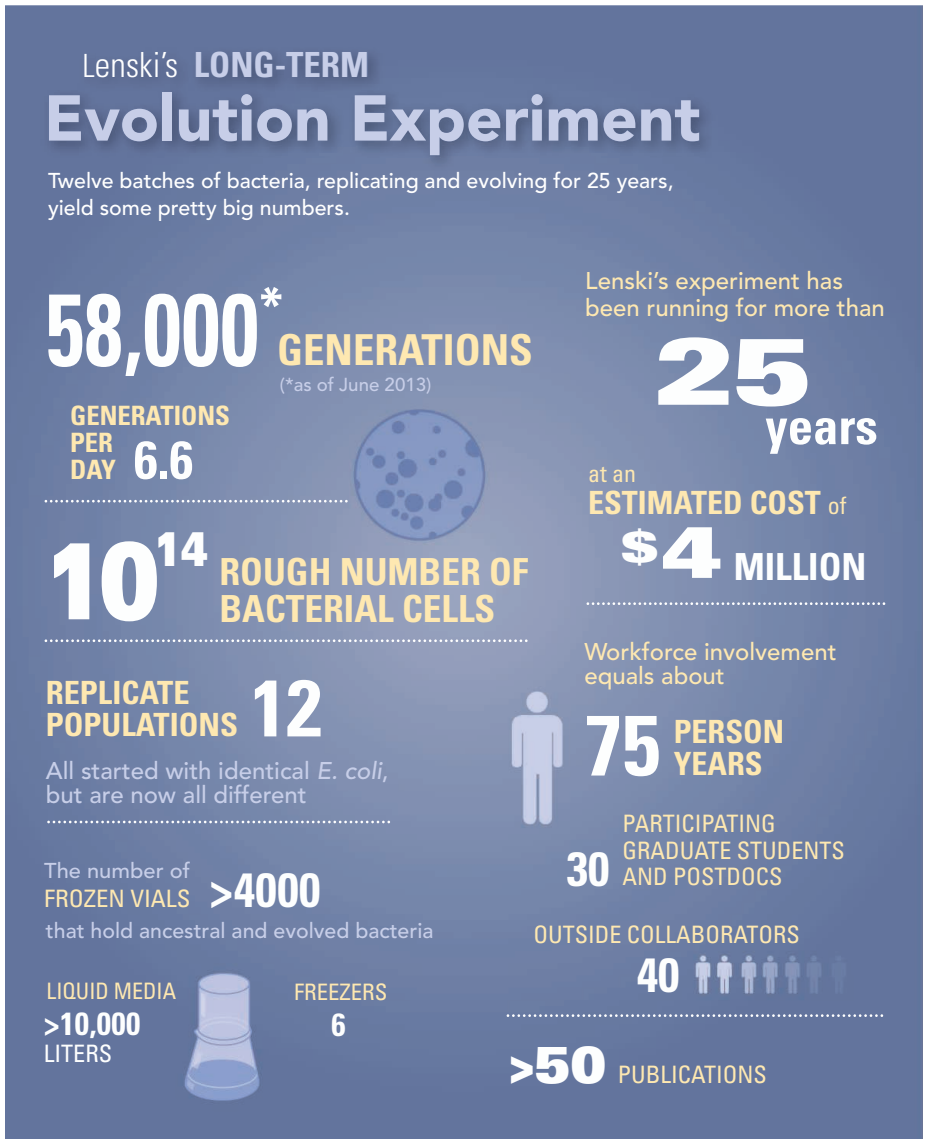

DATA SOURCE: R. LENSKI

Published by AAAS

tricks up their sleeves, a lot more potential to evolve in ways that one cannot anticipate."

One morning, Lenski and his colleagues noticed that the medium in one flask had grown turbid, a sign that it was unusually thick with bacteria. They suspected contamination but could not confirm it, so they dug out the most recent frozen sample of Ara-3, as that population was called, and restarted it. Three weeks later, the turbidity reappeared. This time, they thoroughly tested the culture and ruled out contamination. By growing the Ara-3 bacteria on different types of media, they discovered that the bacteria in that flask had evolved a new way to nourish themselves. Instead of relying on scarce glucose, they drew on a different energy source in their medium, citrate, which enabled them to reach much higher densities than in other flasks. "This was the biggest event in the entire *E. coli* experiment," Adami says. "To have a complex new function develop seemingly from scratch is a big deal and quite remarkable."

It fell to graduate student Zachary Blount to figure out what happened. Was a single mutation responsible? And if so, why hadn't this ability appeared earlier, since the bacteria had already had plenty of time to experience mutations in every possible gene? Or were multiple mutations required, and if so, when and in what order did they arise? To find answers, Blount rewound the tape of life, unfreezing earlier generations and letting them evolve again in the same medium. Citrate use emerged in four of 72 cultures, always in ones derived from more recently frozen samples. That suggested that multiple mutations underlie the trait. Populations from those later generations had already acquired the predisposing mutations and so could more readily take the next step.

Blount and Lenski's results, published in 2008, drew lots of attention, and not just from the media and scientific community. On his website, Conservapedia, conservative Christian Andrew Schlafly questioned the conclusion that the bacteria had evolved this striking new ability and requested Lenski's original data. Lenski referred him to the original paper, but Schlafly persisted. Lenski responded with a sharply worded response that went viral. "He immediately became a rock star of science," Adami says.

Meanwhile, the citrate work continued. The cost of sequencing microbial genomes dropped dramatically, enabling Blount to look at the specific genetic changes involved. He found that citrate users had undergone a duplication of a 2933-base piece of DNA that activated an otherwise silent gene coding for a citrate transporter. Subsequent genetic changes then tuned up the efficiency of that transporter, he and Lenski reported in 2012.

Pileup. Zachary Blount used all these petri dishes to study how one flask of bacteria evolved the ability to consume citrate.

CREDIT: BRIAN BAER/MSU

These citrate users are enabling Blount, now a postdoc in the lab, and Lenski to look at another aspect of evolution: the formation of new species. The usual test of separate species is that they are unable to interbreed successfully, a criterion that can't be applied to bacteria because they don't mate. But because one of *E. coli*'s defining characteristics is the inability to use citrate for energy in the presence of oxygen, the citrate-consuming bacteria could be seen as a new species. And they may even meet the traditional definition. Researchers can't interbreed bacteria, but they can mix the genomes of separate strains. Bacteria that thrive on citrate do poorly on glucose, and melding the citrate users with the parent strain produces a less fit hybrid, Lenski reported at the June evolution meeting.

Evolving endlessly

Lenski no longer thinks about ending his experiment. "It's become more and more apparent that it's not good to just do short-term experiments," he says. "Any microbiology lab with enough people should be thinking about doing a 20-year experiment." Funders agree. The project, once rejected by the National Institutes of Health, now has ongoing NSF support: a 10-year Long Term Research in Environmental Biology grant.

And it is continuing to pay off, Lenski, Wiser, Ribeck, and their colleagues report online this week in *Science* (http://scim.ag/MWiser). Researchers have long assumed that when organisms encounter a new environment, they will adapt very quickly at first, then, as long as conditions are stable, ultimately reach an adapted state. At that point—a "fitness peak"—adaptive evolution should virtually stop. Wiser tested the fitness of all 12 populations at 41 time points during their evolution, traveling back in time with the frozen samples. At 10,000 generations—about 5 years—it seemed the bacteria were reaching that fitness peak. But now, after 50,000 generations, the improvement has slowed down but not leveled off as expected, Lenski's team reports. "The notion of a fitness peak is more elusive than I anticipated," Lenski says. "I think fitness may well continue to increase for a million years." Evolution is endless, it seems, even in a stable environment. "That's a profound insight," Boughman says.

It's also an encouraging portent for the future of Lenski's cultures, which are now passing 58,500 generations. "If you asked me 20 years ago, I thought [the researchers] were running out of new things to learn," Levin says. Now, "I think they should go on indefinitely." Lenski agrees. During his presidential address at the recent evolution meeting, he made a plea: "If you know anyone who would like to endow a million-year experiment, have them get in touch with me." **–ELIZABETH PENNISI**

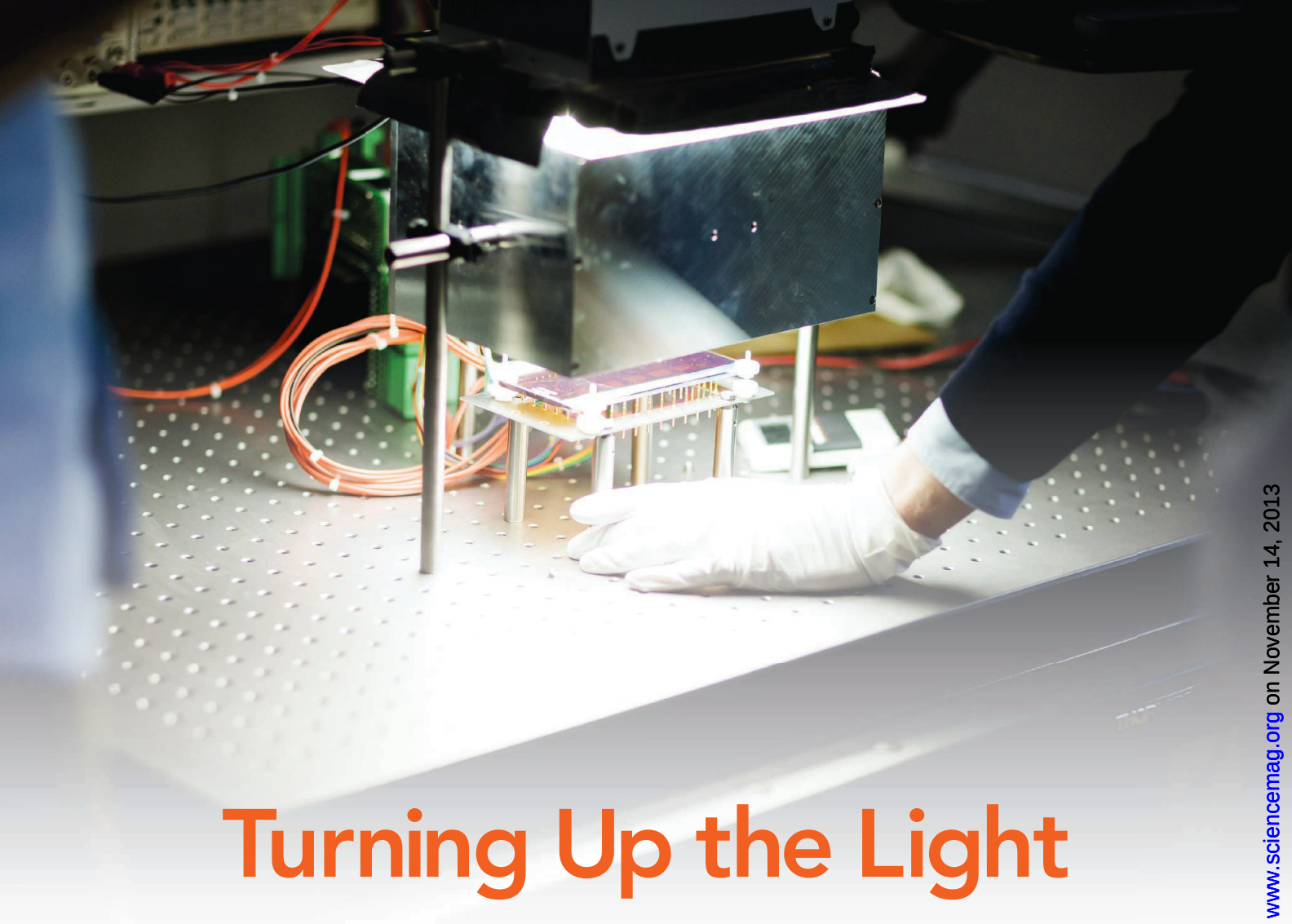

CREDIT: DOUGLAS FRY

Turning Up the Light

Photovoltaic materials called perovskites work wonders in the lab, but will they shine as commercial technology?

Plot the progress of different types of solar cells, and one line stands out. For decades, almost all solar technologies—such as panels made with wafers of crystalline silicon or thin films of cadmium telluride—have made slow, steady progress. A technology that converts 14% of the energy in sunlight to electricity nudges up to 14.1% 2 years later, and so on.

But a new contender, solar cells built with complex crystalline materials called perovskites, is leaping ahead. It tiptoed onto the scene in 2009 with cells that were 3.8% efficient—a ho-hum result when top silicon cells in labs were notching 25%. By the end of 2011, however, that efficiency had nearly doubled to 6.5%. Last year, it climbed to 10%. In 2013, the new cells have hit 15%, surpassing some alternatives that have had decades to mature. "It's amazing," says David Cahen, a materials scientist at the Weizmann Institute of Science in Rehovot, Israel. "We have never seen anything like this in the solar cell community."

The news gets better. Perovskites are made from readily available materials. Unlike some kinds of solar cells, they're cheap and easy to produce. Experts think they have plenty of room for improvement and that their efficiencies could top 20% within the next year. And perhaps best of all, perovskite solar cells have the potential to be integrated with silicon panels, creating tandem cells with efficiencies of 30% or more. "There is a wave of excitement, and it's spreading," says Michael McGehee, a materials scientist at Stanford University in California.

Perovskite cells are a long way from a commercial debut: So far, most are no bigger than a postage stamp, produce just milliamps of electricity, and dissolve on exposure to air. The best of them also contain lead, an environmental toxin. But researchers are scrambling to surmount these challenges. To date, only a couple of dozen papers on the new cells have been published, most by a handful of groups. But that's likely to change quickly. "People are pouring into [the field]," McGehee says. From his extensive contacts in the area, McGehee estimates that more than 100 groups around the world are now working on perovskites.

"It's very competitive," says Michael Grätzel, a chemist at the Swiss Federal Institute of Technology in Lausanne, Switzerland. "The battle is on. One has to move very quickly." Yang Yang, a solar cell expert at the University of California, Los Angeles, agrees. "I don't have enough time to sleep," Yang says.

The right mix

Perovskites have been under the noses of solar cell makers for more than a century. A Russian mineralogist discovered the first,

natural version in 1839. Today, hundreds are known. The category simply refers to materials that adopt the same type of crystal structure with atoms arranged in octahedra that are connected at the corners in all three spatial directions. The solar cell perovskites are semiconductors. But other family members run the gamut from conductors to insulators, the most famous being the high-temperature copper oxide superconductors that burst onto the scene in 1986.

In the 1990s, David Mitzi, a physicist at IBM's Thomas J. Watson Research Center in Yorktown Heights, New York, made thin-film transistors and light-emitting diodes from a semiconducting perovskite. The devices worked. But even though many light-emitting materials also make good light absorbers—and thus potentially good photovoltaics—Mitzi decided his perovskites were too unstable for use in solar cells, which must survive decades to be commercially viable.

Nearly a decade later, Tsutomu Miyasaka took a first step toward solving that problem. Miyasaka, a chemist at Toin University of Yokohama in Japan, and colleagues were working on photovoltaics called dye-sensitized solar cells (DSSCs). Unlike conventional silicon solar cells, DSSCs consist of a blend of organic light-absorbing dyes coating tiny inorganic particles such as titanium dioxide (TiO_2), which in turn are surrounded by a charge-conducting electrolyte. In standard DSSCs, when a dye molecule absorbs a photon, the light boosts the energy of one of the electrons in the dye, enabling it to jump onto a TiO_2 particle. From there, it skips from particle to particle until it reaches an electrode, where it's collected and sent through a circuit to do work. Meanwhile, another electron jumps from the electrolyte to the dye to restore it to its original state.

The trouble, says Grätzel, whose team invented DSSCs in 1991, is that the dyes don't absorb all the light that hits them, reducing the cells' efficiency. Hoping to do better, Miyasaka turned to a perovskite. He says that it took one of his students 2 years to find a recipe to make the material sturdy enough for a brief demonstration. In the 6 May 2009 issue of the *Journal of the American Chemical Society*, they reported building cells that, in place of the dye, contained a thin layer of a light-absorbing perovskite and were 3.8% efficient. Unfortunately, the cells also contained a liquid electrolyte that dissolved the perovskite within minutes, causing them to fail.

Grätzel took the next step, with Nam-Gyu Park and colleagues at Sungkyunkwan University in Suwon, Korea. On 21 August 2012 in *Scientific Reports*, they reported that they had replaced the liquid electrolyte in a perovskite-containing cell with a solid version and achieved efficiency close to 10%. Now things were starting to get interesting.

Grätzel then looked for better ways to grow the perovskites. Previously, his group and others had mixed precursor compounds in a solvent and heated it to drive off the solvent and crystallize the perovskite. But the approach produced perovskite layers that widely varied in thickness. Hoping to control the process better, they came up with a two-step recipe using two different solvents. In the 18 July issue of *Nature*, they reported that the process yielded more even coatings for their TiO_2 and an efficiency of 15%.

Meanwhile, at the University of Oxford in the United Kingdom, Henry Snaith, one of Grätzel's former postdoctoral assistants, took the next step toward all-perovskite cells. Snaith's team wondered whether the TiO_2 played a crucial role in the solid-electrolyte cells. They tried replacing the semiconducting TiO_2 with a porous insulating material made from aluminum oxide (Al_2O_3), thinking that removing the semiconductor would kill the performance of their cells. Instead, the cells worked better than before.

The researchers realized that the perovskite was acting not only as a light absorber, but as a charge-carrying semiconductor as well. In that case, they reasoned, why bother with TiO_2 or Al_2O_3? In the 19 September issue of *Nature*, Snaith and his colleagues reported that they simply grew a thin film of their perovskite, with a couple of additional layers sandwiched around it to help ferry charges to the electrodes, and matched the Grätzel team's efficiency of 15%.

The progress has been so rapid that Snaith says, "I think it could be feasible to get physically addicted to breakthrough results."

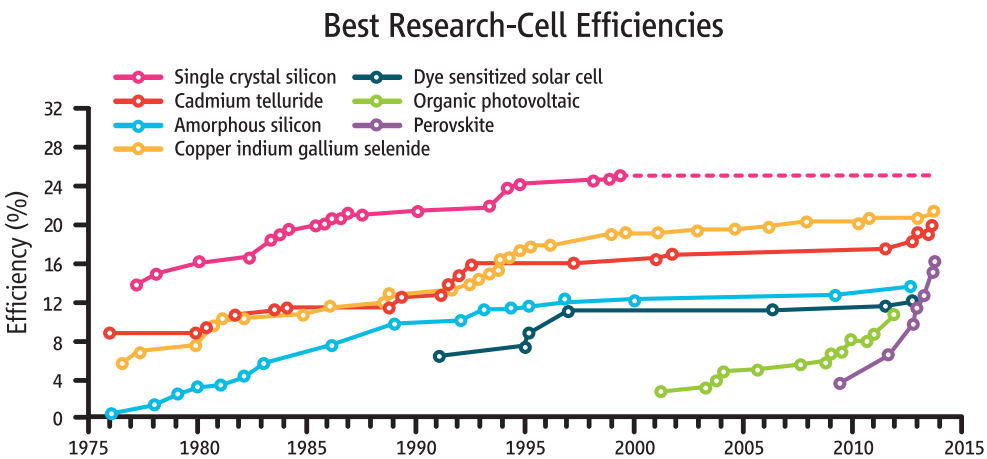

Rapid rise. The efficiency with which perovskite solar cells convert the energy in sunlight to electricity (purple) has soared faster in recent years than any competing solar technology.

CREDIT: CHART ADAPTED FROM P. NAYAK/WEIZMANN INSTITUTE; G. GRULLÓN/*SCIENCE*

Online

sciencemag.org

Podcast interview with author Robert F. Service (http://scim.ag/pod_6160).

Better and better

So why are perovskite solar cells surging ahead when other technologies have been struggling to break 12%? A good part of the answer, Cahen says, is that the perovskites have near-perfect crystallinity. That's a trait shared by today's top solar cell materials, including gallium arsenide and crystalline silicon.

In second-tier cell materials, this crystalline arrangement is typically riddled with defects. When electric charges whizzing through the crystal run into those defects, they stop cold and often give up their excess energy. Growing defect-free crystals normally requires ultrahigh temperatures or multimillion-dollar machines, such as molecular beam epitaxy. But perovskites can be grown at 80°C and simply precipitate out of solution in near-perfect form. "It's a little bit of a dream come true," Cahen says.

In the 18 October issue of *Science*, separate teams that included Snaith and Grätzel reported a consequence of that perfection: Perovskites are excellent at allowing excited electric charges to travel

Published by AAAS

long distances through the material. That property, known as the carrier diffusion length, is critical for all solar cells. It measures how far an electron might travel before it meets up with a positively charged electron vacancy, or hole, and drops into it. In the process, the electron gives up the excess energy that it got from the photon of sunlight, generating heat instead of electricity.

Organic solar cells typically have a diffusion length of about 10 nanometers. In perovskites, by contrast, carriers can travel as much as a micrometer, 100 times as far. "The upshot is, you can collect charges over longer distances," Grätzel says—thus making it more likely that the charges will wind up as useful current.

Perovskites have another highly valued property that boils down to how effective they are at generating an electric voltage. In crystalline silicon solar cells, for example, it takes photons with energies of at least 1.1 electron volts (eV) to kick an electron out of the tight grip of a silicon atom and become freely conducting. By the time those electrons reach an electrode and are dumped into a circuit, their voltage drops to 0.7 (eV), a loss of just 0.4 eV—part of the reason silicon is so commercially successful. For traditional DSSCs and organic solar cells, these losses usually amount to 0.7 to 0.8 eV. Perovskites, however, match the commercial champs with losses of only 0.4 eV. The new solar cells also do a decent job on a third solar cell metric, known as the fill factor, which measures how much power a solar cell produces relative to its theoretical maximum.

"For perovskites, these three parameters are all very good," Yang says. "It's just what we want." Yang's group has spent much of the past 10 years pioneering work on organic solar cells to raise their performance close to 11%. But since they've started tinkering with perovskites, "we've achieved about 13% in 5 months," Yang says.

Such overnight successes have made researchers confident that they can do even better. Grätzel notes that top-flight solar cells have a fill factor of about 80%, out of a theoretical maximum of 90%. But most perovskite cells today are between 60% and 70%. Likewise, early results suggest there is room for improving the amount of current the cells generate as well. As a result, McGehee says, he expects the overall efficiency of perovskite solar cells to keep rising. "We may see 20% before the end of the year," he says.

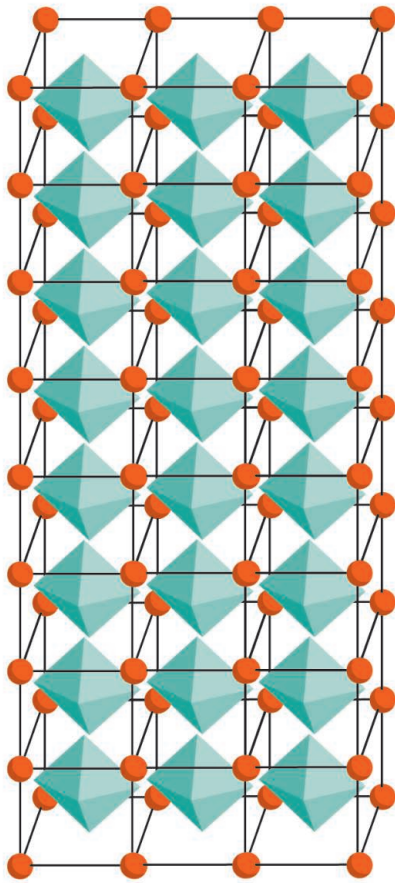

Cagey. Saltlike solar cell perovskites assemble themselves into near-perfect crystalline structures.

CREDIT: G. GRULLÓN/*SCIENCE*

They may go even further with help from today's champion: silicon. Commercial silicon cells already deliver 17% to 23% efficiency. "Making the silicon industry obsolete is very tough," McGehee says. Alternative technologies, such as thin films of copper indium gallium selenide, use far less material and thus are cheaper to make. But they haven't been able to knock silicon from its perch because they are less efficient. Consumers need more panels to generate the same amount of electricity and thus must pay higher installation costs.

> "The mood was **extremely grim in the PV community**. It was the shot in the arm that **we needed**."
>
> —Michael Grätzel, Swiss Federal Institute of Technology in Lausanne

Perovskites, by contrast, might literally piggyback off silicon's success. Perovskites are better than silicon at absorbing higher energy blue and green photons, while silicon excels at snagging lower energy red and infrared photons. And because perovskites can be grown at temperatures below the melting point of glass, engineers may be able to layer them directly onto the top glass coating of a silicon cell. That strategy, McGehee suspects, could produce low-cost tandem cells with about 30% efficiency. No one has done it yet, but McGehee says he expects many researchers are trying.

Hurdles ahead

All of this comes as a much-needed boost for the solar cell industry, which has struggled through a brutal commercial retrenchment in recent years as falling prices for solar cells have caused numerous companies to go bankrupt. Venture capital firms and even scientific funding agencies were getting cold feet about supporting research in slow-moving areas such as organic photovoltaics and DSSCs, Grätzel says. "The mood was extremely grim in the PV community." So perovskites couldn't have come at a better time, he adds. "It was the shot in the arm that we needed."

Even so, perovskite solar cells have a long way to go before they will be ready for the marketplace. For starters, Cahen says, most cells being produced in labs today are tiny, just centimeters on a side. By contrast, silicon panels are meters across. "It's very difficult to grow large continuous films" of perovskites, Cahen says. Nor have researchers solved the durability problem. Perovskite cells are extremely sensitive to oxygen, which reacts to break down the crystal structure, and to water vapor, which dissolves the saltlike perovskites. Even worse, the lead in today's best perovskites could leach out of the solar panel onto rooftops or the soil below.

"There are problems here," Cahen says. "At the moment, I'm an optimist, and a believer in materials research." Between the promise of perovskites and the multiple challenges that still need to be solved, "this field is going to be extremely active for the next few years," Grätzel says. And with the global solar cell market still worth nearly $50 billion a year, researchers have every incentive to keep the progress curve rising.

–ROBERT F. SERVICE

Published by AAAS

LETTERS

edited by Jennifer Sills

Biomedical Research: Strength from Diversity

THE RECENT EDUCATION FORUM BY M. J. GRAHAM AND COLLEAGUES ("INCREASING PERSISTENCE of college students in STEM," 27 September, p. 1455) called for widespread implementation of a much-needed framework for increasing persistence of college students in science, technology, engineering, and mathematics (STEM) fields. The Persistence Framework that they describe is evidence based, drawing from a rich body of research that has identified the relevant education and psychosocial issues that must be addressed, as well as effective strategies.

Recognizing that the biomedical research enterprise would be greatly strengthened by attracting the most talented individuals from all groups, the National Institutes of Health (NIH) has been intensively engaged for more than 2 years in a planning process. As a result, a distinguished working group (*1*) has made a series of bold recommendations that are now in the process of being implemented. These include the systematic evaluation of NIH training programs, the appointment of a Chief Office for Scientific Workforce Diversity, and the launch of a new three-component program that will provide the resources necessary to implement and assess, on a large scale, approaches such as those described by Graham *et al*. Developing new ways to engage college students, sustain their interest in research, and provide trainees at all career stages with the strategies and tools to thrive in the biomedical research workforce are the goals of the "Enhancing the Diversity of the NIH-Funded Workforce" program (*2*). This program will consist of three highly integrated initiatives:

(i) The National Research Mentoring Network (NRMN) will develop transformative approaches to mentoring. The network will engage diverse mentors from many biomedical research disciplines and link them to mentees at multiple career stages.

(ii) The Building Infrastructure Leading to Diversity (BUILD) initiative will support relatively under-resourced academic institutions with a demonstrated commitment to students from highly diverse backgrounds. These institutions will have the opportunity to develop a series of potentially transformative education and training activities that address the many factors underlying student/trainee persistence in biomedical research career paths and successful transition into the research workforce. BUILD emphasizes and requires the provision of research opportunities. The program will seek strength through collaboration across the spectrum of types of institutions.

(iii) The Coordination and Evaluation Center will work with both the BUILD consortium and NRMN to assess the efficacy of the various approaches that are being piloted.

History has revealed that addressing problems that disproportionately affect minority populations has often had a transformative impact for the majority as well (*3*). We predict that transformative approaches to student engagement and training developed through the Common Fund's Diversity Program will have a similar far-reaching impact on training everywhere.

ELIZABETH L. WILDER, LAWRENCE A. TABAK, RODERIC I. PETTIGREW, FRANCIS S. COLLINS*
National Institutes of Health, Bethesda, MD 20892, USA.
*Corresponding author. E-mail: collinsf@mail.nih.gov

References

1. NIH Advisory Committee to the Director, *Diversity in the Biomedical Workforce Working Group Report* (NIH, Bethesda, MD, 2012).
2. NIH, *Enhancing the Diversity of the NIH-Funded Workforce* (http://commonfund.nih.gov/diversity/).
3. M.N. Davidson, *The End of Diversity as We Know It: Why Diversity Efforts Fail and How Leveraging Difference Can Succeed* (Berrett-Koehler Publishers, San Francisco, 2011).

Pest Control: Embrace Marketing

IN HIS NEWS STORY "VIETNAM TURNS BACK a 'tsunami of pesticides'" (special section on Smarter Pest Control, 16 August, p. 737) D. Normile attributes the increase in pesticide use in Asia to "very powerful marketing forces." Yet, the campaigns that convinced Vietnamese rice farmers to use less pesticide also used marketing principles and tools, such as strategic use of posters, leaflets, radio soap operas, and television commercials. Although marketing principles are usually used to communicate the value of a commercial product or service to a cus-

Letters to the Editor

Letters (~300 words) discuss material published in *Science* in the past 3 months or matters of general interest. Letters are not acknowledged upon receipt. Whether published in full or in part, Letters are subject to editing for clarity and space. Letters submitted, published, or posted elsewhere, in print or online, will be disqualified. To submit a Letter, go to www.submit2science.org.

When North Africa was humid

808

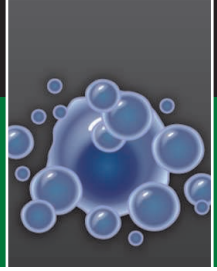

Synthetic lethality genes

809

tomer, they can also be applied to promote the social good, as practitioners in the field of social marketing have done for decades in areas such as public health (*1*).

It is time that those working to mitigate threats to the environment recognize that marketing principles have much to offer by providing a tried and tested framework that can be used to influence human behavior, a key driver of threats to biodiversity worldwide (*2*). For this to happen, marketing needs to be acknowledged as an amoral set of tools that can be used for a variety of ends, depending on who applies them. It is true that marketing has been traditionally used by businesses, and often to promote behaviors that are environmentally unsustainable. This is exactly why we need to engage with these effective principles and level the playing field. After all, why should the devil have all the best tunes (*3*)?

DIOGO VERÍSSIMO

Durrell Institute of Conservation and Ecology, University of Kent, Canterbury, CT2 7NZ, UK. E-mail: dv38@kent.ac.uk

References

1. J. French, C. Blair-Stevens, D. McVey, R. Merritt, *Social Marketing and Public Health: Theory and Practice* (Oxford Univ. Press, Oxford, 2009).
2. D. Veríssimo, *Conserv. Evidence* **10**, 29 (2013).
3. G. Hastings, *Social Marketing: Why Should the Devil Have All the Best Tunes?* (Elsevier, Oxford, 2007).

Pest Control: Biopesticides' Potential

THE SPECIAL SECTION ON SMARTER PEST Control (16 August, p. 728) highlighted the threats that chemical pesticides pose to human health and the environment, and some of the smart alternatives, including genetically modified (GM) crops. However, an important and emerging technology against insect pests was overlooked: biological pesticides.

Biopesticides are "derived from such natural materials as animals, plants, and bacteria" (*1*). They include microbial pesticides produced from fungi, protozoa, nematodes, baculoviruses, and bacteria (such as the widely used *Bacillus thuringiensis*, known as Bt). In the United States, there are about 400 registered biopesticide active ingredients and over 1250 products; there are many fewer in Europe (*2*). There has been substantial growth in biopesticides in recent years, especially in Asia, but they still comprise less than 4% of the global pesticides market (*3*).

Market growth is undermined by the variable efficacy of some biopesticides, smaller market niches, and policy/regulatory barriers (*2*, *4*). However, the potential for biopesticides is substantial, and many constraints can be overcome if, like other crop protection technologies, biopesticides also become smarter through research and innovation. Rather than treating biopesticides as synthetic chemicals, there is scope to develop and adopt novel production and delivery approaches that exploit their positive biological attributes (such as higher target specificity, capacity for secondary cycling, sublethal effects, genetic diversity, and transgenerational transmission) and minimize their negative ones (such as slower speed of kill and greater environmental sensitivity).

GM technologies do have the potential to radically reduce pest damage, but their global-scale acceptability and adoption remain a long way off. In the meantime, biopesticides in general, and microbial pesticides in particular, offer the potential to reduce the chemical burden on the landscape while minimizing the evolution of resistance. In addition to delivering a more environment-friendly alternative to synthetic chemicals that is compatible with organic farming and integrated pest management programs, biopesticides may provide cheaper solutions for crop protection globally if policy and regulatory barriers can be minimized and harmonized (*4*).

KENNETH WILSON,[1]* TIMOTHY G. BENTON,[2] ROBERT I. GRAHAM,[1] DAVID GRZYWACZ[3]

[1]Lancaster Environment Centre, Lancaster University, Lancaster, LA1 4YQ, UK. [2]School of Biology, University of Leeds, Leeds, LS2 9JT, UK. [3]Natural Resources Institute, University of Greenwich, Chatham Maritime, Kent, ME4 4TB, UK.
*Corresponding author: E-mail: ken.wilson@lancaster.ac.uk

References

1. U.S. Environmental Protection Agency, *Pesticides: Regulating Pesticides* (www.epa.gov/pesticides/biopesticides/whatarebiopesticides.htm).
2. D. Chandler *et al.*, *Philos. Trans. R. Soc. London Ser. B* **366**, 1987 (2011).
3. T. Glare *et al.*, *Trends Biotechnol.* **30**, 250 (2012).
4. R. Ehlers, *Regulation of Biological Control Agents* (Springer, Dordrecht, Netherlands, 2011).

Pest Control: Risks of Biochemical Pesticides

IN THE SPECIAL SECTION ON SMARTER PEST Control (16 August, p. 728), scientists propose smarter and safer pesticides. One increasingly popular solution that the section did not discuss is biochemical pesticides. Because of their unique mechanism of action, biochemical pesticides have minimal mammalian toxicity (*1*). However, these pesticides may put other facets of the environment at risk. For example, strobilurin fungicides have become the most widely used biochemical fungicides around the world. Yet, almost all strobilurin fungicides are highly toxic to fish and other aquatic organisms (*2*) and can contaminate surface and ground water (*3*). Statements on the product's labels that warn users to take precautions around water do not adequately address these concerns. As we search for pesticide alternatives, we must bear in mind that abuse or overuse of biochemical pesticides could be incredibly dangerous to our environment.

GEFEI HAO AND GUANGFU YANG*

Key Laboratory of Pesticide and Chemical Biology, Ministry of Education, College of Chemistry, Central China Normal University, Wuhan, 430079, China.
*Corresponding author. E-mail: gfyang@mail.ccnu.edu.cn

References

1. K. M. Meepagala, W. Osbrink, C. Burandt, A. Lax, S. O. Duke, *Pest Manag. Sci.* **67**, 1446 (2011).
2. E. T. Rodrigues, I. Lopes, M. A. Pardal, *Environ. Int.* **53**, 18 (2013).
3. T. J. Reilly, K. L. Smalling, J. L. Orlando, K. M. Kuivila, *Chemosphere* **89**, 228 (2012).

CORRECTIONS AND CLARIFICATIONS

Books *et al.*: "*Artemisia*, malaria, and the Red Queen," by W. Lawley *et al*. (11 October, p. 195). In the book's title, "Contol" should be "Control." The HTML and PDF versions online have been corrected.

News & Analysis: "India aims a probe at Mars—and at earthly prestige" by P. Bagla (20 September, p. 1328). The article incorrectly states that comet Siding Spring (C/2013 A1) is expected to collide with Mars in late 2014. Calculations earlier this year determined that the comet is likely to only make a close approach to the planet, with a negligible probability of colliding with the surface.

News Focus: "A floating lab explores the fringes of science and gastronomy" by K. Kupferschmidt (17 May, p. 809). Kevin Krajick was mistakenly listed as the author in the HTML version online. The author name has been corrected on the article page and the corresponding Table of Contents page.

SCIENCE AND POLICY

Failures to Compute

Cyrus C. M. Mody

Experts sometimes disagree with each other. Dispute and debate, after all, are fundamental to the hammering out of scientific knowledge. But when experts differ on matters of national interest, the public and its policy elites are placed in the uncomfortable position of deciding which experts to believe. Every country referees experts' squabbles, but in the United States such imbroglios are common. As recent historical work on climate change—most notably Naomi Oreskes and Erik Conway's *Merchants of Doubt* (*1*)—has shown, techno-political disputes in the United States are easily amplified by the country's traditions of populist rhetoric, pliant spokes-experts subsidized by vested interests, and journalistic commitment to "balance."

Arguments That Count
Physics, Computing, and Missile Defense, 1949–2012

by Rebecca Slayton
MIT Press, Cambridge, MA, 2013. 337 pp. $35, £24.95. ISBN 9780262019446. Inside Technology.

Rebecca Slayton's *Arguments That Count* examines one such controversy, that over the feasibility and utility of ballistic missile defense (BMD), through the course of almost 70 years. In her conclusion, Slayton (a science policy scholar at Stanford University) suggests that some aspects of the BMD debate can be generalized to other cases—such as climate change or genetically modified organisms—where disputatious experts have tried to craft arguments that will persuade the public or its policy-makers. In particular, she offers a new sociological concept, the "disciplinary repertoire," as a tool for understanding how different kinds of experts latch onto different arguments or present them in varying ways. These repertoires are "the quantitative rules, codified knowledge, and habits of problem solving that enable experts to structure, estimate, and quantify uncertain technological futures. Disciplinary repertoires allow experts to rhetorically distinguish subjective, politically controversial aspects of a problem from putatively objective, technical realities."

In a sense, it's fortunate that Slayton makes the case that BMD can tell us something about climate change, genetically modified organisms, and other controversies where the public struggles to decide which experts to believe. After all, missile defense has not often been a front-page issue during the present presidential administration—although Slayton reminds readers that BMD continues to complicate the United States's relationships with many other countries, and she strongly implies that the Obama administration has hardly been more cautious than its predecessors in throwing money at an expensive, unproven, and potentially destabilizing technology. Ballistic missile defense is similar enough to other politically charged technologies that it can tell us something about that general category of dispute, but even when dormant it is always close enough to erupting into controversy again that the arguments Slayton examines will no doubt resurface in the public sphere once more.

Potential for errors. Programmer Madeleine Carey with the 60,000 punch cards that contained the master program for the SAGE air defense system.

CREDIT: MITRE CORPORATION/COURTESY MIT PRESS

As a continually controversial not-yet-existent technology, BMD has had its history written many times—by technical and policy participants, political scientists, sociologists, and historians. Yet Slayton finds an ingenious and novel way to tell the history of missile defense systems anew: as a stage on which physicists and computing experts—computer professionals? software engineers? this group's muddled identity is part of Slayton's point—performed for one another and for policy-makers and the public, while using those performances to forward their individual and community objectives.

For the most part, Slayton focuses on elite practitioners, both within the physics and science policy establishment and among those trying to forge a professional identity for programmers. We learn quite a bit about the importance of BMD in the careers of scientists and engineers who are more (and justly) famous for other things. These include physicists Herbert York, Hans Bethe, Jerome Wiesner, Dick Garwin, and Harold Brown as well as, on the computing side, Daniel McCracken, Fred Brooks, Edward David, and J. C. R. Licklider. Slayton's focus on the elite gives her narrative an oblique sensibility, because for most of the characters BMD was a sideshow (if an incredibly important one).

Yet there is a strong historical reason for looking to technical elites' relationships with BMD. Since at least the 1930s, plans for knocking enemy weapons out of the sky before they strike the homeland were a critical point of entry for technical experts into the higher strata of war- and policy-making in the United States and allied nations. Even before the atomic bomb made J. Robert Oppenheimer and Edward Teller such influential figures, air defense had done the same for Henry Tizard, P. M. S. Blackett, and Vannevar Bush. Postwar, physicists who developed radar for air defense—particularly at the Radiation Laboratory at the Massachusetts Institute of Technology—rose quickly in both academia and government.

One of Slayton's major contributions is to tease out the continuities and discontinuities between air defense and BMD. Elite physicists leveraged the threat of a Soviet bomber attack to create quintessential Cold

The reviewer is at the Department of History, Rice University, Houston, TX 77251–1892, USA. E-mail: cm6@rice.edu

Published by AAAS

War institutions, such as Lincoln Laboratory, that blurred the lines of academia and government and to pour money into efforts to develop digital computers such as SAGE (Semi-Automatic Ground Environment) and Project Whirlwind. Many of the same elite physicists (e.g., York, Garwin, and Bethe), however, were later opposed to the development of a comprehensive BMD system, largely on the grounds that it could destabilize nuclear diplomacy while providing little protection. Physicists who criticized the Johnson and Nixon administrations' desire for missile defense risked their careers and ultimately contributed to the decline in American politicians' deference toward technical expertise, even if their arguments ought to have counted.

Curiously, physicists who opposed a large-scale missile defense did not initially identify software errors as a potential source of catastrophic failure. As Slayton shows, physicists involved in nuclear policy assumed (somewhat hilariously) that programming such a system would be cheap, fast, easy, and reliable. The reality, of course, was otherwise. Indeed, perhaps Slayton's most notable contribution is to show how much missile defense fostered the formation of professional institutions for software engineering as well as the development of new computer languages, proofs of program reliability (and, more generally, error-checking algorithms), standardization of software across different machines, and administrative methods for managing large programming projects. Ironically, the military's support for the emergence of a self-confident software engineering community yielded a new argument against BMD: that no software program complex enough to control a missile defense system could be shown to be free of errors that would render it inoperative the first (and only) time it was asked to do its job.

That argument remained bottled up through the 1970s—Slayton shows, for instance, that Daniel McCracken's Computer Professionals Against the ABM (Anti-Ballistic Missile) garnered many colleagues' tacit agreement but few offered public support. Later, however, software engineers' arguments counted more, with computer scientist David Parnas's well-publicized resignation from a Strategic Defense Initiative review panel in the 1980s and the contribution of software glitches to Patriot missile failures during the first Gulf War. Physical arguments against BMD, meanwhile, struggled to keep up with the changing technological basis of the proposed system (interceptor nukes in the '60s, space-based lasers in the '80s, and "brilliant pebbles" in the '90s) and the changing political environment of the post–Cold War.

And that is where we are today. Slayton convincingly shows that physical arguments against BMD, however plausible and conservative in their assumptions, are sapped of their force by Americans' profound faith in technological progress and the ability of innovation to solve any problem. Software engineers, meanwhile, could perhaps supply a knockout argument, but doing so would undermine their own progressive narrative of increasing program reliability. And so, we are left with a costly, diplomatically divisive system that we have every reason to think cannot work.

References

1. N. Oreskes, E. M. Conway, *Merchants of Doubt: How a Handful of Scientists Obscured the Truth on Issues from Tobacco Smoke to Global Warming* (Bloomsbury, New York, 2010); reviewed in (*2*).
2. P. Kitcher, *Science* **328**, 1230 (2010).

10.1126/science.1246560

BEHAVIOR

Coming to Grips with Learning with Others

Dorothy M. Fragaszy and Yonat Eshchar

Everyone, it seems, is interested in animals' social lives, including the ways that social partners help others to learn about the world around them and to master skills to thrive in it. Parents and group mates nurturing young animals as they learn to forage (or to fly, to navigate, etc.) are a staple theme of nature documentaries. These often contain gratuitous references by the narrator to teaching or imitation, two processes that lay viewers typically attribute to social species. Such attributions cause behavioral scientists to shudder, because the evidence for both these processes (in the sense that we understand them in humans) in nonhuman species is limited to precious few species and contexts (*1*).

Perhaps we should not be surprised at widespread anthropomorphic conceptions of social learning in other species. All of us have direct experience with social learning, and our experiential understanding of this process in our own species is reinforced by exposure to a long history of learned examination of the topic (for example, in the 20th century, in the works of John Dewey). In contrast, scientific research on social learning in nonhuman animals has blossomed only relatively recently—in the past 40 or so years—as part of the growing fields of animal behavior and evolutionary biology (*1*–*5*). It will be some time before we can explain to the general public how social learning works in nonhuman species well enough to displace superficial attributions of humanlike imitation and teaching.

Meanwhile, those trying to understand social learning in nonhuman animals using the tools of science have much work to do. We are coming to understand that social learning is not restricted to large-brained animals but is instead widely distributed—it is present, for example, in crickets (*6*)—and that it is a powerful participant in evolutionary processes (*7*). Documenting how social learning contributes to the diversity of animal life is challenging. The field is currently overstocked with proposed categories of social learning processes and understocked with sufficiently powerful analytical paradigms. This state of affairs leaves prospective students of social learning wondering where to start.

Behavioral biologists William Hoppitt (Anglia Ruskin University) and Kevin Laland (University of St Andrews) offer a steady hand to those aspiring to study how social learning works or to understand the relevant scientific literature. To our knowledge, *Social Learning* is the first authored—rather than edited—book devoted specifically to the topic. As such, it is more thematically organized than previous volumes about the subject (*1*–*3*). With admirable clarity, the authors review the concepts, experimental designs, and methods used in studies of social learning in nonhuman animals, and they provide suggestions for new analytical approaches

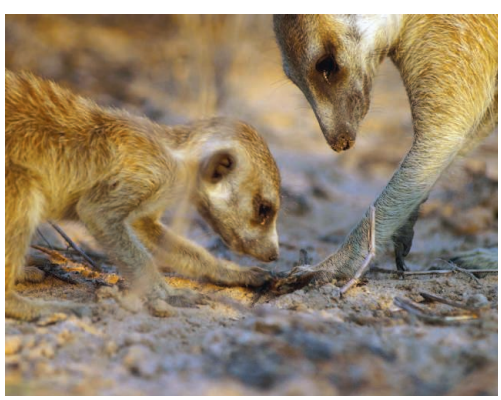

Learning with another. Juvenile meerkat (*Suricata suricatta*) inspects cricket captured by an adult.

CREDIT: ALEX THORNTON/UNIVERSITY OF EXETER

The reviewers are at the Behavioral and Brain Sciences Program, Department of Psychology, University of Georgia, Athens, GA 30602, USA. E-mail: doree@uga.edu; yonat@uga.edu

to enduring problems. They largely achieve their goal to provide "a complete and accessible practical guide" for students and researchers in the field of social learning. The word "practical" is very important here: The book is not primarily about theoretical issues or empirical findings, although it presents some of each. Hoppitt and Laland devote the bulk of the book to describing methods for conducting social learning experiments and observational studies. They illustrate their points by reviewing studies that used particular tools, and explanatory boxes go over relatively less familiar statistical methods in detail (at times to the level of software code). For each method, the authors spell out clearly what questions it can answer, under what circumstances it has been used in the past or might be used in the future, its advantages, and its limitations.

The authors bravely venture into the untidy details of real-world studies, providing guidance on how to handle missing data, incomplete information regarding individuals' histories with a given problem, lack of cross-generational data, and other common deviations from the ideal study design that plague the field. They also devote considerable space to explaining the value of computational modeling and how to use particular methods—for example, network modeling to study diffusion of behavioral traits across individuals and groups; causal modeling to disambiguate relationships among ecological, social, behavioral, and genetic similarity across groups; and modeling the probability and the timing of acquiring a trait. The authors advocate using models to generate hypotheses, explore data, and test theoretical predictions. Their account offers a clear guide to creating and working with models and also reviews published work in social learning using modeling approaches.

The pragmatic approach makes the book a great starting point for researchers who wish to plan a study or to look for ways to analyze data. Students will find it accessible, and the analytical tools can be used by anyone having a basic understanding of statistical methods. The five chapters that focus on methods should go a long way toward providing a clear way forward for the field.

Social Learning
An Introduction to Mechanisms, Methods, and Models

by William Hoppitt and Kevin N. Laland
Princeton University Press, Princeton, NJ, 2013. 319 pp. $75, £52. ISBN 9780691150703. Paper, $49.50, £34.95. ISBN 9780691150710.

Hoppitt and Laland apparently felt compelled (by history more than conviction, it seems) to tackle the thorny problem of defining social learning mechanisms: how the learner is affected by the actions of others. Here, their effort proves less successful than in their presentation of methods. That is hardly surprising, as the field has always suffered from a lack of consensus about such definitions. At present, the phenomenon of "social learning" is broken into several theoretically discrete processes: local enhancement, stimulus enhancement, response facilitation, social facilitation, multiple types of imitation, and more. (The authors' table contains 12 entries.) A fundamental problem is that the separate existence of all these discrete mechanisms is far from clear. To some extent, the categories restate the procedures used to identify them. In addition, different people use the same term to mean different things, and boundaries between categories seem to change with every new publication. Hoppitt and Laland organize these mechanisms as best as possible, choosing clear definitions and delineating—or at least trying to delineate—the borders among them. We doubt, however, that their work in this regard is worth the effort. The authors themselves note that the existing classifications "have overlapping categories, and encompass mechanisms that are almost impossible to tell apart, given the data that are likely to be available." We find little merit in laboriously listing and defining categories that end up being of little to no use. The field would be better served by taking a different, functional approach to understanding how social learning happens.

The authors do, in fact, offer a new approach to frame questions about social learning mechanisms, one based on three simple questions: Is the effect context-specific? Is it sensitive to the outcome? Is it action-specific? This fresh perspective appears more pragmatic and more useful to the field, because it suggests questions that we can actually address with data. Unfortunately, Hoppitt and Laland present their approach almost shyly (in around two pages) and only after dedicating most of the chapter about mechanisms to the cumbersome historical approach. We hope that the field adopts Hoppitt and Laland's new scheme and regret that they did not develop it more fully and advocate it more strongly.

The book should certainly fulfill the authors' intention that it serve as a practical guide to the study of social learning in nonhuman animals. *Social Learning* will advance the field by encouraging and enabling the use of more sophisticated mathematical analytical tools and standardizing the use of particular methods—one hopes as effectively as Jeanne Altmann's seminal work (*8*) oriented researchers to use quantitative sampling methods in observational research. Hoppitt and Laland's accessible writing and the book's clear graphics support its effectiveness. We predict a long and useful life for this welcome volume.

References

1. D. M. Fragaszy, S. Perry, Eds., *The Biology of Traditions and Evidence* (Cambridge Univ. Press, Cambridge, 2003).
2. T. R. Zentall, B. G. Galef, Eds., *Social Learning: Psychological and Biological Perspectives* (Lawrence Erlbaum, Hillsdale, NJ, 1988).
3. C. M. Heyes, B. G. Galef, Eds., *Social Learning in Animals: The Roots of Culture* (Academic Press, San Diego, 1996).
4. M. Nielsen, F. Subiaul, B. Galef, T. Zentall, A. Whiten, *J. Comp. Psychol.* **126**, 109 (2012).
5. B. G. Galef, C. M. Heyes, *Anim. Learn. Behav.* **32**, 1 (2004).
6. I. Coolen, O. Dangles, J. Casas, *Curr. Biol.* **15**, 1931 (2005).
7. E. Jablonka, M. J. Lamb, *Evolution in Four Dimensions: Genetic, Epigenetic, Behavioral, and Symbolic Variation in the History of Life* (MIT Press, Cambridge, MA, 2005).
8. J. Altmann, *Behavior* **49**, 227 (1974).

10.1126/science.1246296

BROWSINGS

Shaping Humanity: How Science, Art, and Imagination Help Us Understand Our Origins.
John Gurche. Yale University Press, New Haven, CT, 2013. 363 pp. $49.95, £30. ISBN 9780300182026.

CREDIT: © JOHN GURCHE/COURTESY YALE UNIVERSITY PRESS

For the Smithsonian's Hall of Human Origins (2010), paleoartist Gurche crafted 15 exquisite sculptures of hominin species (above, *Homo erectus*) from the past 6 million years. Revealing in detail what lies beneath their skin, he presents color photographs of the reconstructions in progress and a personal account of the scientific and aesthetic decisions along the nearly 30-year journey from conception to fully realized art.

CONSERVATION

Protected Areas and Effective Biodiversity Conservation

Increasing the collective contribution of protected areas toward preventing species extinctions requires the strategic allocation of management efforts.

Soizic Le Saout,[1] Michael Hoffmann,[2,3] Yichuan Shi,[2,3] Adrian Hughes,[2] Cyril Bernard,[1] Thomas M. Brooks,[2,4] Bastian Bertzky,[3]* Stuart H. M. Butchart,[5] Simon N. Stuart,[2,3,6,7,8] Tim Badman,[2] Ana S. L. Rodrigues[1]†

Although protected areas (PAs) cover 13% of Earth's land (*1*), substantial gaps remain in their coverage of global biodiversity (*2*). Thus, there has been emphasis on strategic expansion of the global PA network (*3*–*5*). However, because PAs are often understaffed, underfunded, and beleaguered in the face of external threats (*6*, *7*), efforts to expand PA coverage should be complemented by appropriate management of existing PAs. Previous calls for enhancing PA management have focused on improving operational effectiveness of each PA [e.g., staffing and budgets (*6*)]. Little guidance has been offered on how to improve collective effectiveness for meeting global biodiversity conservation goals (*3*). We provide guidance for strategically allocating management efforts among and within existing PAs to strengthen their collective contribution toward preventing global species extinctions.

Strategic Management Across PAs

PAs vary in the extent to which they can contribute to preventing extinctions. The notion of "irreplaceability" reflects a site's potential contribution to conservation goals or, conversely, the extent to which options for meeting those goals are lost if the site is lost (*4*). Irreplaceability has been extensively used to identify potential new PAs [e.g., (*2*, *4*)] but can also be applied to inform allocation of management effort among existing sites (*8*). We highlight a set of exceptionally irreplaceable PAs for which we recommend a particularly high level of management effort and encourage global recognition as World Heritage sites.

We estimated the irreplaceability of each of the world's 173,461 designated PAs, and of 2059 proposed sites (*9*), for ensuring representation of 21,419 vertebrate species, encompassing all amphibians, nonmarine mammals, and birds, of which 4329 are globally threatened (*10*, *11*) [see the supplementary materials (SM)]. Irreplaceability was estimated from the fraction of the global distribution of each species that is contained within each PA, by following a new approach that reduces the effect of the commission errors (falsely assuming species presence in PAs) inherent to the available spatial data (see SM). Irreplaceability scores and relative ranks were obtained both when considering all species (overall irreplaceability) or only those species that are globally at risk of extinction (threatened species irreplaceability), for all taxa combined (multitaxa), as well as separately for each taxonomic group (amphibians, mammals, and birds) (table S1). We highlight a subset of 137 PAs, covering 1.7 million km^2, identified by combining the 100 highest-ranking sites in terms of overall irreplaceability with the 100 most irreplaceable areas for threatened species (see the figure, fig. S1, and table S2).

Mainly located in tropical forest regions, particularly in mountains and on islands, these highly irreplaceable PAs encompass a wide diversity of other ecosystems. PA sizes range from 41 to 364,793 km^2 (table S2). Nearly all are located in biogeographic regions of exceptional levels of endemism (*12*) and nearly all have already been identified as key biodiversity areas (*13*). Collectively, they are responsible for the long-term conservation prospects of 627 species (119 birds, 385 amphibians, and 123 mammals), including 304 globally threatened species (60 birds, 179 amphibians, and 65 mammals) whose global distributions fall mostly (>50%) within these sites. For 88 of these PAs, the conservation stakes are particularly high, as they overlap sites previously identified as holding ≥95% of the global population of at least one highly threatened species, where species extinctions are imminent unless effective conservation action is implemented (*14*).

The Bale Mountains National Park in the Ethiopian highlands is home more than half of the world's estimated 366 Ethiopian wolves, *Canis simensis* (*10*) seen at right.

The United Nations World Heritage Convention (WHC) seeks to encourage the identification and conservation of natural and cultural heritage of "outstanding universal value." Among currently designated World Heritage Sites (WHS), 132 have been inscribed [under criterion (x)] as having outstanding universal value for the in situ conservation of biodiversity (see SM) (*15*). Their very high overall irreplaceability (91% are among the 95th percentile of PA irreplaceability for all species and/or for threatened species examined here) (table S1) suggests a remarkable agreement between outstanding universal value, as defined by the WHC, and

[1]Centre d'Ecologie Fonctionnelle et Evolutive, CEFE-CNRS UMR5175, 34293 Montpellier, France. [2]International Union for Conservation of Nature, CH-1196 Gland, Switzerland. [3]United Nations Environment Programme World Conservation Monitoring Centre, Cambridge CB3 0DL, UK. [4]School of Geography and Environmental Studies, University of Tasmania, Hobart, Tasmania 7001, Australia. [5]BirdLife International, Cambridge CB3 0NA, UK. [6]Conservation International, Arlington, VA, 22202, USA. [7]Department of Biology and Biochemistry, University of Bath, Bath BA2 7AY, UK. [8]Al Ain Zoo, Abu Dhabi, United Arab Emirates.

*Present address: European Commission, Joint Research Centre, Institute for Environment and Sustainability, Ispra, Italy.

†Corresponding author. E-mail: ana.rodrigues@cefe.cnrs.fr

Published by AAAS

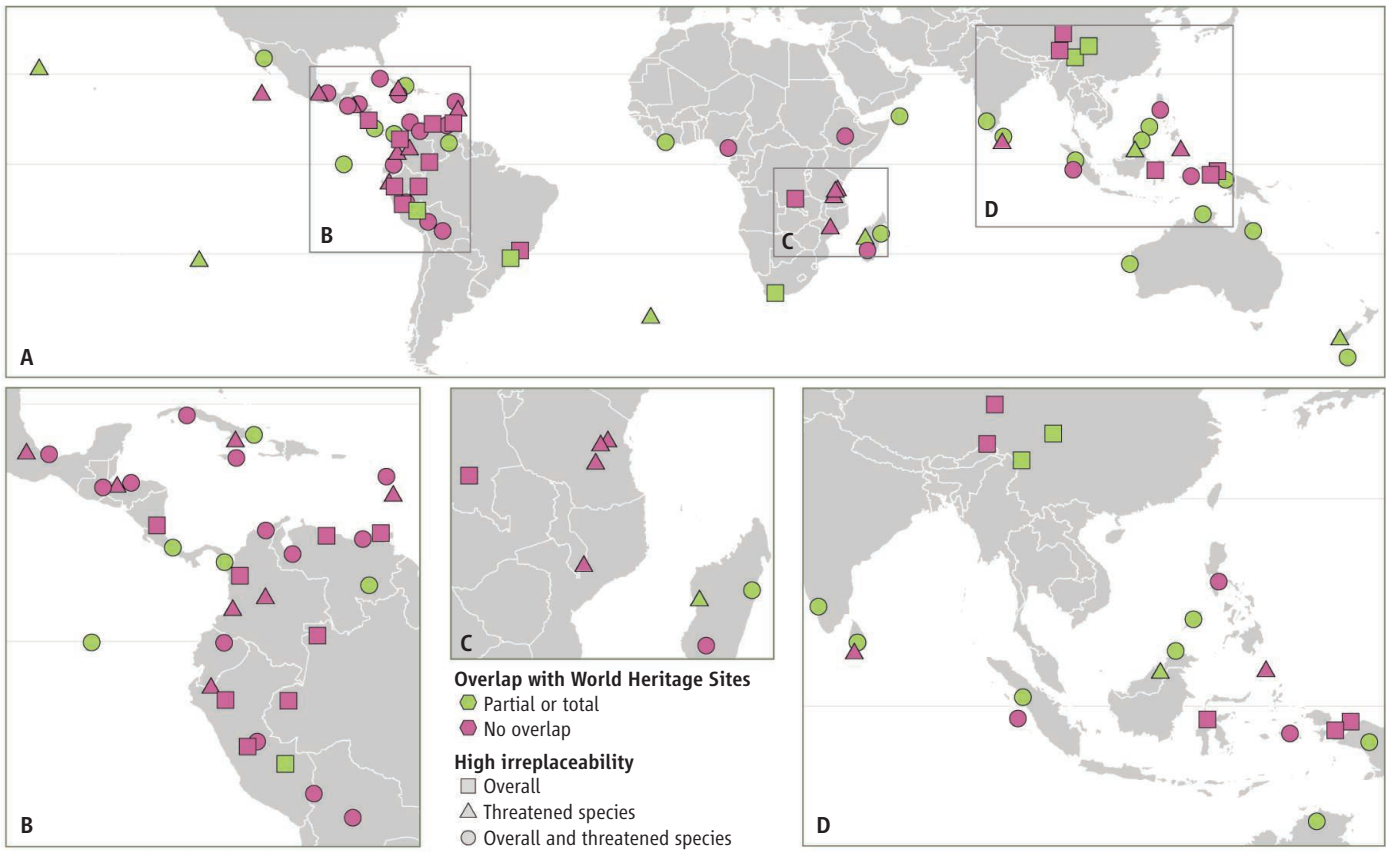

The world's most irreplaceable PAs for conservation of amphibian, bird, and mammal species. (**A**) Global distribution. (**B**) Central and South America. (**C**) East Africa. (**D**) Southern and Southeast Asia. To facilitate representation, clusters of overlapping or nearby sites are presented here as a single symbol; see fig. S1 and table S2 for a full list of sites comprising 137 protected areas in 78 clusters. See SM for details.

high irreplaceability. We thus recommend the inclusion of the latter as an operational indicator of the former in future assessments of World Heritage status for biodiversity (*16*).

However, at present only about half the combined area of the 137 highly irreplaceable PAs highlighted in this study is inscribed as WHS under criterion (x) (table S2). We thus encourage the respective nations and the World Heritage Committee to consider extending World Heritage recognition to the remaining highly irreplaceable territory, either through the nomination of new WHS or the extension of existing sites (see the figure and fig. S1) (*16*). Given that WHS must, as a prerequisite to inscription, meet rigorous standards of integrity, protection, and management, the process to achieve and maintain recognition under the WHC would be a powerful mechanism to ensure effective protection of the exceptionally irreplaceable areas identified in this study.

Furthermore, these areas vary in the urgency of their conservation needs (tables S1 and S2). In areas of high irreplaceability for species at risk of extinction, there is no time to lose in establishing effective management necessary to prevent extinctions. Highly irreplaceable PAs whose uniqueness is driven by nonthreatened species can afford proactive conservation actions that anticipate future threats.

Strategic Management Within PAs

Ensuring that highly irreplaceable PAs are managed as effectively as possible is crucial to the collective performance of the global network of PAs, but in order to be effective, local management must be strategically tailored to the specific biodiversity features of each site. Local management plans often focus on charismatic species, and management decisions favoring these (e.g., habitat protection) will often benefit a whole set of species. However, management objectives established for particular species sometimes deliver no benefits to, or can even jeopardize the persistence of, other species [e.g., (*17*)]. In such cases, we propose that species for which a PA has the highest conservation responsibility should be the first consideration for management and monitoring.

The percentage of each species' global distribution that overlaps each PA can be used as a simple indicator of responsibility (complemented by better data when available; e.g., on population abundance). This percentage can be estimated from global distribution maps already available for some taxonomic groups and being compiled for others (*10*, *18*), but given the coarse nature of such maps, it is only informative for relatively high percentages of overlap (see SM). We provide, for each PA, the list of species for which >5% of their range overlaps the PA, and the extent of such overlap (*19*). For example, Gunung Lorentz National Park, Indonesia, overlaps >5% of the range of 46 mammal species, including two that occur nowhere else, and eight that have more than half their range inside the park, which should be high priorities for management.

Data compiled in the International Union for Conservation of Nature (IUCN) Red List of Threatened Species (*10*) can help guide conservation strategies, particularly in high-biodiversity, poorly known regions (*20*). In Gunung Lorentz National Park, for example, both the Alpine Woolly Rat (*Mallomys gunung*, endangered, 95% overlap) and the Dingiso (*Dendrolagus mbaiso*, endangered, 59% overlap) are montane species threatened by hunting, which suggests that regulating hunting in high-altitude ecosystems should be a management priority within this PA.

Data that we provide are derived from extensive global data sets on species and PAs that are already freely available (SM). Turning these data sets into information useful for the management of individual PAs requires processing and resources that are often not easily available to park managers and decision-makers. We make our results available in an easily accessible format (table S1) (*19*), to complement other information needed for effective protected area management (e.g., on the costs of conservation actions and the value of sites for conservation of biodiversity at levels other than species, such as genes and ecosystems).

PAs are our main hope for meeting ambitious global conservation targets, such as preventing species extinctions (*3*), but the costs of ensuring their effective management are substantial, albeit affordable (*21*). We hope that the conceptual guidance and specific data provided here will support strategic reinforcement of the world's existing PAs, to improve their individual and collective effectiveness for conserving global biodiversity.

References and Notes

1. B. Bertzky *et al*., *Protected Planet Report 2012: Tracking Progress Towards Global Targets for PAs* (IUCN, Gland, Switzerland and UNEP-WCMC, Cambridge, 2012).
2. A. S. L. Rodrigues *et al*., *Bioscience* **54**, 1092 (2004).
3. SCBD, *COP 10 Decision X/2: Strategic Plan for Biodiversity 2011-2020* (Secretariat of the Convention on Biological Diversity, Nagoya, Japan, 2010).
4. R. L. Pressey, C. J. Humphries, C. R. Margules, R. I. Vane-Wright, P. H. Williams, *Trends Ecol. Evol.* **8**, 124 (1993).
5. A. Moilanen, K. A. Wilson, H. Possingham, *Spatial Conservation Prioritization: Quantitative Methods and Computational Tools* (Oxford Univ. Press, Oxford, UK, 2009).
6. F. Leverington, K. L. Costa, H. Pavese, A. Lisle, M. Hockings, *Environ. Manage.* **46**, 685 (2010).
7. W. F. Laurance *et al*., *Nature* **489**, 290 (2012).
8. A. J. Hartley *et al*. *The Assessment of African PAs* (European Commission: Joint Research Centre, Institute for Environment and Sustainability, Luxembourg, 2007).
9. IUCN, UNEP-WCMC, *The World Database on Protected Areas (WDPA): October 2012* (UNEP-WCMC, Cambridge, 2012); www.protectedplanet.net
10. IUCN, *2012 IUCN Red List of Threatened Species. Version 2012.2* (IUCN, Gland, Switzerland and Cambridge, 2012); www.iucnredlist.org.
11. We focus on terrestrial vertebrate groups (for which better spatial information exists) both as targets in their own right and as surrogates for broader global biodiversity. As data improve, the proposed methodology can be extended to marine PAs and to other taxa.
12. T. M. Brooks *et al*., *Science* **313**, 58 (2006).
13. G. Eken *et al*., *Bioscience* **54**, 1110 (2004).
14. T. H. Ricketts *et al*., *Proc. Natl. Acad. Sci. U.S.A.* **102**, 18497 (2005).
15. B. Bertzky *et al*., *Terrestrial Biodiversity and the World Heritage List* (UNEP-WCMC, Cambridge, 2013); www.unep-wcmc.org/biodiversity-wh_975.html.
16. These recommendations are integrated and further developed in (*15*).
17. F. Courchamp *et al*. *Science* **302**, 1532 (2003).
18. M. Hoffmann *et al*., *Science* **330**, 1503 (2010).
19. This information is available for 2370 PAs (covering 6117 species) either through a link from each PA's page on www.protectedplanet.net, or searchable from http://irreplaceability.cefe.cnrs.fr. For the example discussed in the text, Gunung Lorentz National Park, see either the "Irreplaceability Analysis" link in www.protectedplanet.net/sites/1500 or http://irreplaceability.cefe.cnrs.fr/sites/1500.
20. A. S. L. Rodrigues *et al*. *Trends Ecol. Evol.* **21**, 71 (2006).
21. D. P. McCarthy *et al*., *Science* **338**, 946 (2012).

Acknowledgments: This work has been partially funded by the German Federal Agency for Nature Conservation (BfN) and by the MAVA Foundation. We thank N. Burgess, P. Geniez, O. Gimenez, J. Hutton, N. Kingston, S. Ollier, and T. Wilkinson for technical support and discussions, and anonymous referees for constructive comments. We are grateful to those who provided the information on which the World Database on PAs and IUCN Red List of Threatened Species are based.

Supplementary Materials
www.sciencemag.org/content/342/6160/803/suppl/DC1

10.1126/science.1239268

ENVIRONMENTAL SCIENCE

What Does Zero Deforestation Mean?

Ambiguous definitions and metrics create risks for forest conservation and accountability.

Sandra Brown[1]* and Daniel Zarin[2]

Since 2005, negotiations under the United Nations Framework Convention on Climate Change (UNFCCC) have focused considerable attention on the role that reducing emissions from deforestation and forest degradation (REDD+) can play in climate change mitigation. As global interest in reducing deforestation has grown, numerous governments, corporate groups, and civil society organizations have set time-bound targets for achieving "zero deforestation." Some targets specify "net deforestation," some "gross deforestation," and some do not specify at all (see the table). Public- and private-sector policy-makers who commit to deforestation reduction targets, and those who advocate for them, are often unclear about their implications. This lack of clarity may lead to perverse outcomes, including governments celebrating reductions of deforestation when large areas of native forest have been cut down and "zero deforestation" certification of agricultural commodities produced on land recently cleared of native forest cover. Progress toward goals of forest conservation, climate change mitigation, and associated cobenefits would be better served and more readily monitored by setting separate time-bound targets for reductions in the clearing of native forests (gross deforestation) and increases in the establishment of new forests on previously cleared lands (reforestation). Net deforestation targets, inherently and erroneously, equate the value of protecting native forests with that of planting new ones.

[1]Ecosystem Services Unit, Winrock International, Arlington, VA 22202, USA. [2]Climate and Land Use Alliance, San Francisco, CA 94104, USA.

*Corresponding author. E-mail: sbrown@winrock.org

Net Versus Gross Deforestation

The most commonly used source of data on global deforestation is the United Nations Food and Agriculture Organization's Forest Resource Assessment (FAO-FRA) program, which publishes reports at 5-year intervals (*1*). A key metric in the FAO-FRA reports is the annualized net change in forest area. This "net deforestation" is estimated as the difference in forest area between two points in time, taking into account both losses from deforestation and gains from forest regeneration and/or tree plantations, divided by the number of years between the two time periods (*1*, *2*). For most tropical countries, this metric is generally estimated from tabular data, provided to the FAO-FRA by the countries, which are based on periodic forest inventories, land-use surveys, and/or forest area maps but rarely from interpretation of multiyear remote sensing imagery due to the lack of capacity and resources to acquire and process the imagery. Because losses in forest area generally exceed gains due to secondary forest regeneration and tree plantings in tropical countries, the FAO-FRA "net deforestation" metric for those countries is often reported simply as "tropical deforestation" (*3*).

Meanwhile, since 1988, the Brazilian Space Agency (INPE) has monitored

Data that we provide are derived from extensive global data sets on species and PAs that are already freely available (SM). Turning these data sets into information useful for the management of individual PAs requires processing and resources that are often not easily available to park managers and decision-makers. We make our results available in an easily accessible format (table S1) (*19*), to complement other information needed for effective protected area management (e.g., on the costs of conservation actions and the value of sites for conservation of biodiversity at levels other than species, such as genes and ecosystems).

PAs are our main hope for meeting ambitious global conservation targets, such as preventing species extinctions (*3*), but the costs of ensuring their effective management are substantial, albeit affordable (*21*). We hope that the conceptual guidance and specific data provided here will support strategic reinforcement of the world's existing PAs, to improve their individual and collective effectiveness for conserving global biodiversity.

References and Notes

1. B. Bertzky *et al.*, *Protected Planet Report 2012: Tracking Progress Towards Global Targets for PAs* (IUCN, Gland, Switzerland and UNEP-WCMC, Cambridge, 2012).
2. A. S. L. Rodrigues *et al.*, *Bioscience* **54**, 1092 (2004).
3. SCBD, *COP 10 Decision X/2: Strategic Plan for Biodiversity 2011-2020* (Secretariat of the Convention on Biological Diversity, Nagoya, Japan, 2010).
4. R. L. Pressey, C. J. Humphries, C. R. Margules, R. I. Vane-Wright, P. H. Williams, *Trends Ecol. Evol.* **8**, 124 (1993).
5. A. Moilanen, K. A. Wilson, H. Possingham, *Spatial Conservation Prioritization: Quantitative Methods and Computational Tools* (Oxford Univ. Press, Oxford, UK, 2009).
6. F. Leverington, K. L. Costa, H. Pavese, A. Lisle, M. Hockings, *Environ. Manage.* **46**, 685 (2010).
7. W. F. Laurance *et al.*, *Nature* **489**, 290 (2012).
8. A. J. Hartley *et al. The Assessment of African PAs* (European Commission: Joint Research Centre, Institute for Environment and Sustainability, Luxembourg, 2007).
9. IUCN, UNEP-WCMC, *The World Database on Protected Areas (WDPA): October 2012* (UNEP-WCMC, Cambridge, 2012); www.protectedplanet.net
10. IUCN, *2012 IUCN Red List of Threatened Species. Version 2012.2* (IUCN, Gland, Switzerland and Cambridge, 2012); www.iucnredlist.org.
11. We focus on terrestrial vertebrate groups (for which better spatial information exists) both as targets in their own right and as surrogates for broader global biodiversity. As data improve, the proposed methodology can be extended to marine PAs and to other taxa.
12. T. M. Brooks *et al.*, *Science* **313**, 58 (2006).
13. G. Eken *et al.*, *Bioscience* **54**, 1110 (2004).
14. T. H. Ricketts *et al.*, *Proc. Natl. Acad. Sci. U.S.A.* **102**, 18497 (2005).
15. B. Bertzky *et al.*, *Terrestrial Biodiversity and the World Heritage List* (UNEP-WCMC, Cambridge, 2013); www.unep-wcmc.org/biodiversity-wh_975.html.
16. These recommendations are integrated and further developed in (*15*).
17. F. Courchamp *et al. Science* **302**, 1532 (2003).
18. M. Hoffmann *et al.*, *Science* **330**, 1503 (2010).
19. This information is available for 2370 PAs (covering 6117 species) either through a link from each PA's page on www.protectedplanet.net, or searchable from http://irreplaceability.cefe.cnrs.fr. For the example discussed in the text, Gunung Lorentz National Park, see either the "Irreplaceability Analysis" link in www.protectedplanet.net/sites/1500 or http://irreplaceability.cefe.cnrs.fr/sites/1500.
20. A. S. L. Rodrigues *et al. Trends Ecol. Evol.* **21**, 71 (2006).
21. D. P. McCarthy *et al.*, *Science* **338**, 946 (2012).

Acknowledgments: This work has been partially funded by the German Federal Agency for Nature Conservation (BfN) and by the MAVA Foundation. We thank N. Burgess, P. Geniez, O. Gimenez, J. Hutton, N. Kingston, S. Ollier, and T. Wilkinson for technical support and discussions, and anonymous referees for constructive comments. We are grateful to those who provided the information on which the World Database on PAs and IUCN Red List of Threatened Species are based.

Supplementary Materials
www.sciencemag.org/content/342/6160/803/suppl/DC1

10.1126/science.1239268

ENVIRONMENTAL SCIENCE

What Does Zero Deforestation Mean?

Ambiguous definitions and metrics create risks for forest conservation and accountability.

Sandra Brown[1]* and Daniel Zarin[2]

Since 2005, negotiations under the United Nations Framework Convention on Climate Change (UNFCCC) have focused considerable attention on the role that reducing emissions from deforestation and forest degradation (REDD+) can play in climate change mitigation. As global interest in reducing deforestation has grown, numerous governments, corporate groups, and civil society organizations have set time-bound targets for achieving "zero deforestation." Some targets specify "net deforestation," some "gross deforestation," and some do not specify at all (see the table). Public- and private-sector policy-makers who commit to deforestation reduction targets, and those who advocate for them, are often unclear about their implications. This lack of clarity may lead to perverse outcomes, including governments celebrating reductions of deforestation when large areas of native forest have been cut down and "zero deforestation" certification of agricultural commodities produced on land recently cleared of native forest cover. Progress toward goals of forest conservation, climate change mitigation, and associated cobenefits would be better served and more readily monitored by setting separate time-bound targets for reductions in the clearing of native forests (gross deforestation) and increases in the establishment of new forests on previously cleared lands (reforestation). Net deforestation targets, inherently and erroneously, equate the value of protecting native forests with that of planting new ones.

Net Versus Gross Deforestation

The most commonly used source of data on global deforestation is the United Nations Food and Agriculture Organization's Forest Resource Assessment (FAO-FRA) program, which publishes reports at 5-year intervals (*1*). A key metric in the FAO-FRA reports is the annualized net change in forest area. This "net deforestation" is estimated as the difference in forest area between two points in time, taking into account both losses from deforestation and gains from forest regeneration and/or tree plantations, divided by the number of years between the two time periods (*1*, *2*). For most tropical countries, this metric is generally estimated from tabular data, provided to the FAO-FRA by the countries, which are based on periodic forest inventories, land-use surveys, and/or forest area maps but rarely from interpretation of multiyear remote sensing imagery due to the lack of capacity and resources to acquire and process the imagery. Because losses in forest area generally exceed gains due to secondary forest regeneration and tree plantings in tropical countries, the FAO-FRA "net deforestation" metric for those countries is often reported simply as "tropical deforestation" (*3*).

Meanwhile, since 1988, the Brazilian Space Agency (INPE) has monitored

[1]Ecosystem Services Unit, Winrock International, Arlington, VA 22202, USA. [2]Climate and Land Use Alliance, San Francisco, CA 94104, USA.

*Corresponding author. E-mail: sbrown@winrock.org

Illustrative Examples of Deforestation Reduction Targets from Government, Private-Sector, and Nongovernmental Organizations

Government	Commitment	Source
Brazil	Pledged to cut **gross** deforestation in the Legal Amazon by 80% from historic levels (1996–2005) by 2020	Ref (*4*) and http://www.planalto.gov.br/ccivil_03/_Ato2007-2010/2010/Decreto/D7390.htm
Pará State, (Brazil)	Announced at Rio+20 a target of zero **net** deforestation by 2020	http://www.loterpa.pa.gov.br/?q=node/368
Peru	Target of zero **net** deforestation of primary and natural forests by 2021	http://www.unfccc.int/files/meetings/cop_15/copenhagen_accord/application/pdf/perucphaccord_app2.pdf
European Union	Considers that significant financial support must be provided to developing countries to halt **gross** tropical deforestation by 2020 at the latest	http://eur-lex.europa.eu/LexUriServ/LexUriServ.do?uri=OJ:C:2010:184E:0041:0043:EN:PDF
Corporate	**Commitment**	**Source**
Asia Pulp and Paper	From 1st February 2013 all natural forest clearance has been suspended…. No further clearance of areas identified as forest will take place (**not specified**)	http://www.asiapulppaper.com/system/files/APP%20Forest%20Conservation%20Policy-ENGLISH.pdf
Consumer Goods Forum	Board of the CGF has agreed a resolution pledging to mobilize resources within the respective businesses to help achieve zero **net** deforestation by 2020	http://www.theconsumergoodsforum.com/PDF/WorkingGroups-Accordion/Sustainability/10.Board_Resolutions_on_Deforestation_and_Refrigeration.pdf
Golden Agri-Resources	GAR wants to ensure that its palm oil operations have no deforestation footprint (**not specified**)	http://www.goldenagri.com.sg/pdfs/sustain_policies/GAR_Forest_Conservation_Policy.pdf
Nestlé	Nestlé's ambition is to ensure that its products have not led to deforestation (**not specified**)	http://www.nestle.com/asset-library/documents/media/statements/2012-october/2011-nestle_commitments_on_deforestation_forest_stewardship.pdf
Nongovernment	**Commitment**	**Source**
Greenpeace	Campaigning for zero deforestation (**not specified**) globally, by 2020	http://www.greenpeace.org/usa/en/campaigns/forest/solutions-to-deforestation/
World Wildlife Fund	Call for zero **net** deforestion by 2020 supported by delegates of 67 countries at the Ninth Conference of Parties to the Convention of Biological Diversity in 2008	http://www.panda.org/zerodeforestation

Table 1. Illustrative examples of deforestation reduction targets from government, private-sector, and nongovernmental organizations. In bold, we specify whether these deforestation commitments are gross, net, or not specified.

and reported annually the amount of gross deforestation in the 59% of Brazilian territory defined as the "Legal Amazon" (*4*). INPE's analysis, methods, and data are transparent and credible. Nationally and internationally, these data are reported as deforestation, just like the FAO-FRA data, although their meaning is quite different.

In contrast to net deforestation, gross deforestation is the loss in forest area over a given time period caused by conversion of forest to nonforested land (*5*). An estimate of gross deforestation begins with an agreed-upon definition of forest (commonly based on forest cover, i.e., the proportion of ground surface covered by tree canopies) and the derivation of a map from satellite imagery for the first time period (year 1) that classifies pixels as either forest or nonforest. A second map developed for the same area at the second time period (year 2), using the identical methodology, provides the basis for comparison to identify which forest pixels in year 1 changed to nonforest pixels at year 2. The sum of the area of the pixels that were converted to nonforest in the time interval is the amount of gross deforestation. Although this methodology does not distinguish between loss of forest cover caused by intentional clearing and loss of forest due to natural disturbances, additional analysis can be used to separate the two (*6*). Tree plantations also can be identified in the imagery and mapped separately from native forests, and any harvesting of them can be excluded from estimates of gross deforestation.

With a large suite of satellites to choose from, freely available data from some providers, robust algorithms for the interpretation of the imagery, and increased computing power, monitoring changes in forest cover is no longer a technical challenge (*6*). Numerous bilateral and multilateral agreements are now providing assistance to overcome the institutional and technical capacity and resource constraints in many tropical countries (*7*).

Carbon Emissions and Cobenefits

If the intent is to reduce carbon emissions, conserve biodiversity, and protect hydrological services, then reducing gross deforestation will generally have a better outcome than reducing net deforestation. Net deforestation targets are mostly ambiguous with respect to carbon emissions, biodiversity, and hydrological services because, according to the FAO-FRA methodology, low or even negative net deforestation may be reported even when there are large losses of native forests, if those losses are offset by increases in young secondary forests or tree plantations with inferior carbon, biodiversity, and hydrological service values. For this reason, and to safeguard the customary rights to native forests of indigenous and other local people, UNFCCC negotiators agreed to prohibit counting any carbon accumulation in plantations that substitute for native forests within countries' voluntary commitments to REDD+ (*8*). Sixty-seven countries that have pledged their support to a World Wildlife Fund's (WWF) 2020 goal of zero net deforestation have adopted a definition that, in contrast to the FAO-FRA methodology, explicitly excludes plantations (see the table).

For the purpose of climate change mitigation, it is particularly important to clarify that zero net deforestation does not mean zero net carbon emissions. For example, a zero net deforestation commitment may include conversion of 100,000 ha per year (ha $year^{-1}$) of native forest, with high carbon stocks, to agricultural commodity production and the reforestation of an equivalent area with secondary forest regrowth or new plantations that remove smaller quantities of carbon. If we assume that native forest biomass has an average carbon stock of

150 Mg C ha^{-1} (*9*) and the reforested area sequesters carbon at an annual rate of 5 Mg C ha^{-1} yr^{-1} (*10, 11*), the net annual emissions would be 14.5 Tg C yr^{-1}. Achieving zero net emissions in this example would require that for every 1 ha deforested, 30 ha would have to be reforested.

A Pragmatic Approach

At the national scale, the empirically derived "forest-transition" model has been used to classify countries into phases characterized by little loss of native forest area (pretransition), accelerating rate of forest loss (early transition), decelerating rate of forest loss (late transition), and reforestation (posttransition) (*12*). Efforts to reduce deforestation globally have prioritized the early- and late-transition countries and have helped to slow the loss of diverse, carbon-dense, "primary" forests. Brazil and Indonesia are emblematic examples of these "transition" countries, and Brazil has been the most successful at both setting and making progress toward a clear and ambitious deforestation reduction target (see the table). Pretransition countries like Gabon and Guyana may achieve their forest transitions with proportionally less deforestation, and they should be encouraged to do so. Posttransition countries like Costa Rica and India are actively reforesting, and in Costa Rica's case, this is part of a plan to reach economy-wide carbon neutrality by 2021 (*13*). Although the boundaries between these phases are porous and each country remains its own idiosyncratic case, at a general level, the phases define important differences among countries.

Deforestation in the Tesso Nilo National Park, Riau province, Indonesia, May 2013.

CREDIT: BAGUS INDAHONO/EPA/NEWSCOM

Global zero deforestation targets are particularly challenging. On the one hand, if the target is zero gross deforestation globally, as urged by the European Parliament (see the table), it cannot accommodate any expansion of infrastructure or agricultural production in native forest areas, including in pretransition countries. This seems both infeasible and inequitable. On the other hand, a global zero net deforestation target equates protecting high carbon/biodiversity/hydrologic-service–value native forests with the planting of lower-value new forests.

Ambitious targets for reductions in gross deforestation and for reforestation that take into account differences in forest-transition phases among countries are likely to prove more actionable than a one-size-fits-all approach. For example, the goal of eliminating deforestation from agricultural commodity production is possible at the global scale because big gains in productivity can be achieved by improving agricultural practices with existing technologies and because there are large expanses of previously cleared, underused land in some of the major commodity-producing countries like Brazil (*14*) and Indonesia (*15*). Hence, there are broad synergies, both globally and within these transition countries, among the goals of eliminating deforestation for commodity production, intensifying agricultural production, and restoring degraded lands. Indeed, two major commodity-producing companies with large historic responsibility for deforestation in Indonesia (Golden Agri-Resources and Asia Pulp and Paper) have announced their own zero deforestation policies (see the table) where others have not (see the figure).

In tropical countries that have little nonforested land either suitable or available for agriculture, including several in Latin America and Central Africa, zero deforestation would mean halting agricultural expansion. Without compelling economic development alternatives, this may prove difficult to sustain, especially when global demand for food, fiber, and bioenergy continues to grow (*16*). In these pre- to early-transition countries, nonzero targets for deforestation—integrated within robust land-use planning, rural development, and governance initiatives—can be both ambitious and suited to national circumstances.

As an idea, zero deforestation is compelling. It seems simple and precise, and therefore attractive. But as a global target, it means much more than what is achievable if the meaning is "gross," and much less if it is "net." Intentionally or not, these terms are being used ambiguously and sometimes interchangeably, which fosters confusion and sets the stage for perverse outcomes. Governments, corporations, and nongovernmental organizations should instead set separate, ambitious targets for reductions in gross deforestation and for reforestation. Some gross deforestation targets, including for commodity production in transition countries, could be actionable at or near zero; others could not. Until targets are clarified, and metrics agreed upon, zero may mean nothing at all.

References and Notes

1. FAO-FRA, "Global forest resources assessment 2010" (FAO forestry paper 163, FAO, Rome, 2010); www.fao.org/forestry/fra/fra2010/en.
2. FAO-FRA, "On definitions of forest and forest change" (Working paper 33, FAO, Rome, 2000).
3. A. Grainger, *Proc. Natl. Acad. Sci. U.S.A.* **105**, 818 (2008).
4. INPE, Projeto Prodes; www.obt.inpe.br/prodes/index.php.
5. GOFC-GOLD, "A sourcebook of methods and procedures for monitoring and reporting anthropogenic greenhouse gas emissions and removals associated with deforestation, gains and losses of carbon stocks in forests remaining forests, and forestation" (GOFC-GOLD Report version COP18-1, GOFC-GOLD Land Cover Project Office, Wageningen University, Netherlands, 2012).
6. M. C. Hansen *et al.*, *Proc. Natl. Acad. Sci. U.S.A.* **105**, 9439 (2008).
7. D. J. Baker *et al.*, *Environ. Sci. Policy* **13**, 249 (2010).
8. UNFCCC, CP/2010/7/Add.1; http://unfccc.int/resource/docs/2010/cop16/eng/07a01.pdf#page=2.
9. S. S. Saatchi *et al.*, *Proc. Natl. Acad. Sci. U.S.A.* **108**, 9899 (2011).
10. IPCC (*11*), reports an average rate of C sequestration in reforested natural tropical forests of 10 Mg biomass ha^{-1} year^{-1} during the first 20-year period, converted assuming 1 Mg biomass = 0.5 Mg C.
11. IPCC, *2006 IPCC Guidelines for National Greenhouse Gas Inventories* vol. 4, *Agriculture, Forestry, and Other Land Use* (IGES, Hayama, Japan, 2007), chapt. 4.
12. N. Hosonuma *et al.*, *Environ. Res. Lett.* **7**, 044009 (2012).
13. BBC News, Costa Rica bids to go carbon neutral, 12 August 2008; http://news.bbc.co.uk/1/hi/americas/7508107.stm.
14. P. Barreto, D. da Silva, How can one develop the rural economy without deforesting the Amazon? [Amazon Institute of People and Environment (IMAZON), Belém, Brazil 2013]; www.imazon.org.br/publications/books/how-can-one-develop-the-rural-economy-without-deforesting-the-amazon.
15. N. Sizer, The False Choice Between Palm Oil and Indonesian Forests, WRI Insights, World Resource Institute (2013); http://insights.wri.org/news/2012/11/false-choice-between-palm-oil-and-indonesian-forests
16. OECD-FAO, "OECD-FAO agricultural outlook 2013" (OECD Publishing, Paris, 2013); http://dx.doi.org/10.1787/agr_outlook-2013-en.

Acknowledgments: S.B. received a grant from the ClimateWorks Foundation, a member of the Climate and Land Use Alliance. D.Z. conceived the idea for the paper, S.B. undertook the analysis and review of the literature, and both prepared the manuscript. We thank E. Burrows and E. Swails of Winrock, as well as D. Lee.

10.1126/science.1241277

CLIMATE CHANGE

Out of the African Humid Period

Edouard Bard

Data from an East African marine core help to explain the transition from the more humid conditions in the early Holocene to today's arid climate.

During the last deglaciation, climatic changes allowed human societies to develop and flourish in the subtropical zone from North Africa to Asia. On page 843 of this issue, Tierney and deMenocal (*1*) report details of these climatic changes in North Africa. They show that between 21,000 and 11,500 calendar years before present (cal. yr B.P.), millennium-long periods of subtropical aridity corresponded to transient phases of intense iceberg melting into the North Atlantic. The Holocene period, starting ~11,500 cal. yr B.P., was characterized by a prominent increase in rainfall triggered by summer insolation values higher than those of today. The spatial extent and temporal limits of this period, called the African Humid Period in North Africa, are still debated (see the figure).

From the early Holocene to the present day, summer insolation in the subtropical zone has slowly decreased as a result of changes in Earth's orbit around the Sun. This gradual change over 10 millennia contrasts with the complexity of rainfall proxy observations gathered from marine coastal sediments, lake sediments, and cave stalagmites. The African Humid Period ended abruptly ~5000 cal. yr B.P. in many locations, such as western North Africa (*2*, *3*) and northern Kenya (*4*). In other places, changes occurred gradually over several millennia—for example, in the central Sahara (*5*) and the southern Arabian Peninsula (*6*).

The increasingly arid conditions at the end of the African Humid Period forced human agropastoral societies to improve their organization in order to optimize natural resources, in particular freshwater supplies (*7*). As a result of growing demographic pressure in an environment that was again becoming hostile, Neolithic communities were forced to concentrate in river valleys and to develop irrigation systems. These complex transformations help explain the rise of the Egyptian, Sumerian, and Harappan civilizations that flourished along major rivers such as the Nile, Euphrates, Tigris, and Indus.

Climate projections for the next century show that the subtropical zone is likely to experience major rainfall changes (*8*). It is thus crucial to understand how some ancient societies could adapt through technical and political innovations, whereas other human groups were forced to migrate. The spatial variability of the mid-Holocene arid transition provides a further complication. The exposure of some Neolithic societies to a stronger climatic forcing than others may explain their different fates: success and domination, or collapse and exodus.

Why was there so much spatial variability at the end of the African Humid Period? The prevailing theory is that the disappearance of vegetation accelerated the drying of the continent through regional changes of albedo, water storage in roots and soils, and evapotranspiration by plants. Simulations with climate models representing the vegetation and its effect on regional climate (*9*) suggest that the efficiency of this biogeophysical feedback may have varied with longitude, which would be compatible with observations. In some places, vegetation diversity may have promoted a gradual termination of the African Humid Period (*10*).

However, Tierney and deMenocal show that the biogeophysical feedback may not be the only cause of the abrupt climate response, particularly in regions that were not covered by abundant vegetation in the early Holocene. This was probably the case for the northeastern corner of Africa, which prompted Tierney and deMenocal to look for a new record from the Horn of Africa. In a marine sediment core from the Gulf of Aden (see the figure), they analyzed leaf waxes transported by winds from the African continent. This site is under the double influence of the African climate and the Indian Ocean, with its summer monsoon winds bringing moisture to the region and picking up dust

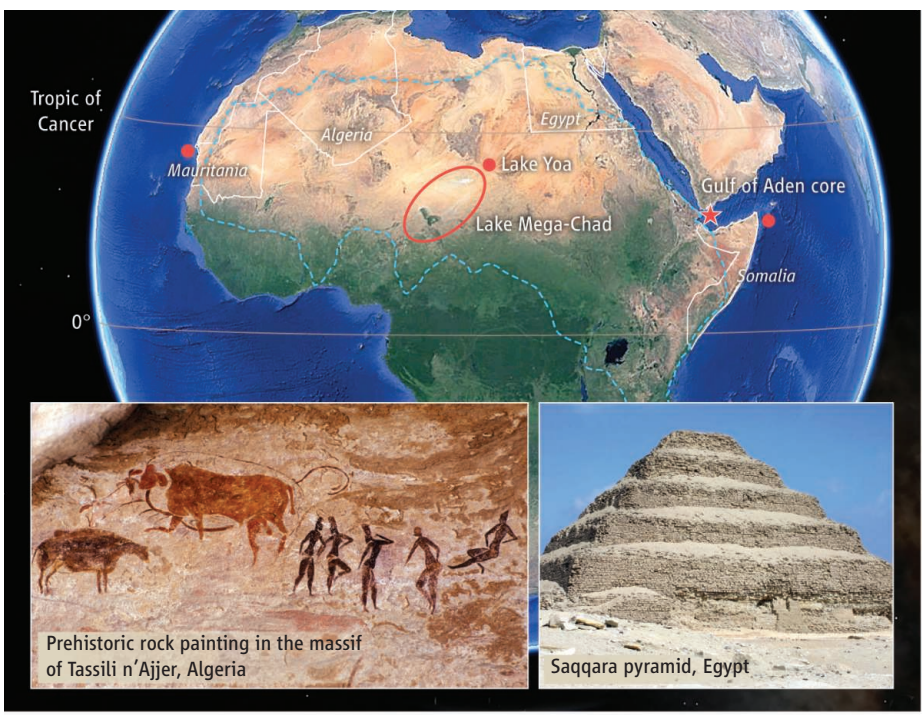

North African climate, then and now. The Landsat image shows modern forests in green and sandy and rocky deserts in yellow and brown. During the African Humid Period ~11,500 to 5000 years ago, this region was much more humid, as shown by the contours (dashed line) marking the zone of high water levels (*15*). Tierney and deMenocal have studied a sediment core from the Gulf of Aden that provides detailed insights into the beginning and end of the African Humid Period. The work complements previous studies of sediment cores taken off the coasts of Mauritania (*2*, *3*) and Somalia (*11*) and from Lake Yoa (*5*, *12*) and Lake Chad (*14*). The African Humid Period and its termination affected human civilizations, as illustrated by a rock painting from the Tassili n'Ajjer, Algeria, and the pyramid of pharaoh Djoser in Saqqara, Egypt.

Collège de France and CEREGE (Aix-Marseille University, CNRS, IRD, CdF), Aix-en-Provence F-13545, France. E-mail: bard@cerege.fr

Published by AAAS

over the East African continent. In a nearby deep-sea sediment core off the Somalian coast, Holocene aridification over the course of 2000 years was recorded from the radiogenic isotope signature of wind-transported dust (*11*). Tierney and deMenocal instead measured the deuterium-to-hydrogen ratio (D/H) of the leaf waxes; this ratio is directly linked to the isotopic composition of precipitation and hence to total rainfall.

By comparing their Gulf of Aden record with published records, Tierney and deMenocal conclude that the African Humid Period ended abruptly within a few centuries and was synchronous in the western and eastern part of Africa. By considering modern climate observations and model simulations, they propose that East African rainfall responded in a nonlinear way to surface temperatures in the Indian Ocean.

Tierney and deMenocal's Gulf of Aden record provides key information for understanding North African climate during the Holocene. However, much research is still needed to build a comprehensive view of hydroclimatic changes during the African Humid Period. Most published records are based on proxies that are difficult to link unequivocally to rainfall changes. For example, records of wind-transported material reflect both the decrease in vegetation cover and the increase in the dust source area caused by widespread lake desiccation. Documenting these parameters requires information from multiple proxies measured in the same continental or marine archives. The time resolution of records must also be improved by increasing the sampling rate for these proxies. Decadal-to-seasonal profiles measured with geochemical scanners (*12*) allow studying African Humid Period transitions without relying on statistical corrections.

More continuous records are needed from north of the Gulf of Aden, along the Nile Valley and the Red Sea. Obtaining new data from central North Africa is also crucial for backing up observations made in sediments of the small Lake Yoa (*5*, *12*). Of particular importance is the Holocene history of Lake Chad, which was at least 10 times as large during the African Humid Period than it is today (*13*). Pollen data from Lake Chad (*14*) indicate that vegetation changes occurred progressively over about two millennia, but that century-scale variability was superimposed on the mid-Holocene drying trend. Additional proxies remain to be measured and longer continuous cores to be collected and studied from Lake Chad to advance understanding of the African Humid Period.

References

1. J. E. Tierney, P. B. deMenocal, *Science* **342**, 843 (2013); 10.1126/science.1240411.
2. P. B. deMenocal *et al.*, *Quat. Sci. Rev.* **19**, 347 (2000).
3. D. McGee, P. B. deMenocal, G. Winckler, J. B. W. Stuut, L. I. Bradtmiller, *Earth Planet. Sci. Lett.* **371-372**, 163 (2013).
4. Y. Garcin, D. Melnick, M. R. Strecker, D. Olago, J.-J. Tiercelin, *Earth Planet. Sci. Lett.* **331**, 322 (2012).
5. S. Kröpelin *et al.*, *Science* **320**, 765 (2008).
6. D. Fleitmann *et al.*, *Quat. Sci. Rev.* **26**, 170 (2007).
7. R. Kuper, S. Kröpelin, *Science* **313**, 803 (2006).
8. Intergovernmental Panel on Climate Change, Working Group I Contribution to the IPCC Fifth Assessment Report, T. Stocker *et al.*, Eds. (World Meteorological Organization and United Nations Environment Programme, Geneva, Switzerland, 2013).
9. V. Brovkin, M. Claussen, *Science* **322**, 1326 (2008).
10. M. Claussen, S. Bathiany, V. Brovkin, T. Kleinen, *Nat. Geosci.* 10.1038/ngeo1962 (2013).
11. S. Jung, G. R. Davies, G. M. Ganssen, D. Kroon, *Earth Planet. Sci. Lett.* **221**, 27 (2004).
12. P. Francus *et al.*, *Sedimentology* **60**, 911 (2013).
13. M. Schuster *et al.*, *Quat. Sci. Rev.* **24**, 1821 (2005).
14. P. G. C. Amaral *et al.*, *Clim. Past* **9**, 223 (2013).
15. N. Roberts, *The Holocene, An Environmental History* (Blackwell, Oxford, 1998).

10.1126/science.1246519

CANCER

Potential of the Synthetic Lethality Principle

Elucidating the first principles of synthetic lethality in cancer, including biological context, will assist clinical translation.

Sebastian M. B. Nijman[1] and Stephen H. Friend[2]

Most cancer mutations, including those causing a loss of function, are not directly "druggable" with conventional small-molecule drugs or biologicals, such as antibodies. Thus, despite our growing knowledge of mutations that drive cancer progression, there remains a frustrating gap in translating this information into the development of targeted treatments that kill only cancer cells. An approach that exploits a concept from genetics called "synthetic lethality" could provide a solution. But it has been over 15 years since that framework was proposed (*1*). Does the synthetic lethality principle still have the potential for treating cancer?

Synthetic lethality, first observed in the fruit fly *Drosophila melanogaster* almost a century ago, describes a phenomenon where only the simultaneous perturbation of two genes results in a deadly combination. Thus, cancer aberrations that are not readily targetable [e.g., tumor suppressor proteins such as retinblastoma protein 1 (RB1) and p53 (*TP53*); oncogenes such as *RAS* and c-*MYC*] could be indirectly exploited by inhibiting the product of another gene (*2*–*4*). The broader definition of synthetic lethality has also been referred to as "nononcogene addiction" or "induced essentiality" to distinguish it from its classical meaning in genetics. In the budding yeast *Saccharomyces cerevisiae*, most genes display numerous synthetic lethal interactions (*5*, *6*), which may also apply to many human cancer genes. Furthermore, "passenger" mutations, which do not directly contribute to tumorigenesis, and even rewiring of cellular networks that give rise to a cancerous state, may also be exploited with the synthetic lethal principle. However, to date, only a single synthetic lethal interaction has shown therapeutic promise. Why have synthetic lethal therapies largely failed to deliver?

The proof of principle that the synthetic lethality concept is clinically translatable is the efficacy of drugs that target the single-strand DNA repair enzyme poly(ADP-ribose) polymerase (PARP) in tumors with mutations in the *BRCA1* and *BRCA2* genes (*7*). These genes encode tumor suppressor proteins that help repair damaged DNA. The remarkable ability of tumors to acquire resistance to PARP inhibitors by regaining BRCA function shows that PARP-targeting drugs act through a synthetic lethal mechanism (*8*). This finding triggered an intensive search for synthetic lethal drug targets akin to PARP. In particular, large-scale RNA interference screens (in which RNA molecules block the expression of specific genes) have led to a growing list of potential synthetic lethal

[1]CeMM Research Center for Molecular Medicine of the Austrian Academy of Sciences, Vienna, Austria. [2]Sage Bionetworks, 1100 Fairview Avenue North, Seattle, WA 98109, USA. E-mail: snijman@cemm.oeaw.ac.at; friend@sagebase.org

gene targets. It is too soon to know if any of these new drug targets can be translated to the clinic. A major obstacle is that genetic and pharmacological perturbations do not always have the same functional outcome. This means that a genetic synthetic lethal relationship may never be realized pharmacologically. Despite this understanding, there is a growing concern that many synthetic lethal interactions are not easily transferred beyond the models used for screening, challenging synthetic lethality as a broadly applicable therapeutic concept. Indeed, only a few synthetic lethal drug targets are in clinical development, and none are as compelling as the BRCA-PARP paradigm.

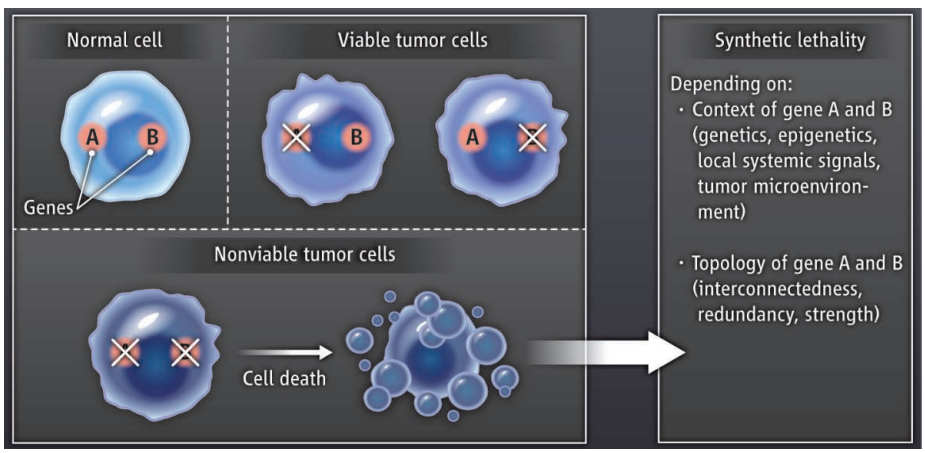

Context and topology. Identifying synthetic lethal interactions (when simultaneous mutations in two genes are lethal to the cell) must consider the context of their interactions, such as genetic and epigenetic variability, the microenvironment, and local systemic signals. Topological characteristics (strength, connectivity, degree, and redundancy) of human synthetic lethal interaction networks are also an important consideration, but are largely unknown.

A major obstacle to achieving synthetic lethal therapies is a lack of insight into the first principles that govern the phenomenon in cancer cells. For example, there is little understanding of how variability in genetics, epigenetics, systemic signals, and the microenvironment influences synthetic lethal interactions (see the figure). Too often, a line of investigation focuses on "what works" without considering the context or analyzing unexpected or even contradictory results. Phenotypes are rarely conserved across a panel of biologically diverse replicates (humans), indicating that context matters. This is especially important in cancer, where molecular heterogeneity (contextual variability) is greater than for any other disease. Indeed, delving into biological context can be highly informative and provide therapeutic leads. For instance, colon cancer cells with activating and oncogenic mutations in the gene *BRAF* fail to respond to BRAF inhibitors. However, these cancer cells display a feedback mechanism that induces signaling by the epidermal growth factor receptor, negating the effects of BRAF inhibition. This "bigger picture" view yielded a rationale to combine BRAF inhibitors with epidermal growth factor inhibitors, a solution that blocked growth of seemingly "drug-resistant" cancer cells (*9*, *10*).

Synthetic lethal interactions may be no less context dependent than other cellular phenotypes. The opposite actually may be true. In yeast, single gene perturbations that lead to fitness defects (mutations in essential genes) are evolutionarily more conserved than defects induced by two mutations (*11*). As clonal evolution during tumorigenesis results in a divergence of cell states (through the progressive accumulation of genetic and epigenetic abnormalities in multiple and different genes), context dependencies may be even more pronounced for drugs that exploit synthetic lethality than for those that target "oncogene addiction," in which only one gene that is required for maintaining malignancy is targeted.

The importance of context is also revealed in the comparison of genes that are differentially essential in two yeast strains (*12*). It was predicted that some of these conditional essential genes could be explained by mutations in synthetic lethal interactors in the affected strain. However, crossing the two strains and analyzing the frequency of viable spores showed that most of the conditional essential interactions are due to multiple genes acting in concert. This implies that synthetic interactions may also be susceptible to genetic modifiers and that quantitative differences in gene activity (between cell types, tumors, and individuals) can affect synthetic lethality. Moreover, stochastic variation in gene activity in the worm *Caenorhabditis elegans* can affect the penetrance of synthetic lethal interactions (*13*). This suggests that context will impact synthetic lethality in human cancer cells and argues for a systematic study of this phenomenon to guide more successful clinical translation. Such studies should focus on identifying co-occurring mutations in tumors that can modify the penetrance of synthetic lethal interactions. This can be achieved, for instance, by testing the synthetic lethal interaction in a large panel of well-characterized cancer cell lines or by using engineered isogenic cell lines that model the variability observed in patients in a defined genetic context. Although these cell culture studies would not directly address the role of the tumor microenviroment, any identified genetic modifiers could serve as biomarkers to predict which tumors are most likely to display the synthetic lethal interaction. Ultimately, performing a genome-wide screen for genetic modifiers that enhance or suppress a specific synthetic lethal interaction could reveal those that are least sensitive to contextual variability, and thus would be more likely to be of general use in the clinic. Results of such suppressor-enhancer screens from a variety of candidate synthetic lethal interactions may reveal more fundamental rules that govern context dependency.

There are several additional fundamental aspects of synthetic lethal interactions in human cells that have yet to be systematically explored. Some of these relate to network topology—the parameters that describe the connectivity structure of synthetic lethal interaction. For example, quantitative insights into the strength of synthetic lethality in human cells are lacking; yet this may determine the eventual therapeutic index—the concentration of a drug required for toxic effects divided by the concentration required for therapeutic effects—that can be achieved in patients. Such knowledge will be instructive for selecting the most promising synthetic lethal interactions for drug discovery and development (*4*). Indeed, compared to normal cells, cells lacking *BRCA1/2* are almost three orders of magnitude more sensitive to PARP inhibitors. By contrast, most other described synthetic lethal interactions in human cells are much less striking, and some may not even conform to the strictest definition requiring that each single gene perturbation alone has no effect on cell viability.

Topological information may point to the best cellular processes for identifying syn-

CREDIT: C. BICKEL/*SCIENCE*

thetic lethal interactions. Which types of genes or cellular processes tend to display the most interactions (interconnectivity) may instruct functional genomics efforts. Screens in model organisms such as yeast and worm indicate that proteins involved in chromatin regulation such as histone deacetylases display the most frequent genetic interactions (*5*, *14*).One explanation is that transcriptional regulation is well positioned for buffering perturbations by tuning the expression of multiple genes simultaneously. However, there are no experiments to corroborate this hypothesis in human cancer cells. Even for DNA synthesis and repair pathways that represent highly conserved functional modules (an obvious place to look for synthetic lethality), an inventory of synthetic lethal interactions in human cells has still not materialized.

Other largely uncharted topological areas concern the number of synthetic lethal connections between genes and their distribution and redundancy. The complexity of a human cell compared to a yeast cell may suggest that human cells display more redundancy, making them more resilient to perturbations and implying that synthetic lethal interactions would be less frequent. Current and next-generation genomics tools will help to answer these questions.

In the near term, the ability to perform personalized screens for synthetic lethal interactions on ex vivo tissue samples may provide clinically useful knowledge until the long-term goal of better understanding the biological rules can be achieved. Until a thorough understanding of synthetic interactions and the ability to assess their promise is in hand, their validation and translation will remain hit-and-miss. Recognizing the challenges facing gene therapy and immune therapy paved the way for moving from concept to clinical reality, and there is hope that learning the principles that govern synthetic lethal interactions in cancer will do the same.

References

1. L. H. Hartwell, P. Szankasi, C. J. Roberts, A. W. Murray, S. H. Friend, *Science* **278**, 1064 (1997).
2. W. G. Kaelin, Jr., *Nat. Rev. Cancer* **5**, 689 (2005).
3. J. Luo, N. L. Solimini, S. J. Elledge, *Cell* **136**, 823 (2009).
4. A. Ashworth, C. J. Lord, J. S. Reis-Filho, *Cell* **145**, 30 (2011).
5. M. Costanzo *et al.*, *Science* **327**, 425 (2010).
6. M. E. Hillenmeyer *et al.*, *Science* **320**, 362 (2008).
7. P. C. Fong *et al.*, *N. Engl. J. Med.* **361**, 123 (2009).
8. S. L. Edwards *et al.*, *Nature* **451**, 1111 (2008).
9. A. Prahallad *et al.*, *Nature* **483**, 100 (2012).
10. R. B. Corcoran *et al.*, *Cancer Discov.* **2**, 227 (2012).
11. A. Roguev *et al.*, *Science* **322**, 405 (2008).
12. R. D. Dowell *et al.*, *Science* **328**, 469 (2010).
13. A. Burga, M. O. Casanueva, B. Lehner, *Nature* **480**, 250 (2011).
14. B. Lehner, C. Crombie, J. Tischler, A. Fortunato, A. G. Fraser, *Nat. Genet.* **38**, 896 (2006).

10.1126/science.1244669

CHEMISTRY

A Nickel Finish Protects Silicon Photoanodes for Water Splitting

Ultrathin nickel coatings allow silicon to act as the oxygen-generating electrode in the direct formation of hydrogen from water with sunlight.

John A. Turner

The large-scale generation of hydrogen from water with sunlight could provide a sustainable source of this industrially important gas, but could also provide fuel for vehicles and a storage medium for solar energy. The direct photoelectrochemical (PEC) splitting of water into hydrogen and oxygen, which combines a photovoltaic cell and an electrolyzer into a single device, remains an important goal (*1*). One problem is that some of the materials that work well for photovoltaics, such as n-type silicon (Si), corrode in electrolyzer solutions. On page 836 of this issue, Kenney *et al*. (*2*) show that a 2-nm-thick nickel (Ni) film on an n-type silicon semiconductor not only provides some stability against corrosion when used for oxygen evolution in a PEC configuration, but also generates a high voltage via a metal-insulator-semiconductor (MIS) configuration.

Hydrogen is used today primarily in the petroleum refining industry and for ammonia synthesis. More than 50 million tons of hydrogen are produced worldwide every year from fossil fuel feedstocks that generate CO_2 emissions. In a carbon-free energy system, however, hydrogen must be produced from water splitting by means of renewable resources such as wind and solar energy. As solar energy is our largest resource, combining photovoltaics with electrolysis would seem to be the clear choice for renewable hydrogen production (*3*), but to date the only commercially available pathway in this scheme is the electrolysis step. Unfortunately, hydrogen from electrolysis with photovoltaic-generated electricity is far too expensive to be commercially viable, so other pathways must be considered.

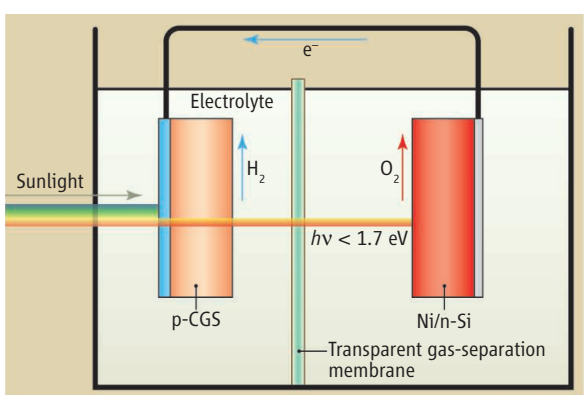

Doubling up for solar hydrogen production. A design configuration is shown where two separate semiconductors with different band gaps are illuminated in series to form a tandem system for water splitting. Sunlight illuminates the p-type electrode, which absorbs the visible light and transmits the red and near-infrared light that then illuminates the n-type electrode. The work of Kenney *et al*. shows that a thin nickel film can protect n-type silicon from corrosion by the electrolyte.

In a PEC water-splitting system, a semiconductor electrode is immersed in an aqueous solution, and when illuminated it splits water directly at the semiconductor's surface. For the use of n-type silicon, the study of Kenney *et al*. presents several critical results. The 2-nm Ni film combined with the thin native silicon oxide layer (SiO_x) that forms on silicon exposed to air, and the surface of the nickel oxidized in the electrolyte to form nickel oxide (NiO_x). The resulting NiO_x/Ni/SiO_x/Si device generated a voltage of 500 mV when exposed to light, with no need for the thermally grown SiO_x layer that has traditionally been required to achieve that voltage (*4*).

National Renewable Energy Laboratory, 1617 Cole Boulevard, Golden, CO 80401, USA. E-mail: john.turner@nrel.gov

This combination stabilized and catalyzed the interface for oxygen evolution. An unexpected finding is that lithium ions from the electrolyte further improved the stability.

Formally, this device could be viewed as a buried junction, where the charge carriers form at the junction buried underneath the 2-nm nickel layer (the MIS structure). However, thicker 5- and 10-nm nickel films did not display the same high voltage, so the aqueous solution must play a role in the operation of this device. The authors attribute this effect to incomplete screening of the solution by the Ni/NiO_x layer.

Recent technoeconomic analysis (*5*) shows that to produce cost-competitive hydrogen via a PEC process, the solar-to-hydrogen efficiency should be at least 15% and perhaps greater than 20% (*6*). Other studies have shown that to achieve this efficiency, not only must the semiconductor electrode have the same solid-state properties as current photovoltaic devices, it also must have a tandem configuration (*7*–*9*). In a tandem configuration, two semiconductors with different band gaps are illuminated in series, so that the top semiconductor with the higher band gap absorbs the visible light and transmits the rest through to the bottom cell with a lower band gap. Thus far, the only PEC system that shows greater than 10% water-splitting efficiency is a tandem device composed of high-efficiency III-V semiconducting materials (*10*), such as gallium arsenide. This tandem configuration limits the semiconductors that can be used to pairs of highly crystalline materials that have matching crystal lattices.

An alternative tandem scheme presented by Nozik (*11*, *12*) relaxes these requirements by making use of separated p-type and n-type photoelectrodes with two different band gaps. This separated p-n arrangement eliminates the need to either match lattices or create stacks of dissimilar materials, and further allows the use of polycrystalline materials. Nozik showed that this configuration could perform unassisted water splitting, but the efficiency was limited by the photoanode. There are a number of excellent p-type photoelectrodes, including silicon, that can produce hydrogen with high efficiency, but no known n-type photoelectrodes (photoanodes) can produce oxygen with high efficiency.

The reason why n-type silicon was thought to be unsuitable for oxygen evolution was its instability in basic conditions and the formation of a thick oxide film that blocks the reaction in acidic conditions. However, the results of Kenney *et al*. show that a thin Ni film can protect the n-Si surface for oxygen evolution, as well as afford a good photovoltage. Thus, their result opens up the possibility of using this electrode in a p-n tandem configuration by coupling it with a photocathode that has a wider band gap, such as p-type copper gallium diselenide (p-CGS).

A tandem configuration of these two materials has a maximum theoretical efficiency greater than 25% (*9*). As shown in the figure, sunlight first illuminates p-CGS, which has a band gap of 1.68 V. The light that is not adsorbed illuminates the Ni-coated Si photoanode; when CGS is deposited on transparent conducting glass substrates, it shows good transparency for the longer-wavelength light below its band gap (*13*). Such a configuration illustrates the ability of a PEC system to integrate polycrystalline thin films with single-crystal photoelectrodes into a viable tandem device; this would be more difficult to accomplish with a solid-state device.

The results of Kenney *et al*. are a long way from being integrated into a viable water-splitting device. However, they do point the way toward reconsideration of a long-held belief about n-type silicon as a photoanode for oxygen evolution. The results open up some additional possibilities for a solar water-splitting system with efficiencies of 15% or greater.

References

1. A. Bard, M. A. Fox, *Acc. Chem. Res.* **28**, 141 (1995).
2. M. J. Kenney *et al*., *Science* **342**, 836 (2013).
3. D. V. Esposito, I. Levin, T. P. Moffat, A. A. Talin, *Nat. Mater.* **12**, 562 (2013).
4. J. A. Turner, *Science* **285**, 687 (1999).
5. B. A. Pinaud *et al*., *Energy, Environ. Sci.* **6**, 1983 (2013).
6. D. James, G. N. Baum, J. Perez, K. N. Baum, *Technoeconomic Analysis of Photoelectrochemical (PEC) Hydrogen Production* (Directed Technologies Inc., Arlington, VA, 2009).
7. R. Rocheleau, E. Miller, *Int. J. Hydrogen Energy* **22**, 771 (1997).
8. M. Hanna, A. Nozik, *J. Appl. Phys.* **100**, 074510 (2006).
9. S. Hu, C. Xiang, S. Haussener, A. D. Berger, N. S. Lewis, *Energy Environ. Sci.* **6**, 2984 (2013).
10. O. Khaselev, J. A. Turner, *Science* **280**, 425 (1998).
11. A. J. Nozik, *Appl. Phys. Lett.* **30**, 567 (1977).
12. A. J. Nozik, *Annu. Rev. Phys. Chem.* **29**, 189 (1978).
13. J. Kaneshiro *et al*., in *Photovoltaic Specialists Conference (PVSC), 2010 35th IEEE* (2010), pp. 002448–002451; 10.1109/PVSC.2010.5614163.

10.1126/science.1246766

EVOLUTION

Transposons Up the Dosage

Edward B. Chuong and Cédric Feschotte

A family of transposable elements have played an important role in the evolution of dosage compensation in fruit flies.

It took more than three decades—and a Nobel Prize in 1983—for Barbara McClintock's discovery of transposition and mobile genetic elements to become widely accepted. However, her vision of transposons as "controlling elements" and architects of genome organization has remained controversial. On page 846 of this issue, a report by Ellison and Bachtrog brings McClintock's prescient ideas back to center stage (*1*). They show that transposition has shaped the regulatory landscape of an entire chromosome at least twice in the evolutionary history of *Drosophila*, facilitating the emergence of novel sex chromosomes.

In species such as humans and fruit flies, where sex is established by an XX/XY chromosome system, the X chromosome is present in two copies in females (XX) and one copy in males (XY). A dosage compensation mechanism is necessary to ensure that genes located on the X chromosome are expressed at equivalent levels in both sexes. Curiously, humans and flies achieve this feat in opposite ways: in humans, one of the X chromosomes is inactivated in females, whereas in flies the transcription of X-linked genes is up-regulated by about twofold in males (*2*). Mechanisms of dosage compensation are remarkable in that they must be established rapidly during evolution for a new sex chromosome system to be able to emerge, and they must act at the level of an entire chromosome to regulate hundreds of genes. How do such mechanisms evolve?

Several lineages of *Drosophila*, which have recently evolved sex chromosomes, provide a unique system to address this question. *Drosophila miranda*, in addition to its ancestral >60 million year old "XL" chromosome, which is homologous to the X of *D. melanogaster*, has a younger

Department of Human Genetics, University of Utah School of Medicine, Salt Lake City, UT 84112, USA. E-mail: edwardc@genetics.utah.edu; cedric@genetics.utah.edu

15-million-year-old "XR" chromosome, and a "neo-X" that emerged just 1 million years ago (*1*) and that is unique to *D. miranda* (see the figure). Whereas XL and XR exhibit full dosage compensation, the dosage compensation on the neo-X is still incomplete—a sign of its relative youth.

In *D. melanogaster,* dosage compensation requires the male-specific lethal (MSL) complex, which binds to MSL recognition elements (MREs) along the male X chromosome, from which it spreads to create a localized chromatin state that promotes a two-fold increase in gene transcription levels (*3*). Previous experiments in *D. miranda*, including mapping of MSL binding sites using chromatin immunoprecipitation followed by deep sequencing (ChIP-seq), revealed that the MSL complex is also responsible for establishing dosage compensation on the ancestral XL chromosome and on the newly evolved XR and neo-X chromosomes (*4*).

Ellison and Bachtrog delved more deeply into the evolutionary origins of the MRE on the neo-X of *D. miranda*. Unexpectedly, they uncovered that about half of 41 sites most robustly bound by MSL on the neo-X map to repetitive elements derived from a single transposon family named ISX. They found that ISX elements were amplified shortly after the formation of the neo-X, about 1 million years ago, and are almost entirely absent from the rest of the genome. But where did ISX come from? The ISX family is nearly identical, except for a 10–base pair (bp) internal deletion, to another family of *Helitron*-type transposons called ISY, which unlike ISX is dispersed throughout the *D. miranda* genome. By creating transgenic lines of *D. melanogaster* where various ISX or ISY elements are individually inserted into an autosomal chromosome, the authors demonstrate that ISX—but not ISY—successfully recruited the MSL complex at the ectopic insertion site and that the 10-bp deletion was necessary to create a functional MRE in ISX.

Ellison and Bachtrog go on to show that the recruitment of ISX for dosage compensation on the neo-X mirrors a previous episode of transposon recruitment on the 15-million-year-old XR chromosome. They found that the XR chromosome is highly enriched for yet another related family of *Helitrons*, named ISXR, which also recruits the MSL complex. The distribution of ISXR on the XR chromosome parallels that of ISX in the neo-X. Individual copies of ISXR show many more changes in their sequence compared with ISX (and ISY) but, paradoxically, exhibit stronger MSL binding. Thus, the same lineage of transposons has been co-opted or "domesticated" at two different time points to facilitate the evolution of dosage compensation in *Drosophila*. As such, ISX and ISXR provide evolutionary snapshots capturing different phases of the transposon domestication process.

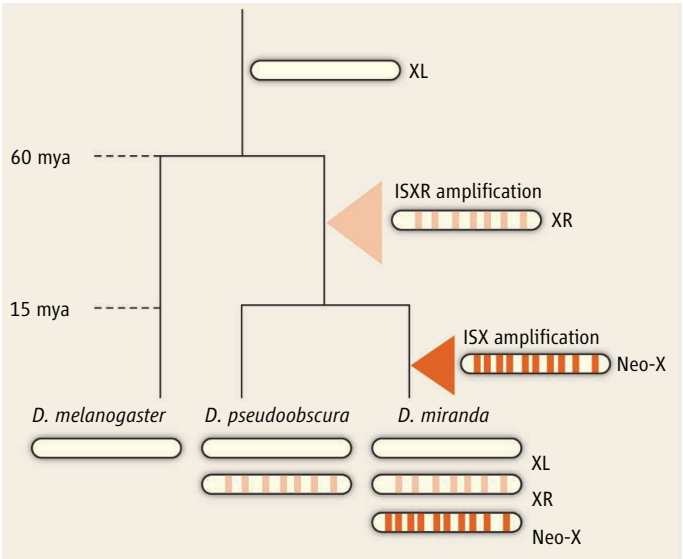

Jumping genes drive evolution of dosage compensation. A schematic depicting the phylogenetic relationship between *D. melanogaster*, *D. pseudoobscura*, and *D. miranda*. Triangles represent waves of transposon amplification that distributed MSL binding sites across the XR and neo-X, facilitating the evolution of dosage compensation in novel sex chromosomes. Million years ago (mya).

Based on these results, the authors propose a three-step model for transposon-mediated evolution of dosage compensation: (i) A mutation introduces a functional MRE binding site in a progenitor transposon; (ii) the newly "functional" transposon replicates throughout the genome, and adaptive insertions on the nascent X chromosome are selectively retained; and (iii) binding sites are gradually fine-tuned while nonfunctional regions of the transposon are eroded by point mutations. The authors speculate that ISX has entered the third stage of domestication, whereas ISXR has essentially completed the process, as attested by its stronger MSL recruitment activity and the more profound sequence divergence of its nonfunctional parts. Importantly, the model predicts that the sequence signatures of domesticated transposons in *Drosophila* may disappear completely within a few million years, leaving only the functional binding sites as vestiges of the domestication process.

Several outstanding questions remain. For example, is there a special feature of *Helitrons* or the specific progenitor of the ISX/ISXR families that predisposed these elements to evolve a MRE? Is MSL binding to ISX and ISXR indispensable for proper dosage compensation in *D. miranda*? This question might be tested using newly developed genome-editing technologies to delete the MRE located within these elements (*5*).

Intriguingly, this is not the first time that transposons have been implicated in the process of dosage compensation. In mammals, LINE-1 retroelements are enriched on the X chromosome and have long been thought to play a role in the process of X-chromosome inactivation (*6*, *7*). Although the putative mechanism by which LINE-1 appears to contribute to mammalian X inactivation is distinct from ISX-mediated MSL recruitment in *D. miranda*, it shares a common theme of a chromosome-wide regulatory activity spread by transposon amplification.

This work adds another example of transposition acting as a rapid evolutionary mechanism to wire up a genomic regulatory network (*8*–*13*). It also suggests that many transposon domestications are likely to go undetected due to the rapid erasure of their sequence signatures. Although we now understand that controlling gene expression is not the raison d'être of transposons, we are gaining a better appreciation of their propensities to promote regulatory evolution, which led McClintock to originally call them "controlling elements."

References

1. C. E. Ellison, D. Bachtrog, *Science* **342**, 846 (2013).
2. V. B. Kaiser, D. Bachtrog, *Annu. Rev. Genet.* **44**, 91 (2010).
3. A. A. Alekseyenko *et al.*, *Cell* **134**, 599 (2008).
4. A. A. Alekseyenko *et al.*, *Genes Dev.* **27**, 853 (2013).
5. P. Mali, K. M. Esvelt, G. M. Church, *Nat. Methods* **10**, 957 (2013).
6. M. F. Lyon, *Cytogenet. Cell Genet.* **80**, 133 (1998).
7. J. C. Chow *et al.*, *Cell* **141**, 956 (2010).
8. C. Feschotte, *Nat. Rev. Genet.* **9**, 397 (2008).
9. G. Kunarso *et al.*, *Nat. Genet.* **42**, 631 (2010).
10. V. J. Lynch, R. D. Leclerc, G. May, G. P. Wagner, *Nat. Genet.* **43**, 1154 (2011).
11. D. Schmidt *et al.*, *Cell* **148**, 335 (2012).
12. R. Rebollo, M. T. Romanish, D. L. Mager, *Annu. Rev. Genet.* **46**, 21 (2012).
13. E. B. Chuong *et al.*, *Nat. Genet.* **45**, 325 (2013).

Acknowledgments: Work in the Feschotte laboratory is supported by grant R01-GM077582 from the NIH.

10.1126/science.1246659

GENETICS

Can Cancer Drugs Treat Immunodeficiency?

Genome sequencing has defined the genetic basis for a primary immunodeficiency disease.

Mary Ellen Conley[1] and David A. Fruman[2]

The usual arduous path to the discovery and implementation of a new medical therapy is to start at the "bench" with the characterization of a molecular aberration in a specific disease (such as a type of cancer), assess its function, design a drug, and eventually bring that intervention to "bedside" through clinical trials. Rarely, if ever, does the path start at bedside with patients who share a profile of symptoms, lead back to the bench where the gathering of mutation data defines a new disease, and then move forward again to bedside. But on page 866 of this issue, Angulo *et al*. (*1*) show that just such a route has led to the discovery of a new genetic immune deficiency disease, with a drug that is potentially at-the-ready for therapy (see the figure). The study emphasizes the power of exome (DNA coding regions) sequencing to identify causative mutations in rare diseases.

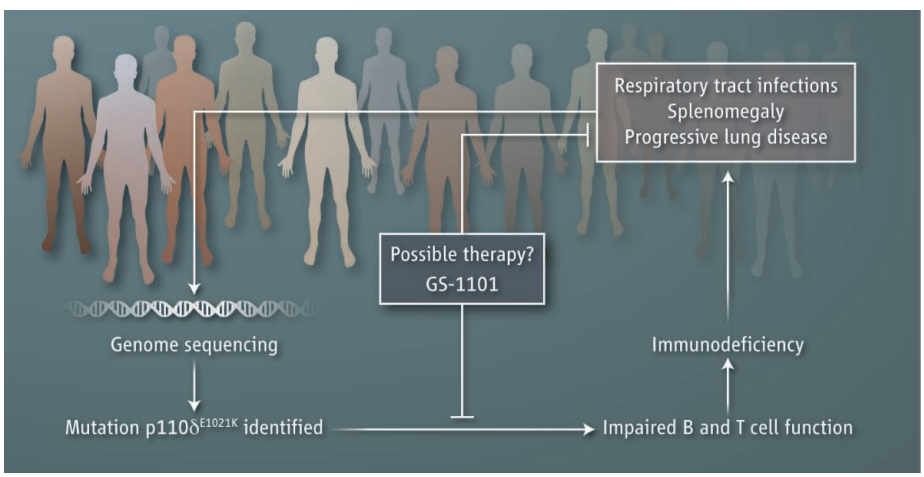

Genetic disease discovery. Patients with common symptoms were found to have the same mutation in p110δ. The mutation results in aberrant B cell and T cell function and immunodeficiency, thus revealing a new primary immunodeficiency syndrome (APDS). The p110δ inhibitor GS-1101 has shown encouraging results in clinical trials in patients with chronic lymphocytic leukemia and some non-Hodgkin's lymphomas. p110δ inhibitors are also under development for certain inflammatory diseases (*15*). The new primary immunodeficiency disease may be sensitive to the drug.

Angulo *et al.* examined 17 members of seven unrelated families for whom the clinical phenotype was quite variable, but most affected patients had recurrent respiratory tract infections, splenomegaly (enlarged spleen), and progressive lung disease. The authors identified the exact same heterozygous mutation (Glu^{1021} → Lys, or E1021K) in the gene *PIK3CD* in all 17 individuals. *PIK3CD* encodes the protein p110δ, the catalytic subunit of an enzyme that belongs to the phosphoinositide 3-kinase (PI3K) family. As the E1021K mutation results in inappropriate activation of the kinase, the authors aptly named the condition activated PI3Kδ syndrome (APDS).

The class IA PI3Ks are a highly conserved family of enzymes that phosphorylate the membrane lipid phosphatidylinositol 4,5-bisphosphate (*2*). These heterodimeric enzymes are composed of one of three catalytic p110 subunits (p110α, p110β, and p110δ encoded by *PIK3CA*, *PIK3CB*, and *PIK3CD*, respectively) and a regulatory subunit (encoded by *PIK3R1*, *PIK3R2*, or *PIK3R3*). Whereas p110α and p110β are broadly expressed, p110δ is mainly expressed in cells found in the blood. Activation of PI3K enzymes downstream of cell surface receptors can induce cell growth, proliferation, survival, migration, metabolism, angiogenesis, and differentiation, depending on the cell lineage, the specific PI3K isoform, and cooperating cellular signals (*2*).

Our understanding of how PI3K family members function has been greatly informed by murine models and by patients who have genetic alterations in the components of these kinases. In mice, loss of p110α or p110β is lethal, causing embryonic death, but loss of p110δ results in a more focused phenotype characterized by a partial block in B cell differentiation and impaired function of mature B cells and T cells (*3*–*5*). Mice lacking p110δ have decreased concentrations of serum immunoglobulins and severely reduced antibody responses to T cell–independent and T cell–dependent antigens. Loss of the regulatory subunit encoded by *Pik3r1* causes a similar B cell immunodeficiency in mice (*6*, *7*). A single patient has been reported with a homozygous premature stop codon in the 5′ part of the *PIK3R1* gene (*8*). This patient had agammaglobulinemia (no immunoglobulin production) and a complete failure of B cell development, a phenotype that is similar to but much more severe than that seen in mice with loss of *Pik3r1*.

Genetic studies of human cancer have shown that most tumors have mutations that activate cell signaling pathways that involve PI3Ks (*9*). Frequent gain-of-function mutations in *PIK3CA* or *PIK3R1* are prominent examples. Activating mutations in *PIK3CA* and *PIK3R2* are also seen in affected tissues of patients with megalencephaly (enlargement of the brain) and somatic overgrowth syndromes (*10*–*12*). Of interest, many of the cancer-promoting mutations in *PIK3CA* cluster around the site in the catalytic domain that is mutated in the patients with activated *PIK3CD*. Angulo *et al*. confirmed through biochemical and cellular assays that the E1021K mutation increases p110δ enzyme activity and its association with cellular membranes.

The clinical phenotype in the patients with the E1021K activating mutation in *PIK3CD* has some surprises. The most consistent feature is recurrent infections with encapsulated bacteria, but this is a rather

CREDIT: H. MCDONALD/*SCIENCE*

[1]Department of Pediatrics, University of Tennessee College of Medicine, Memphis, TN 38163, USA. [2]Department of Molecular Biology & Biochemistry and Institute for Immunology, University of California, Irvine, CA 92697, USA. E-mail: mconley@uthsc.edu; dfruman@uci.edu

Published by AAAS

common, nonspecific finding. Although the serum concentration of immunoglobulin M (IgM; the first antibody produced in response to infection) was sometimes elevated, the total serum immunoglobulin G (IgG, the high-affinity antibody) was normal. Serum antibody titers to tetanus toxoid, a very strong T cell–dependent antigen, were normal, but titers to the T cell–independent antigens *Streptococcus pneumoniae* and *Haemophilus influenzae* were low despite the use of conjugate vaccines. The mice lacking *Pik3cd* also had poor responses to T cell–dependent and –independent antigens, suggesting that just the right amount of p110δ is needed at just the right time.

Strikingly, the progressive lung disease in these patients appears to be out of proportion to the degree of antibody deficiency. Requirements for normal p110δ activity for neutrophil function have been reported, but Angulo *et al*. did not observe neutrophil dysfunction in their patients. However, in vitro assays do not always reflect in vivo function.

One might expect patients with activated p110δ to have a high incidence of malignancy and autoimmune disease. Although these disorders were seen, they were not predominant. This may be because patient lymphocytes are highly susceptible to activation-induced cell death. Angulo *et al*. also noted that the 17 patients have an increased proportion of transitional B cells, which are newly released from the bone marrow. The authors suggest that this might be due to a late block in B cell development or enhanced death of mature B cells, but there is also the possibility that there is increased production of early B cell precursors in the bone marrow. The early onset of splenomegaly and enlarged lymph nodes before the development of recurrent infections supports this possibility. The fact that multiple patients with this newly recognized activated PI3Kδ syndrome were identified in a relatively small cohort suggests that other physicians have similar patients. Indeed, activating *PIK3CD* mutations in 14 immunodeficiency patients from seven families were recently identified (*13*). A particularly exciting aspect of this work is that a viable treatment for these individuals might soon be available. The selective p110δ inhibitor GS-1101 has shown impressive efficacy and tolerability in patients with certain B cell cancers and is in phase III clinical trials (*14*). GS-1101 and a related compound, IC87114, both blocked the activity of the E1021K mutant; moreover, IC87114 protected T cells from activation-induced cell death. Whether such compounds can restore immune function and forestall organ damage in the patients will be interesting to evaluate. At a broader level, it is remarkable that one enzyme is a potential drug target for indications as diverse as leukemia, immunodeficiency, and inflammation.

References

1. I. Angulo *et al*., *Science* **342**, 866 (2013); 10.1126/science.1243292.
2. B. Vanhaesebroeck, J. Guillermet-Guibert, M. Graupera, B. Bilanges, *Nat. Rev. Mol. Cell Biol.* **11**, 329 (2010).
3. E. Clayton *et al*., *J. Exp. Med.* **196**, 753 (2002).
4. S. T. Jou *et al*., *Mol. Cell. Biol.* **22**, 8580 (2002).
5. K. Okkenhaug *et al*., *Science* **297**, 1031 (2002).
6. D. A. Fruman *et al*., *Science* **283**, 393 (1999).
7. H. Suzuki *et al*., *Science* **283**, 390 (1999).
8. M. E. Conley *et al*., *J. Exp. Med.* **209**, 463 (2012).
9. P. Liu, H. Cheng, T. M. Roberts, J. J. Zhao, *Nat. Rev. Drug Discov.* **8**, 627 (2009).
10. M. J. Lindhurst *et al*., *Nat. Genet.* **44**, 928 (2012).
11. J. B. Rivière *et al*., *Nat. Genet.* **44**, 934 (2012).
12. J. H. Lee *et al*., *Nat. Genet.* **44**, 941 (2012).
13. C. L. Lucas *et al*., *Nat. Immunol.* 10.103/ni.2771 (2013).
14. D. A. Fruman, C. Rommel, *Cancer Discov.* **1**, 562 (2011).
15. K. D. Puri, M. R. Gold, *Front. Immunol.* **3**, 256 (2012).

10.1126/science.1246760

ECOLOGY

Understanding Lakes Near and Far

Satellite and in situ sensor data complement long-term studies of individual lakes to provide insights into the effects of climate change and pollution.

Stephanie E. Hampton

Scientists have long viewed lakes as microcosms in which to study fundamental ecosystem processes (*1*). A large, heterogeneous body of multidecadal data has been accumulated around the world, documenting historical conditions, capturing temporal dynamics of complex ecological phenomena that could not be observed within shorter time periods. Building on this legacy of long-term data collection, innovations in sensor applications and computing are creating new opportunities for integrating data across different scales in space and time, enriching long-term research and stimulating collaboration.

A shared characteristic of long-term lake studies is that they address questions far beyond those posed at inception. Lake Washington is a famous story of lake restoration (*2*). In 1955, Edmondson and colleagues noted a sudden shift in microalgae suggestive of nutrient pollution, and so began long-term studies that examined algal-nutrient relationships, informed the public process leading to sewage diversion, and documented the restoration of water clarity. The case could have been closed here, but further water clarity increases shifted attention to food web interactions that transpired across decades, providing insights into trophic cascades (*2*) and continuing through the present to reveal subtle responses to climate change, such as temperature controls on the timing of plankton growth that appear to be general across many lakes (*3*).

Meanwhile in Siberia, three generations of a family of Russian scientists and their colleagues were maintaining comparable records on the world's most voluminous freshwater lake—Lake Baikal—to study drivers of plankton dynamics (*4*). From 1945 to the present, the exceptional duration and continuity of the temperature record turned out to be uniquely suited for deciphering seasonal timing shifts attributable to decadal climate oscillations. The detailed data revealed that changes in the timing of seasonal transitions in lake temperature, and potentially throughout the region, are predictably forced by changes in the trajectory and strength of the jet stream and its storm tracks (*5*).

Other examples of long-term lake research have been a result of sustained government support. In England's Lake District, research since the 1930s has produced seminal work from physics to food webs and ultimately documented complex effects of climate change that could not have been discerned in shorter studies. Researchers working with the long-term Lake District data were among the first to recognize and demonstrate the relationship of lake processes with large-scale climate dynamics such as the North Atlantic Oscillation (*6*).

Until 2012, Canada boasted similar strong governmental support for the crown jewel of its environmental science programs, the Experimental Lakes Area (ELA). From elucidating effects of acid rain and nutrient pollution on freshwater to pathways for

National Center for Ecological Analysis and Synthesis, University of California, Santa Barbara, CA 93101, USA. E-mail: hampton@nceas.ucsb.edu

mercury contamination in food webs, ELA has produced a broad range of work with immediate policy relevance and transformative effects on science. With the withdrawal of stable federal support, ELA is challenged to remain the engine of innovation that it has been for four decades (*7*).

Traditionally, long-term lake research programs have been local efforts, and collaborative data synthesis has lagged behind that seen in marine research. Notable exceptions exist, particularly in Europe, where the 2000 EU Water Framework Directive has incentivized ongoing large-scale scientific collaboration. Grounded in theory and guided by well-defined questions, these large-scale syntheses of empirical data have produced generalizable principles and specific recommendations for managers of freshwater resources in the EU, including biological indicators that identify effects of previously underappreciated pressures of human uses such as shoreline and water level modification (*8*).

Such syntheses have been rare because they are difficult. Even if data access can be negotiated, the lack of standardization across the community makes it difficult to compare data from different locations. When comparable data are finally aligned, analytical challenges remain; the statistical frameworks for integrating and analyzing disparate time series exist, but such techniques remain relatively unfamiliar to environmental scientists (*9*). This community increasingly requires greater access to robust computational infrastructure for data archiving, sharing, and analysis—and training in its use—particularly as sensors create new opportunities for integrative studies.

From portable in situ devices to instrumented satellites, sensors allow investigators to be in many places at once and in otherwise inaccessible places. A vast amount of information can be collected quickly, allowing for rapid delivery of novel scientific discoveries while a long-term research program matures. The Global Lake Ecological Observatory Network (GLEON) is a grassroots network of lake researchers that aims to build a persistent monitoring network in lakes using in situ instrumentation. Recently, Solomon *et al*. (*10*) integrated data from 25 GLEON lakes to examine lake metabolism. The fine temporal scale provided by the sensors and the broad spatial extent facilitated by the collaborative network created an unprecedented opportunity to empirically test theories about the drivers of in situ microbial activity, quantifying variation attributable to ecological processes that previously would have been subsumed within measurement error.

The fine spatial scale of in situ sensors is complemented by remote sensing data, providing coarser resolution but with broadest spatial extent (see the figure). Remote sensing is particularly promising for inferring lake temperatures, water levels, and algal dynamics. A global analysis of satellite-derived lake temperatures demonstrated the rapid warming of lakes worldwide over recent decades, with lakes warming faster than the air in some regions such as the Laurentian Great Lakes and northern Europe (*11*). The satellite data allowed analysis across a much broader spatial extent than would have been possible with in situ data and fueled subsequent efforts to pair satellite-derived data with long-term in situ lake data (*12*).

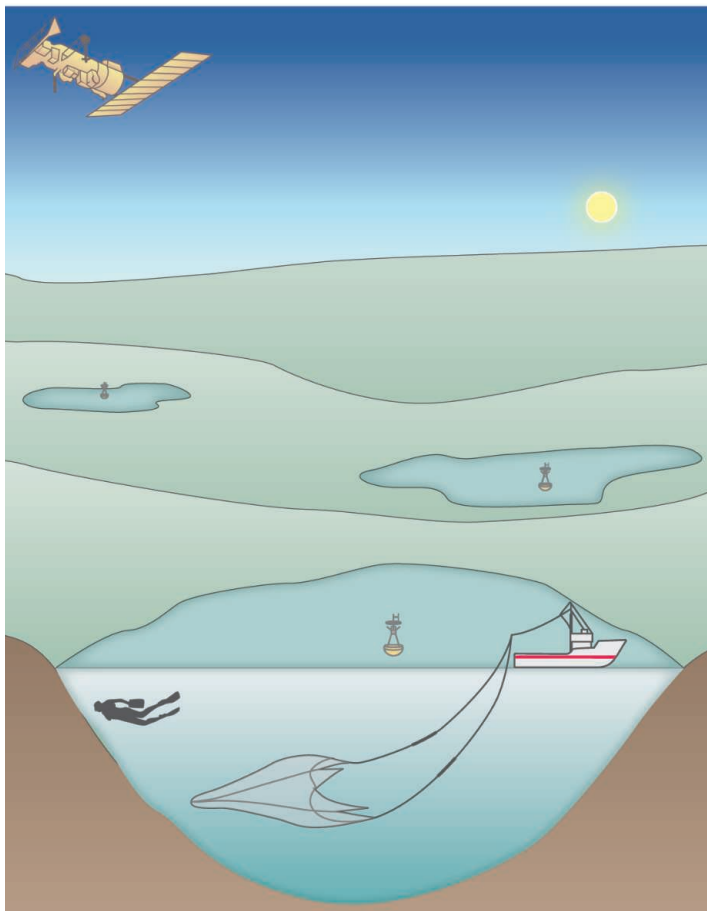

Complementary routes. Remote sensing approaches allow broad spatial coverage, complementing the finer-scale understanding facilitated by long-term in situ lake monitoring programs. In situ programs may include sensors deployed in the water and collections carried out by hand, and can be particularly powerful when coordinated across multiple lakes.

Current sensors complement, but do not replace, in situ measurements. For example, sensors do not provide organismal data necessary for guiding fisheries management, and the relation between satellite-derived data and in situ data is not yet well understood. It is vital that research and monitoring programs are not driven by the sensors available but by the fundamental questions at hand.

Globally, less than 3% of water resources are fresh, and most of this freshwater is bound in ice, leaving a scant 0.01% readily available at the surface. However, the value of lakes extends beyond immediate human requirements for clean, fresh water. Lying at the lowest points on landscapes, lakes aggregate materials from the watershed and airshed, integrating regional signals, ultimately acting as sentinels of ecosystem change (*13*). Freshwater science is now in a position to leverage decades of empirical data to develop broader integrative studies that are facilitated by new technologies and to transform scientific practice and understanding of these critical ecosystems.

References

1. B. Moss, *Sci. Total Environ.* **434**, 130 (2012).
2. W. T. Edmondson, *Lake Reservior Manage.* **10**, 75 (1994).
3. D. Straile, R. Adrian, D. E. Schindler, *PLOS ONE* **7**, e45497 (2012).
4. O. M. Kozhova, L. R. Izmest'eva, *Lake Baikal: Evolution and Biodiversity* (Backhuys Publishers, Leiden, 1998).
5. S. L. Katz, S. E. Hampton, L. R. Izmest'eva, M. V. Moore, *PLOS ONE* **6**, e14688 (2011).
6. S. C. Maberly, J. A. Elliott, *Freshw. Biol.* **57**, 233 (2012).
7. B. E. Beisner, *J. Plankton Res.* **34**, 849 (2012).
8. A. Lyche-Solheim *et al*., *Hydrobiologia* **704**, 57 (2013).
9. S. E. Hampton *et al*., *Ecology* **94**, 2663 (2013).
10. C. T. Solomon *et al*., *Limnol. Oceanogr.* **58**, 849 (2013).
11. P. Schneider, S. J. Hook, *Geophys. Res. Lett.* **37**, L22405 (2010).
12. J. D. Lenters, S. J. Hook, P. B. McIntyre, *Eos Trans. AGU* **93**, 427 (2012).
13. C. E. Williamson, J. E. Saros, W. F. Vincent, J. P. Smol, *Limnol. Oceanogr.* **54**, 2273 (2009).

10.1126/science.1244732

PRESIDENTIAL ADDRESS

What's So Special About Science (And How Much Should We Spend on It?)

William H. Press

Scientific research probes the deepest mysteries of the universe and of living things, and it creates applications and technologies that benefit humanity and create wealth. This "Beauty and Benefits of Science" is the theme of this 2013 AAAS Annual Meeting.

The subject of my address is a different kind of mystery, although it is also related to this theme. It is the mystery of why society is willing to support an endeavor as abstract and altruistic as basic scientific research and an enterprise as large and practical as the research and development (R&D) enterprise as a whole. Put differently, it is the mystery that a unified scientific enterprise can be simultaneously the seed corn for economic advance and the confectionary corn syrup of pure, curiosity-driven scientific discovery.

The view that science can be supported as a contribution to the intellectual richness of the world has a distinguished list of adherents. In 1969, Robert Wilson explained what Fermilab would do for the country by saying, "It has nothing to do directly with defending our country except to make it worth defending" (*1*). And, almost two centuries earlier, in his first annual address to Congress, George Washington wrote, "[t]here is nothing which can better deserve your patronage, than the promotion of Science and Literature. Knowledge is in every country the surest basis of publick happiness" (*2*).

Indeed, U.S. taxpayers are, to some extent, willing to pay for activities that enrich American social and cultural capital without having a direct economic benefit. Congress, up to now, has appropriated about $150 million a year for the National Endowment for the Arts (NEA) and about $170 million a year for the National Endowment for the Humanities (NEH) (*3*). However, by contrast, Congress appropriates about $40 billion a year for basic research (*4*). If you plot a bar graph with these three numbers, you can barely see that the NEA and NEH numbers are not zero.

It is evident that society is willing to pay much more for curiosity-driven research in science than for the analogous thought- and beauty-driven practice of the arts and humanities. It is easy to guess the reason: the link, sometimes subtle but repeatedly established over time, between investment in basic research and macroeconomic growth. Discovery leads to technology and invention, which lead to new products, jobs, and industries.

Such is the case that we scientists need to reinforce in the austere times that we face. However, mere repetition is not an effective strategy. In today's lean times, we need to articulate our case more powerfully and in a more sophisticated way than in more prosperous times. A skeptical and stressed Congress is entitled to wonder whether scientists are the geese that lay golden eggs or just another group of pigs at the trough.

More Than a Century of Exponential Growth

Figure 1 shows the growth in U.S. gross domestic product (GDP) per capita over the past 130 years. If we ignore a few bumps with time scales of a decade or so, the curve is surprisingly well fit by a pure exponential. Note that the curve is not plotting GDP, which would grow with population and the overall size of the U.S. economy, but GDP per capita, which reflects something like the average income of each individual. Ameri-

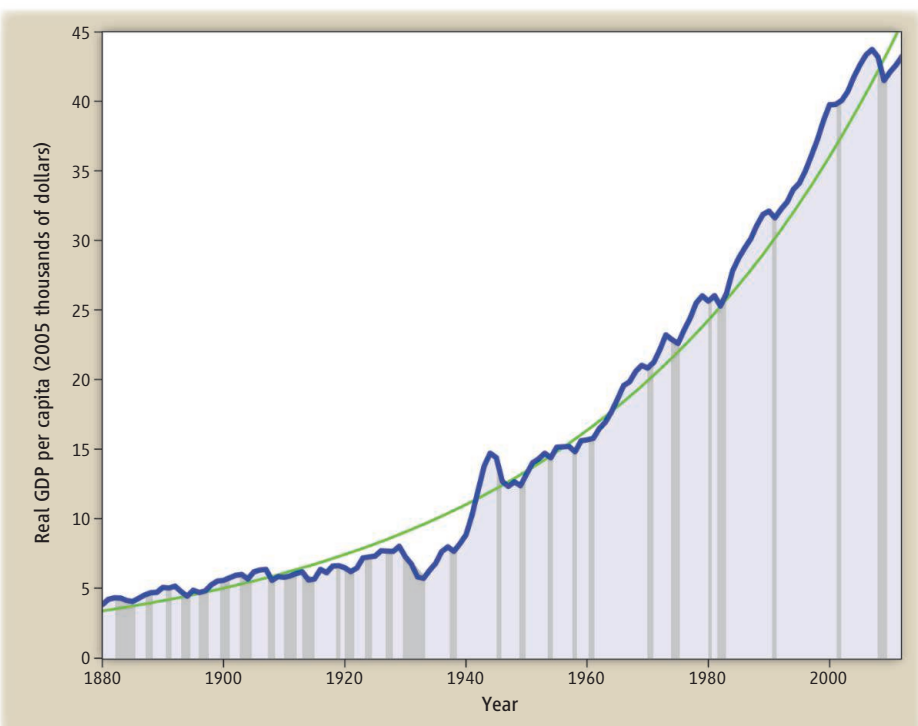

Fig. 1. U.S. GDP per capita, corrected for inflation in 2005 dollars. The smooth green curve is an exponential fit to the data. Shaded date ranges show official periods of recession. On average, an individual's income in the United States has increased by about 2% per year for more than 130 years.

CREDIT: DATA SOURCE: MEASURINGWORTH.COM, WIKIPEDIA

William H. Press is the Warren J. and Viola M. Raymer Professor in Computer Science and Integrative Biology at the University of Texas at Austin. He is a member of President Obama's Council of Advisors on Science and Technology. He previously served as Deputy Laboratory Director at Los Alamos National Laboratory from 1999 to 2005 and was earlier Professor of Astronomy and of Physics at Harvard University. He was president of AAAS from February 2012 to February 2013. This article is based on the Presidential Address he delivered at the AAAS annual meeting in Boston, MA, on 14 February 2012. E-mail: wpress@cs.utexas.edu

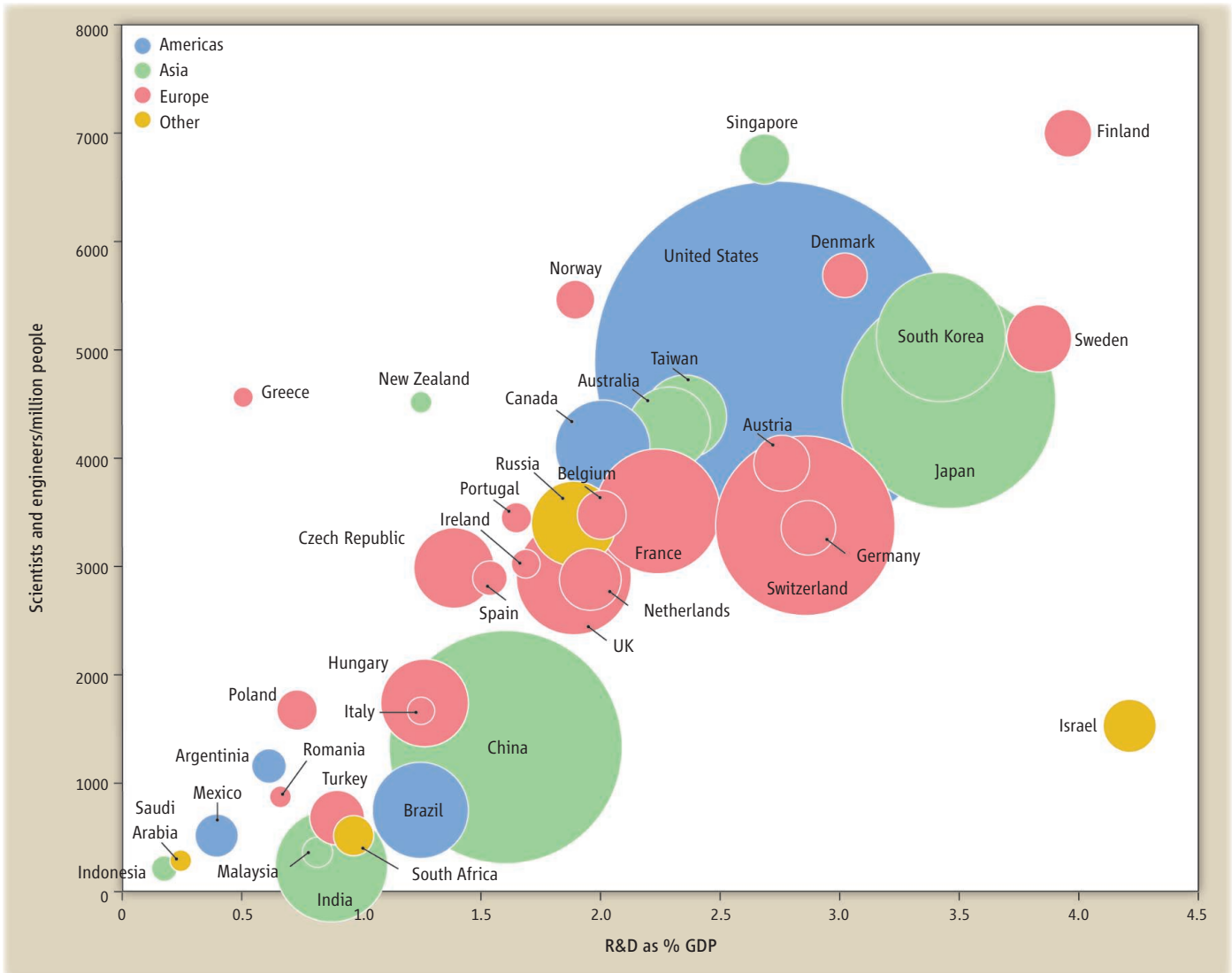

Fig. 2. R&D spending by country in 2011 by percent of GDP and percent of population who are scientists and engineers. The size of the circles show the country's total R&D spending.

CREDIT: REPRINTED WITH PERMISSION FROM THE BATTELLE MEMORIAL INSTITUTE AND R&D MAGAZINE (DECEMBER 2011)

can individual income has grown exponentially. (That is on average. The distribution of that income within the population is another matter entirely.)

In the wake of the financial crisis, economist Robert Gordon advanced the theory that 2008 was the beginning of a new normal where exponential growth could no longer be assumed (*5*). However, one sees plenty of other temporary blips in the historical record, the Great Depression of the 1930s being most visible. Any of these fluctuations might have been mistakenly overinterpreted. Indeed, from a low in 2009, GDP per capita has increased in each of the past 3 years (*6*).

Turn now to Fig. 2, from the Battelle Memorial Institute and R&D Magazine (*7*). The horizontal axis shows the fraction of their GDP that countries of the world spend on research and development. The vertical axis shows what fraction of their populations are scientists or engineers. Unsurprisingly, these are highly correlated. The area of each country's circle is its total R&D spending. The United States is the largest circle, just short of 3% of GDP, and at about a half percent scientists and engineers in the population. Notice that the United States is not the most intensive investor, neither as a percentage of GDP nor as a fraction of its population.

It is striking that the powerhouse industrial nations of the past 50 years (e.g., United States, Germany, Japan, and South Korea), lead the pack at the upper right, together with the Scandinavian countries and (recently) Singapore. These countries might thus be identified as the technology leaders. The United States ranks third or fourth among large economies in what we spend per capita on R&D and ranks eighth among all countries (*8*).

A second cluster of developed nations spends about a third less and has correspondingly fewer scientists and engineers: United Kingdom, France, Canada, Australia, and Russia, among others. These industrialized countries might thus be identified as the technology followers. A third cluster at the lower left comprises the developing countries of the world, China being by far the largest.

It would be overly simplistic to ask, "Which of these three clubs do you want to be in?" and to then equate spending on research with the sustained economic growth that gives the powerhouse industrial nations their high standard of living. Correlation, we know, is not the same as causality. Are we richer because we spend more on R&D? Or do we spend more on R&D because we are richer, and can afford to do so? Or is there some other factor, causative of both?

The Solow Residual Is Technology

Luckily, we know the answer, thanks to intensive study by economists, starting with Robert Solow (who won a Nobel Prize for this work) (*9*), as well as luminaries such as Ken Arrow, Zvi Griliches, and many others. Starting after World War II and continuing in the 1970s and 1980s, economists have largely settled the question of where the exponential growth of the U.S. economy has come from and what the factors that produced it were.

Although I am not an economist, I want to give you a simple version of the story, because it is one that I think scientists need to understand as part of making the case for what we do. Exponential growth comes from positive feedback, where the production of something enables you to produce even more. In other words, during the exponential growth that we have experienced, something produced must itself have been a factor of production. Economists have been studying factors of production since the time of Adam Smith and David Ricardo more than 200 years ago. The classic factors of production are land, labor, and capital. Leaping over two centuries of economic history, we might modernize these by adding various forms of human capital, such as investment in education. We might also add intellectual property as capital, which today is no less important than factories and machinery. [Interestingly, this change was formally made by the U.S. Bureau of Economic Analysis only this year, resulting in a $560 billion "increase" in the U.S. GDP (*10*).]

A relatively fixed factor of production such as land (today we would include all natural resources) cannot produce positive feedback for exponential growth. Land does not multiply to produce more land. Other natural resources are at best augmented by one-time discoveries; at worst, they are depleted. Labor can multiply to produce more labor, in the sense of a GDP that increases in proportion to population growth. But growth of labor cannot by itself produce more income per person. Therefore, it is uniquely what economists call capital (albeit in its broadest sense, including human, intellectual, and environmental capital) that can fuel exponential growth of the economy.

Solow and subsequent researchers studied this and attempted a detailed accounting of how much growth was due to each of the known factors of production. Their finding was that at most half of the historical growth could be explained by known factors. The unexplained part, sometimes estimated as large as 85%, was termed the Solow residual. Subsequent work showed that the bulk of the Solow residual could in fact be explained by positing a new factor of production: technological progress. Technology is not exactly a form of capital (although it is related to human and intellectual capital), because the technology state of the art is not exactly owned by anyone. Yet it is capable of generating positive feedback. As a factor of production, technology produces wealth and produces more technological progress, enabling a virtuous cycle of exponential growth (*11*, *12*).

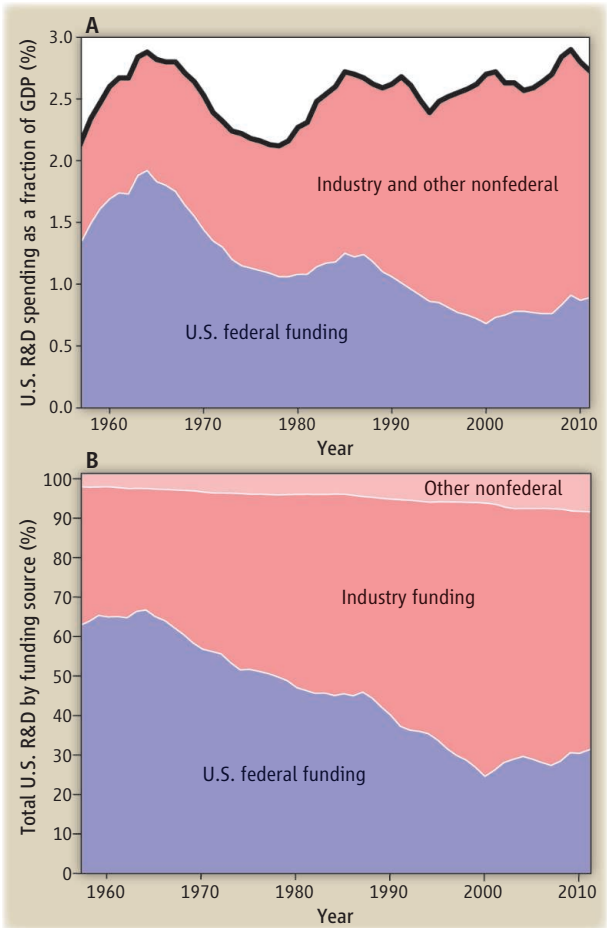

Fig. 3. Two views of R&D spending. (**A**) U.S. total R&D spending as a percent of U.S. GDP. Total spending has fluctuated between about 2.2% and 2.8% since 1957. (**B**) Same data plotted as a fraction of total R&D spending. Over the period shown, industry's share of R&D funding has increased from about 1/3 to about 2/3. Other nonfederal funding has also grown in share. The U.S. government share has correspondingly decreased.

Once this new factor was identified, many studies from the 1970s forward have taken small, studiable slices of the economy and tried to estimate the annual rates of return on investment (ROI) in basic research—the fuel for technological progress. As AAAS members, we may all be gratified that these studies nearly all show high rates of return. Many institutions, including our universities and retirement funds, accept 5% sustained ROI as a decent return. Yet investments in basic research are variously estimated as ultimately returning between 20% and 60% per year (*13*).

The Appropriability Conundrum

If that were the whole story, my advice today would be simple enough: Withdraw all your retirement funds and invest them in your laboratory! But, of course, it's not the whole story. What makes this advice bad (apart from its being a risky undiversified investment) is another important concept from neoclassical economics, appropriability. Appropriability means the following: How well do the rewards flow back to the investor who actually takes the risk and puts up the money?

The returns from basic research are large, but they are not very appropriable. The nature of basic research is that its results flow to the rest of the world. Although basic research can be turned into applied research—into patents, products, and eventually economic growth—this may not necessarily occur in the laboratory where the work is originally done or even in the same country. So the appropriability of basic research is low. The investor generally does not get enough of the reward.

Basic research leading to scientific discovery is thus a public good. It will benefit all. But,

CREDIT: DATA SOURCE: NATIONAL SCIENCE FOUNDATION (NSF)

because the private incentive to pay for basic research is therefore attenuated, the private sector as a matter of economic self-interest is likely to underinvest in it. Therefore, if the full social potential of this public good is to be realized, the investment must come from government. Indeed, government in the United States does support the lion's share of the nation's basic research endeavors.

Figure 3, based on data from the National Science Foundation (NSF) (*14*), shows total U.S. support of R&D over the past 50 years as a percentage of GDP and how it is divided between federal and nonfederal (dominantly industry) funding. Looking now at all R&D (not just basic research), one sees that, post-Sputnik, total R&D per GDP has fluctuated between about 2.2 and 2.8%. Without minimizing the importance of the up-and-down fluctuations (these are, respectively, beneficial or destructive to the research enterprise), U.S. investment in R&D has largely kept pace with the size of the U.S. economy. Indeed, following Solow's theory, it is likely responsible for up to 85% of U.S. economic growth.

What has changed dramatically over 50 years is the fraction of total R&D support from the federal government. In the years immediately after Sputnik, about two-thirds of total R&D was federally funded, whereas one-third was funded by the private sector. Today the proportions are almost exactly reversed: About two-thirds of U.S. R&D is paid for by industry.

This change drives a shift toward appropriable R&D, that is, more "D" and less "R," because that is the kind of investment that more likely yields products and services that can get to the market quickly, thus yielding returns for the investors who invest in the companies that fund the work. The federally funded fraction, which has been decreasing, is the less appropriable part, the part that is a public good—the seed corn.

What has driven this trend? (I am again simplifying a complicated piece of economic history.) In 1945, just after World War II, the United States accounted for 50% of the total world GDP. Therefore, federal investment in R&D was almost guaranteed to be at least 50% appropriable, with its returns accruing to the U.S. economy. In fact, the appropriability was likely even larger, because, until as late as the 1960s, America's potential competitors, Japan and Europe, lacked the full capacity to absorb the results of U.S.-funded basic research. By contrast, information flows today are so rapid that anyone, anywhere, can potentially be the entrepreneur who recognizes the economic potential of scientific discoveries. U.S. scientific results used to be exported at the speed of ocean mail or international student Ph.D. programs; today, they are exported at Internet speeds.

Fast forward to the 1990s. The industrialized world is a much more competitive place. In the United States, the era of regulated monopolies (such as the Bell System, which paid for the hugely productive Bell Laboratories) is over. Large multinational corporations are becoming more dominant. Quarter-by-quarter accountability to shareholders is now an influential pressure point. Increased industry investment in R&D is a rational response, because R&D is (as discussed) a good investment. However, industry investment in non-appropriable R&D, such as basic research, is becoming harder to justify, both because of its longer time horizon and because of the risk that others will appropriate the results.

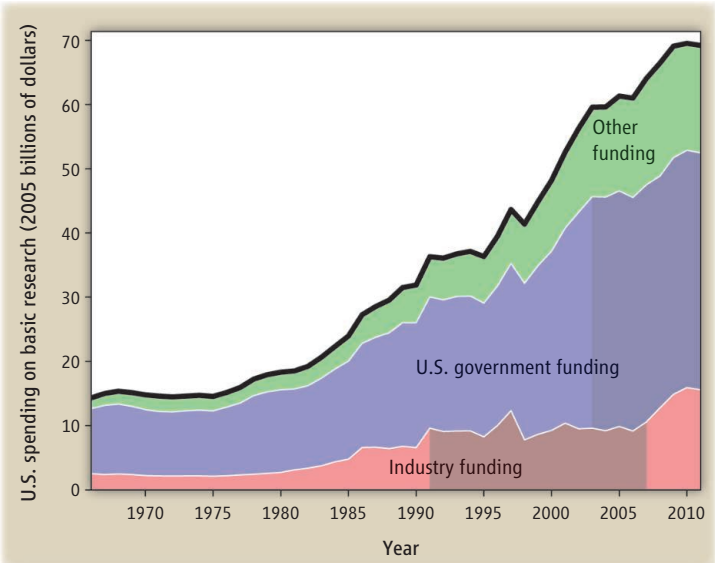

Fig. 4. U.S. R&D spending on basic research in constant 2005 dollars (top curve). Funding sources are shown by the color bands. "Other" includes state and local government and nonprofit organizations. Industry funding of basic research stagnated at about $10 billion in the period 1991–2007, while federal support has stagnated at about $37 billion since 2003 (periods of stagnation shown as shaded).

Indeed, the data from 1990 to 2007 support this interpretation. During this whole period, industry investment in basic research stagnated at about $10 billion (constant 2005 dollars). Thanks to increased federal and other funding during most of this period, the total amount of basic research did increase (even faster than the overall size of the economy). However, only in 2008 to 2010 in the wake of the financial crisis, did industry increase its spending on basic research, and this may be simply an artifact of renewed attention by industry to R&D generally in that period. In fact, industry spending on basic research again decreased in 2011. Figure 4 shows the data for total annual investment in U.S. basic research from 1965 to 2011 and how it has been divided among industry, the federal government, and other funding sources.

Overgrazing the Commons of Basic Research

The stagnation of industry's funding of basic research in the period from 1990 to 2007 presages an even more alarming trend, also shown in Fig. 4: Total federal spending on basic research has stagnated since 2003 at about $37 billion (2005 dollars). This creates an extremely dangerous situation, and for two related reasons.

First, 10 years into this trend, the federal budget is now facing a time of unprecedented austerity. Basic research needs to grow at least as fast as the economy because it is part of the feedback loop for most of the economy's growth. Industry support, even if it proves to be on the rise, supplies only a small fraction of what is needed; therefore, federal funding must make up the bulk of the difference. In today's environment of austerity, the rate of increase in federal support needed to make up for a decade of neglect, and to keep pace with the recovering economy, will be a very tough sell.

Second, the traditional bipartisan support enjoyed by federal spending on basic research has always been conditioned on its being a public good whose benefit accrues to the U.S. taxpayer. Therefore, any decrease in that investment's appropriability—now on the

CREDIT: DATA SOURCE: NSF

scale of nations, not individual corporations—decreases the attractiveness of the investment. In other words, the danger of the 2010s is that nations such as the United States will make the same decision that individual corporations made in the 1990s and invest relatively less in basic research. In effect, the federal government already made this decision around 2003, because its support of basic research has stagnated in constant dollars since then. If other countries follow suit, this could lead to what we have never seen before in 150 years of exponential growth: a zero-sum world of research. This would be a world in which every country tries to gain the benefit of whatever basic research is funded by others, but no country is willing to make investments themselves. Rather, all scramble to compete over diminishing returns from past investments.

"America is a country of wonderful, frontier, short-term pragmatism. That benefits us in many ways, but it may not put the United States in the best competitive position in a game of international competition that favors long time horizons."

This scenario is what economists call the tragedy of the commons. No one will invest to maintain something that benefits all, given the option of instead being a free rider. The classic tragedy of the commons is a piece of grassland owned in common. Everyone is entitled to graze their sheep, and no one pays for the land's upkeep. And, after a while, there are a lot of hungry sheep and no grass.

Basic research is a commons. It can be overgrazed and underreplenished. There is no Global Science Foundation that has an annual appropriation of the world's taxes to invest for the ultimate good of everyone in the world. Yet, not all nations can be free riders, especially not the United States.

The current situation is dangerous. Short-term actions in a time of budget crisis and financial austerity might become the triggers of long-term underinvestment in the ultimate fuel of economic growth, basic research in science. Can this tragedy be avoided? Possibly. Let me sketch two paths forward for avoiding such a negative outcome.

Geographical Anchors and Nonmonetizable Benefits

The first path forward is to adopt policies that maintain the appropriability of returns from U.S. basic research to the U.S. economy. This requires finesse because policies that conflict with the fundamental openness of such research are sure to be counterproductive. Yet, even in the Internet age, there are strategies that can geographically anchor the transformation of research discoveries into economic growth. One such phenomenon is the growth of research hubs around America's great research universities. The older examples are Silicon Valley on the West Coast and Route 128 around Boston, but examples now include established and growing high-tech corridors in or near New York (Silicon Alley), Washington (Dulles Technology Corridor), Chicago (Golden Corridor), Portland (Silicon Forest), Raleigh-Durham (Research Triangle), and other places.

The point is that research universities are geographically rooted communities, and they are not easily exported. One can imagine a corporation moving its R&D overseas, but it is difficult to imagine that Stanford or the Massachussetts Institute of Technology will decide to up and relocate. Proximity and day-to-day human social interactions breed more efficient technology transfer. Thus, research universities and the industry that they engender serve to increase the appropriable return for the nations and regions that host them. A recent report (*15*) by the President's Council of Advisors on Science and Technology (PCAST), in which I participated, delves further into the new importance of the outstanding U.S. research universities. That report emphasizes their new dual mission, to protect and advance basic research and to make that basic research more easily translatable into application and technology in a way that remains geographically rooted.

There are also other kinds of rooted infrastructure, such as research parks, research incubators, national user facilities (such as synchrotron light sources), and so forth. These may geographically anchor all stages of the R&D process (*16*).

Let me approach my second, less conventional, path forward indirectly. A 2009 Harris poll (*17*) asked the public to name the most prestigious occupations. The answers (in order) were firefighter, scientist, doctor, nurse, teacher, and military officer. What struck me immediately when I saw this result is that every one of these, except scientist, is an immediate helper occupation. These people save us from fires, prevent attacks, teach our children, and heal us. By contrast, the value of scientists and the benefit they produce can be very long term. Yet the public perceives scientists as belonging in the same basket of high-prestige helper occupations. This tells us something. Another poll, by Pew (*18*), finds that the majority of Americans think that government investments in basic scientific research (73%) and engineering and technology (74%) pay off in the long run, with only small differences between Democrats and Republicans. That also tells us something.

When I ask nonscientists, "what is science good for?", only rarely do I hear the answer that it promotes economic growth. Instead, most answers are about science creating a better world in ways not easily monetizable: enabling longer, healthier lives; protecting the planet; feeding humanity; deterring (or winning) international conflicts; bringing us resiliency to engage future challenges of an uncertain world, with climate change as one example. People also talk about the basic human need for discovery and understanding of the natural world, about the almost-mysterious power of science at engaging the natural idealism of young people, and empowering them to participate in the world in ways that they otherwise would not.

There are numerous respected occupations that are closer to the business of business; that is, they enable industry to create jobs. Yet these are not at the top of the Harris poll. My theory is that the poll results, and also the public's appreciation of science's nonmonetizable benefits, are related effects: Both are the result of the public's intuitive understanding of something well known to statisticians as heavy-tailed distributions. When you bet on a heavy-tailed distribution that has positive outcomes, you can not only win, you can win big.

What It Means for Scientific Discovery to Be Heavy-Tailed

To the statistician, a heavy-tailed distribution describes a certain kind of pattern for how often random events with various magnitudes occur. Heavy-tailed means that extremely large events are only a bit rarer than mid-sized events. In other words, the tail of the probability distribution extends out to the right, so as to allow events of truly huge consequence to occur once in a while—and more than one might think.

(This is the opposite of the so-called normal distribution, where very large events are so exponentially improbable that, in practice, they never occur.)

Looking at the history of science over the last couple of centuries, it seems evident to me that the benefits of scientific discovery have been heavy-tailed. A typical medical advance might save many thousands of lives. The discovery of penicillin (and its publicly supported development, leading to further antibiotics) saved hundreds of millions of lives. In a single century (the 20th), a confluence of fundamental discoveries in quantum mechanics and atomic structure led to all of modern electronics, the computer, and the Internet. This stemmed from what, in the 1920s and 1930s, were arcane areas of very basic science. Thus large, incredibly consequential discoveries do occur relatively often.

Science's heavy tail allows us to expect even greater future discoveries, even if we cannot predict when they will occur or even what fields they will occur in. This might seem like a lot to load on two polls. However, many surrogates for measuring the distribution of returns from scientific discovery [such as patterns of patent citations (*19*, *20*) or frequency of citation of scientific papers (*21*)] demonstrate a heavy-tailed pattern.

If basic research is a heavy-tailed investment opportunity, as I claim, then what is the optimal investment strategy for nations to make in it? It turns out that the optimal strategy is not just to put some money into the bank account and watch it grow by compound interest, nor is it to try to pick winners (as my previous bad investment advice to you suggested). The former of these strategies simply misses the heavy-tailed rewards, whereas the latter is almost certain to lead to gambler's ruin, that is, losing everything on a mere temporary run of bad luck.

The optimal strategy for heavy tails is in effect the mathematical opposite of gambler's ruin. I call it patient investor's bounty. The player who stays in the game, investing on a continuing, sustainable basis, will be there to reap the rewards of the rare-but-huge heavy-tailed events (*22*). Stability of investment over the long run is likely to be the best predictor of success in this game.

The policy-maker might say this: All right, you need stability. But what is the right amount to invest in basic research (or, for that matter, in total R&D)? I can think of a couple of possible answers to this reasonable question.

First, we can look back at Fig. 2 for historical guidance. As nations compete for economic growth opportunities, it appears that those who spend close to 3% of their GDP on R&D are the ones that compete most successfully. The United States is in that club now. We don't want to fall out of it.

Second, we can look inward at ourselves. How patient we can be as patient investors is a matter of social and national character. It is a question of intergenerational social choice. What kind of world do we want our children and grandchildren to have? Does our planning horizon extend beyond two generations? Can we think about what kind of world we want for our great-great-great-great-grandchildren, who will be living a century from now? That is a very short time in the great scheme of things.

America is a country of wonderful, frontier, short-term pragmatism. That benefits us in many ways, but it may not put the United States in the best competitive position in a game of international competition that favors long time horizons. Europeans look up and see 500-year-old cathedrals. European science has developed mechanisms for obligating nation states to make investments over long periods, for example, to CERN (*23*), where the Higgs boson was discovered. Chinese culture sees itself as having continuity over millennia. China's investment in R&D as a fraction of GDP is under 2%, but that number is on a trajectory of amazingly rapid and sustained increase (*24*).

The American public already highly values science and scientists and seems to have an intuitive grasp of heavy-tailed, not immediately monetizable, returns. Through communication with the public, we must continue to provide the evidence that may justify those beliefs—indeed, this is the mission of AAAS. But also as individuals, we must seize every opportunity to demonstrate that what we do is altruistic and idealistic and that it is also economically vital. Our message is that science is a single, unified, long-term enterprise in which basic science discoveries, and research accomplishments of applied science and engineering, are things to be admired in their own right that also, often unpredictably, lead to better jobs and better lives, new products and new industries. Both of these perspectives will be well served if the United Statesis able to keep itself (and help to put the rest of the world) on a Solow-inspired trajectory of technology-enabled exponential growth.

References

1. R. R. Wilson, Congressional Testimony (April 1969); available online at http://history.fnal.gov/testimony.html.
2. G. Washington, "The first State of the Union address" (8 January 1790); available online at http://ahp.gatech.edu/first_state_union_1790.html.
3. Wikipedia, "National Endowment for the Arts" and "National Endowment for the Humanities," http://en.wikipedia.org.
4. National Science Foundation, Science and Engineering Indicators 2012, chapter 4; available online at www.nsf.gov/statistics/seind12/c4/c4s1.htm#s4.
5. R. J. Gordon, "Is U.S. Economic Growth Over? Faltering Innovation Confronts the Six Headwinds" (NBER Working Paper No. 18315, National Bureau of Economic Research, Cambridge, MA, August 2012); available online at www.nber.org/papers/w18315.
6. Federal Reserve Bank of St. Louis, "Real GDP Per Capita in the United States (USARGDPC)" (10 December 2012); available online at http://research.stlouisfed.org/fred2/series/USARGDPC.
7. "R&D Spending Growth Continues While Globalization Accelerates," *Battelle Memorial Institute and R&D Magazine* (December 2011); available online at http://battelle.org/docs/default-document-library/2012_global_forecast.pdf.
8. Organization for Economic Cooperation and Development (OECD), "International comparisons" in *Main Science and Technology Indicators*, **2011**, 2, OECD Publishing, Paris (2011).
9. R. M. Solow, *Rev. Econ. Stat.* **39**, 312 (1957).
10. J. Bernstein, D. Baker, "What Is 'Seinfeld' Worth?" *New York Times*, 31 July 2013, p. A21; available online at www.nytimes.com/2013/08/01/opinion/what-is-seinfeld-worth.html.
11. K. Arrow, in *The Rate and Direction of Inventive Activities*, R. Nelson, Ed. (Princeton Univ. Press, Princeton, NJ, 1962), pp. 609–625.
12. Z. Griliches, in *Handbook of Industrial Innovation*, P. Stoneman, Ed. (Blackwell, London, 1995), pp. 52–89.
13. A. J. Salter, B. R. Martin, *Res. Policy* **30**, 509 (2001). doi:10.1016/S0048-7333(00)00091-3
14. NSF National Center for Science and Engineering Statistics, "National patterns of R&D resources: 2010–11 data update," NSF 13-318; available online at www.nsf.gov/statistics/natlpatterns/.
15. President's Council of Advisors on Science and Technology, "Report to the President: Transformation and opportunity, the future of the U.S. research enterprise" (November 2012); available online at www.whitehouse.gov/sites/default/files/microsites/ostp/pcast_future_research_enterprise_20121130.pdf.
16. A. B. Jaffe, M. Trajtenberg, R. Henderson, *Q. J. Econ.* **108**, 577 (1993).
17. HarrisInteractive, "Firefighters, scientists and doctors seen as most prestigious occupations" (4 August 2009); available online at www.harrisinteractive.com/vault/Harris-Interactive-Poll-Research-Pres-Occupations-2009-08.pdf.
18. Pew Research Center for the People and The Press, "Public Praises Science; Scientists Fault Public, Media: Scientific Achievements Less Prominent Than a Decade Ago" (9 July 2009); available online at www.people-press.org/2009/07/09/public-praises-science-scientists-fault-public-media/.
19. M. Trajtenberg, *Rand J. Econ.* **21**, 172 (1990).
20. D. Harhoff, F. Narin, F. M. Scherer, K. Vopel, *Rev. Econ. Stat.* **81**, 511 (1999).
21. E. Garfield, paper presented at the International Congress on Peer Review and Biomedical Publication, Chicago, IL, 16 to 18 September 2005.
22. W. H. Press, *Science* **339**, 627 (2013). doi:10.1126/science.1235227
23. "Convention for the establishment of a European organization for nuclear research," 1 July 1953, amended 17 January 1971; available online at http://council.web.cern.ch/council/en/governance/Convention.html.
24. OECD, "Main Science and Technology Indicators"; available online at www.oecd.org/sti/msti.htm.

The Consequence of Tree Pests and Diseases for Ecosystem Services

I. L. Boyd,* P. H. Freer-Smith, C. A. Gilligan, H. C. J. Godfray

READ THE FULL ARTICLE ONLINE
http://dx.doi.org/10.1126/science.1235773

Cite this article as I. L. Boyd *et al.*, *Science* **342**, 1235773 (2013).
DOI: 10.1126/science.1235773

Background: Trees are major components of many terrestrial ecosystems and are grown in managed plantations and orchards to provide a variety of economically important products, including timber, pulp, fiber, and food. They are subject to a wide range of pests and diseases, of which the most important causative agents are viruses, bacteria, fungi, oomycetes, and insect herbivores. Research on tree pests and diseases has had a historical focus on trees of direct economic importance. However, some epidemics and infestations have damaged and killed common trees that are integral parts of natural ecosystems. These have harmed valuable landscapes and highlighted the wide-ranging consequences arising from tree pests and diseases. There is also growing concern that aspects of globalization—in particular, higher volumes and new forms of trade—may increase the risk of disease spread.

Advances: We review the challenges in maintaining tree health in natural and managed ecosystems. It is argued that it is helpful to consider explicitly the consequences of pests and diseases for the full range of ecosystem services provided by trees. In addition to forest and orchard products, tree pests and diseases can affect the ability of forests to sequester and store carbon, reduce flood risk, and purify water. They can affect the biodiversity supported by trees and the recreational and cultural values accorded to woodland by people. Many of these benefits are uncosted and enjoyed by different classes of stakeholders, which raises difficult questions about who should be responsible for measures to protect tree health. Changes in the risk of pest and disease introduction, the increasing prevalence of genetic reassortment leading to novel disease threats, and the potential role of climate change are all highlighted.

Outlook: Modern pest and disease management is based on an extensive science base that is rapidly developing, spurred in particular by modern molecular technologies. A research priority is to build a better understanding of why certain pathogens and insects become major pests and diseases. This will involve a better understanding of the molecular basis of pathogenicity and herbivory, as will ecological insights into why some species reach epidemic prevalence or abundance. It will also help anticipate which species may become a problem if they are transported to new geographical regions, recombine with other organisms, or experience new climatic conditions. However, identifying all species that may become pests will be impossible, and the Review stresses the importance of risk management at the "pathway of introduction" level, especially when modern trade practices provide potential new routes of entry. Last, when ecosystem services are provided by woods and forests rather than individual tree species, we need to understand better the consequences of pests and diseases that attack or feed on particular species.

ARTICLE OUTLINE

SUPPLEMENTARY MATERIALS

Supplementary Text
References

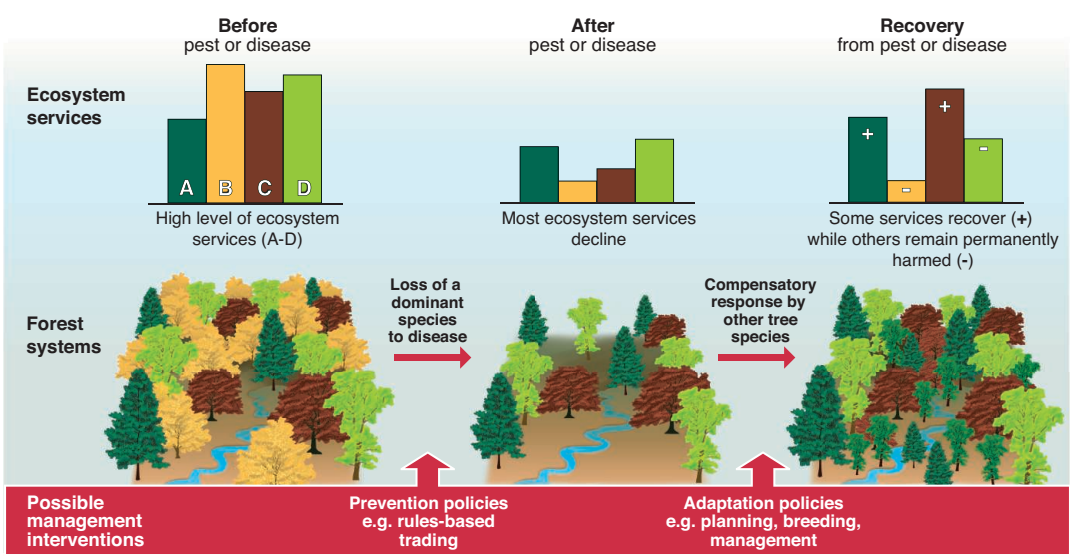

A forest providing numerous ecosystem services is subject to a disease epidemic that reduces the abundance of a dominant native species, resulting in a change in forest structure. Initially, a wide range of ecosystem services (**A** to **D**) are harmed. But as trees grow to replace lost species, some (perhaps carbon storage or water purification) are regained, whereas others (perhaps the biodiversity supported by the diseased tree species) are permanently disrupted. Policy measures can both help prevent new diseases being introduced (the first stage) or improve recovery through management practices or planting resistant trees.

The list of author affiliations is available in the full article online.
*Corresponding author. E-mail: ilb@st-andrews.ac.uk

The Consequence of Tree Pests and Diseases for Ecosystem Services

I. L. Boyd,[1]* P. H. Freer-Smith,[2] C. A. Gilligan,[3] H. C. J. Godfray[4]

Trees and forests provide a wide variety of ecosystem services in addition to timber, food, and other provisioning services. New approaches to pest and disease management are needed that take into account these multiple services and the different stakeholders they benefit, as well as the likelihood of greater threats in the future resulting from globalization and climate change. These considerations will affect priorities for both basic and applied research and how trade and phytosanitary regulations are formulated.

Trees support a broad array of organisms that feed on or infect them. When these herbivores or infections are perceived to reduce the value of trees to people, they are termed pests and diseases (*1*, *2*). Recent examples of the near extermination of common tree species over large geographical areas—including that of the American chestnut (*Castanea dentata*) in North America because of chestnut blight (*3*) and elms (*Ulmus* spp.) in Europe and North America because of Dutch elm disease (*4*)—have highlighted the vulnerability of trees to disease and our lack of preparedness to deal with these threats. Current trends in pest and disease outbreaks suggest that greater vigilance and new approaches may be needed.

The management of pests and diseases has historically been concerned with species grown for wood and pulp, for fruit and other food, and to a lesser extent, for their arboricultural and amenity value. Reduction of the direct economic harm of tree pests and disease will continue to be very important, but there is an increasing understanding that trees provide additional benefits to society. Trees can be thought of as key components of natural or artificial ecosystems that provide a wide variety of different ecosystem services (*5*, *6*). Explicit consideration of how pests and diseases affect the multiple services provided by trees can change both research priorities and management strategies (Fig. 1) (*7*).

In this Review, we explore how pests and diseases influence the range of services provided by trees and look at how future trends such as increasing trade and climate change may interact with pests and diseases to affect the benefits we obtain from trees. We use the terms "pest" and "disease" to describe all pathogens and small- to medium-size herbivores that—by causing death, morbidity, or other harm—disrupt the ecosystem services provided by trees. We ask in particular whether the way we research and manage tree pests and diseases, with its historical preoccupation with tree products, is best placed to protect the multiple services we require from trees.

[1]College Gate, University of St. Andrews, St. Andrews KY18 9LB, UK. [2]Forest Research, Alice Holt Lodge, Farnham, Surrey, GU10 4LH, UK. [3]Department of Plant Science, University of Cambridge, Cambridge, CB2 3EA, UK. [4]Department of Zoology, University of Oxford, Oxford, OX1 3PS, UK.

*Corresponding author. E-mail: ilb@st-andrews.ac.uk

The Pests and Diseases of Trees

Trees are attacked by a wide range of pathogens, including bacteria (*8*), helminths (*9*), viruses (*10*), and many fungi and oomycetes (*11*). Insects and other invertebrates attack all parts of the plant, with defoliators and borers causing most direct damage; other insects may be more evident as disease vectors (*8*, *12*). An illustrated account of some of the most important tree natural enemies is provided in Fig. 2 and the supplementary materials. Pests and pathogens can also interact; for example, trees suffering defoliation by an insect pest are typically more vulnerable to systemic pathogens (*10*). Pest and disease problems may be caused by native organisms attacking native trees, although many of the most pernicious threats arise from introduced species feeding on or infecting trees outside their native range.

In the past 50 years, there have been several major pathogen outbreaks that have drastically reduced the densities of particular tree species. Widespread diebacks have alarmed the public and raised tree health higher on the policy agenda. The most important of these pathogens have been fungi and oomycetes (water molds); the latter are curious organisms once classified as fungi but now recognized as distant relatives of diatoms and algae. The most damaging bacterial disease of trees is probably Citrus greening or huanglongbing caused by *Candidatus Liberibacter asiaticus*, which although of Asian origin is now present in many countries worldwide. The disease was largely ignored until its introduction to the Americas and it is now a substantial challenge in newly infected citrus production areas (*13*). Pine wilt is a problem caused by the nematode *Bursaphelenchus xylophilus*, which is spread by *Monochamus* beetles and with the movement of infested wood. Its native range covers much of Canada, the United States, and Mexico, where it does not kill trees, but it is now present in China, Japan, Korea, Taiwan, and Portugal, where it is causing substantial losses of susceptible trees, especially pines (*9*).

Fungi are behind the devastation of the American chestnut (*Castanea dentata)* in eastern North American forests. The introduced fungus *Cryphonectria parasitica* (chestnut blight) led to a decline in the frequency of this iconic tree from 36% in 1934 to 0.5% in 1993 and its replacement by oak, maple, and hemlock species (*14*, *15*). Dutch elm disease is also a fungal pathogen (*Ophiostoma novo-ulmi*) and is transmitted by bark beetles; it has eliminated mature elms (*Ulmus* spp.) from European and North American landscapes from the late 1960s (*4*, *15*). Today, there is intense concern that another major European tree species, ash (*Fraxinus excelsior*), could suffer a similar fate as an emergent fungal pathogen (*Chalara fraxinea*), first observed to kill trees in Poland in the 1990s, inexorably increases its geographic range (*16*).

The most notable oomycetes are species of *Phytophthora*, which cause disease in both trees and other plants (they include the pathogen responsible for the Irish potato famine). The introduction of *Phytophthora cinnamomi* to Western Australia caused dieback of Jarrah (*Eucalyptus marinata*) over an area of 282,000 ha. *Phytophthora* spp. often have broad host ranges, and in addition to Jarrah, plants in 34 other genera have also been killed by *P. cinnamoni* in Australia (*17*). *Phytophthora ramorum* is another species with a broad host range (*18*). It was probably introduced into North America and Europe from Asia and leads to sudden oak death in the United States (*19*), although in the UK, it unexpectedly causes most problems as a disease of Japanese larch (*Larix kaempferi*).

Insects can also be major tree pests. For example, Asian longhorn beetle (*Anoplophora glabripennis*) is a wood-boring insect that has spread in packaging material from southeast Asia to the United States, Canada, and Europe, with devastating consequences for indigenous broad-leaved trees in several countries (*20*). Oak processionary moth (*Thaumetopoea processionea*) is an invasive tree defoliator that can cause local defoliation of oak (*Quercus* spp.), although it is of greater concern because the urticarial hairs shed by its larvae are a threat to human health (*21*). Recent infestations of bark beetles and defoliating insects in North America have been more intense than at any time in recorded history (*22*, *23*). Mountain pine beetle (*Dendroctonus ponderosae*) has a wide tree host range, and outbreaks occur when the beetle experiences several years of favorable weather (*23*). Over 1 million ha of western yellow pine (*Pinus ponderosa*) and 1.5 million ha of piñon pine (*Pinus edulis*) have been killed on the Colorado Plateau and central Rocky Mountains, and over 37 million ha of forest are likely to be affected in British Columbia between 2000 and 2020 (*24*). Emerald ash borer (*Agrilus planipennis*), an insect pest introduced from Asia, is a further threat to ash species in addition to ash dieback in North America and Europe (*7*, *25*).

Tree Health and Ecosystem Services

Thinking about pests and diseases in terms of ecosystem services highlights potential risks that might otherwise be overlooked and reveals who

benefits from improved tree health and hence who might be expected or required to invest in pest and disease management. A simple classification of the ecosystem services provided by trees includes the direct products used by man (provisioning services), the indirect benefits that occur through modification of the environment (regulating services), and improved human well-being (cultural services).

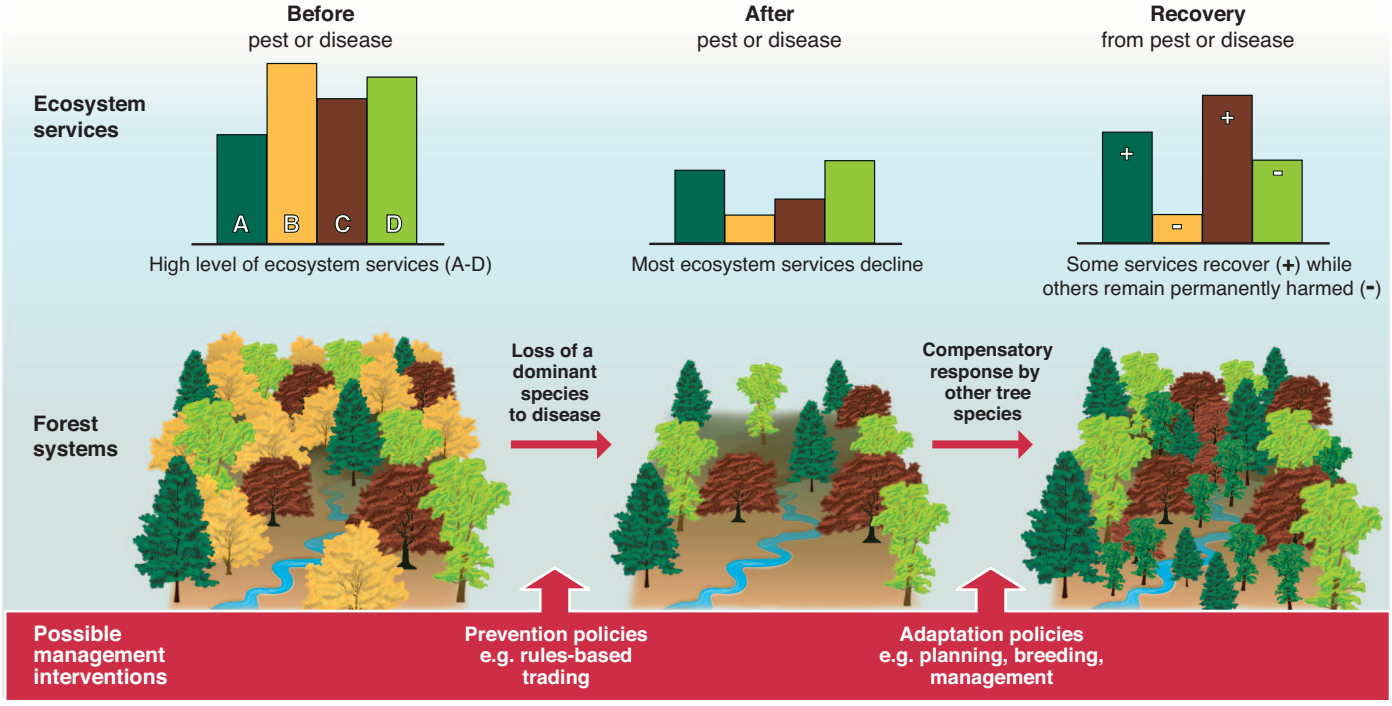

Fig. 1. A forest providing numerous ecosystem services is subject to a disease epidemic that reduces the abundance of a dominant native species, resulting in a change in forest structure. Initially, a wide range of ecosystem services (**A** to **D**) are harmed. But as trees grow to replace lost species, some (perhaps carbon storage or water purification) are regained, whereas others are permanently disrupted (perhaps the biodiversity supported by the diseased tree species). Policy measures can both help prevent new diseases being introduced (the first stage) or improve recovery through management practices or planting resistant trees.

Fig. 2. Tree pests and pathogens. In recent years, landscape-scale pest and pathogen problems have drawn attention to the potential threat to trees and forest ecosystems globally. Examples include (**A**) Chestnut blight caused by the fungus (*Cryphonectria parasitica*, top left) on American chestnut (*Castanea dentata*) (bottom left), and European chestnut (*C. sativa*) in Slovakia (main image); (**B**) the oomycete *Phytophthora cinnamomi* (inset) causing mortality in a 4-year-old plantation of sand pine (*Pinus clausa*) in the United States; and (**C**) the mountain pine beetle *Dendroctonus ponderosae* (inset) infesting a lodgepole pine (*Pinus contorta*) plantation in Canada. Illustrated accounts of major tree diseases and outbreaks caused by bacteria, helminths, oomycetes, bark beetles, boring insects and phloem feeders are provided in the supplementary materials. [Photos provided by E. Bush, Virginia Polytechnic Institute and State University; E. L. Barnard, Florida Department of Agriculture and Customer Services; J. O'Brien, U.S. Department of Agriculture (USDA) Forest Services; A. Kunca, National Forest Centre, Slovakia; USDA Forest Service, Region 2, Rocky Mountain Region Archive and R. F. Billings, Texas Forest Service, respectively; all from www.bugwood.org. Top left image, Biodisc/Visuals Unlimited.]

Much of the historical focus on tree pests and diseases has been on the damage they do to provisioning services (*1*, *2*): to timber and pulp or to fruit, nuts, and vegetable oil. Forest products alone are estimated to be worth ~$120 billion annually (*26*). Because many biotic threats cannot be controlled at the level of the individual landholding, state authorities become involved in regulating trade, setting biosanitary standards, and providing information and training to reduce risk. Although it was long assumed in most countries that the state had a direct role in subsidizing provisioning services in agriculture and forestry, many nations now seek to shift the burden to those that benefit financially, a move naturally resisted by industry. Debates about where the balance of responsibility should lie between the different beneficiaries and public good (*27*, *28*) can be very complex. For example, in many countries there is a thriving industry importing saplings, but if this results in the introduction of a new pest or disease, the cost is largely borne not by the industry but by foresters and farmers (*2*). At the international level, a balance has to be struck between the rights of nations to restrict the spread of agents that will harm their tree-based industries and ecosystems and the risk of this being used as a barrier to free trade.

From a societal point of view, major tree health problems reduce the flow of a particular product—pine bark beetles affect the availability of pine wood, for example—leading to a price response. However, in most cases one type of timber or food type can substitute for another without great disruption, especially in a global marketplace, again underlining the point that for provisioning resources, it is the farmer or forester that suffers most in cases of poor tree health. However, forests are a particular asset class with a very delayed return on investment, and the concern that market mechanisms may not always secure long-time supply of forest products (and associated rural economic activity) has led to arguments for state involvement.

Because of the longevity of tree species, threats to tree health are of particular economic importance to provisioning service providers, such as farmers and forest owners, because long-term investment is threatened and it takes time to replace a damaged or destroyed tree. Society may take a view that to encourage assured supply of timber and other tree resources (or associated rural livelihoods), it may want to absorb some component of this risk in order to increase the attractiveness of investing in forestry.

Trees dominate many landscapes and have a major effect on the regulating services provided by these ecosystems. These services include climate regulation, carbon storage (*29*–*31*), carbon sequestration [~30% of global CO_2 emissions are taken up by forests (*32*)], flood control, and water purification (*33*, *34*). The forests and woodlands that provide these services contain individual tree species that typically are the targets of specific pests and diseases. In diverse natural forests, the loss or dramatic reduction in density of one species may be readily compensated by other species filling the gap (*14*, *35*), as was seen by the replacement of American chestnut by other trees after the chestnut blight epidemic. The net effect on carbon stocks or other ecosystem services such as water management may thus be small, although regulating services may be affected during the transition period. The degree to which the functional integrity of the ecosystem is resilient to pests and disease may differ from one place to another. Some North American forests are dominated by foundation or keystone species whose loss to pests and diseases can fundamentally alter the value of the ecosystem services provided by forests (*36*, *37*). For example, much of the northern boreal zone is of low diversity and hence probably reduced functional redundancy, and here a threat to an individual species may have much more impact (*26*, *38*).

This Review has excluded discussion of large mammalian herbivores, but their greater polyphagy (deer eat most young saplings) or role as ecosystem engineers (for example, beavers) mean they have a potentially much larger effect on regulating services than do most other pests and diseases.

In many areas of the world, humans largely determine the distribution of forest and woodland. However, pests and diseases can affect regulating services indirectly by influencing land-use decisions. This could happen by reducing the perceived economic returns from forests (including through increased financial risk of return on investment) or by reducing the societal desirability of woodlands.

Regulating services can benefit the landowner (for example, flood control), the region (for example, water management), or everyone (for example, carbon sequestration). Thus, who should pay to reduce the threat from pests and diseases is complex and context-specific and may depend on the scale over which benefits are provided.

Trees and forests are of enormous importance for individuals who cherish particular landscapes, tree species, tree-dominated parks and cityscapes, and even individual trees (*1*, *39*). Attempts to ascribe an economic value to these cultural services are fraught with difficulties. For example, the value of identical woodlands may depend on their proximity to a city or be influenced by an individual's sociocultural background and economic circumstances (*40*, *41*). The mere act of assigning value can influence how a resource is regarded by society, and some have argued for a more explicit ethical, values-driven approach to decisions of this type (*42*).

Tree pests and diseases affect cultural services in different ways (*43*). As with regulating services, we need to understand how a reduction in tree health affects the value placed on these resources—for example, on the importance of woodland and forests to society. This again is complex because it may include how enjoyment of landscapes is transiently affected by the presence of tree pests and diseases. Some of the greatest harm to cultural services occurs when iconic species are severely affected by disease, as noted already for chestnut blight and Dutch elm disease. One concern about the spread of the oak processionary moth is that its larvae's urticarial hairs will affect the amenity value of woodland.

It is often not straightforward to predict which threats to trees will elicit the greatest concern in the general public. The nonmonetary nature of cultural services means it is difficult to track their value, and this can lead to unexpected and apparently rapid shifts in the public value placed on them. Social amplification is a term used to describe dramatic switches in public concern, often

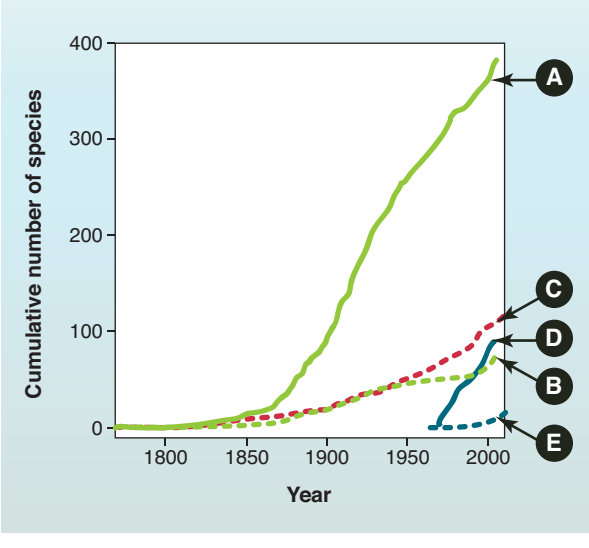

Fig. 3. A composite representation of the increasing number of pests and pathogens affecting different regions. Solid lines indicate the number of introduced species, and dashed lines indicate the number of pests and/or pathogens. Common colors indicate the same geographical region (green, United States; red, Europe; blue, United Kingdom or Great Britain). (**A**) Cumulative number of nonnative insects introduced and found in association with trees to the United States during 1800 to 2006 (*90*). (**B**) Cumulative number of "high-impact" nonnative tree insect pests and pathogens introduced to the United States during 1800 to 2006 (*90*). (**C**) Cumulative number of nonnative tree pathogens introduced to Europe during 1800 to 2009 (*57*). (**D**) Cumulative number of nonnative invertebrates introduced to Great Britain during 1970 to 2004 (*91*). (**E**) Cumulative number tree pests and pathogens introduced to the UK during 1965 to 2012 (*92*). Additional information about the data sources is provided in the supplementary materials.

caused by positive feedback through new and old media (*44*). Such events can greatly increase the pressure on policy-makers to respond to threats to cultural services (*45*). The nonmonetary nature of most cultural services clearly places a duty on the state to underpin their protection, although other sectors are also involved. In high-income countries, for example, civil society and nongovernmental organizations play a role in protecting forested areas, whereas private individuals owning trees in gardens, as well as the horticultural sector that supports them, have major interests in tree health.

Trees and forests also provide supporting services for other ecosystem components. In particular, they are home to many species of plants and animals that may themselves constitute provisioning services (such as wild honey bees or harvested animals), regulating services (pollinators or the natural enemies of pests), or cultural services [a major fraction of the earth's biodiversity lives in forests, particularly tropical forests (*46*–*48*)]. There are disservices (*49*) as well as services: Forest elephants and deer can cause economic damage in surrounding farmland, and sylvan mosquitoes spread malaria in the Brazilian Amazon (*50*). Some insect herbivores damage both trees and human health through shedding urticarial hairs, or the loss of trees can be associated with increased risk to health (*51*). Native nonpest herbivores that rely on specific tree species are especially vulnerable to disease of their host species; for example, the loss of mature elms in Europe has dramatically decreased the abundance of the white-letter hairstreak butterfly *Satyrium w-album*, which feeds only on this host plant (*52*).

Global Change and Tree Pests and Diseases

Globalization and Pest and Disease Movement

People have moved trees beyond their native range since at least the beginning of agriculture, and international trade has increased greatly over recent decades (*53*). The threat presented by pests and pathogens can be represented by the number of new species of potential pests and pathogens being imported, whether or not they end up becoming pests or causing disease. Based on experience from Great Britain and the United States, there is an apparent constant rate of ingress of new forest invertebrate species (Fig. 3; line A compared with line D), and a similar trend exists for Europe and Africa (*54*). The constant rates illustrated by these data suggest that plant health inspection regimes could be keeping pace with the increased threats from increasing volumes of trade (*55*, *56*).

However, not all of these species cause harm. In contrast to the steady ingress of species that threaten to cause infestations or diseases, there has been a recent acceleration in the occurrence of harmful pests and pathogens in the United States (Fig. 3, line B), Europe (Fig. 3, line C), and the UK (Fig. 3, line E). Santini *et al.* (*57*) found that at least 68% of harmful pathogens introduced to Europe have been assisted in some way by trade. It is also possible that a further proportion of those that have unknown routes of entry (22%) are connected to trade because not all forms of trade can be monitored effectively. This acceleration in the appearance of damaging infestations and disease, especially in recent years, is a cause for concern, and it is not clear why this pattern differs from the relatively constant rate of importation of new species. One possible conclusion is that an increasing proportion of the species that are imported are causing infestations or disease.

Globalization and Genetic Reassortment

Species that may be commensals or only mildly pathogenic within their original tree hosts can become pests or pathogens when moved elsewhere. In some cases, especially among pathogens, new

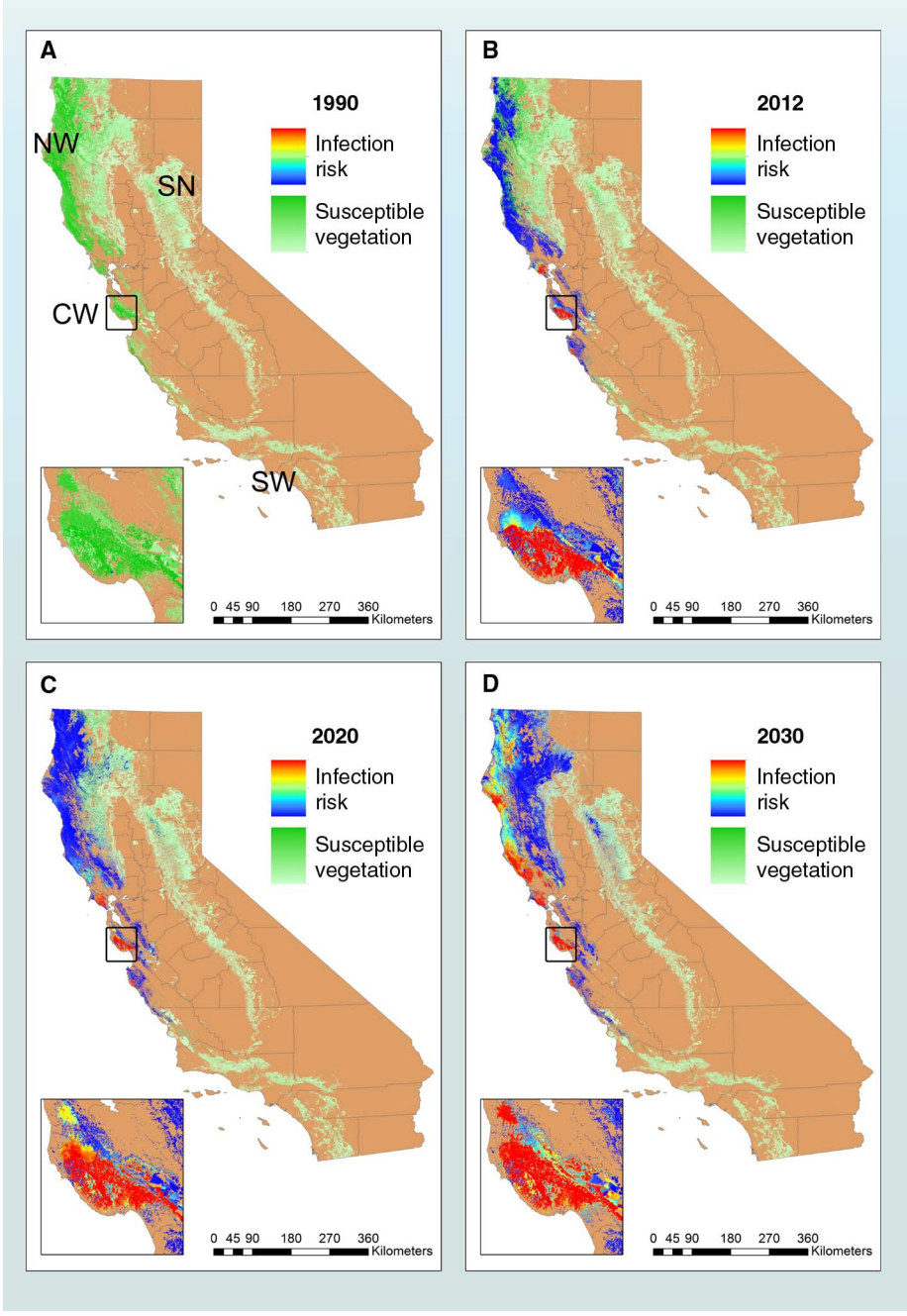

Fig. 4. Predicted spread of sudden oak death (SOD). Shown is from 1990 (putative date of introduction to the San Francisco Bay area) to 2030 in California by using a stochastic, spatially explicit epidemiological model (*79*). The model used two scales of dispersal, involving local spread (~0.1 to 3 km) of *P. ramorum* by spores in rain and wind (*80*) coupled with long-distance movement (~3 to 100 km). Despite its name, SOD has a wide host range (>50 woody species). (**A**) The distribution of susceptible vegetation in California. (**B** to **D**) Model predictions for the risk of spread.

diseases can arise spontaneously because of genetic change in the infecting species. Further problems occur when introduced species escape their own natural enemies or encounter hosts that have no evolved resistance mechanisms.

Several tree diseases have arisen from introduced species that hybridized with or acquired genes from resident species. For example, when the causal agent of Dutch elm disease, *O. novo-ulmi*, spread across the northern hemisphere, it acquired major genes through hybridization with the native species *O. ulmi*. This gene transfer probably prevented the attenuation of infection in elms by *O. novo-ulmi*, which proved to be a very damaging pathogen (*58*). In addition, many invasive pathogens may initially arrive as a single genotype or clone, and sometimes the invasive clone has been a single mating or compatibility type. Some genotypes are more aggressive pathogens than others (*11*), and the presence of compatible mating types and occurrence of sexual reproduction increases the opportunity for the development of pathogenicity. Examples include *Phytophthora cinnamomi*, *P. ramorum*, and *Dothistroma septosporum* (a fungus that causes needle blight on conifers). Genetic reassortment allows introduced pathogens to acquire specific virulence factors that enable them to colonize native hosts. But, genetic exchange may also be facilitated when the nursery trade brings together numerous species and their pathogens in close proximity. The highly aggressive *Phytophthora* of alder arose out of a swarm of new interspecific hybrids, and the spread of the new aggressive subspecies *P. alni* subsp. *Alni* along Bavarian rivers was associated with infested alder nursery stock (*11*).

Outside of the major pathogens of commercial trees, we still know relatively little about the diversity of tree pathogens in the field, and frequently a poor understanding of their taxonomy is an impediment to their study. Molecular phylogenetics have allowed the geographic and evolutionary origins of a number of fungal pathogens to be identified (*11*), but taxonomic uncertainty can still be a problem in the diagnosis and response to new diseases. In 2006, the causal agent of ash dieback in Europe, the fungus *Chalara fraxinea*, was wrongly identified as the asexual form of an indigenous saprotrophic fungus, *Hymenoscyphus albidus* (in fungi, sexual and asexual forms of the same species can be given different Linnean binomials, and the asexual form of *C. fraxinea* is now known as *Hymenoscyphus pseudoalbidus*) (*59*). This meant that it was not designated as a controlled organism, and trade in ash was allowed to continue (*60*).

Insect pests can also adapt to new hosts but are less likely to hybridize and acquire new genes. However, many rely on bacterial symbionts, and the acquisition of new associates can give rise to tree disease. The scolytid beetle *Dendroctonus valens* has recently colonized China, where it has acquired novel indigenous isolates of its fungal associate *Leptographium procerum* (*61*). The new symbiosis increases the severity of the pest, partly because the fungus releases volatiles that attract further beetles that help to overwhelm the tree's defenses.

Climate Change

Climate change may influence the susceptibility of trees to pest and disease, which in turn may affect forest ecosystem services such as the regulation of carbon and water cycles (*32*–*34*). Pest and disease outbreaks are often triggered by abiotic stress that weakens trees (*1*), and because climate change is predicted to increase the frequency of drought, flooding, severe gales, and extreme temperature events, it is reasonable to expect more frequent outbreaks. The northern boreal forests of North America are typically carbon sinks but can become sources when severe pest infestations occur (*24*, *62*, *63*), contributing to a positive feedback. Climate warming is possibly the major proximate driver of changes in cover in boreal forests (*64*–*66*), and pests or pathogens are likely to be an important ultimate factor determining tree growth and survival.

There is evidence that climate warming has already resulted in increased tree mortality from disease in boreal Alaska (*66*), where the area damaged by pests and pathogens exceeds that affected by fire (*67*). Spruce beetle outbreaks (*Dendroctonus rufipennis*) occur in Alaska at ~50-year intervals but have increased in frequency and extent in recent years, possibly because of shorter beetle life cycles in a warmer environment (*65*, *68*). Insects such as the mountain pine beetle (*D. ponderosae*) kill large discrete patches of trees and are a major driver of forest disturbance dynamics (*69*). This is a natural element of boreal forest ecology (*70*, *71*) but might make forests more susceptible to the effects of increased fire and wind damage due to a changing climate (*24*).

There is most likely a reporting bias toward the negative effects involving climate change and pests and diseases. Some effects of climate change may be positive. For example, pest insects can overwinter beneath an insulating blanket of snow, and reduced snow cover can increase their exposure to low temperatures, causing the insects to die (*1*). Greater disturbance and hence more dead wood can be positive for those components of biodiversity that require this resource (often rare in managed forests when dead wood is removed). More sophisticated integrated assessments are needed that capture the many different consequences of climate warming in order to understand how the ecosystem services provided by forests will change over the coming decades (*38*).

Priorities for the Future

Research

Parasites and herbivores are both components of natural ecological communities and have the potential to become outbreak pathogens and pests, respectively. Despite substantial advances, there is still much we do not know about tree antagonists in natural communities, including their role in maintaining community diversity (*46*, *72*–*74*), which may be important for the delivery of ecosystem services. Only a small fraction of the many diseases and herbivores affecting any tree species cause major harm to tree health. A better understanding of the natural regulation of herbivores and pathogens and under which circumstances this relationship breaks down and results in the emergence of pest and disease would help improve the management of these threats (*24*, *75*, *76*). Many of the most important recent emergent diseases, as well as some insect pests, have switched to feed on new host plants. Understanding the precise molecular mechanisms that allow successful host plant infection by a pathogen, or that lead an insect to recognize a particular plant species as food, are currently major research themes, with progress greatly facilitated by advances in genomics and other areas of molecular biology (*11*, *77*).

The ability to predict the spatial spread of pests and diseases, especially introduced or emerging species, is critical in managing their damage. The connectivity of the susceptible host population is important in determining the rate and extent of local spread by tree pathogens (*78*). However, many plant pathogens are capable of long-distance dispersal. Daughter foci can occur well ahead of the major region of an invasion, as in the case of the isolated outbreaks of *P. ramorum* in Northern California and Oregon that appeared beyond the main regions of sudden oak death in the central coastal regions of California (*79*). One of the principal challenges in the epidemiology of tree diseases is to characterize dispersal kernels and transmission rates for emerging pathogens, often from limited data such as aerial photographs (*80*) or remote sensing.

Epidemiological modeling can combine an understanding of the disease process with meteorological and detailed geographic data to help predict spread and the optimal design of surveillance programs (Fig. 4). These models can provide generalized predictions of disease spread based on fitting the models to data of historical spread (*81*). The case of sudden oak death in California (Fig. 4) illustrates predicted heterogeneous spread within different regions that reflect interactions of environmental conditions, the density and contiguity of susceptible host vegetation, and the inherent epidemiological scales of dispersal. Outputs from models such as this can be used to help optimize sampling strategies so as to detect disease spread, inform management strategies (*79*, *80*), and predict effects on ecosystem services (*19*).

The longevity of trees and the delay before they reproduce has always been a hindrance to breeding for disease resistance. Today, some of these problems can be mitigated by use of modern genetic techniques, such as marker-assisted selection, which should save several years by allowing rapid identification of resistant genotypes

for breeding. The development of resistant hybrids has also proved effective, such as in the case of forest restoration of American chestnut (*3*). However, in *C. dentata* a number of candidate genes for host resistance to chestnut blight fungus (*C. parasitica*) have been identified (*77*), and as for other tree species, understanding the molecular basis of resistance will facilitate the breeding of resistant genotypes. As the full genome sequences of trees become available, progress is likely to accelerate, as will the opportunities to capitalize on genetic modification in countries that permit this technology.

Management

There is considerable scope for both technical and organizational innovation in controlling the spread of tree disease. Risk-based approaches are at the center of the management of tree disease (*82*, *83*) and are governed globally through the World Trade Organization Sanitary and Phytosanitary (WTO SPS) agreement and the International Plant Protection Convention. Regional plant protection organizations (such as the European and Mediterranean Plant Protection Organization) coordinate regional activities. Adoption of risk-based approaches means the acceptance that measures to prevent incursions are implemented in a manner that is proportionate to the severity and likelihood of the hazard. At the moment, however, most assessments of risk focus on direct economic damage to provisioning services rather than on the broader set of ecosystem services explored above. Assessment of risk needs to consider the full range of ecosystem services provided by different host species, including nonmonetary cultural services and their role in supporting other biodiversity. It is also important for all parties to communicate a balanced and realistic assessment of the likely risks of incursions of tree pests and diseases so as to avoid disproportionate public concern (*44*) when infestations do occur.

Current plant health regimes are mainly based on pest risk assessments (PRAs) and control measures against identified, listed organisms, but it is impossible to identify all potential pathogens and to develop risk-based approaches to deal with each on an individual basis. A better approach is to identify different classes of threat defined by (i) type of disease-causing agent (for example, fungal pathogen or insect defoliator); (ii) pathways of movement (for example, natural pathways such as wind, water, animal or man-made pathways, including shipping containers, wood imports, dunnage, and bulk cargos); and (iii) the type of ecosystem service at threat (for example, a tree species valuable for its timber, its keystone role in natural forest, or its conservation importance). It is also critical to anticipate new pathways that may emerge through changing patterns in global trade and the adoption of new technology. For example, recent trends such as the use of containers and refrigeration, the use of wood products as bulk packaging material, as well as the trade in rooted plants in pots with soil provide new potential entry pathways (*55*). In our view, the implementation of voluntary and regulatory measures to address these new pathways has nearly always happened after the fact and are often inadequate.

Biological control—the deliberate release of another organism to control a pest or disease—has had a mixed history for tree pests (*84*) and in managed forests and plantations has to be applied within the context of integrated pest management (*85*). A typical situation in which biological control can be very successful is when a tree is being grown outside its native distribution and an insect from its original range is introduced and becomes a pest. Often, the pest is only an issue because it has escaped its own natural enemies, and their deliberate introduction can solve the problem. Introduction of the Australian predatory Vedalia beetle (*Rodolia cardinalis*) in the late 1800s probably saved the Californian citrus industry, which was being ravaged by a scale insect on which the beetle fed (*86*). The next two decades are likely to see the development of radical new forms of genetics-based biological control: genes that can spread through targeted pest or disease populations despite imposing fitness costs, leading to population suppression (*87*). Whether such approaches will be acceptable to civil society is not yet clear.

Last, increasing resilience to pests and diseases should be a key management goal to help maintain the ecosystem services provided by trees. In orchards and commercial plantations, this is likely to involve greater emphasis on genetic diversity, a move that will be helped by a better understanding of the molecular basis of resistance. For mixed use, amenity, and restored forest, this will require the careful choice of species composition, and for planted forests, improved management practices will be required to restore specific ecosystem services (*88*, *89*). These methods need to be extended to include resilience to possible interactions between climate change and pests and diseases.

Conclusions

There is rising concern that the increase in tree pests and diseases is one of the most tangible manifestations of increasing anthropogenic stresses on life systems. This concern is built on growing evidence that trees, forests, and woodlands are essential parts of sustainable, productive, and safe environments. Trade is an integral part of a modern, globalized economy but, if unregulated, has potentially severe costs for some of the most important ecosystem services involving trees. The evidence suggests that there is likely to be no reduction in this pressure. Although quantifying this cost is likely to be an active research field in the near future, we already know enough to justify substantial investment in novel and practical forms of mitigation. But, science can provide only part of the solution. Policy-makers and civil society need to understand the very many benefits that trees provide beyond timber, fuel, and food and develop and implement evidence-based policies to protect this invaluable component of our natural capital from the extra burdens of pests and diseases to which they are increasingly exposed.

References and Notes

1. M. P. Ayres, M. J. Lombardero, Assessing the consequences of global change for forest disturbance from herbivores and pathogens. *Sci. Total Environ.* **262**, 263–286 (2000). doi: 10.1016/S0048-9697(00)00528-3; pmid: 11087032
2. J. E. Aukema *et al.*, Economic impacts of non-native forest insects in the continental United States. *PLOS ONE* **6**, e24587 (2011). doi: 10.1371/journal.pone.0024587; pmid: 21931766
3. D. F. Jacobs, Toward development of silvical strategies for forest restoration of American chestnut (Castanea dentata) using blight-resistant hybrids. *Biol. Conserv.* **137**, 497–506 (2007). doi: 10.1016/j.biocon.2007.03.013
4. C. Potter, T. Harwood, J. Knight, I. Tomlinson, Learning from history, predicting the future: The UK Dutch elm disease outbreak in relation to contemporary tree disease threats. *Philos. Trans. R. Soc. London B Biol. Sci.* **366**, 1966–1974 (2011). doi: 10.1098/rstb.2010.0395; pmid: 21624917
5. R. K. Turner, G. C. Daily, The ecosystem services framework and natural capital conservation. *Environ. Resour. Econ.* **39**, 25–35 (2008). doi: 10.1007/s10640-007-9176-6
6. I. J. Bateman *et al.*, Bringing ecosystem services into economic decision-making: Land use in the United Kingdom. *Science* **341**, 45–50 (2013). doi: 10.1126/science.1234379; pmid: 23828934
7. W. C. Johnson *et al.*, Forty years of vegetation change on the Missouri River floodplain. *Bioscience* **62**, 123–135 (2012). doi: 10.1525/bio.2012.62.2.6
8. S. E. Halbert, K. L. Manjunath, Asian citrus psyllids (Sternorrhyncha : Psyllidae) and greening disease of citrus: A literature review and assessment of risk in Florida. *Fla. Entomol.* **87**, 330 (2004).
9. E. Bergseng *et al.*, Combining ecological and economic modelling in analysing a pest invasion contingency plan—The case of pine wood nematode in Norway. *Scand. J. For. Res.* **27**, 337–349 (2012). doi: 10.1080/02827581.2011.637509
10. G. Dwyer, J. Dushoff, J. S. Elkinton, S. A. Levin, Pathogen-driven outbreaks in forest defoliators revisited: Building models from experimental data. *Am. Nat.* **156**, 105–120 (2000). doi: 10.1086/303379; pmid: 10856195
11. D. E. L. Cooke, A. Drenth, J. M. Duncan, G. Wagels, C. M. Brasier, A molecular phylogeny of *Phytophthora* and related oomycetes. *Fungal Genet. Biol.* **30**, 17–32 (2000). doi: 10.1006/fgbi.2000.1202; pmid: 10955905
12. C. M. Brasier, S. A. Kirk, Rapid emergence of hybrids between the two subspecies of *Ophiostoma novo-ulmi* with a high level of pathogenic fitness. *Plant Pathol.* **59**, 186–199 (2010). doi: 10.1111/j.1365-3059.2009.02157.x
13. T. R. Gottwald, Current epidemiological understanding of citrus huanglongbing. *Annu. Rev. Phytopathol.* **48**, 119–139 (2010).
14. K. J. Elliott, W. T. Swank, Long-term changes in forest composition and diversity following early logging (1919-1923) and the decline of American chestnut (*Castanea dentata*). *Plant Ecol.* **197**, 155–172 (2008). doi: 10.1007/s11258-007-9352-3
15. J. Loo, Ecological impacts of non-indigenous invasive fungi as forest pathogens. *Biol. Invasions* **11**, 81–96 (2009). doi: 10.1007/s10530-008-9321-3
16. T. Kowalski, *Chalara fraxinae* sp. Nov. associated with dieback of ash (*Fraxinus excelsior*) in Poland. *Forest Pathol.* **36**, 246–270 (2006).
17. D. M. Cahill, J. E. Rookes, B. A. Wilson, L. Gibson, K. L. McDougal, *Phytophthora cinnamomi* and Australia's biodiversity: Impacts, predictions and progress towards control. *Aust. J. Bot.* **56**, 279–310 (2008).

18. N. J. Grünwald, E. M. Goss, C. M. Press, *Phytophthora ramorum*: A pathogen with a remarkably wide host causing sudden oak death on oaks and ramorum blight on woody ornamentals. *Mot. Plant Pathol.* **9**, 729–740 (2008).
19. R. C. Cobb, J. A. N. Filipe, R. K. Meentemeyer, C. A. Gilligan, D. M. Rizzo, Ecosystem transformation by emerging infectious disease: Loss of large tanoak from California forests. *J. Ecol.* **100**, 712–722 (2012).
20. M. J. Wingfield, B. Slippers, B. D. Wingfield, Novel associations between pathogens, insects snd tree species threaten world forests. *N. Z. J. Forest. Sci.* **40**, S95 (2010).
21. H. Maier *et al*., The oak processionary caterpillar as the cause of an epidemic airborne disease: Survey and analysis. *Br. J. Dermatol.* **149**, 990 (2003).
22. C. J. Fettig *et al*., The effectiveness of vegetation management practices for prevention and control of bark beetle infestations in coniferous forests of the western and southern United States. *For. Ecol. Manage.* **238**, 24–53 (2007). doi: 10.1016/j.foreco.2006.10.011
23. H. K. Preisler, J. A. Hicke, A. A. Ager, J. L. Hayes, Climate and weather influences on spatial temporal patterns of mountain pine beetle populations in Washington and Oregon. *Ecology* **93**, 2421–2434 (2012). doi: 10.1890/11-1412.1; pmid: 23236913
24. W. A. Kurz *et al*., Mountain pine beetle and forest carbon feedback to climate change. *Nature* **452**, 987–990 (2008). doi: 10.1038/nature06777; pmid: 18432244
25. T. K. BenDor, S. S. Metcalf, L. E. Fontenot, B. Sangunett, B. Hannon, Modeling the spread of the Emerald Ash Borer. *Ecol. Modell.* **197**, 221–236 (2006). doi: 10.1016/j.ecolmodel.2006.03.003
26. Food and Agriculture Organization of the United Nations (FAO), *Global Forest Resource Assessment 2010* (FAO, Rome, 2010).
27. A. Chhatre, A. Agrawal, Trade-offs and synergies between carbon storage and livelihood benefits from forest commons. *Proc. Natl. Acad. Sci. U.S.A.* **106**, 17667–17670 (2009). doi: 10.1073/pnas.0905308106; pmid: 19815522
28. M. R. W. Rands *et al*., Biodiversity conservation: Challenges beyond 2010. *Science* **329**, 1298–1303 (2010). doi: 10.1126/science.1189138; pmid: 20829476
29. S. Piao *et al*., The carbon balance of terrestrial ecosystems in China. *Nature* **458**, 1009–1013 (2009). doi: 10.1038/nature07944; pmid: 19396142
30. S. L. Lewis *et al*., Increasing carbon storage in intact African tropical forests. *Nature* **457**, 1003–1006 (2009). doi: 10.1038/nature07771; pmid: 19225523
31. S. Luyssaert *et al*., Old-growth forests as global carbon sinks. *Nature* **455**, 213–215 (2008). doi: 10.1038/nature07276; pmid: 18784722
32. J. G. Canadell, M. R. Raupach, Managing forests for climate change mitigation. *Science* **320**, 1456–1457 (2008). doi: 10.1126/science.1155458; pmid: 18556550
33. X. Lee *et al*., Observed increase in local cooling effect of deforestation at higher latitudes. *Nature* **479**, 384–387 (2011). doi: 10.1038/nature10588; pmid: 22094699
34. G. B. Bonan, Forests and climate change: Forcings, feedbacks, and the climate benefits of forests. *Science* **320**, 1444–1449 (2008). doi: 10.1126/science.1155121; pmid: 18556546
35. P. F. Hessburg, B. G. Smith, R. B. Salter, R. D. Ottmar, E. Alvarado, Recent changes (1930s-1990s) in spatial patterns of interior northwest forests, USA. *For. Ecol. Manage.* **136**, 53–83 (2000). doi: 10.1016/S0378-1127(99)00263-7
36. G. M. Lovett, C. D. Canham, M. A. Arthur, K. C. Weathers, R. D. Fitzhugh, Forest ecosystem responses to exotic pests and pathogens in eastern North America. *Bioscience* **56**, 395 (2006). doi: 10.1641/0006-3568(2006)056[0395:FERTEP]2.0.CO;2
37. A. M. Ellison *et al*., Loss of foundation species: Consequences for the structure and dynamics of forested ecosystems. *Front. Ecol. Environ* **3**, 479–486 (2005). doi: 10.1890/1540-9295(2005)003[0479:LOFSCF]2.0.CO;2
38. S. N. Aitken, S. Yeaman, J. A. Holliday, T. L. Wang, S. Curtis-McLane, Adaptation, migration or extirpation: Climate change outcomes for tree populations. *Evol. Appl.* **1**, 95–111 (2008). doi: 10.1111/j.1752-4571.2007.00013.x
39. D. B. Lindenmayer, W. F. Laurance, J. F. Franklin, Ecology. Global decline in large old trees. *Science* **338**, 1305–1306 (2012). www.ncbi.nlm.nih.gov/entrez/query.fcgi?cmd=Retrieve&db=PubMed&list_uids=23224548&dopt=Abstract. doi: 10.1126/science.1231070; pmid: 23224548
40. T. Wu, Y. S. Kim, M. D. Hurteau, Investing in natural capital: Using economic incentives to overcome barriers to forest restoration. *Restor. Ecol.* **19**, 441 (2011).
41. T. C. Daniel *et al*., Contributions of cultural services to the ecosystem services agenda. *Proc. Natl. Acad. Sci. U.S.A.* **109**, 8812–8819 (2012). doi: 10.1073/pnas.1114773109; pmid: 22615401
42. S. M. J., *What Money Can't Buy: The Moral Limits of Markets* (Farrar, Straus and Giroux, New York, 2012).
43. I. J. Bateman, G. M. Mace, C. Fezzi, G. Atkinson, K. Turner, Economic analysis for ecosystem service assessments, economic analysis for ecosystem service assessments. *Environ. Resour. Econ.* **48**, 177–218 (2011). doi: 10.1007/s10640-010-9418-x
44. R. E. Kasperson *et al*., The social amplification of risk—A conceptual framework. *Risk Anal.* **8**, 177 (1988).
45. P. Mills *et al*., Integrating natural and social science perspectives on plant disease risk, management and policy formulation. *Philos. Trans. R. Soc. B* **366**, 2035–2044 (2011).
46. S. Azaele, S. Pigolotti, J. R. Banavar, A. Maritan, Dynamical evolution of ecosystems. *Nature* **444**, 926–928 (2006). doi: 10.1038/nature05320; pmid: 17167485
47. C. K. Feld *et al*., Indicators of biodiversity and ecosystem services: A synthesis across ecosystems and spatial scales. *Oikos* **118**, 1862 (2009). doi: 10.1111/j.1600-0706.2009.17860.x
48. L. Gibson *et al*., Primary forests are irreplaceable for sustaining tropical biodiversity. *Nature* **478**, 378–381 (2011). doi: 10.1038/nature10425; pmid: 21918513
49. S. Roy, J. Byrne, C. Pickering, A systematic quantitative review of urban tree benefits, costs, and assessment methods across cities in different climatic zones. *Urban For. Urban Green.* **11**, 351 (2012).
50. D. Valle, J. Clark, Conservation efforts may increase malaria burden in the Brazilian Amazon. *PLOS ONE* **8**, e57519 (2013). doi: 10.1371/journal.pone.0057519; pmid: 23483912
51. G. H. Donovan *et al*., The relationship between trees and human health: Evidence from the spread of the emerald ash borer. *Am. J. Prev. Med.* **44**, 139–145 (2013). doi: 10.1016/j.amepre.2012.09.066; pmid: 23332329
52. J. Thomas, R. Lewington, *The Butterflies of Britain & Ireland* (British Wildlife Publishing, Dorset, UK, 1991).
53. A. Roques, Alien forest insects in a warmer world and a globalised economy: Impacts of changes in trade, tourism and climate on forest biosecurity. *N. Z. J. For. Sci.* **40**, S77 (2010).
54. J. K. Waage *et al*., Patterns of plant pest introductions in Europe and Africa. *Agric. Syst.* **99**, 1–5 (2008). doi: 10.1016/j.agsy.2008.08.001
55. T. T. Work, D. G. McCullough, J. F. Cavey, R. Komsa, Arrival rate of nonindigenous insect species into the United States through foreign trade. *Biol. Invasions* **7**, 323–332 (2005). doi: 10.1007/s10530-004-1663-x
56. M. A. McGeoch *et al*., Global indicators of biological invasion: Species numbers, biodiversity impact and policy responses. *Divers. Distrib.* **16**, 95–108 (2010). doi: 10.1111/j.1472-4642.2009.00633.x
57. A. Santini *et al*., Biogeographical patterns and determinants of invasion by forest pathogens in Europe. *New Phytol.* **197**, 238–250 (2013). doi: 10.1111/j.1469-8137.2012.04364.x; pmid: 23057437
58. M. Paoletti, K. W. Buck, C. M. Brasier, Selective acquisition of novel mating type and vegetative incompatibility genes via interspecies gene transfer in the globally invading eukaryote *Ophiostoma novo-ulmi*. *Mol. Ecol.* **15**, 249 (2006).
59. L. V. McKinney, I. M. Thomsen, E. D. Kjaer, S. B. K. Bengtsson, L. R. Nielsen, Rapid invasion by an aggressive pathogenic fungus (Hymenoscyphus pseudoalbidus) replaces a native decomposer (Hymenoscyphus albidus): A case of local cryptic extinction? *Fungal Ecol.* **5**, 663–669 (2012). doi: 10.1016/j.funeco.2012.05.004
60. Department for Environmental, Food and Rural Affairs, Tree health and plant biosecurity expert task force: Final report (2013); available at www.gov.uk/government/publications/tree-health-and-plant-biosecurity-expert-taskforce-final-report.
61. M. Lu, M. J. Wingfield, N. Gillette, J. H. Sun, Do novel genotypes drive the success of an invasive bark beetle-fungus complex? Implications for potential reinvasion. *Ecology* **92**, 2013 (2011).
62. D. R. Gray, W. E. MacKinnon, Outbreak patterns of the spruce budworm and their impacts in Canada. *For. Chron.* **82**, 550 (2006).
63. C. C. Dymond *et al*., Future spruce budworm outbreak may create a carbon source in eastern Canadian forests. *Ecosystems (N.Y.)* **13**, 917–931 (2010). doi: 10.1007/s10021-010-9364-z
64. D. Verbyla, The greening and browning of Alaska based on 1982-2003 satellite data. *Glob. Ecol. Biogeogr.* **17**, 547–555 (2008). doi: 10.1111/j.1466-8238.2008.00396.x
65. E. E. Berg, J. D. Henry, C. L. Fastie, A. D. De Volder, S. M. Matsuoka, Spruce beetle outbreaks on the Kenai Peninsula, Alaska, and Kluane National Park and Reserve, Yukon Territory: Relationship to summer temperatures and regional differences in disturbance regimes. *For. Ecol. Manage.* **227**, 219–232 (2006). doi: 10.1016/j.foreco.2006.02.038
66. A. J. Soja *et al*., Climate-induced boreal forest change: Predictions versus current observations. *Global Planet. Change* **56**, 274–296 (2007). doi: 10.1016/j.gloplacha.2006.07.028
67. C. M. Malmstrom, K. F. Raffa, Biotic disturbance agents in the boreal forest: Considerations for vegetation change models. *Glob. Change Biol.* **6**, 35–48 (2000). doi: 10.1046/j.1365-2486.2000.06012.x
68. R. A. Werner, E. H. Holsten, S. M. Matsuoka, R. E. Burnside, Spruce beetles and forest ecosystems in south-central Alaska: A review of 30 years of research. *For. Ecol. Manage.* **227**, 195–206 (2006). doi: 10.1016/j.foreco.2006.02.050
69. F. Magnani *et al*., The human footprint in the carbon cycle of temperate and boreal forests. *Nature* **447**, 848–850 (2007). doi: 10.1038/nature05847; pmid: 17568744
70. P. M. Attiwill, T. H. E. Dros, The disturbance of forest ecosystems—The ecological basis for conservative management. *For. Ecol. Manage.* **63**, 247–300 (1994). doi: 10.1016/0378-1127(94)90114-7
71. D. B. Lindenmayer *et al*., Ecology. Salvage harvesting policies after natural disturbance. *Science* **303**, 1303 (2004). doi: 10.1126/science.1093438; pmid: 14988539
72. J. R. Garnas, M. P. Ayres, A. M. Liebhold, C. Evans, Subcontinental impacts of an invasive tree disease on forest structure and dynamics. *J. Ecol.* **99**, 532 (2011).
73. E. S. Eveleigh *et al*., Fluctuations in density of an outbreak species drive diversity cascades in food webs. *Proc. Natl. Acad. Sci.* **104**, 16976 (2007).
74. G. von Oheimb, J. Brunet, Dalby Soderskog revisited: Long-term vegetation changes in a south Swedish deciduous forest. *Acta Oecol.-Int. J. Ecol.* **31**, 229 (2007).
75. C. D. Allen, Interactions across spatial scales among forest dieback, fire, and erosion in northern New Mexico landscapes. *Ecosystems* **10**, 797 (2007).
76. J. A. McLaughlin, M. T. Dumas, in *Pathological Implications of Partial Cutting in Boreal Mixedwood Stands*, C. R. Smith, G. W. Crook, Eds. (Advancing Boreal Mixedwood Management in Ontario: Proceedings of a Workshop, Sault Ste. Marie, Canada, 1996), pp. 167–169.
77. A. Barakat *et al*., Comparison of the transcriptomes of American chestnut (*Castanea dentata*) and Chinese chestnut (*Castanea mollissima*) in response to the chestnut blight infection. *BMC Plant Biol.* **9**, 51 (2009). doi: 10.1186/1471-2229-9-51 pmid: 19426529

78. A. R. Cook, G. J. Gibson, T. R. Gottwald, C. A. Gilligan, Constructing the effect of alternative intervention strategies on historic epidemics. *J. R. Soc. Interface* **5**, 1203–1213 (2008). doi: 10.1098/rsif.2008.0030; pmid: 18302995
79. R. K. Meentemeyer *et al.*, Epidemiological modeling of invasion in heterogeneous landscapes: Spread of sudden oak death in California (1990–2030). *Ecosphere* **2**, art17 (2011). doi: 10.1890/ES10-00192.1
80. J. A. N. Filipe *et al.*, Landscape epidemiology and control of pathogens with cryptic and long-distance dispersal: Sudden oak death in northern Californian forests. *PLOS Comput. Biol.* **8**, e1002328 (2012). doi: 10.1371/journal.pcbi.1002328; pmid: 22241973
81. C. A. Gilligan, F. van den Bosch, Epidemiological models for invasion and persistence of pathogens. *Annu. Rev. Phytopathol.* **46**, 385–418 (2008). doi: 10.1146/annurev.phyto.45.062806.094357; pmid: 18680429
82. S. Parnell, T. R. Gottwald, F. van den Bosch, C. A. Gilligan, Optimal strategies for the eradication of Asiatic citrus canker in heterogeneous landscapes. *Phytopathology* **99**, 1370–1376 (2009).
83. T. D. Harwood, X. Xu, M. Pautasso, M. J. Jeger, M. W. Shaw, Epidemiological risk assessment using linked network and grid based modelling: *Phytophthora ramorum* and *Phytophthora kernoviae* in the UK. *Ecol. Model.* **220**, 3353–3361 (2009). doi: 10.1016/j.ecolmodel.2009.08.014
84. F. Moscardi, Assessment of the application of baculoviruses for control of *Lepidoptera*. *Annu. Rev. Entomol.* **44**, 257–289 (1999). doi: 10.1146/annurev.ento.44.1.257; pmid: 15012374
85. K. M. Waring, K. L. O'Hara, Silvicultural strategies in forest ecosystems affected by introduced pests. *For. Ecol. Manage.* **209**, 27–41 (2005). doi: 10.1016/j.foreco.2005.01.008
86. L. E. Caltagirone, R. L. Doutt, The history of the vedalia beetle importation to California and its impact on the development of biological control. *Annu. Rev. Entomol.* **34**, 1–16 (1989). doi: 10.1146/annurev.en.34.010189.000245
87. S. P. Sinkins, F. Gould, Gene drive systems for insect disease vectors. *Nat. Rev. Genet.* **7**, 427–435 (2006). doi: 10.1038/nrg1870; pmid: 16682981
88. E. G. Brockerhoff, H. Jactel, J. A. Parrotta, S. F. B. Ferraz, Role of eucalypt and other planted forests in biodiversity conservation and the provision of biodiversity-related ecosystem services. *For. Ecol. Manage.* **301**, 43–50 (2013). doi: 10.1016/j.foreco.2012.09.018
89. H. Jactel, E. G. Brockerhoff, Tree diversity reduces herbivory by forest insects. *Ecol. Lett.* **10**, 835–848 (2007). doi: 10.1111/j.1461-0248.2007.01073.x; pmid: 17663717
90. J. E. Aukema *et al.*, Historical accumulation of nonindigenous forest pests in the continental United States. *Bioscience* **60**, 886–897 (2010). doi: 10.1525/bio.2010.60.11.5
91. R. M. Smith *et al.*, Recent non-native invertebrate plant pest establishments in Great Britain: Origins, pathways, and trends. *Agric. For. Entomol.* **9**, 307–326 (2007). doi: 10.1111/j.1461-9563.2007.00349.x
92. Department for Environment, Food and Rural Affairs, Independent panel on Forest: final report (2012); available at www.defra.gov.uk/forestrypanel.

Supplementary Materials

www.sciencemag.org/content/342/6160/1235773/suppl/DC1
Supplementary Text
References

10.1126/science.1235773

Molecular Architecture of a Eukaryotic Translational Initiation Complex

Israel S. Fernández,* Xiao-Chen Bai,* Tanweer Hussain, Ann C. Kelley, Jon R. Lorsch,† V. Ramakrishnan,† Sjors H. W. Scheres†

READ THE FULL ARTICLE ONLINE
http://dx.doi.org/10.1126/science.1240585

Cite this article as I. S. Fernández *et al.*, *Science* **342**, 1240585 (2013).
DOI: 10.1126/science.1240585

Introduction: Initiation of protein synthesis is a key step in the control of gene expression. In eukaryotes, initiation is a highly complex process that requires almost a dozen protein factors. The last step involves joining of the large and small subunits of the ribosome to form the 80*S* initiation complex with the transfer RNA (tRNA) in the P-site base paired to the start codon. This step is catalyzed by the guanosine triphosphatase (GTPase) factor eIF5B. In addition, eIF5B is thought to play a role in ensuring that translation initiation takes place only on mature ribosomes.

Methods: The development of fast, direct electron detectors and new methods of image analysis for cryo–electron microscopy allow high-resolution reconstructions from much smaller numbers of particles than previously possible. We used these new methods to provide feedback to improve the biochemical preparation of samples for structure determination of the eukaryotic translation initiation complex with initiator tRNA and eIF5B, which was trapped on the ribosome with the non-hydrolyzable GTP analog GDPCP.

Results: Although the structure of the fully assembled complex was calculated from only 5143 particles, representing just 3% of the population in the sample, it was possible to obtain a resolution of 6.6 Å. This allowed us to propose a molecular model for the initiation complex. The structure shows that the subunits of the ribosome are rotated relative to the canonical state after initiation. The long helix and C-terminal domain of eIF5B have changed conformation and moved into the ribosome, where the C-terminal domain interacts with the initiator tRNA. The tRNA is stabilized in a distorted conformation, with its 3′-CCA end out of the peptidyl transferase center.

Discussion: The conformational change in eIF5B may be induced upon binding to the small (40*S*) subunit when it specifically recognizes initiator tRNA. In its altered conformation, eIF5B interacts simultaneously with the initiator tRNA and the GTPase center of the ribosome, thus coupling GTP hydrolysis with tRNA recognition in the ribosome. The large number of contacts made by eIF5B with the ribosomal subunits and tRNA is consistent with its role in subunit joining. A close contact with the eukaryote-specific ribosomal protein L40 would not be possible in the immature ubiquitinated form of L40, thus precluding the recruitment of immature 60*S* subunits. A comparison with previous work on the bacterial homolog IF2 suggests that the mechanism of this step of initiation is conserved across kingdoms. Finally, the use of recent advances in cryo-EM to determine a relatively high-resolution structure of the eIF5B-ribosome complex from a very small fraction of a sample could be a general approach for the study of other dynamic or transient biological complexes.

FIGURES IN THE FULL ARTICLE

SUPPLEMENTARY MATERIALS

Materials and Methods
Movies S1 to S3

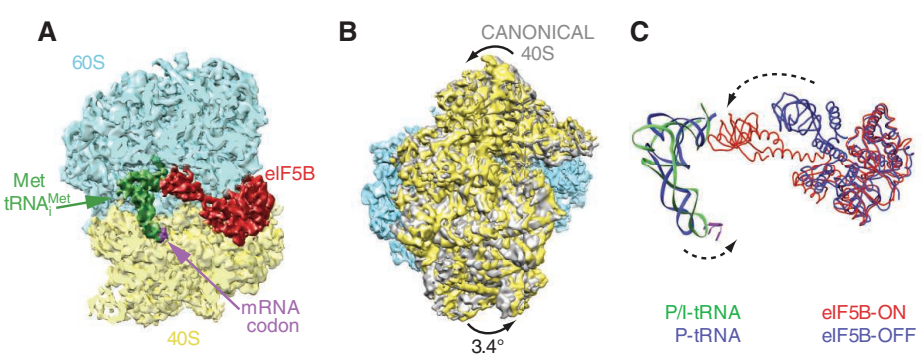

The complex of the ribosome with eIF5B and initiator tRNA determined by cryo-EM, showing conformational changes in all three components. (**A**) The structure of the initiation complex of the ribosome with initiation factor eIF5B, initiator tRNA, and mRNA start codon. (**B**) Comparison with the canonical ribosome (gray) reveals a rotation of the two subunits relative to each other. (**C**) There are large conformational changes in eIF5B and initiator tRNA relative to the isolated structures.

The list of author affiliations is available in the full article online.
*These authors contributed equally to this work.
†Corresponding author. E-mail: jon.lorsch@nih.gov (J.R.L.); ramak@mrc-lmb.cam.ac.uk (V.R.); scheres@mrc-lmb.cam.ac.uk (S.H.W.S.)

Molecular Architecture of a Eukaryotic Translational Initiation Complex

Israel S. Fernández,[1]* Xiao-Chen Bai,[1]* Tanweer Hussain,[1] Ann C. Kelley,[1] Jon R. Lorsch,[2]†‡ V. Ramakrishnan,[1]† Sjors H. W. Scheres[1]†

The last step in eukaryotic translational initiation involves the joining of the large and small subunits of the ribosome, with initiator transfer RNA (Met-tRNA$_i^{Met}$) positioned over the start codon of messenger RNA in the P site. This step is catalyzed by initiation factor eIF5B. We used recent advances in cryo–electron microscopy (cryo-EM) to determine a structure of the eIF5B initiation complex to 6.6 angstrom resolution from <3% of the population, comprising just 5143 particles. The structure reveals conformational changes in eIF5B, initiator tRNA, and the ribosome that provide insights into the role of eIF5B in translational initiation. The relatively high resolution obtained from such a small fraction of a heterogeneous sample suggests a general approach for characterizing the structure of other dynamic or transient biological complexes.

Initiation of protein synthesis is a key step in the control of gene expression in all kingdoms of life (*1*). Specific exogenous factors, called initiation factors, assist the ribosome in positioning the initiation codon of the messenger RNA (mRNA) and a charged initiator transfer RNA (Met-tRNA$_i^{Met}$) in the P site of the ribosome. Whereas, bacteria use just three initiation factors, eukaryotes use almost a dozen initiation factors, many of which are large multisubunit complexes themselves [reviewed in (*2*–*4*)].

Despite substantial differences in the mechanism of initiation, all kingdoms of life share a subset of universally conserved initiation factors (*5*). In particular, the three bacterial initiation factors IF1, IF2, and IF3 are functionally related to the eukaryotic initiation factors eIF1A, eIF5B, and eIF1, respectively. Of these, IF2 and eIF5B (and the archaeal aIF5B) are universally conserved guanosine triphosphatases (GTPases) that promote recruitment of the large ribosomal subunit at the final step of initiation. Recruitment of the large subunit and recognition of the initiator tRNA results in GTP hydrolysis and dissociation of the factor, leaving the ribosome in a competent state for elongation (*6*). Recent reports also relate eIF5B to the last step of pre-40*S* subunit maturation (*7*). The GTPase activity of eIF5B is essential for a pseudo-translational initiation cycle, where eIF5B helps to position the 60*S* subunit for the last cleavage of 20*S* pre-rRNA (*8*).

Crystal structures of a starvation-stalled 80*S* ribosome (*9*), the 40*S* subunit in complex with eIF1 (*10*), and the 60*S* subunit in complex with eIF6 (*11*) have provided the first high-resolution snapshots of the eukaryotic translational machinery. However, the difficulty of obtaining large amounts of homogeneous complexes trapped in a specific state of translation presents a major barrier to crystallography. Cryo–electron microscopy (cryo-EM) makes it possible to determine the structure of a minor population in a heterogeneous sample, from several orders of magnitude less material (*12*). Moreover, recent developments in electron detectors and statistical image processing now make it feasible to rapidly determine cryo-EM structures for the ribosome to near-atomic resolutions from relatively small data sets (*13*). These advances enable the combined use of EM and biochemistry to guide the preparation of appropriate samples to characterize a specific functional state. Here, we exploited these developments to determine the structure at 6.6 Å resolution of the complex of the 80*S* ribosome, Met-tRNA$_i^{Met}$, mRNA, and eIF5B with the nonhydrolyzable GTP analog β-γ-methyleneguanosine 5′-triphosphate (GDPCP), which provides a snapshot of the last step in eukaryotic initiation.

Results

Interplay Between Cryo-EM and Sample Preparation

We used rapid but high-quality single-particle reconstructions by cryo-EM to characterize ribosomal samples and provide feedback for optimizing preparation of the initiation complex of eIF5B (Fig. 1). Initially, we isolated 80*S* ribosomes directly from *Saccharomyces cerevisiae* strain YAS2488 using cells that were collected in mid-log phase. Despite harvesting in mid-log phase, cryo-EM reconstructions showed that the majority of ribosomes contained Stm1 (Fig. 1, step 1), a protein that previously was considered to be bound to the ribosome as a result of glucose starvation and required for its crystallization (*9*). The ribosomes from this sample also crystallized in the same form as previously reported. As seen in the crystal structure of the 80*S* ribosome (*9*), this protein partially overlaps with P-site tRNA on the 60*S* as well as with the mRNA channel in the 40*S*, thus precluding the formation of most functional complexes.

To obtain ribosomes free of Stm1, we purified 60*S* and 40*S* ribosomal subunits and reassociated them. The density corresponding to Stm1 was absent in the reassociated 80*S* ribosomes, but initial attempts of complex formation with Met-tRNA$_i^{Met}$, eIF5B, and mRNA showed no density for the factor (Fig. 1, step 2).

We then proceeded to form the eIF5B complex by using the method for reconstituting translational initiation in yeast (*14*). To stabilize eIF5B on the ribosome, we used a mutant defective in GTP hydrolysis (*15*) in conjunction with GDPCP. The eIF5B used lacks the N-terminal unstructured tail (*15*, *16*) and consists of four domains: an N-terminal nucleotide binding domain (G-domain) followed by domains II to IV.

When we analyzed the resulting sample by cryo-EM, we observed a mixture of 80*S* ribosomes and free subunits, as well as a very noisy background that we attributed to unbound initiation factors. However, an initial reconstruction of 2000 selected 80*S* particles showed a prominent density near the GTPase center of the 80*S*, which was unambiguously assigned to the G-domain and domain II (Fig. 1, step 3).

Reducing the excess concentration of eIF1 and eIF2/eIF5 from a 3× to a 1× molar ratio relative to ribosomal subunits resulted in an increased fraction of 80*S* ribosomes in the sample. We observed reasonable amounts of 80*S* particles per micrograph (~100 particles per 0.5 μm^2; Fig. 2A), and reconstructions showed good density for eIF5B. However, only the G-domain and domain II of the factor were clearly visible. Moreover, the tRNA was in a hybrid P/E state interacting with the L1 stalk. This suggested that the tRNA had become deacylated (Fig. 1, step 4) and the eIF5B had become partially disordered.

To prevent deacylation, we synthesized a Met-NH-tRNA$_i^{Met}$ version of the yeast initiator tRNA, in which the ester bond between the methionine and the 3′ carbon of A76 of the tRNA$_i^{Met}$ is replaced by an amide bond, thus exhibiting much slower deacylation under our experimental conditions (*17*). With this improved sample, we collected a cryo-EM data set that comprised 130,030 particles. An elaborated classification protocol (Fig. 2B) showed for the first time a class of 5143 particles for which all four domains of eIF5B and the Met-NH-tRNA$_i^{Met}$ were well defined in the reconstruction, with the tRNA in the P site (Fig. 1, step 5). The resolution of this reconstruction was improved to 6.6 Å by statistical movie processing (*13*) (Fig. 2C). At this resolution, secondary structure elements were clearly resolved in the density (Fig. 2D, left) and could be assigned unambiguously to the factor and tRNA. A molecular model of the complex was obtained by rigid-body fitting of

[1]MRC Laboratory of Molecular Biology, Cambridge Biomedical Campus, Cambridge CB2 0QH, UK. [2]Johns Hopkins University School of Medicine, Baltimore, MD 21205, USA.

*These authors contributed equally to this work.
†Corresponding author. E-mail: jon.lorsch@nih.gov (J.R.L.); ramak@mrc-lmb.cam.ac.uk (V.R.); scheres@mrc-lmb.cam.ac.uk (S.H.W.S.)
‡Present address: Laboratory on the Mechanism and Regulation of Protein Synthesis, Eunice K. Shriver Institute of Child Health and Human Development, Bethesda, MD 20892, USA.

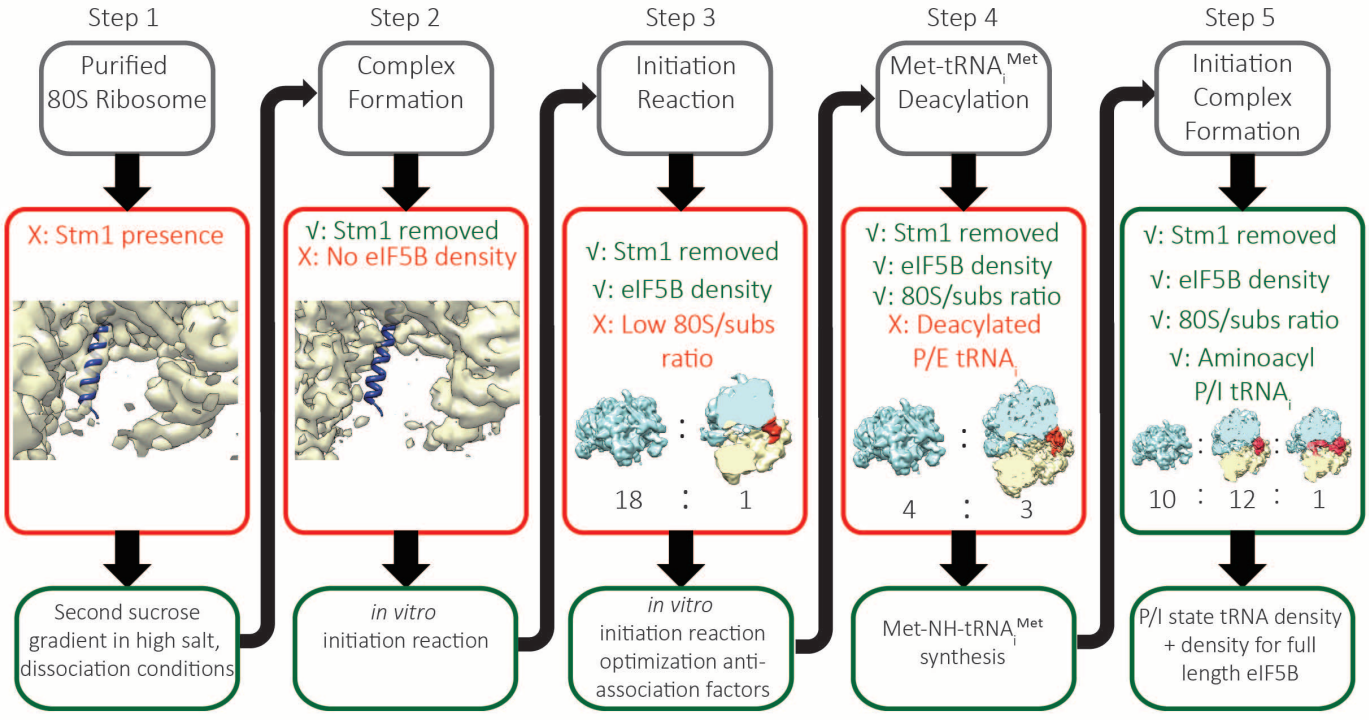

Fig. 1. Sample optimization strategy. Our sample preparation procedure was based on structural feedback provided by cryo-EM reconstructions and consists of five steps that are described in the text. Cryo-EM reconstructed density for 60*S* subunits is indicated in cyan, density for the 40*S* in yellow, density for eIF5B/tRNA in red, and Stm1 protein as a blue ribbon. A similar color scheme is used throughout all figures.

crystal structures of yeast 80*S* (*9*) and domains of eIF5B and tRNA, followed by molecular dynamics flexible fitting (MDFF) on the factor and tRNA (*18*). A second class of 40,729 80*S* particles was identified as the class described in step 4 of Fig. 1. This class, which had an ordered G-domain and domain II of eIF5B, as well as a hybrid P/E tRNA interacting with the L1 stalk, yielded a final resolution of 4.3 Å (Fig. 2C) at which amino acid side chains could be seen (Fig. 2D, right).

Overview of the Structure

Relative to its conformation in the canonical ribosome, the 40*S* subunit in the complex is rotated anticlockwise by approximately 3.4° with respect to the 60*S* subunit (Fig. 3A and movie S1). There is no additional swiveling of the head of the 40*S* subunit.

The conformation of eIF5B in the initiation complex is markedly different from its crystal structure in isolation, either in complex with GDP or with the GTP nonhydrolyzable analog GDPNP (Fig. 3, B to D, and movie S2) (*19*). Domains III and IV, including the long α-helix h12 that links the two, move in a coordinated manner to adopt a position deep inside the intersubunit space of the 80*S*. In this position, the β barrel of domain IV is in close contact with the 3′-CCA end of the Met-tRNA$_i^{Met}$ and in the vicinity of the peptidyl transferase center (PTC). A similar conformational change was also observed for the bacterial ortholog of eIF5B (IF2) on the bacterial initiation

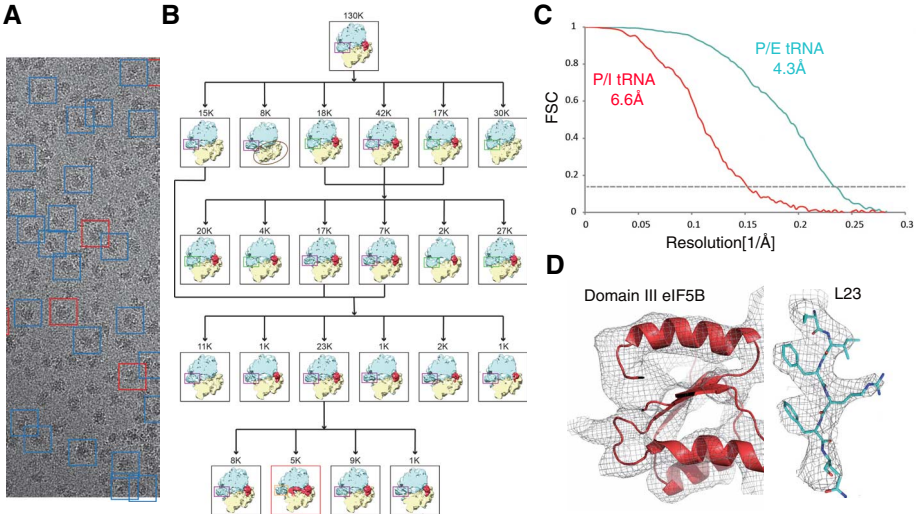

Fig. 2. Micrograph example, maximum-likelihood classification scheme, and final maps. (**A**) Example of a micrograph obtained after the protocol optimization. (**B**) Maximum-likelihood classification scheme used to localize the subpopulation of particles where density for all four domains of eIF5B could be identified. (**C**) Gold-standard Fourier shell correlation (FSC) curves for the small class (P/I tRNA, red) and the larger class (P/E tRNA, cyan) after refinement and statistical movie processing in RELION (*34*). (**D**) Representative densities for the two maps.

complex (*20*). In this conformation, eIF5B stabilizes the initiator tRNA in a conformation different from the canonical P-site orientation (*17*), preventing the 3′-CCA of the tRNA from reaching the PTC (Fig. 4 and movie S3). In addition, the anticodon stem loop (ASL) of the Met-tRNA$_i^{Met}$ appears to form a base pair with the start codon of mRNA and is slightly displaced from the position adopted by a canonical P-site tRNA (Fig. 4A and movie S3). A similar change in the conformation of the P-site tRNA was also described in the bacterial initiation complex (*20*).

Initiator-tRNA recognition is coupled to GTPase activation by the simultaneous interaction of eIF5B with the initiator tRNA via domain IV at the C-terminal end and the G-domain with

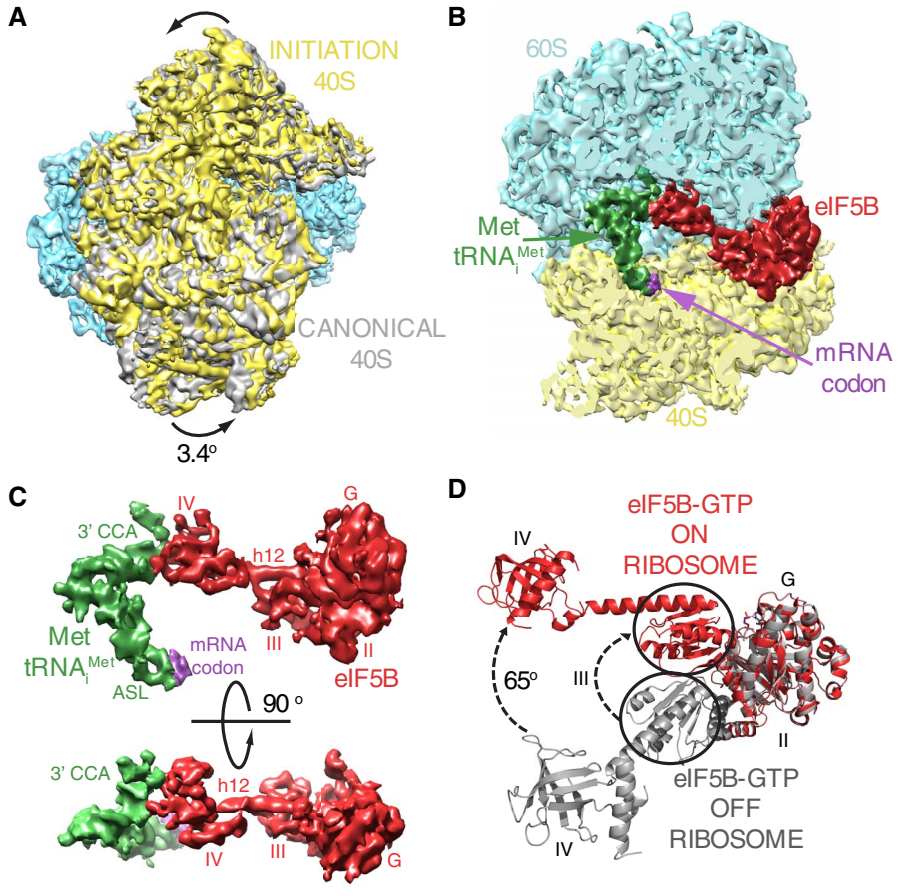

Fig. 3. The eukaryotic 80*S*–Met-tRNA$_i^{Met}$–eIF5B initiation complex. (**A**) Ratcheted overall conformation of the eukaryotic initiation complex. The 40*S* in the initiation complex (yellow) is rotated anticlockwise approximately 3.4° from its position in the canonical 80*S* (gray) (*39*). (**B**) eIF5B (red), Met-tRNA$_i^{Met}$ (green), and mRNA start codon (purple) bound to the 80*S* ribosome (60*S* in cyan, 40*S* in yellow). (**C**) Cryo-EM density showing the interaction between Met-tRNA$_i^{Met}$ (green) and eIF5B (red) in two orientations. Domain IV of eIF5B contacts the 3′ CCA aminoacyl end of Met-tRNA$_i^{Met}$. (**D**) Conformational changes in eIF5B induced during formation of the initiation complex on the ribosome. A coordinated displacement of domains III (circled) and IV, together with the linker α-helix 12 of eIF5B, is observed with respect to the crystal structure of eIF5B in isolation (*19*).

the sarcin-ricin loop (SRL) of 28*S* RNA in the 60*S* subunit at the N-terminal end (Fig. 5A). This coupling is made possible by a shift of domain III relative to domain II and the G-domain. In the ribosome-bound conformation, the shifted domain III repositions the base of the connecting α helix 12 (residues 835 to 840) to directly contact the SRL of the 28*S* rRNA (Fig. 5B). This interaction aligns the SRL with the GTP-binding site on the G-domain in a conformation similar to what has been seen for the activated form of EF-Tu (*21*). A sequence alignment with the bacterial and archaeal orthologs of eIF5B (Fig. 5C) reveals a universally conserved sequence for these residues, providing further evidence for their importance in eIF5B function.

As expected, the G-domain is closely packed against the GTPase center of the 80*S* (Fig. 6). The GTP analog GDPCP is directly adjacent to the SRL of the 28*S* rRNA (nucleotides 3014 to 3039). Ribosomal protein L9 (the eukaryotic ortholog of the bacterial protein L6) is within interaction distance of helix 6 of eIF5B and orients the SRL for optimal contact with the G-domain. Moreover, the eukaryote-specific ribosomal protein L40 is in the vicinity of the GTPase center, and its N-terminal end is in close contact with helix 6 (Fig. 6, top left). This protein is expressed as an N-terminally tagged ubiquitin fusion protein, and the cleavage of the ubiquitin moiety is required for 40*S* subunit maturation (*22*). This close contact between the G-domain and the N terminus of the cleaved L40 protein suggests that binding of translational GTPases is possible only after cleavage of the ubiquitin domain (*11*).

Domains II and III of eIF5B make interactions with the 40*S* subunit (Fig. 6). An interaction between domain II and the 40*S* subunit was suggested by previous genetic and biochemical data on rRNA suppressor mutations in the body of the 40*S* that are able to restore the wild-type phenotype of a GTPase-deficient eIF5B mutant (*16*). Our structure also identifies a second major interaction through domain III of eIF5B and ribosomal protein S23, which is the yeast ortholog of bacterial protein S12 (Fig. 5A).

The P stalk of the 60*S* is the equivalent of the L12 stalk in bacteria that is implicated in interaction with translational GTPases (*23*). Upon interaction with eIF5B, the P stalk as a whole moves downward relative to its position in the empty 80*S*, to closely contact the G-domain of eIF5B. In particular, the element of secondary structure formed by the P-stalk rRNA residues 1265 to 1275 is projected toward eIF5B, contacting the G-domain of the initiation factor (Fig. 6, center). The result is a further stabilization of eIF5B in the active conformation by the P stalk.

Discussion

Our work shows how recent developments in cryo-EM that allow reconstructions to high resolution from an order of magnitude fewer particles than previously required (*13*) can accelerate the determination of structures by guiding the biochemistry of sample preparation. The rapidity of cryo-EM reconstructions from a relatively small number of particles provided iterative feedback to efficiently steer us toward an optimized strategy for increasing the fraction of the sample that had the initiation complex of eIF5B (Fig. 1). Even with this optimization, the fraction of this complex in the population was very small. However, when combined with new, powerful image classification algorithms (*12*), we were able to determine a 6.6 Å resolution structure of the eIF5B initiation complex on the ribosome from only ~5000 particles, comprising fewer than 3% of the particles in our sample.

The structure allows for comparison with a previous, lower-resolution structure of the corresponding bacterial complex (*20*) and sheds light on the mechanism of this step in both kingdoms. The rotation of the small subunit relative to the large subunit, the change in the orientation of the initiator tRNA from the canonical P-site conformation, and the change in the orientation of the long connecting helix in the factor that allows it to make contact with the 3′ end of tRNA in the ribosome are all features that appear to be common to both eukaryotes and bacteria. They therefore represent essential features of subunit joining and eIF5B/IF2 function. In addition, the molecular model derived from the substantially higher resolution of the current structure provides further mechanistic insights into eIF5B function.

The large conformational change in eIF5B relative to the isolated structure couples initiator tRNA recognition to GTP hydrolysis. It is known that the A1-U72 base pair is an essential discriminating feature of initiator tRNA (*24*). The C-terminal domain of eIF5B makes extensive contacts around this base pair, thus possibly specifically recognizing initiator tRNA. The Met-tRNA$_i^{Met}$ is also bent at the anticodon stem exactly in the region characterized by three consecutive GC pairs that are the hallmark of all initiator tRNAs. It is possible that this sequence allows the stabilization of the bent conformation by eIF5B. The result is that the tRNA is stabilized by eIF5B in a conformation that places the aminoacyl 3′ end out

of the PTC, thus preventing the formation of an elongation-competent complex until GTP hydrolysis and dissociation of eIF5B from the ribosome takes place.

Simultaneously, the altered conformation places the base of the long connecting helix 12 of eIF5B in contact with the SRL. This in turn places the catalytic site of eIF5B in a conformation seen in the activated forms of EF-Tu and EF-G (*21*, *25*). Thus, the conformational change in eIF5B, by simultaneously stabilizing the GTPase-activated catalytic site and the unusual conformation of the initiator tRNA, couples GTP hydrolysis to specific recognition of the initiator tRNA in the 40*S* subunit.

The large number of contacts made by eIF5B with both the 40*S* and 60*S* subunits is consistent with its role in facilitating subunit joining. However, it is known that eIF5B also accelerates the rate of 60*S* recruitment (*26*, *27*). It is likely that the conformational changes in eIF5B upon binding to the 40*S* subunit are stabilized by its specific interaction with initiator tRNA. These result in additional contacts with both the 60*S* and 40*S* subunits. Moreover, the P stalk of the ribosome is also stabilized as a result of factor binding. Acceleration of forward rates has often been suggested to be the result of induced conformational changes [e.g., (*28*)], and it is likely that the induced changes in the ribosome, tRNA, and eIF5B during the formation of this initiation complex lead to an acceleration of the forward rate here. Finally, the close contact of eIF5B with the P stalk RNA and proteins L9 and L40 at its base (Fig. 6) would be sterically impossible with the immature ubiquitinated form of L40, thus precluding the recruitment of immature 60*S* subunits, which is another essential feature of eIF5B.

Our work shows that the structure of a macromolecular complex can be determined by cryo-EM to sufficiently high resolution to resolve secondary structures with relatively small numbers of particles that represent a very small fraction of the sample population. Because the preparation of sufficient amounts of homogeneous sample is a major barrier in the structural biology of large complexes, this approach is likely to be useful in the study of a variety of important processes.

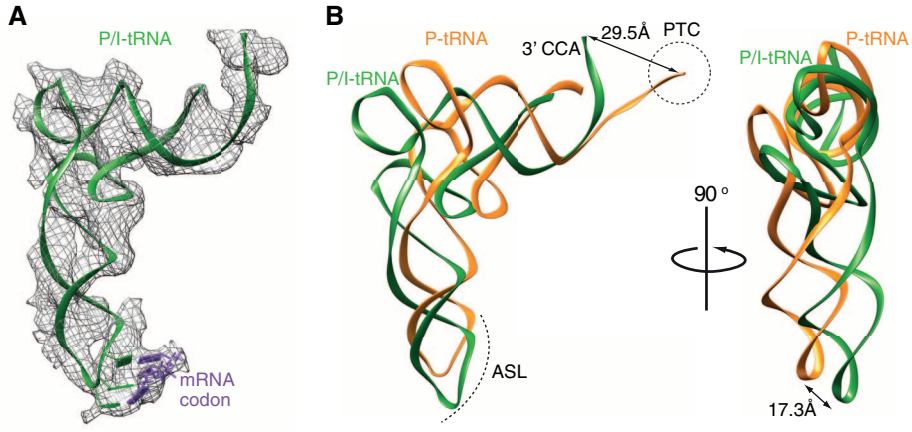

Fig. 4. Met-tRNA$_i^{Met}$ conformation on the initiation complex. (**A**) Cryo-EM density for the Met-tRNA$_i^{Met}$ allowed unambiguous docking of the tRNA (green) and the start codon of mRNA (purple). (**B**) Met-tRNA$_i^{Met}$ (green) in the initiation complex compared to canonical P-site tRNA conformation (orange, PDB ID 2WDK/2WDL) (*17*). A displacement in the ASL is indicated. The 3′ CCA of the Met-tRNA$_i^{Met}$ is stabilized in a conformation that prevents its entering the PTC, circled.

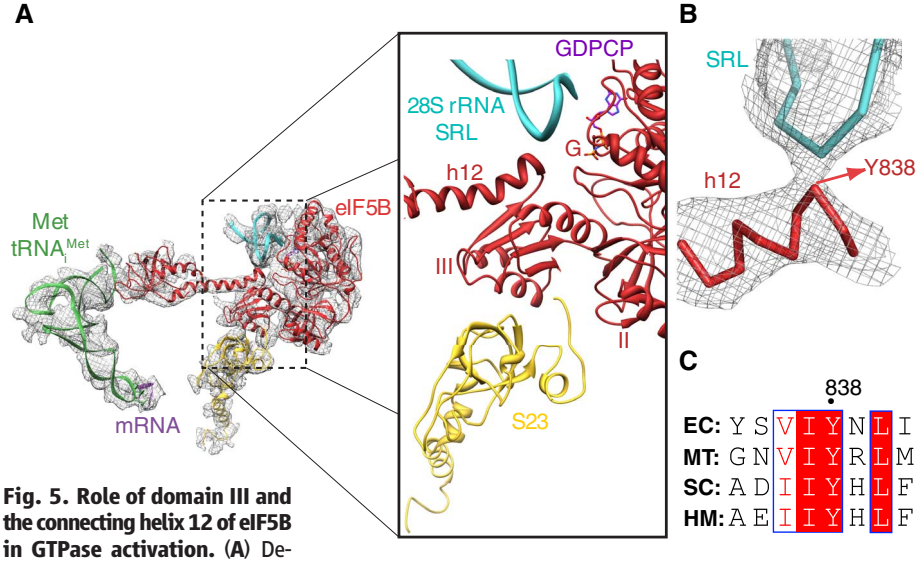

Fig. 5. Role of domain III and the connecting helix 12 of eIF5B in GTPase activation. (**A**) Details showing the interaction of domain III of eIF5B with ribosomal protein S23 from the 40*S* (yellow) and the base of helix 12 with the SRL of the 28*S* rRNA (**B**) Zoomed-in view of the interaction between helix 12 and the SRL around residue Tyr^{838}. (**C**) A sequence alignment of IF2 from the bacteria *Escherichia coli* (EC), aIF5B from the archaea *Methanothermobacter thermautotrophicus* (MT), and eIF5B from the eukaryotes *S. cerevisiae* (SC) and humans (HM) highlights the conservation of Tyr^{838} and surrounding residues suggesting the importance of this interaction. Amino acid abbreviations: A, Ala; D, Asp; E, Glu; I, Ile; L, Leu; M, Met; N, Asn; R, Arg; S, Ser; V, Val; Y, Tyr.

Materials and Methods

Preparation of Ribosomes and Initiation Factors

Ribosomes were purified from the *S. cerevisiae* strain YAS-2488. Cells were harvested in mid-log phase (OD_{600} = 2 to 4) and resuspended in 20 mM Hepes-KOH (pH 7.45), 150 mM KCl, 150 mM K-acetate, 10 mM Mg^{2+}-acetate, heparin (1 mg/ml), 0.1 mM phenylmethylsulfonyl fluoride (PMSF), 0.1 mM benzamidine, and 2 mM dithiothreitol (DTT). Cell pellets frozen in liquid nitrogen were mechanically disrupted by a blender. The lysate was thawed at 4°C and clarified by centrifugation for 20 min at 14,500*g*. Ribosomes in the supernatant were pelleted through a sucrose cushion for 4 hours at 45,000 rpm in a Ti45 rotor (Beckman Coulter) in the same buffer supplemented with 1 M sucrose. The pellets were resuspended in sucrose gradient buffer without sucrose [20 mM Hepes-KOH (pH 7.45), 50 mM KCl, 5 mM Mg^{2+}-acetate, 0.1 mM PMSF, 0.1 mM benzamidine, and 2 mM DTT] and incubated for 15 min with 1 mM puromycin on ice. The sample was loaded on a 10 to 40% sucrose gradient and centrifuged for 16 hours at 28,000 rpm in a Ti25 zonal rotor (Beckman Coulter). The single 80*S* peak was concentrated. For subunit purification, 80*S* ribosomes were exchanged into dissociation buffer [20 mM Hepes-KOH (pH 7.45), 600 mM KCl, 8 mM Mg^{2+}-acetate, 1 mg/ml heparin, 0.1 mM PMSF, 0.1 mM benzamidine, and 2 mM DTT] before loading onto a sucrose gradient in the same buffer and centrifuged for 19 hours at 28,500 rpm in the Ti25 rotor. For reassociation, the 60*S* and 40*S* subunits were exchanged separately to reassociation buffer [3 mM Hepes-KOH (pH 7.45), 6.6 mM Tris-acetate (pH 7.2), 3 mM NH_4Cl, 6.6 mM NH_4-acetate, 48 mM K-acetate, 4 mM Mg^{2+}-acetate, and 2.4 mM DTT], concentrated to 6 μM, and stored at –80°C after being flash-frozen in liquid nitrogen.

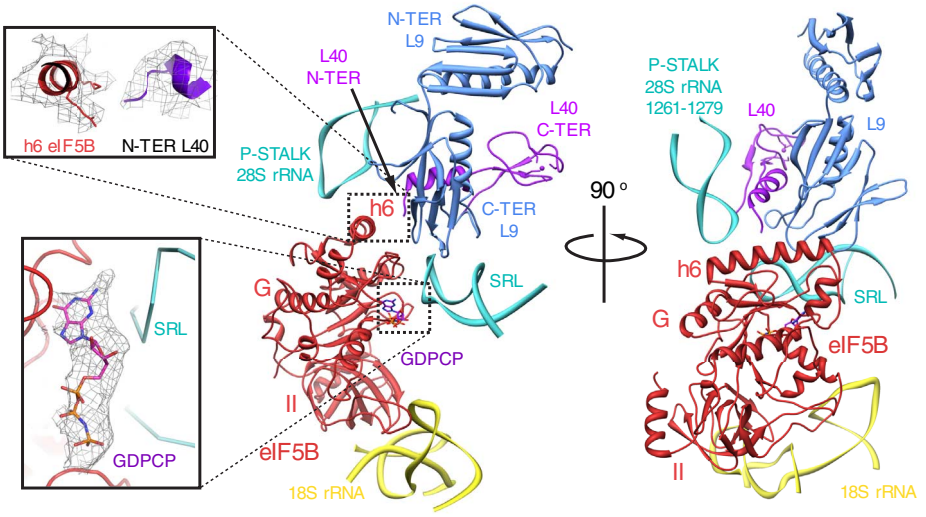

Fig. 6. Two views of the eukaryotic ribosomal GTPase center. The G-domain and domain II of eIF5B (red) contact the GTPase center of the 80*S* formed by the ribosomal proteins L9 (blue), L40 (purple) and regions of the 28*S* rRNA (cyan) and the 18*S* rRNA (yellow). Helix 6 of eIF5B packs tightly against the C-terminal domain of L9 and the N-terminal domain of the eukaryote-specific protein L40 (inset, top left). Density for the GTP analog GDPCP was clearly seen in the G-domain of eIF5B facing the 28*S*-rRNA SRL (inset, bottom left).

Initiation factors eIF1, eIF1A, eIF2, and eIF5 were produced as described (*29*). An N-terminally truncated eIF5B version (residues 396 to 1002, with a molecular weight of 68 kD) was cloned in a T7-based expression vector that added a 6×His tag followed by a TEV protease cleavage site at the N terminus. A point mutation eIF5B-T439A was introduced using a QuickChange Mutagenesis Kit (Invitrogen) and was confirmed by DNA sequencing. Overexpression in *E. coli* strain BL21-AI (Invitrogen) was followed by chromatography using HisTrap, Q-HP and Sephacryl S-200 (GE Healthcare). The resulting highly pure protein that was concentrated to 100 µM and snap-frozen in liquid nitrogen.

tRNA and mRNA Production

Yeast $tRNA_i^{Met}$ purification was purified as described (*30*) with minor modifications: After phenol extraction of cell lysate, the aqueous phase was ethanol precipitated and the resuspended pellet was applied to a Q sepharose column in buffer A [20 mM Tris/HCl (pH 7.5), 5 mM MgCl, and 300 mM NaCl]. tRNA was eluted with a linear gradient with buffer B [20 mM Tris/HCl (pH 7.5), 5 mM MgCl, and 1 M NaCl]. The eluted peak was further purified using a TSK phenyl 5PW hydrophobic column in buffer A [10 mM ammonium acetate (pH 6.3) and 1.7 M ammonium sulfate] and eluted with an inverse ammonium sulfate gradient in the same buffer. A final purification step was performed in a C18 reverse-phase HPLC column using, as solvent A, 20 mM Tris-acetate (pH 6), 20 mM Mg^{2+}-acetate, and 400 mM NaCl, and as solvent B, 20 mM Tris-acetate (pH 6), 20 mM Mg^{2+}-acetate, 400 mM NaCl, and 60% v/v methanol. The acylated version of $tRNA_i^{Met}$ as well as the Met-NH-$tRNA_i^{Met}$ were produced following previously established protocols (*17*). The mRNA with sequence 5′ GGAA[UC]$_4$UAUG[CU]$_4$C 3′ was commercially synthesized by Integrated DNA Technologies.

Complex Formation

Initially, ribosomes were reassembled by mixing equimolar amounts of 40*S* and 60*S* subunits, either by themselves or with an excess of Met-$tRNA_i^{Met}$, mRNA, and eIF5B with GDPCP. Subsequently, the complex of eIF5B via the initiation pathway using 60*S*, 40*S*, Met-NH-$tRNA_i^{Met}$, and initiation factors was assembled following procedures previously described (*31*) with modifications to the final concentrations of eIF1, eIF2, and eIF5 (1:1 molar ratio each with respect to ribosomal subunits). The 40*S* mix (40*S*, eIF1, eIF1A, and mRNA), the ternary complex mix (eIF2, GTP, and Met- $tRNA_i^{Met}$), and the 60*S* mix (60*S*, eIF5, eIF5B, and GDPCP) were incubated separately for 5 min at 30°C. The ternary complex was added to the 40*S* mix and incubated for an additional 5 min before addition of the 60*S* mix. After a further incubation of 5 min, the sample was cooled to 4°C and used immediately to make cryo-EM grids.

Electron Microscopy

Aliquots of 3 µl of the 80*S* initiation complex at a concentration of ~80 nM were incubated for 30 s on glow-discharged holey carbon grids (Quantifoil R2/2), on which a home-made continuous carbon film (estimated to be ~30 Å thick) had previously been deposited. Grids were blotted for 2.5 s and flash-cooled in liquid ethane using an FEI Vitrobot. Grids were transferred to an FEI Polara G2 microscope that was operated at 300 kV. Defocus values in the final data set ranged from 1.6 to 4.6 µm. Images were recorded manually on a back-thinned FEI Falcon II detector at a calibrated magnification of 79,096 (yielding a pixel size of 1.77 Å). A system built in house was used to intercept the videos from the detector at a speed of 16 frames for the 1-s exposures (*13*). All electron micrographs that showed noticeable signs of astigmatism or drift were discarded.

Image Processing

All reconstructions described in Fig. 1 were calculated using semi-automated image processing as outlined below. We used the swarm tool in the e2boxer.py program of EMAN2 (*32*) for semi-automated particle picking. For our final data set, we selected 193,297 particles from 1012 micrographs. Contrast transfer function parameters were estimated using CTFFIND3 (*33*). All 2D and 3D refinements were performed using RELION (*34*).

We used reference-free 2D class averaging to discard 60*S* subunits and defective particles, resulting in 130,030 particles of the final data set for subsequent 3D refinement and classification. Refinement of all particles against a single model [60 Å low-pass filtered version of EMDB-2275 (*13*)] yielded a preliminary consensus reconstruction with local fuzzy density for the 40*S* subunit, the L1 stalk, and the factor. Subsequently, we used a cascaded 3D classification scheme (Fig. 2B) to identify a class of 5143 particles, for which all four domains of the factor showed clear density. A second class of 40,729 80*S* ribosomes with tRNA in the P/E site and only density for the G-domain and domain II of eIF5B were identified by a separate classification of all particles into 10 classes.

To further increase the resolution of both classes, we performed statistical movie processing as described (*13*). In this procedure, we used running averages of five movie frames, a standard deviation of 1° for the priors on the Euler angles, and a standard deviation of 1 pixel for the translations. Reported resolutions are based on the gold-standard FSC = 0.143 criterion (*35*) and involved only soft masking. (Note that the gold-standard approach yields refinements that are free from overfitting, and that the previously common FSC = 0.5 criterion would severely underestimate resolution in the absence of overfitting.) Before visualization, all density maps were corrected for the modulation transfer function (MTF) of the detector and then sharpened by applying a negative B factor that was estimated using automated procedures (*36*) (–217 $Å^2$ for the small class; –155 $Å^2$ for the larger class).

Rigid-body and flexible fitting of 80*S*, tRNA, and eIF5B crystal structures were performed using UCSF Chimera and MDFF (*18*, *37*), respectively. We split the structure into multiple rigid-body substructures (comprising 40*S* and 60*S* subunits, eIF5B, tRNA, L1 stalk, and P stalk) and used COOT (*38*) to manually rebuild those parts that were outside the cryo-EM density. MDFF refinements for the reported structures were performed at 300 K for 200,000 steps using both hydrogen bond and dihedral angle restraints and a weight on

the EM density (GSCALE) of 0.3 kcal/mol. After MDFF, another 5000 steps of energy minimization were performed using GSCALE = 5.0 kcal/mol. Relative to the rigid-body fit, numerous attempts at flexible fitting (with varying GSCALEs) of the entire 80*S* did not improve FSCs between the model and the map beyond the resolution used in MDFF. This lack of improvement suggests that at this resolution, the flexible fitting procedure generally results in overfitting. However, the eIF5B, the tRNA, and the parts of the ribosome that are in contact with those (e.g., the L1 stalk and the P stalk) showed large and obvious conformational changes with respect to available crystal structures. For these entities, rigid-body fitting was done for the various domains, followed by minor adjustments of the interface between the domains using flexible fitting. A manual inspection using COOT was performed to check the accuracy of the final fit. For the tRNA, the anticodon stem loop and the rest of the molecule were fit as rigid bodies, followed by flexible fitting of the acceptor region, which shows considerable deviation from canonical tRNA (*17*). Additional density corresponding to the mRNA start codon was clearly visible next to the anticodon in a conformation consistent with codon-anticodon base pairing. The rest of the mRNA appears disordered in the map. Because the fitted coordinates of the G-domain and domain II of eIF5B showed no obvious differences between the small and the larger class (with an RMSD of 1.2 Å between the two), we used the coordinates from the higher-resolution map of the larger class to describe the GTPase center of the 80*S* interacting with the G-domain and domain II of eIF5B.

References and Notes

1. A. Marintchev, G. Wagner, Translation initiation: Structures, mechanisms and evolution. *Q. Rev. Biophys.* **37**, 197–284 (2004). doi: 10.1017/S0033583505004026; pmid: 16194295
2. N. Sonenberg, A. G. Hinnebusch, Regulation of translation initiation in eukaryotes: Mechanisms and biological targets. *Cell* **136**, 731–745 (2009). doi: 10.1016/j.cell.2009.01.042; pmid: 19239892
3. R. J. Jackson, C. U. Hellen, T. V. Pestova, The mechanism of eukaryotic translation initiation and principles of its regulation. *Nat. Rev. Mol. Cell Biol.* **11**, 113–127 (2010). doi: 10.1038/nrm2838; pmid: 20094052
4. C. E. Aitken, J. R. Lorsch, A mechanistic overview of translation initiation in eukaryotes. *Nat. Struct. Mol. Biol.* **19**, 568–576 (2012). doi: 10.1038/nsmb.2303; pmid: 22664984
5. A. Roll-Mecak, B. S. Shin, T. E. Dever, S. K. Burley, Engaging the ribosome: Universal IFs of translation. *Trends Biochem. Sci.* **26**, 705–709 (2001). doi: 10.1016/S0968-0004(01)02024-2; pmid: 11738593
6. A. G. Hinnebusch, J. R. Lorsch, The mechanism of eukaryotic translation initiation: New insights and challenges. *Cold Spring Harb. Perspect. Biol.* **4**, a011544 (2012). doi: 10.1101/cshperspect.a011544; pmid: 22815232
7. B. S. Strunk, M. N. Novak, C. L. Young, K. Karbstein, A translation-like cycle is a quality control checkpoint for maturing 40S ribosome subunits. *Cell* **150**, 111–121 (2012). doi: 10.1016/j.cell.2012.04.044; pmid: 22770215
8. S. Lebaron *et al.*, Proofreading of pre-40S ribosome maturation by a translation initiation factor and 60S subunits. *Nat. Struct. Mol. Biol.* **19**, 744–753 (2012). doi: 10.1038/nsmb.2308; pmid: 22751017
9. A. Ben-Shem *et al.*, The structure of the eukaryotic ribosome at 3.0 Å resolution. *Science* **334**, 1524–1529 (2011). doi: 10.1126/science.1212642; pmid: 22096102
10. J. Rabl, M. Leibundgut, S. F. Ataide, A. Haag, N. Ban, Crystal structure of the eukaryotic 40S ribosomal subunit in complex with initiation factor 1. *Science* **331**, 730–736 (2011). doi: 10.1126/science.1198308; pmid: 21205638
11. S. Klinge, F. Voigts-Hoffmann, M. Leibundgut, S. Arpagaus, N. Ban, Crystal structure of the eukaryotic 60S ribosomal subunit in complex with initiation factor 6. *Science* **334**, 941–948 (2011). doi: 10.1126/science.1211204; pmid: 22052974
12. S. H. Scheres, A Bayesian view on cryo-EM structure determination. *J. Mol. Biol.* **415**, 406–418 (2012). doi: 10.1016/j.jmb.2011.11.010; pmid: 22100448
13. X. C. Bai, I. S. Fernandez, G. McMullan, S. H. Scheres, Ribosome structures to near-atomic resolution from thirty thousand cryo-EM particles. *Elife* **2**, e00461 (2013). doi: 10.7554/eLife.00461; pmid: 23427024
14. M. G. Acker, S. E. Kolitz, S. F. Mitchell, J. S. Nanda, J. R. Lorsch, Reconstitution of yeast translation initiation. *Methods Enzymol.* **430**, 111–145 (2007). doi: 10.1016/S0076-6879(07)30006-2; pmid: 17913637
15. B. S. Shin *et al.*, Uncoupling of initiation factor eIF5B/IF2 GTPase and translational activities by mutations that lower ribosome affinity. *Cell* **111**, 1015–1025 (2002). doi: 10.1016/S0092-8674(02)01171-6; pmid: 12507428
16. B. S. Shin *et al.*, rRNA suppressor of a eukaryotic translation initiation factor 5B/initiation factor 2 mutant reveals a binding site for translational GTPases on the small ribosomal subunit. *Mol. Cell. Biol.* **29**, 808–821 (2009). doi: 10.1128/MCB.00896-08; pmid: 19029250
17. R. M. Voorhees, A. Weixlbaumer, D. Loakes, A. C. Kelley, V. Ramakrishnan, Insights into substrate stabilization from snapshots of the peptidyl transferase center of the intact 70S ribosome. *Nat. Struct. Mol. Biol.* **16**, 528–533 (2009). doi: 10.1038/nsmb.1577; pmid: 19363482
18. L. G. Trabuco *et al.*, Applications of the molecular dynamics flexible fitting method. *J. Struct. Biol.* **173**, 420–427 (2011). doi: 10.1016/j.jsb.2010.09.024; pmid: 20932910
19. A. Roll-Mecak, C. Cao, T. E. Dever, S. K. Burley, X-Ray structures of the universal translation initiation factor IF2/eIF5B: Conformational changes on GDP and GTP binding. *Cell* **103**, 781–792 (2000). doi: 10.1016/S0092-8674(00)00181-1; pmid: 11114334
20. G. S. Allen, A. Zavialov, R. Gursky, M. Ehrenberg, J. Frank, The cryo-EM structure of a translation initiation complex from *Escherichia coli*. *Cell* **121**, 703–712 (2005). doi: 10.1016/j.cell.2005.03.023; pmid: 15935757
21. R. M. Voorhees, T. M. Schmeing, A. C. Kelley, V. Ramakrishnan, The mechanism for activation of GTP hydrolysis on the ribosome. *Science* **330**, 835–838 (2010). doi: 10.1126/science.1194460; pmid: 21051640
22. T. Lacombe *et al.*, Linear ubiquitin fusion to Rps31 and its subsequent cleavage are required for the efficient production and functional integrity of 40S ribosomal subunits. *Mol. Microbiol.* **72**, 69–84 (2009). doi: 10.1111/j.1365-2958.2009.06622.x; pmid: 19210616
23. J. P. Ballesta, M. Remacha, The large ribosomal subunit stalk as a regulatory element of the eukaryotic translational machinery. *Prog. Nucleic Acid Res. Mol. Biol.* **55**, 157–193 (1996). doi: 10.1016/S0079-6603(08)60193-2; pmid: 8787610
24. L. D. Kapp, J. R. Lorsch, GTP-dependent recognition of the methionine moiety on initiator tRNA by translation factor eIF2. *J. Mol. Biol.* **335**, 923–936 (2004). doi: 10.1016/j.jmb.2003.11.025; pmid: 14698289
25. D. S. Tourigny, I. S. Fernández, A. C. Kelley, V. Ramakrishnan, Elongation factor G bound to the ribosome in an intermediate state of translocation. *Science* **340**, 1235490 (2013). doi: 10.1126/science.1235490; pmid: 23812720
26. T. V. Pestova *et al.*, The joining of ribosomal subunits in eukaryotes requires eIF5B. *Nature* **403**, 332–335 (2000). doi: 10.1038/35002118; pmid: 10659855
27. M. G. Acker *et al.*, Kinetic analysis of late steps of eukaryotic translation initiation. *J. Mol. Biol.* **385**, 491–506 (2009). doi: 10.1016/j.jmb.2008.10.029; pmid: 18976658
28. T. Pape, W. Wintermeyer, M. Rodnina, Induced fit in initial selection and proofreading of aminoacyl-tRNA on the ribosome. *EMBO J.* **18**, 3800–3807 (1999). doi: 10.1093/emboj/18.13.3800; pmid: 10393195
29. M. A. Algire *et al.*, Development and characterization of a reconstituted yeast translation initiation system. *RNA* **8**, 382–397 (2002). doi: 10.1017/S1355838202029527; pmid: 12008673
30. L. D. Kapp, J. R. Lorsch, The molecular mechanics of eukaryotic translation. *Annu. Rev. Biochem.* **73**, 657–704 (2004). doi: 10.1146/annurev.biochem.73.030403.080419; pmid: 15189156
31. M. G. Acker, B. S. Shin, T. E. Dever, J. R. Lorsch, Interaction between eukaryotic initiation factors 1A and 5B is required for efficient ribosomal subunit joining. *J. Biol. Chem.* **281**, 8469–8475 (2006). doi: 10.1074/jbc.M600210200; pmid: 16461768
32. G. Tang *et al.*, EMAN2: An extensible image processing suite for electron microscopy. *J. Struct. Biol.* **157**, 38–46 (2007). doi: 10.1016/j.jsb.2006.05.009; pmid: 16859925
33. J. A. Mindell, N. Grigorieff, Accurate determination of local defocus and specimen tilt in electron microscopy. *J. Struct. Biol.* **142**, 334–347 (2003). doi: 10.1016/S1047-8477(03)00069-8; pmid: 12781660
34. S. H. Scheres, RELION: Implementation of a Bayesian approach to cryo-EM structure determination. *J. Struct. Biol.* **180**, 519–530 (2012). doi: 10.1016/j.jsb.2012.09.006; pmid: 23000701
35. S. H. Scheres, S. Chen, Prevention of overfitting in cryo-EM structure determination. *Nat. Methods* **9**, 853–854 (2012). doi: 10.1038/nmeth.2115; pmid: 22842542
36. P. B. Rosenthal, R. Henderson, Optimal determination of particle orientation, absolute hand, and contrast loss in single-particle electron cryomicroscopy. *J. Mol. Biol.* **333**, 721–745 (2003). doi: 10.1016/j.jmb.2003.07.013; pmid: 14568533
37. E. F. Pettersen *et al.*, UCSF Chimera—A visualization system for exploratory research and analysis. *J. Comput. Chem.* **25**, 1605–1612 (2004). doi: 10.1002/jcc.20084; pmid: 15264254
38. P. Emsley, B. Lohkamp, W. G. Scott, K. Cowtan, Features and development of Coot. *Acta Crystallogr. D* **66**, 486–501 (2010). doi: 10.1107/S0907444910007493; pmid: 20383002
39. J. P. Armache *et al.*, Cryo-EM structure and rRNA model of a translating eukaryotic 80S ribosome at 5.5-A resolution. *Proc. Natl. Acad. Sci. U.S.A.* **107**, 19748–19753 (2010). doi: 10.1073/pnas.1009999107; pmid: 20980660

Acknowledgments: We thank S. Chen for technical support with cryo-EM, G. McMullan for help in movie data acquisition, T. Darling and J. Grimmett for help with computing, D. Tourigny for discussions, and one of the reviewers for suggestions on properly modeling the P/I tRNA. X.-C.B. is supported by a EU FP7 Marie Curie postdoctoral fellowship. Supported by grants from the UK Medical Research Council (MC_U105184332 to V.R. and MC_UP_A025_1013 to S.H.W.S.); a Wellcome Trust Senior Investigator award (WT096570), the Agouron Institute, and the Jeantet Foundation (V.R.); and the Human Frontiers Science Program (grant RGP 28/2009 to V.R. and J.R.L.). The cryo-EM density maps have been deposited in the Electron Microscopy Data Bank with accession numbers EMD-2421 (for the large class with P/E tRNA) and EMD-2422 (for the small class with P/I tRNA). Fitted atomic coordinates have been deposited in the Protein Data Bank, with entry codes 4byl, 4byn, 4byo, 4byp, 4byq, 4byr, and 4bys for the large class and entry codes 4byt, 4byu, 4byv, 4byw, and 4byx for the small class.

Supplementary Materials

www.sciencemag.org/content/342/6160/1240585/suppl/DC1
Movies S1 to S3

16 May 2013; accepted 5 September 2013
10.1126/science.1240585

Iron(IV)hydroxide pK_a and the Role of Thiolate Ligation in C–H Bond Activation by Cytochrome P450

Timothy H. Yosca, Jonathan Rittle, Courtney M. Krest, Elizabeth L. Onderko, Alexey Silakov, Julio C. Calixto, Rachel K. Behan, Michael T. Green*

Cytochrome P450 enzymes activate oxygen at heme iron centers to oxidize relatively inert substrate carbon-hydrogen bonds. Cysteine thiolate coordination to iron is posited to increase the pK_a (where K_a is the acid dissociation constant) of compound II, an iron(IV)hydroxide complex, correspondingly lowering the one-electron reduction potential of compound I, the active catalytic intermediate, and decreasing the driving force for deleterious auto-oxidation of tyrosine and tryptophan residues in the enzyme's framework. Here, we report on the preparation of an iron(IV)hydroxide complex in a P450 enzyme (CYP158) in ≥90% yield. Using rapid mixing technologies in conjunction with Mössbauer, ultraviolet/visible, and x-ray absorption spectroscopies, we determine a pK_a value for this compound of 11.9. Marcus theory analysis indicates that this elevated pK_a results in a >10,000-fold reduction in the rate constant for oxidations of the protein framework, making these processes noncompetitive with substrate oxidation.

The cytochrome P450 class of thiolate-ligated heme proteins uses dioxygen and the formal equivalents of molecular hydrogen ($2H^+ + 2e^-$) to oxidize a broad spectrum of biologically active molecules. P450s are potent catalysts. They have been likened to a biological blowtorch for their ability to oxidize chemically inert hydrocarbons (*1*). Compound I, the active intermediate in P450 catalysis, is capable of cleaving unactivated C–H bonds with an observed rate constant of $1.1 \times 10^7\ M^{-1}s^{-1}$. The oxidation of bound substrate can exceed $1000\ s^{-1}$ (*2*). A major goal of bioinorganic chemistry has been to elucidate the factors that govern these transformations (*3*–*5*).

Experiments have shown that, during the course of productive C–H bond activation, compound I abstracts hydrogen from substrate to yield an iron(IV)hydroxide species (compound II) and a substrate radical (Fig. 1) (*2*, *6*). An enigmatic aspect of P450 catalysis is the enzyme's ability to perform this demanding oxidation $E^{\circ\prime}_{CH/C\bullet} \sim 1.5$ V (*7*, *8*) without damage to its own relatively fragile protein framework: The oxidation of tyrosine and tryptophan residues found throughout the tertiary structures of these enzymes represents an energetically favorable "short circuit" for compound I's oxidizing equivalents. Indeed, tyrosine oxidation ($E^{\circ\prime}_{Tyr\text{-}OH/O\bullet}$), which is known to dominate nonproductive decay in P450s, requires ~13 kcal/mol less driving force than alkane oxidation (*9*–*11*).

These unfavorable thermodynamics prompt a kinetic explanation of P450's preference for C–H bond activation. However, the intramolecular oxidation of tyrosine via long-range proton-coupled electron transfer (PCET) can be rapid, with rate constants approaching $10^6\ s^{-1}$ (*12*–*14*). Given rate constants of this magnitude and the substantial difference in pathway energetics, what mechanism precludes nonproductive oxidations of the protein framework and biases P450 toward substrate C–H bond activation?

We have argued that P450's axial thiolate ligand promotes C–H bond activation through the generation of basic iron(IV)oxo (or ferryl) species (*15*, *16*). To understand this proposal, it is useful to consider the free energies of the productive and nonproductive pathways illustrated in Fig. 1. The driving force for C–H bond activation, ΔG_p, is given by the difference between the energies of the C–H bond broken, D(C–H), and the O–H bond made, D(O–H) (Eq. 1).

$$\Delta G_p = D(\text{C–H}) - D(\text{O–H}) \quad (1)$$

In heme systems, D(O–H) is determined by the one-electron reduction potential of compound I and the pK_a (where K_a is the acid dissociation constant) of compound II, making ΔG_p a function of both of these thermodynamic parameters (Eq. 2). C is a constant that depends on the solvent and reference electrode. Its value is 57.6 for aqueous solution with $E°$ versus normal hydrogen electrode (NHE) (*8*).

$$D(\text{O–H}) = 23.06 \times E^{\circ}_{I} + 1.37 \times \text{p}Ka_{II} + C \pm 2\ \text{kcal/mol} \quad (2)$$

In contrast, ΔG_{np}, the driving force for nonproductive oxidations, is determined by the one-electron reduction potential of compound I, E°_{I}, and the proton-coupled reduction potential of tyrosine ($E^{\circ\prime}_{Tyr}$, which includes the energetics of proton transfer to a basic residue or solvent, shown as **B:** in Fig. 1) (Eq. 3).

$$\Delta G_{np} = 23.06(E^{\circ\prime}_{Tyr} - E^{\circ}_{I})\ \text{kcal/mol} \quad (3)$$

This means that a change in the compound II pK_a alters the energetics of the system. To illustrate this point, we construct the relative free energy, ΔG_{rel} (Eqs. 4 and 5 and supplementary materials eqs. S20 to S25), which is the difference between the free energies of the productive and nonproductive pathways. The sign of ΔG_{rel} indicates the thermodynamically preferred process. When $\Delta G_{rel} < 0$, the productive pathway is preferred. Note that ΔG_{rel} is independent of the reduction potential of compound I. For a given tyrosine potential, ΔG_{rel} depends only upon the compound II pK_a, with a unit increase in the pK_a shifting the energetics of the system 1.37 kcal/mol toward the productive pathway (Fig. 1).

$$\Delta G_{rel} = \Delta G_p - \Delta G_{np} \quad (4)$$

$$\Delta G_{rel} = D(\text{C–H}) - 1.37 \times \text{p}Ka - C - 23.06 \times E^{\circ\prime}_{Tyr} \pm 2\ \text{kcal/mol} \quad (5)$$

For a given ΔG_p, a change in the compound II pK_a affects not only the energetics but also the kinetics of the system. The rate constant for nonproductive oxidations can be linked directly to E°_{I}, which decreases (by 59 mV per unit) with increasing pK_a. Thus, a highly elevated pK_a can dramatically attenuate the rate of nonproductive decay.

Based on these arguments, we propose that a critical role of thiolate ligation in P450 is to alter the free energy landscape, shifting the relative free energy for the productive and nonproductive pathways to a regime where the rate constant for C–H bond activation dominates that for nonproductive decay.

Results from theoretical investigations and reactivity studies with model systems lend support to this hypothesis (*16*–*20*), but an experiment (or experimental parameter) that could provide a quantitative measure of the thiolate's impact on P450 catalysis has proven elusive. In what follows, we report the identification of a P450 that can be prepared in the compound II form in high yield over a wide pH range. This discovery has allowed us to determine an iron(IV)hydroxide pK_a precisely.

Determination of an Iron(IV)hydroxide pK_a

Iron(IV)oxo moieties are generally thought to be electrophilic in nature and hence rarely protonated. Although examples of synthetic ferryl porphyrins are numerous (*21*), a definitive characterization of a synthetic iron(IV)hydroxide has not been reported. The same is true for histidine ligated iron centers in peroxidase and globin enzymes. A battery of spectroscopic measurements have shown that the compound II forms of these enzymes have pK_a values ≤3.5. They are best described as iron(IV)oxo species (*22*). These results stand in stark contrast to those obtained for thiolate ligated heme systems, where only the iron(IV)hydroxide state has been observed (*16*).

Department of Chemistry, Pennsylvania State University, University Park, PA 16802, USA.

*Corresponding author. E-mail: mtg10@psu.edu

Although a number of spectroscopic investigations have confirmed the basic nature of thiolate ligated ferryls (*15*, *16*, *23*–*26*), poor yields and the inability to prepare compound II at high pH have precluded efforts to pinpoint the iron(IV)hydroxide pK_a. Recently, we identified a P450 (CYP158 with a large, solvent exposed, active site) in which the compound II form of the enzyme can be prepared in high yield over a wide pH range.

CYP158 is one of 18 P450 enzymes found in the prototypic soil bacterium *Streptomyces coelicolor* (*27*, *28*). The enzyme is thought to play a role in the synthesis of secondary metabolites that afford *S. coelicolor* protection against the harmful effects of ultraviolet (UV) irradiation. During efforts to characterize high-valent intermediates in the catalytic cycle of CYP158, we found that compound II (CYP158-II) could be prepared by reacting ferric enzyme with *meta*-chloroperbenzoic acid (*m*-CPBA).

The use of *m*-CPBA, a two-electron oxidant, to prepare P450 compound II (which is only one oxidizing equivalent above ferric enzyme) can be understood in terms of the highly reactive nature of P450-I, which in the absence of substrate can strip an electron from the protein framework to form compound II and a protein-based radical (*9*–*11*): To avoid the uncoupling of redox equivalents during normal aerobic turnover, P450s rely on precise control of proton delivery. Two protons must be delivered to the distal oxygen of the reduced ferrous-oxy complex to generate compound I, while subsequent delivery of protons to the ferryl oxygen must be avoided to prevent its reduction to water (*29*, *30*). In substrate free enzyme, solvent-derived protons can readily access the iron(IV)oxo unit. The coupling of ferryl protonation to the reduction of compound I increases the driving force for oxidation of the protein framework. Under turnover conditions with substrates that fit poorly in the active site, these processes are known to lead to oxidase chemistry (*31*–*33*). In rapid mixing experiments with *m*-CPBA, they can present a major obstacle to the isolation of P450-I (*9*–*11*). As we will show, CYP158 allows us to use this facet of P450 chemistry to our advantage.

The reaction of CYP158 with *m*-CPBA generates compound II in good yield in the pH range from 7 to 10, with maximum formation (>90%) (fig. S1) occurring at pH 9. The intermediate is relatively stable at this pH, decaying at ~0.01s^{-1}. The UV/visible spectrum of CYP158-II at pH 9.0 is hyperporphyrin-like: It features a split Soret band with absorption maxima at 370 and 426 nm and Q bands at 532 and 565 nm (Fig. 2). Mössbauer measurements confirm that this species is best described as an iron(IV)-hydroxide complex.

The ^{57}Fe Mössbauer spectrum of CYP158-II at pH 9 consists of a single quadrupole doublet (Fig. 3A). Best fits of the data provide a quadrupole splitting of ΔE_Q = 2.05 mm/s and an isomer shift of δ = 0.10 mm/s. These values are in good agreement with Mössbauer parameters reported for other thiolate-ligated compound II species (*23*, *26*).

Given the high yield and stability of CYP158-II at pH 9, we wondered if the pH 9 intermediate could serve as a platform from which CYP158-II could be prepared at higher pH via rapid sequential mixing, allowing a well-bounded pK_a measurement. Figures 2 and 3 show spectra of CYP158A-II samples prepared from pH 9.0 to pH 14.0. With increasing pH, the iron(IV)hydroxide complex converts cleanly to a new species. The UV/visible spectrum of the high pH intermediate is also hyperporphyrin-like, with absorption maxima at 371 and 437 nm and a single Q band centered at 545 nm. Mössbauer measurements at pH 13.3 again reveal the presence of a single iron(IV) species. This species has a reduced quadrupole splitting that is indicative of an iron(IV)oxo porphyrin (δ = 0.09 mm/s, ΔE_Q = 1.30 mm/s) (*22*).

Figure 2 reveals that the UV/visible spectra obtained as a function of pH possess multiple isosbestic points, indicating that pH-driven changes in the spectra result only from the hydroxo to oxo reaction. This result is consistent with our Mössbauer experiments (Fig. 3) as well as the observed decay

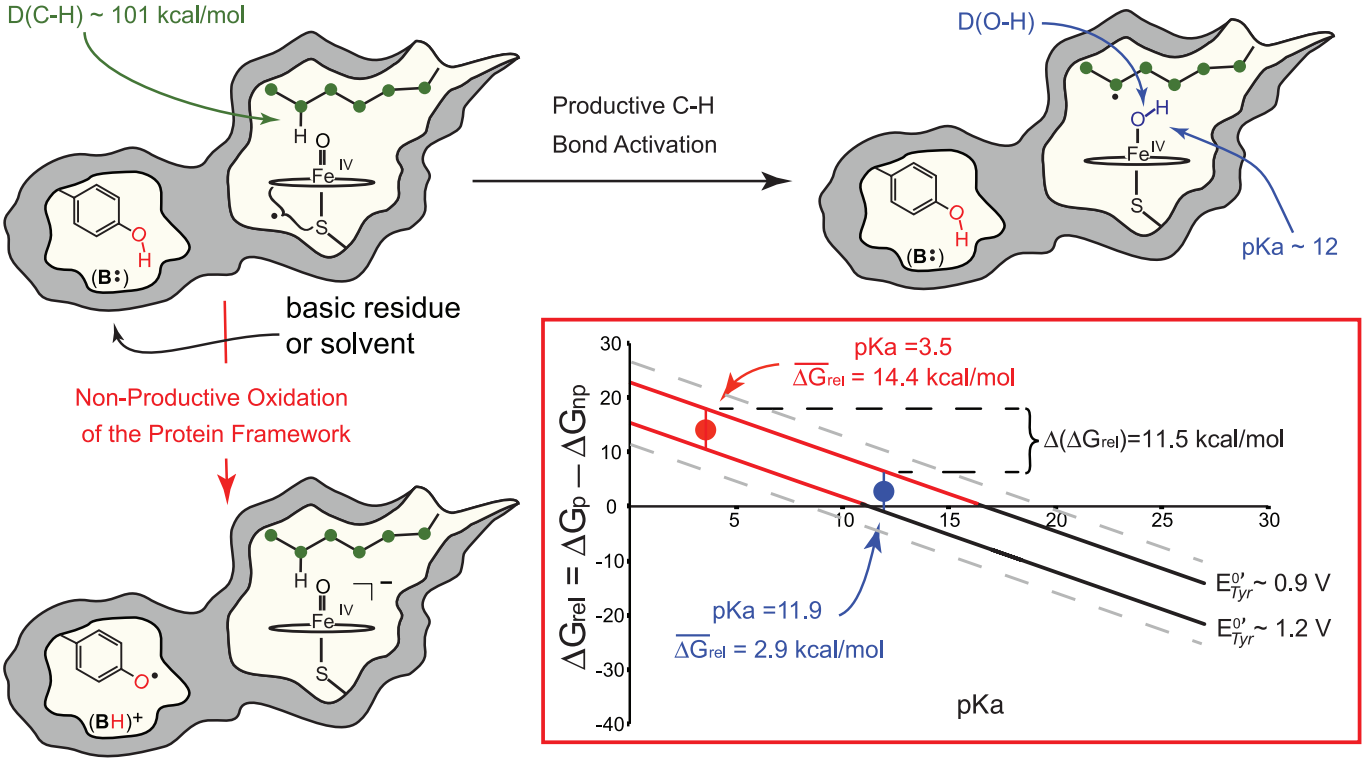

Fig. 1. Productive and nonproductive pathways for compound I decay. During productive C–H bond activation, compound I (a ferryl-radical species) abstracts hydrogen from substrate to yield compound II [an iron(IV)hydroxide complex] and a substrate radical. The nonproductive pathway shown involves the oxidation of a tyrosine residue contained within the protein framework, with the phenolic proton being transferred to **B:**, a basic residue or solvent molecule, upon tyrosine oxidation. The inset shows the relative free energies (ΔG_{rel}) (Eq. 5) for the productive and nonproductive pathways as a function of the compound II pK_a for the range of aqueous tyrosine potentials. When ΔG_{rel} is negative, the productive pathway is thermodynamically preferred. As a result of the ±2 kcal/mol error in Eq. 2, a small range of tyrosine potentials could yield a given ΔG_{rel}. The uncertainty in the solid lines as a result of this error is ±0.1 V.

rates, which indicate that there is minimal degradation (<3% at pH 14) (fig. S3) during the time required for our measurements. Analyses of the data reveal that the iron(IV) species are in equilibrium: Plotting either the change in UV/visible absorbance or the relative concentration of the oxo species as a function of pH results in the pH titration curves shown in Fig. 4. Fits of these curves provide an iron(IV)hydroxide pK_a of 11.9. The reversibility of this transition was confirmed using triple-mix stopped-flow experiments, in which the oxo form (prepared at pH 13.5) was protonated to the hydroxo form (at pH 9) by an additional mixing stage with 1 M low-pH Tris-HCl (fig. S4).

Given the extreme pH at which this transition occurs, could a pH-driven conformational change result in the loss of thiolate ligation and associated driving force for ferryl protonation? The observation of a split Soret band at high pH effectively rules out this possibility. A split Soret, or hyperporphyrin spectrum, is known to be a key indicator of thiolate ligation in heme proteins. The Soret band typically arises from porphyrin $\pi \rightarrow \pi^*$ electronic transitions, but in thiolate-ligated systems this band is split through interactions with a sulfur $\rightarrow$ porphyrin charge-transfer band (*34*). The two Soret bands at 371 and 437 nm in the UV/visible spectrum of the high-pH intermediate are the hallmarks of this interaction. Their presence indicates the retention of thiolate ligation at high pH.

Iron *K*-edge x-ray absorption measurements (Fig. 5) further confirm the retention of thiolate ligation and support the assignment of the compound II pK_a. Both the high- and low-pH forms of the intermediate have an absorption edge that lies ~1.5 eV above the ferric edge, consistent with the presence of an iron(IV) state. Fits of the extended x-ray absorption fine structure (EXAFS) data yield Fe–O/Fe–S distances of 1.68/2.36 Å at pH 13.3 and 1.84/2.27 Å at pH 9.0. The short Fe–O distance at pH 13.3 is indicative of an iron(IV)oxo species. With decreasing pH, the Fe–O bond length increases by 0.15 Å, consistent with protonation of the ferryl moiety (*15*).

Examination of the CYP158 crystal structure suggests a number of candidates for the location of the protein-derived reducing equivalent that converts P450-I to P450-II in our rapid mixing experiments (*27*) (PDB accession code 1S1F). Chief among them is Tyr-352, a solvent-exposed residue, which is adjacent to the Cys-353 thiolate ligand (fig. S5). Incorporation of a phenylalanine at this position, through site-directed mutagenesis, results in protein that generates P450-I in high (~80%) yield (figs. S6 to S8). Samples of the Y352F CYP158-I variant show the presence of residual compound II (~3%) as well as a protein-based radical (~5%). Both can be completely eliminated through the removal of a second tyrosine at position 318. The Y318F/Y352F variant shows increased CYP158-I production (~90% yield) and a compound I electron paramagnetic resonance spectrum that is devoid of protein radicals (figs. S6 to S8).

Using insights gained from these site-directed mutagenesis studies, we sought to determine the compound II pK_a in a second P450. The reaction of the thermophilic CYP119 with *m*-CPBA is known to produce P450-I in high (~75%) yield: Compound II does not accumulate. Incorporation of a tyrosine residue at the position corresponding to that of Tyr-352 in CYP158 results in an L316Y CYP119 variant that generates compound II in high yield. Similar pH jump experiments set the pK_a of the CYP119-II variant at 12.2 (figs. S9 to S12).

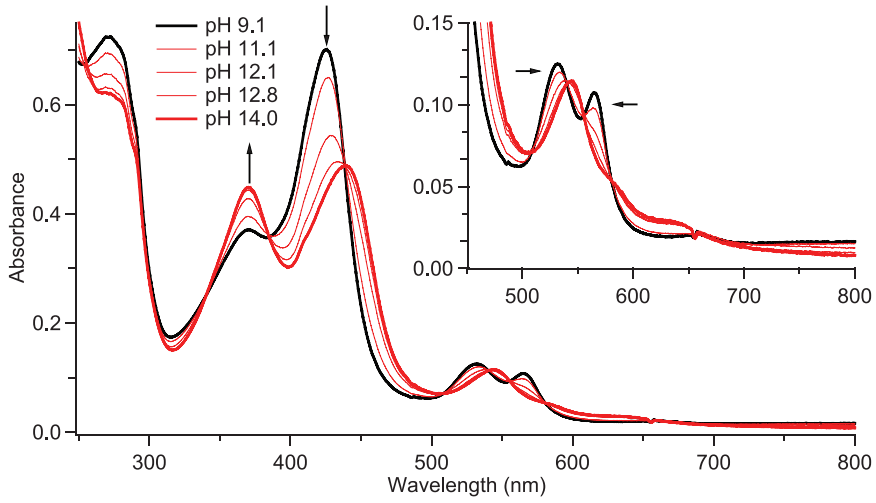

Fig. 2. UV/visible spectra of CYP158-II at varying pH. Samples were prepared in a double-mix stopped-flow experiment. Ferric CYP158 (30 μM, 10 mM Tris-HCl, pH 9.0) was first mixed with 150 μM *m*-CPBA and held until maximum formation of CYP158-II was achieved (2.5 s). This solution was then mixed with a strongly buffered solution (containing 200 mM phosphate, 200 mM carbonate, pH adjusted with KOH) to obtain the desired final pH. Mixing was 1:1:1. The inset shows a magnification of the 450- to 800-nm region.

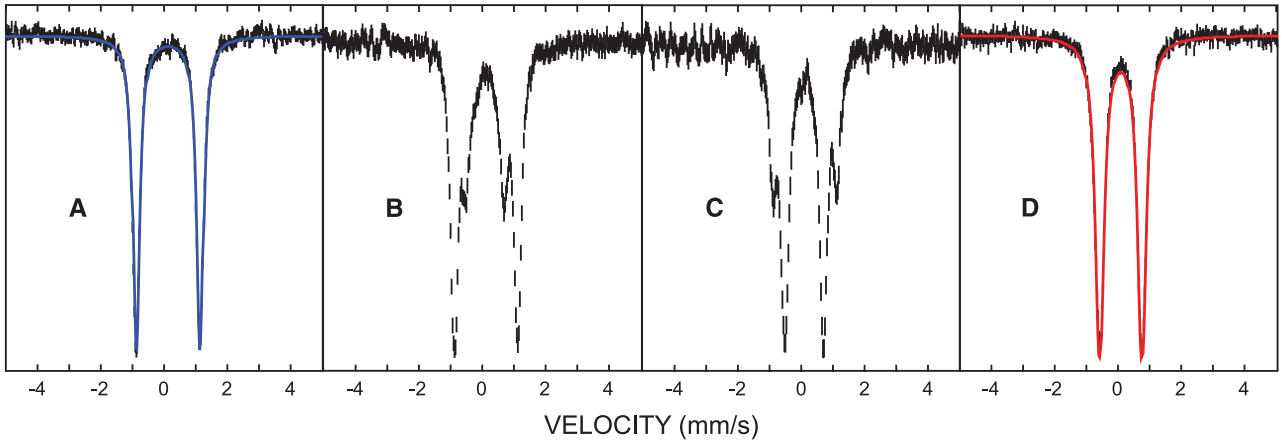

Fig. 3. Mössbauer spectra of CYP158-II at varying pH. (**A**) pH 9.0, (**B**) 11.8, (**C**) 12.2, and (**D**) 13.3. Samples were prepared in a double-mix freeze-quench experiment. Protein (6 mM) was mixed 2:1 with 60 mM *m*-CPBA to form CYP158-II at pH 9. This species was then mixed 3:1 with an arginine/NaOH buffer (pH 14). The strength of the arginine/NaOH buffer was varied (10 mM to 108.16 mM) to achieve the desired final pH. The reaction mixture was sprayed into liquid ethane 7 ms after the first mix (see supplementary materials). Fits for the intermediate pH samples [(B) and (C)] are shown in fig. S2.

It is conceivable that an electron-deficient residue adjacent to the proximal cysteine could diminish the electron-donating ability of the thiolate ligand, thereby decreasing the iron(IV)hydroxide pK_a. However the solvent-exposed nature of the tyrosine residues under consideration renders this possibility unlikely. To alleviate any concerns that a neighboring Tyr-O• might suppress the compound II pK_a from its natural value, density functional theory calculations were performed on an active-site model, using implicit solvation. These calculations, which examined the energy of ferryl protonation in the presence and absence of tyrosine oxidation, revealed that the Tyr-O• has little (if any) effect on the pK_a of the iron(IV)hydroxide complex. When "solvated" in a dielectric continuum with dielectric constant ε = 4.0 (a value typically chosen for the protein matrix) (*35*), the Tyr-O• suppresses the iron(IV)hydroxide pK_a by only 0.3 units. In water (ε = 80), the effect is less than 0.1 units (fig. S13).

The observation of a similar compound II pK_a (~12) in both CYP119 and CYP158 is important. These P450s have different active-site pockets and substrate preferences (*27*, *28*, *36*, *37*). Our results suggest that an elevated iron(IV)hydroxide pK_a is a general feature of P450s and thiolate-ligated hemes.

Implications for Reactivity and the Role of Thiolate Ligation in P450 Catalysis

A central question in the field of P450 catalysis has been the thiolate's role in hydrocarbon oxidations. A number of spectroscopic studies have revealed the impact of thiolate ligation on the electronic and geometric structures of the P450 active site. These investigations have provided clear evidence for the strong electron-donating character of the axial thiolate ligand (*38*, *39*), but they have not provided a quantitative measure of the thiolate's impact on reactivity. A compound II pK_a of ~12 provides such a measure.

A pK_a of ~12 is notable for an iron(IV)hydroxide, given the (typically) electrophilic nature of ferryl species. The compound II pK_a values reported here are at least 8.5 units higher than the pK_a values of histidine-ligated hemes in peroxidase and globin enzymes. An increase of ≥8.5 units in the compound II pK_a shifts the energetics of the system ≥11.5 kcal/mol toward the productive pathway (Eq. 5). This is illustrated in the inset of Fig. 1, where ΔG_{rel} is shown for the full range of aqueous tyrosine reduction potentials, indicated by the dashed gray lines ($E^{\circ}_{Tyr\text{-}O/Tyr\text{-}O\bullet}$ = 0.7 V to $E^{\circ}_{Tyr\text{-}OH/Tyr\text{-}OH\bullet+}$ = 1.4 V). The solid line at ~0.9 V in Fig. 1 separates the low- and mid-potential regions. It corresponds to the reduction potential of a solvent-exposed tyrosine. The incorporation of a tyrosine residue into the protein framework is expected to place its reduction potential near or above this value (*40*, *41*). The line at $E^{\circ'}_{Tyr}$ ~ 1.2 V separates mid- and high-potential regions: For tyrosines with reduction potentials above $E^{\circ'}_{Tyr}$ ~ 1.2 V, ΔG_{rel} changes sign as the iron(IV)hydroxide pK_a increases from 3.5 to 12. That is, with thiolate ligation, the productive pathway becomes thermodynamically preferred.

This behavior is not observed in the important midpotential region, which lies at the intersection of tyrosine potentials most likely to be found in P450s with those most readily oxidized by compound I. For these systems, with a compound II pK_a of 3.5, nonproductive tyrosine oxidation is favored over C–H bond activation by an average of 14 kcal/mol. As the pK_a increases, the energetics of the system shift toward the productive pathway. With a pK_a of 12, the preference for the nonproductive pathway has been reduced to an average of only 3 kcal/mol.

We argue that this shift in the relative free energy places C–H bond activation in a regime of kinetic control. For a given ΔG_p, a decrease of ≥11.5 kcal/mol in ΔG_{rel} corresponds to a reduction of ≥0.5 V in E°_I. This drop in reduction potential dramatically attenuates the rate constants for nonproductive oxidations, biasing the system toward C–H bond activation.

The impact of thiolate ligation on the nonproductive rate constants can be illustrated through the application of Marcus theory. Although originally proposed to describe outer-sphere electron transfer reactions, Marcus theory has been shown to be applicable to a broad range of PCET processes (*42*, *43*), with the rate constant for PCET being given by Eq. 6

$$k(s^{-1}) = Ae^{-(\Delta G+\gamma)^2/4\gamma RT} \quad (6)$$

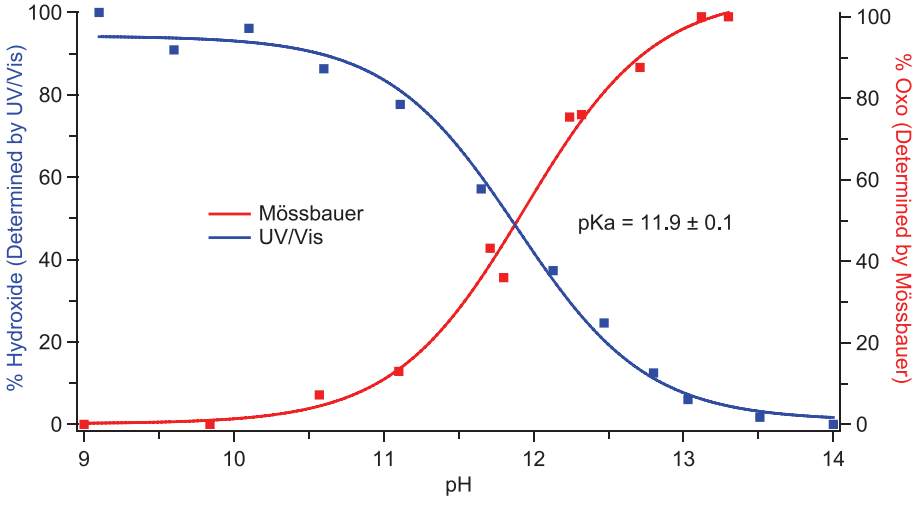

Fig. 4. pH titration curves for CYP158-II. Data obtained from stopped-flow UV/visible (blue) and Mössbauer spectroscopies (red) yield the same pK_a value of 11.9. UV/visible data points were obtained from the change in absorbance at 423 nm (Fig. 2). Mössbauer data points were obtained from the ratio of the areas of the iron(IV)oxo and iron(IV)hydroxide subspectra (fig. S2).

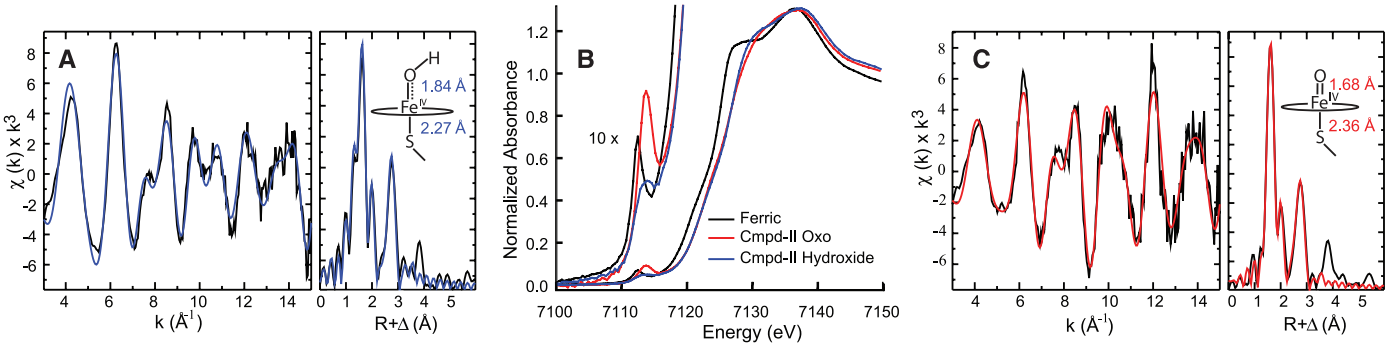

Fig. 5. X-ray absorption spectroscopy. (**A**) EXAFS of CYP158-II at pH 9.0. (**B**) X-ray absorption edges. (**C**) EXAFS of CYP158-II at pH 13.3. All EXAFS samples were analyzed by Mössbauer spectroscopy before data collection. See tables S1 and S2 for further details.

Where ΔG is the driving force for the reaction, γ is the intrinsic barrier (*44*), and A is a function of the coupling between the donor and acceptor states.

Examinations of the intra- and intermolecular oxidations of tyrosine and substituted phenols have revealed that γ is large in these systems. Analyses of reactions employing oxidants with reduction potentials as high as 1.3 V indicate that $2\gamma >> \Delta G$ (*13*, *45*–*47*). Given PCET within this regime, Eq. 7 (derived in eqs. S1 to S19) allows a comparison of rate constants for nonproductive oxidation by compound I species, k^{np}, as a function of compound II pK_a values.

$$\frac{k_1^{np}}{k_2^{np}} = 10^{\left(\frac{\Delta pK_a}{2}\right)} \qquad (7)$$

Implicit in the derivation of Eq. 7 is the assumption of an invariant driving force for productive substrate oxidations (i.e., ΔG_p). Equation 7 can be used to determine the magnitude by which thiolate ligation suppresses nonproductive oxidations. Inserting $\Delta pK_a \geq 8.5$ (the difference between histidine- and thiolate-ligated compound II pK_a values) into Eq. 7 reveals that (relative to histidine ligation) thiolate ligation provides—*ceteris paribus*—a >10,000-fold reduction in the rate constant for nonproductive oxidations. The ability of thiolate ligation to suppress these nonproductive pathways is of critical importance given the apparent endergonic nature of C–H bond activation.

The O–H bond strength of P450-II is unknown, but theoretical methods predict that cleavage of an unactivated C–H bond by P450-I is ~6 kcal/mol endergonic (*48*). To achieve similar energetics, a histidine-ligated compound I would require a one-electron reduction potential of at least 1.4 V, yielding $\Delta G_{np} \sim 0.2$ to 0.5 V for the tyrosine potentials displayed in Fig. 1. Experiments on biological and synthetic model systems possessing similar driving forces have shown that the oxidation of tyrosines by long-range intramolecular PCET can be rapid, with experimentally determined rate constants ranging from 10^4 to 10^6 s^{-1} (*12*, *13*, *49*). The preceding analysis suggests that thiolate ligation lowers rate constants of even this magnitude to less than 50 s^{-1}, making them noncompetitive with C–H bond activation (<5% uncoupling). Thus, we argue that thiolate ligation buys time for P450-I to accomplish endergonic oxidations, creating what is effectively a controlled burn of inert organic compounds.

Our analysis provides insight into the absence of histidine-ligated P450-like enzymes in nature. The degree of uncoupling (via the nonproductive oxidation of aromatic residues) in such a system would be unsustainable. Oxidations by the ferryl intermediates of nonheme enzymes such as AlkB, SyrB2, and TauD (*50*–*53*) and by the 5′-deoxyadenosyl 5′-radical of radical SAM enzymes (*54*–*56*) appear to be additional examples of this scheme in action (*57*–*60*).

References and Notes

1. I. Schlichting *et al*., *Science* **287**, 1615–1622 (2000).
2. J. Rittle, M. T. Green, *Science* **330**, 933–937 (2010).
3. S. G. Sligar, *Science* **330**, 924–925 (2010).
4. J. M. Bollinger Jr., J. B. Broderick, *Curr. Opin. Chem. Biol.* **13**, 51–57 (2009).
5. J. T. Groves, *Proc. Natl. Acad. Sci. U.S.A.* **100**, 3569–3574 (2003).
6. J. T. Groves, G. A. McClusky, R. E. White, M. J. Coon, *Biochem. Biophys. Res. Commun.* **81**, 154–160 (1978).
7. P450s are known to activate inert C–H bonds with bond dissociation energies (BDEs) on the order of 98 to 101 kcal/mol. In this work, we consider a hypothetical C–H bond with a BDE that equals the average of this range, BDE = 99.5 kcal/mol. Assuming $S^0_{solv}(CH) = S^0_{solv}(C\bullet)$ for hydrocarbons adds 1.8 kcal/mol to the BDE (*8*), for a bond dissociation free energy (BDFE) of ~101 kcal/mol. Using this value, we obtain the thermodynamic potential $E^{o'}_{CH/C\bullet} \sim 1.47$ V for hydrocarbon oxidation at pH 7. The oxidation of tyrosine at this pH requires a potential of $E^{o'}_{Tyr\text{-}OH/O\bullet} \sim 0.9$ V. The difference in these potentials is equivalent to ~13 kcal/mol.
8. J. J. Warren, T. A. Tronic, J. M. Mayer, *Chem. Rev.* **110**, 6961–7001 (2010).
9. In the absence of substrate, P450-I decays predominantly through the oxidation of tyrosine residues (*10*, *11*). The oxidation of tryptophan is energetically feasible, but tyrosine with its (generally) lower potential is the preferred target. Tryptophan radicals have been observed after P450-I decay, but these species constituted only a minor component of the decay product (*10*). The treatment of tyrosine oxidation presented here is an archetype for nonproductive one-electron processes. It may be applied equally well to tryptophan oxidation.
10. C. Jung, V. Schünemann, F. Lendzian, *Biochem. Biophys. Res. Commun.* **338**, 355–364 (2005).
11. V. Schünemann *et al*., *J. Biol. Chem.* **279**, 10919–10930 (2004).
12. T. Irebo, O. Johansson, L. Hammarström, *J. Am. Chem. Soc.* **130**, 9194–9195 (2008).
13. M. Sjödin, S. Styring, B. Åkermark, L. Sun, L. Hammarström, *J. Am. Chem. Soc.* **122**, 3932–3936 (2000).
14. R. Ahlbrink *et al*., *Biochemistry* **37**, 1131–1142 (1998).
15. M. T. Green, J. H. Dawson, H. B. Gray, *Science* **304**, 1653–1656 (2004).
16. M. T. Green, *Curr. Opin. Chem. Biol.* **13**, 84–88 (2009).
17. Y. Kang *et al*., *Chemistry* **15**, 10039–10046 (2009).
18. T. H. Parsell, M.-Y. Yang, A. S. Borovik, *J. Am. Chem. Soc.* **131**, 2762–2763 (2009).
19. K. A. Prokop, S. P. de Visser, D. P. Goldberg, *Angew. Chem. Int. Ed.* **49**, 5091–5095 (2010).
20. C. V. Sastri *et al*., *Proc. Natl. Acad. Sci. U.S.A.* **104**, 19181–19186 (2007).
21. J. Terner *et al*., *J. Inorg. Biochem.* **100**, 480–501 (2006).
22. R. K. Behan, M. T. Green, *J. Inorg. Biochem.* **100**, 448–459 (2006).
23. R. K. Behan, L. M. Hoffart, K. L. Stone, C. Krebs, M. T. Green, *J. Am. Chem. Soc.* **128**, 11471–11474 (2006).
24. M. T. Green, *J. Am. Chem. Soc.* **128**, 1902–1906 (2006).
25. K. L. Stone, R. K. Behan, M. T. Green, *Proc. Natl. Acad. Sci. U.S.A.* **103**, 12307–12310 (2006).
26. K. L. Stone, L. M. Hoffart, R. K. Behan, C. Krebs, M. T. Green, *J. Am. Chem. Soc.* **128**, 6147–6153 (2006).
27. B. Zhao *et al*., *J. Biol. Chem.* **280**, 11599–11607 (2005).
28. B. Zhao, F. P. Guengerich, M. Voehler, M. R. Waterman, *J. Biol. Chem.* **280**, 42188–42197 (2005).
29. P. R. O. de Montellano, Ed., *Cytochrome P450: Structure, Mechanism, and Biochemistry* (Kluwer Academic/Plenum Publishers, New York, ed. 3, 2004).
30. S. Kadkhodayan, E. D. Coulter, D. M. Maryniak, T. A. Bryson, J. H. Dawson, *J. Biol. Chem.* **270**, 28042–28048 (1995).
31. L. D. Gorsky, D. R. Koop, M. J. Coon, *J. Biol. Chem.* **259**, 6812–6817 (1984).
32. W. M. Atkins, S. G. Sligar, *J. Am. Chem. Soc.* **109**, 3754–3760 (1987).
33. Y. V. Grinkova, I. G. Denisov, M. A. McLean, S. G. Sligar, *Biochem. Biophys. Res. Commun.* **430**, 1223–1227 (2013).
34. L. K. Hanson *et al*., *J. Am. Chem. Soc.* **98**, 2672–2674 (1976).
35. M. K. Gilson, B. H. Honig, *Biopolymers* **25**, 2097–2119 (1986).
36. J. K. Yano *et al*., *J. Biol. Chem.* **275**, 31086–31092 (2000).
37. S. Y. Park *et al*., *J. Inorg. Biochem.* **91**, 491–501 (2002).
38. Dawson and co-workers (*39*) have shown that exogenous thiol ligands bound trans to the proximal thiolate of P450 have enhanced basicity relative to analogous myoglobin adducts.
39. M. Sono, L. A. Andersson, J. H. Dawson, *J. Biol. Chem.* **257**, 8308–8320 (1982).
40. S. Hay, K. Westerlund, C. Tommos, *Biochemistry* **44**, 11891–11902 (2005).
41. C. Tommos, K. G. Valentine, M. C. Martínez-Rivera, L. Liang, V. R. Moorman, *Biochemistry* **52**, 1409–1418 (2013).
42. J. M. Mayer, *J. Phys. Chem. Lett.* **2**, 1481–1489 (2011).
43. J. M. Mayer, *Acc. Chem. Res.* **44**, 36–46 (2011).
44. J. J. Warren, J. R. Winkler, H. B. Gray, *FEBS Lett.* **586**, 596–602 (2012).
45. M.-T. Zhang, T. Irebo, O. Johansson, L. Hammarström, *J. Am. Chem. Soc.* **133**, 13224–13227 (2011).
46. T. F. Markle, I. J. Rhile, A. G. Dipasquale, J. M. Mayer, *Proc. Natl. Acad. Sci. U.S.A.* **105**, 8185–8190 (2008).
47. I. J. Rhile *et al*., *J. Am. Chem. Soc.* **128**, 6075–6088 (2006).
48. S. P. de Visser, D. Kumar, S. Cohen, R. Shacham, S. Shaik, *J. Am. Chem. Soc.* **126**, 8362–8363 (2004).
49. C. E. Immoos *et al*., *Inorg. Chem.* **43**, 3593–3596 (2004).
50. M. L. Matthews *et al*., *Biochemistry* **48**, 4331–4343 (2009).
51. J. C. Price, E. W. Barr, B. Tirupati, J. M. Bollinger Jr., C. Krebs, *Biochemistry* **42**, 7497–7508 (2003).
52. C. Krebs, D. Galonić Fujimori, C. T. Walsh, J. M. Bollinger Jr., *Acc. Chem. Res.* **40**, 484–492 (2007).
53. J. M. Simmons, T. A. Müller, R. P. Hausinger, *Dalton Trans.* (38): 5132–5142 (2008).
54. S. J. Booker, *Curr. Opin. Chem. Biol.* **13**, 58–73 (2009).
55. M. R. Challand, R. C. Driesener, P. L. Roach, *Nat. Prod. Rep.* **28**, 1696–1721 (2011).
56. K. S. Duschene, S. E. Veneziano, S. C. Silver, J. B. Broderick, *Curr. Opin. Chem. Biol.* **13**, 74–83 (2009).
57. D. M. Davies, P. Jones, D. Mantle, *Biochem. J.* **157**, 247–253 (1976).
58. G. Annino, M. Cassettari, M. Martinelli, *IEEE Trans. Microw. Theory Tech.* **57**, 775–783 (2009).
59. E. Reijerse, F. Lendzian, R. Isaacson, W. Lubitz, *J. Magn. Reson.* **214**, 237–243 (2012).
60. Gaussian 09, Revision C.01 (Gaussian Inc., Wallingford, CT, 2009).

Acknowledgments: We thank M. Latimer and E. Nelson for onsite assistance at the synchrotron. This work was supported by NIH (R01-GM101390). Portions of this research were carried out at the Stanford Synchrotron Radiation Lightsource (SSRL), a Directorate of SLAC National Accelerator Laboratory and an Office of Science User Facility operated for the U.S. Department of Energy (DOE) Office of Science by Stanford University. The SSRL Structural Molecular Biology Program is supported by the DOE Office of Biological and Environmental Research and by the NIH National Institute of General Medical Sciences (including P41GM103393).

Supplementary Materials

www.sciencemag.org/content/342/6160/825/suppl/DC1
Materials and Methods
Supplementary Text
Figs. S1 to S13
Tables S1 to S4

7 August 2013; accepted 17 October 2013
10.1126/science.1244373

Room-Temperature Quantum Bit Storage Exceeding 39 Minutes Using Ionized Donors in Silicon-28

Kamyar Saeedi,[1] Stephanie Simmons,[2] Jeff Z. Salvail,[1] Phillip Dluhy,[1] Helge Riemann,[3] Nikolai V. Abrosimov,[3] Peter Becker,[4] Hans-Joachim Pohl,[5] John J. L. Morton,[6] Mike L. W. Thewalt[1]*

Quantum memories capable of storing and retrieving coherent information for extended times at room temperature would enable a host of new technologies. Electron and nuclear spin qubits using shallow neutral donors in semiconductors have been studied extensively but are limited to low temperatures (≲10 kelvin); however, the nuclear spins of ionized donors have the potential for high-temperature operation. We used optical methods and dynamical decoupling to realize this potential for an ensemble of phosphorous-31 donors in isotopically purified silicon-28 and observed a room-temperature coherence time of over 39 minutes. We further showed that a coherent spin superposition can be cycled from 4.2 kelvin to room temperature and back, and we report a cryogenic coherence time of 3 hours in the same system.

A long-term, portable quantum storage register operating at room temperature would be an important advance in realizing the potential of quantum computation (*1*, *2*) and new technologies such as quantum money (*3*, *4*). Solid-state quantum systems have reached a coherent storage time (T_2) of ~2 s for the nuclear spin of a ^{13}C atom coupled to a nitrogen-vacancy (NV) center in diamond at room temperature (*5*). Another promising semiconductor qubit system uses the electron and/or nuclear spins of neutral shallow donor impurities (D^0) such as ^{31}P in Si (*6*–*8*). The nuclear spin of neutral ^{31}P in isotopically purified ^{28}Si can reach a coherence time of 180 s (*9*); however, like all shallow D^0, this is an inherently low-temperature system. Even at 4.2 K, the nuclear spin T_2 is limited by the electron spin relaxation time, T_1 (*9*), which decreases very rapidly with increasing temperature, dropping to a few milliseconds at 10 K (*10*); in addition, the donors begin to thermally ionize above ~30 K.

Here we show that the nuclear spin of the ionized donor (D^+) has important advantages over that of D^0 and is not limited to operation at cryogenic temperatures. In two recent studies on the D^+ nuclear spin in natural Si at cryogenic temperatures, one on an ensemble (*11*) and one on a single ^{31}P atom (*12*), the nuclear spin T_2 for D^+ was found to be considerably longer than that for D^0, because the removal of the electron spin eliminated decoherence associated with the electric field noise arising from the nearby electrodes and Si/SiO_2 interface. The resulting D^+ T_2

[1]Department of Physics, Simon Fraser University, Burnaby, BC, V5A 1S6, Canada. [2]Department of Materials, Oxford University, Oxford OX1 3PH, UK. [3]Leibniz-Institut für Kristallzüchtung, 12489 Berlin, Germany. [4]PTB Braunschweig, 38116 Braunschweig, Germany. [5]VITCON Projectconsult, 07743 Jena, Germany. [6]London Centre for Nanotechnology, University College London, London WC1H 0AH, UK.

*Corresponding author. E-mail: thewalt@sfu.ca

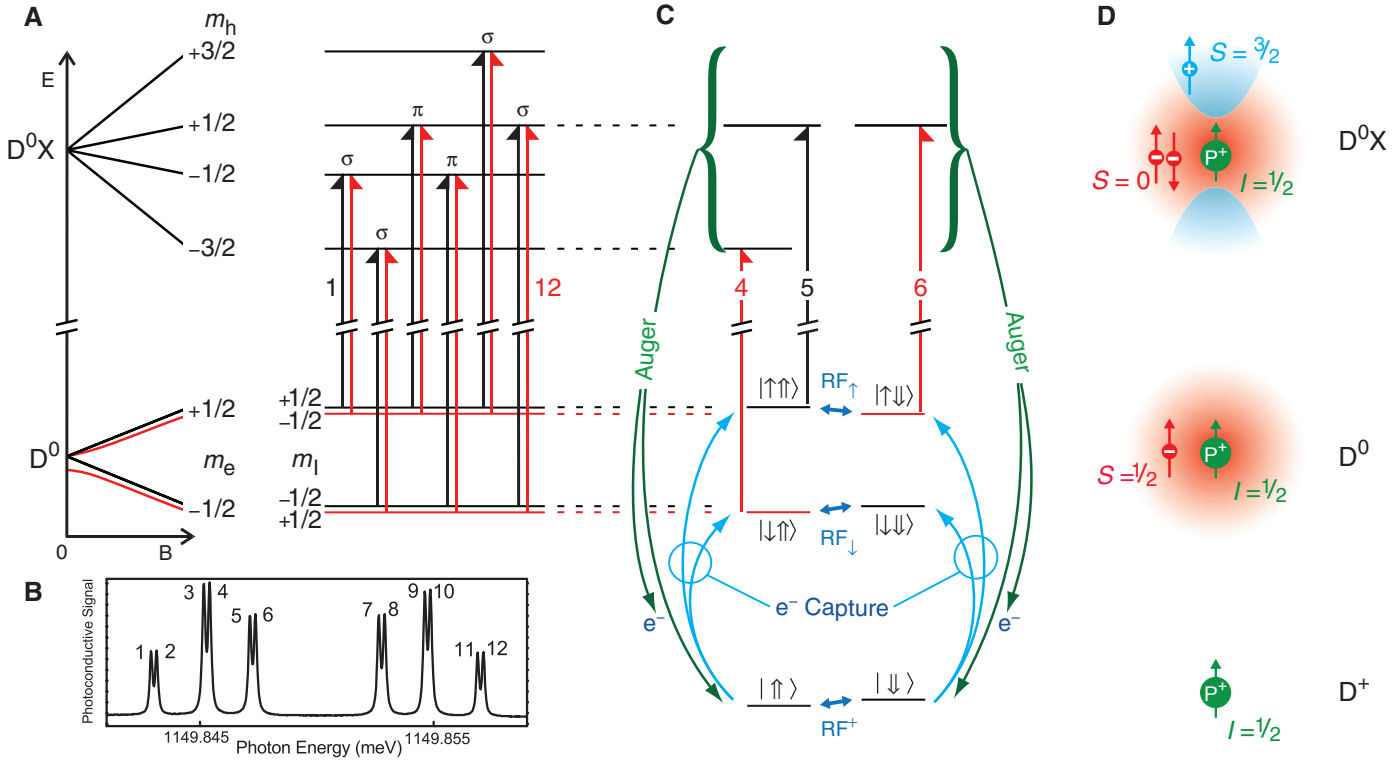

Fig. 1. Energy levels and transitions of the P neutral donor (D^0), donor bound exciton (D^0X), and ionized donor (D^+). (**A**) The Zeeman splittings of the D^0 and D^0X states are shown from $B_0 = 0$ to $B_0 = 845.3$ G, along with the dipole-allowed optical transitions. (**B**) Photoconductive readout spectrum without any D^0 hyperpolarization. (**C**) The specific optical transitions (lines 4, 5, and 6) and nuclear magnetic resonance transitions ($RF_\uparrow$, $RF_\downarrow$, and RF^+) used here to hyperpolarize, manipulate, and read out the nuclear spins. The magnitude of the D^+ Zeeman splitting (RF^+) has been exaggerated to show the ordering of the D^+ states, and the small nuclear Zeeman energy is ignored for the D^0X states. Although the energy differences between the D^0 and D^0X levels are precisely fixed in ^{28}Si, the D^+ energy is not well defined because of the kinetic energy of the e^-. (**D**) Sketches of the spins and charge densities of D^+, D^0, and D^0X.

of tens of milliseconds was well accounted for (*11*, *12*) by spectral diffusion from the ~5% of ^{29}Si occurring in the natural Si samples (*13*). We removed this source of spectral diffusion by using highly enriched ^{28}Si and dynamic decoupling.

The sample used here and in the previous study of D^0 (*9*) was enriched to 99.995% ^{28}Si and contained ~5×10^{11} cm^{-3} of ^{31}P and 5×10^{13} cm^{-3} of the acceptor B, making it p-type (*14*). In equilibrium at low temperature one would expect all donors to be D^+, with an equal number of ionized acceptors, but this equilibrium is reached very slowly at these low concentrations (*15*). Weak above-gap excitation provided by a 1047-nm laser photoneutralizes almost all of the donors and acceptors. Highly enriched ^{28}Si provides a "semiconductor vacuum" host for dopants, allowing for the optical hyperpolarization and readout of D^0 nuclear spin states (*9*, *16*). We additionally used optical transitions to fully ionize the spin-polarized D^0 at low temperature, after which T_1 or T_2 measurements can be carried out on D^+ at either cryogenic or room temperature. After this, with the sample at cryogenic temperature, the D^+ atoms are optically reneutralized, and the remaining D^0 polarization is read out optically. Once ionized, virtually all donors will remain ionized indefinitely, independent of temperature, provided that above-gap light is excluded. Above ~30 K, the excess acceptors ionize, providing a background of free holes, and nearer room temperature, thermally generated free electrons will also be present (*14*). These free carriers could affect the D^+ nuclear spin polarization and coherence times, but our results show that long-term coherent storage at room temperature is still possible.

The optical transitions between D^0 and the donor bound exciton (D^0X) used for hyperpolarization, readout, and donor ionization are shown in Fig. 1. In Fig. 1C, the four D^0 hyperfine levels are labeled by their electron spin (↑ or ↓) and nuclear spin (⇑ or ⇓) (the $|\uparrow\Downarrow\rangle$ and $|\downarrow\Uparrow\rangle$ labels are approximate at low B_0 because of hyperfine mixing). The D^0X atoms decay with near-unity efficiency through the Auger process (*17*) to give D^+ and free electrons (e^-), which are eventually recaptured to return D^+ to D^0. The Auger decay process is central to both the D^0 hyperpolarization and hyperfine state readout using resonant D^0X photoconductivity, as illustrated in the sequence used to measure the coherence time of D^+ nuclear spins [Fig. 2A and (*14*)]. It consists of optical and radio-frequency (RF) pulses to hyperpolarize the nuclear spins (steps {1 to 3}), fully ionize the donors {4}, coherently manipulate the D^+ nuclear spin {6 to 8}, reneutralize the donors {10}, and read out the resulting spin populations {11 to 14}. By step {5}, we estimate that over 90% of the ^{31}P atoms are both ionized and polarized into $|\Uparrow\rangle$. Single-shot readouts of D^+, polarized into either $|\Uparrow\rangle$ or $|\Downarrow\rangle$ and then reneutralized, are shown in Fig. 2, B to D, contrasting our previous (*9*) readout method optimized for D^0 (Fig. 2B) with the improved readout used here (Fig. 2, C and D). Details of the preparation and readout schemes are found in (*14*). Analysis of the data in Fig. 2, C and D, shows that the $D^0 \rightarrow D^0X \rightarrow D^+ \rightarrow D^0$ readout cycle can be repeated at least 250 times before the nuclear polarization decays by 1/e (*14*), which is an underestimate given that much of the decay in Fig. 2D is due to imperfections in the readout π pulses. A similar insensitivity of the nuclear spin polarization to repeated donor charge cycles has been reported for readout of a single ^{31}P nuclear spin (*12*) and for ensemble measurements using electrically detected magnetic resonance (*18*).

We used two different temperature profiles to measure T_1 and T_2, as shown above Fig. 2A; either a fixed temperature at or below 4.2 K, or T_1 or T_2 measurements at room temperature (298 K), with the polarization and readout steps at 4.2 K. The measurement RF pulse sequence is shown for a simple Hahn echo (π/2 - π - π/2). The temperature is changed only while the D^+ nuclear spin is in an eigenstate in the Z basis (i.e., in the $|\Downarrow\rangle$ or $|\Uparrow\rangle$ state). This ensures that the nuclear spin is sensitive only to T_1 relaxation processes while the temperature is changing. Later we explored a third profile, changing the temperature while the nuclear spin was in a superposition state.

In Fig. 3A we show the D^+ nuclear spin T_1 measured at 1.9 K and room temperature [the Hahn echo sequence is replaced with either no operations, leaving the nuclear spin polarization unchanged, or a π pulse, which inverts it (*14*)]. The D^+ T_1 at cryogenic temperature was so long that no decay could be observed over 2 hours, and at room temperature T_1 was over an hour.

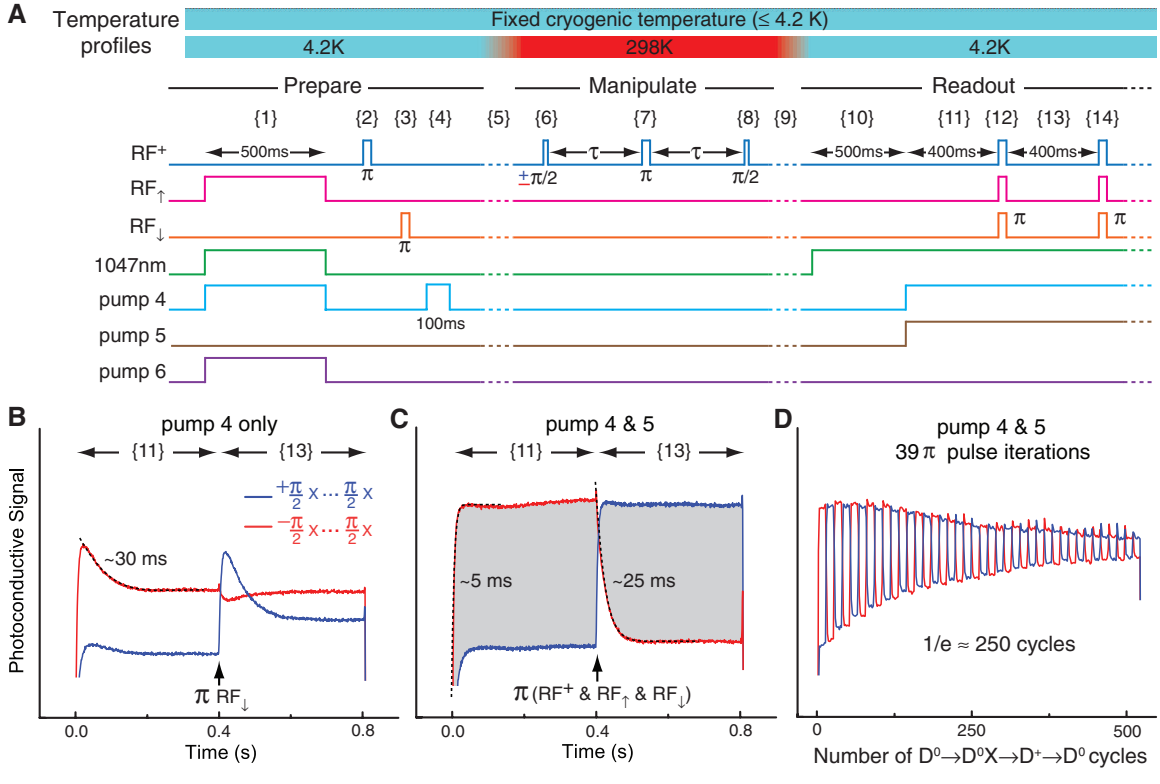

Fig. 2. Initialization, manipulation, and readout protocols. (**A**) The laser and RF sequences used to prepare D^+ in the $|\Uparrow\rangle$ state (steps {1} to {4}), manipulation of D^+ spins for the case of a Hahn echo ({6} to {8}), and readout of the resulting Z component ({10} to {14}…). At the top are the two temperature profiles relevant to Fig. 3: either a constant temperature ≤4.2 K or 4.2 K during preparation and readout, with a ramp up to 298 K taking ~6 min {5}, a constant 298 K during the D^+ manipulation period, and a ramp down to 4.2 K taking ~4 min {9}. Each measurement was performed twice, with opposite signs of the initial π/2 pulse {6}. (**B**) Single-shot readout of D^+ polarized $|\Uparrow\rangle$ (red) or $|\Downarrow\rangle$ (blue) using our previous method optimized for D^0 readout is compared with (**C**), the improved scheme for D^+ readout (*14*). The detected signal is proportional to the shaded area. (**D**) The cycle shown in (C) extended to 39 π pulse inversions (16 s).

Even a short thermal cycle up to room temperature and back resulted in a ~30% loss in nuclear spin polarization as compared to the same measurement at a constant 4.2 K, so all room-temperature decay data are normalized to unity for the shortest time (2 min at 298 K). Figure 3B shows single-shot Hahn echo decay data at 4.2 K revealing increasing phase noise with increasing delay time, probably arising from low-frequency magnetic field fluctuations. This phase noise was eliminated from the 1.9 K data by using maximum magnitude detection (*14*). The Hahn echo T_2 of about 30 s measured at or below 4.2 K is well explained by spectral diffusion due to the residual (46 parts per million) ^{29}Si nuclear spins present in the sample (*13*). Also shown is single-shot Hahn echo data at room temperature, where the long cycle time made the use of maximum magnitude detection impractical, so that the phase noise could not be eliminated, and the apparent Hahn echo T_2 was reduced to ~8 s.

We have demonstrated (*9*) that dynamic decoupling using the XY-16 sequence of π pulses (*19*) is effective for reducing the effect of low-frequency noise on donor nuclear spins while maintaining arbitrary initial states. In Fig. 3C we show the results of using this sequence to replace the single π pulse of the Hahn echo (for all XY-16 results shown here, the time 2τ between π pulses was 8 ms). At 1.2 K the coherence decay follows a single exponential, with a T_2 of 180 min, whereas at 1.9 K and 4.2 K there is an early component of a faster decay (time constant ~12 min), followed by a decay consistent with a T_2 of 180 min. We believe that this initial faster decay is due to charge dynamics in the sample after illumination, probably from D^- and A^+ centers, which are frozen out at the lowest temperature (*20*). It may be related to the ~30% loss in nuclear polarization observed in even short cycles from cryogenic to room temperature and back. In Fig. 3D we show a room-temperature T_2 decay of 39 min. This is a lower bound, because the same XY-16 sequence applied to a ±Z state yields a decay constant of 50 min, which is substantially shorter than the

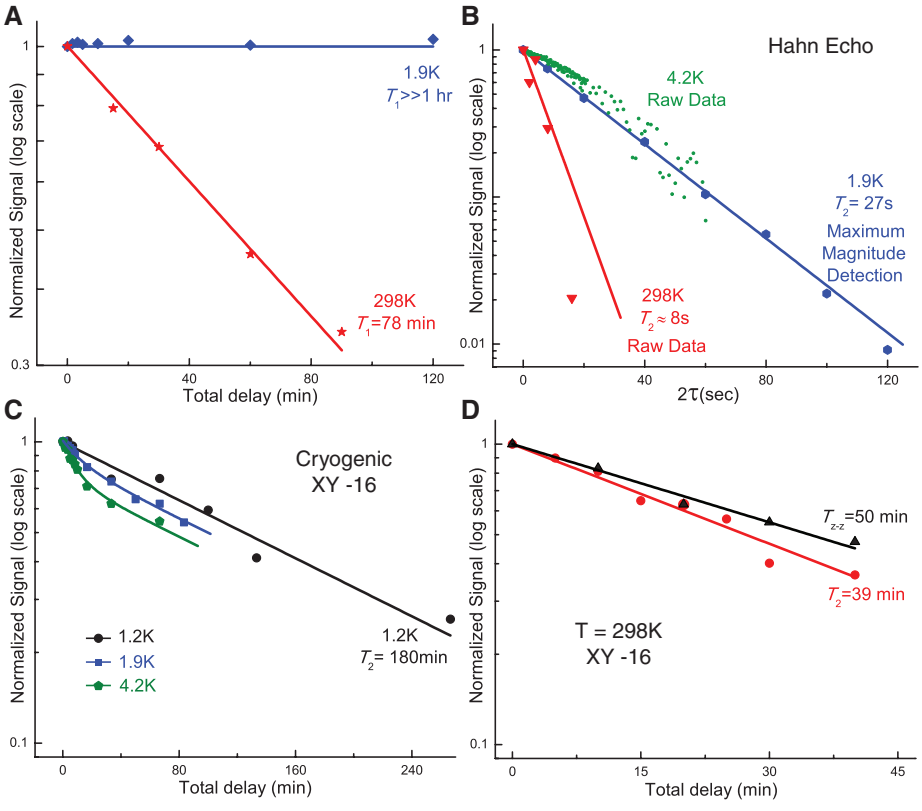

Fig. 3. Measured T_1 and T_2 times for the $^{31}P^+$ nuclear spin at cryogenic and room temperature. (**A**) The decay of the nuclear spin polarization (along Z), parameterized by T_1, is shown for 1.9 and 298 K. (**B**) Single-shot Hahn echo T_2 measurements are shown at 298 and 4.2 K, the latter (green dots) showing increasing phase noise with increasing delay. The effect of phase noise can be suppressed by using maximum magnitude detection (*14*), as shown for data taken at 1.9 K. (**C**) T_2 decays using the XY-16 decoupling sequence at cryogenic temperatures. The 1.9 and 4.2 K data were fit using biexponentials, with the longer component set to 180 min. (**D**) The T_2 decay at 298 K using XY-16 decoupling, together with the observed decay of a ±Z state using XY-16 decoupling under identical conditions.

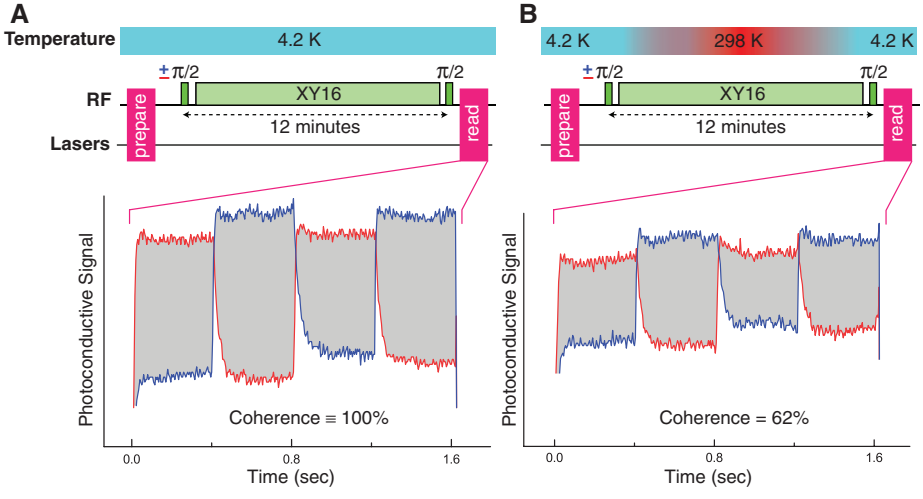

Fig. 4. Cycling D^+, while in a nuclear spin superposition state, from 4.2 K to room temperature and back. (**A**) A measurement at a constant temperature of 4.2 K, with XY-16 decoupling over a 12-min period, is compared to (**B**), where the nuclear spins are placed into a coherent superposition at 4.2 K and the XY-16 decoupling sequence is begun, followed by a ~6-min ramp to 298 K, 2 min at 298 K, and a ~4-min ramp back down to 4.2 K, after which the remaining coherence is read out. The preparation and readout sequences are as in Fig. 2A. A comparison of (A) and (B) shows that 62% of the spin coherence remains after the temperature cycle, which is equivalent to a state fidelity of 81%.

78-min T_1, indicating that pulse errors in the XY-16 sequence contribute significantly to the observed decay and are also likely to contribute to the 180-min T_2 observed at cryogenic temperatures.

The low-temperature nuclear spin T_2 of ≥180 min demonstrates that the XY-16 sequence is very effective in suppressing decoherence arising from slow spectral diffusion caused by the remaining ^{29}Si. Whereas the cryogenic Hahn echo T_2 reported here for D^+ is slightly shorter than that reported earlier (*10*) for D^0, XY-16 dynamic decoupling extends the observed coherence time by a factor of 400 for D^+ but only by ~4.4 for D^0. This suggests a very different decoherence process for the D^0 case (*14*).

These long coherence times for the D^+ nuclear spin should be achievable even when the donor is placed near an interface in a nanodevice, as long as the temperature is low enough that flips or flip-flops of electron spins at the interface are suppressed. The shorter 39-min T_2 measured at room temperature could arise from carrier-induced magnetic field fluctuations, whose effect is not completely suppressed by the dynamical decoupling, combined with a higher error in the RF pulses (*15*). The observed room-temperature T_2 is also compatible with the accumulated phase error from the small probability of the donor being in the D^0 ground state at room temperature. The observed room-temperature T_2 considerably exceeds that reported (*21*) for ^{29}Si in natural Si using homonuclear decoupling. Given that ^{29}Si should not be more sensitive to free carriers than D^+, this probably results from difficulty in completely decoupling the ^{29}Si at the high concentration present in natural Si.

Finally, we demonstrated the ability to change the sample temperature while the D^+ nuclear spin was in a coherent superposition state. Figure 4A shows a reference measurement at 4.2 K using the sequence shown in Fig. 2A, but with XY-16 decoupling. In Fig. 4B, the D^+ nuclear spins are placed into a coherent superposition at 4.2 K, the XY-16 sequence is begun, and then the temperature is ramped to room temperature in ~6 min. It is held there for 2 min before being ramped back down to 4.2 K in ~4 min. Once the sample is reimmersed in liquid He, the XY-16 sequence ends and the remaining coherence is projected back into a ±Z state for readout after reneutralization. By comparing the two readout signals we see that it is possible to bring a coherent state from cryogenic temperature to room temperature and back while retaining 62% of the coherence signal, which is equivalent to a state fidelity of 81% (*22*). This loss of coherence can be largely attributed to the ~30% drop in nuclear spin polarization observed over one thermal cycle to room temperature and back.

These results support the possibility of truly long-term storage of quantum information at room temperature. To make use of the D^+ state as a quantum memory for, say, a donor-based electron spin qubit, as has already been done with the nuclear spin of D^0 (*23*), it will be necessary to find a way to ionize and neutralize the donor without disturbing the coherent state of the nuclear spin. Whereas ^{31}P donors in ^{28}Si at this time require low temperatures for initialization and readout, the ability to bring coherent information reversibly between cryogenic and room temperatures suggests ways to exploit this system. It may also be possible to initialize and read out this system at elevated temperatures, or to find similar but more robust systems with larger electron binding energies, in which charge control can still be used to turn a hyperfine interaction on for initialization and readout and off for long-term storage. In Si, one possibility would be to use much deeper donors such as chalcogens, where an optically accessible hyperfine splitting has already been observed for $^{77}Se^+$ in ^{28}Si (*24*) and where the hyperfine coupling can be removed by placing the donor into either D^0 or D^{2+} charge states. Another promising possibility would be deep defects in wider-gap materials such as diamond and SiC (*25*), which can also be isotopically purified to remove background spins and where the method of charge-state control could be combined with initialization and readout at room temperature.

References and Notes

1. D. Deutsch, *Proc. R. Soc. London Ser. A* **400**, 97–117 (1985).
2. T. D. Ladd *et al.*, *Nature* **464**, 45–53 (2010).
3. S. Wiesner, *ACM SIGACT News* **15**, 78–88 (1983).
4. F. Pastawski, N. Y. Yao, L. Jiang, M. D. Lukin, J. I. Cirac, *Proc. Natl. Acad. Sci. U.S.A.* **109**, 16079–16082 (2012).
5. P. C. Maurer *et al.*, *Science* **336**, 1283–1286 (2012).
6. B. E. Kane, *Nature* **393**, 133–137 (1998).
7. J. J. Morton, D. R. McCamey, M. A. Eriksson, S. A. Lyon, *Nature* **479**, 345–353 (2011).
8. D. D. Awschalom, L. C. Bassett, A. S. Dzurak, E. L. Hu, J. R. Petta, *Science* **339**, 1174–1179 (2013).
9. M. Steger *et al.*, *Science* **336**, 1280–1283 (2012).
10. G. Feher, E. A. Gere, *Phys. Rev.* **114**, 1245–1256 (1959).
11. L. Dreher, F. Hoehne, M. Stutzmann, M. S. Brandt, *Phys. Rev. Lett.* **108**, 027602 (2012).
12. J. J. Pla *et al.*, *Nature* **496**, 334–338 (2013).
13. W. M. Witzel, M. S. Carroll, Ł. Cywiński, S. Das Sarma, *Phys. Rev. B* **86**, 035452 (2012).
14. Supplementary materials are available on *Science* Online.
15. P. Dirksen, A. Henstra, W. Th. Wenckebach, *J. Phys. Condens. Matter* **1**, 7085–7092 (1989).
16. M. Steger *et al.*, *J. Appl. Phys.* **109**, 102411 (2011).
17. W. Schmid, *Phys. Status Solidi* **84**, 529–540 (1977) (b).
18. D. R. McCamey, J. Van Tol, G. W. Morley, C. Boehme, *Science* **330**, 1652–1656 (2010).
19. T. Gullion, D. B. Baker, M. S. Conradi, *J. Magn. Reson.* **89**, 479–484 (1990).
20. W. Burger, K. Lassmann, *Phys. Rev. Lett.* **53**, 2035–2037 (1984).
21. T. D. Ladd, D. Maryenko, Y. Yamamoto, E. Abe, K. M. Itoh, *Phys. Rev. B* **71**, 014401 (2005).
22. R. Jozsa, *J. Mod. Opt.* **41**, 2315–2323 (1994).
23. J. J. L. Morton *et al.*, *Nature* **455**, 1085–1088 (2008).
24. M. Steger *et al.*, *Phys. Rev. B* **80**, 115204 (2009).
25. W. F. Koehl, B. B. Buckley, F. J. Heremans, G. Calusine, D. D. Awschalom, *Nature* **479**, 84–87 (2011).

Acknowledgments: The work at Simon Fraser University was supported by the Natural Sciences and Engineering Research Council of Canada. S.S. is supported by the Violette and Samuel Glasstone Fellowship and St. John's College, Oxford. J.J.L.M. is supported by the Royal Society.

Supplementary Materials

www.sciencemag.org/content/342/6160/830/suppl/DC1
Materials and Methods
Supplementary Text
Figs. S1 to S3
References (*26*–*37*)

24 April 2013; accepted 15 October 2013
10.1126/science.1239584

Layer-Resolved Graphene Transfer via Engineered Strain Layers

Jeehwan Kim,*† Hongsik Park,*† James B. Hannon, Stephen W. Bedell, Keith Fogel, Devendra K. Sadana, Christos Dimitrakopoulos*‡

The performance of optimized graphene devices is ultimately determined by the quality of the graphene itself. Graphene grown on copper foils is often wrinkled, and the orientation of the graphene cannot be controlled. Graphene grown on SiC(0001) via the decomposition of the surface has a single orientation, but its thickness cannot be easily limited to one layer. We describe a method in which a graphene film of one or two monolayers grown on SiC is exfoliated via the stress induced with a Ni film and transferred to another substrate. The excess graphene is selectively removed with a second exfoliation process with a Au film, resulting in a monolayer graphene film that is continuous and single-oriented.

Graphene offers great potential for high-performance electrical and optical devices such as radio-frequency transistors, high-speed photodetectors, and optical modulators (*1*–*5*). The most common approach used to build graphene devices is to grow the polycrystalline graphene via chemical vapor deposition on a thin metal foil, followed by transfer of the graphene to the substrate of interest (*6*, *7*). This process can produce large areas of graphene with good control over the thickness. However, the graphene is often wrinkled because the metal foil substrate is rough. Furthermore, the relative crystallographic orientation of the domains is random because of the lack of registry with the substrate.

High-quality flat monolayer graphene can be epitaxially grown on the Si face of SiC (0001) wafers via a practically self-limiting sublimation of Si (*8*–*10*). Because of the high cost of SiC

IBM T. J. Watson Research Center, 1101 Kitchawan Road, Yorktown Heights, NY 10598, USA.

*Corresponding author. E-mail: jeehwkim@us.ibm.com (J.K.); hpark@us.ibm.com (H.P.); dimitrak@umass.edu (C.D.)
†These authors contributed equally to this work.
‡Present address: University of Massachusetts, 686 North Pleasant Street, Amherst, MA 01003, USA.

wafers and the need for integration of graphene devices with conventional Si integrated circuits, the transfer of graphene from SiC surfaces is of interest. However, the transfer of monolayer graphene directly from a SiC surface has not been demonstrated yet. The difficulty arises from the strong binding of graphene to the SiC surface. Graphene layers from multilayer graphene stacks formed on SiC could be transferred, possibly because of the weak graphene/graphene interaction (*11*, *12*), but multilayer stacks have varying thickness, are defective, and/or are rotationally disordered (*9*, *10*, *13*, *14*). Although the high-quality graphene formed by self-limiting Si sublimation is nominally monolayer and highly ordered, precisely controlling the graphene layer thickness on a SiC surface is difficult because of the presence of narrow "stripes" of thicker graphene decorating the vicinal steps of the SiC wafer (*8*, *10*). Thus, a method for transferring epitaxial graphene from a SiC surface is highly desired and, furthermore, a technique for selectively removing any residual excess graphene layers is required.

To enable uniform and reproducible exfoliation and transfer of epitaxial graphene directly from a SiC surface onto another substrate, we have developed a method for manipulating graphene layers with a single-atom–thickness precision, based on the binding energy difference at specific interfaces (such as graphene/graphene and graphene/SiC). A schematic of our graphene transfer method is illustrated in Fig. 1A. A 4-inch-diameter (~10 cm) monolayer graphene sheet with a single azimuthal orientation was grown on the Si face of a SiC wafer (*15*). The graphene was completely exfoliated from the SiC wafer by using an adhesive-strained layer (Ni) and the handling layer (thermal release tape). The graphene released from the SiC surface was then transferred onto a wafer, and then the thermal tape and Ni were removed [see the supplementary materials for the details of graphene growth and transfer (*16*)]. This technique enables the reuse of one SiC wafer for further growth and transfers.

In our method, the exfoliation of the graphene from the SiC wafer was induced by the accumulated internal strain of the adhesive-strained layer strongly bound to graphene. It was critical to select a proper adhesive-strained material that satisfied the following conditions for uniform and reproducible exfoliation with a high yield: (i) no chemical reaction with C and no solubility in C (and vice versa) to maintain the purity of the graphene; (ii) stronger adhesion to the graphene than between graphene and SiC (*15*); and (iii) high stress to apply strain energy to separate the graphene/SiC interface. We investigated Ni, Cu, Pd, and Au adhesive-strained layers, as these metals are inert to graphene at room temperature. The binding energies per atom between graphene and these materials ($\gamma_{Ni-G} \approx 140$ meV, $\gamma_{Pd-G} \approx 70$ meV, $\gamma_{Cu-G} \approx 60$ meV, and $\gamma_{Au-G} \approx 60$ meV) have been reported (*17*), but the binding energy between the graphene and SiC (γ_{G-SiC}) has not been reported yet. The measured internal stresses for the investigated metals were tensile. The stress of Ni was ~1 GPa, whereas those of Cu, Au, and Pd were between 100 and 250 MPa under the same deposition conditions and thickness. This difference indicates that Ni is under the highest strain at the same thickness.

In order to verify whether these metals have a sufficient binding energy to graphene, we exfoliated graphene from a SiC surface by applying these metals. We obtained a yield of graphene transfer of more than 95% by using Ni, whereas Cu, Pd, and Au could barely exfoliate graphene. This result implies that γ_{Ni-G} is larger than γ_{G-SiC}, but γ_{Pd-G}, γ_{Cu-G}, and γ_{Au-G} are smaller than γ_{G-SiC}. Thus, Ni is a proper adhesive-strained material whose binding energy to graphene is sufficient and strain can be efficiently controlled by film thickness because of its high stress. For uniform and reproducible exfoliation of graphene, it is desired to induce high Ni strain energy without self-exfoliation in the deposition chamber. Thus, we need to estimate γ_{G-SiC} in order to control the thickness of Ni in a given internal stress. Assuming that graphene is delaminated from a SiC surface when the accumulated strain energy in Ni reaches γ_{G-SiC} at a critical thickness, the relation between γ_{G-SiC} and the critical thickness for graphene self-exfoliation (t^{C}_{Ni}) is given by

$$\gamma_{G\text{-}SiC} = \frac{(1-\nu_{Ni})}{2Y_{Ni}} t^{c}_{Ni} \sigma^{2}_{Ni} \qquad (1)$$

where ν_{Ni}, Y_{Ni}, and σ_{Ni} are Poisson's ratio, Young's modulus, and the internal stress of Ni, respectively (*18*, *19*). We measured t^{C}_{Ni} under different σ_{Ni} by monitoring the Ni thickness for self-exfoliation in the metal deposition chamber [see the supplementary materials for more detail about Eq. 1, deposition methods, and conditions to vary σ_{Ni} (*16*)]. We extracted the quantitative value of γ_{G-SiC} = 106.2 meV from the slope of the fitted linear $t^{C}_{Ni} - 1/\sigma_{Ni}^{2}$ plot (Fig. 1B). The measured γ_{G-SiC} is 25% smaller than γ_{Ni-G} and >2 times larger than the reported value of the graphene-graphene binding energy in graphite (γ_{G-G} = 40 to 50 meV) (*20*, *21*). This result shows a good agreement with the aforementioned conclusion that γ_{Ni-G} (≈ 140 meV) > γ_{G-SiC} (≈ 106 meV) > γ_{Pd-G} (≈ 70 meV), γ_{Cu-G} (≈ 60 meV), and γ_{Au-G} (≈ 60 meV), and the substantial dif-

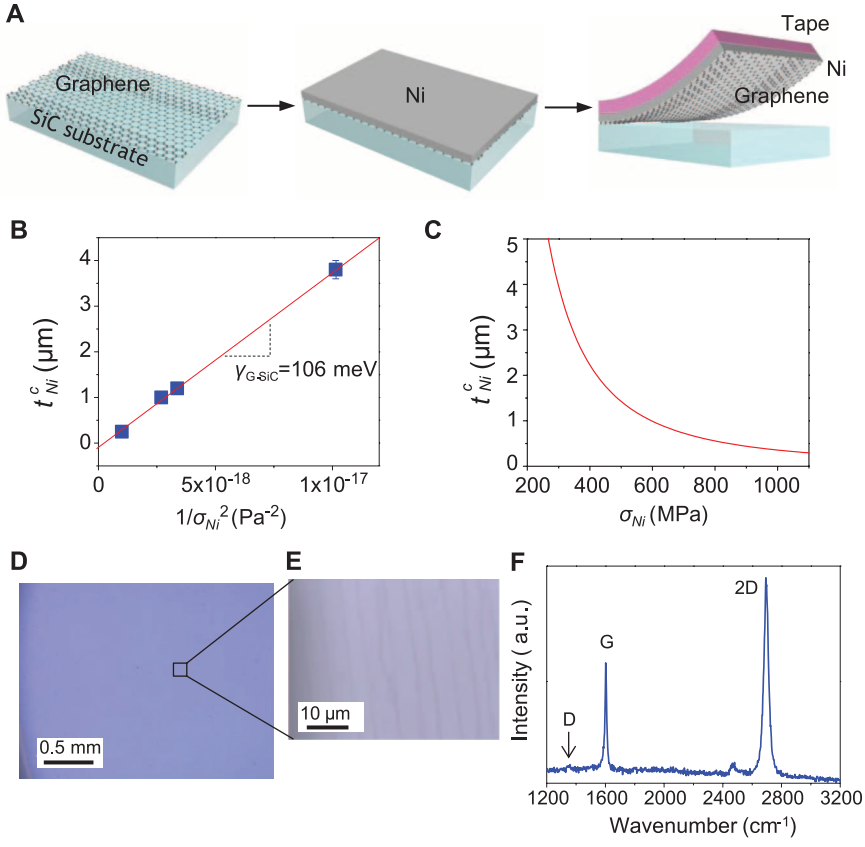

Fig. 1. (**A**) Schematic of a method for transferring graphene directly from a SiC surface onto a SiO_2/Si wafer. An adhesive-strained layer (Ni) is deposited on graphene grown on a SiC wafer. The graphene/Ni layer is exfoliated by using a handling layer (thermal release tape) for transfer. (**B**) The binding energy between graphene and a SiC surface (γ_{G-SiC}) was determined from the measured critical Ni thicknesses for self-exfoliation (t^{C}_{Ni}) of graphene at various internal stresses of Ni. (**C**) Critical Ni thickness as a function of the internal stress (σ_{Ni}) of Ni deposited on graphene. (**D** and **E**) Optical microscope images of the graphene transferred from a reused SiC wafer, showing a high yield of the transfer. (**F**) Representative Raman spectrum of the graphene transferred from a resued SiC wafer, indicating that the transferred graphene is a single layer and the graphene layer is not damaged during the transfer (no D peak). a.u., arbitrary units.

ference between γ_{G-SiC} and γ_{G-G} explains why it has been difficult to exfoliate monolayer graphene directly from the surface of SiC.

Figure 1C shows the t^{C}_{Ni} as a function of σ_{Ni}. Based on this plot, we designed the thickness and stress of Ni deposited on graphene/SiC. A yield of graphene transfer higher than 95% could be obtained when the induced strain energy was higher than 80% of the critical strain for self-exfoliation of graphene, whereas exfoliation dominated by an external force rather than the internal strain of Ni typically resulted in no exfoliation or a low yield and non-uniform coverage of a transferred graphene sheet (fig. S1).

Graphene was completely exfoliated from a 4-inch SiC wafer and transferred onto an 8-inch Si wafer coated with 90 nm of SiO_2 (fig. S2). The SiC wafer used for the first transfer was regraphitized, and we repeated the exfoliation and transfer onto another wafer. Throughout five growth and transfer processes with a single SiC wafer, the transfer yield and quality of graphene were maintained [see the supplementary materials (*16*) and fig. S2]. The optical microscope images in Fig. 1, D and E, show that this transfer process completely exfoliates the epitaxial graphene layer, including double-layer stripes from the SiC surface, and the Raman spectrum in Fig. 1F indicates that the quality of the graphene is maintained during the transfer (no D peak in the spectra). However, for obtaining perfect monolayer graphene, it is essential to selectively remove any residual graphene layers. The decomposition of SiC to produce graphene occurs primarily at vicinal steps on the SiC surface, and double-layer stripes are inherently formed at the edge of the steps (*8*, *10*). Eliminating the double-layer stripes is important because they degrade the electrical properties of the graphene (such as carrier mobility) as well as the ballistic nature of charge transport (*22*–*24*). There is no existing technique for selectively removing additional graphene layers from monolayer graphene, although the embedded stripe layers are exposed after exfoliation from SiC.

In this work, we developed a method of selective graphene exfoliation with a single-layer precision based on the binding energy contrast among graphene and different metals. The devised process is illustrated in Fig. 2A. After the exfoliation of an epitaxial graphene layer from SiC by using Ni as the first adhesive-strained layer (first exfoliation), we separated the exposed additional graphene stripes from the monolayer graphene sheet on Ni, using a second adhesive-strained layer (second exfoliation) followed by transfer onto another wafer. For a selective exfoliation of double-layer graphene, we used Au as a second adhesive-strained layer because γ_{Au-G} is much less than γ_{Ni-G} ($\gamma_{Ni-G} \approx 2.6\,\gamma_{Au-G}$), which prevents tearing or exfoliation of graphene from the Ni surface, and γ_{Au-G} is larger than γ_{G-G}, which allows selective removal of the graphene stripes from the underlying monolayer. Figure 2, B and C, show the optical microscope image and the map of the 2D/G peak ratio from Raman spectra taken on the graphene layer transferred by the first exfoliation, respectively (A-1). In Fig. 2C, the representative Raman spectra show that the blue and red regions in the Raman map correspond to monolayer and double-layer graphene, respectively. As determined from the distribution of the 2D/G peak ratio (Fig. 2D), about 20% of the area of the graphene sheets from the first exfoliation was a double-layer region. The microscope image (Fig. 2E) and Raman map (Fig. 2F) from the graphene transferred by two-step exfoliation (the first and second exfoliation) show that the double-layer stripes were successfully removed. The distribution of the 2D/G peak ratio (Fig. 2G) indicates that 99% of the area of the transferred graphene by the two-step exfoliation was a monolayer region. The Raman spectra from the monolayer showed no enhancement of the D peak (Fig. 2F), which indicates that the monolayer graphene was not damaged during the two-step exfoliation process, as expected based on the binding energy difference between the layer interfaces. For direct verification of the exfoliation selectivity, we also transferred the graphene stripes attached to the Au layer onto a SiO_2/Si substrate (A-3). Figure 2, H to J, show the optical microscope image and Raman analysis. The black and blue areas in the Raman map of the 2D peak intensity (Fig. 2I) correspond to a SiO_2 surface and monolayer graphene stripes, respectively. This result confirms that the stripes in A-1 are double layers and the second exfoliation selectively removes the additional graphene layers.

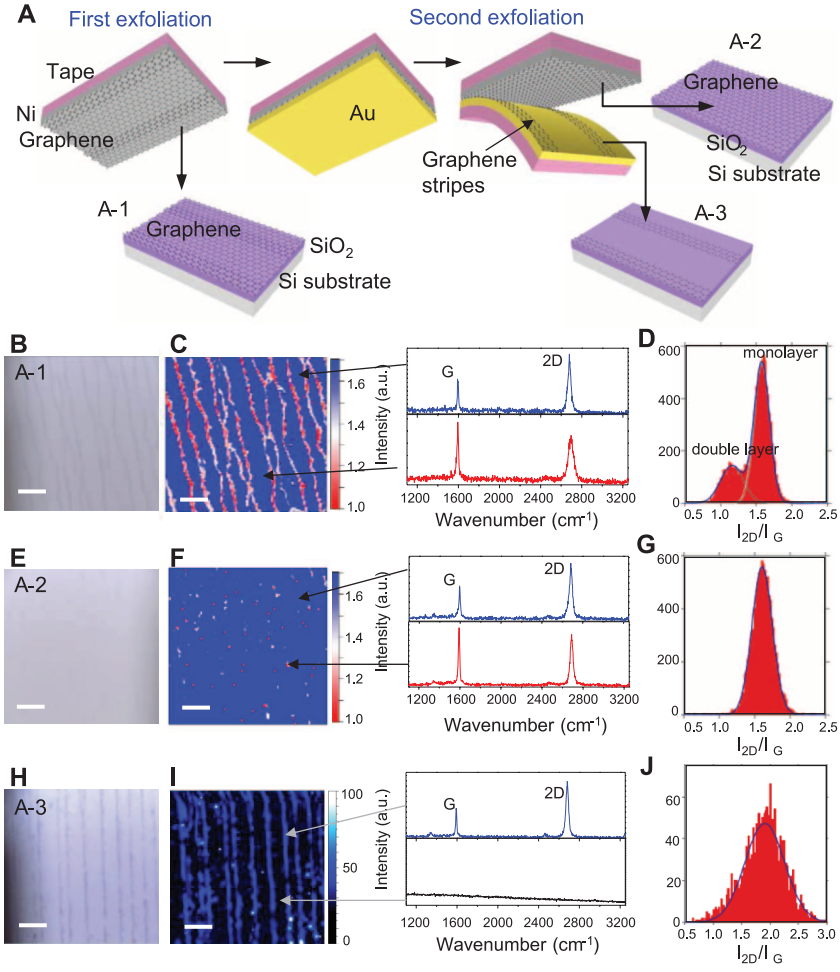

Fig. 2. (**A**) Schematic of a method for removing double-layer stripes from graphene exfoliated from a SiC substrate. A second adhesive-strained layer (Au) is deposited on the graphene/Ni/tape stack that is exfoliated from the SiC substrate. The graphene stripes forming double layers are selectively removed by Au, and the complete monolayer graphene sheet without the stripes is then transferred onto a SiO_2/Si substrate (A-2). The removed graphene stripes are also transferred onto another substrate (A-3). Optical microscope image (**B**), the map of the 2D/G peak ratio from Raman spectra (**C**), and the distribution of the 2D/G peak ratio (**D**) of the graphene transferred after the first exfoliation (A-1), showing that about 20% of the transferred graphene is double-layered. Optical image (**E**), the map of the 2D/G peak ratio from Raman spectra (**F**), and the distribution of the 2D/G peak ratio (**G**) of the graphene transferred after the second exfoliation (A-2), indicating that the second exfoliation selectively removed the graphene stripes without damage on the monolayer graphene. Optical image (**H**), the map of the 2D peak intensity from Raman spectra (**I**), and the distribution of the 2D peak intensity (**J**) of the transferred graphene stripes (A-3), confirming that the stripes in A-1 are double layers and the Au layer removes the graphene stripes with an excellent selectivity. Scale bars, 10 μm.

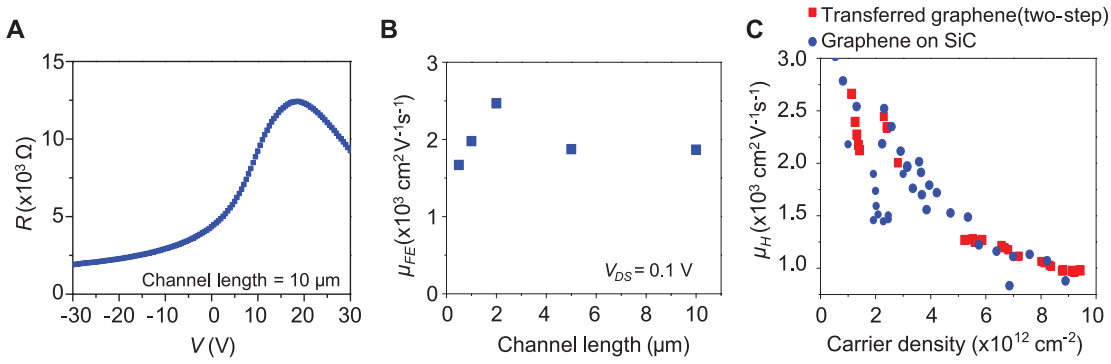

Fig. 3. (**A**) A representative plot of the channel resistance (R) as a function of the gate voltage (V_G) measured from the transistors at the drain voltage (V_{DS}) of 0.1 V. (**B**) The field-effect mobility (μ_{FE}) with various channel lengths. (**C**) Mobility measured from Hall bars (μ_H) as a function of a carrier density. The Hall mobility of the transferred graphene is comparable to that of graphene on SiC before transferring.

The Raman spectroscopy measurements show conclusively that the two-step transfer process can produce uniform graphene films of single-layer thickness. To assess the crystallinity of the films, we performed microspot electron diffraction measurements in a low-energy electron microscope (*25*). Specifically, after the two-step transfer, we illuminated the graphene film with a narrow electron beam having a diameter of about 2 μm. A diffraction pattern of the graphene film recorded with 40-eV electrons (fig. S4) revealed typical characteristics of monolayer graphene on SiO (*26*). To determine the long-range order and domain size, we recorded diffraction patterns as we scanned the sample under the electron beam. The measurements show that graphene covered about 95% of the surface. Furthermore, no rotated graphene domains were observed. All the diffraction patterns recorded across the sample were identical, indicating that the graphene layer has a single orientation [see the supplementary materials (*16*) and fig. S5].

To evaluate the electrical properties of the monolayer graphene formed by the two-step exfoliation method, we fabricated field-effect transistors (FETs) and Hall bars on the graphene transferred on oxidized Si wafers (90 nm SiO_2). A representative plot of the channel resistance (R) as a function of the gate voltage (V_G) measured from the FETs is shown in Fig. 3A. In contrast to graphene on SiC, which is highly negatively doped by the substrate (*27*, *28*), the graphene transferred from SiC onto SiO_2 is positively doped like other typical graphene layers transferred from graphite or Cu on SiO_2 (*29*, *30*). The field-effect mobility (μ_{FE}) calculated from the maximum transconductance was 1700 to 2500 $cm^2\ V^{-1}\ s^{-1}$ (Fig. 3A). Similarly, the mobility measured from Hall bars (μ_H) was in the range from 1000 to 2700 $cm^2\ V^{-1}\ s^{-1}$, depending on the carrier density (Fig. 3B). These mobility values are comparable to Hall mobility values measured from flat graphene layers grown on SiC terrace regions without any effects of SiC vicinal steps. These electrical measurement results indicate that graphene maintains its quality after the two-step exfoliation process.

References and Notes

1. Y.-M. Lin *et al.*, *Science* **327**, 662 (2010).
2. Y.-M. Lin *et al.*, *Science* **332**, 1294–1297 (2011).
3. F. Xia, T. Mueller, Y.-M. Lin, A. Valdes-Garcia, Ph. Avouris, *Nat. Nanotechnol.* **4**, 839–843 (2009).
4. M. Liu *et al.*, *Nature* **474**, 64–67 (2011).
5. K. S. Novoselov *et al.*, *Nature* **490**, 192–200 (2012).
6. X. Li *et al.*, *Science* **324**, 1312–1314 (2009).
7. K. S. Kim *et al.*, *Nature* **457**, 706–710 (2009).
8. K. V. Emtsev *et al.*, *Nat. Mater.* **8**, 203–207 (2009).
9. S. Tanaka *et al.*, *Phys. Rev. B* **80**, 121406R (2009).
10. Ph. Avouris, C. Dimitrakopoulos, *Mater. Today* **15**, 86–97 (2012).
11. S. Unarunotai *et al.*, *ACS Nano* **4**, 5591–5598 (2010).
12. J. D. Caldwell *et al.*, *ACS Nano* **4**, 1108–1114 (2010).
13. J. B. Hannon, R. M. Tromp, *Phys. Rev. B* **77**, 241404R (2008).
14. N. Luxmi *et al.*, *J. Vac. Sci. Technol. B* **28**, C5C1 (2010).
15. During graphene formation on the Si face of a SiC wafer by Si sublimation from the surface, an interfacial C buffer layer [the $(6\sqrt{3} \times 6\sqrt{3})R30$ reconstruction of the 0001 surface of SiC] that is covalently bonded to the SiC surface is also formed. For simplicity, we express a C buffer/SiC substrate as a SiC substrate.
16. Materials and methods are available as supplementary materials on *Science* Online.
17. I. Hamada, M. Otani, *Phys. Rev. B* **82**, 153412 (2010).
18. J. Kim, D. Inns, D. K. Sadana, *J. Appl. Phys.* **107**, 073507 (2010).
19. W. D. Nix, *Metall. Mater. Trans. A Phys. Metall. Mater. Sci.* **20**, 2217–2245 (1989).
20. R. Podeszwa, *J. Chem. Phys.* **132**, 044704 (2010).
21. R. Zacharia, H. Ulbricht, T. Hertel, *Phys. Rev. B* **69**, 155406 (2004).
22. S.-H. Ji *et al.*, *Nat. Mater.* **11**, 114–119 (2011).
23. C. Dimitrakopoulos *et al.*, *Appl. Phys. Lett.* **98**, 222105 (2011).
24. Y.-M. Lin *et al.*, *IEEE Electron Device Lett.* **32**, 1343–1345 (2011).
25. E. Bauer, *Rep. Prog. Phys.* **57**, 895–938 (1994).
26. K. R. Knox *et al.*, *Phys. Rev. B* **78**, 201408R (2008).
27. T. Ohta, A. Bostwick, T. Seyller, K. Horn, E. Rotenberg, *Science* **313**, 951–954 (2006).
28. C. Riedl, A. A. Zakharov, U. Starke, *Appl. Phys. Lett.* **93**, 033106 (2008).
29. F. Xia, V. Perebeinos, Y.-M. Lin, Y. Wu, Ph. Avouris, *Nat. Nanotechnol.* **6**, 179–184 (2011).
30. A. D. Franklin, S.-J. Han, A. A. Bol, W. Haensch, *IEEE Electron Device Lett.* **32**, 1035–1037 (2011).

Acknowledgments: The authors thank J. Bacchignano and S. Dawes for technical assistance with electron-beam lithography; E. Kim for assistance with figure illustration; and F. M. Ross, B. Shin, S. J. Chey, and S.-J. Han for helpful discussions. C.D. was partially supported for this work by Defense Advanced Research Projects Agency contract HR0011-12-C-0038.

Supplementary Materials

www.sciencemag.org/content/342/6160/833/suppl/DC1
Materials and Methods
Supplementary Text
Figs. S1 to S6
References (*31*, *32*)

10 July 2013; accepted 16 October 2013
Published online 31 October 2013;
10.1126/science.1242988

High-Performance Silicon Photoanodes Passivated with Ultrathin Nickel Films for Water Oxidation

Michael J. Kenney,* Ming Gong,* Yanguang Li,* Justin Z. Wu, Ju Feng, Mario Lanza, Hongjie Dai†

Silicon's sensitivity to corrosion has hindered its use in photoanode applications. We found that deposition of a ~2-nanometer nickel film on n-type silicon (n-Si) with its native oxide affords a high-performance metal-insulator-semiconductor photoanode for photoelectrochemical (PEC) water oxidation in both aqueous potassium hydroxide (KOH, pH = 14) and aqueous borate buffer (pH = 9.5) solutions. The Ni film acted as a surface protection layer against corrosion and as a nonprecious metal electrocatalyst for oxygen evolution. In 1 M aqueous KOH, the Ni/n-Si photoanodes exhibited high PEC activity with a low onset potential (~1.07 volts versus reversible hydrogen electrode), high photocurrent density, and durability. The electrode showed no sign of decay after ~80 hours of continuous PEC water oxidation in a mixed lithium borate–potassium borate electrolyte. The high photovoltage was attributed to a high built-in potential in a metal-insulator-semiconductor–like device with an ultrathin, incomplete screening Ni/NiO_x layer from the electrolyte.

Sunlight's intermittent nature is one of the issues limiting widespread harvesting of solar energy for societal power infrastructure (*1*, *2*). A potential solution is the use of sunlight to drive uphill electrochemical reactions that produce chemical fuels, which can be stored and

transported. Photoelectrochemical (PEC) water splitting is such a reaction; toward this end, tremendous efforts have been invested in the pursuit of photoactive and durable semiconductor materials, especially for photoanodes operating under highly oxidizing potentials. Oxides such as TiO_2 and WO_3 are relatively stable under these conditions but suffer from poor PEC activity under visible light. Silicon and III-V semiconductors, important materials in the electronics industry, are excellent light absorbers with high carrier mobilities but are extremely prone to photoanodic corrosion (*3*). Although this problem can also be avoided by using photovoltaic-coupled electrolysis schemes (*4*, *5*), PEC water splitting may be attractive for its reduced fabrication costs (*6*). Passivating the semiconductor surface with a layer of stable material could suppress or retard the photocorrosion; such a layer could also serve as an electrocatalyst to expedite the otherwise sluggish oxygen evolution reaction (OER).

Limited success has been achieved with a variety of protection layers for Si photoanodes, including transition metal oxides (*7*–*12*), doped SiO_2 (*13*), noble metal silicides (*14*), and polymer-coated gold films (*15*). For example, MnO_x (*8*) and NiO_x (*9*) films on Si were recently shown to afford high PEC activity in KOH and potassium sulfate electrolytes, but stability was limited (<2 hours). Thin layers (2 nm) of TiO_2 deposited by atomic layer deposition and coated with iridium (3 nm) have shown both good stability (8 hours) and PEC activity (*16*). However, longer-term stability is needed and the precious metal iridium is costly and therefore undesirable. Silicon nanowires protected by $NiRuO_x$ are active, but performance degrades after 1.5 hours (*12*). A cheap and highly stable protection film that does not absorb too much of the incident light and/or hinder charge transfer across the semiconductor-electrolyte interface has yet to be achieved.

Here, we investigated the use of a thin Ni layer to both protect the surface of n-type Si (n-Si) and serve as an OER catalyst in basic conditions. Nickel offers corrosion resistance, high OER activity, and Earth abundance, making it an excellent candidate material for such a layer. Nickel-based electrocatalysts have been widely used as the most active and stable Earth-abundant materials for water oxidation (*17*–*21*), and nickel-based anodes have long been used in industrial water electrolysis with excellent stability over several years (*22*). However, nickel's integration into PEC systems has been relatively unexplored.

We deposited Ni films (2 to 20 nm) on phosphorus-doped [100] n-Si wafers (resistivity = 0.3 to 0.5 ohm·cm) with native oxide by electron beam evaporation to form a metal-insulator-semiconductor (MIS) photoanode (see supplementary materials). Ohmic contact was made to the backside of the wafer by electron beam deposition of a 20-nm layer of Ti (Fig. 1). The nickel-modified anodes were found to be highly active for PEC water oxidation in both 1 M KOH (pH = 14) and 1 M potassium borate (K-borate) buffered (pH = 9.5) aqueous electrolytes (Fig. 2, A and B; cyclic voltammetry data without any iR compensation). The 2-nm Ni/n-Si photoanode afforded PEC water oxidation onset at ~0.00 V versus SCE (saturated calomel electrode) in aqueous KOH solution and ~0.38 V versus SCE in aqueous K-borate solution [corresponding to ~1.07 V versus RHE (reversible hydrogen electrode) and ~1.18 V versus RHE, respectively], below the thermodynamic electrochemical potential of 1.23 V versus RHE for water oxidation. Dark currents for the 2-nm Ni-coated n-Si anodes were zero over the potentials applied in this study (Fig. 2, A and B; dark yellow curves). The flatband voltages (V_{FB}) for the electrodes used in this study were found to be shifted ~600 mV negative of the observed photocurrent onset (figs. S1 and S2), similar to a previous report (*11*). The discrepancy between V_{FB} and the photocurrent onset is likely due to OER overpotential losses and voltage drops in the circuit. In aqueous KOH, this performance was similar to that of the most active silicon photoanodes reported (*8*, *16*). Previous work investigated Ni anodization (*23*) and OER electrocatalysis in aqueous K-borate solutions (*17*, *18*). Here, we observed water oxidation with a silicon photoanode in aqueous K-borate solutions (pH = 9.5) at an onset potential below the thermodynamic limit. The same Ni/n-Si photoanodes were slightly less active in the aqueous K-borate electrolyte than in aqueous KOH; we attribute this difference to higher solution resistance (40 to 50 ohms versus 10 to 15 ohms) and ohmic loss.

The photovoltage generated by the 2-nm Ni/n-Si photoanode was ~500 mV, as manifested by the OER onset shift of ~500 mV between the photoanode under illumination and a metallic (heavily doped) n++ silicon (0.001 to 0.005 ohm·cm) coated with 2 nm of Ni and measured in the dark (green curve in Fig. 2A). Under illumination, the Ni^{2+}/Ni^{3+} redox peaks (*21*, *24*) (below the OER onset potential) shifted negative by ~500 mV for the Ni/n-Si photoanode relative to the metallic n++Si coated with 2 nm of Ni (fig. S3), suggesting a photovoltage consistent with the OER onset shift. The photovoltage was further confirmed by comparing the voltage at which a current density of 20 mA/cm^2 was reached for a two-electrode cell containing a Ni foam cathode and a 2-nm Ni/n++Si anode with a two-electrode cell in 1 M KOH containing a Ni foam cathode and a 2-nm Ni-coated n-Si photoanode under illumination in 1 M KOH. The voltage difference was found to be ~500 mV (fig. S4).

The PEC water oxidation onset increased sharply to a more positive potential by ~300 mV

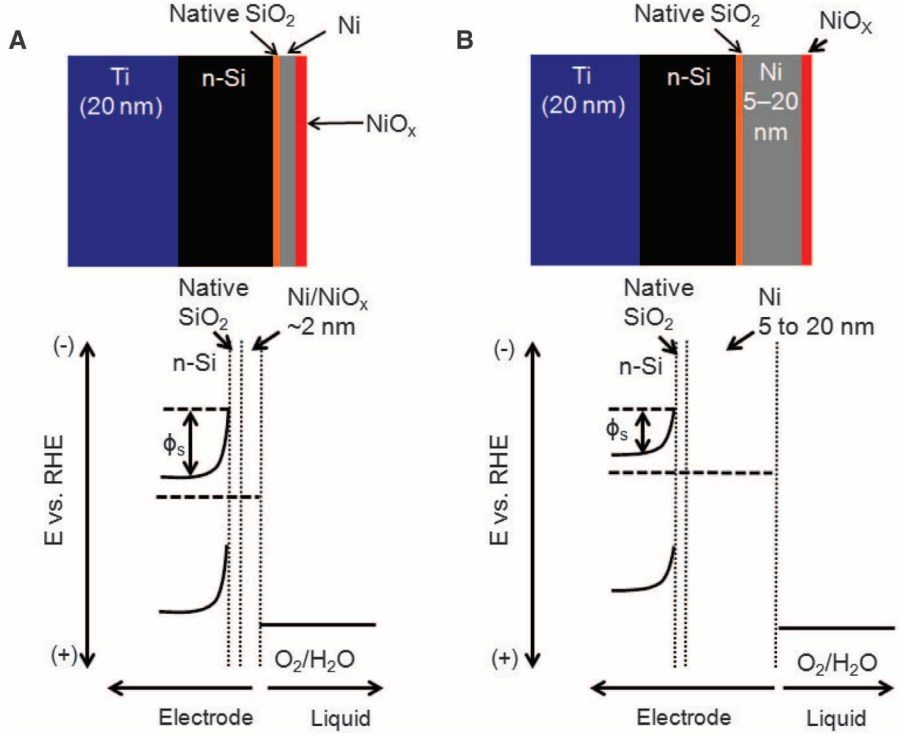

Fig. 1. Schematic of Ni/n-Si photoanode. (**A**) Structure of 2-nm Ni-coated n-Si anode (top) and proposed approximate energy band diagram (bottom). The ultrathin Ni/NiO_x and the electrolyte form an effective layer interfacing with Si, affording a high built-in potential ϕ_s and photovoltage. (**B**) Structure of 5- to 20-nm Ni-coated n-Si anode (top) and a typical Ni/n-Si Schottky barrier formed between 5- to 20-nm Ni and n-Si, with built-in potential ϕ_s and photovoltage lower than the 2-nm Ni/n-Si case in (**A**).

Department of Chemistry, Stanford University, Stanford, CA 94305, USA.

*These authors contributed equally to this work.
†Corresponding author. E-mail: hdai@stanford.edu

with an increase in Ni film thickness from 2 to 5 nm (Fig. 2, A and B); further increases in Ni film thickness up to 20 nm showed no further change in the photocurrent onset potential. Thicker Ni films (10 nm and 20 nm) afforded smaller saturation current densities, which we attributed to reduced light transmittance through the Ni film (see fig. S5 for optical transmittance measurement of film transparency).

We then investigated the stability of the 2-nm Ni/n-Si photoanode. Although the anode was able to retain nearly all of its PEC activity after ~24 hours of continuous operation at a constant current density of 10 mA/cm^2 in 1 M KOH (Fig. 2, C and D, and fig. S6), scanning electron microscopy (SEM) imaging and Auger electron spectroscopy chemical mapping showed that the film was slowly corroded in aqueous KOH, as manifested by the appearance of etch holes (fig. S7A). Etch pits were beginning to form at 5 hours (fig. S7A) and Auger mapping confirmed that silicon was exposed inside the pit (fig. S7B). After 12 hours, the Ni/n-Si was further corroded with more holes and silicon was exposed (fig. S7, C and D). Si and its oxide are known to corrode in the presence of 1 M KOH, and unprotected Si photoanodes can only last tens of minutes under similar PEC reaction conditions (*16*). Clearly, the 2-nm Ni film was able to substantially slow corrosion of the underlying silicon in the aqueous KOH solution.

Corrosion of the Ni/n-Si photoanode was greatly alleviated in the aqueous K-borate electrolyte, because the high stability of Ni in aqueous K-borate yielded better protection under anodization and OER conditions (*17*, *18*, *23*). After 12 hours of PEC at a current density of 10 mA/cm^2, we observed that the Ni/n-Si photoanode retained its activity (Fig. 2, C and D); in addition, microscopy and Auger mapping revealed no etch pits and no Si exposure to the electrolyte (fig. S5, E and F). The 2-nm Ni/n-Si photoanode in aqueous K-borate electrolyte showed activity decay only after ~24 hours of operation (fig. S6). Remarkably, replacement of a fraction of the potassium counterions with lithium ions imparted superior stability to the 2-nm Ni/n-Si photoanode over long PEC operation (>3 days; see supplementary materials). A 2-nm Ni/n-Si photoanode in an aqueous solution of 0.65 M K-borate and 0.35 M lithium borate (Li-borate) was able to maintain a photocurrent of 10 mA/cm^2 for ~80 hours (Fig. 2E) without any sign of decay in PEC activity or of surface corrosion, as measured by SEM and Auger mapping (fig. S7, G and H). Even after 80 hours of operation, gas bubbles were still generated at the electrode surface (Fig. 2E, inset). Cyclic voltammograms taken before and after 80 hours also showed no noticeable decay of PEC activity (fig. S8).

The Li^+ does not necessarily need to be present in the electrolyte for the stability to be maintained once a stable film is formed in the mixed K-borate/Li-borate electrolyte. This was confirmed by maintaining a constant current density of 10 mA/cm^2 in the lithiated electrolyte for 1 day under illumination and then switching to 1 M K-borate for ~65 additional hours (fig. S9). The addition of Li^+ to aqueous KOH was found to improve the cell stability, but corrosion was still seen over the course of 48 hours (fig. S10).

In addition to the PEC stability tests, we also evaluated the chemical stability of Ni/n-Si, NiO_x/Ni/n-Si (generated by 30 min of PEC), and bare Si in 1 M KOH or 1 M K-borate. After 24 hours of exposure to 1 M K-borate, all samples showed no corrosion as evaluated by SEM. However, Ni-coated samples exposed to 1 M KOH for 24 hours showed slight surface morphology change via conversion of metallic nickel to nickel hydroxide (fig. S11). Unprotected Si exposed to 1 M KOH showed severe corrosion, as expected. These data confirm that Ni and Si are intrinsically more

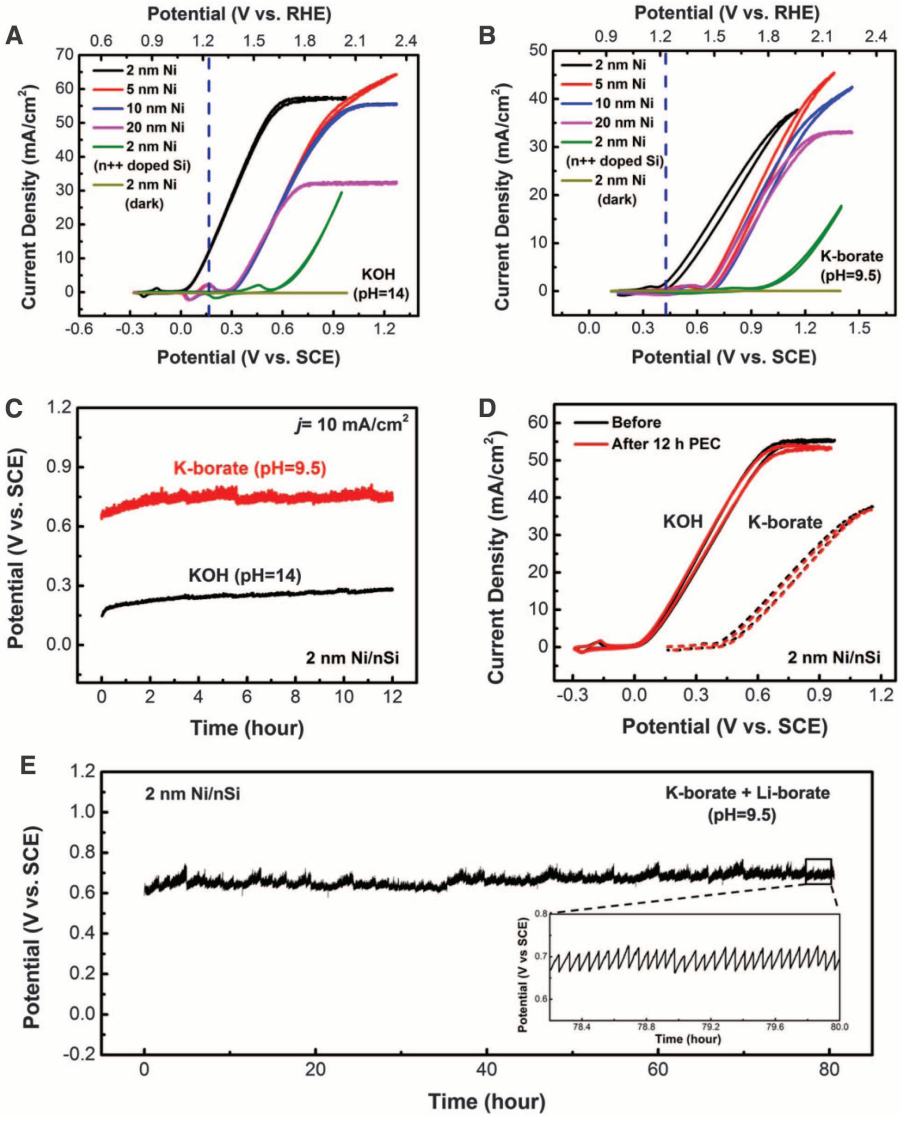

Fig. 2. High-performance Ni/n-Si photoanode with ultrahigh stability. (**A**) Cyclic voltammograms of 2-, 5-, 10-, and 20-nm Ni-coated n-Si anodes in 1 M KOH under illumination with a xenon lamp (150 W; 225 ± 10 mW/cm^2, approximately twice that of the Sun), 2-nm Ni-coated n-Si anode in the dark, and 2-nm Ni on metallic, heavily doped n++Si in the dark. (**B**) Cyclic voltammograms of 2-, 5-, 10-, and 20-nm Ni-coated n-Si anodes in 1 M K-borate electrolyte under illumination, 2-nm Ni-coated n-Si anode in the dark, and 2-nm Ni on metallic, heavily doped n++Si in the dark. (**C**) Potential versus time data, under constant current density of 10 mA/cm^2, of two 2-nm Ni/n-Si anodes in 1 M KOH and 1 M K-borate, respectively, for 12 hours under constant illumination. (**D**) Cyclic voltammograms taken before and after 12-hour stability tests in (C). All voltammograms were taken at 100 mV/s with no iR compensation applied. (**E**) Potential versus time data, under constant current density of 10 mA/cm^2, of a 2-nm Ni/n-Si anode in 0.65 M K-borate and 0.35 M Li-borate (pH = 9.5) for 80 hours (>3 days) under constant illumination. No PEC activity decay was observed. Inset shows details of current fluctuations caused by oxygen gas bubble release. The increased saturation current in the 5-nm Ni-coated electrodes is highly reproducible, but the cause is currently unknown.

stable in borate-based electrolytes, leading to the higher PEC stability observed when they are used.

To ascertain the Ni/n-Si photoanode surface composition, we carried out x-ray photoelectron spectroscopy (XPS) depth profiling experiments by slow Ar ion milling of n-Si samples with 2-nm or 5-nm Ni coatings after 5 hours and 12 hours of PEC operation in aqueous 1 M KOH (Fig. 3). The Ni and O signal intensities peaked at the surface of the 2-nm Ni/n-Si sample and decreased as depth increased (Fig. 3A). The Si signal increased continuously and became dominant after ~1 min of ion milling. High-resolution Ni spectra at different milling times (Fig. 3B) revealed that Ni at the surface was close to a +3 oxidation state because of anodization of Ni in the aqueous KOH solution (*25*, *26*) while the Ni underneath remained in the metallic state. No nickel oxide or hydroxide was detected at the Si interface. A similar depth profile was seen with the 5-nm Ni/n-Si sample after 12 hours of PEC operation, implying that the silicon is still fully protected in this case as well (Fig. 3, C and D).

We attribute the dependence of Ni/n-Si photoanode activity on Ni thickness to the nature of the Si-SiO_2-Ni-NiO_x-electrolyte interfaces. With a relatively thick Ni layer (≥5 nm), a typical MIS junction was formed with a built-in potential ϕ_s dictated by the Schottky barrier height and silicon doping level (Fig. 1B). In a MIS device, the photovoltage depends on the built-in potential and scales linearly with the Schottky barrier height (*27*). A higher photovoltage is attainable between n-Si and a metal with a high work function, such as Pt or Pd (*27*), and between p-Si and a metal with a low work function in MIS photocathodes (*28*). In the case of Ni with thickness of >5 nm, a photovoltage of 200 mV was measured and the photoanode was essentially a Ni-SiO_2-Si MIS solar cell coupled with an OER catalyst (NiO_x) at the surface.

In contrast, the 2-nm Ni/NiO_x films on n-Si appeared not to act as bulk nickel because of their ultrathin nature and associated ability to only partially screen charge, unlike thicker metal films, as shown in previous studies on metal thickness–dependent screening at semiconductor interfaces (*29*). This resulted in an interface formed between the n-Si/native SiO_2 and a combination of the Ni/NiO_x layer and the electrolyte solution potential. The higher photovoltage observed in the 2-nm Ni/n-Si case suggested a higher effective work function of the Ni/NiO_x/electrolyte than that of bulk nickel (Fig. 1A), affording a higher built-in voltage across the interface by an impressive ~300 mV (see figs. S12 and S13 for work function effect).

The thin Ni film on Si played multiple roles during PEC water oxidation. First, the metallic Ni at the n-Si interface formed a junction to afford band bending, thereby favoring charge separation and motion of photoexcited holes toward the OER catalyst-electrolyte interface. The Ni film thickness provides a degree of tuning of the built-in potential and photovoltage. Second, surface Ni species served as the active electrocatalyst for OER. It is well known that Ni-based catalysts exhibit the highest OER activity in basic conditions among first-row transition metals (*6*). At high potentials, oxidized Ni species are formed in situ and act as the OER active sites (*18*), and the OER activity is only slightly inferior to that of precious metal catalysts (i.e., RuO_x and IrO_x). Finally, the Ni/NiO_x film provided excellent protection to Si. In particular, remarkable stability was conferred by a 2-nm Ni coating on the Si photoanode in a mixed aqueous K-borate/Li-borate (pH = 9.5) electrolyte. Electrolyte lithiation has been suggested (through Edison's Ni battery research) to eliminate the formation of a more oxidized α-phase $Ni(OH)_2$ during Ni anodization, which avoids large volume expansion [relative to the dense β-phase $Ni(OH)_2$] and weakening of the oxidized Ni layer, thus imparting higher stability to anodized Ni (*25*, *26*). The Ni/n-Si photoanodes were not stable for PEC water oxidation in other electrolytes tested, including H_2SO_4 (pH = 0), K_2SO_4 (pH = 7), potassium phosphate (pH = 7), and HCO_3^-/CO_3^{2-} (2:1 ratio for pH = 10) because of dissolution of Ni under these conditions.

The low cost of Si and its instability under anodic conditions make it an ideal material to demonstrate the effectiveness of our protection scheme. However, its band gap (1.1 eV) limits the amount of photovoltage that can be generated for water splitting (*6*). The use of semiconductors with larger band gaps than Si under similar surface protection/electrolyte conditions should result in a shift of the OER photocurrent onset to more negative potentials.

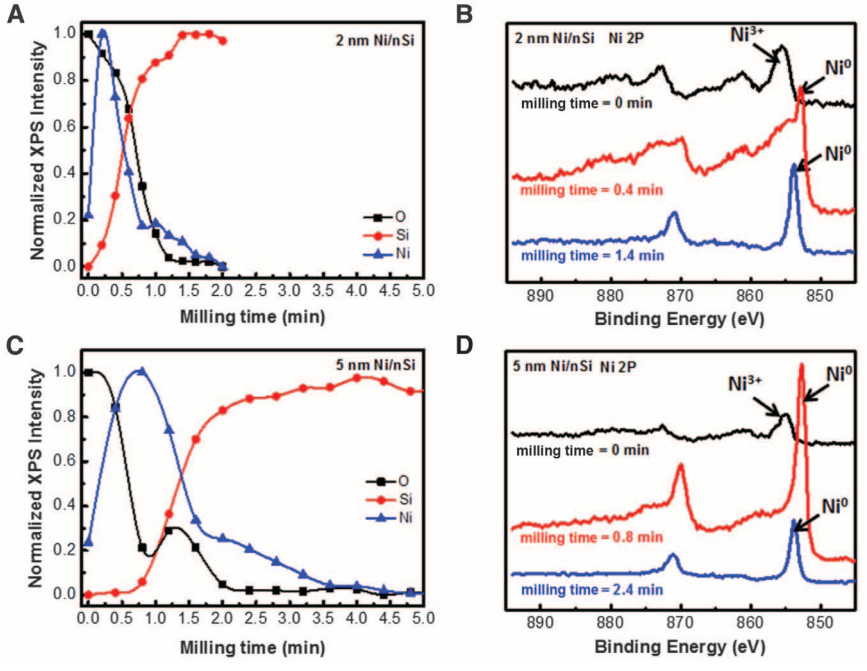

Fig. 3. X-ray photoelectron spectroscopy depth profiling of Ni/n-Si photoanodes. (**A**) Elemental depth profile of a 2-nm Ni-coated n-Si photoanode after 5 hours of continuous PEC operation (10 mA/cm^2) in 1 M KOH under illumination. A thin oxidized Ni layer ($Ni^{\delta+}$, $\delta \approx 3$) is evident above metallic nickel. (**B**) Ni 2p spectra for the sample in (A) taken after three different ion milling times into the Si substrate. Oxidized Ni peaks are seen at ~856 eV with metallic Ni peaks appearing at 854 eV. (**C**) Elemental depth profile of a 5-nm Ni-coated n-Si photoanode after 12 hours of continuous PEC operation (10 mA/cm^2) in 1 M KOH under illumination. The metallic layer is clearly thicker than in the 2-nm case. (**D**) Ni 2p spectra for the sample in (C) taken after three different ion milling times into the Si substrate.

References and Notes

1. N. S. Lewis, D. G. Nocera, *Proc. Natl. Acad. Sci. U.S.A.* **103**, 15729–15735 (2006).
2. H. B. Gray, *Nat. Chem.* **1**, 7 (2009).
3. H. Gerischer, *Faraday Discuss. Chem. Soc.* **70**, 137–151 (1980).
4. C. R. Cox, M. T. Winkler, J. J. H. Pijpers, T. Buonassisi, D. G. Nocera, *Energy Environ. Sci.* **6**, 532–538 (2013).
5. S. Y. Reece *et al.*, *Science* **334**, 645–648 (2011).
6. M. G. Walter *et al.*, *Chem. Rev.* **110**, 6446–6473 (2010).
7. R. C. Kainthla, B. Zelenay, J. O. Bockris, *J. Electrochem. Soc.* **133**, 248–253 (1986).
8. N. C. Strandwitz *et al.*, *J. Phys. Chem. C* **117**, 4931–4936 (2013).
9. K. Sun *et al.*, *Energy Environ. Sci.* **5**, 7872–7877 (2012).
10. G. Li, S. Wang, *J. Electroanal. Chem.* **227**, 213–221 (1987).
11. K. Jun, Y. S. Lee, T. Buonassisi, J. M. Jacobson, *Angew. Chem.* **51**, 423–427 (2012).
12. K. Sun *et al.*, *Nano Lett.* **13**, 2064–2072 (2013).
13. A. Q. Contractor, J. O. M. Bockris, *Electrochim. Acta* **29**, 1427–1434 (1984).
14. F. R. F. Fan, R. G. Keil, A. J. Bard, *J. Am. Chem. Soc.* **105**, 220–224 (1983).
15. F. R. F. Fan, B. L. Wheeler, A. J. Bard, R. N. Noufi, *J. Electrochem. Soc.* **128**, 2042–2045 (1981).
16. Y. W. Chen *et al.*, *Nat. Mater.* **10**, 539–544 (2011).
17. M. Dincă, Y. Surendranath, D. G. Nocera, *Proc. Natl. Acad. Sci. U.S.A.* **107**, 10337–10341 (2010).

18. D. K. Bediako *et al.*, *J. Am. Chem. Soc.* **134**, 6801–6809 (2012).
19. R. D. L. Smith *et al.*, *Science* **340**, 60–63 (2013).
20. D. A. Corrigan, R. M. Bendert, *J. Electrochem. Soc.* **136**, 723–728 (1989).
21. M. Gong *et al.*, *J. Am. Chem. Soc.* **135**, 8452–8455 (2013).
22. R. L. LeRoy, *Int. J. Hydrogen Energy* **8**, 401–417 (1983).
23. B. MacDougall, D. F. Mitchell, M. J. Graham, *J. Electrochem. Soc.* **127**, 1248–1252 (1980).
24. D. A. Corrigan, S. L. Knight, *J. Electrochem. Soc.* **136**, 613–619 (1989).
25. D. Tuomi, *J. Electrochem. Soc.* **112**, 1–12 (1965).
26. P. Oliva *et al.*, *J. Power Sources* **8**, 229–255 (1982).
27. S. K. Behura, P. Mahala, A. Ray, *J. Electron Devices* **10**, 471–482 (2011).
28. D. V. Esposito, I. Levin, T. P. Moffat, A. A. Talin, *Nat. Mater.* **12**, 562–568 (2013).
29. X. Wu, E. S. Yang, *IEEE Electron Device Lett.* **11**, 315–317 (1990).

Acknowledgments: Supported by a Stinehart/Reed Award from the Stanford Precourt Institute for Energy, a Stanford GCEP grant, and an NSF Graduate Fellowship (M.J.K.). We thank C. Chidsey for helpful discussions.

Supplementary Materials
www.sciencemag.org/content/342/6160/836/suppl/DC1
Materials and Methods
Figs. S1 to S13
Tables S1 to S6

3 June 2013; accepted 7 October 2013
10.1126/science.1241327

Enantioselective Lewis Acid Catalysis of Intramolecular Enone [2+2] Photocycloaddition Reactions

R. Brimioulle and T. Bach*

Asymmetric catalysis of photochemical cycloadditions has been limited by the challenge of suppressing the unselective background reaction. Here, we report that the high cross-section ππ* transition of 5,6-dihydro-4-pyridones, a versatile class of enone substrates, undergoes a >50 nanometer (nm) bathochromic absorption shift upon Lewis acid coordination. Based on this observation, enantioselective intramolecular [2+2] photocycloaddition reactions (82 to 90% enantiomeric excess) were achieved with these substrates using 0.5 equivalents of a chiral Lewis acid upon irradiation at a wavelength of 366 nm. One of the products was applied as a key intermediate in the total synthesis of (+)-lupinine and the formal synthesis of (+)-thermopsine. Several enones show similar bathochromic shifts in the presence of a Lewis acid, indicating that chiral Lewis acid catalysis may be a general approach toward enantioselective enone [2+2] photocycloadditions.

The [2+2] photocycloaddition (PCA) of enones was discovered in 1908 by Ciamician and Silber (*1*), early pioneers (*2*) of organic photochemistry. Over the years this reaction has become one of the most widely applied photochemical transformations (*3*–*7*). The reaction occurs on the triplet manifold and can be initiated by direct excitation or sensitization (*8*). The key intermediate is the lowest-lying triplet (T_1) state of the enone, which has ππ* character and to which another olefin can add, leading via a 1,4-diradical to four-membered cyclobutane rings. With the advent of enantioselective synthesis and with increasing attention given to enantiomerically pure products (*9*), attempts were undertaken to render the enone [2+2] PCA enantioselective. Although a chiral auxiliary-based approach—first demonstrated by Tolbert and Ali (*10*)—is viable, it lacks brevity (two steps are required to attach and remove the auxiliary) and general applicability (many enones are cyclic compounds without a possible site for auxiliary attachment).

Nonauxiliary-based approaches have been restricted to aromatic α,β-unsaturated lactones and lactams with a narrow substitution pattern and with very limited use in natural product synthesis. Examples include the intermolecular [2+2] PCA of axially chiral coumarins (*11*), the sensitized intramolecular [2+2] PCA of N-unsubstituted quinolones (*12*), or the Lewis acid–catalyzed intramolecular [2+2] PCA of 4-substituted coumarins (*13*, *14*). Unlike for typical enones, the T_1 state of the latter substrates cannot be accessed upon direct excitation because internal conversion from the first excited singlet state (S_1) to the ground state (S_0) is rapid (*15*). Intramolecular [2+2] PCA proceeds on the singlet hypersurface with medium efficiency at wavelength λ = 300 nm (*14*) and with low efficiency at λ = 366 nm (*13*). The known fact (*15*–*17*) that Lewis acid coordination to coumarins enhances the lifetime of the S_1 state and allows for the population of the T_1 state via S_1 was exploited to catalyze the [2+2] PCA at λ = 366 nm. Fluorescence experiments confirmed an increased lifetime of the S_1 state (*14*), and the catalyzed reaction was shown to occur on the triplet hypersurface (*13*).

The present study was concerned with a synthetically useful class of enones, 5,6-dihydro-4-pyridones, and their intramolecular [2+2] PCA reactions in the presence of a chiral Lewis acid. This reaction was first described in its intermolecular variant by Neier *et al.* (*18*–*20*). The intramolecular variant has been later applied to natural product synthesis, in particular by Comins *et al.* (*21*–*23*). The substrates attracted our interest because they exhibit an extensive bathochromic

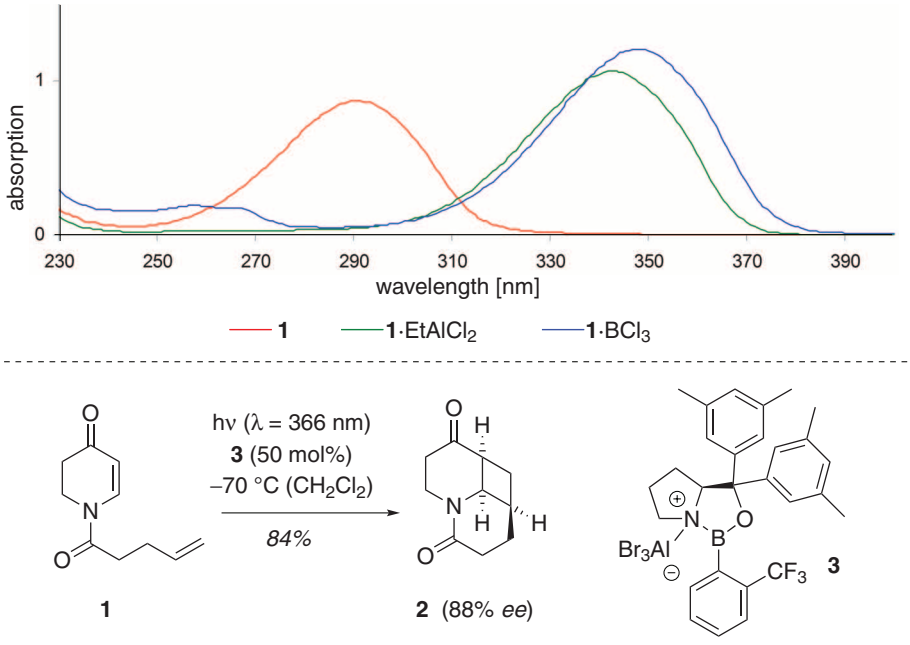

Fig. 1. Ultraviolet-visible spectra of substrate 1 in the presence of the Lewis acids and formation of compound 2 in an enantioselective [2+2] PCA reaction using chiral Lewis acid 3. Et, ethyl; h, Planck's constant; ν, frequency.

Lehrstuhl für Organische Chemie I and Catalysis Research Center, Technische Universität München, D-85747 Garching, Germany.

*Corresponding author. E-mail: thorsten.bach@ch.tum.de

absorption shift in the presence of Lewis acids (Fig. 1). The ultraviolet-visible spectrum of compound **1** in CH_2Cl_2 (molar concentration c = 0.5 mM) shows, in the absence of a Lewis acid, a strong absorption at λ_{max} = 291 nm (molar absorption coefficient ε = 17,400) and a weak, broad absorption at $\lambda_{max} \cong 360$ nm ($\varepsilon \cong 70$). In analogy to other enones (*24*), the former band can be assigned to an allowed $\pi\pi^*$-transition, whereas the latter band is probably due to a forbidden $n\pi^*$-transition. Lewis acid addition changed the absorption spectrum dramatically, and the strong absorption appeared at λ_{max} = 343 nm (ε = 21,400) with $EtAlCl_2$ as Lewis acid and λ_{max} = 348 nm (ε = 24,200) with BCl_3 as Lewis acid. A shift of the weak absorption was not detectable.

Based on the idea of selectively exciting the Lewis acid–complexed enone, irradiation experiments were performed at long wavelengths in the presence of the chiral Lewis acid **3** (Fig. 1). Attempted reactions at λ = 419 nm (for emission spectra, see fig. S1) were not successful, yielding very little product even after prolonged irradiation time. However, at λ = 366 nm and a reaction temperature of –70°C, a clean reaction was observed, which led to the formation of the desired [2+2] PCA product **2**. The reaction was regio- and diastereoselective; that is, only a single product was obtained as a mixture of enantiomers. Different attempts to determine the enantiomeric purity of this product failed, and it was necessary to derivatize the product before measuring the enantiomeric excess (ee). The preferred derivatization method included diastereoselective reduction of the ketone to a secondary alcohol and subsequent benzoylation with 3,5-dinitrobenzoyl chloride (see fig. S2). Under optimized conditions, the PCA product **2** was obtained in 84% yield and with 88% ee.

The success of the reaction depends on the concentration and the solvent purity. The optimum substrate concentration was found to be 20 mM. A decrease of the catalyst loading leads to a decrease in enantioselectivity [64% ee at 40 mole % (mol %); 50% ee at 30 mol %], which is likely related to the mode of action of the catalyst (see below). The solvent (CH_2Cl_2) had to be dried over 4 Å molecular sieves to a residual water content of <1 parts per million and was carefully degassed. The Lewis acid was prepared in situ, as described previously (*14*). The generality of the method was shown by employing several other acylated 5,6-dihydro-4-pyridones as substrates (Fig. 2); these compounds delivered products **4** to **9** in high yields (75 to 87%) and enantioselectivities (80 to 90% ee). The lower yield of product **5** is due to concomitant formation of by-product **10**, which appears at first sight to be the product of a subsequent Norrish type II fragmentation. However, monitoring the reaction course indicated that the formation of product **10** occurs parallel to the formation of product **5** (see fig. S3).

After reduction of product **8** to the respective alcohol, an acylation with (*R*)-(–)-α-methoxy-α-trifluoromethylphenylacetyl chloride was possible, which delivered the (S)-configured ester **11** (Fig. 2). Analysis of this ester according to the Mosher method (*25*, *26*) suggests the absolute configuration of the 10-methyl-6-oxodecahydro-1-10-methanopyrido[1,2-a]azepine skeleton to be (1S, 2R, 10R, 10aS). This outcome is in agreement with a postulated coordination of the precursor of product **8**, substrate **12**, to the Lewis acid as depicted in Fig. 2 (*27*), and an intramolecular approach of the olefin to the double bond in a Si-face attack relative to the enone α-carbon atom.

Applications to the synthesis of lupin alkaloids were pursued to further substantiate the configuration assignment and to show the synthetic utility of the enantioselective enone [2+2] PCA reaction. Many of these alkaloids exhibit a central quinolizidine skeleton, which is built up with high selectivity in the course of the photochemical reaction and which represents the core structure of compounds **2**, **4**, **5**, **6**, and **9**. Cleavage of the cyclobutane ring between carbon atoms C8 and C8a in the hexahydro-1H,5H-cyclobuta[ij]quinolizine-1,5-dione ring system would enable ready access to quinolizidines. Although this ring cleavage is already implemented in product **10**, further functionalization appeared difficult. However, it was possible to displace the chlorine substituent of product **9** by various nucleophiles in an elimination-addition reaction.

For the synthesis of the prototypical quinolizidine alkaloid lupinine (*28*, *29*), the introduction of an oxygen atom was required (Fig. 3). Employing *para*-methoxybenzyl alcohol (PMBOH) as nucleophile, product **13** was obtained in 59% yield as a single enantiomer after appropriate purification. Reductive ring opening of the C8-C8a bond was best achieved via the respective xanthate (*30*). Diastereoselective reduction of ketone **13** gave the secondary alcohol **14**, which was converted into xanthate **15**. Generation of the secondary radical with azobis(isobutyronitrile) (AIBN) as the initiator led to the desired fragmentation, and the primary PMBO-substituted radical was trapped with tributyltin hydride. Conversion of ring-opening product **16** to lupinine (**18**) was performed by lactam reduction to amine **17**, followed by concomitant double bond hydrogenation and ether hydrogenolysis. The enantiomerically pure product turned out to be dextrorotatory (specific rotation

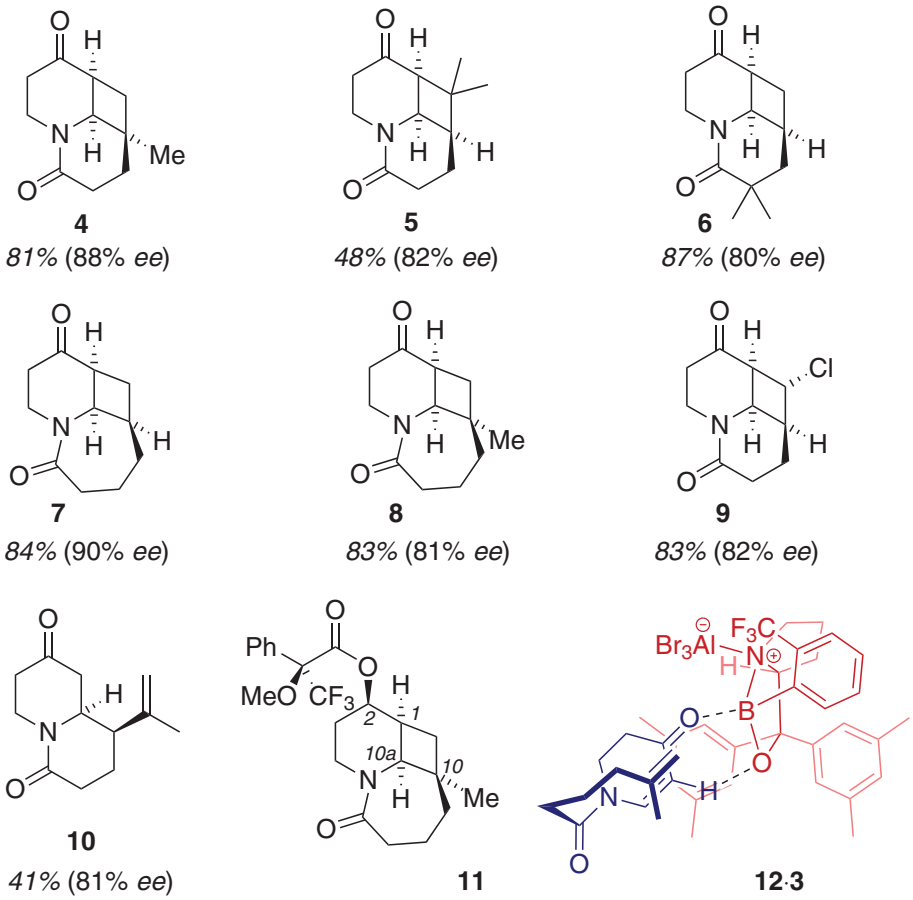

Fig. 2. Structures of compounds 4 to 10, which were formed in the enantioselective enone [2+2] PCA reaction using chiral Lewis acid 3. Compounds **5** and **10** were formed simultaneously from the same irradiation precursor in 89% combined yield. Mosher ester **11** was obtained starting from photoproduct **8** in two steps, confirming the absolute configuration of the enantiomers formed in the [2+2] PCA reaction (see supplementary materials). The configuration of compound **8** can be explained by the proposed conformation of the complex of **12** with Lewis acid **3**. Me, methyl; Ph, phenyl.

$[\alpha]_D^{20}$ = +18.5), proving its absolute configuration and confirming the initial configuration assignment for products **2** and **4** through **9**.

The more complex (relative to lupinine) α-pyridone–type quinolizidine alkaloid thermopsine (*31*) could be accessed in a similar fashion (Fig. 4). Displacement of the chlorine substituent in product **9** by 2-pyridone was facile, producing precursor **19** for the cyclobutane bond cleavage. Reduction to alcohol **20** and formation of xanthate **21** preceded the radical fragmentation reaction, which led to the desired intermediate **22**. Attempts to achieve the desired bond cleavage by reduction of ketone **19** with SmI_2 (*21*, *23*) remained less successful, leading under a variety of conditions to a mixture of product and starting material. A selective reduction of the double bond in intermediate **22** was facilitated by hydrogen and Raney nickel–providing compound **23**, which had been previously synthesized in racemic form by a different route and has been shown to be converted into racemic thermopsine in three steps (*32*). The synthesis of compound **23** thus constitutes a formal synthesis of (+)-thermopsine.

Extensive mechanistic studies elucidating the effect of the Lewis acid on the reaction course have not yet been performed. However, we showed that many enones manifest a similarly strong absorption shift in the presence of Lewis acids (see figs. S4 and S5), which should open the possibility to extend the enantioselective Lewis acid–catalyzed enone [2+2] PCA to other substrates. It is evident that the mode of action in the case of enones is different from that in the specific case of coumarin [2+2] PCA. There is no increase in fluorescence due to Lewis acid coordination (see fig. S6), and the bathochromic shift induced by the Lewis acid is large (≥50 nm), as opposed to the minimal shift (≤10 nm) observed upon Lewis acid coordination to coumarins. Apart from the successful enantioface differentiation, the most relevant argument to explain the enantioselectivity is the fact that the strong absorption of the enone–Lewis acid complex prevents a reaction of uncomplexed enone and suppresses the racemic background reaction by avoiding an excitation of the nπ* band at λ ≅ 360 nm. At lower catalyst loading, the concentration of uncomplexed enone increases, and the reaction is less enantioselective.

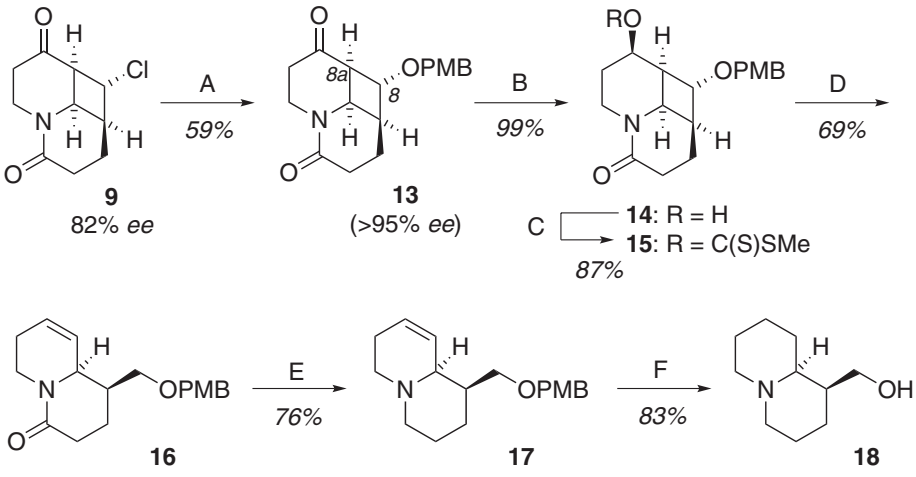

Fig. 3. Enantioselective total synthesis of (+)-lupinine starting from 9. (**A**) (i) *para*-Methoxybenzyl alcohol, *i*-Pr_2NEt, room temperature (r.t.), 20 hours; (ii) chiral high-performance liquid chromatography (HPLC) separation. *i*-Pr, isopropyl. (**B**) $NaBH_4$, −78°C → r.t., 16 hours (solvent: MeOH). OPMB, *para*-methoxybenzyloxy. (**C**) (i) NaH, 0°C, 30 min [*N*,*N*-dimethylformamide (DMF)]; (ii) CS_2, 0°C, 30 min, r.t., 2.5 hours (DMF); (iii) MeI, r.t., 3 hours (DMF). (**D**) $HSnBu_3$, AIBN, 75°C, 4 hours (PhH). Bu, butyl. (**E**) $LiAlH_4$, reflux, 3 hours (tetrahydrofuran). (**F**) H_2, [Pd/C], r.t., 5 days, (MeOH/HOAc). OAc, acetate.

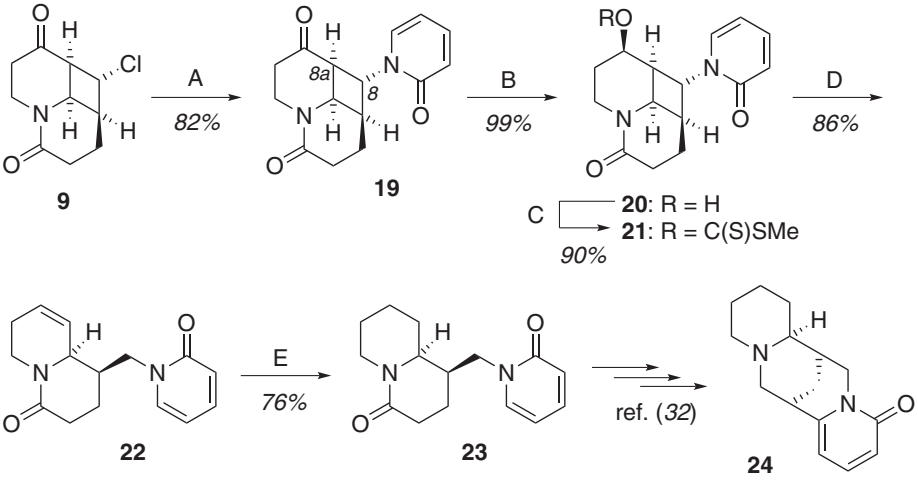

Fig. 4. Enantioselective formal synthesis of (+)-thermopsine starting from 9. (**A**) 2-Pyridone, K_2CO_3, r.t., 16 hours (DMF). (**B**) $NaBH_4$, −78°C → r.t., 16 hours (MeOH). (**C**) (i) NaH, 0°C, 30 min (DMF); (ii) CS_2, 0°C, 30 min, r.t., 2.5 hours (DMF); (iii) MeI, r.t., 3 hours (DMF). (**D**) $HSnBu_3$, AIBN, reflux, 3.5 hours (PhMe). (**E**) Raney-Ni, H_2, 20 hours (EtOH).

References and Notes

1. G. Ciamician, P. Silber, *Ber. Dtsch. Chem. Ges.* **41**, 1928–1935 (1908).
2. G. Ciamician, *Science* **36**, 385–394 (1912).
3. M. T. Crimmins, T. L. Reinhold, *Org. React.* **44**, 297–588 (1993).
4. J. P. Hehn, C. Müller, T. Bach, in *Handbook of Synthetic Photochemistry*, A. Albini, M. Fagnoni, Eds. (Wiley-VCH, Weinheim, Germany, 2009), pp. 171–215.
5. J. D. Winkler, C. M. Bowen, F. Liotta, *Chem. Rev.* **95**, 2003–2020 (1995).
6. J. Iriondo-Alberdi, M. F. Greaney, *Eur. J. Org. Chem.* **2007**, 4801–4815 (2007).
7. T. Bach, J. P. Hehn, *Angew. Chem. Int. Ed.* **50**, 1000–1045 (2011).
8. D. I. Schuster, G. N. Lem, A. Kaprinidis, *Chem. Rev.* **93**, 3–22 (1993).
9. W. A. Nugent, T. V. RajanBabu, M. J. Burk, *Science* **259**, 479–483 (1993).
10. L. M. Tolbert, M. B. Ali, *J. Am. Chem. Soc.* **104**, 1742–1744 (1982).
11. M. Sakamoto *et al.*, *J. Am. Chem. Soc.* **130**, 1132–1133 (2008).
12. C. Müller, A. Bauer, T. Bach, *Angew. Chem. Int. Ed.* **48**, 6640–6642 (2009).
13. H. Guo, E. Herdtweck, T. Bach, *Angew. Chem. Int. Ed.* **49**, 7782–7785 (2010).
14. R. Brimioulle, H. Guo, T. Bach, *Chemistry* **18**, 7552–7560 (2012).
15. F. D. Lewis, S. V. Barancyk, *J. Am. Chem. Soc.* **111**, 8653–8661 (1989).
16. F. D. Lewis, D. K. Howard, J. D. Oxman, *J. Am. Chem. Soc.* **105**, 3344–3345 (1983).
17. H. Görner, T. Wolff, *Photochem. Photobiol.* **84**, 1224–1230 (2008).
18. P. Guerry, R. Neier, *Chimia (Aarau)* **41**, 341–342 (1987).
19. P. Guerry, R. Neier, *J. Chem. Soc. Chem. Commun.* **1989**, 1727–1728 (1989).
20. P. Guerry, P. Blanco, H. Brodbeck, O. Pasteris, R. Neier, *Helv. Chim. Acta* **74**, 163–178 (1991).
21. D. L. Comins, X. Zheng, *J. Chem. Soc. Chem. Commun.* **1994**, 2681–2682 (1994).
22. D. L. Comins, Y.-M. Zhang, X. Zheng, *Chem. Commun.* **1998**, 2509–2510 (1998).
23. D. L. Comins, X. Zheng, R. R. Goehring, *Org. Lett.* **4**, 1611–1613 (2002).
24. D. I. Schuster, in *The Photochemistry of Enones, Part 2*, S. Patai, Z. Rappoport, Eds. (Wiley, Chicester, UK, 1989), pp. 623–756.
25. J. A. Dale, H. S. Mosher, *J. Am. Chem. Soc.* **95**, 512–519 (1973).
26. T. R. Hoye, C. S. Jeffrey, F. Shao, *Nat. Protoc.* **2**, 2451–2458 (2007).

27. E. Canales, E. J. Corey, *J. Am. Chem. Soc.* **129**, 12686–12687 (2007).
28. P. Karrer, F. Canal, K. Zohner, R. Widmer, *Helv. Chim. Acta* **11**, 1062–1084 (1928).
29. M. Hajri, C. Blondelle, A. Martinez, J.-L. Vasse, J. Szymoniak, *Tetrahedron Lett.* **54**, 1029–1031 (2013).
30. G. Adamson, A. L. J. Beckwith, M. Kaufmann, A. C. Willis, *J. Chem. Soc. Chem. Commun.* **1995**, 1783–1784 (1995).
31. D. J. Robins, D. S. Rycroft, *Magn. Reson. Chem.* **30**, 1125–1127 (1992).
32. D. Gray, T. Gallagher, *Angew. Chem. Int. Ed.* **45**, 2419–2423 (2006).

Acknowledgments: This work was supported by the Deutsche Forschungsgemeinschaft (Graduiertenkolleg GRK 1626 Chemical Photocatalysis) and by the Fonds der Chemischen Industrie (scholarship to R.B.). We thank O. Ackermann for help in conducting HPLC analyses.

Supplementary Materials
www.sciencemag.org/content/342/6160/840/suppl/DC1
Supplementary Text
Figs. S1 to S8
NMR Spectra
HPLC Spectra
References (*33*–*42*)

16 August 2013; accepted 16 October 2013
10.1126/science.1244809

Abrupt Shifts in Horn of Africa Hydroclimate Since the Last Glacial Maximum

Jessica E. Tierney[1]* and Peter B. deMenocal[2]

The timing and abruptness of the initiation and termination of the Early Holocene African Humid Period are subjects of ongoing debate, with direct consequences for our understanding of abrupt climate change, paleoenvironments, and early human cultural development. Here, we provide proxy evidence from the Horn of Africa region that documents abrupt transitions into and out of the African Humid Period in northeast Africa. Similar and generally synchronous abrupt transitions at other East African sites suggest that rapid shifts in hydroclimate are a regionally coherent feature. Our analysis suggests that the termination of the African Humid Period in the Horn of Africa occurred within centuries, underscoring the nonlinearity of the region's hydroclimate.

During the Early Holocene epoch between roughly 11 to 5 thousand years ago (ka), the presently hyperarid Saharan desert was dotted with large and small lakes, savannah grasslands, and in some regions, humid tropical forests and shrubs (*1*, *2*). This "African Humid Period" (AHP) was a unique hydrological regime and has been a focal point of African paleoclimate studies, both for its climatological implications (*3*, *4*) and its influence on the emergence of pharaonic civilization along the Nile (*5*, *6*). The fundamental cause of the AHP—dramatic increases in summer precipitation triggered by orbital forcing of African monsoonal climate and amplified by oceanic and terrestrial feedbacks—is well understood (*7*, *8*). However, the abruptness with which the AHP began and, most particularly, ended is still debated. Dust proxy data from the west coast of Africa indicate a rapid, century-scale termination of the AHP near 5 ka (*9*). In contrast, isotopic proxies from central Africa (*10*, *11*) and pollen and sedimentological data from a lake in the eastern Sahara (*12*, *13*) suggest a more gradual reduction in rainfall during the mid-Holocene tracking the orbital decline in boreal summer insolation. The discrepancy remains unresolved. Previous studies have attributed the difference in climate response to differing proxy sensitivities; for example, dust may respond nonlinearly to a gradual drying of the Sahara (*14*), and conversely, pollen data may be smoothed because of mixed contributions from distal terrains (*2*). Alternatively, there may be regional heterogeneity in both the timing and duration of the AHP termination, reflecting the variable sensitivity of different regions to certain feedback mechanisms (in particular, vegetation feedbacks) (*3*, *4*, *6*, *15*, *16*).

East Africa and the Arabian Peninsula also experienced humid conditions during the Early Holocene (*17*, *18*). Speleothem $\delta^{18}O$ data from southern Oman (Qunf Cave) and dust strontium isotopes off of Somalia suggest a gradual attenuation of humid conditions during the Holocene, much like the eastern Saharan pollen data (*19*, *20*). These observations have led to the suggestion that the eastern Sahara and northeast Africa experienced a gradual end to the AHP (*3*, *4*, *12*, *15*, *21*) and that abrupt responses were therefore limited to the western Sahara.

We revisited the timing and abruptness of transitions into and out of the AHP in northeast Africa using a new record of hydroclimate from a key, yet previously understudied, region: the Horn of Africa. This record is derived from a marine core (P178-15P) located in the Gulf of Aden (Fig. 1). The Gulf of Aden receives substantial amounts of terrestrial material during the summer monsoon season, when prevailing southwesterly winds transport dust from the Horn (Fig. 1 and fig. S1). Therefore, the terrestrial components (including organic matter) in the sediments predominantly reflect conditions in the Horn and Afar regions (supplementary materials). Twenty radiocarbon dates constrain the chronology of P178-15P and indicate an average sedimentation rate of 32 cm per thousand years (supplementary materials).

We used the hydrogen isotopic composition of leaf waxes (δD_{wax}) as a proxy for aridity and, more generally speaking, hydroclimate, including precipitation/evaporation balance and changes in regional convection. δD_{wax} has been widely used in African paleoclimate and is an effective indicator of changes in the isotopic composition of precipitation (δD_P) and aridity, with enriched isotopic values corresponding to drier conditions and depleted values to wetter conditions (*10*, *22*). More generally, tropical water isotopes are good tracers of large-scale changes in atmospheric circulation (*18*, *23*) and therefore reflect regional, rather than local, shifts in the hydrological cycle. Because Congo basin moisture is effectively blocked by the Ethiopian highlands and the Horn of Africa receives the majority of its rainfall from the Indian Ocean (*24*), we interpret the δD_{wax} values to primarily represent changes in western Indian Ocean hydroclimate.

The δD_{wax} record from the Gulf of Aden indicates that Horn of Africa hydroclimate has changed dramatically during the past 40,000 years (Fig. 2). After the arid conditions of the Last Glacial Maximum (LGM) (26 to 19 ka), the Horn region experienced a severe dry period coincident with the North Atlantic cooling event, Heinrich Event 1 (H1) (Fig. 2), which is consistent with previous proxy (*25*) and model (*23*) evidence

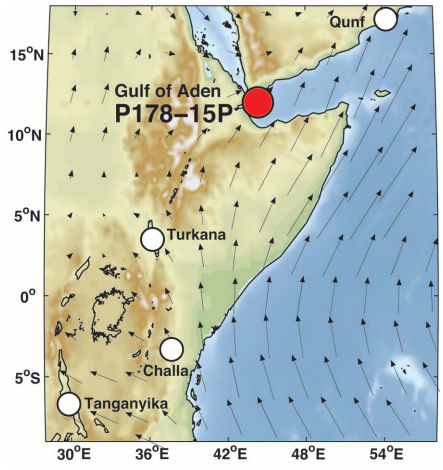

Fig. 1. A map of East Africa. The map includes topography, wind climatology for June-July-August (JJA) (*46*), the location of the study site (Gulf of Aden P178-15P; 11° 57.3′ N, 44° 18′ E, 869 m water depth), and other sites mentioned in the text.

[1]Woods Hole Oceanographic Institution, 266 Woods Hole Road, Woods Hole, MA 02540, USA. [2]Lamont Doherty Earth Observatory, Palisades, NY 10964, USA.

*Corresponding author. E-mail: tierney@whoi.edu

from the Afro-Asian monsoon domain. After H1, there was a rapid transition to intermediate conditions coincident with the Bölling-Allerød (B/A) period and then a reversal into dry conditions during the Younger Dryas (YD), another North Atlantic cold event (Fig. 2). Upon the termination of the YD, the Horn of Africa rapidly moved into the most humid conditions of the past 40,000 years, coincident with the AHP (Fig. 2). These conditions persisted until ~5 ka.

The δD_{wax} record from the Gulf of Aden is dominated by abrupt transitions that occur more rapidly than would be predicted from orbital forcing alone (Fig. 3). Two other δD_{wax} records from East Africa—from Lake Tanganyika (*22*) and Lake Challa (*26*)—show similar and generally coeval abrupt transitions at the end of H1, the YD, and the AHP, even though these sites sit ~2000 km to the south of the Gulf of Aden (Figs. 1 and 3). The overall similarity between the three records attests to the ability of water isotope proxies, specifically δD_{wax}, to record large-scale hydroclimatic patterns in tropical Africa.

The perceived timing and abruptness of the transitions in each δD_{wax} record is subject to dating uncertainties as well as sedimentary properties. Therefore, we used a Monte Carlo method (*27*) to create empirical probability distributions for the midpoint and duration of each identified transition and more clearly assess the duration and synchronicity of these key climate transitions (supplementary materials). We used these distributions to assess the timing of the transitions in a statistical fashion by applying a *T* test for contemporaneity (*28*) to test against the null hypothesis that the transitions are synchronous between two sites, or a χ^2 test to test against the null hypothesis that the transitions at all three sites derive from the same mean and are therefore likely synchronous. In both cases, we accepted the null hypothesis if $P > 0.05$.

Several findings emerged from this analysis. First, we found that the termination of H1 and the YD are not likely synchronous at all sites. All age model iterations indicate an older timing for the H1–B/A transition at Lake Tanganyika than at the Gulf of Aden site [Lake Challa does not have a detectable H1 termination (supplementary materials)]. The median date of the transition in the Gulf of Aden record [14,680 years before the present (B.P.)] is close to the generally accepted timing of 14,700 years B.P. (*29*), whereas the transition at Lake Tanganyika occurs nearly 1000 years earlier (median = 15,760 years B.P.). For the Challa and Tanganyika sites, the termination of the YD is likely synchronous (*t* test, $P = 0.99$) and the timing (median of both = 11,600 years B.P.) is in good agreement with the transition (11,570 years B.P.) dated by tree-ring chronologies (*30*), but the transition in the Gulf of Aden record occurs later in all iterations (median = 10,850 years B.P.).

The observed offsets in the Tanganyika and Aden δD_{wax} data across the H1 and YD terminations, respectively, could reflect meaningful local climatic deviations; however, because these millennial-scale events are remotely forced by North Atlantic processes, it seems more likely that they reflect unconstrained changes in site radiocarbon (^{14}C) reservoirs. Lake Tanganyika has a substantial ^{14}C reservoir today (~1000 years) owing to its meromixis (*22*), and although the evolution of this reservoir is constrained by paired bulk organic matter and terrestrial plant macrofossil dates from the LGM to present (*22*), no data are available for H1, during which time the lake was stratified (*31*). Likewise, we lack sufficient information to constrain how the Gulf of Aden ^{14}C reservoir has evolved through time. Although our site sits outside of the upwelling zone, it is still likely that the regional radiocarbon reservoir was modulated by the intensity of Arabian Sea upwelling, especially during the deglaciation, when large changes

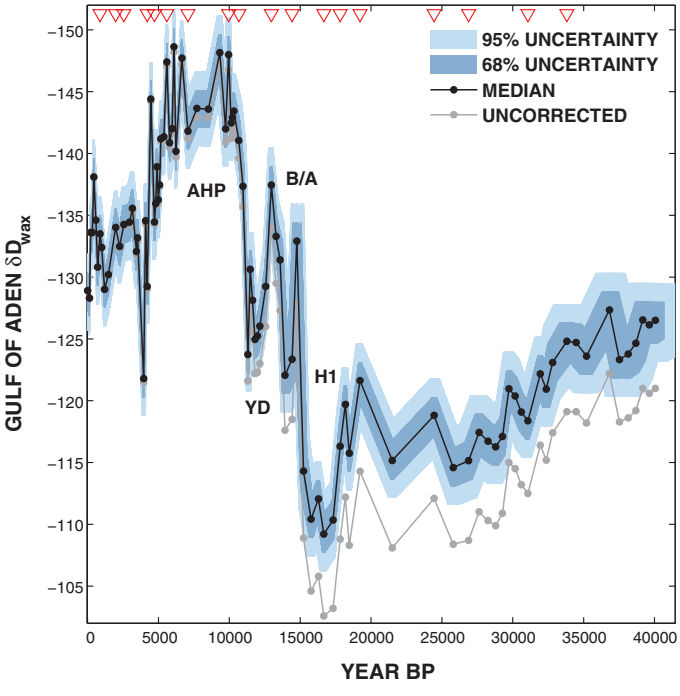

Fig. 2. δD_{wax} data from Gulf of Aden core P178-15P. δD_{wax} data is in per mil versus Vienna standard mean ocean water (VSMOW). Black line denotes median values, with the effect of changing ice volume on the isotopic values removed to isolate the regional hydroclimatic component (supplementary materials). Gray line shows the δD_{wax} data uncorrected for ice volume changes. Shadings indicate empirical 68 and 95% uncertainty bounds (including both analytical- and time-uncertainty) calculated via a Monte Carlo method (*27*). Red triangles denote the stratigraphic locations of radiocarbon dates.

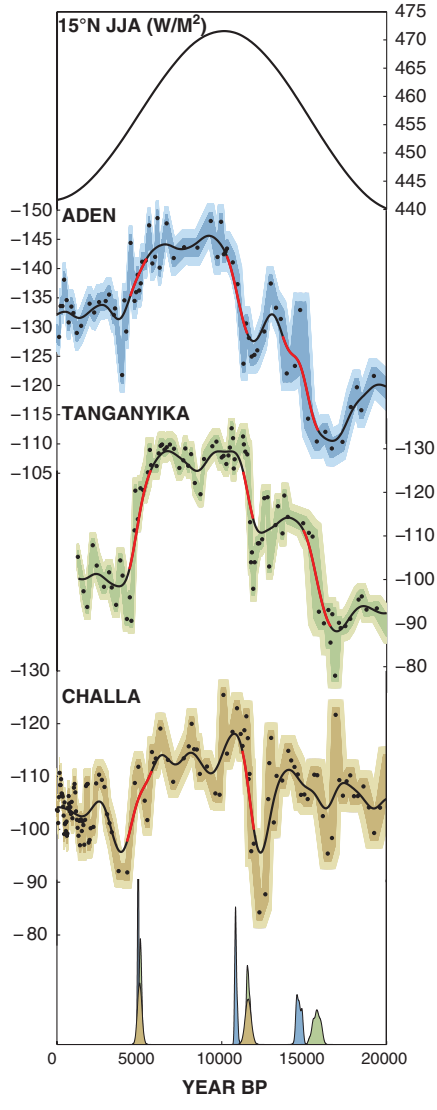

Fig. 3. JJA insolation at 15°N, δD_{wax} data from three sites in East Africa, and the timing of their abrupt transitions. JJA insolation is in watts per square meter, and δD_{wax} data is in per mil versus VSMOW. The effect of changing ice volume on the isotopic values has been removed to isolate the regional hydroclimatic component (supplementary materials). Black markers denote median values, and shadings indicate empirical 68 and 95% uncertainty bounds (including both analytical- and time-uncertainty) calculated via a Monte Carlo method (*27*). Black line indicates the 2000-year Gaussian smoothed time series for each site, with the identified transitions highlighted in red. Probability distributions (bottom) represent the timing of each highlighted transition given the dating uncertainties. Lake Challa δD_{wax} does not indicate a large drying associated with H1 and therefore lacks a H1–B/A transition (supplementary materials).

are known to have occurred and, at least in the eastern Arabian Sea, shifted the ^{14}C reservoir (*32*).

In contrast to the deglacial transitions, our analysis suggests that the termination of the AHP is likely synchronous between all three sites (χ^2 test, $P = 0.25$). Because the mid-Holocene is less likely to be affected by unknown uncertainties in the ^{14}C reservoir (*22*, *32*), we have more confidence that the inferred synchronicity is meaningful. Using Gaussian error reduction, the average timing of the AHP termination from these three East African sites is 4960 ± 70 years B.P. (2σ). This is similar to the revised AHP termination estimate from west Africa of 4900 ± 400 years B.P. (2σ) and is likely synchronous (*t* test, $P = 0.77$).

The observed durations of the identified transitions vary from centuries to millennia (Fig. 4); however, sedimentary factors (sedimentation rates and bioturbation) as well as the sampling rate of the proxy influence how the duration is expressed and attenuated in the time series. As evidence of this, we observed a strong relationship between the duration of the transition and proxy sampling interval (ΔT) [correlation coefficinet (r) = 0.95, $P = 0.0005$] (fig. S2). Normalizing the duration distributions by this sedimentation effect, we arrived at "theoretical" durations representing the most probable duration given a hypothetical infinite sampling rate (Fig. 4). We found that the calculated theoretical durations are short—occurring within centuries—and broadly similar between sites (Fig. 4). The theoretical duration of the termination of the AHP in our Gulf of Aden record ranges from 280 to 490 years. This duration is in accord with a recent analysis of lake level changes in Lake Turkana in northern Kenya: Detailed radiocarbon dating of exposed paleoshoreline horizons revealed that the water level in Lake Turkana dropped permanently by ~50 m within a few centuries at 5270 ± 300 years B.P. (also synchronous with our analyzed timing; *t* test, $P = 0.46$) (*33*). Taken together with our new data from the Gulf of Aden, this suggests that the termination of the AHP was abrupt across a relatively large sector of northeast Africa.

We recognize, however, that there is heterogeneity in terms of the timing and abruptness of the AHP termination across Africa according to the currently available proxy data. Although at low-resolution ($n = 29$ samples; mean ΔT = 470 years), a δD_{wax} record from Lake Victoria has been interpreted as reflecting a gradual termination of the AHP (*34*). Farther to the west, a δD_{wax} record that integrates the Congo drainage basin also shows a gradual termination (*10*), as does a record of the oxygen isotopic composition of seawater from the Gulf of Guinea (*11*). Likewise, to the north of our study site, $\delta^{18}O$ data measured on a Oman stalagmite from Qunf Cave (Fig. 1) suggests a gradual reduction in precipitation across the Arabian Peninsula (*19*). Collectively, these data suggest that abrupt behavior is not a universal feature across Africa and may be restricted to the western Sahara and East Africa.

If this is so, then the feedback mechanisms leading to the observed abrupt shifts may be relatively specific to these regions. In the Sahara and Sahel region, the nonlinear change in rainfall associated with the termination of the AHP likely involves vegetation feedbacks, which enhance the orbitally driven response by changing surface albedo and soil moisture (*35*, *36*). In contrast, vegetation feedbacks are not likely to have occurred within the humid central African zone, where proxy data suggest that vegetation has not shifted substantially (*10*). This may explain the lack of abrupt response in that region. Vegetation feedbacks are also hypothesized to be weaker in the eastern Saharan region because of regional differences in vegetation and soil moisture (*3*, *4*, *15*). In the extreme case, the Arabian Peninsula may not have acquired enough vegetation in the Early Holocene to promote a feedback in spite of more pluvial conditions; limited pollen data suggest a predominance of steppe and grassland but no development of shrubland or dry woodland (*1*, *37*). It is not clear whether vegetation feedbacks universally contributed to the abrupt shifts in East African hydroclimate. Carbon isotopes measured on the same leaf waxes at the sites analyzed here suggest that a vegetation feedback is plausible at Lake Tanganyika, which experienced a dramatic shift from a mixed humid woodland to a more open shrubland (fig. S3). However, there was relatively little shift in the vegetation near Lake Challa and in the Horn of Africa (fig. S3), suggesting that, as with the Arabian Peninsula, a vegetation-driven feedback is unlikely in arid East Africa.

Alternatively, we hypothesize that nonlinear behavior in East African rainfall, including the termination of the AHP, reflects convection feedbacks associated with Indian Ocean sea-surface temperatures (SSTs). This mechanism may explain the difference between the northeast African region and southern Oman. SSTs in the western Indian Ocean hover near the lower bound of the threshold for deep convection (26° to 28°C), and their relationship with deep convection is nonlinear (*38*). Therefore, very small changes in western Indian Ocean SSTs—such as those that occur during Indian Ocean Dipole or El Niño events, as well as oscillations on the multidecadal time scale—can alter the Walker Circulation in the Indian Ocean and induce anomalous deep convection and heavy rainfall in East Africa (*39*, *40*). Rainfall over the southern Arabian Peninsula, although susceptible to such variability (*41*), primarily falls from July through August in association with the Indian summer monsoon, and the influence of the latter likely dominates on orbital time scales (*19*, *21*). Therefore, whereas the gradual trend in the Qunf Cave speleothem record represents the direct response of Arabian hydroclimate to the orbitally driven waning of the boreal summer Indian monsoon, the abrupt shift in East Africa conceivably reflects a convective feedback with a different seasonal dimension. Model simulations suggest that during the Early Holocene, the northward migration of the summer monsoon winds in response to orbital forcing decreased latent heat flux out of the western Indian Ocean, leading to warmer SSTs during the following September-November ("short") rainy season, a reduced east-west SST gradient, and enhanced convection and rainfall over East Africa (*18*, *42*). As the winds migrated south during the Holocene in response to orbital forcing, a critical SST threshold may have been crossed, causing an abrupt cessation of deep convection during the short rainy season and regional aridity. Existing proxy data from the Arabian Sea indicate that Early Holocene SSTs were similar to, or perhaps slightly warmer than, present-day SSTs (*43*, *44*). Meanwhile, eastern Indian Ocean temperatures were slightly cooler (*45*), suggesting a reduced east-west temperature gradient that may have facilitated enhanced convection over East Africa, which is in agreement with the modeling results. It is unclear, however, whether these proxy data are reflecting a change in SSTs during a particular season.

Although further research is needed to investigate the role of Indian Ocean SSTs, the δD_{wax} data presented here suggest that the hydroclimate

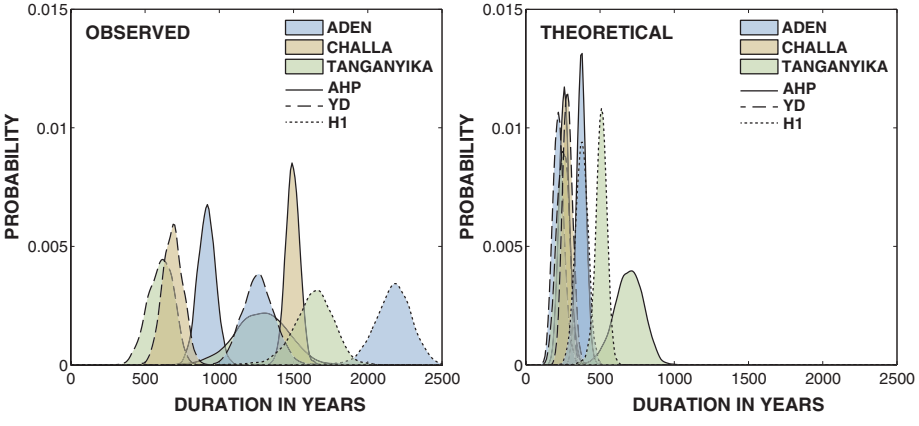

Fig. 4. Observed and theoretical probability distributions. Probability distributions are for the duration of the H1, YD, and AHP terminations at each East African site, corrected for the sampling interval effect (supplementary materials).

of East Africa can rapidly shift from dry and wet conditions. More generally, the Gulf of Aden δD_{wax} record provides a new benchmark of hydroclimatic history for the understudied Horn of Africa region. This study revises our understanding of Holocene climate change in northeast Africa, providing firm evidence that the abrupt termination of the AHP is not limited to the western Sahara. Although the forcings driving the abrupt shifts seen in the paleorecord since the LGM are large and not directly analogous to climate changes experienced today, the possibility of rapid changes in rainfall on human-relevant time scales (centuries) deserves further attention. Paleoclimate data from the past millennium suggest that easternmost Africa was much wetter than present only 300 years ago (*40*), attesting to the dynamic nature of the hydrological cycle in this region. Identifying the mechanisms driving these dramatic and rapid shifts in East African hydroclimate would greatly improve our understanding of the region's climatology, as well as future predictions of food and water security.

References and Notes

1. D. Jolly *et al.*, *J. Biogeogr.* **25**, 1007–1027 (1998).
2. A.-M. Lézine, C. Hély, C. Grenier, P. Braconnot, G. Krinner, *Quat. Sci. Rev.* **30**, 3001–3012 (2011).
3. V. Brovkin, M. Claussen, V. Petoukhov, A. Ganopolski, *J. Geophys. Res.* **103**, 31613 (1998).
4. M. Claussen *et al.*, *Geophys. Res. Lett.* **26**, 2037–2040 (1999).
5. P. Hoelzmann, B. Keding, H. Berke, S. Kröpelin, H.-J. Kruse, *Palaeogeogr. Palaeoclimatol. Palaeoecol.* **169**, 193–217 (2001).
6. R. Kuper, S. Kröpelin, *Science* **313**, 803–807 (2006).
7. J. E. Kutzbach, B. L. Otto-Bliesner, *J. Atmos. Sci.* **39**, 1177–1188 (1982).
8. M. Claussen, V. Gayler, *Global Ecol. Biogeo. Lett.* **6**, 369–377 (1997).
9. P. B. deMenocal *et al.*, *Quat. Sci. Rev.* **19**, 347–361 (2000).
10. E. Schefuß, S. Schouten, R. R. Schneider, *Nature* **437**, 1003–1006 (2005).
11. S. Weldeab, D. W. Lea, R. R. Schneider, N. Andersen, *Science* **316**, 1303–1307 (2007).
12. S. Kröpelin *et al.*, *Science* **320**, 765–768 (2008).
13. P. Francus *et al.*, *Sedimentology* **60**, 911–934 (2013).
14. J. A. Holmes, *Science* **320**, 752–753 (2008).
15. V. Brovkin, M. Claussen, *Science* **322**, 1326b (2008).
16. S. Bathiany, M. Claussen, K. Fraedrich, *Clim. Dyn.* **38**, 1775–1790 (2012).
17. F. A. Street-Perrott, D. S. Marchand, N. Roberts, S. P. Harrison, *U.S. Department of Energy Technical Report* 46 (U.S. Department of Energy Washington, DC, 1989).
18. J. E. Tierney, S. C. Lewis, B. I. Cook, A. N. LeGrande, G. A. Schmidt, *Earth Planet. Sci. Lett.* **307**, 103–112 (2011).
19. D. Fleitmann *et al.*, *Science* **300**, 1737–1739 (2003).
20. S. Jung, G. Davies, G. Ganssen, D. Kroon, *Earth Planet. Sci. Lett.* **221**, 27–37 (2004).
21. D. Fleitmann *et al.*, *Quat. Sci. Rev.* **26**, 170–188 (2007).
22. J. E. Tierney *et al.*, *Science* **322**, 252–255 (2008).
23. F. Pausata, D. Battisti, K. Nisancioglu, C. Bitz, *Nat. Geosci.* **4**, 474–480 (2011).
24. J. Slingo, H. Spencer, B. Hoskins, P. Berrisford, E. Black, *Philos. Trans. A Math. Phys. Eng. Sci.* **363**, 25–42 (2005).
25. J. C. Stager, D. B. Ryves, B. M. Chase, F. S. Pausata, *Science* **331**, 1299–1302 (2011).
26. J. E. Tierney, J. M. Russell, J. S. Sinninghe Damsté, Y. Huang, D. Verschuren, *Quat. Sci. Rev.* **30**, 798–807 (2011).
27. K. J. Anchukaitis, J. E. Tierney, *Clim. Dyn.* **41**, 1291–1306 (2013).
28. A. Long, B. Rippeteau, *Am. Antiq.* **39**, 205 (1974).
29. K. A. Hughen, T. I. Eglinton, L. Xu, M. C. Makou, *Science* **304**, 1955–1959 (2004).
30. M. Friedrich, B. Kromer, M. Spurk, J. Hofmann, K. Felix Kaiser, *Quat. Int.* **61**, 27–39 (1999).
31. J. E. Tierney, J. M. Russell, *Geophys. Res. Lett.* **34**, L15709 (2007).
32. M. Staubwasser, F. Sirocko, P. M. Grootes, H. Erlenkeuser, *Paleoceanography* **17**, 15-1–15-2 (2002).
33. Y. Garcin, D. Melnick, M. R. Strecker, D. Olago, J.-J. Tiercelin, *Earth Planet. Sci. Lett.* **331**, 322–334 (2012).
34. M. A. Berke *et al.*, *Quat. Sci. Rev.* **55**, 59–74 (2012).
35. J. G. Charney, *Q. J. R. Meteorol. Soc.* **101**, 193–202 (1975).
36. J. Shukla, Y. Mintz, *Science* **215**, 1498–1501 (1982).
37. A. Parker *et al.*, *J. Quaternary Sci.* **19**, 665–676 (2004).
38. C. Zhang, *J. Clim.* **6**, 1898–1913 (1993).
39. E. Black, J. Slingo, K. R. Sperber, *Mon. Weather Rev.* **131**, 74–94 (2003).
40. J. E. Tierney, J. E. Smerdon, K. J. Anchukaitis, R. Seager, *Nature* **493**, 389–392 (2013).
41. A. Chakraborty, S. K. Behera, M. Mujumdar, R. Ohba, T. Yamagata, *Mon. Weather Rev.* **134**, 598–617 (2006).
42. Y. Zhao *et al.*, *Clim. Dyn.* **25**, 777–800 (2005).
43. F. Rostek, E. Bard, L. Beaufort, C. Sonzogni, G. Ganssen, *Deep Sea Res. Part II Top. Stud. Oceanogr.* **44**, 1461–1480 (1997).
44. P. Anand *et al.*, *Paleoceanography* **23**, PA4207 (2008).
45. M. Mohtadi, S. Steinke, A. Lückge, J. Groeneveld, E. Hathorne, *Earth Planet. Sci. Lett.* **292**, 89–97 (2010).
46. E. Kalnay *et al.*, *Bull. Am. Meteorol. Soc.* **77**, 437–471 (1996).

Acknowledgments: This study was supported by National Science Foundation grant OCE-1203892 to J.E.T., National Oceanic and Atmospheric Administration award NAO80AR4320912 to P.B.d.M., and the Lamont-Doherty Earth Observatory (LDEO) Climate and Life Initiative. We thank E. Hamilton and C. Johnson for assistance with the stable isotope measurements; J.-B. Stuut, G. Ganssen, and C. Cleroux for assistance with core sampling; J. Fang and T. Guilderson for assistance with the radiocarbon dating; and C. Ummenhofer for comments on the initial versions of the manuscript. We thank the Captain and crew of the *R/V Pelagia* for their remarkable professionalism during the penultimate leg (Cruise 178; April to May 2001) of the scientific circumnavigation of the African continent. With co-chief scientist G. Ganssen, we were able to obtain valuable samples from this remote and geopolitically challenging region. This is LDEO contribution number 7739.

Supplementary Materials

www.sciencemag.org/content/342/6160/843/suppl/DC1
Materials and Methods
Figs. S1 to S3
Tables S1 and S2
References

13 May 2013; accepted 26 September 2013
Published online 10 October 2013;
10.1126/science.1240411

Dosage Compensation via Transposable Element Mediated Rewiring of a Regulatory Network

Christopher E. Ellison and Doris Bachtrog*

Transposable elements (TEs) may contribute to evolutionary innovations through the rewiring of networks by supplying ready-to-use cis regulatory elements. Genes on the *Drosophila* X chromosome are coordinately regulated by the male specific lethal (MSL) complex to achieve dosage compensation in males. We show that the acquisition of dozens of MSL binding sites on evolutionarily new X chromosomes was facilitated by the independent co-option of a mutant helitron TE that attracts the MSL complex (TE domestication). The recently formed neo-X recruits helitrons that provide dozens of functional, but suboptimal, MSL binding sites, whereas the older XR chromosome has ceased acquisition and appears to have fine-tuned the binding affinities of more ancient elements for the MSL complex. Thus, TE-mediated rewiring of regulatory networks through domestication and amplification may be followed by fine-tuning of the cis-regulatory element supplied by the TE and erosion of nonfunctional regions.

Active transposable elements (TEs) impose a substantial mutational burden on the host genome (*1*–*4*). However, there is growing evidence implicating TEs as drivers of key evolutionary innovations by creating or rewiring regulatory networks (*5*–*11*). Many TEs harbor a variety of regulatory motifs, and TE amplification may allow for the rapid accumulation of a specific motif throughout the genome, thus recruiting multiple genes into a single regulatory network (*12*).

In *Drosophila miranda*, multiple sex chromosome/autosome fusions have created a series of X chromosomes of differing ages (Fig. 1). The ancestral X chromosome, XL, is homologous to the *D. melanogaster* X and is at least 60 million years old (*13*). Chromosome XR became a sex chromosome ~15 million years ago and is shared among members of the *affinis* and *pseudoobscura* subgroups, whereas the neo-X chromosome is specific to *D. miranda* and originated only 1 million years ago (*14*, *15*). The male specific lethal (MSL) complex coordinates gene expression on the *Drosophila* male X to achieve dosage compensation (*16*). This complex is recruited to the X chromosome in males to high-affinity chromatin entry sites (CES) containing a conserved, roughly 21–base

Department of Integrative Biology, University of California, Berkeley, Berkeley, CA 94720, USA.
*Corresponding author. E-mail: dbachtrog@berkeley.edu

pair (bp)–long GA-rich sequence motif termed the MSL recognition element (MRE) (*17*). Once bound, the MSL-complex spreads from the CES in cis to actively transcribed genes, where it catalyzes the deposition of the activating histone modification H4K16ac, which ultimately results in a chromosome-wide twofold increase in gene expression levels (*16*). *D. miranda* males show MSL binding specific to the X chromosomes, associated with full dosage compensation of chromosomes XL and XR. In contrast, the neo-X shows incomplete dosage compensation (*18*).

The evolution of dosage compensation on XR and the neo-X involved co-option of the MSL machinery (*19*) and the creation of CES capable of recruiting this machinery, via MRE sequence motifs at a few hundred locations along the two X chromosomes. We used chromatin immunoprecipitation sequencing (ChIP-seq) profiling of MSL binding to conservatively define 132 CES on chromosome XL, 215 on XR, and 68 on the neo-X (*18*), and a more realistic estimate identifies 219 CES on XL, 383 on XR, and 175 on the neo-X (fig. S1) (*20*); we refer to these two groups as our "strict" versus "broad" set of CES. The CES on XR and the neo-X likely arose within the past 15 and 1 million years, respectively, after these chromosomes became X-linked in an ancestor of *D. miranda*.

Comparison of the genomic regions at strict neo-X CES sequences to their homologous regions in *D. pseudoobscura*, which are not X-linked and do not recruit the MSL complex, identified the mutational paths responsible for the formation of a MRE at 41 CES on the neo-X (*21*). In half of these sites, point mutations and short indels at prebinding sites created a stronger MRE. For the remaining half, however, the new MREs appeared to have been gained via a relatively large (~1 kb), *D. miranda*–specific insertion. Sanger resequencing and manual curation of the genome assembly at these sites allowed us to determine that these insertions are derived from a transposable element [homologous to the ISY element (*22*)] that is highly abundant in the genome of *D. miranda* and its relatives (>1000 copies in *D. miranda* and *D. pseudoobscura*) (Fig. 2A). The ISY element (~1150 bp) is a nonautonomous helitron (figs. S2 and S3) (*20*), a class of DNA-transposable elements that replicate through a rolling-circle mechanism (*23*, *24*). All 21 elements found at strict CES on the neo-X share a 10-bp deletion relative to the consensus ISY element, and we refer to the ISY sequence containing this deletion as ISX (Fig. 3A and fig. S4). ISX is also found at 24 of our broad CES and is present at 43% of strict CES and 30% of broad CES on the neo-X (figs. S5 and S6) (*20*). This 10-bp deletion creates a sequence motif more similar to the consensus MRE motif inferred from XL relative to the consensus ISY sequence (Fig. 2B) and thus might create a strong recruitment signal for the MSL-complex. The ISX element—but not ISY—is specific to *D. miranda* and highly enriched on the neo-X relative to other chromosomes (Fig. 3C and fig. S7) and strongly bound by the MSL complex

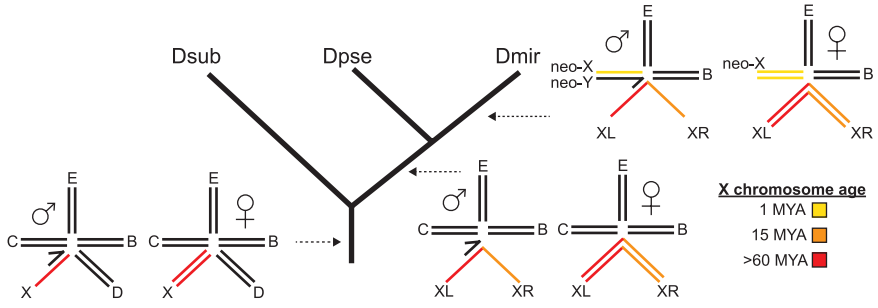

Fig. 1. Evolutionary history of *Drosophila miranda* sex chromosomes. The ancestral X chromosome shared by all members of the *Drosophila* genus (red) fused to an autosome ~15 million years ago, creating chromosome XR (orange). Another autosome fused to the Y chromosome ~1 million years ago, creating the neo-X chromosome (yellow). *D. miranda* thus harbors three X chromosomes of different ages. Dsub, *D. subobscura*; Dpse, *D. pseudoobscura*; and Dmir, *D. miranda*.

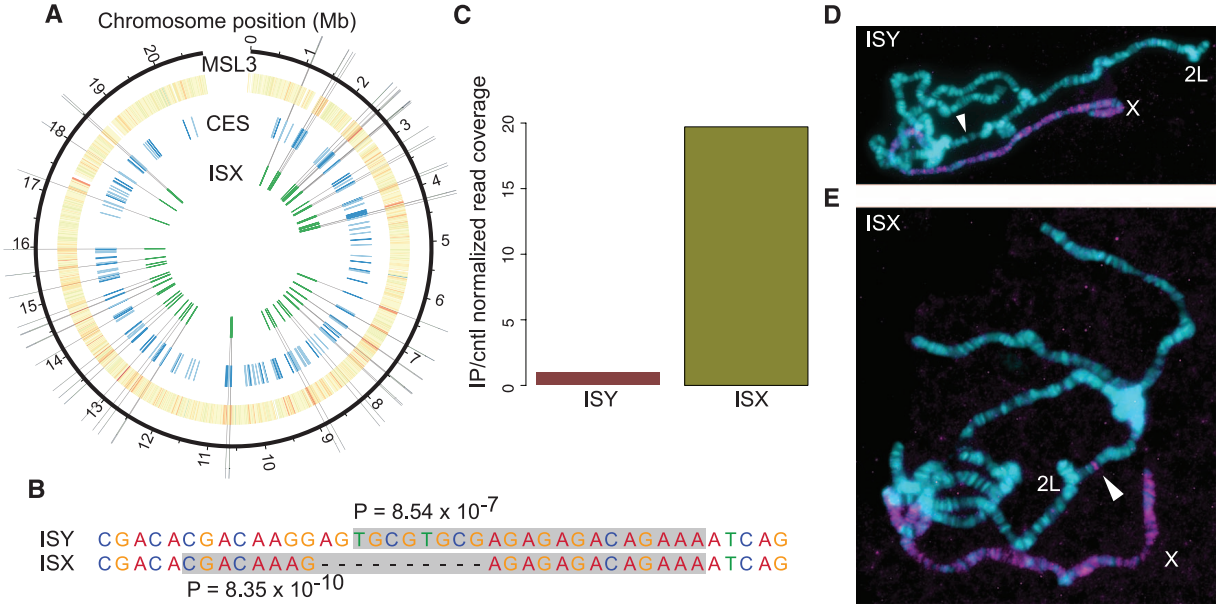

Fig. 2. ISX is a domesticated helitron TE that is associated with CES on the neo-X chromosome and recruits the MSL complex in transgenic assays. (**A**) Twenty-one of 68 strict MSL complex CES on the neo-X chromosome overlap *D. miranda*–specific insertions of the ISX element, and 69 (out of 77 total) neo-X–linked ISX elements lie within broad CES. (**B**) A derived 10-bp deletion differentiates ISX from the related ISY element and creates a stronger match to the MRE consensus motif identified from chromosome XL. *P* values are from FIMO (*27*) and are based on log-likelihood ratio scores between the *D. melanogaster* canonical MRE consensus motif and the sequence highlighted in gray. (**C**) MSL3 ChIP-seq data show that MSL complex binds ISX but not ISY elements. (**D** and **E**) Ectopic MSL-targeting by the ISX element from *D. miranda*, and lack of activity from the corresponding ISY element. Transgenic polytene chromosomes were stained with antibody to MSL2 (purple) to identify regions targeted by the MSL-complex, and 4′,6-diamidino-2-phenylindole to identify all chromosome arms (blue). An ISY and ISX element were each targeted to cytosite 37B7 (location denoted by white arrow) on chromosome 2L in *D. melanogaster*. (D) No staining is detected at 37B7 when the insertion contains ISY, (E) but we find robust MSL immunostaining at the location when the insertion contains ISX.

in vivo (Fig. 2C). Additionally, the sequence similarity among ISX elements found at CES on the neo-X (Fig. 3, A and B) is consistent with their recent acquisition on the neo-X, after the formation of the neo-sex chromosomes (*20*). Together, these results suggest that within the past 1 million years, the *D. miranda* lineage was invaded by a domesticated helitron that recruits hundreds of genes into the MSL regulatory network on the neo-X. This process involved the formation of a high-affinity MRE sequence motif via a 10-bp deletion, followed by amplification and fixation of this element at dozens of sites along the neo-X chromosome (figs. S8 and S9) (*20*).

We used a transgenic assay in *D. melanogaster* to functionally verify that the ISX element attracts the MSL complex and functions as a CES. We targeted our construct to the previously characterized autosomal landing site 37B7 in *D. melanogaster* (*25*). Immunostaining of male polytene chromosomes shows that the ISX element can recruit the MSL complex of *D. melanogaster*, but no staining was detected with the ISY element (Fig. 2, D and E, and figs. S10 and S11). A higher affinity of the MSL complex to ISX versus ISY was also confirmed by means of ChIP–quantitative polymerase chain reaction (fig. S12). We also used mutagenesis assays to convert this ISX element into ISY by inserting the 10-bp sequence (ISX → ISY) and deleted the 10-bp fragment from the ISY element to create ISX (ISY → ISX). Immunostaining confirmed that the ISX → ISY construct could no longer recruit the MSL-complex to an autosomal location, whereas the ISY → ISX transgene was now able to attract MSL to an autosomal landing site in *D. melanogaster* (fig. S13). Thus, the ISX element alone is able and sufficient to attract the MSL complex, and the 10-bp deletion creates a functional MSL recruitment site. This experimentally confirms that the amplification of this TE along the neo-X chromosome may have resulted in the rapid wiring of neo-X–linked genes

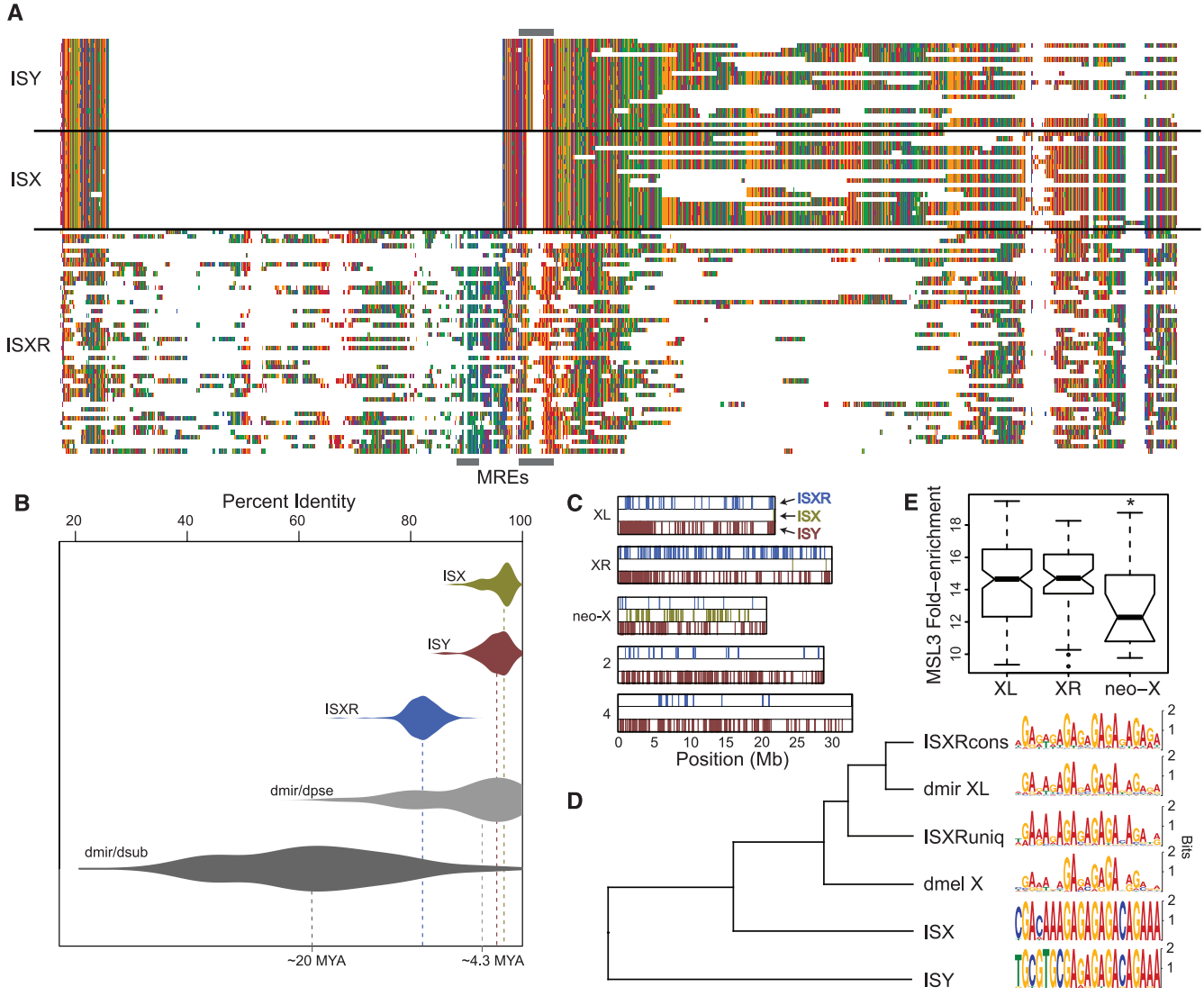

Fig. 3. The ISXR helitron is associated with CES on chromosome XR. (**A**) Multiple-sequence alignment showing helitrons from within neo-X CES (ISX), XR CES (ISXR), and the related ISY element. Gray boxes indicate approximate location of the MRE motifs in the alignment. (**B**) Divergence of elements from their consensus sequence places the burst of ISXR amplification after the divergence of *D. subobscura* from the *miranda*/*pseudoobscura* ancestor (>15 million years ago) and the ISX burst after the divergence of *D. pseudoobscura* and *D. miranda* (~4 million years ago) (*20*). (**C**) The ISY element is distributed evenly among *D. miranda* chromosomes [permutation test $P > 0.08$ in all cases, except for chromosome 4, where it is depleted (permutation test $P < 0.0001$)], whereas ISXR is enriched on XR, and ISX is enriched on the neo-X (permutation test $P < 0.0001$ in both cases) (additional details are available in table S2). (**D**) Clustering of the canonical *D. miranda* and *D. melanogaster* MRE motifs inferred from the ancient X chromosome along with the consensus from each helitron TE. ISXRcons refers to the ISXR MRE that is conserved with ISX, and ISXRuniq refers to the MRE that is specific to ISXR (*20*). (**E**) MSL3 ChIP-seq data show that XR CES–overlapping ISXR elements have a higher affinity for the MSL complex in vivo as compared with that of the neo-X CES that overlap ISX elements (comparing the distribution of MSL-enrichment from 21 strict CES created by ISX, versus 47 strict CES created by ISXR; Wilcoxon test, $P = 0.01$).

into the dosage compensation network. Dosage compensation of neo-X genes is advantageous because ~40% of homologous neo-Y genes are pseudogenized (*26*); however, because of its ability to recruit the MSL complex and induce dosage compensation, the ISX element should be selected against from autosomal locations. Indeed, out of a total of 82 copies of the ISX element, only two exist on an autosome, within repeat-rich and supposedly silenced regions on the dot chromosome (fig. S14) (*20*).

In the ancestor of the *affinis* and *pseudoobscura* subgroups (~15 million years ago), Muller element D became incorporated into the dosage compensation network after it fused to the ancestral X to form chromosome XR (Fig. 1). We compared all CES sequences on XR to determine whether they were enriched for sequence elements besides the MRE motif that would be indicative of a TE burst. Three repeat elements were present in ~22% of strict (and in 14.4% of broad) XR CES sequences, but not in the homologous regions from *D. subobscura*, where this chromosome is an autosome (Fig. 1). Furthermore, these elements were all determined to be conserved fragments from a single TE (hereafter referred to as ISXR), which is derived from the same helitron family as the ISY/ISX elements (Fig. 3A and fig. S15). Individual ISXR copies are less similar to each other than the ISX elements, and sequence divergence among the different copies of this TE is consistent with a burst of transposition activity coinciding with the formation of chromosome XR (Fig. 3B). Additionally, ISXR is enriched on chromosome XR (Fig. 3C), and similar to ISX/ISY, its autosomal homologs show less sequence similarity to the MRE consensus motif and cannot recruit the MSL-complex in vivo (fig. S16). ISXR contains a ~350-bp region that is not present in any of the ISY or ISX elements, and this region specific to ISXR contains an additional MRE motif in close proximity to the MRE whose location is conserved between the ISX and ISXR elements (Fig. 3, A and D, and fig. S17). In addition, although the location of the 3′ ISXR MRE is conserved with ISX, there is no evidence of the 10-bp deletion seen in ISX. The presence of this particular sequence region suggests that although ISX and ISXR evolved from a similar helitron progenitor TE, they represent independent TE domestications and chromosomal expansions at different time points (Fig. 3A and fig. S18) (*20*). Consistent with the more ancient expansion of ISXR, nonfunctional parts of the TE are severely eroded (Fig. 3A and fig. S15).

Similarity-based clustering of the MRE consensus motifs from each helitron subtype reveal that both ISXR MRE motifs are more similar to the canonical XL MRE motif, compared with the ISX MRE motif (Fig. 3D). This suggests that MSL binding motifs supplied by ISX may be suboptimal, whereas ISXR binding affinity is optimized. A large number of substitutions observed at MRE motifs among ISXR copies across the genome (fig. S19) (*20*) and elevated rate of evolution at homologous ISXR MRE sites relative to XL MREs across species (fig. S20) suggest that the ISXR element initially may have also harbored a suboptimal MRE motif (*20*). Over time, mutation and selection may have fine-tuned the nucleotide composition at ISXR independently across elements and species, to maximize MSL recruitment by increasing their similarity to the canonical XL MRE motif (Fig. 3D). In agreement with this observation, the TE-derived XR CES show a higher affinity for MSL complex in vivo as compared with that of those on the neo-X (Fig. 3E).

The recently formed sex chromosomes of *D. miranda* provide insights into the role of TEs in rewiring regulatory networks. The evolutionary pressure driving the acquisition of dosage compensation as well as the molecular mechanism of MSL function and targeting provide clear expectations of which genes should be recruited into the dosage compensation network, as well as when and how. Additionally, the comparison of XR and the neo-X allows us to study the dynamic process of TE-mediated wiring of chromosomal segments into the dosage-compensation network at two different evolutionary stages: both the initial incorporation of the neo-X chromosome by amplification of a domesticated TE and possible subsequent fine-tuning of the regulatory element supplied by the TE on XR, together with the erosion of TE sequence not required for MSL-binding. Our data support a three-step model for TE-mediated rewiring of regulatory networks (domestication, amplification, and potential fine-tuning) followed by erosion of nonfunctional parts of the transposon (Fig. 4). Eventually, the footprints left behind by TE-mediated rewiring will completely vanish, and many ancient bursts of domesticated TEs that rewired regulatory networks are likely to go undetected. Indeed, we do not observe any TE relics within the CES of chromosome XL that acquired MSL-mediated dosage compensation over 60 million years ago, either because they evolved via a different mechanism or deletions and substitutions have degraded the signal of TE involvement to the point at which they are no longer recognizable.

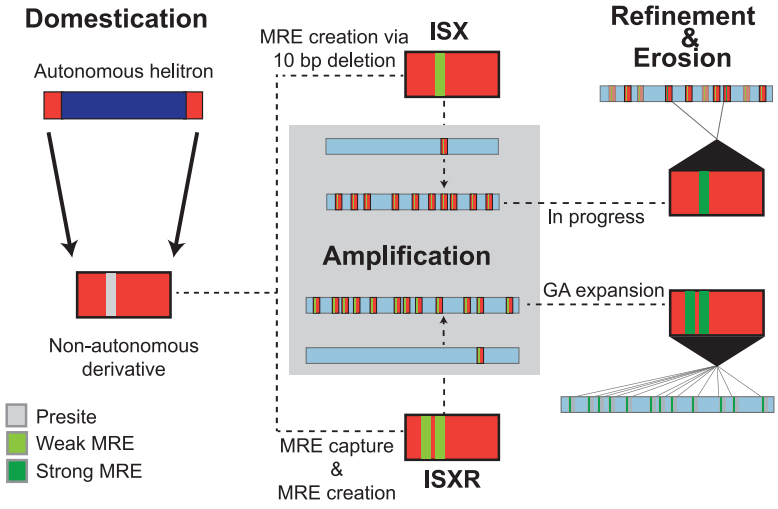

Fig. 4. TE-mediated evolution of MSL complex CES. Comparison of the two evolutionary time points of acquiring chromatin entry sites on XR and the neo-X suggest a three-step model for the TE-mediated wiring of a newly evolved X chromosome into the dosage compensation network followed by erosion of nonfunctional elements of the TE. The first step, domestication, involves the acquisition of a MRE sequence motif capable of acting as a CES for the MSL complex. The domesticated TE is amplified across the genome and beneficial on a newly formed X chromosome but selected against on autosomal locations. This results in the accumulation of the domesticated TE, along with the MRE motif that it carries, on the X. The amplified MRE motif may initially be suboptimal, as seen with the younger ISX elements on the neo-X, but over time, secondary fine-tuning mutations within each MRE can refine the ability to recruit optimal levels of MSL complex, as seem to have occurred with the older ISXR elements on XR. This is accompanied by erosion of TE sequences that are not required for MSL-binding, eventually degrading the signature of TE involvement for supplying CES.

References and Notes

1. B. Charlesworth, D. Charlesworth, *Genet. Res.* **42**, 1 (1983).
2. W. F. Doolittle, C. Sapienza, *Nature* **284**, 601–603 (1980).
3. D. A. Hickey, *Genetics* **101**, 519–531 (1982).
4. L. E. Orgel, F. H. Crick, *Nature* **284**, 604–607 (1980).
5. V. J. Lynch, R. D. Leclerc, G. May, G. P. Wagner, *Nat. Genet.* **43**, 1154–1159 (2011).
6. G. Bourque *et al.*, *Genome Res.* **18**, 1752–1762 (2008).
7. G. Kunarso *et al.*, *Nat. Genet.* **42**, 631–634 (2010).
8. T. Wang *et al.*, *Proc. Natl. Acad. Sci. U.S.A.* **104**, 18613–18618 (2007).
9. R. Johnson *et al.*, *Nucleic Acids Res.* **34**, 3862–3877 (2006).
10. F. Bringaud *et al.*, *PLOS Pathog.* **3**, 1291–1307 (2007).
11. M. Cowley, R. J. Oakey, *PLOS Genet.* **9**, e1003234 (2013).
12. C. Feschotte, *Nat. Rev. Genet.* **9**, 397–405 (2008).
13. S. Richards *et al.*, *Genome Res.* **15**, 1–18 (2005).
14. A. B. Carvalho, A. G. Clark, *Science* **307**, 108–110 (2005).
15. D. Bachtrog, B. Charlesworth, *Nature* **416**, 323–326 (2002).

16. T. Conrad, A. Akhtar, *Nat. Rev. Genet.* **13**, 123–134 (2011).
17. A. A. Alekseyenko *et al.*, *Cell* **134**, 599–609 (2008).
18. A. A. Alekseyenko *et al.*, *Genes Dev.* **27**, 853–858 (2013).
19. I. Marín, A. Franke, G. J. Bashaw, B. S. Baker, *Nature* **383**, 160–163 (1996).
20. Materials and methods are available as supplementary materials on *Science* Online.
21. Q. Zhou, C. E. Ellison, V. B. Kaiser, A. A. Alekseyenko, A. A. Gorchakov, D. Bachtrog, *PLoS Biol.* **11**, e1001711 (2013).
22. M. Steinemann, S. Steinemann, *Proc. Natl. Acad. Sci. U.S.A.* **89**, 7591–7595 (1992).
23. J. Jurka, *Repbase Reports* **12**, 1376 (2012).
24. V. V. Kapitonov, J. Jurka, *Trends Genet.* **23**, 521–529 (2007).
25. J. R. Bateman, A. M. Lee, C. T. Wu, *Genetics* **173**, 769–777 (2006).
26. Q. Zhou, D. Bachtrog, *Science* **337**, 341–345 (2012).
27. C. E. Grant, T. L. Bailey, W. S. Noble, *Bioinformatics* **27**, 1017–1018 (2011).

Acknowledgments: This work was funded by NIH grants (R01GM076007 and R01GM093182) and a Packard Fellowship to D.B. and a NIH postdoctoral fellowship to C.E.E. All DNA-sequencing reads generated in this study are deposited at the National Center for Biotechnology Information Short Reads Archive (www.ncbi.nlm.nih.gov/sra) under the accession no. SRS402821. The genome assemblies are available at the National Center for Biotechnology Information under BioProject PRJNA77213. We thank Z. Walton and A. Gorchakov for technical assistance.

Supplementary Materials

www.sciencemag.org/content/342/6160/846/suppl/DC1
Materials and Methods
Supplementary Text
Figs. S1 to S20
Tables S1 to S3
References (*28*–*54*)

23 April 2013; accepted 30 September 2013
10.1126/science.1239552

High-Resolution Global Maps of 21st-Century Forest Cover Change

M. C. Hansen,[1]* P. V. Potapov,[1] R. Moore,[2] M. Hancher,[2] S. A. Turubanova,[1] A. Tyukavina,[1] D. Thau,[2] S. V. Stehman,[3] S. J. Goetz,[4] T. R. Loveland,[5] A. Kommareddy,[6] A. Egorov,[6] L. Chini,[1] C. O. Justice,[1] J. R. G. Townshend[1]

Quantification of global forest change has been lacking despite the recognized importance of forest ecosystem services. In this study, Earth observation satellite data were used to map global forest loss (2.3 million square kilometers) and gain (0.8 million square kilometers) from 2000 to 2012 at a spatial resolution of 30 meters. The tropics were the only climate domain to exhibit a trend, with forest loss increasing by 2101 square kilometers per year. Brazil's well-documented reduction in deforestation was offset by increasing forest loss in Indonesia, Malaysia, Paraguay, Bolivia, Zambia, Angola, and elsewhere. Intensive forestry practiced within subtropical forests resulted in the highest rates of forest change globally. Boreal forest loss due largely to fire and forestry was second to that in the tropics in absolute and proportional terms. These results depict a globally consistent and locally relevant record of forest change.

Changes in forest cover affect the delivery of important ecosystem services, including biodiversity richness, climate regulation, carbon storage, and water supplies (*1*). However, spatially and temporally detailed information on global-scale forest change does not exist; previous efforts have been either sample-based or employed coarse spatial resolution data (*2*–*4*). We mapped global tree cover extent, loss, and gain for the period from 2000 to 2012 at a spatial resolution of 30 m, with loss allocated annually. Our global analysis, based on Landsat data, improves on existing knowledge of global forest extent and change by (i) being spatially explicit; (ii) quantifying gross forest loss and gain; (iii) providing annual loss information and quantifying trends in forest loss; and (iv) being derived through an internally consistent approach that is exempt from the vagaries of different definitions, methods, and data inputs. Forest loss was defined as a stand-replacement disturbance or the complete removal of tree cover canopy at the Landsat pixel scale. Forest gain was defined as the inverse of loss, or the establishment of tree canopy from a nonforest state. A total of 2.3 million km^2 of forest were lost due to disturbance over the study period and 0.8 million km^2 of new forest established. Of the total area of combined loss and gain (2.3 million km^2 + 0.8 million km^2), 0.2 million km^2 of land experienced both loss and subsequent gain in forest cover during the study period. Global forest loss and gain were related to tree cover density for global climate domains, ecozones, and countries (refer to tables S1 to S3 for all data references and comparisons). Results are depicted in Fig. 1 and are viewable at full resolution at http://earthenginepartners.appspot.com/science-2013-global-forest.

The tropical domain experienced the greatest total forest loss and gain of the four climate domains (tropical, subtropical, temperate, and boreal), as well as the highest ratio of loss to gain (3.6 for >50% of tree cover), indicating the prevalence of deforestation dynamics. The tropics were the only domain to exhibit a statistically significant trend in annual forest loss, with an estimated increase in loss of 2101 km^2/year. Tropical rainforest ecozones totaled 32% of global forest cover loss, nearly half of which occurred in South American rainforests. The tropical dry forests of South America had the highest rate of tropical forest loss, due to deforestation dynamics in the Chaco woodlands of Argentina, Paraguay (Fig. 2A), and Bolivia. Eurasian rainforests (Fig. 2B) and dense tropical dry forests of Africa and Eurasia also had high rates of loss.

Recently reported reductions in Brazilian rainforest clearing over the past decade (*5*) were confirmed, as annual forest loss decreased on average 1318 km^2/year. However, increased annual loss of Eurasian tropical rainforest (1392 km^2/year), African tropical moist deciduous forest (536 km^2/year), South American dry tropical forest (459 km^2/year), and Eurasian tropical moist deciduous (221 km^2/year) and dry (123 km^2/year) forests more than offset the slowing of Brazilian deforestation. Of all countries globally, Brazil exhibited the largest decline in annual forest loss, with a high of over 40,000 km^2/year in 2003 to 2004 and a low of under 20,000 km^2/year in 2010 to 2011. Of all countries globally, Indonesia exhibited the largest increase in forest loss (1021 km^2/year), with a low of under 10,000 km^2/year from 2000 through 2003 and a high of over 20,000 km^2/year in 2011 to 2012. The converging rates of forest disturbance of Indonesia and Brazil are shown in Fig. 3. Although the short-term decline of Brazilian deforestation is well documented, changing legal frameworks governing Brazilian forests could reverse this trend (*6*). The effectiveness of Indonesia's recently instituted moratorium on new licensing of concessions in primary natural forest and peatlands (*7*), initiated in 2011, is to be determined.

Subtropical forests experience extensive forestry land uses where forests are often treated as a crop and the presence of long-lived natural forests is comparatively rare (*8*). As a result, the highest proportional losses of forest cover and the lowest ratio of loss to gain (1.2 for >50% of tree cover) occurred in the subtropical climate domain. Aggregate forest change, or the proportion of total forest loss and gain relative to year-2000 forest area [(loss+gain)/2000 forest], equaled 16%, or more than 1% per year across all forests within the domain. Of the 10 subtropical humid and dry forest ecozones, 5 have aggregate forest change >20%, three >10%, and two >5%. North American subtropical forests of the southeastern United States are unique in terms of change dynamics because of short-cycle tree planting and harvesting (Fig. 2C). The disturbance rate of this ecozone was four times that of South American

[1]Department of Geographical Sciences, University of Maryland, College Park, MD 20742, USA. [2]Google, Mountain View, CA, USA. [3]Department of Forest and Natural Resources Management, State University of New York, Syracuse, NY, USA. [4]Woods Hole Research Center, 149 Woods Hole Road, Falmouth, MA 02540, USA. [5]Earth Resources Observation and Science, United States Geological Survey, 47914 252nd Street, Sioux Falls, SD 57198, USA. [6]Geographic Information Science Center of Excellence, South Dakota State University, Brookings, SD, USA.

*Corresponding author. E-mail: mhansen@umd.edu

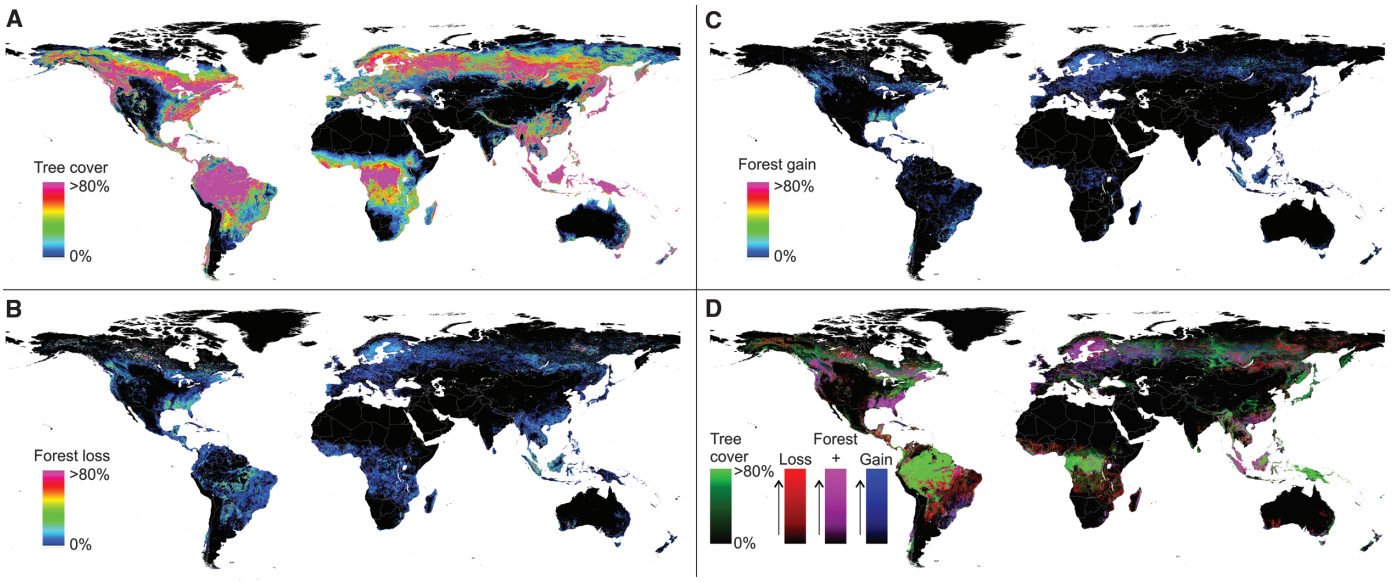

Fig. 1. (A) Tree cover, (B) forest loss, and (C) forest gain. A color composite of tree cover in green, forest loss in red, forest gain in blue, and forest loss and gain in magenta is shown in (**D**), with loss and gain enhanced for improved visualization. All map layers have been resampled for display purposes from the 30-m observation scale to a 0.05° geographic grid.

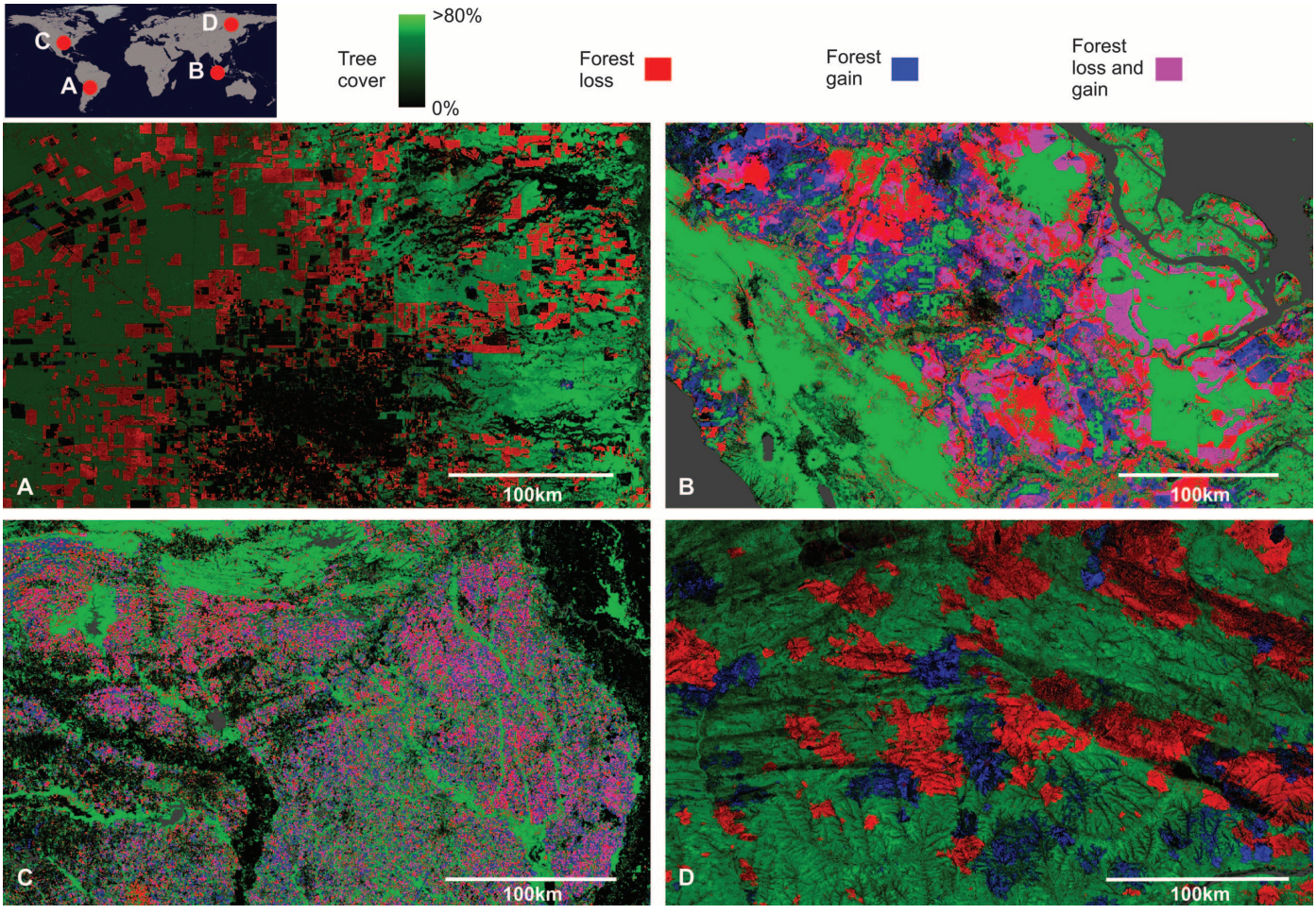

Fig. 2. Regional subsets of 2000 tree cover and 2000 to 2012 forest loss and gain. (**A**) Paraguay, centered at 21.9°S, 59.8°W; (**B**) Indonesia, centered at 0.4°S, 101.5°E; (**C**) the United States, centered at 33.8°N, 93.3°W; and (**D**) Russia, centered at 62.1°N, 123.4°E.

rainforests during the study period; over 31% of its forest cover was either lost or regrown. Areas of colocated loss and gain (magenta tones in Fig. 1D), indicating intensive forestry practices, are found on all continents within the subtropical climate domain, including South Africa, central Chile, southeastern Brazil, Uruguay, southern China, Australia, and New Zealand.

The temperate climatic domain has a forestry-dominant change dynamic and a relatively low ratio of loss to gain (1.6 for >50% of tree cover). Oceanic ecozones, in particular, are similar to the subtropics in the intensity of indicated forest land use. The northwest United States is an area of intensive forestry, as is the entire range of temperate Canada. The intermountain West of North America exhibits a loss dynamic, largely due to fire, logging, and disease [for example, large-scale tree mortality due to mountain pine bark beetle infestation, most evident in British Colombia, Canada (*9*)]. Temperate Europe has a forestry dynamic with Estonia and Latvia exhibiting a high ratio of loss to gain. Portugal, which straddles the temperate and subtropical domains, has a complicated dynamic of forestry and forest loss due to fire; the resulting aggregate change dynamic is fourth in intensity globally. Elevated loss due to storm damage is indicated for a few areas. For example, a 2005 extratropical cyclone led to a historic blowdown of southern Sweden temperate forests, and a 2009 windstorm leveled extensive forest areas in southwestern France (*10*).

Fire is the most significant cause of forest loss in boreal forests (*11*), and it occurred across a range of tree canopy densities. Given slower regrowth dynamics, the ratio of boreal forest loss to gain is high over the study period (2.1 for >50% of tree cover). Boreal coniferous and mountain ecozones are similar in terms of forest loss rates, with North America having a higher overall rate and Eurasia a higher absolute area of loss. Forest gain is substantial in the boreal zone, with Eurasian coniferous forests having the largest area of gain of all global ecozones during the study period, due to forestry, agricultural abandonment (*12*), and forest recovery after fire [as in European Russia and the Siberia region of Russia (Fig. 2D)]. Russia has the most forest loss globally. Co-located gain and loss are nearly absent in the high-latitude forests of the boreal domain, reflecting a slower regrowth dynamic in this climatic domain. Areas with loss and gain in close proximity, indicating forestry land uses, are found within nearly the entirety of Sweden and Finland, the boreal/temperate transition zone in eastern Canada, parts of European Russia, and along the Angara River in central Siberia, Russia.

A goal of large-area land cover mapping is to produce globally consistent characterizations that have local relevance and utility; that is, reliable information across scales. Figure S1 reflects this capability at the national scale. Two measures of change, (i) proportion of total aggregate forest change relative to year-2000 forest area [(loss + gain)/2000 forest], shown in column q of table S3; and (ii) proportion of total change that is loss [loss/(loss + gain)], calculated from columns b and c in table S3, are displayed. The proportion of total aggregate forest change emphasizes countries with likely forestry practices by including both loss and gain in its calculation, whereas the proportion of loss to gain measure differentiates countries experiencing deforestation or another loss dynamic without a corresponding forest recovery signal. The two ratio measures normalize the forest dynamic in order to directly compare national-scale change regardless of country size or absolute area of change dynamic. In fig. S1, countries that have lost forests without gain are high on the *y* axis (Paraguay, Mongolia, and Zambia). Countries with a large fraction of forest area disturbed and/or reforested/afforested are high on the *x* axis (Swaziland, South Africa, and Uruguay). Thirty-one countries have an aggregate dynamic >1% per year, 11 have annual loss rates >1%, and 5 have annual gain rates of >1%. Figure S2 compares forest change dynamics disaggregated by ecozone (http://foris.fao.org/static/data/fra2010/ecozones2010.jpg).

Brazil is a global exception in terms of forest change, with a dramatic policy-driven reduction in Amazon Basin deforestation. Although Brazilian gross forest loss is the second highest globally, other countries, including Malaysia, Cambodia, Cote d'Ivoire, Tanzania, Argentina, and Paraguay, experienced a greater percentage of loss of forest cover. Given consensus on the value of natural forests to the Earth system, Brazil's policy intervention is an example of how awareness of forest valuation can reverse decades of previous widespread deforestation. International policy initiatives, such as the United Natons Framework Convention of Climate Change Reducing Emissions from Deforestation and forest Degradation (REDD) program (*13*), often lack the institutional investment and scientific capacity to begin implementation of a program that can make use of the global observational record; in other words, the policy is far ahead of operational capabilities (*14*). Brazil's use of Landsat data in documenting trends in deforestation was crucial to its policy formulation and implementation. To date, only Brazil produces and shares spatially explicit information on annual forest extent and change. The maps and statistics we present can be used as an initial reference for a number of countries lacking such data, as a spur to capacity building in the establishment of national-scale forest extent and change maps, and as a basis of comparison in evolving national monitoring methods.

Global-scale studies require systematic global image acquisitions available at low or no direct

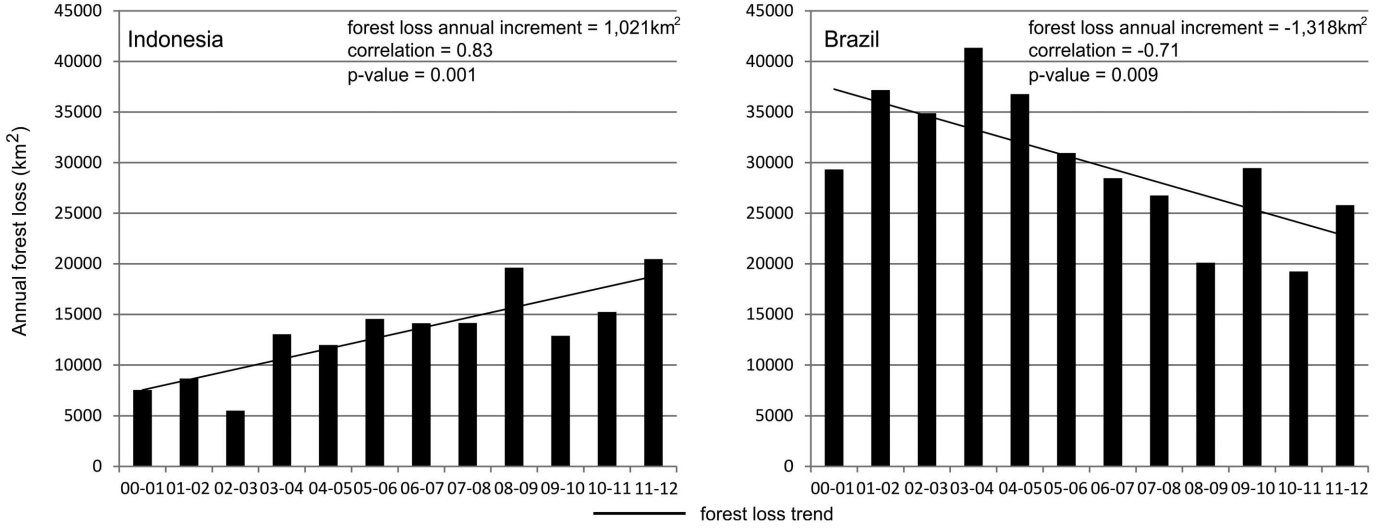

Fig. 3. Annual forest loss totals for Brazil and Indonesia from 2000 to 2012. The forest loss annual increment is the slope of the estimated trend line of change in annual forest loss.

cost and the preprocessing of geometric and radiometric corrections of satellite imagery, exemplified by the Landsat program. Given such progressive data policies and image processing capabilities, it is now possible to use advanced computing systems, such as the Google cloud, to efficiently process and characterize global-scale time-series data sets in quantifying land change. There are several satellite systems in place or planned for collecting data with similar capabilities to Landsat. Similar free and open data policies would enable greater use of these data for public good and foster greater transparency of the development, implementation, and reactions to policy initiatives that affect the world's forests.

The information content of the presented data sets, which are publicly available, provides a transparent, sound, and consistent basis on which to quantify critical environmental issues, including (i) the proximate causes of the mapped forest disturbances (*15*); (ii) the carbon stocks and associated emissions of disturbed forest areas (*16*–*18*); (iii) the rates of growth and associated carbon stock gains for both managed and unmanaged forests (*19*); (iv) the status of remaining intact natural forests of the world and threats to biodiversity (*20*, *21*); (v) the effectiveness of existing protected-area networks (*22*); (vi) the economic drivers of natural forest conversion to more intensive land uses (*23*); (vii) the relationships between forest dynamics and social welfare, health, and other relevant human dimensions data; (viii) forest dynamics associated with governance and policy actions—and many other regional-to-global–scale applications.

References and Notes

1. J. A. Foley *et al.*, *Science* **309**, 570–574 (2005).
2. M. C. Hansen, S. V. Stehman, P. V. Potapov, *Proc. Natl. Acad. Sci. U.S.A.* **107**, 8650–8655 (2010).
3. Food and Agricultural Organization of the United Nations, *Global Forest Land-Use Change 1990-2005, FAO Forestry Paper No. 169* (Food and Agricultural Organization of the United Nations, Rome, 2012).
4. M. Hansen, R. DeFries, *Ecosystems* **7**, 695–716 (2004).
5. Instituto Nacional de Pesquisas Especias, *Monitoring of the Brazilian Amazonian Forest by Satellite, 2000-2012* (Instituto Nacional de Pesquisas Especias, San Jose dos Campos, Brazil, 2013).
6. G. Sparovek, G. Berndes, A. G. O. P. Barretto, I. L. F. Klug, *Environ. Sci. Policy* **16**, 65–72 (2012).
7. D. P. Edwards, W. F. Laurance, *Nature* **477**, 33 (2011).
8. M. Drummond, T. Loveland, *Bioscience* **60**, 286–298 (2010).
9. W. A. Kurz *et al.*, *Nature* **452**, 987–990 (2008).
10. B. Gardiner *et al.*, *Destructive Storms in European Forests: Past and Forthcoming Impacts* (European Forest Institute, Freiburg, Germany, 2010).
11. P. Potapov, M. Hansen, S. Stehman, T. Loveland, K. Pittman, *Remote Sens. Environ.* **112**, 3708–3719 (2008).
12. A. Prishchepov, D. Muller, M. Dubinin, M. Baumann, V. Radeloff, *Land Use Policy* **30**, 873–884 (2013).
13. United Nations Framework Convention on Climate Change, *Reducing Emissions from Deforestation in Developing Countries: Approaches to Stimulate Action – Draft Conclusions Proposed by the President* (United Nations Framework Convention on Climate Change Secretariat, Bonn, Germany, 2005).
14. R. Houghton *et al.*, *Carbon Manage.* **1**, 253–259.
15. H. Geist, E. Lambin, *Bioscience* **52**, 143–150 (2002).
16. S. S. Saatchi *et al.*, *Proc. Natl. Acad. Sci. U.S.A.* **108**, 9899–9904 (2011).
17. A. Baccini *et al.*, *Nature Clim. Change* **2**, 182–185 (2012).
18. N. L. Harris *et al.*, *Science* **336**, 1573–1576 (2012).
19. R. Waterworth, G. Richards, C. Brack, D. Evans, *For. Ecol. Manage.* **238**, 231–243 (2007).
20. P. Potapov *et al.*, *Ecol. Soc.* **13**, 51 (2008).
21. T. M. Brooks *et al.*, *Science* **313**, 58–61 (2006).
22. A. S. Rodrigues *et al.*, *Nature* **428**, 640–643 (2004).
23. T. Rudel, *Rural Sociol.* **63**, 533–552 (1998).

Acknowledgments: Support for Landsat data analysis and characterization was provided by the Gordon and Betty Moore Foundation, the United States Geological Survey, and Google, Inc. GLAS data analysis was supported by the David and Lucile Packard Foundation. Development of all methods was supported by NASA through its Land Cover and Land Use Change, Terrestrial Ecology, Applied Sciences, and MEaSUREs programs (grants NNH05ZDA001N, NNH07ZDA001N, NNX12AB43G, NNX12AC78G, NNX08AP33A, and NNG06GD95G) and by the U.S. Agency for International Development through its CARPE program. Any use of trade, firm, or product names is for descriptive purposes only and does not imply endorsement by the U.S. government. Results are depicted and viewable online at full resolution: http://earthenginepartners.appspot.com/science-2013-global-forest.

Supplementary Materials

www.sciencemag.org/content/342/6160/850/suppl/DC1
Materials and Methods
Supplementary Text
Figs. S1 to S8
Tables S1 to S5
References (*24*–*40*)

14 August 2013; accepted 15 October 2013
10.1126/science.1244693

Changes in Cytoplasmic Volume Are Sufficient to Drive Spindle Scaling

James Hazel,[1] Kaspars Krutkramelis,[2] Paul Mooney,[1] Miroslav Tomschik,[1] Ken Gerow,[3] John Oakey,[2] J. C. Gatlin[1]*

The mitotic spindle must function in cell types that vary greatly in size, and its dimensions scale with the rapid, reductive cell divisions that accompany early stages of development. The mechanism responsible for this scaling is unclear, because uncoupling cell size from a developmental or cellular context has proven experimentally challenging. We combined microfluidic technology with *Xenopus* egg extracts to characterize spindle assembly within discrete, geometrically defined volumes of cytoplasm. Reductions in cytoplasmic volume, rather than developmental cues or changes in cell shape, were sufficient to recapitulate spindle scaling observed in *Xenopus* embryos. Thus, mechanisms extrinsic to the spindle, specifically a limiting pool of cytoplasmic component(s), play a major role in determining spindle size.

Organelles and other intracellular structures must scale with cell size in order to function properly. Maintenance of these dimensional relationships is challenged by the rapid and reductive cell divisions that characterize early embryogenesis in many organisms. The cellular machine that drives these divisions, the mitotic spindle, functions to segregate chromosomes in cells that vary greatly in size while also adapting to rapid changes in cell size. The issue of scale is epitomized during *Xenopus* embryogenesis, where a rapid series of divisions reduces cell size 100-fold: from the 1.2-mm-diameter fertilized egg to ~12-μm-diameter cells in the adult frog (*1*). In large blastomeres, spindle length reaches an upper limit that is uncoupled from changes in cell size. However, as cell size decreases, a strong correlation emerges between spindle length and cell size (*2*). Although this scaling relationship has been characterized in vivo for several different organisms, little is known about the direct regulation of spindle size by cell size or the underlying mechanism(s) (*2*–*4*). Spindle size may be directly dictated by the physical dimensions of a cell, perhaps through microtubule-mediated interaction with the cell cortex [i.e., boundary sensing (*5*–*7*)]. Alternatively, cell size could constrain spindle size by providing a fixed and finite cytoplasmic volume and, therefore, a limiting pool of resources such as cytoplasmic spindle assembly or length-determining components [i.e., component limitation (*8*, *9*)]. Last, mechanisms intrinsic to the spindle could be actively tuned in response to systematic changes in cytoplasmic composition occurring during development [i.e., developmental cues (*10*, *11*)].

To elucidate the responsible scaling mechanism(s), we developed a microfluidic-based platform to confine spindle assembly in geometrically defined volumes of *Xenopus* egg extract (*12*). Interphase extract containing *Xenopus* sperm nuclei was induced to enter mitosis and immediately pumped into a microfluidic droplet-generating device before nuclear envelope breakdown and the onset of spindle assembly. At the same time, a fluorinated oil/surfactant mixture was pumped into the device through a second inlet. These two discrete, immiscible phases merged at a T-shaped junction within the device to produce stable emulsions of extract droplets in a continuous oil phase (Fig. 1, A and C). Changing the T-junction channel dimensions and relative flow rates of the two phases

[1]Department of Molecular Biology, University of Wyoming, Laramie, WY 82071, USA. [2]Department of Chemical and Petroleum Engineering, University of Wyoming, Laramie, WY 82071, USA. [3]Department of Statistics, University of Wyoming, Laramie, WY 82071, USA.

*Corresponding author. E-mail: jgatlin@uwyo.edu

enabled us to tune droplet volume. Droplet shape could be controlled independently by changing the geometry and dimensions of the device's collection region. In this way, we were able to produce three distinct geometries: spheres, flattened discs, and axially elongated "slugs" (Fig. 1, B and C). After encapsulation, nuclei size and shape resembled those of their unencapsulated counterparts (Fig. 1C), suggesting that the process of droplet generation did not appreciably perturb nuclear morphology.

To examine the relationship between steady-state spindle length and cytoplasmic volume, we encapsulated interphase nuclei within spherical droplets ranging in diameter from 20 to 120 μm. Bipolar spindle assembly was observed in droplets of greater than ~30 μm diameter, permitting measurements of spindle length by using fluorescence microscopy (Fig. 2, A and B). Spindles exhibited isometric scaling, so we used the single metric of spindle length to serve as a reasonable proxy for spindle size (Fig. 2A). This also allowed direct comparisons with previously published scaling data in which length was the only reported spindle dimension. These measurements defined two distinct regimes that described the relationship between spindle length and droplet

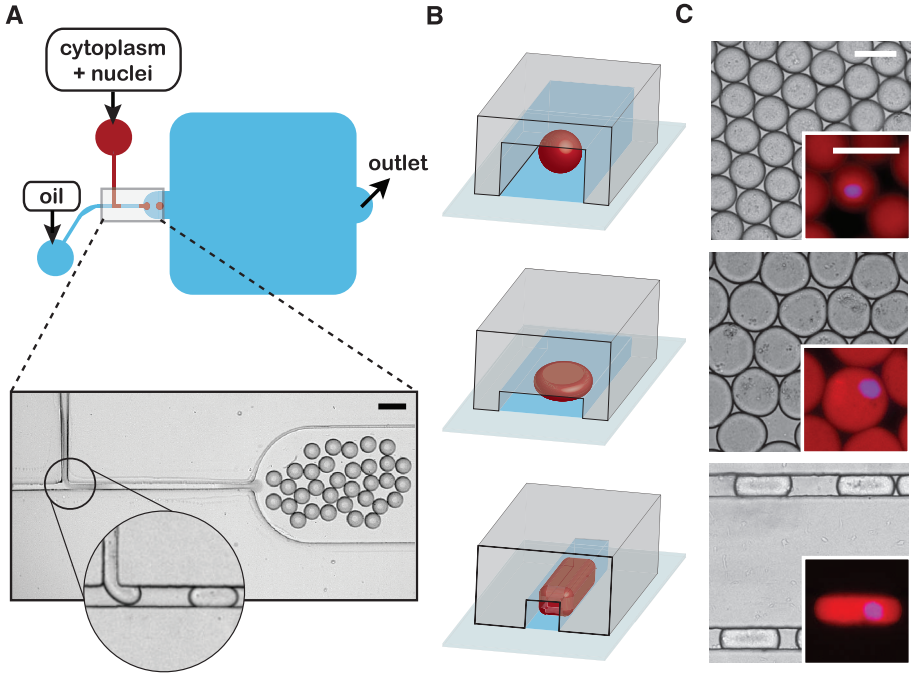

Fig. 1. Microfluidic encapsulation of nuclei in cytoplasmic volumes of defined size and shape. (**A**) (Top) Simplified schematic of a polydimethylsiloxane microfluidic device featuring a classic T-junction droplet generator and collection reservoir (blue rounded square). An extract phase containing nuclei (red) is continuous until sheared off into droplets by the oil/surfactant phase (blue). (Bottom) A representative image of droplet generation at a standard T-junction. (Inset) A formed droplet moving toward the collection reservoir and another about to be sheared from the extract phase (movie S1). Scale bar indicates 100 μm. (**B**) Alternative droplet shapes result from changing the collection reservoir geometry: spheres (top), flattened disks (middle), and elongated slug-shaped droplets (bottom). (**C**) Representative micrographs of spheres, discs, and slugs contained within reservoirs or channels. Scale bar, 50 μm. (Insets) Magnified images of droplets encapsulating "cycled" interphase sperm nuclei. Nuclear DNA was stained with 4′,6-diamidino-2-phenylindole (DAPI) to access nuclear morphology (blue), and soluble tubulin (pseudo-colored red, labeled with Atto-488) was used to visualize droplet boundaries. All droplets are roughly isovolumetric. Inset scale bar, 50 μm.

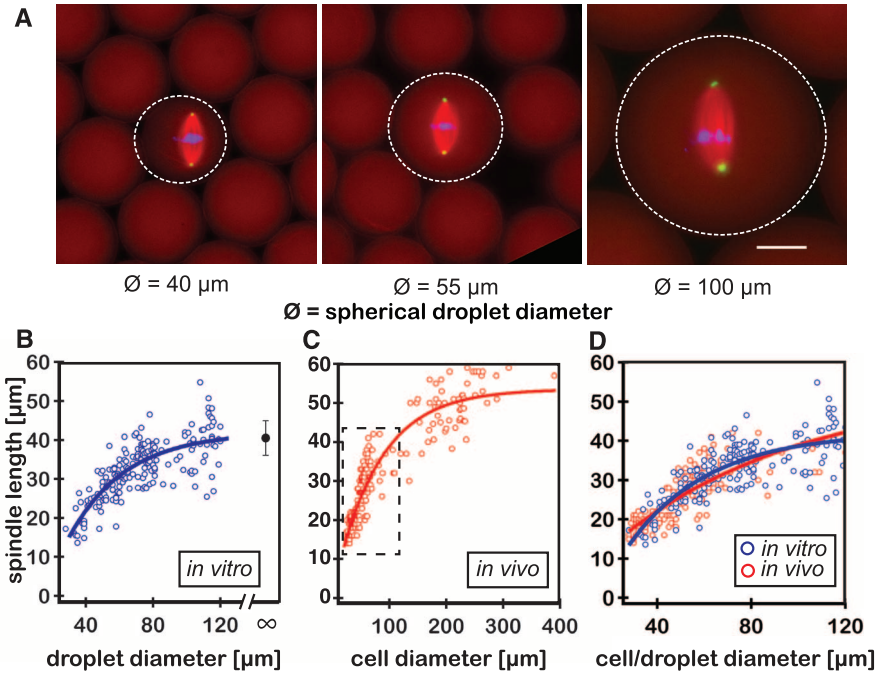

Fig. 2. Developmental spindle scaling can be recapitulated in vitro in the absence of developmental cues or a functional cell cortex. (**A**) Representative fluorescent images of spindles assembled in spherical extract droplets of various sizes. Spindles were labeled by adding fluorophores to the extract before droplet formation; tubulin was added to visualize microtubules (pseudo-colored red, labeled with Atto-488); DAPI, to visualize DNA (blue); and antibodies against nuclear mitotic apparatus protein (NuMA), to visualize spindle poles (pseudo-colored green, directly labeled with Atto-568). Dashed circles indicate droplet boundaries as visualized by the extent of soluble labeled tubulin. Scale bar, 25 μm. (**B**) Spindle length plotted as a function of encapsulating droplet diameter (blue open circles, n = 96 spindles). The single black circle indicates the average spindle length in unencapsulated extract (mean ± SD; n = 81 spindles). (**C**) Spindle length at metaphase plotted as a function of cell size during early (stages 8 to 9) *Xenopus* embryo development [red open circles; adapted from (*2*)]. (**D**) Comparison of spindle scaling in vitro and in vivo (blue and red open circles, respectively, with corresponding fits). Each data set was fit by using a three-parameter equation that assumes asymptotic growth [solid lines in (B) to (D) and figs. S1 and S2].

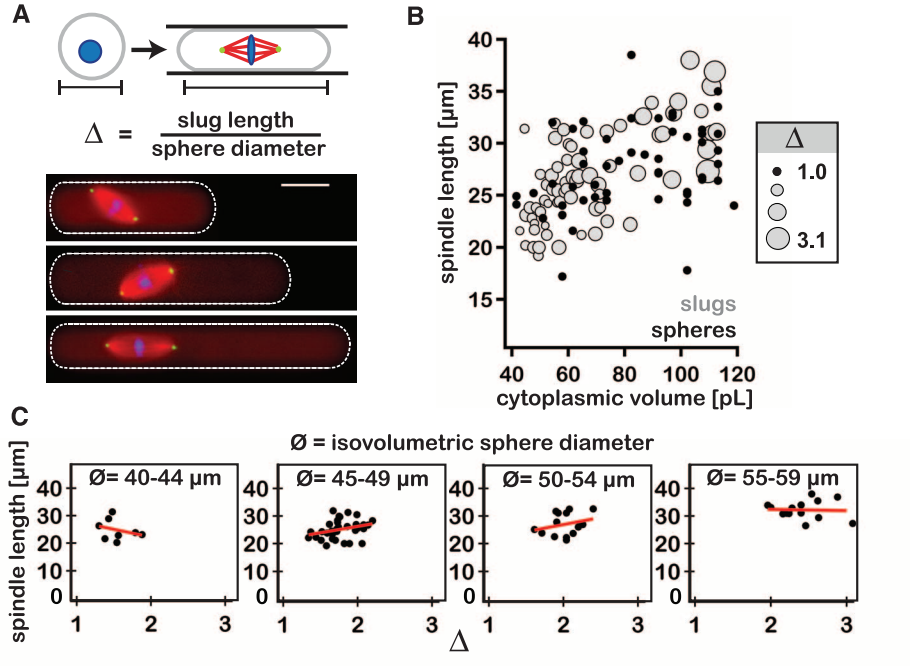

Fig. 3. Reductions in cytoplasmic volume account for the spindle scaling observed in vitro. (**A**) (Top) Cartoon depicting the transformation of a spherical droplet into an isovolumetric slug and the calculation of extent of elongation (Δ). (Bottom) Fluorescent images of representative spindles assembled in slugs of increasing Δ. Fluorophores were added to the extract as described in Fig. 2. (**B**) Spindle length plotted as a function of droplet cytoplasmic volume. For shaded markers (gray circles, n = 71 spindles), marker size is proportional to the ratio of slug long-axis length over the diameter of an isovolumetric sphere (i.e., extent of elongation, denoted as Δ). Solid markers (black circles) represent data derived from spherical droplets (i.e., Δ = 1, n = 96 spindles). (**C**) Spindle length as a function of extent of elongation under near-isovolumetric conditions (i.e., binned by isovolumetric sphere diameter, Ø). Linear trend lines (red) exhibit variable slopes, indicating a lack of a constant relationship between the two measurements.

diameter: In droplets with diameters larger than ~80 μm, spindle length was relatively constant, reaching an upper limit similar to the average spindle length found in unencapsulated extract (~40.5 ± 4.4 μm; mean ± SD), whereas in smaller droplets spindle length scaled almost linearly with droplet diameter (Fig. 2B).

These results share notable similarity with spindle scaling observed during *Xenopus* development, particularly in the linear scaling regime (*2*) (Fig. 2, C and D). Within their respective scaling regimes, asymptotic growth fits to the in vivo and in vitro data sets were statistically indistinguishable (solid lines in Fig. 2, B to D; figs. S1 and S2), suggesting that our in vitro system recapitulated the scaling observed in vivo. Scaling was observed in droplets ranging in diameter from ~30 to 80 μm, corresponding to cell sizes typical of stages 8 and 9 of *Xenopus* development (Fig. 2D), a temporal window that encompasses the mid-blastula transition and the onset of zygotic transcription (*13*, *14*). Because *Xenopus* egg extracts are effectively static in a developmental context, changes in cytoplasmic composition that might affect scaling in the intact embryo do not occur in our system [e.g., (*15*)]. Thus, developmental cues can be eliminated as a potential model for the spindle scaling observed in these droplets, leaving the two remaining hypothetical mechanisms, component limitation and/or boundary sensing.

A boundary-sensing mechanism predicts that changing the physical dimensions of the encapsulating droplet, while holding droplet volume constant, should affect spindle length. To test this model, we compared the lengths of spindles assembled in spheres with those assembled in longer, isovolumetric slugs. The use of slugs as opposed to flattened spheres allowed spindle assembly to be restricted in two of three dimensions over a broader aspect ratio range (Fig. 3A). To ensure that encapsulated spindle lengths could vary in response to changes in droplet shape, we generated slugs by geometrically confining spheres ranging in diameter from 40 to 60 μm

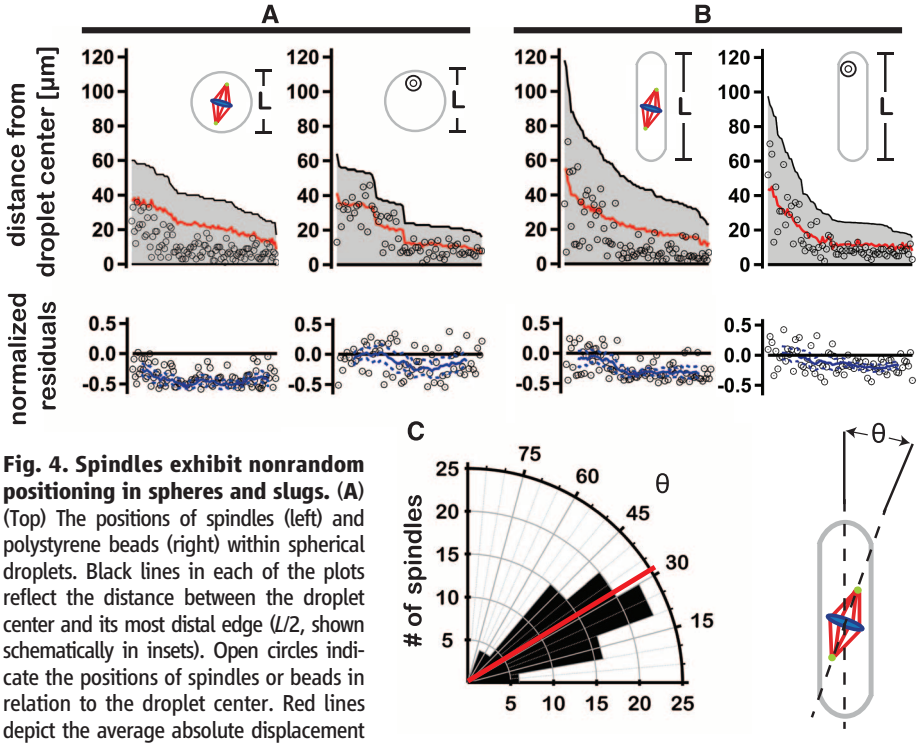

Fig. 4. Spindles exhibit nonrandom positioning in spheres and slugs. (**A**) (Top) The positions of spindles (left) and polystyrene beads (right) within spherical droplets. Black lines in each of the plots reflect the distance between the droplet center and its most distal edge (*L*/2, shown schematically in insets). Open circles indicate the positions of spindles or beads in relation to the droplet center. Red lines depict the average absolute displacement of spindles/beads expected for uniform random positioning (see supplementary materials). (Bottom) Corresponding residual plots show the normalized difference between the center-to-center position of the spindle or bead and the theoretical random position. Solid blue lines represent the moving average of residual values (with upper and lower 95% confidence intervals indicated by dashed blue lines). (**B**) As in (A), spindle and bead positions in axially elongated slugs. (**C**) Spindle orientation in slugs. (Left) Polar histogram plot showing the angle θ between the interpolar spindle axis and the long axis of the confining slug (red line indicates the average orientation angle; n = 89 spindles). (Right) Cartoon depicting the determination of angle θ.

(the approximate midpoint of the scaling regime; movie S2). Differences in spindle lengths for these two extract droplet geometries were statistically indistinguishable (Student's t test, $P = 0.2$ for all slug and sphere data between 40 and 60 μm). Furthermore, spindle length remained relatively constant despite threefold increases in slug length over a narrow range of cytoplasmic volumes (Fig. 3, B and C, and fig. S3). Collectively, these results oppose the predictions of a boundary-sensing model for spindle length regulation and suggest that cytoplasmic shape is not likely a major determinant of spindle length.

Through a variety of different mechanisms, spindles in vivo demonstrate a remarkable ability to correctly position themselves near the cell center before the onset of anaphase and cytokinesis. (*16*–*20*). Each implicitly requires the spindle be able to "sense" its position relative to cellular boundaries. In the absence of boundary sensing, spindle position within a cell (or a confining extract volume) is expected to be random. To test this prediction, we plotted spindle position relative to the volumetric centers of confining spheres and slugs (Fig. 4, A and B). In both geometries, spindles tended to localize toward the droplet center to a greater extent than expected for uniform random positioning (Fig. 4, A and B, and movie S3). This trend was more pronounced in smaller droplets (Fig. 4, A and B, residual plots). In contrast, the positions of encapsulated polystyrene beads aligned more closely with average random positions (Fig. 4, A and B, residual plots; figs. S1 and S2; and movie S4). This suggested that the weak convective flows observed in some slugs were likely not responsible for spindle centering (e.g., movie S5). The distribution of spindle orientations relative to the slug long axis was found to be 31° ± 16° (Fig. 4C), indicating that, like in cells, a spindle is more likely to align parallel to the long axis of its enclosure (*21*), even in the absence of a cortical membrane and associated pulling forces. Indeed, peripheral spindle microtubules extend well beyond the spindle proper, effectively increasing its size (*22*). Perhaps these peripheral microtubules exert pushing forces against droplet boundaries that result in centering (*23*). Alternatively, spindle proximity to a droplet boundary might influence the distribution of forces generated by microtubule-associated motors pulling against the bulk cytoplasm (*19*, *24*). Thus, a boundary-sensing mechanism might indeed work to affect spindle position but contributes little, if at all, to determining spindle length.

Collectively, our data indicate that changes in cytoplasmic volume are sufficient to account for spindle scaling as it occurs in vivo (*2*). By eliminating alternative hypothetical models, the data support a scaling mechanism in which a limiting pool of cytoplasmic component(s) regulates spindle length (*8*, *11*). In large droplets or cells, like in unbounded extract, spindle length appears to be constrained by mechanisms intrinsic to the spindle (*2*, *25*). Once cytoplasmic volume is reduced to a critical threshold, components become limited, which produces smaller spindles. This process serves as a passive yet robust way for cells to control the size of their spindles and possibly other internal structures.

References and Notes

1. M. Montorzi, M. H. Burgos, K. H. Falchuk, *Mol. Reprod. Dev.* **55**, 75–82 (2000).
2. M. Wühr *et al.*, *Curr. Biol.* **18**, 1256–1261 (2008).
3. A. Courtois, M. Schuh, J. Ellenberg, T. Hiiragi, *J. Cell Biol.* **198**, 357–370 (2012).
4. Y. Hara, A. Kimura, *Curr. Biol.* **19**, 1549–1554 (2009).
5. S. L. Bird, R. Heald, K. Weis, *Mol. Biol. Cell* **24**, 2506–2514 (2013).
6. T. Kiyomitsu, I. M. Cheeseman, *Nat. Cell Biol.* **14**, 311–317 (2012).
7. D. J. Sharp *et al.*, *Mol. Biol. Cell* **11**, 241–253 (2000).
8. M. Decker *et al.*, *Curr. Biol.* **21**, 1259–1267 (2011).
9. W. B. Ludington, L. Z. Shi, Q. Zhu, M. W. Berns, W. F. Marshall, *Curr. Biol.* **22**, 2173–2179 (2012).
10. Y. H. Chan, W. F. Marshall, *Organogenesis* **6**, 88–96 (2010).
11. N. W. Goehring, A. A. Hyman, *Curr. Biol.* **22**, R330–R339 (2012).
12. A. Desai, A. W. Murray, T. Mitchison, C. E. Walczak, in *Mitosis and Meiosis*, C. L. Rieder, vol. 61 of *Methods in Cell Biology* (Academic Press, New York, 1999), pp. 385–412.
13. J. Newport, M. Kirschner, *Cell* **30**, 675–686 (1982).
14. P. D. Nieuwkoop, J. Faber, Eds., *Normal Table of* Xenopus laevis *[Daudin] - A Systematical and Chronological Survey of the Development from the Fertilized Egg Till the End of Metamorphosis* (North-Holland, Amsterdam, ed. 2, 1967).
15. J. D. Wilbur, R. Heald, *Elife* **2**, e00290 (2013).
16. P. Gönczy, S. Grill, E. H. Stelzer, M. Kirkham, A. A. Hyman, in *The Cell Cyle and Development*, G. R. Bock, G. Cardew, J. A. Goode, Eds. (Novartis Foundation Symposium no. 237, Wiley, Chichester, UK, 2008), pp. 164–181.
17. L. Lee *et al.*, *Science* **287**, 2260–2262 (2000).
18. N. Minc, D. Burgess, F. Chang, *Cell* **144**, 414–426 (2011).
19. T. Mitchison *et al.*, *Cytoskeleton* **69**, 738–750 (2012).
20. I. M. Tolić-Nørrelykke, L. Sacconi, G. Thon, F. S. Pavone, *Curr. Biol.* **14**, 1181–1186 (2004).
21. M. Wühr, E. S. Tan, S. K. Parker, H. W. Detrich 3rd, T. J. Mitchison, *Curr. Biol.* **20**, 2040–2045 (2010).
22. J. C. Gatlin *et al.*, *Curr. Biol.* **19**, 287–296 (2009).
23. T. E. Holy, M. Dogterom, B. Yurke, S. Leibler, *Proc. Natl. Acad. Sci. U.S.A.* **94**, 6228–6231 (1997).
24. M. Wühr, S. Dumont, A. C. Groen, D. J. Needleman, T. J. Mitchison, *Cell Cycle* **8**, 1115–1121 (2009).
25. S. Dumont, T. J. Mitchison, *Curr. Biol.* **19**, R749–R761 (2009).

Acknowledgments: We thank T. Salmon and T. Mitchison for their insightful reviews of the manuscript; M. Wuhr for comments on the work and for providing access to raw data originally presented in (*2*); L. Edens, C. Geisler, D. Fay, and D. Levy in the Molecular Biology Department at the University of Wyoming for their critical review of the manuscript and helpful suggestions; and A. Groen for providing labeled anti-NuMA used in these studies. This work was supported by NIH grants R01 GM102428 (to J.C.G.) and R15 GM101636 (to J.O.) and by the NIH-funded Wyoming IDeA Networks of Biomedical Research Excellence program (P20RR016474 and P20GM103432).

Supplementary Materials

www.sciencemag.org/content/342/6160/853/suppl/DC1
Materials and Methods
Supplementary Text
Figs. S1 to S3
References (*26*–*31*)
Movies S1 to S5

12 July 2013; accepted 15 October 2013
10.1126/science.1243110

Cytoplasmic Volume Modulates Spindle Size During Embryogenesis

Matthew C. Good,[1,2,3] Michael D. Vahey,[2] Arunan Skandarajah,[2] Daniel A. Fletcher,[2,4]* Rebecca Heald[1]*

Rapid and reductive cell divisions during embryogenesis require that intracellular structures adapt to a wide range of cell sizes. The mitotic spindle presents a central example of this flexibility, scaling with the dimensions of the cell to mediate accurate chromosome segregation. To determine whether spindle size regulation is achieved through a developmental program or is intrinsically specified by cell size or shape, we developed a system to encapsulate cytoplasm from *Xenopus* eggs and embryos inside cell-like compartments of defined sizes. Spindle size was observed to shrink with decreasing compartment size, similar to what occurs during early embryogenesis, and this scaling trend depended on compartment volume rather than shape. Thus, the amount of cytoplasmic material provides a mechanism for regulating the size of intracellular structures.

Although mechanisms that set eukaryotic cell size by coordinating growth and division rates have been uncovered (*1*–*3*), much less is known about how the size and the shape of a cell affect its physiology. Recent work has suggested mechanisms by which cell boundaries or size can control biochemical reactions (*2*), constrain cytoskeletal assembly (*4*–*6*), and dictate the positioning of internal structures (*7*, *8*). The size-scaling problem is most acute during early embryo development, when cell size changes rapidly. For example, over the first 10 hours of amphibian embryogenesis, cell diameter may decrease 100-fold, from a 1.2-mm egg to 12-μm-diameter blastomeres, because of cell division in

[1]Department of Molecular and Cellular Biology, University of California–Berkeley, Berkeley, CA 94720, USA. [2]Department of Bioengineering and Biophysics Group, University of California–Berkeley, Berkeley, CA 94720, USA. [3]Miller Institute for Basic Research in Science, University of California–Berkeley, Berkeley, CA 94720, USA. [4]Physical Biosciences Division, Lawrence Berkeley National Laboratory, Berkeley, CA 94720, USA.

*Corresponding author. E-mail: bheald@berkeley.edu (R.H.), fletch@berkeley.edu (D.A.F.)

the absence of growth (*9*). Although micrometer-scale organelles and intracellular structures have been shown to adapt and function across a wide spectrum of cell sizes (*10*–*14*), mechanisms of size scaling remain poorly understood.

We focused on the mitotic spindle, a dynamic bipolar structure consisting of microtubules and many associated factors that must be appropriately sized to accurately distribute chromosomes to daughter cells. During development, spindle size correlates with cell size in the embryos of invertebrates (*15*, *16*), amphibians (*9*) (fig. S1), and mammals (*17*). However, it is unknown whether spindle size is governed by compositional changes as part of a developmental blueprint or whether spindle size is coupled directly to physical properties of the cell, such as size and shape. Although molecular mechanisms of spindle size regulation have been proposed (*9*–*13*), the existence of a causal link between cell size and spindle size remains unclear.

Because of the difficulty of modulating cell size in vivo, we investigated spindle size scaling by developing an in vitro system of cell-like droplets of varying size containing *Xenopus* egg or embryo cytoplasm. *Xenopus* egg extracts transit the cell cycle in the absence of cell boundaries and recapitulate many cell biological activities in vitro, including spindle assembly (*18*, *19*). To match cell size changes during *Xenopus* embryogenesis, we tuned compartment volume 1,000,000-fold by using microfluidic systems (Fig. 1A and fig. S2). A polyethylene glycol (PEG)–ylated stearate served as a surfactant to prevent droplets from coalescing and to prevent cytoplasmic proteins from interacting with the boundary (Fig. 1A).

Metaphase spindle length and width scaled with droplet size in vitro (Fig. 1, B and C, and fig. S3). Spindles, which normally have a steady-state length of 35 to 40 μm in bulk egg extract (*20*), became smaller as the size of the encapsulating droplet decreased (Fig. 1C and fig. S3). Spindle size scaling was roughly linear in droplet diameters ranging from 20 to 80 μm (Fig. 1C), whereas in larger droplets spindle size matched that of unencapsulated egg extracts. Spindle assembly efficiency decreased in very small droplets and dropped to zero in droplets with a diameter less than 20 μm (fig. S3, C and D). Thus, two regimes of scaling were observed: one in which spindle size was coupled to droplet diameter and a second in which they were uncoupled. These two regimes were similar to spindle scaling trends observed in vivo during early *Xenopus* embryogenesis (Fig. 1, C and D, and fig. S1B) (*9*). Thus, compartmentalization is sufficient to recapitulate spindle size scaling during embryogenesis in the absence of any developmental cues (e.g., transcription).

We considered two possible explanations for the scaling of spindle size with cell or droplet size. The position of cell or droplet boundaries could directly influence spindle size through interaction with microtubules. Alternatively, cytoplasmic volume could limit the amount of material for assembly, which has been proposed for centrosome size regulation in *Caenorhabditis elegans* (*12*, *21*) and spindle size regulation in mouse and sea snail embryos (*17*, *22*). To distinguish

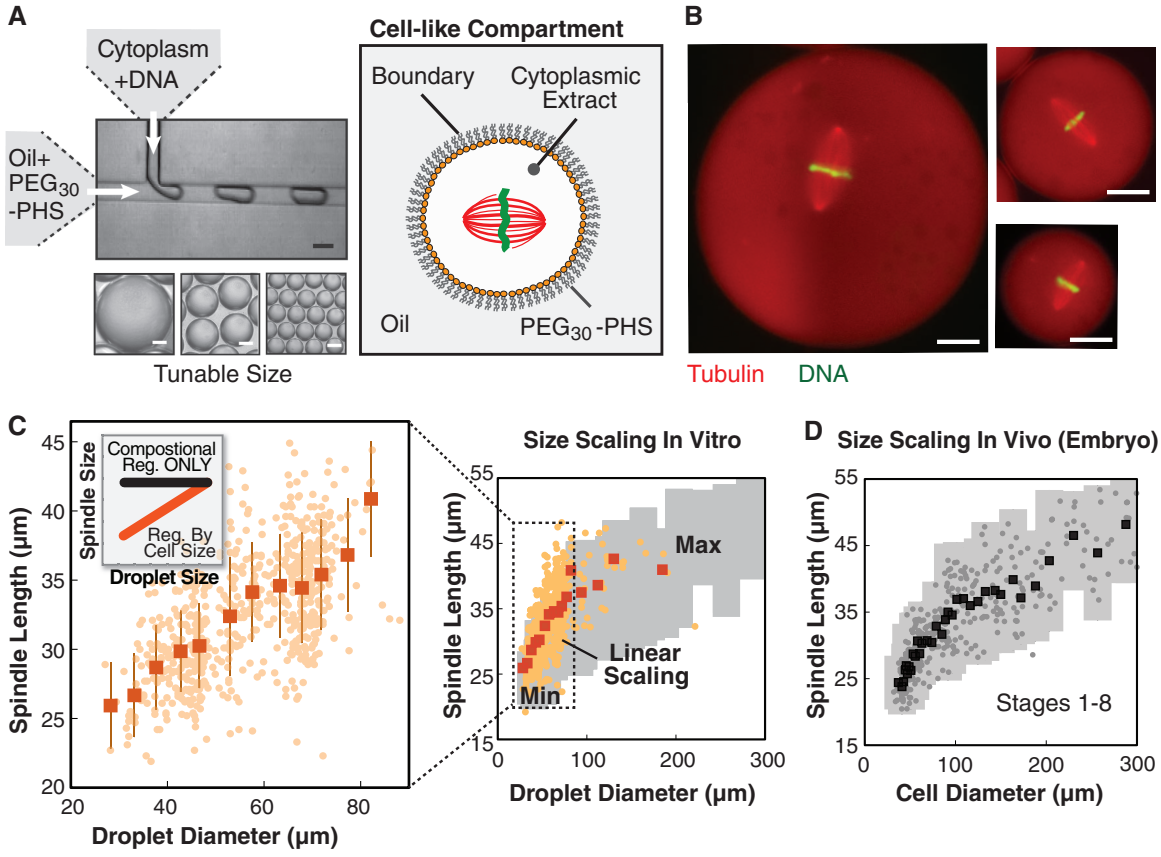

Fig. 1. Spindle length scales with compartment size in vitro and in vivo. (**A**) System for creating cell-like compartments in vitro, including a passivated boundary, cell-free cytoplasm capable of assembling metaphase spindles (*Xenopus* egg or embryo extracts), and tunable compartment size. PHS, polyhydroxystearate. (**B**) Spindles in droplets, compressed to improve image quality, corresponding to spheres 80, 55, and 40 μm in diameter. Uneven shading is due to image stitching. Scale bars indicate 20 μm. (**C**) Spindle length in encapsulated *X. laevis* egg extract scaled with droplet size in vitro. (Left) Linear scaling regime. (Inset) Scaling prediction. Raw data (orange circles) and average spindle length (orange squares) ± SD across 5-μm intervals in droplet diameter are shown. *P* value ($<10^{-60}$) and R^2 (0.34) calculated from linear fit to raw droplet data in 20- to 80-μm diameter range. (Right) Full scaling curve in vitro. For comparison, gray bars indicate two standard deviations from average embryo data in (D). (**D**) Spindle length scaling in vitro mirrored length scaling in the *X. laevis* embryo through stage 8, with similar linear scaling regimes and a plateau where spindle size was uncoupled from compartment size. Raw data from embryos across 5-μm intervals in cell diameter (gray circles) and average spindle length (black squares) ± 2 SD (thick error bars) are shown.

between these two possibilities, we compared spindle size scaling in droplets that were spherical or compressed into a disklike shape (z-height ~ 25 μm) (fig. S4B). Spindle length and assembly efficiency in differently shaped droplets collapsed onto the same curve when plotted against volume but not diameter, suggesting that spindle assembly is dependent on the amount of cytoplasm rather than the position of the compartment boundaries (Fig. 2 and fig. S4C). Although spindles were positioned near the center of cells in the embryo, they were more randomly distributed when formed in droplets (fig. S4D) (*23*). Although the cell boundary plays a crucial role in positioning and could affect spindle size in vivo, we did not observe an effect in droplets. Thus compartment volume, not boundary interactions, dictates spindle size in our system.

To elucidate how spindle size scales with compartment volume, we considered a limiting component mechanism, in which the amount of particular molecules per cell regulates spindle assembly. Although multiple components could become limiting, we focused our attention on tubulin, the subunit of microtubules and the major structural component of the spindle, whose levels have been implicated in regulating spindle size (*24*). Because the cellular tubulin concentration and the number and length of microtubules in the egg extract spindle have been characterized (*25*, *26*), it was possible to determine what fraction of soluble tubulin within a given volume remained in the cytoplasm after spindle assembly. We used this information to create a simplified quantitative model that predicted spindle size on the basis of compartment volume (Fig. 3A and fig. S5). The model assumes an available pool of soluble αβ-tubulin dimers, which is depleted as the spindle assembles, and depends on both cytoplasmic volume and spindle volume. Because tubulin concentration is known to affect microtubule dynamics (*27*, *28*), we hypothesized that this depletion might drive volume-dependent spindle scaling. Combining this idea with measured spindle parameters (*25*, *26*) and the observation that tubulin density in the spindle does not change with spindle size (fig. S6B, inset) (*29*), we derived an analytical model for volume-dependent spindle scaling that agrees quantitatively with our data both in droplets (Fig. 3B and fig. S5C) and in cells during embryogenesis (fig. S5D) (*23*).

A key prediction of this model is that the soluble tubulin concentration after spindle assembly should be lower for smaller cells. We measured the fluorescence intensity of tubulin in the cytoplasm and spindle as a function of cell volume (fig. S6A) and found that cytoplasmic tubulin was significantly depleted in cells smaller than 150 μm in diameter, with up to 60% of the total cellular tubulin incorporated into the spindle in the smallest cells (Fig. 3C and fig. S6B). This result is quantitatively consistent with our model (Fig. 3C) and rules out other models in which the spindle assembles from a constant fraction of cellular material. Although our analysis suggests that tubulin is necessary to maintain spindle size, it is not likely to be sufficient. The addition of tubulin to egg extracts did not alter spindle scaling in droplets (fig. S7), presumably because the levels of other spindle assembly factors were also limiting. In summary, although the model described here is general and can be applied to other molecular components that are enriched in the spindle, its quantitative agreement with measured data suggests that tubulin depletion plays an important role in volume-dependent spindle scaling.

Volume offers a useful mechanism for directly modulating spindle size throughout development. Because cell size varies within an embryo and even within individual stages of development (fig. S8A), scaling mechanisms based only on developmental timing or cytoplasmic composition would not couple spindle size to cell size, potentially leading to spindle positioning errors. We found that spindle length and cell volume correlated across most stages of *X. laevis* early embryogenesis (Fig. 4A) and within individual developmental stages (fig. S8, B and C), in support of volume-dependent scaling in vivo. To demonstrate that cytoplasmic volume regulates spindle size independent of developmental stage, we encapsulated stage 4 (8-cell) and stage 8 (~4000-cell) embryo extracts. In the largest droplets, maximum spindle size was consistent with results in unencapsulated extracts (*30*) and depended on developmental stage (Fig. 4B). Nonetheless, encapsulated mitotic spindles from both extracts exhibited volume-dependent scaling (Fig. 4B), showing that cytoplasmic volume and composition together control spindle size during *X. laevis* embryogenesis.

To determine whether cytoplasmic volume-dependent spindle scaling is conserved in other organisms, we encapsulated egg extracts from a related frog species, *Xenopus tropicalis*, which generate smaller spindles than *X. laevis* extracts, in part because of higher microtubule-severing activity of p60 katanin (*20*, *31*). Like *X. laevis* spindles, *X. tropicalis* spindles scaled with compartment volume, both in vitro (fig. S9, A and B) and in vivo (fig. S10B). Combined with recent data for spindle size in embryos of the mammal *Mus musculus* (*17*), these findings indicate conservation of volume-dependent scaling in vertebrate evolution. Although the upper limits to spindle size vary in embryonic cells among these organisms (fig. S10C), large portions of the scaling curves closely overlapped (fig. S10D).

Taken together, these results suggest that volume-dependent spindle size scaling is conserved across spindle architectures (meiotic and mitotic), developmental stages, and vertebrate species. Previous reports on spindle scaling factors have focused primarily on compositional differences between cells or cytoplasmic extracts. We have identified cell volume as a physicochemical scaling mechanism that regulates spindle size through limiting amounts of cytoplasmic material, acting in concert with other mechanisms that alter activity of microtubule regulatory factors (*26*, *29*–*31*). All together, mechanisms altering

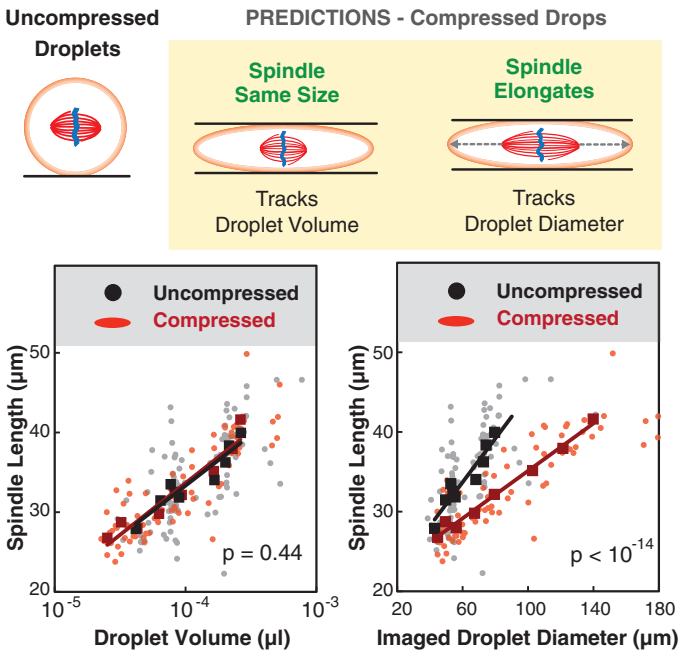

Fig. 2. Cytoplasmic volume sets spindle size in vitro. To distinguish between boundary- and volume-sensing models, we compared spindle length scaling in uncompressed (spherical) and compressed (disklike) droplets (details in fig. S4B). Spindle length scaling in both droplet geometries appeared identical when plotted as a function of droplet volume, supporting a volume-sensing mechanism. Spindle scaling curves did not overlay when plotted as a function of projected (imaged) droplet diameter, ruling out boundary sensing. Raw data points (circles; gray, uncompressed; red, compressed) and spindle length, averaged across 10 droplets (squares; black, uncompressed; red, compressed), are shown. Raw data were fit to a log function in volume plot [black line, R^2 = 0.42 (uncompressed), and red line, R^2 = 0.79 (compressed)] and linear function in diameter plot [black line, R^2 = 0.45 (uncompressed), and red line, R^2 = 0.79 (compressed)]. *P* values indicate statistical differences between *y* intercepts of compressed versus uncompressed regression lines, calculated by using an analysis of covariance.

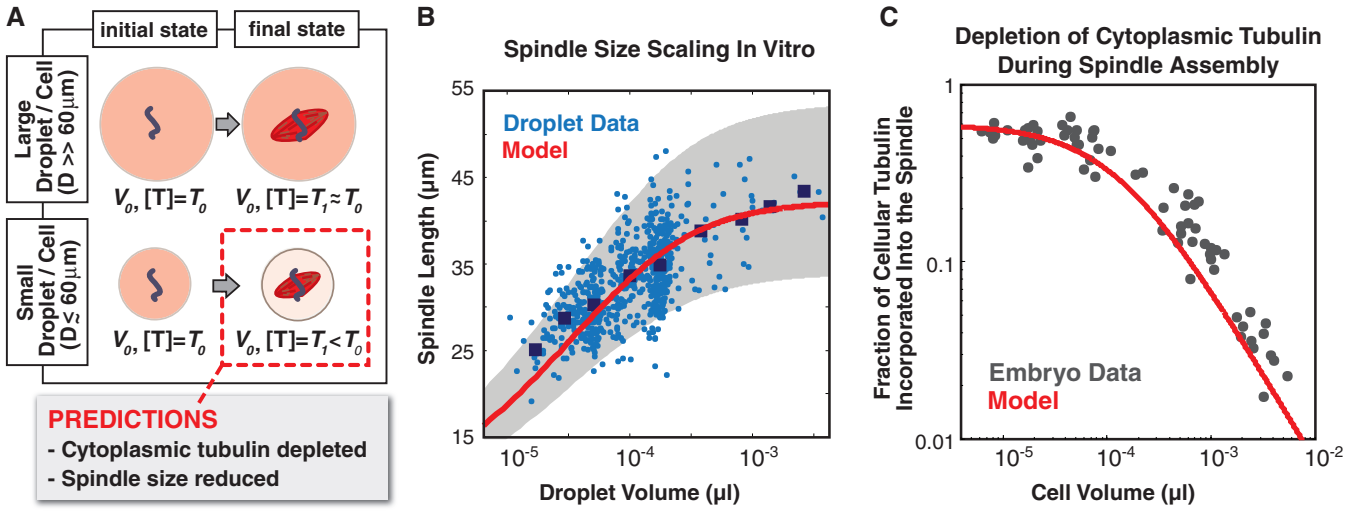

Fig. 3. A limiting-component model for spindle size regulation. (**A**) Schematic of limiting-component model (for more details, see fig. S5A and supplementary text). (**B**) Limiting tubulin model accurately predicted *X. laevis* spindle length from droplet volume in vitro. Raw data from droplets (blue circles) and binned averages (dark blue squares) were compared to the model. Shaded gray regions represent model predictions across a range of parameter values (fig. S5B); the red line shows the prediction for intermediate values. (**C**) Cytoplasmic tubulin became substantially depleted as cell size decreased during *X. laevis* embryogenesis. Comparison of model prediction (red) and experimental data (gray) for the fraction of total cellular tubulin incorporated in the spindle as a function of cell volume. Model used parameter values that gave best agreement in fig. S5, C and D.

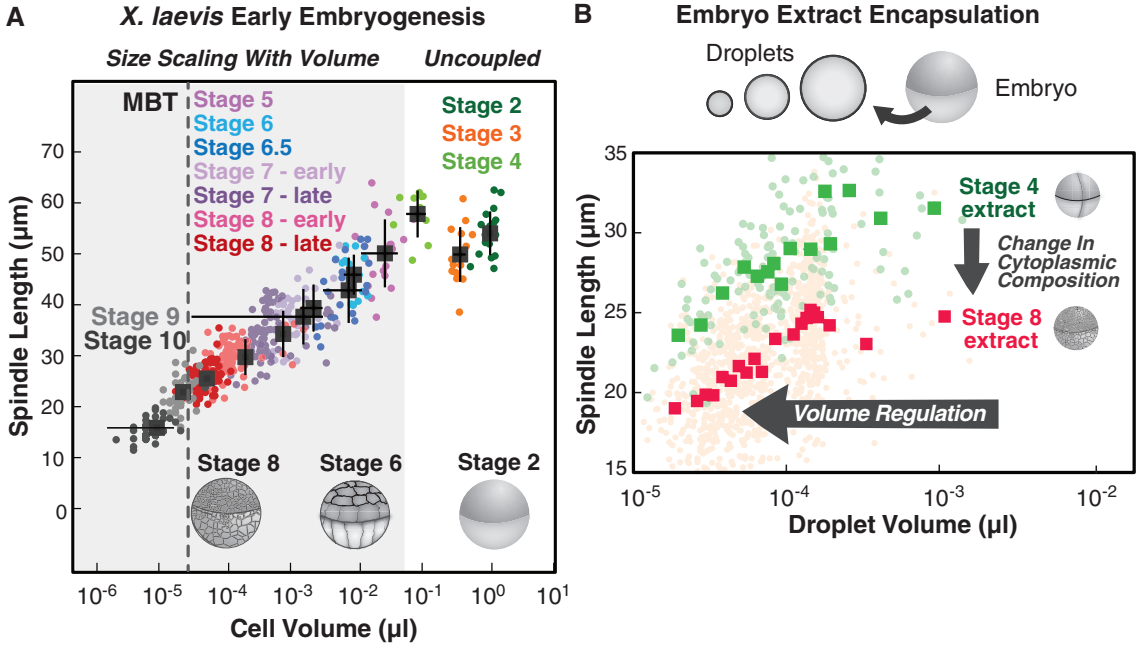

Fig. 4. Cell volume and composition control spindle size during *Xenopus* early embryogenesis. (**A**) Spindle length scaled linearly with cell volume across a broad range of developmental stages during early *X. laevis* embryogenesis (stages 5 to 10). Spindle length had an upper limit and was uncoupled from cell volume in stages 2 to 4. Raw data (colored circles) and stage-averaged cell diameter and spindle length (black squares) ± SD are shown. (**B**) Despite having distinct maximum spindle lengths coupled to developmental stage (stage 4, green; stage 8, red), the length of *X. laevis* embryo extract mitotic spindles scaled with compartment volume in vitro. This result suggested that changes in cytoplasmic volume and composition work in concert to regulate spindle size. Raw data points (light circles) and bin-averaged spindle length (squares), calculated for 5-μm intervals in droplet diameter across the 20- to 80-μm range of droplet diameters (wider intervals were used for averaging in largest droplets because data were sparse), are shown.

the concentration or activity of cytoplasmic scaling factors appear to modulate maximum and minimum spindle size, whereas cytoplasmic volume couples spindle size to cell size (fig. S11). We propose that the amounts of certain molecules known to be important for spindle assembly, including but not limited to tubulin, are responsible for this coupling, which weakens as cell volume increases and the components required for assembly are no longer limiting.

References and Notes

1. R. Kafri *et al.*, *Nature* **494**, 480–483 (2013).
2. J. J. Turner, J. C. Ewald, J. M. Skotheim, *Curr. Biol.* **22**, R350–R359 (2012).
3. A. Tzur, R. Kafri, V. S. LeBleu, G. Lahav, M. W. Kirschner, *Science* **325**, 167–171 (2009).
4. M. Pinot *et al.*, *Curr. Biol.* **19**, 954–960 (2009).
5. M. Pinot *et al.*, *Proc. Natl. Acad. Sci. U.S.A.* **109**, 11705–11710 (2012).
6. L. Laan *et al.*, *Cell* **148**, 502–514 (2012).
7. N. Minc, D. Burgess, F. Chang, *Cell* **144**, 414–426 (2011).
8. O. M. Lancaster *et al.*, *Dev. Cell* **25**, 270–283 (2013).
9. M. Wühr *et al.*, *Curr. Biol.* **18**, 1256–1261 (2008).
10. Y. H. Chan, W. F. Marshall, *Science* **337**, 1186–1189 (2012).

11. S. Dumont, T. J. Mitchison, *Curr. Biol.* **19**, R749–R761 (2009).
12. N. W. Goehring, A. A. Hyman, *Curr. Biol.* **22**, R330–R339 (2012).
13. G. Goshima, J. M. Scholey, *Annu. Rev. Cell Dev. Biol.* **26**, 21–57 (2010).
14. D. L. Levy, R. Heald, *Annu. Rev. Cell Dev. Biol.* **28**, 113–135 (2012).
15. G. Greenan *et al.*, *Curr. Biol.* **20**, 353–358 (2010).
16. Y. Hara, A. Kimura, *Mol. Biol. Cell* **24**, 1411–1419 (2013).
17. A. Courtois, M. Schuh, J. Ellenberg, T. Hiiragi, *J. Cell Biol.* **198**, 357–370 (2012).
18. A. Desai, A. Murray, T. J. Mitchison, C. E. Walczak, *Methods Cell Biol.* **61**, 385–412 (1998).
19. E. Hannak, R. Heald, *Nat. Protoc.* **1**, 2305–2314 (2006).
20. K. S. Brown *et al.*, *J. Cell Biol.* **176**, 765–770 (2007).
21. M. Decker *et al.*, *Curr. Biol.* **21**, 1259–1267 (2011).
22. E. G. Conklin, *J. Exp. Zool.* **12**, 1–98 (1912).
23. A description of the spindle centering analysis and a detailed derivation of the limiting component model can be found in the supplementary materials.
24. R. Lattao, S. Bonaccorsi, M. Gatti, *J. Cell Sci.* **125**, 584–588 (2012).
25. J. Brugués, V. Nuzzo, E. Mazur, D. J. Needleman, *Cell* **149**, 554–564 (2012).
26. R. Loughlin, R. Heald, F. Nédélec, *J. Cell Biol.* **191**, 1239–1249 (2010).
27. L. Brun, B. Rupp, J. J. Ward, F. Nédélec, *Proc. Natl. Acad. Sci. U.S.A.* **106**, 21173–21178 (2009).
28. M. E. Janson, M. E. de Dood, M. Dogterom, *J. Cell Biol.* **161**, 1029–1034 (2003).
29. S. B. Reber *et al.*, *Nat. Cell Biol.* **15**, 1116–1122 (2013).
30. J. D. Wilbur, R. Heald, *eLife* **2**, e00290 (2013).
31. R. Loughlin, J. D. Wilbur, F. J. McNally, F. J. Nédélec, R. Heald, *Cell* **147**, 1397–1407 (2011).

Acknowledgments: This work was supported by fellowships from the Miller Institute for Basic Science Research (M.C.G.), NIH (M.D.V.), and NSF (A.S.). This work was also supported by NIH grants (GM074751, D.A.F.) and (GM098766, R.H.). We thank J. Wilbur, K. Helmke, F. Nedelec, K. Weis, M. Welch, H. Ramage, K. Nyberg, N. Metrakos, the Berkeley BioChIP NSF Research Experience for Undergraduates program, and members of the Heald and Fletcher labs. The authors declare no competing financial interests. Data described can be found in the main figures and supplementary materials.

Supplementary Materials

www.sciencemag.org/content/342/6160/856/suppl/DC1
Materials and Methods
Supplementary Text
Figs. S1 to S11
References (*32*–*39*)

12 July 2013; accepted 15 October 2013
10.1126/science.1243147

ERF115 Controls Root Quiescent Center Cell Division and Stem Cell Replenishment

Jefri Heyman,[1,2] Toon Cools,[1,2] Filip Vandenbussche,[3] Ken S. Heyndrickx,[1,2] Jelle Van Leene,[1,2] Ilse Vercauteren,[1,2] Sandy Vanderauwera,[1,2] Klaas Vandepoele,[1,2] Geert De Jaeger,[1,2] Dominique Van Der Straeten,[3] Lieven De Veylder[1,2]*

The quiescent center (QC) plays an essential role during root development by creating a microenvironment that preserves the stem cell fate of its surrounding cells. Despite being surrounded by highly mitotic active cells, QC cells self-renew at a low proliferation rate. Here, we identified the ERF115 transcription factor as a rate-limiting factor of QC cell division, acting as a transcriptional activator of the phytosulfokine PSK5 peptide hormone. ERF115 marks QC cell division but is restrained through proteolysis by the APC/C^{CCS52A2} ubiquitin ligase, whereas QC proliferation is driven by brassinosteroid-dependent *ERF115* expression. Together, these two antagonistic mechanisms delimit ERF115 activity, which is called upon when surrounding stem cells are damaged, revealing a cell cycle regulatory mechanism accounting for stem cell niche longevity.

Plant root growth and development depend on the continuous generation of new cells by the stem cell niche that is located in the proximal zone of the root meristem. Key to the maintenance of the stem cell niche are a small group of organizing cells, the quiescent center (QC) (*1*–*4*). QC cells divide with a frequency lower by a factor of 3 to 10 than mitotically active root cells (*2*, *5*–*7*). Combined with the suppression of stem cell differentiation, a low QC proliferation rate is fundamental to maintain root structure and meristem function (*7*). Whereas inhibition of stem cell differentiation is controlled through the retinoblastoma pathway (*8*), the molecular components that control the QC cell division rate remain unknown. The *Arabidopsis thaliana* CELL CYCLE SWITCH 52 A2 (CCS52A2) activating subunit of the anaphase-promoting complex/cyclosome (APC/C), a highly conserved E3 ubiquitin ligase that marks cell cycle proteins for destruction, restrains QC cell division (*9*).

[1]Department of Plant Systems Biology, VIB, B-9052 Gent, Belgium. [2]Department of Plant Biotechnology and Bioinformatics, Ghent University, B-9052 Gent, Belgium. [3]Laboratory of Functional Plant Biology, Department of Physiology, Faculty of Sciences, Ghent University, B-9000 Gent, Belgium.

*Corresponding author. E-mail: lieven.deveylder@psb.vib-ugent.be

CCS52A2 copurifying proteins identified through tandem-affinity purification (fig. S1) (*10*) were screened for their ability to promote QC cell proliferation upon ectopic expression. Among these, the ethylene response factor 115 (ERF115) resulted in a QC cell division phenotype that mimicked that of *ccs52a2-1* knockout plants (Fig. 1, A to C). Expression of the WOX5-GFP (green fluorescent protein) marker confirmed that it was the QC cells that divided (fig. S2).

ERF115 (At5g07310) belongs to the ETHYLENE RESPONSE FACTOR family of transcription factors that control the transcription of genes linked to various biological processes related to growth and development. Biochemical data validated that ERF115 is a proteolytic target of APC/C^{CCS52A2}. The proteasome inhibitor MG132 stabilized the chimeric ERF115-GFP reporter in a *CCS52A2*-dependent manner (Fig. 1, D to G, and fig. S3). In contrast, knockout of the paralogous *CCS52A1* gene, which controls the timing of cell cycle exit of the root cells within the cell elongation zone through cyclin destruction (*6*, *11*), did not affect proteolysis of ERF115 (Fig. 1, H and I). ERF115 has two putative destruction (D)–box sequences (amino acids 115 to 118 and 150 to 153) that are recognized by the APC/C (fig. S4A). Inactivation of the proximal D-box stabilized ERF115, whereas its stability was increased by mutation of the second D-box (Fig. 1J and fig. S4B).

In agreement with ERF115 being a proteasome target, within translation reporter lines, ERF115-GFP fluorescence could only be detected upon MG132 treatment, revealing a QC cell–specific accumulation pattern (fig. S5). Correspondingly, *ERF115* promoter activity was observed in the QC cells (Fig. 2A), albeit only in 11.7% of the examined roots (n = 60 root tips). As observed previously (*6*), a modest temperature increase promoted QC cell division (31.0% at 24°C versus 15.0% at 21°C; n = 20 and 29 roots, respectively), coinciding with a temperature-dependent rise in *pERF115:GUS*-positive QC cells (Fig. 2C), of which 32.3%, corresponding to the QC cell division frequency at 24°C, showed signs of a recent cell division, as indicated by the presence of two adjacent blue cells (Fig. 2B). When grown with the cell cycle inhibitory drug hydroxyurea, plants had fewer *pERF115:GUS*-positive QC cells (Fig. 2C). Thus, *ERF115* expression marks dividing QC cells.

Ethylene plays a putative role in QC cell division (*5*) and regulates some members of the *ERF* gene family. However, the frequency of *pERF115:GUS*-positive QC cells did not vary upon treatment with the ethylene precursor 1-aminocyclopropane-1-carboxylic acid (ACC) or ethylene itself, nor upon treatment with the ethylene inhibitor silver nitrate (fig. S6), suggesting that ERF115 is not involved in ethylene perception or signaling. Brassinosteroids also promote QC cell division (*12*). Correspondingly, *ERF115* expression appeared to depend on brassinosteroids, because treatment with brassinolide increased the number of *pERF115:GUS*-positive QC cells (Fig. 2C and fig. S7) and reached up to 86.6% (n = 82 root tips) at 24°C. Because of the link between *ERF115* expression and QC cell division, we investigated whether the brassinosteroid-dependent QC cell proliferation phenotype was ERF115 dependent. QC cells of *erf115*^{KO} lines still divided in response to brassinosteroid treatment, perhaps due to gene redundancy in the 122-member *ERF* gene family. To circumvent this problem, we converted

ERF115 into a dominant negative form by fusing it with the SUPERMAN repression domain (SRDX) (*13*). Wild-type plants treated with brassinolide displayed disorganized root meristems due to hyperproliferation of the QC. In contrast, *ERF115*^{SRDX} plants treated with brassinolide showed reduced QC hyperproliferation (Fig. 2D and fig. S8). Thus, the brassinosteroid-induced QC divisions depend at least in part on the ERF115 activity. Contrasting, in line with the absence of transcriptional control of *ERF115* by ethylene, no effect on ethylene-dependent QC cell division was observed in the *ERF115*^{SRDX} plants (fig. S9), indicating that brassinosteroids and ethylene control QC cell division through different pathways.

To identify the mechanism by which ERF115 drives QC cell division, we screened for genes controlled by ERF115 through transcriptome analysis on *ERF115*^{OE} plants and tandem chromatin-affinity purification analysis (Fig. 3A). Compared with the wild type, 259 genes were activated in *ERF115*^{OE} root tips (table S1), of which 20 were bound by the ERF115 transcription factor (tables S2 and S3). In this group, we found one of the five *PHYTOSULFOKINE PRECURSOR*–encoding genes of *Arabidopsis thaliana*, which give rise to a sulfonated pentapeptide hormone molecule, known to control root growth, cell proliferation, cell elongation, and callus formation (*14*–*17*). *PSK5* was more than 8-fold transcriptionally upregulated and was bound by ERF115 in its promoter region (Fig. 3B and fig. S10). *PSK5* induction in the *ERF115*^{OE} line was confirmed through quantitative reverse transcription polymerase chain reaction analysis (Fig. 3C). In the dominant negative *ERF115*^{SRDX} roots, *PSK5* expression was more than 60% repressed, supporting a role for ERF115 as transcriptional activator of this particular *PSK* gene (Fig. 3C). Increased *PSK5* transcript levels were also observed in the *ccs52a2-1* mutant, in which the ERF115 protein is stabilized, validating the *PSK5* transcriptional activation by ERF115 (Fig. 3D). Similar to the *ERF115* gene, upon brassinolide treatment, *PSK5* transcription is activated in a manner that depends on the brassinosteroid-insensitive 1 receptor (Fig. 3E), in agreement with the recent observation that PSK signaling is brassinosteroid dependent (*18*). As PSK peptides are predominantly sensed by the leucine-rich repeat receptor kinase PSKR1 (*19*, *20*), we introduced the *ERF115*^{OE} construct into *pskr1-3* plants. Absence of a functional PSKR1 receptor resulted in a normal QC cell division phenotype (Fig. 3F and fig. S11), demonstrating that the ERF115-induced QC cell divisions depend on PSK signaling.

Our data suggest that the APC/C^{CCS52A2} and brassinosteroid pathways regulate the QC cell division through their antagonistic effect on the ERF115 abundance, a mechanism that might account for the low proliferation rate of the QC cells, in which APC/C^{CCS52A2} dampens the activity of brassinosteroid-induced ERF115 activity through its proteolytic turnover (fig. S12). Next to brassinosteroids, QC cell division is observed upon treatment with other stress signaling hormones (*5*, *21*). Reminiscent to the law of Bergonié and Tribondeau stating that the reproductive activity of cells is proportional to their sensitivity toward genotoxic signals (*22*), we postulated that the low division rate of QC cells would mark them as less vulnerable to stress in comparison with other stem cells and that the QC cells might represent a reservoir of cells that are called upon to replenish damaged stem cells. As verified under our conditions, treatment of *Arabidopsis* roots for 24 hours with the radiomimetic drug bleomycin triggered programmed cell death of stem cells neighboring the QC, as visualized by the uptake of the cell death marker propidium iodide (*23*) (Fig. 4, A and B). In contrast, cell death was suppressed in the QC cells (Fig. 4B and fig. S13), which might in part be attributed to the significant enriched expression of DNA damage repair genes ($P < 0.001$) (table S4). Upon retransfer of the bleomycin-treated plants to drug-free medium, the QC expression domain increased through cell division (Fig. 4C), displacing dead cells from the stem cell niche within 2 to 4 days (Fig. 4, D and E). In plants hemizygous for *ERF115*^{SRDX}, the *WOX5* expression domain expanded as well but through ectopic acquirement of QC cell identity rather than cell division (Fig. 4, F and G), in agreement with the observation that ERF115 activity is required for QC cell division. As a consequence, the original QC cells lost their cell identity, whereas the newly formed QC cells remained in direct contact with dead cells, even after transfer to drug-free medium (Fig. 4, H to J). This phenotype was more notable in homozygous *ERF115*^{SRDX} plants that lost meristem organization completely within 2 days on recovery medium (fig. S14). Root-growth measurement illustrated that clearance of all dead stem cells in wild-type plants allowed roots to resume growth after release from the stress, whereas in *ERF115*^{SRDX} growth was inhibited (fig. S15). These data are reminiscent of pioneering work in maize showing that root apex regeneration upon x-ray radiation occurs through proliferation of the QC cells (*24*) and indicate that the ERF115-PSK signaling pathway not only may account for the low QC cell proliferation rate but also contributes to ensuring the longevity of the stem cell niche. Coexistence of quiescent and actively dividing adjoining stem cells is not plant-specific, but rather appears to be a general principle, found as well within hair follicle, gut, and bone marrow stem cell niches (*25*). Therefore, maintaining a stem cell subpopulation that is used to replace damaged stem cells might represent a general mechanism to maintain a functional stem cell niche under stress conditions.

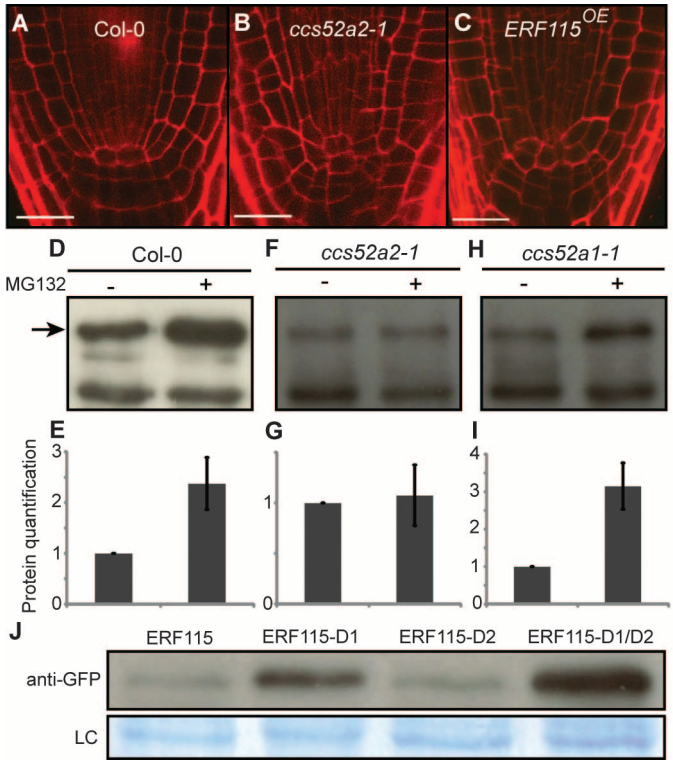

Fig. 1. ERF115 drives QC cell division and is a substrate of the APC/C^{CCS52A2}. (**A** to **C**) QC cells of 1-week-old wild-type (Col-0) (A), *ccs52a2-1* mutant (B), and *ERF115*^{OE} (C) plants visualized by confocal microscopy. Cell walls were counterstained with propidium iodide. Scale bars, 20 μm. (**D** to **I**) ERF115-GFP protein gel blot analysis with an antibody against GFP on 5-day-old wild-type (D), *ccs52a2-1* mutant (F), and *ccs52a1-1* mutant (H) seedlings control-treated (–) or treated (+) with the MG132 proteasome inhibitor (100 μM). Arrow indicates the position of ERF115-GFP fusion protein. A nonspecific cross-reacting protein was used as a loading control. Quantified proteins levels are corrected for the expression levels [(E), (G), and (I)]. The protein level of ERF115-GFP without MG132 was arbitrarily set to one. Data represent mean ± SD (n = 2 independent pull-down assays). (**J**) ERF115-GFP protein gel blot analysis with an antibody against GFP on *Nicotiana benthamiana* leaf spots infiltrated with constructs encoding ERF115-GFP and its D-box mutated variants ERF115-D1 (N-terminal D-box mutated; RVWL→AVWA), ERF115-D2 (C-terminal D-box mutated; RAQL→AAQA), and ERF115-D1/D2 (both D-boxes mutated). LC, loading control of Coomassie-stained nonspecific bands.

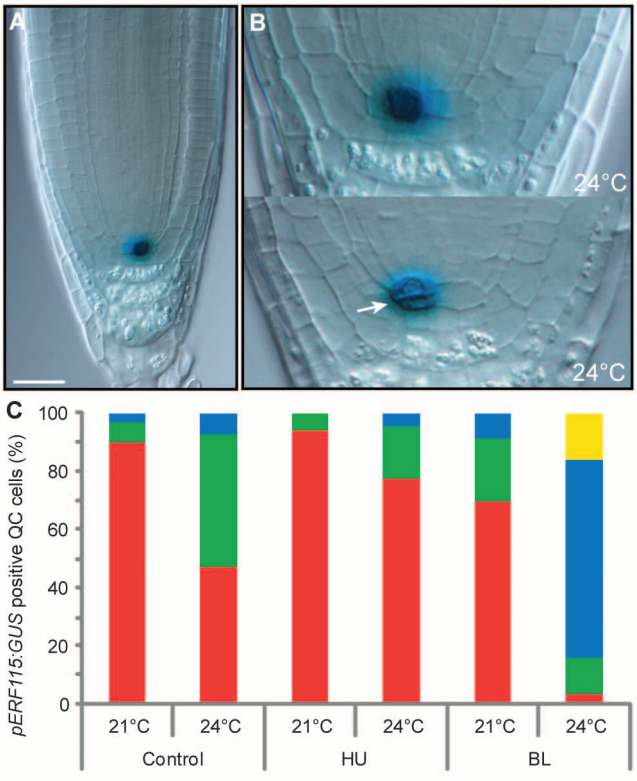

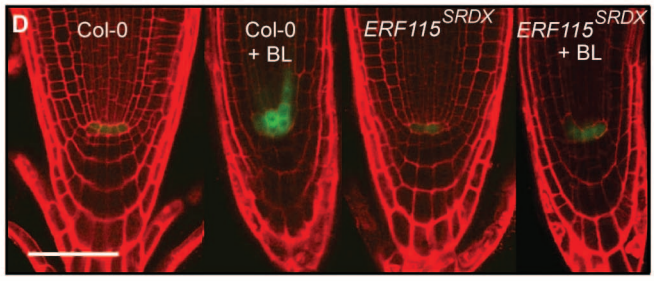

Fig. 2. *ERF115* expression correlates with QC cell division and is regulated by brassinosteroids. (**A**) pERF115:GUS activity in QC cells of a 1-week-old seedling. Scale bar, 20 μm. (**B**) *pERF115:GUS*-positive cells marking a divided QC cell (arrow). (**C**) Quantification of *pERF115:GUS*-positive QC cells in control, hydroxyurea-treated (0.75 mM HU), and brassinolide-treated (0.5 nM BL) 1-week-old seedlings, grown at 21°C and 24°C. Red represents the percentage of plants with unstained QC cells, whereas green, blue, and yellow indicate the percentage of root tips with either one, two, or more positive QC cells ($n > 57$ root tips). (**D**) Root tip organization of 1-week-old wild-type (Col-0) and $ERF115^{SRDX}$ seedlings control-treated or treated with 0.5 nM brassinolide (BL+). QC cells are visualized by the WOX5-GFP marker. Cells were counterstained with propidium iodide. Scale bar, 50 μm.

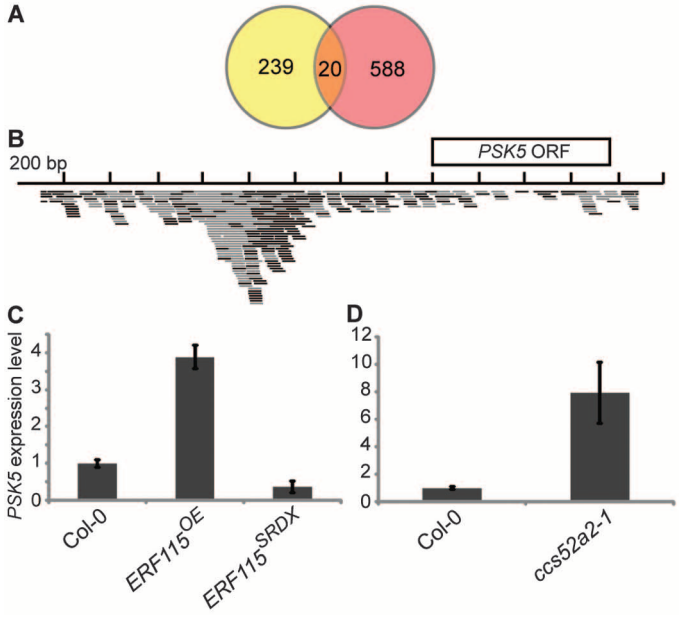

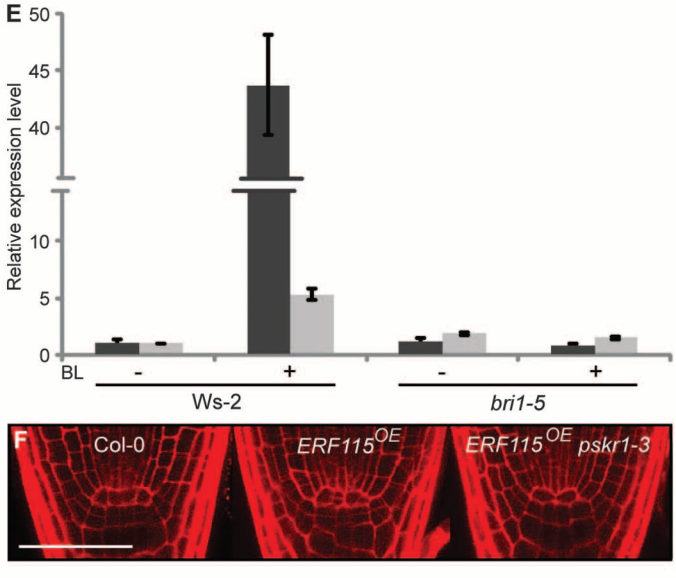

Fig. 3. ERF115 controls QC cell division through PSK5 signaling. (**A**) Venn diagram depicting the overlap between the 259 genes up-regulated in the $ERF115^{OE}$ root tip (yellow) and the 608 genes bound by ERF115 (red). This overlap is higher than expected by chance ($P < 0.05$; hypergeometric distribution). (**B**) Graphical representation of the reads resulting from tandem chromatin-affinity purification sequencing mapping to the *PSK5* gene. Gray and black bars represent reads mapped to the forward and reverse strand, respectively. (**C**) Relative *PSK5* expression levels in 5-day-old wild-type (Col-0), $ERF115^{OE}$, and $ERF115^{SRDX}$ mutant root tips. Expression levels of the wild type were arbitrarily set to one. Data represent mean ± SE ($n = 3$ independent RNA extractions). (**D**) Relative *PSK5* expression levels in 5-day-old wild-type (Col-0) and *ccs52a2-1* mutant roots. Expression levels of the wild type were arbitrarily set to one. Data represent mean ± SE ($n = 3$ independent RNA extractions). (**E**) Relative *ERF115* (black) and *PSK5* (gray) expression levels in 1-week-old wild-type (Ws-2) and *brassinosteroid-insensitive 1 receptor* (bri1-5) mutant roots control-treated (BL-) or treated with 0.5 nM brassinolide (BL+). Expression levels of the wild type were arbitrarily set to one. Data represent mean ± SE ($n = 3$ independent RNA extractions). (**F**) Confocal microscopy image of 1-week-old wild-type (Col-0), $ERF115^{OE}$, and $ERF115^{OE}$ *pskr1-3* mutant root meristems. Scale bar, 50 μm.

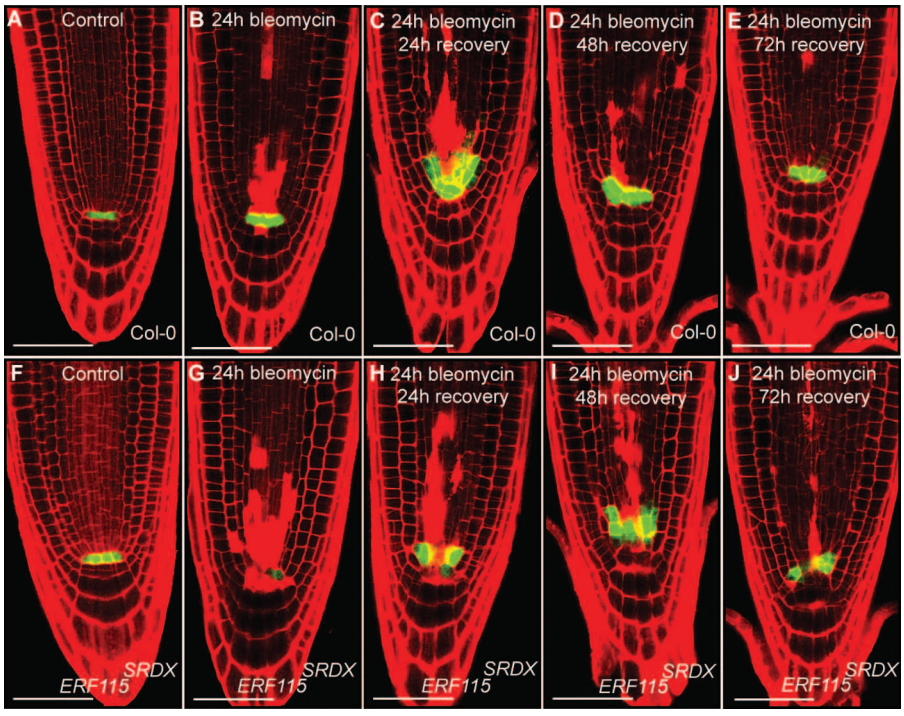

Fig. 4. ERF115 maintains the QC identity domain upon damage of the stem cell niche. (**A** to **E**) Wild-type (Col-0) root tips before (A) and after treatment with 0.6 μg/mL bleomycin for 24 hours (B) and upon recovery on bleomycin-free medium for 24 hours (C), 48 hours (D), and 72 hours (E). (**F** to **J**) *ERF115*^{SRDX} root tips before (F) and after treatment with 0.6 μg/mL bleomycin for 24 hours (G) and upon recovery on bleomycin-free medium for 24 hours (H), 48 hours (I), and 72 hours (J). QC cells are visualized by the WOX5-GFP marker. Cells were counterstained with propidium iodide. Scale bars, 50 μm.

References and Notes

1. C. van den Berg, V. Willemsen, W. Hage, P. Weisbeek, B. Scheres, *Nature* **378**, 62–65 (1995).
2. C. van den Berg, V. Willemsen, G. Hendriks, P. Weisbeek, B. Scheres, *Nature* **390**, 287–289 (1997).
3. F. A. Clowes, *Exp. Cell Res.* **25**, 529–534 (1961).
4. M. Fujie, H. Kuroiwa, T. Suzuki, S. Kawano, T. Kuroiwa, *J. Exp. Bot.* **44**, 689–693 (1993).
5. O. Ortega-Martínez, M. Pernas, R. J. Carol, L. Dolan, *Science* **317**, 507–510 (2007).
6. C. Kidner, V. Sundaresan, K. Roberts, L. Dolan, *Planta* **211**, 191–199 (2000).
7. A. K. Sarkar *et al.*, *Nature* **446**, 811–814 (2007).
8. M. Wildwater *et al.*, *Cell* **123**, 1337–1349 (2005).
9. M. Vanstraelen *et al.*, *Proc. Natl. Acad. Sci. U.S.A.* **106**, 11806–11811 (2009).
10. J. Van Leene *et al.*, *Mol. Syst. Biol.* **6**, 397 (2010).
11. V. Boudolf *et al.*, *Plant Physiol.* **150**, 1482–1493 (2009).
12. M. P. González-García *et al.*, *Development* **138**, 849–859 (2011).
13. M. Ikeda, M. Ohme-Takagi, *Plant Cell Physiol.* **50**, 970–975 (2009).
14. A. Kutschmar *et al.*, *New Phytol.* **181**, 820–831 (2009).
15. Y. Matsubayashi, T. Goto, Y. Sakagami, *Plant Cell Rep.* **23**, 155–158 (2004).
16. N. Stührwohldt, R. I. Dahlke, B. Steffens, A. Johnson, M. Sauter, *PLOS ONE* **6**, e21054 (2011).
17. H. Yang, Y. Matsubayashi, K. Nakamura, Y. Sakagami, *Plant Physiol.* **127**, 842–851 (2001).
18. J. Hartmann, N. Stührwohldt, R. I. Dahlke, M. Sauter, *Plant J.* **73**, 579–590 (2013).
19. Y. Amano, H. Tsubouchi, H. Shinohara, M. Ogawa, Y. Matsubayashi, *Proc. Natl. Acad. Sci. U.S.A.* **104**, 18333–18338 (2007).
20. Y. Matsubayashi, M. Ogawa, A. Morita, Y. Sakagami, *Science* **296**, 1470–1472 (2002).
21. Q. Chen *et al.*, *Plant Cell* **23**, 3335–3352 (2011).
22. J. Bergonié, L. Tribondeau, *C. R. Acad. Sci.* **143**, 983–985 (1906).
23. N. Fulcher, R. Sablowski, *Proc. Natl. Acad. Sci. U.S.A.* **106**, 20984–20988 (2009).
24. F. A. L. Clowes, *Ann. Bot. (London)* **23**, 205–210 (1959).
25. L. Li, H. Clevers, *Science* **327**, 542–545 (2010).

Acknowledgments: The authors thank M. Sauter for sharing the *pskr1-3* mutant and A. Bleys and M. De Cock for help in preparing the manuscript. This work was supported by Ghent University (Multidisciplinary Research Partnership Bioinformatics: From nucleotides to networks); theInteruniversity Attraction Poles Programme (IUAP P7/29 MARS), initiated by the Belgian Science Policy Office; Ghent University-Bijzonder Onderzoeksfonds (to D.V.D.S.); and Research Foundation-Flanders (grants G.029809 and G.022.10N to D.V.D.S. and L.D.V., respectively). K.S.H. is indebted to the Agency for Innovation by Science and Technology for a predoctoral fellowship. T.C., F.V., and J.V.L. are Postdoctoral Fellows of the Research Foundation-Flanders. Microarray and sequencing data have been deposited in the Gene Expression Omnibus (GEO) database, www.ncbi.nlm.nih.gov/geo under accession nos. GSE48836 and GSE48793, respectively. J.H. and L.D.V. are inventors on a patent application filed by Ghent University and Vlaams Instituut voor Biotechnologie that covers the use of ERF115 to modulate plant growth through phytosulfokine gene expression.

Supplementary Materials

www.sciencemag.org/content/342/6160/860/suppl/DC1
Materials and Methods
Figs. S1 to S15
Tables S1 to S5
References (*26*–*38*)

17 May 2013; accepted 15 October 2013
Published online 24 October 2013;
10.1126/science.1240667

Staphylococcus aureus Degrades Neutrophil Extracellular Traps to Promote Immune Cell Death

Vilasack Thammavongsa, Dominique M. Missiakas, Olaf Schneewind*

Bacterial invasion of host tissues triggers polymorphonuclear leukocytes to release DNA [neutrophil extracellular traps (NETs)], thereby immobilizing microbes for subsequent clearance by innate defenses including macrophage phagocytosis. We report here that *Staphylococcus aureus* escapes these defenses by converting NETs to deoxyadenosine, which triggers the caspase-3–mediated death of immune cells. Conversion of NETs to deoxyadenosine requires two enzymes, nuclease and adenosine synthase, that are secreted by *S. aureus* and are necessary for the exclusion of macrophages from staphylococcal abscesses. Thus, the pathogenesis of *S. aureus* infections has evolved to anticipate host defenses and to repurpose them for the destruction of the immune system.

Staphylococcus aureus is a leading cause of skin and soft-tissue infections, bacteremia, sepsis, and endocarditis (*1*). The vast spectrum of human morbidity and mortality has been attributed to the ability of staphylococci to evade innate and adaptive immune responses (*2*). The hallmark of *S. aureus* infection is the formation of abscesses, which comprise a bacterial community surrounded by fibrin deposits and a cuff of host immune cells (*3*) (Fig. 1 and fig. S1). Such lesions evolve by the infiltration of neutrophils, which release their DNA in the form of neutrophil extracellular traps (NETs) that immobilize the pathogen and enhance the bactericidal activity of antimicrobial peptides (*4*). *S. aureus* produces a spectrum of virulence factors that counter neutrophil defenses and include proteins that kill neutrophils (*2*); block their extravasation (*5*), chemotaxis (*6*), opsonization, and phagocytosis (*7*); and inhibit reactive oxygen–mediated killing (*8*). Earlier work has reported that staphylococcal nuclease, secreted by *S. aureus*, degrades NETs (*9*). Thus, staphylococci persist and replicate within

Department of Microbiology, University of Chicago, 920 East 58th Street, Chicago, IL 60637, USA.
*Corresponding author. E-mail: oschnee@bsd.uchicago.edu

abscesses and seed new lesions at different sites or disseminate to other hosts via the purulent exudate (*3*).

Although the interactions between *S. aureus* and neutrophils have been studied in detail, comparatively little is known about the contributions of macrophages toward the establishment of abscesses and the potential clearance of staphylococcal infections. In this work, we combined immunohistochemical staining of abscesses and the genetic analysis of *S. aureus* to explore the fate of macrophages during staphylococcal infections in mice (see supplementary materials and methods). Immunohistochemical examination of renal tissues isolated 5 days after intravenous injection of *S. aureus* into BALB/c mice revealed bacteria surrounded by infiltrates of immune cells, primarily composed of Ly-6G–positive neutrophils (Fig. 1, A and J). Macrophages, identified by F4/80-specific staining, were observed to accumulate only at the periphery of abscesses and were absent from the cuff of neutrophils surrounding bacteria (Fig. 1, D and G). We used a collection of *S. aureus* mutants with insertional lesions in virulence genes (*10*) to search for variants with phenotypic defects in which macrophages entered abscesses and the frequency of lesions was reduced (table S1). Two mutants, with mutations in staphylococcal nuclease (*nuc*) or adenosine synthase A (*adsA*), were selected. Abscesses that had been caused by the *nuc* mutant harbored staphylococci surrounded by a cuff of neutrophils and with infiltrates of F4/80-positive macrophages at the periphery of the immune cell cuff, but not in the central part of the abscess (Fig. 1, B, E, and H). In contrast, abscesses caused by the *adsA* mutant were characterized by diffuse infiltrates of F4/80-positive macrophages throughout the neutrophil cuff (Fig. 1, C, F, and I). Expression of plasmid-encoded *nuc* and *adsA* in the mutant strains restored the wild-type (WT) phenotype (figs. S1 and S2). As a control, *S. aureus* variants with mutations in the genes for clumping factor A (*clfA*) or coagulase (*coa*) (*3*) did not affect the frequency or structure of the abscesses (fig. S1). Taken together, these results indicate that macrophages are excluded from *S. aureus*–induced abscesses by mechanisms requiring staphylococcal secretion of nuclease and AdsA.

We wondered whether secreted virulence factors of *S. aureus* affect the viability of mouse or human macrophages. Incubation of *S. aureus*–conditioned culture medium with mouse or human macrophages (see below) or the human macrophage cell line U937 did not increase trypan blue staining, which serves as an indicator of loss of cell viability (Fig. 2A). To test whether a host product contributed we first incubated bacterial cultures with human blood neutrophils and then added macrophages. Incubation of *S. aureus* culture media with macrophages alone did not cause an increase in cytotoxicity (Fig. 2A). However, treatment of neutrophils with phorbol 12-myristol 13-acetate (PMA), an inducer of NET formation (*4*), caused staphylococci to generate a product that, when transferred to U937 cells, triggered a loss of macrophage viability [8 ± 1.6% (SEM) trypan blue–positive cells for *S. aureus* plus NETs compared with 1.5 ± 0.6% (SEM) for NETs alone; $P < 0.05$] (Fig. 2A). This cytotoxic activity was reduced when *S. aureus* NET samples were derived from *nuc* or *adsA* variant strains (Fig. 2A). Nuclease is a DNA cleavage enzyme with endo- and exonuclease activity (*11*), and AdsA has been reported to function as a 5′-nucleotidase (*12*). Nuclease is secreted via its N-terminal signal peptide into the extracellular medium. AdsA is anchored to the envelope and subsequently released into the extracellular medium (*13*).

To identify the toxic product generated by staphylococci, we treated NETs with staphylococcal culture medium and analyzed the products with reversed-phase high-performance liquid chromatography (rpHPLC) and matrix-assisted laser desorption/ionization–time-of-flight (MALDI-TOF) mass spectrometry (Fig. 2C). A single ion [mass/charge ratio (*m/z*) 251.074] that was absent from mock-treated NETs was identified in NET samples treated with staphylococci. The mass was consistent with 2′-deoxyadenosine (dAdo), a deoxyribonucleoside base of DNA (Fig. 2C). NETs treated with either the *nuc* or *adsA* mutants, which stimulated less macrophage cytotoxicity, had less dAdo. NETs that had not been exposed to staphylococci did not have dAdo. The extracellular medium of staphylococcal cultures also lacked dAdo (Fig. 2C). These data indicate that staphylococcal nuclease and AdsA are both required to release dAdo from NETs, and dAdo may be responsible for the observed cytotoxic effect on macrophages. To test this model, we incubated human HL60 neutrophils, THP-1 monocytes, and U937 macrophages with purified dAdo or with adenosine, another immune-suppressive product that staphylococcal AdsA generates from adenosine triphosphate (ATP) released by damaged host tissues (*13*). Purified dAdo, but not adenosine, induced cytotoxicity of U937 macrophages and THP-1 monocytes, whereas HL60 neutrophils were insignificantly affected (Fig. 2D).

Treatment of human or animal cells with dAdo causes accumulation of intracellular dATP, which quenches DNA synthesis and triggers apoptosis (*14*). Rapidly dividing cells of the hematopoietic lineage are particularly susceptible to dAdo-induced apoptosis (*14*). Under physiological conditions, accumulation of dAdo and adenosine

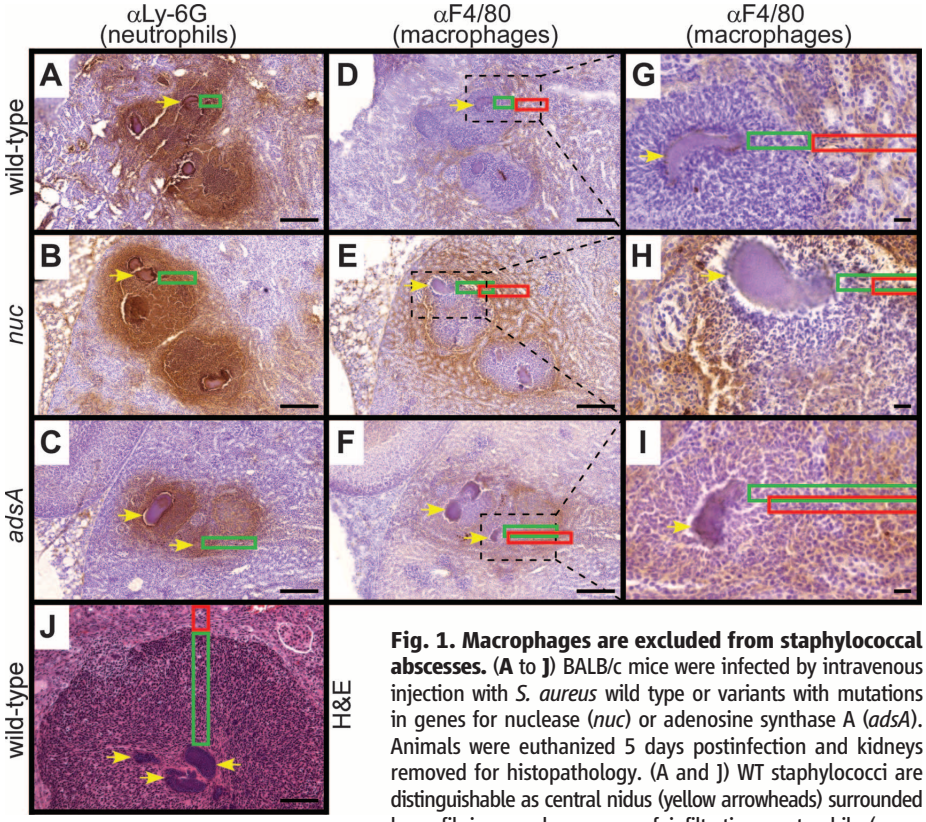

Fig. 1. Macrophages are excluded from staphylococcal abscesses. (**A** to **J**) BALB/c mice were infected by intravenous injection with *S. aureus* wild type or variants with mutations in genes for nuclease (*nuc*) or adenosine synthase A (*adsA*). Animals were euthanized 5 days postinfection and kidneys removed for histopathology. (A and J) WT staphylococci are distinguishable as central nidus (yellow arrowheads) surrounded by a fibrin capsule, a zone of infiltrating neutrophils (green boxes, immune cell cuffs), and macrophages at the periphery of these lesions [red box in (J), hematoxylin-and-eosin stained tissue]. Cryo-sections of renal tissues were examined by immunohistochemistry with αLy-6G antibodies [neutrophils stained as brown pigment (A to C)] or αF4/80 antibodies [macrophages (D to I)] and counterstained with hematoxylin. (G to I) Magnifications of the areas framed by the black boxes in (D) to (F). Macrophages (red boxes) are excluded from the neutrophil cuff of abscesses formed by WT *S. aureus* (green boxes), but not from those formed by the *nuc* or *adsA* mutants. Images are representative of similar data from kidneys of each cohort ($N = 4$) of infected mice. Scale bars: (A to F) 200 μm; (G to I) 20 μm; (J) 100 μm.

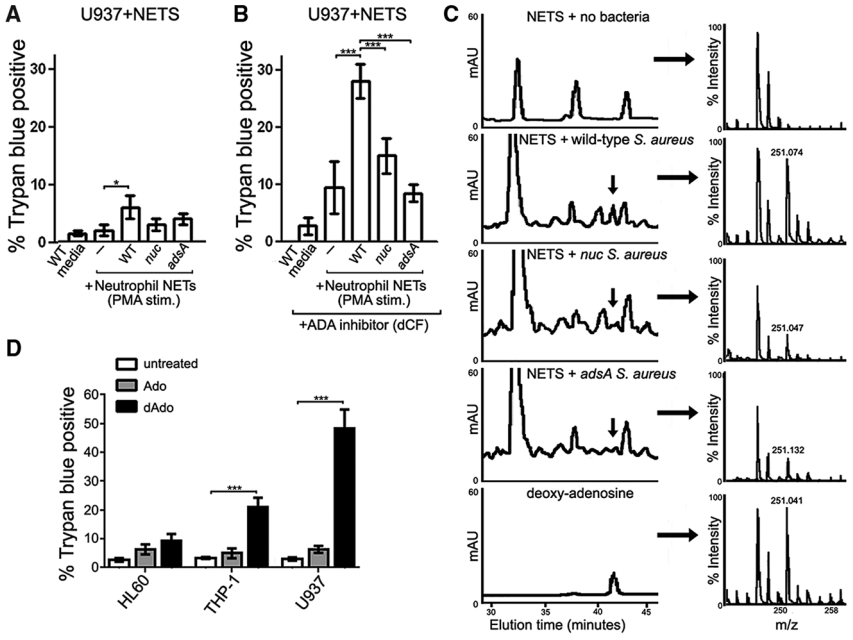

Fig. 2. *S. aureus* generates deoxyadenosine from NETs to induce macrophage cytotoxicity. (**A**) Death of U937 macrophages was measured as trypan blue uptake. Human neutrophils were induced with PMA to form NETs that were then exposed to staphylococcal cultures and used to treat human U937 macrophages. Pairwise comparisons of mock/phosphate-buffered saline PBS (–) with the extracellular medium from WT, *nuc*, or *adsA* mutant *S. aureus* cultures were conducted. Data are the mean ± SEM ($N = 3$ replicates). Statistical significance was examined with the two-tailed Student's *t* test; $^*P < 0.05$. (**B**) U937 macrophages were treated with the adenosine deaminase inhibitor dCF and with NETs that were mock treated or incubated with staphylococcal culture medium ($N = 3$); $^{***}P < 0.005$. (**C**) NET cleavage reactions (A) were subjected to rpHPLC. Absorbance at 260 nm was monitored (left panels); eluate was analyzed by MALDI-TOF mass spectrometry (right panels), which identified *m/z* 251.074 as deoxyadenosine (dAdo, arrows). mAU, milliabsorbance units. (**D**) Differentiated human HL60 neutrophil, THP-1 monocyte, and U937 macrophage cell lines were incubated overnight with 10 μM adenosine (Ado) or dAdo and monitored for cell death. Data are the mean ± SEM ($N = 3$). Statistical significance was examined with the two-tailed Student's *t* test; $^{***}P < 0.005$.

is prevented by adenosine deaminases (ADAs), enzymes of the purine salvage pathway that deaminate dAdo and adenosine to generate inosine or deoxyinosine, respectively (*15*). Inability to degrade Ado or dAdo, as occurs in individuals with heritable defects in ADA expression, causes severe combined immunodeficiency (*15*). Activity of ADA is observed both within cells and in plasma. Two isoenzymes, designated ADA1 and ADA2, are expressed in mammalian tissues. In plasma, ADA activity is predominantly derived from macrophage ADA2, and depending on cell or tissue type, intracellular activities are attributable to ADA1 and/or ADA2 (*16*). Conditioned media collected from HL60, THP-1, and U937 cell overnight cultures cleaved [^{14}C] adenosine to generate [^{14}C] inosine, as observed by thin-layer chromatography (fig. S3). Erythro-9-(2-hydroxy-3-nonyl)adenine (EHNA), an effective inhibitor of ADA1 (*17*), quenched adenosine deaminase activity of HL60 and THP-1 cells, but not of U937 macrophages. Similarly, the activity of purified recombinant ADA1 was blocked by EHNA, whereas the activity of U937 cells was only slightly reduced (fig. S3). Treatment with 2′-deoxycoformycin (dCF), a potent ADA1/2 inhibitor, blocked the adenosine deaminase activity of U937, HL60, and THP-1 cells (fig. S3). dCF treatment also increased the macrophage cytotoxicity of NETs incubated with *S. aureus* (Fig. 2B). Cytotoxic activity was abolished in the *S. aureus adsA* mutant and reduced in the *nuc* variant. Together, these data indicate that the phosphodiesterase activity of nuclease, which predominantly cleaves DNA and RNA into 3′phosphomononucleotides and dinucleotides

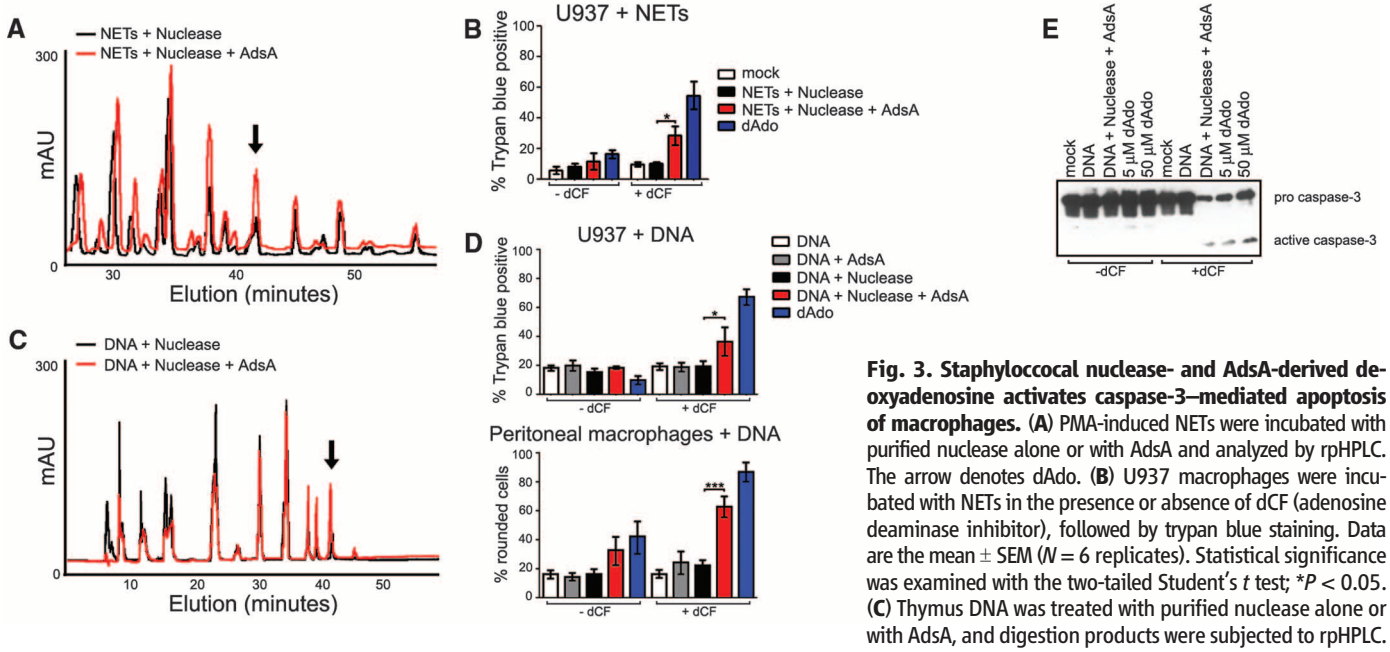

Fig. 3. Staphyloccocal nuclease- and AdsA-derived deoxyadenosine activates caspase-3–mediated apoptosis of macrophages. (**A**) PMA-induced NETs were incubated with purified nuclease alone or with AdsA and analyzed by rpHPLC. The arrow denotes dAdo. (**B**) U937 macrophages were incubated with NETs in the presence or absence of dCF (adenosine deaminase inhibitor), followed by trypan blue staining. Data are the mean ± SEM ($N = 6$ replicates). Statistical significance was examined with the two-tailed Student's *t* test; $^*P < 0.05$. (**C**) Thymus DNA was treated with purified nuclease alone or with AdsA, and digestion products were subjected to rpHPLC. (**D**) U937 macrophages or mouse macrophages were treated with thymus DNA samples that had been incubated with nuclease alone or with AdsA in the presence or absence of dCF, followed by trypan blue staining. Digestions of DNA with either purified nuclease or AdsA alone and undigested thymus DNA were included as controls. Data are the mean ± SEM ($N = 3$). Statistical significance was examined with the two-tailed Student's *t* test; $^*P < 0.05$; $^{***}P < 0.005$. (**E**) U937 macrophages were incubated with thymus DNA pretreated with nuclease alone or with AdsA. Cell lysates were subjected to immunoblotting with α-caspase-3 antibodies ($N = 3$).

(*11*), degraded NETs into products that AdsA subsequently converted into dAdo. In agreement with this model, rpHPLC analysis of 2′-deoxyadenosine-3′-monophosphate and 2′-deoxyadenosine-5′-monophosphate treated with purified AdsA revealed the generation of dAdo, indicating that AdsA also functions as a 3′-nucleotidase in addition to its reported 5′-nucleotidase function (fig. S4) (*12*).

We sought to reconstitute dAdo production from NETs using purified nuclease and AdsA. Treatment of NETs with nuclease generated a spectrum of cleavage products, mostly mononucleotides such as 2′-deoxyadenosine-3′-phosphate, whereas treatment with nuclease and AdsA produced dAdo (Fig. 3A). When added to U937 macrophages, we observed a corresponding increase in cytotoxicity from nuclease- and AdsA-treated NETs (Fig. 3B). Cytotoxicity was increased even further when NETs were added to U937 cells in the presence of dCF, which prevents cleavage of dAdo to deoxyinosine (Fig. 3B). NETs consist of DNA and associated granule proteins, including calprotectin, elastase, myeloperoxidase, and antimicrobial peptides (*4*). After neutrophil degranulation and NET formation, granule proteins contribute to tissue damage and trigger inflammatory responses (*18*). We sought to discern whether dAdo from NET DNA was sufficient to induce macrophage apoptosis or whether granule proteins were also required. Purified thymus DNA devoid of granular enzymes was incubated with nuclease and AdsA. The reaction products were analyzed by rpHPLC, which showed that dAdo was produced (Fig. 3C). Thymus DNA digestion products were cytotoxic for U937 macrophages and primary human monocytes but not for neutrophils (Fig. 3 and fig. S5). Cell death in U937 cells and human monocytes was associated with annexin V staining, indicating that treatment with nuclease- and AdsA-digested DNA products induces apoptosis (fig. S6) (*19*). These data indicate that staphylococcal nuclease- and AdsA-derived NET cytotoxicity selectively targets monoctyes and macrophages. This phenotype is attributable to the production of dAdo and is not dependent on the concomitant release of neutrophil granular enzymes.

Treatment of U937 macrophages with dAdo triggered the conversion of procaspase-3 to active caspase-3, a potent inducer of apoptosis (Fig. 3E) (*20*). Although thymus DNA alone did not activate caspase-3, nuclease and AdsA digestion of DNA triggered U937 macrophage conversion of procaspase-3 to active caspase-3, which was also detected when ADA activity was blocked with dCF (Fig. 3E). Inhibition of caspase-3 with the Z-DEVD-FMK peptide significantly reduced dAdo-induced cell death (fig. S7). Caspase-3 activation was observed in *S. aureus* abscesses with immunohistochemical staining (fig. S8). Less caspase-3 staining was observed in abscesses from the *nuc* mutant strain and was not detectable in lesions caused by the *adsA* mutant strain (fig. S8).

Here, we present evidence that *S. aureus* infection of host tissues is associated with the production of dAdo from NETs that are cleaved by two secreted bacterial products, nuclease and AdsA. Production of dAdo by AdsA is sufficient to induce apoptosis of macrophages via the activation of caspase-3. This mechanism restricts the survival of macrophages entering the immune cell cuff that surrounds staphylococcal abscess communities, thereby antagonizing phagocytosis of the invading pathogen and promoting the establishment of persistent infections. Nuclease facilitates the production of dAdo through the degradation of NET DNA into deoxyadenosine monophosphate, a substrate for AdsA, thereby supporting macrophage exclusion at the periphery of the immune cell cuff. These insights may aid in the design of therapies that enhance macrophage survival and staphylococcal clearance from infected tissues.

References and Notes

1. A. J. Kallen *et al.*, *JAMA* **304**, 641–648 (2010).
2. A. N. Spaan, B. G. J. Surewaard, R. Nijland, J. A. G. van Strijp, *Annu. Rev. Microbiol.* **67**, 629–650 (2013).
3. A. G. Cheng *et al.*, *PLOS Pathog.* **6**, e1001036 (2010).
4. V. Brinkmann *et al.*, *Science* **303**, 1532–1535 (2004).
5. J. Bestebroer *et al.*, *Blood* **113**, 328–337 (2009).
6. A. J. Laarman *et al.*, *EMBO J.* **31**, 3607–3619 (2012).
7. S. H. M. Rooijakkers *et al.*, *Nat. Immunol.* **10**, 721–727 (2009).
8. G. Y. Liu *et al.*, *J. Exp. Med.* **202**, 209–215 (2005).
9. E. T. Berends *et al.*, *J. Innate Immun.* **2**, 576–586 (2010).
10. T. Bae *et al.*, *Proc. Natl. Acad. Sci. U.S.A.* **101**, 12312–12317 (2004).
11. K. K. Reddi, *Nature* **187**, 74–75 (1960).
12. V. Thammavongsa, O. Schneewind, D. M. Missiakas, *BMC Biochem.* **12**, 56 (2011).
13. V. Thammavongsa, J. W. Kern, D. M. Missiakas, O. Schneewind, *J. Exp. Med.* **206**, 2417–2427 (2009).
14. D. A. Carson, J. Kaye, S. Matsumoto, J. E. Seegmiller, L. Thompson, *Proc. Natl. Acad. Sci. U.S.A.* **76**, 2430–2433 (1979).
15. E. R. Giblett, J. E. Anderson, F. Cohen, B. Pollara, H. J. Meuwissen, *Lancet* **300**, 1067–1069 (1972).
16. R. Franco, R. Pacheco, J. M. Gatell, T. Gallart, C. Lluis, *Crit. Rev. Immunol.* **27**, 495–509 (2007).
17. N. M. Kredich, D. V. J. Martin Jr., *Cell* **12**, 931–938 (1977).
18. A. Hakkim *et al.*, *Proc. Natl. Acad. Sci. U.S.A.* **107**, 9813–9818 (2010).
19. G. Koopman *et al.*, *Blood* **84**, 1415–1420 (1994).
20. N. Niitsu, Y. Yamaguchi, M. Umeda, Y. Honma, *Blood* **92**, 3368–3375 (1998).

Acknowledgments: We thank J. D. Sauer for macrophages. This work was supported by grants from the National Institute of Allergy and Infectious Diseases (AI038897, AI052474, and AI057153) and the American Heart Association (POST4590023). We declare no conflicting financial interests. V.T. performed experiments; V.T., D.M.M., and O.S. interpreted data, designed experiments, and wrote the paper.

Supplementary Materials

www.sciencemag.org/content/342/6160/863/suppl/DC1
Materials and Methods
Supplementary Text
Figs. S1 to S8
Table S1
References (*21*–*23*)

21 June 2013; accepted 16 October 2013
10.1126/science.1242255

Phosphoinositide 3-Kinase δ Gene Mutation Predisposes to Respiratory Infection and Airway Damage

Ivan Angulo,[1]* Oscar Vadas,[2]*† Fabien Garçon,[3]* Edward Banham-Hall,[3]* Vincent Plagnol,[4] Timothy R. Leahy,[5,6] Helen Baxendale,[7] Tanya Coulter,[6,8] James Curtis,[1] Changxin Wu,[1] Katherine Blake-Palmer,[1] Olga Perisic,[2] Deborah Smyth,[9] Mailis Maes,[1] Christine Fiddler,[1] Jatinder Juss,[1] Deirdre Cilliers,[10] Gašper Markelj,[11] Anita Chandra,[7] George Farmer,[12] Anna Kielkowska,[13] Jonathan Clark,[13] Sven Kracker,[14,15] Marianne Debré,[16] Capucine Picard,[15,16,17] Isabelle Pellier,[18] Nada Jabado,[19] James A. Morris,[20] Gabriela Barcenas-Morales,[21] Alain Fischer,[14,15,16] Len Stephens,[3] Phillip Hawkins,[3] Jeffrey C. Barrett,[20] Mario Abinun,[5] Menna Clatworthy,[1] Anne Durandy,[14,15,16,17] Rainer Doffinger,[7] Edwin R. Chilvers,[1] Andrew J. Cant,[5] Dinakantha Kumararatne,[7] Klaus Okkenhaug,[3] Roger L. Williams,[2] Alison Condliffe,[1]‡ Sergey Nejentsev[1]‡§

Genetic mutations cause primary immunodeficiencies (PIDs) that predispose to infections. Here, we describe activated PI3K-δ syndrome (APDS), a PID associated with a dominant gain-of-function mutation in which lysine replaced glutamic acid at residue 1021 (E1021K) in the p110δ protein, the catalytic subunit of phosphoinositide 3-kinase δ (PI3Kδ), encoded by the *PIK3CD* gene. We found E1021K in 17 patients from seven unrelated families, but not among 3346 healthy subjects. APDS was characterized by recurrent respiratory infections, progressive airway damage, lymphopenia, increased circulating transitional B cells, increased immunoglobulin M, and reduced immunoglobulin G2 levels in serum and impaired vaccine responses. The E1021K mutation enhanced membrane association and kinase activity of p110δ. Patient-derived lymphocytes had increased levels of phosphatidylinositol 3,4,5-trisphosphate and phosphorylated AKT protein and were prone to activation-induced cell death. Selective p110δ inhibitors IC87114 and GS-1101 reduced the activity of the mutant enzyme in vitro, which suggested a therapeutic approach for patients with APDS.

Respiratory infections are the most common illnesses of people worldwide. Recurrent respiratory infections may lead to bronchiectasis, a permanent, abnormal dilation of bronchi (*1*). Susceptibility to recurrent respiratory infections and bronchiectasis may be conferred by an underlying primary immunodeficiency (PID) (*1*, *2*). PIDs have variable penetrance, and

those that have a milder course may remain undiagnosed. Mutations in more than 200 genes are known to cause various PIDs (*3*). Recent improvements in DNA sequencing technology provide an opportunity to study the patient's whole genome or its coding part, known as the exome (*4*). This technological advancement has improved the genetic diagnostics of PIDs in patients with recurrent and severe infections and facilitated the identification of novel causative genes and mutations.

We used exome sequencing to search for causative mutations in 35 PID patients from the United Kingdom who suffered recurrent infections and had a family history of susceptibility to infections (*5*). After identification of genetic variants in these patients, we excluded common polymorphisms previously detected in the 1000 Genomes and National Heart, Lung, and Blood Institute (NHLBI) projects (table S1) (*5*). When cross-checking the remaining rare variants, we noted that three patients from one family (P1, P2, and P3 in family A) and one patient from another family (P5 in family B) had the same heterozygous G to A mutation at position 9,787,030 on chromosome 1, c.3061G>A in the *PIK3CD* gene (Fig. 1). This mutation was not present in the other exomes and was the only rare variant shared among all patients in these two unrelated families. It encodes an amino-acid substitution, a glutamic acid for a lysine, at position 1021 (E1021K) of the p110δ protein, the catalytic subunit of phosphoinositide 3-kinase δ (PI3Kδ). Sanger sequencing confirmed the presence of the E1021K mutation in these patients and four additional affected family members. In both families, the mutation cosegregated with the clinical phenotype (Fig. 1).

We then designed a genotyping assay for this E1021K mutation and screened 3346 healthy subjects, including 2296 from the United Kingdom and 1050 representing 51 different populations from around the world (*5*). No healthy carriers of E1021K were identified in these two large cohorts, supporting our hypothesis that this is a pathogenic mutation rather than a rare neutral polymorphism. We then studied DNA samples of an additional heterogeneous cohort of 134 PID patients from the United Kingdom and Ireland (*5*). In this cohort, we identified five further patients from three unrelated families (C, D, and E) who had the same heterozygous E1021K mutation (Fig. 1A). The apparent high frequency of the mutation among PID patients and the fact that P8 (family C) had previously been diagnosed with hyper-immunoglobulin M (hyper-IgM) syndrome prompted us to study an additional cohort from France comprising 15 hyper-IgM patients from 13 families that had previously undergone exome sequencing. Among these, we found three patients from two unrelated families, F and G, with the same mutation, indicating that E1021K may cause a typical hyper-IgM syndrome. One additional patient was identified among family members, bringing the overall number of patients with the E1021K mutation to 17.

Sequencing of the healthy parents of P8 in family C showed that both were homozygous for the normal allele (Fig. 1A). Genome-wide identity-by-descent analysis in family C confirmed the relationship of both parents to P8, thus classifying this E1021K mutation as de novo. The mutation was present in DNA isolated from both fibroblast and blood samples of P8 and therefore is likely to be germline, rather than somatic. Then, in families A to E, we studied genotypes of 149 markers in a 2-Mb interval on chromosome 1 flanking the mutation (*5*). We found no shared long-range haplotypes across any pair of families and no flanking markers that were consistently in linkage disequilibrium with the mutation across all five families. These data strongly suggest a recurrent mutation, rather than a founder effect. Nucleotide G in position 9,787,030 is part of a CpG dinucleotide (Fig. 1B) that is known to be ~30 times more prone to transition mutations (e.g., G>A) than an average nucleotide in the genome (*6*).

Before our genetic analysis, patients from families A to G were not considered to have the same disease etiology. The discovery of the same causative mutation in these patients prompted us to compare their clinical and immunological histories (table S2), revealing the phenotype of this PID, which is characterized by recurrent respiratory infections and progressive airway damage (Table 1, supplementary text, and figs. S1 and S2). Whereas the immunological phenotype was largely consistent between patients, the clinical presentation and disease course have been variable (e.g., mild disease in P10) (table S2). Such clinical variability may be explained by differences in lifestyle, exposure to pathogens, treatment efficacy, and possibly by modifying genetic factors.

To understand how the E1021K mutation caused immunodeficiency, we first studied its effect on p110δ function. The p110δ protein is a catalytic subunit that, together with a regulatory subunit, forms PI3Kδ, a heterodimeric lipid kinase. PI3Kδ phosphorylates phosphatidylinositol 4,5-bisphosphate (PIP_2), generating phosphatidylinositol 3,4,5-trisphosphate (PIP_3), an important second messenger molecule. We cloned the cDNA of p110δ and introduced the E1021K change by site-directed mutagenesis. Subsequently, we expressed both normal and mutant p110δ proteins, together with the regulatory subunit p85α, in baculovirus-infected insect cells and purified the proteins (fig. S3A). We measured lipid kinase activity using a modified membrane capture assay (*7*) and found that the basal PIP_3 production by PI3Kδ containing the mutant $p110\delta^{E1021K}$ subunit was higher by up to a factor of 6 than that produced by the wild-type PI3Kδ (Fig. 2A and fig. S3B). After stimulation with a platelet-derived growth factor (PDGF) receptor's bis-phosphorylated peptide (pY), the activity of both wild-type and mutant PI3Kδ increased, but PIP_3 production by the mutant PI3Kδ was still up to 3 times as high (Fig. 2A and fig. S3C). We used two structurally related isoform-selective PI3Kδ inhibitors, IC87114 and GS-1101 (*8*, *9*), and found that both reduced the activity of the mutant PI3Kδ as efficiently as that of the wild-type PI3Kδ (Fig. 2B), suggesting that these compounds may be effective in patients with the E1021K mutation.

To understand the mechanism by which E1021K increases PI3Kδ activity, we first modeled the structure of the mutant p110δ protein (*5*). p110δ is organized similarly to other PI3K catalytic subunits (Fig. 2C) (*10*, *11*). The E1021K mutation is located in the C lobe of the kinase domain that interacts with cellular membrane, accommodates lipid substrate, and binds the cSH2 domain of the regulatory subunit (Fig. 2D). Structural modeling showed that E1021K of p110δ is positioned similarly to the somatic mutation H1047R of another PI3K isoform, p110α, which is known to increase PI3K activity in cancer cells by enhancing its association with membranes (*12*, *13*). Therefore, we used a protein-lipid fluorescence resonance energy transfer (FRET) assay to study interaction between lipid vesicles and either wild-type p110δ or the mutant $p110\delta^{E1021K}$. We found that $p110\delta^{E1021K}$ has a much higher basal affinity for lipid vesicles than the wild-type p110δ (Fig. 2E). After pY stimulation, the affinity of $p110\delta^{E1021K}$ was also increased, although the difference with respect to the pY-activated wild-type p110δ was less striking (Fig. 2E). These results suggest that stronger binding to membranes contributes to the increased activity of the mutant $p110\delta^{E1021K}$ protein. Another potential activating mechanism of E1021K may involve interaction of p110δ with the regulatory subunit p85α (*14*). Our structural

[1]Department of Medicine, University of Cambridge, Cambridge, UK. [2]Medical Research Council, Laboratory of Molecular Biology, Cambridge, UK. [3]The Babraham Institute, Cambridge, UK. [4]University College London Genetics Institute, University College London, London, UK. [5]Primary Immunodeficiency Group, Institute of Cellular Medicine, Newcastle University, Newcastle upon Tyne, UK. [6]Our Lady's Children's Hospital, Crumlin, Dublin, Ireland. [7]Department of Clinical Biochemistry and Immunology, Addenbrooke's Hospital, Cambridge, UK. [8]Department of Immunology, School of Medicine, Trinity College, Dublin, Ireland. [9]Juvenile Diabetes Research Foundation/Wellcome Trust Diabetes and Inflammation Laboratory, Department of Medical Genetics, Cambridge Institute for Medical Research, University of Cambridge, Cambridge, UK. [10]Department of Clinical Genetics, Oxford University Hospitals, Oxford, UK. [11]Department of Allergology, Rheumatology and Clinical Immunology, University Children's Hospital, University Medical Center, Ljubljana, Slovenia. [12]Raigmore Hospital, Inverness, UK. [13]Babraham Bioscience Technologies Ltd, Babraham Research Campus, Cambridge, UK. [14]National Institute of Health and Medical Research INSERM U768, Necker Children's Hospital, Paris, France. [15]Descartes-Sorbonne Paris Cité University of Paris, Imagine Institute, Paris, France. [16]Department of Immunology and Hematology, Assistance Publique-Hopitaux de Paris, Necker Children's Hospital, Paris, France. [17]Center for Primary Immunodeficiencies (CEDI), Assistance Publique-Hopitaux de Paris, Necker Children's Hospital, Paris, France. [18]Department of Pediatrics, Centre Hospital Universitaire, Angers, France. [19]Department of Pediatrics, McGill University and McGill University Health Center, Montreal, Canada. [20]Wellcome Trust Sanger Institute, Wellcome Trust Genome Campus, Hinxton, UK. [21]Laboratorio de Inmunologia, Unam, Fes-Cuautitlan, Mexico.

*These authors contributed equally to this work.
†Present address: Department of Pharmaceutical Sciences, University of Geneva, Geneva, Switzerland.
‡These authors contributed equally to this work.
§Corresponding author. E-mail: sn262@cam.ac.uk

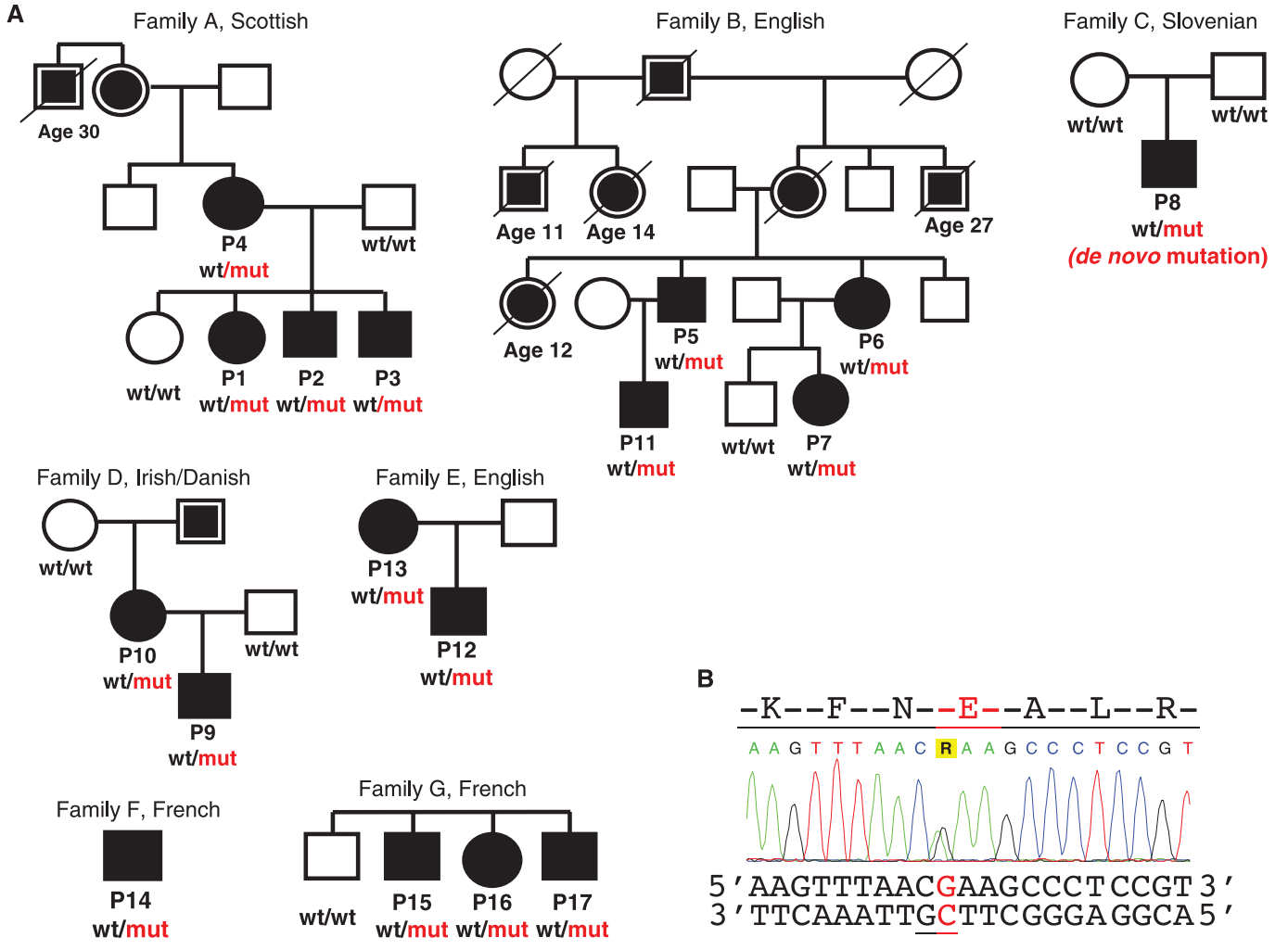

Fig. 1. Families with the E1021K p110δ mutation. (**A**) Open circles and squares, unaffected; filled circles and squares, affected; partly filled circles and squares, available data indicate recurrent infections. Age at the time of death is shown for patients who died ≤30 years of age. *PIK3CD* genotype is shown if known. wt, wild-type allele encoding glutamic acid (E1021); mut, mutant allele encoding lysine (K1021). (**B**) Sequence chromatogram showing heterozygous mutation c.3061G>A in the *PIK3CD* gene leading to the E1021K amino acid change in p110δ. CpG dinucleotide is underlined.

Table 1. Summary of clinical and immunological features of patients with the E1021K p110δ mutation. CT, computed tomography; HSV, herpes simplex virus; CMV, cytomegalovirus; VZV, varicella-zoster virus; EBV, Epstein-Barr virus.

Clinical or immunological manifestation	Patients	Frequency, *n*/total studied (%)
Recurrent respiratory and ear infections (*H. influenzae* and *S. pneumoniae*)	P1–17	17/17 (100)
CT evidence of large (bronchiectasis) or small (mosaic attenuation) airway disease	P1–7, 9, 11–13, 17	12/16 (75)
Splenomegaly (before the onset of recurrent infections)	P2, 3, 5, 6, 8, 9, 13–16	10/17 (59)
Skin, salivary gland, lacrimal gland, or dental abscess formation; orbital cellulitis	P1, 3, 5–8, 10	7/17 (41)
Infection caused by herpes group viruses (HSV, CMV, VZV, and EBV)	P3, 8, 12, 13 (and the deceased sister of P5/P6)	4/17 (24)
Marginal zone lymphoma	P13	1/17 (6)
Low/intermittent low-serum IgG2 levels	P2–7, 10–13	10/11 (91)
High/intermittent high-serum IgM levels	P1–6, 8–11, 13–16	14/17 (82)
Low levels of antibodies to *S. pneumoniae*	P1–4, 7, 9, 11–13, 17	10/10 (100)
Low levels of antibodies to *H. influenzae* type B	P1–4, 8, 9, 12, 13	8/10 (80)
Decreased circulating T cells (total $CD3^+$) and/or $CD4^+$ and/or $CD8^+$ T cells	P1–9, 13, 14, 17	12/17 (71)
Decreased circulating B cells (total $CD19^+$)	P2–9, 13, 14-16	12/17 (71)
Increased circulating transitional B cells ($CD19^+CD38^+IgM^+$)	P1–4, 7–14, 16, 17	14/16 (88)
Decreased circulating class-switched memory B cells ($CD19^+CD27^+IgD^-$)	P1–3, 8, 9, 12, 13, 16	8/16 (50)

model shows that E1021K may impair binding of p110δ to the inhibitory cSH2 domain (Fig. 2D), leading to increased PI3Kδ activity. However, it is unlikely to affect binding of another inhibitory p85α domain, nSH2 (Fig. 2D). This is consistent with our observation that pY stimulation further activates the mutant enzyme, probably by removing the nSH2 inhibition.

PI3Kδ is expressed predominantly in cells of hematopoietic lineage and is the major PI3K isoform signaling downstream of T and B cell antigen receptors (TCR and BCR), Toll-like receptors (TLRs), costimulatory molecules, and cytokine receptors in T, B, and myeloid cells (*15*). Therefore, we studied the activity of the mutant PI3Kδ ex vivo in patients' leukocytes. We measured levels of PIP_3 using a high-performance liquid chromatography–mass spectrometry–based assay (*16*) in $CD4^+$ and $CD8^+$ T cells isolated from fresh peripheral blood. In both T lymphocyte lineages we found consistently higher PIP_3 levels in patients than in controls before stimulation and 10, 20, 30, and 60 s after stimulation (Fig. 3A). In patient cells treated with IC87114, the levels of PIP_3 were significantly reduced (Fig. 3A). Furthermore, in stimulated patients' T cells, we found increased levels of phosphorylated AKT protein, a major downstream mediator of PIP_3 signaling (Fig. 3B). Levels of p110δ expression were normal in the patients' T cells (Fig. 3B). We then cloned in a retroviral vector the wild-type p110δ, the mutant $p110\delta^{E1021K}$, and $p110\delta^{D911A}$ with mutation D911A that inactivates the kinase domain, and transduced these constructs into T blasts isolated from the p110δ-knockout mouse (*5*). After stimulation, cells with $p110\delta^{E1021K}$ had more phosphorylated AKT than other cells (Fig. 3C and fig. S4). Together, these results strongly suggest that the E1021K mutation increases PI3K signaling in vivo as well as in vitro.

To study T cell responses, we stimulated purified $CD4^+$ and $CD8^+$ cells with antibodies to CD3 and CD28. Unexpectedly, we observed that both T cell lineages from patients were prone to cell death (Fig. 3D and fig. S5A). This phenomenon was reversed by the addition of IC87114 but not interleukin-2 (IL-2) (Fig. 3D and fig. S5B), suggesting that it is caused by the increased PI3Kδ activity. Cytokine production after stimulation of T cells was profoundly reduced in the patients and was not rescued by exogenous IL-2 (fig. S6), suggesting that T cell death occurs before any considerable cytokine response. However, stimulation with CytoStim, which did not induce T cell death, also led to reduced cytokine production by the patient-derived T cells (fig. S7). The propensity to activation-induced cell death (AICD) is consistent with the T cell lymphopenia found in our patients. It may relate in part to the increased proportion of T cells with

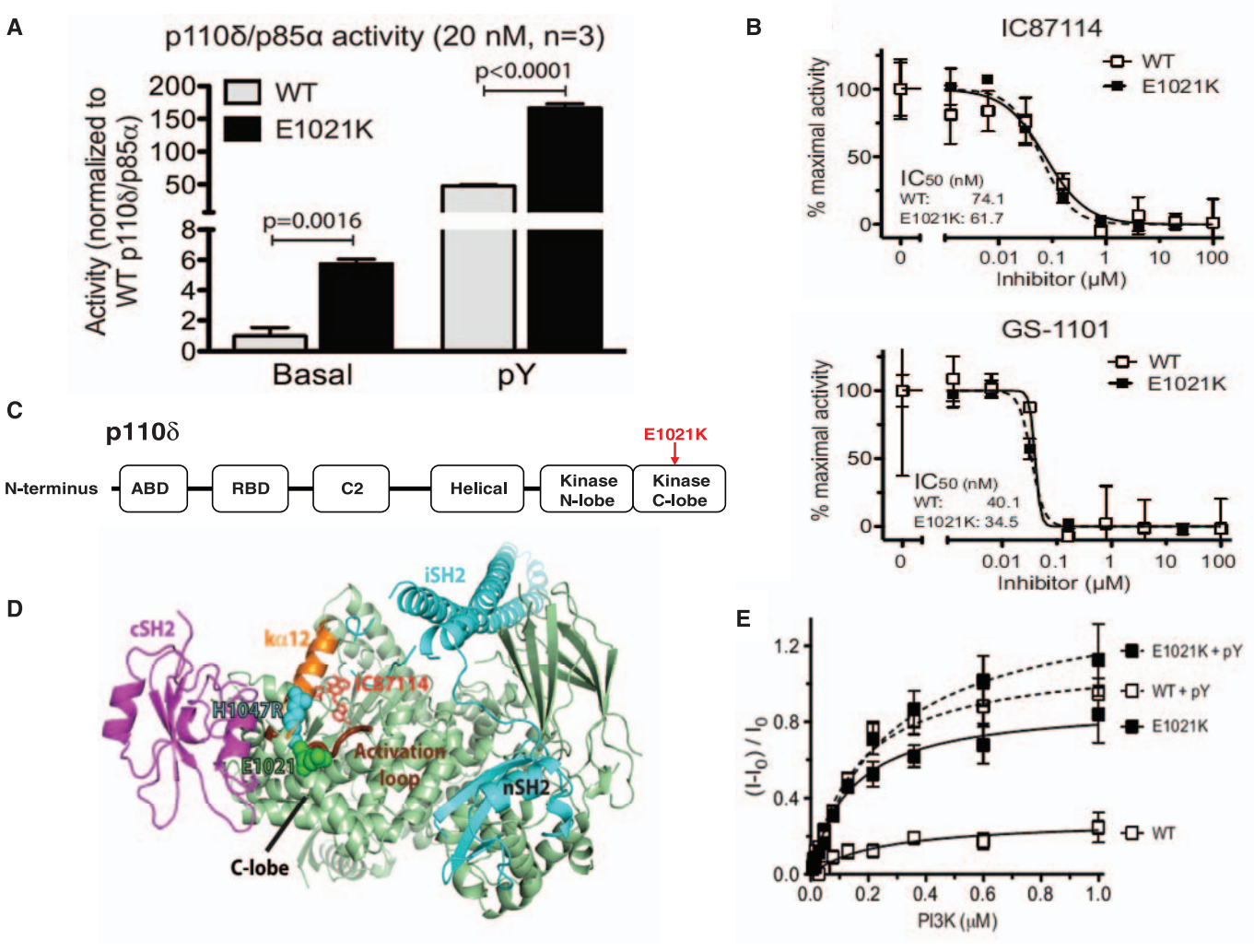

Fig. 2. In vitro activity and structure of p110δ. (**A**) Basal and pY-stimulated PI3K activity at 20-nM concentration. Graphs are mean ± SD of three independent experiments. *P* values were calculated by a two-tailed *t* test. (**B**) Inhibition of mutant and wild-type p110δ/p85α as a function of IC87114 or GS-1101 concentration (data are mean ± SD, *N* = 3 experiments). (**C**) Domain organization of p110δ. (**D**) Structural model of the p110δ/p85α heterodimer. p110δ catalytic subunit (pale green); nSH2 and iSH2 domains of the p85 regulatory subunit (cyan); cSH2 domain (magenta); p110δ activation loop (thick chocolate tube beneath kα12); residue E1021 of p110δ (green spheres); and the analogous residue in H1047R mutant of p110α (cyan spheres). The IC87114 inhibitor bound in the active site is shown in stick representation. (**E**) Membrane binding of p110δ. FRET between the PI3K complex and Dansyl-PS–containing membrane vesicles in the absence (solid lines) or presence (dashed lines) of the pY peptide (data are mean ± SD, *N* = 3 experiments).

an activated/memory phenotype (table S2) (*17*). Moreover, given that p110δ inhibitor reduces AICD of the patient-derived T cells, the activated p110δ may increase the AICD per se, possibly by enhancing TCR signaling.

In the patients' B lymphocytes, we also found increased amounts of phosphorylated AKT, both before and after stimulation, although this analysis was complicated by enhanced protein degradation in the patient-derived cells (fig. S8). Studies in transgenic mice deficient for phosphatase and tensin homolog (PTEN), an enzyme that dephosphorylates PIP_3, have shown that PI3Kδ activity, PIP_3, and phosphorylated AKT suppress immunoglobulin class-switch recombination (CSR) in B cells. These mice have impaired B cell function, increased IgM, decreased IgG and IgA levels, and impaired antibody responses after immunization (*18*–*21*). Immunological presentation of our patients resembles this phenotype and indicates a B cell defect. However, normal total IgG and IgA levels that were found in most of our patients suggest that CSR may be only partially affected. Nevertheless, inefficient antibody production impairs responses to *Streptococcus pneumoniae* and *Hemophilus influenzae type B* vaccinations in our patients, leading to recurrent infections with these pathogens. An increased population of circulating transitional B cells may reflect a block in late stages of B cell maturation or an enhanced death of mature B cells.

PI3Kδ is also highly expressed in neutrophils. We found that patient-derived neutrophils retained their ability to undergo a respiratory burst, degranulation, chemotaxis, and apoptosis (fig. S9). We measured PIP_3 accumulation in tumor necrosis factor–α–primed neutrophils in response to *N*-formyl-Met-Leu-Phe (*f*MLP) stimulation at 6 s (a PI3Kγ-dependent response) and at 60 s (a predominantly PI3Kδ-mediated signal) (*22*) and found no significant difference between patients and controls in either response (fig. S9). Thus, the

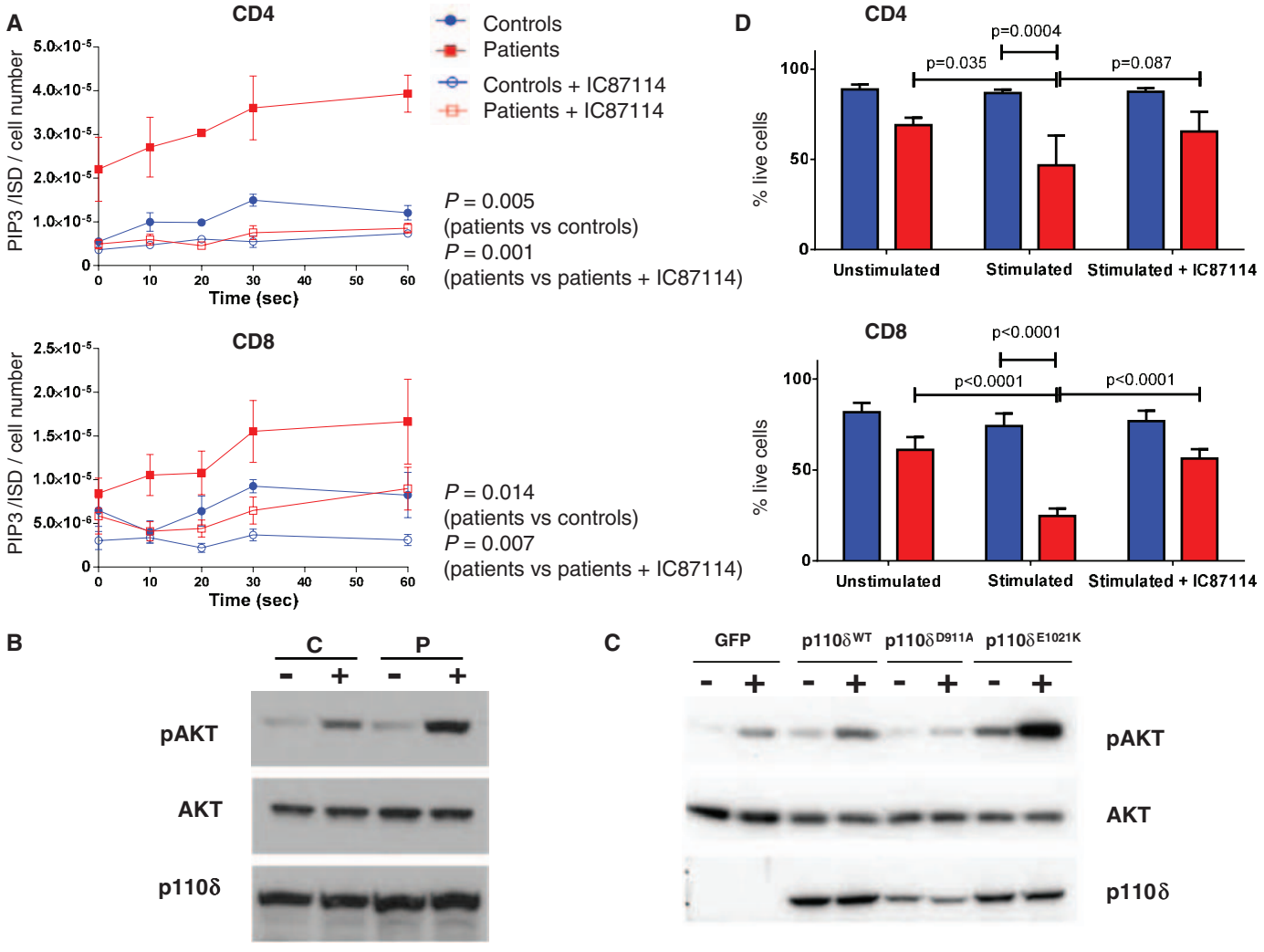

Fig. 3. Functional analyses of T cells in patients with APDS. (**A**) Intracellular PIP_3 levels in $CD4^+$ and $CD8^+$ T lymphocytes of patients (red squares, *N* = 6 subjects) and controls (blue circles, *N* = 5 subjects) at indicated times after stimulation with antibodies to CD3 and CD28 in the presence or absence of IC87114. The data are expressed as the ratio of the quantity of PIP_3 divided by that of the internal standard (ISD) and normalized according to the cell number. The data show mean ± SEM. *P* values were calculated using two-way analysis of variance (ANOVA) with Bonferroni correction. (**B**) Representative (*N* = 3 experiments) Western blot showing levels of p110δ, AKT, and phospho-AKT (pAKT) proteins in $CD4^+$ T cells isolated from fresh blood samples of a healthy control (C) and a patient (P) without stimulation (–) or after 10 min stimulation (+) with antibodies to CD3 and CD28. (**C**) Representative (*N* = 2 experiments) Western blot showing levels of p110δ, and pAKT proteins in $CD4^+$ T cell blasts of a p110δ knockout mouse transduced with retroviral constructs expressing either green fluorescent protein (GFP) or wild-type p110δ ($p110\delta^{WT}$) or kinase dead p110δ ($p110\delta^{D911A}$) or $p110\delta^{E1021K}$ without stimulation (–) or after stimulation (+) with antibodies to CD3 and CD28. An expanded view of this blot is shown as fig. S4. (**D**) Quantification of surviving $CD4^+$ and $CD8^+$ T cells as indicated by percentage of cells excluding viability dye. Cells of patients (red, *N* = 4 subjects) and controls (blue, *N* = 7 subjects) were studied without stimulation and after stimulation with antibodies to CD3 and CD28 and in the presence of IC87114. Each subject was studied in triplicate. The data show mean ± SEM. *P* values were calculated using a two-way ANOVA with Sidak's multiple comparisons test.

effect of the E1021K mutation on the PI3Kδ activity may be cell-type or stimulus-specific, or it may be compensated for by effects of other PI3K isoforms or PTEN. Nevertheless, we cannot exclude that a subtle defect in neutrophil function may contribute to the disease pathogenesis in these patients.

In summary, we have described a PID caused by a recurrent autosomal-dominant germline mutation E1021K in the *PIK3CD* gene that encodes p110δ. We found it in 17 patients from seven unrelated families, suggesting that it is frequent among PID patients and may explain a substantial fraction of patients with recurrent respiratory infections and bronchiectasis. Our rapid genotyping assay should facilitate screening for the E1021K mutation in existing PID and bronchiectasis cohorts, as well as new patients. The E1021K mutation was previously noted in one Taiwanese patient with recurrent respiratory infections and PID; however, its causative and pathogenic role has not been demonstrated (*23*). Here, we have shown that E1021K increases PI3Kδ activity, augmenting the production of PIP_3 and activating the downstream AKT protein in lymphocytes. This leads to defects in T and B cell function and inefficient immune responses to bacterial pathogens, predisposing to recurrent respiratory infections and eventually to bronchiectasis. We named this disorder activated PI3K-δ syndrome (APDS).

Activation of the PI3K pathway is associated with malignant transformations, and it has been shown that overexpression of p110δ can transform cells (*24*). To date, only one of our APDS patients, P13, has been diagnosed with lymphoma (Table 1). Nonetheless, the oncogenic potential of PI3K up-regulation can be enhanced by additional mutations (*25*, *26*). Therefore, APDS patients may be at increased risk of leukemia or lymphoma if they acquire additional somatic mutations.

The APDS patients described here had been treated with immunoglobulin replacement and antibiotics. Despite this, there is evidence of considerable airway damage in most cases. Because of progressive severe disease after splenectomy, patient P8 underwent allogeneic hematopoietic stem cell transplantation (HSCT) at the age of 8 years. One year after HSCT, his clinical condition had improved dramatically, suggesting that HSCT may be a long-term treatment option for young patients. Nevertheless, our results raise the possibility that selective p110δ inhibitors, such as GS-1101, may be an alternative effective therapeutic approach in APDS patients. GS-1101 (CAL-101 or Idelalisib) has been tested in phase 1 and 2 clinical trials for treatment of chronic lymphocytic leukemia (www.clinicaltrials.gov). The possibility of treating APDS patients with p110δ inhibitors should therefore be considered.

References and Notes

1. A. F. Barker, *N. Engl. J. Med.* **346**, 1383–1393 (2002).
2. A. Durandy, S. Kracker, A. Fischer, *Nat. Rev. Immunol.* **13**, 519–533 (2013).
3. W. Al-Herz *et al.*, *Front Immunol* **2**, 54 (2011).
4. M. J. Bamshad *et al.*, *Nat. Rev. Genet.* **12**, 745–755 (2011).
5. Materials and methods are available as supplementary materials on *Science* Online.
6. A. Hodgkinson, A. Eyre-Walker, *Nat. Rev. Genet.* **12**, 756–766 (2011).
7. Z. A. Knight, M. E. Feldman, A. Balla, T. Balla, K. M. Shokat, *Nat. Protoc.* **2**, 2459–2466 (2007).
8. C. Sadhu, B. Masinovsky, K. Dick, C. G. Sowell, D. E. Staunton, *J. Immunol.* **170**, 2647–2654 (2003).
9. B. J. Lannutti *et al.*, *Blood* **117**, 591–594 (2011).
10. E. D. Scheeff, P. E. Bourne, *PLOS Comput. Biol.* **1**, e49 (2005).
11. O. Vadas, J. E. Burke, X. Zhang, A. Berndt, R. L. Williams, *Sci. Signal.* **4**, re2 (2011).
12. D. Mandelker *et al.*, *Proc. Natl. Acad. Sci. U.S.A.* **106**, 16996–17001 (2009).
13. J. E. Burke, O. Perisic, G. R. Masson, O. Vadas, R. L. Williams, *Proc. Natl. Acad. Sci. U.S.A.* **109**, 15259–15264 (2012).
14. J. E. Burke *et al.*, *Structure* **19**, 1127–1137 (2011).
15. K. Okkenhaug, *Annu. Rev. Immunol.* **31**, 675–704 (2013).
16. J. Clark *et al.*, *Nat. Methods* **8**, 267–272 (2011).
17. F. Sallusto, J. Geginat, A. Lanzavecchia, *Annu. Rev. Immunol.* **22**, 745–763 (2004).
18. A. N. Anzelon, H. Wu, R. C. Rickert, *Nat. Immunol.* **4**, 287–294 (2003).
19. A. Suzuki *et al.*, *J. Exp. Med.* **197**, 657–667 (2003).
20. S. A. Omori *et al.*, *Immunity* **25**, 545–557 (2006).
21. M. L. Janas *et al.*, *J. Immunol.* **180**, 739–746 (2008).
22. A. M. Condliffe *et al.*, *Blood* **106**, 1432–1440 (2005).
23. S. T. Jou *et al.*, *Int. J. Immunogenet.* **33**, 361–369 (2006).
24. S. Kang, A. Denley, B. Vanhaesebroeck, P. K. Vogt, *Proc. Natl. Acad. Sci. U.S.A.* **103**, 1289–1294 (2006).
25. J. A. Engelman, *Nat. Rev. Cancer* **9**, 550–562 (2009).
26. K. M. Kinross *et al.*, *J. Clin. Invest.* **122**, 553–557 (2012).

Acknowledgments: S.N. is a Wellcome Trust Senior Research Fellow in Basic Biomedical Science (095198/Z/10/Z). S.N. is also supported by the European Research Council (ERC) Starting grant 260477 and the European Union (EU) FP7 collaborative grant 261441 (PEVNET project). S.N., A.C., D.K., and R.D. are supported by the National Institute for Health Research (NIHR) Cambridge Biomedical Research Centre. O.V. was supported by a Swiss National Science Foundation fellowship (grant PA00P3_134202) and a European Commission fellowship (FP7-PEOPLE-2010-IEF, no. 275880). R.L.W. was supported by the Medical Research Council (file reference U105184308). T.C. is supported by the National Children's Research Centre, Our Lady's Children's Hospital, Crumlin, Dublin, Ireland. E.B.-H. is supported by a Wellcome Trust Translational Medicine and Therapeutics award. A.C. is supported by the Medical Research Council UK and the British Lung Foundation. K.O. is supported by a strategic grant from the Biotechnology and Biological Sciences Research Council and a New Investigator Award from the Wellcome Trust. P.H. and L.S. are funded by an Institute Programme grant from the Biotechnology and Biological Sciences Research Council (BB/J004456/1). S.K. is a Centre National de la Recherche Scientifique (CNRS) researcher. A.D., A.F., and S.K. are funded by Institut National de la Santé et de la Recherche Médicale; A.D. is supported by the EU FP7 EUROPAD contract 201549, Association Contre Le Cancer, and Agence Nationale de la Recherche (grant 2010-CSRD). A.F. is supported by the EU FP7 ERC PIDIMMUNE grant 249816. G.B.-M. was supported by a sabbatical grant from PASPA-DGAPA-UNAM. E.C. is a paid consultant for GlaxoSmithKline, Roche, and Novartis; A.C. is a paid consultant for GlaxoSmithKline; P.H. and L.S are paid consultants for GlaxoSmithKline and Karus Therapeutics Ltd; K.O. is a paid consultant for GlaxoSmithKline. Requests for DNA of individual patients will require informed consent from the patients and samples will be available under a material transfer agreement. The p110δ knockout mice are available from the Babraham Institute under a material transfer agreement. The mutation has been submitted to the ClinVar database; accession no. SCV000083058.

Supplementary Materials

www.sciencemag.org/content/342/6160/866/suppl/DC1
Materials and Methods
Supplementary Text
Figs. S1 to S9
Tables S1 and S2
References (*27*–*37*)

16 July 2013; accepted 23 September 2013
Published online 17 October 2013;
10.1126/science.1243292

Complete Mitochondrial Genomes of Ancient Canids Suggest a European Origin of Domestic Dogs

O. Thalmann,[1*] B. Shapiro,[2] P. Cui,[3] V. J. Schuenemann,[4] S. K. Sawyer,[3] D. L. Greenfield,[5] M. B. Germonpré,[6] M. V. Sablin,[7] F. López-Giráldez,[8] X. Domingo-Roura,[9†] H. Napierala,[10] H-P. Uerpmann,[4] D. M. Loponte,[11] A. A. Acosta,[11] L. Giemsch,[12,13] R. W. Schmitz,[12] B. Worthington,[14] J. E. Buikstra,[15] A. Druzhkova,[16] A. S. Graphodatsky,[16] N. D. Ovodov,[17] N. Wahlberg,[1] A. H. Freedman,[5] R. M. Schweizer,[5] K.-P. Koepfli,[18] J. A. Leonard,[19] M. Meyer,[3] J. Krause,[4] S. Pääbo,[3] R. E. Green,[20] R. K. Wayne[5*]

The geographic and temporal origins of the domestic dog remain controversial, as genetic data suggest a domestication process in East Asia beginning 15,000 years ago, whereas the oldest doglike fossils are found in Europe and Siberia and date to >30,000 years ago. We analyzed the mitochondrial genomes of 18 prehistoric canids from Eurasia and the New World, along with a comprehensive panel of modern dogs and wolves. The mitochondrial genomes of all modern dogs are phylogenetically most closely related to either ancient or modern canids of Europe. Molecular dating suggests an onset of domestication there 18,800 to 32,100 years ago. These findings imply that domestic dogs are the culmination of a process that initiated with European hunter-gatherers and the canids with whom they interacted.

Dogs are one of the best known examples of domestication, the process of species modification over time by human-induced selection (*1*). Domestication often leads to increased phenotypic variation and a geographic distribution that can be heavily influenced by human dispersal. The extensive phenotypic variation among dog breeds hinders a simple inference of dog origins based on the presence of traits shared between dogs and any specific population of the

gray wolf (*Canis lupus*) from which dogs derive (*2*–*4*). Furthermore, inferences from genetic data are confounded by a long history of trade and admixture among dogs from disparate geographic areas, ancient and ongoing local admixture with wolves, intense inbreeding within some lineages, and the stochastic effects of incomplete lineage sorting. Nevertheless, centers of dog origins from genetic data have been proposed, including the Middle East and East Asia (*5*–*7*). However, the oldest putative dog remains are found in Western Europe and Siberia and date from 15,000 to 36,000 years ago (*2*, *8*), although the classification of these specimens remains contentious (*9*). The earliest putative dog remains from the Middle East and East Asia are no older than about 13,000 years ago [see table S3 (*10*)].

DNA extracted from the earliest canids showing phenotypic evidence of domestication (*2*, *8*, *11*–*14*) can potentially be used to test hypotheses about the origin of modern dogs. We generated complete and partial mitochondrial genomes from 18 prehistoric canids and 20 modern wolves of Eurasian and American origin (Table 1 and table S2) by performing DNA capture followed by high-throughput sequencing (*15*). The DNA fragments recovered from these samples show patterns expected of ancient DNA, including a correlation between sequence length and sample age (fig. S1) and deamination patterns typical of ancient DNA (*15*) (fig. S2). After filtering, iterative assembly, and exclusion of mitochondrial genomes with less than 50% of the length recovered, we obtained a median 12-fold (1.9 to 625.7) coverage of the 18 ancient genomes, with on average 15,014 (8667 to 16,415) nucleotides supported by at least twofold coverage. These mtDNA assemblies from ancient canids were compared with complete mitochondrial genome sequences from 49 wolves; 77 dogs, including divergent dog breeds such as Basenji and Dingo; three recently published Chinese indigenous dogs (*7*); and four coyotes totaling 148 mitochondrial genomes.

Phylogenetic analyses of the mitochondrial genome data using maximum likelihood, coalescence and Bayesian approaches all reveal a well-resolved phylogeny (Fig. 1). Although dogs and wolves are not reciprocally monophyletic, all modern dogs and many wolf populations fall within one of several well-supported clades (Fig. 1 and fig. S9). Within this tree topology, dogs fall within one of four clades (Dog A to D) (Fig. 1 and fig. S9), with clade A containing the majority of dog sequences (64%). Three haplotypes from ancient Belgian canids form the most deeply diverging group in the tree. Although the cranial morphology of one of these, the Goyet dog (Belgium *36,000*) (Table 1 and table S1) has been interpreted as dog-like (*2*), its mtDNA relation to other canids places it as an ancient sister-group to all modern dogs and wolves rather than a direct ancestor of dogs. One of the Belgian specimens (Belgium *26,000*) has been found to be uniquely large (*2*) and could be related to a genetically and morphologically distinct form of wolves from Late Pleistocene deposits of the High Arctic permafrost (*16*). However, none of the sequences from the three northerly permafrost wolves (Alaska *28,000*, Alaska *21,000*, and Alaska *20,800*) (Fig. 1) fall within or are sister to this clade. Given their mitochondrial distinctiveness, the Belgian canids, including the Goyet dog, may represent an aborted domestication episode or a phenotypically distinct, and not previously recognized, population of gray wolf.

Dog clades A, C, and D, which make up 78% of dog sequences in our study, are each sister to one or more ancient canids of Europe. The most diverse of these groups is clade A, which includes divergent breeds, such as Basenji and Dingo, and two of the Chinese indigenous dogs (*7*). Moreover, three pre-Colombian New World dogs, ranging in age from 1000 to 8500 years ago, fall within dog clade A (Table 1 and table S1). The calculated time to the most recent common ancestor (MRCA) of dog clade A and ancient New World dog sequences is ~18,800 years ago [95% highest posterior density (HPD): 15,100 to 22,600] (fig. S10), which supports the hypothesis that pre-Colombian dogs in the New World share ancestry with modern dogs. Thus, these dogs likely arrived with the first humans in the New World (*17*, *18*). The clade comprising these ancient New World dogs and modern dog clade A is most closely related to an ancient wolf sequence from the Kesslerloch cave in Switzerland (Switzerland 2 *14,500*) with a MRCA that existed ~32,100 years ago (95% HPD: 27,500 to 36,700).

The lowest diversity dog clade (D) contains only sequences from two Scandinavian breeds and is sister to an ancient wolflike canid from Switzerland with a common ancestor that existed ~18,300 years ago (95% HPD: 15,300 to 21,900). This grouping is most closely related to another sequence from ancient European wolves, as well as extant wolves from Poland and Italy, and is rooted with the sequence from a putative early dog from the Altai Mountains in Russia (*13*). The grouping of clade D with ancient wolf lineages and the association of the Altai specimen with this clade do not support recent common ancestry of the Altai specimen lineage with the great majority of modern dogs. However, clade D dog haplotypes could have been captured as a result of interactions between ancient wolves and early humans that migrated into Scandinavia (*19*).

The closest sister group for dogs in clade C, which makes up 12% (9 of 77) of modern dog sequences, are two morphologically distinct ancient dogs from Bonn-Oberkassel (*12*) and the Kartstein cave in Germany (*14*) (Germany *14,700* and Germany *12,500*, respectively) having a MRCA that existed ~16,000 to 24,000 years ago (95% HPD: 13,500 to 28,100). Last, dog clade B, which contains 22% (17 of 77) of dog sequences has the closest phylogenetic associations with sequences from modern wolves from Sweden and the Ukraine and shares a MRCA with them some ~9200 years ago (95% HPD: 6500 to 12,300).

The association of sequences from modern dogs in clades A, C, and D with ancient European canid specimens and of modern dogs from clade B with European wolves suggests an origin of dogs in Europe, rather than the Middle East or East Asia, as previously suggested (*5*–*7*). Critically, none of the modern wolf sequences from other putative centers of origins such as the Middle East (Saudi Arabia, Oman, Israel, Iran, and India) or East Asia (China, Japan, and Mongolia) show close affinity with modern dog clades. Bayesian analysis of divergence times implies a European origin of the domestic dog dating to as much as 18,800 to 32,100 years ago, given an upper limit of the MRCA of an ancient wolf sequence and dogs clustered in clade A and the MRCA of the most diverse dog clade as a lower limit (Fig. 1). Consequently, our results support the hypothesis that dog domestication preceded the emergence of agriculture (*20*) and occurred in the context of European hunter-gatherer cultures.

Previous research suggested that modern dogs experienced a two-phase bottleneck. The first was at the origin of the domestication process, and the second was more recent during breed formation over the past several hundred years (*21*). To investigate the demographic history of dogs, we used a Bayesian Skygrid analysis (*22*) applied to dog clade A and the closely related pre-Columbian dogs. We find a continuous population size increase from the

[1]Department of Biology, Section of Genetics and Physiology, University of Turku, Itäinen Pitkäkatu 4, 20014 Turku, Finland. [2]Department of Ecology and Evolutionary Biology, University of California Santa Cruz, 1156 High Street, Santa Cruz, CA 95064, USA. [3]Max Planck Institute for Evolutionary Anthropology, Deutscher Platz 6, 04103 Leipzig, Germany. [4]Institute for Archaeological Sciences, University of Tübingen, Rümelinstrasse 23, Tübingen, Germany. [5]Department of Ecology and Evolutionary Biology, University of California Los Angeles, 2149 Terasaki Life Science Building, Los Angeles, CA 90095, USA. [6]Operational Direction "Earth and History of Life," Royal Belgian Institute of Natural Sciences, Vautierstraat 29, 1000 Brussels, Belgium. [7]Zoological Institute, Russian Academy of Sciences, Universitetskaya nab. 1, 199034 Saint Petersburg, Russia. [8]Yale Center for Genome Analysis, Yale University, West Haven, CT 06516, USA. [9]Genètica de la Conservació, Institut de Recerca i Tecnologia Agroalimentàries (IRTA), Carretera de Cabrils km 2, 08348, Cabrils, Barcelona, Spain. [10]Institute of Palaeoanatomy and History of Veterinary Medicine, Ludwig-Maximilian-University Munich, and ArchaeoBioCenter LMU, Kaulbachstrasse 37, 80539 Munich, Germany. [11]Instituto Nacional de Antropología y Pensamiento Latinoamericano, Consejo Nacional de Investigaciones Científicas y Técnicas (CONICET), 3 de Febrero 1378, CJN1429 Buenos Aires, Argentina. [12]Landschaftsverband Rheinland (LVR)–Landesmuseum Bonn, Bachstrasse 5-9, D-53115 Bonn, Germany. [13]Department of Prehistoric and Protohistoric Archaeology, Institute for Archaeology and Cultural Anthropology, University of Bonn, Regina-Pacis-Weg 7, 53113 Bonn, Germany. [14]Southeastern Archaeological Research, Inc., 315 Northwest 138th Terrace, Newberry, FL 32669, USA. [15]Center for Bioarchaeological Research, School of Human Evolution and Social Change, Arizona State University, Tempe, AZ 85287–2402, USA. [16]Department of Genomic Diversity and Evolution, Institute of Molecular and Cellular Biology, Siberian Branch of the Russian Academy of Sciences, Novosibirsk, Russia. [17]Institute of Archaeology and Ethnography, Siberian Branch of the Russian Academy of Sciences, Novosibirsk, Russia. [18]Theodosius Dobzhansky Center for Genome Bioinformatics, Saint Petersburg State University, 41A Sredniy Prospekt, Saint Petersburg 199034, Russia. [19]Estación Biológica de Doñana, Conservation and Evolutionary Genetics Group (EBD-CSIC), Avenida Américo Vespucio s/n, 41093 Seville, Spain. [20]Department of Biomolecular Engineering, University of California Santa Cruz, 1156 High Street, Santa Cruz, CA 95064, USA.

*Corresponding author. E-mail: olatha@utu.fi (O.T.); rwayne@eeb.ucla.edu (R.K.W.)
†Deceased.

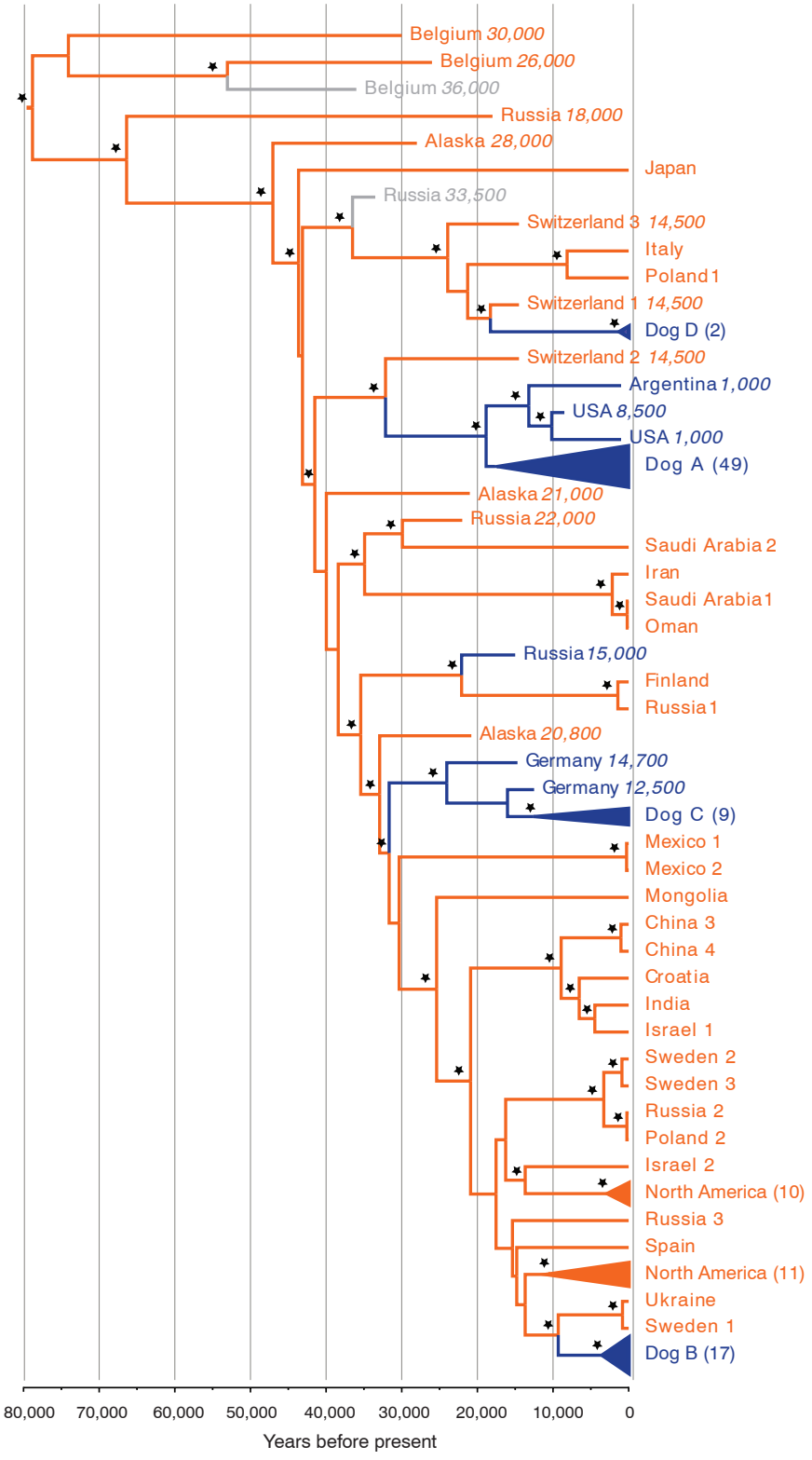

Fig. 1. Phylogenetic arrangement of modern and ancient dog (blue) and wolf sequences (orange) as obtained from coalescence-based, maximum likelihood, and Bayesian methods. The outgroup (four coyotes) and two Chinese wolf sequences were excluded [see (*15*) for more details]. Ancient specimens are labeled with the respective country of origin and their approximate reported age (italicized; in years before present). Fossil specimens with ambiguous taxonomic classification are indicated by a gray color. Whenever modern canid sequences form a monophyletic cluster, the number of sequences in the cluster is indicated in brackets. Asterisks highlight statistical support whenever both bootstrap values are >90% and posterior support is >0.9 for the maximum likelihood and Bayesian analyses, respectively.

time of the MRCA to about 5000 years ago, which may be attributable to the earliest domestication phase (Fig. 2). A more recent decline occurred between 5000 and 2500 years ago and was followed by a sharp increase in population size (Fig. 2). This increase parallels the trajectory of human population size (*23*), which suggests demographic dependence of dogs on human populations. In contrast, wolf numbers declined during this period, consistent with the emergence of agrarian cultures and the loss of vital wolf habitat and wild game.

Our findings support the conclusion that the mitochondrial legacy of dogs derives from wolves of European origin. Past mitochondrial and Y chromosome analyses that suggested a non-European location for the onset of domestication were more limited in sampling of modern or ancient wolves or prehistoric dogs and had weak statistical support for phylogenetic branching points (*4*, *6*, *24*). The modern dog clades A to D are well-supported in our tree of complete mtDNA sequence. We find that the sequence diversity that exists today in dogs can all be found in ancient (clades A, C, and D) or modern (clade B) European canids. The inferred recent divergence of clade B from wolves now found in Sweden and the Ukraine implies that it might represent a mitochondrial genome introgressed from wolves rather than one established by domestication, because dogs were clearly domesticated by this time (*8*, *12*, *14*).

Notably, our ancient panel does not contain specimens from the Middle East or China, two proposed centers of origin (*5*, *6*). In fact, no ancient dog remains older than ~13,000 years are known from these regions (*10*). However, ancient wolf and dog remains from these areas would need to be rooted more closely to the four dominant dog clades than any ancient or modern European canids to contradict our primary conclusions. We consider this scenario unlikely as it would require a common recent coalescence of these ancestral wolf and dog sequences from geographically disparate areas. Nevertheless, a more complete and nuanced picture of dog domestication will likely emerge with the addition of ancient canine mtDNA data from the Middle East and Asia. A further caveat to our conclusions is that although the mtDNA sequence tree is well supported, it represents a single genetic locus. The rapid coalescence of mtDNA genomes and the lack of recombination are important advantages; however, both mitochondrial and nuclear genomes suffer from incomplete lineage sorting, which, given the recent divergence of dogs and wolves, can potentially confound evolutionary inference. The availability of multiple independent loci in the nuclear genome potentially offers more power to resolve phylogenetic relations. We attempted to capture multiple nuclear loci using a densely tiled capture array, but were not able to obtain sufficient coverage to call genotypes confidently in any of the ancient specimens, which reflects their poor state of DNA preservation (*15*). Nonetheless, our mtDNA genome tree shows that three of four

Table 1. Ancient specimens used and summary of sequencing statistics. (**A**) Ancient specimens captured using custom designed capture arrays. (**B**) Specimens enriched for mtDNA using long range PCR-products and custom designed biotinylated adapters (*15*). Morphological classification and approximate age are from the respective references (see table S1). Ancient specimens with ambiguous morphological classification are shown in italic font. Nucleotides were retained with a minimum of two reads per base. Further information on filtering parameters is available (*15*).

Identification	Origin	Morphological classification	Approximate age (years B.P.)	Average mt-genome coverage	Retained nucleotides
A					
Belgium *26,000*	Belgium, Trou des Nutons	Wolflike	26,000	8.3	16,170
Belgium *36,000*	Belgium, Goyet niveau 4	*Doglike*	36,000	4.1	12,020
Belgium *30,000*	Belgium, Goyet niveau 4	Wolflike	30,000	20.4	16,348
Russia *18,000*	Russia, Medvezya cave	Wolflike	18,000	137.7	16,414
Russia *15,000*	Russia, Eliseevichi	Doglike	15,000	6.0	14,340
USA *8500*	USA; Koster site, Illinois	Doglike	8500	7.9	16,154
Argentina *1000*	Argentina, Cerro Lutz	Doglike	1000	27.8	16,369
Russia *22,000*	Russia, Kostenki	Wolflike	22,000	21.5	16,397
USA *1000*	USA, Florida	Doglike	1000	53.7	16,414
B					
Switzerland 1 *14,500*	Switzerland, Kesslerloch cave	Wolflike	14,500	14.7	16,357
Alaska *28,000*	Alaska, Eastern Beringia	Wolflike	28,000	90.1	16,415
Alaska *21,000*	Alaska, Eastern Beringia	Wolflike	21,000	2.1	9073
Alaska *20,800*	Alaska, Eastern Beringia	Wolflike	20,800	625.7	16,412
Switzerland 2 *14,500*	Switzerland, Kesslerloch cave	Wolflike	14,500	4.2	13,965
Russia *33,500*	Russia, Razboinichya cave	*Doglike*	33,500	100.8	16,411
Germany *14,700*	Germany, Bonn-Oberkassel	Doglike	14,700	1.9	8667
Germany *12,500*	Germany, Kartstein cave	Doglike	12,500	8.6	16,239
Switzerland 3 *14,500*	Switzerland, Kesslerloch cave	Wolflike	14,500	9.2	16,089

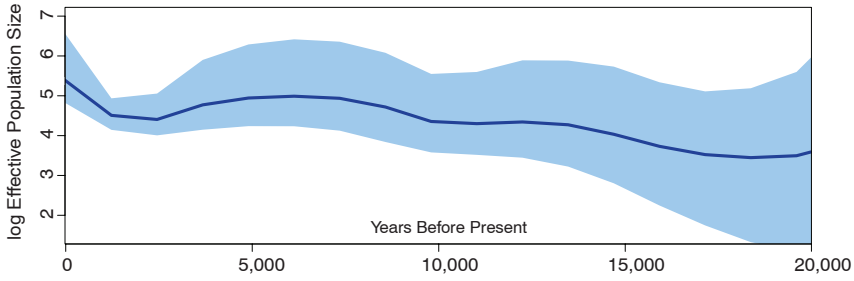

Fig. 2. Bayesian Skygrid plot depicting the demographic trajectory of dog clade A and closely related pre-Columbian dogs. Times are given in years before present and the effective population size is indicated in median logN_e (solid line) with the accompanying 95% HPD interval.

modern dog clades are more closely related to sequences from ancient European rather than extant wolves. Further, analysis of coalescence times support a dog-wolf divergence time of >15,000 years ago. An evolutionary scenario consistent with these results is that dog domestication was initiated close to the Last Glacial Maximum when hunter-gathers preyed on megafauna (*25*). Conceivably, proto-dogs might have taken advantage of carcasses left on site by early hunters, assisted in the capture of prey, or provided defense from large competing predators at kills. Finally, our results imply that some of the earliest putative dog remains, such as the Goyet dog from Belgium (*2*) or Altai Mountain specimen from Russia (*13*), may represent aborted domestication episodes. If true, this suggests that the conditions for dog domestication were not unique to one place or time and adds a role for serendipity to the process that led to the early and singular domestication of a large and dangerous carnivore.

References and Notes

1. G. Larson, J. Burger, *Trends Genet.* **29**, 197–205 (2013).
2. M. Germonpré *et al.*, *J. Archaeol. Sci.* **36**, 473–490 (2009).
3. S. J. Olsen, J. W. Olsen, *Science* **197**, 533–535 (1977).
4. C. Vilà *et al.*, *Science* **276**, 1687–1689 (1997).
5. B. M. vonHoldt *et al.*, *Nature* **464**, 898–902 (2010).
6. P. Savolainen, Y. P. Zhang, J. Luo, J. Lundeberg, T. Leitner, *Science* **298**, 1610–1613 (2002).
7. G. D. Wang *et al.*, *Nat Commun* **4**, 1860 (2013).
8. M. Sablin, G. Khlopachev, *Curr. Anthropol.* **43**, 795–799 (2002).
9. S. J. Crockford, Y. V. Kuzmin, *J. Archaeol. Sci.* **39**, 2797–2801 (2012).
10. G. Larson *et al.*, *Proc. Natl. Acad. Sci. U.S.A.* **109**, 8878–8883 (2012).
11. H. Napierala, H.-P. Uerpmann, *Int. J. Osteoarchaeol.* **22**, 127–137 (2012).
12. G. Nobis, *Umschau* **79**, 610 (1979).
13. N. D. Ovodov *et al.*, *PLOS ONE* **6**, e22821 (2011).
14. M. Baales, *Mongraphien RGZM, Mainz* **38**, 106 (1996).
15. Supplementary materials are available on *Science* Online.
16. J. A. Leonard *et al.*, *Curr. Biol.* **17**, 1146–1150 (2007).
17. J. A. Leonard *et al.*, *Science* **298**, 1613–1616 (2002).
18. B. van Asch *et al.*, *Proc. Biol. Soc.* **280**, 20131142 (2013).
19. H. Malmström *et al.*, *BMC Evol. Biol.* **8**, 71 (2008).
20. E. Axelsson *et al.*, *Nature* **495**, 360–364 (2013).
21. K. Lindblad-Toh *et al.*, *Nature* **438**, 803–819 (2005).
22. M. S. Gill *et al.*, *Mol. Biol. Evol.* **30**, 713–724 (2013).
23. J. A. Tennessen *et al.*, Broad GO, Seattle GO, on behalf of the NHLBI Exome Sequencing Project, *Science* **337**, 64–69 (2012).
24. Z. L. Ding *et al.*, *Heredity* **108**, 507–514 (2012).
25. J. Alroy, *Science* **292**, 1893–1896 (2001).

Acknowledgments: Mitochondrial sequences have been deposited at the NCBI database with the accession numbers (KF661036 to KF661096), and a complete alignment is available as a supplementary file. We would like to thank all colleagues who provided samples for this study, the Illinois State Museum and the Center for American Archeology for allowing us to sample the material from the Koster site, and the American Museum of Natural History, New York. O.T. is grateful to D. Wegmann and D. Schwochow-Thalmann for helpful discussions and comments on the manuscript; M. Bruneaux for help with R; and A. v. Haeseler for helpful advice with TREE-PUZZLE and IQ-TREE. We thank D. Ward, M. Riesenberg, J. Beier, I. Bergmann, H. Mutlu, and S. Bealek for assistance with ancient DNA extractions. R.E.G. is president of Dovetail Genomics. Financial support for this study was provided from the E. Aaltonen foundation and the Turun Yliopistosäätiö to O.T.; Molecular and Cellular Biology, Siberian Branch of the Russian Academy of Sciences, and Russian Foundation for Basic Research grants to A.S.G.; and NSF support to R.K.W. and B.S. (OPP 9617068, EF-1021387). J.K. and V.J.S. were supported by the Carl Zeiss Foundation. This work was further supported by the Max Planck Society. O.T. is financed by a Marie Curie Intra European Fellowship within the 7th European Community Framework Program. The authors declare no conflict of interest.

Supplementary Materials

www.sciencemag.org/content/342/6160/871/suppl/DC1
Materials and Methods
Supplementary Text
Figs. S1 to S9
Tables S1 to S5
References (*26*–*78*)

23 July 2013; accepted 3 October 2013
10.1126/science.1243650

abcam®
discover more

SimpleStep™ ELISA kits – make your life easier

Mix → Wash → Read. It's that easy.

Discover our new single wash sandwich ELISA assay offering improved performance.

Discover more at abcam.com/SimpleStep

SimpleStep™

259a_13_CT

Better results — on any sequencing platform

Get the most from your NGS

Discover new and innovative solutions, dedicated for use with any NGS workflow

Streamline your next-generation sequencing (NGS) workflow and achieve high-quality results you can rely on.

- **Highly specific and selective nucleic acid purification and target enrichment**
- **Unbiased whole genome amplification from a single cell**
- **High DNA library yields using optimized workflows that allow ~50% time-savings**
- **Outstanding results on any sequencing platform**
- **Intuitive, knowledge-based data interpretation for deeper insight into NGS results**

Visit www.qiagen.com/goto/NGS to learn more!

QIAGEN®

Sample & Assay Technologies

BioTianfu Incubator: Create Value For Bioscience & Technology Ecosystem in Chengdu

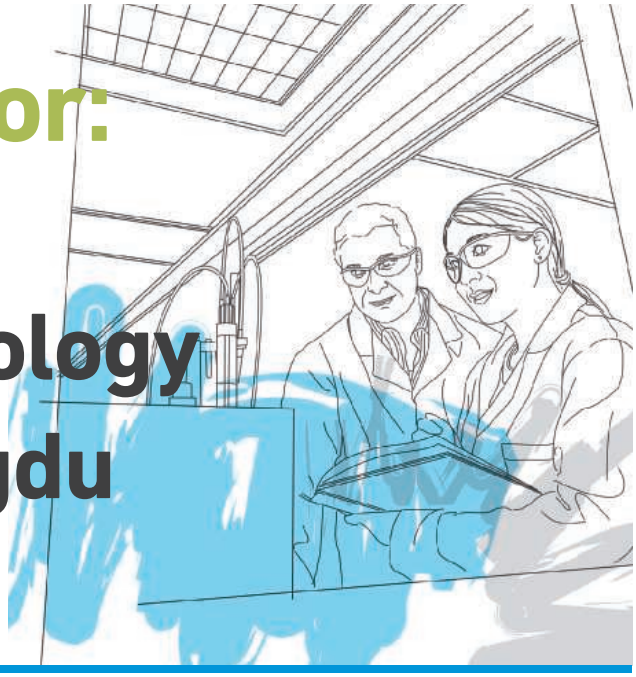

—— Building Up a Spectrum of R&D Capabilities

When Dr. Lin PU, tenured professor of University of Virginia, an expert in organic chemistry, Pharmaceutical synthesis and nano material, decided to establish a biotech company emphasis on anti-cancer drugs, he chose BioTianfu Incubator." This is an ideal place to start up innovation." he said. He was the winner of Thousand Talents Program, China's top talent program which introduces overseas distinguished scholars to China. Now he is the co-founder of Zeple Technology in Chengdu.

The general climate in China created by the resources and the policy slant toward entrepreneurism has been successful in the promotion of talent retention, job creation and incubation model. There are now more than 1,000 incubators in China, and according to the national science and technology enterprise incubator "Twelfth Five-Year Development Planning", the number of incubators will be amounted to 1500 in 2015.

BioTianfu Incubator, at the heart of Tianfu Life Science Park based in Chengdu, Sichuan province, will celebrate the first anniversary in January 2014 of its formal completion. The incubator management team believes that great incubators must create value for the ecosystem and have strong post-incubation performance. In total till October, 23 returnee teams have arrived.

BioTianfu Incubator Building

Chengdu: West China's Innovation Capital

Chengdu, as the capital city of Sichuan Province, has one of the highest concentrations of colleges and universities in China. In the municipality, there are 52 higher education institutions. In 2012, the universities and colleges here produced over 20, 000 graduates for the local labor market specializing in life science related subjects. For the past three years, Chengdu has been attracting attention from all over the world due to its rapid economic development. In 2010, the city was rated as No.1 of the World's Next Decade's Fastest-Growing Cities by Forbes Magazine; in 2012, it was ranked as one of the 40 Fastest Growing Global Cities by The Economist; and for three consecutive years, it was rated by the United States Chamber of Commerce as the preferred city for foreign investment in China.

In 2012, Chengdu rolled out a massive program to attract talent such as technicians and entrepreneurs. The top award it offered was CNY 5 million ($810,000), according to China Daily. This year, Chengdu had attracted 167 overseas top talents to settle down in this city, among whom 29 were from The Thousand Talents Program.

It was part of the city's campaign to lure talented people to sharpen its technological edge and encourage innovation. The city government offered CNY 5 million to the "top innovation and entrepreneurship team", CNY 500,000 to a "youth team," CNY 500,000 to "overseas short term entrepreneurship," and CNY 1 million to "overseas long term entrepreneurship".

Chengdu High-tech Zone: Building World First-Class Park with Trillions in overall Industrial Output

On October 16, 2013 Chengdu High-tech Zone (CDHT) launched an ambitious project called "the 3rd entrepreneurship stage", aiming to build a World First-class Park with one trillion in overall industrial output.

A new and ambitious hi-tech zone in Chengdu, is striving to establish its own Silicon Valley. CDHT already ranks fourth among China's national hi-tech zones, with its comprehensive strength and the growing support of 7 strategic burgeoning industrial clusters, namely Next Generation of Internet, Electronics Core, High-end Software and Burgeoning Information Service, Bio-pharmaceuticals, Bio-medicine, Aeronautic Equipment and Advanced Environmental Protection.

Technological innovation and industrial upgrading are the core enablers in the deployment of the strategy. In line with the Endogenous Development model, Chengdu Hi-tech Zone aims to continue to be the center of a booming cluster of biotechnological innovations enterprises and collaborations.

Under the guide of transcendence strategy and

Chengdu High-tech Zone

BioTianfu Incubator Management Team

West China Hospital Translation Medicine Center

TLSP Pubilc Laboratories

ambition, CDHT is willing to take a leadership role in the burgeoning technology industry, and make a great-leap-forward. The strategy will not only enhance CDHT's comprehensive strength significantly, but also extend to benefit the ability of economies of scale, self-independent innovation and international participation as well.

BioTianfu Incubator: A Hotspot for Startups in the Biotechnology industry

Set among the sculptured green spaces of Chengdu High-tech Zone, Tianfu Life Science Park consists of an area covering a 221,553 sq.m. and has established itself as a top bioscience center in the booming cluster. As the gateway for the life science industry in Western China, TLSP is an important innovation and incubation center for biomedical research and development and serves as a platform for the cooperation between medical/clinical institutions at home and abroad.

With nine floors of flexible work spaces, state-of-the-art equipments to fuel ideas, 6 open labs and 78 offices(incubation units), BioTianfu Incubator covers over 28,000 sq.m. and offers a full range of superior innovation incubation conditions for returnees and domestic excellent R&D teams. It is dedicated to promoting Chengdu bioscience industry and to foster the commercial development of promising biotechnology by providing tangible assets and services to viable startups.

The leading-edge offices, laboratories and facilities in BioTianfu Incubator enable scientists, technologists and enterprises to save development costs and time to market. They can nurture ideas, innovate and develop through the dynamic environment provided by TLSP and BioTianfu Incubator and also expand their business opportunities by strengthening collaboration with growing network of partners.

BioTianfu Incubator Entrance Hall

Incubation Unit

CAS & TLSP Information Center

The expertise and commitment of incubator managers is critical to success. Good managers are essential in selecting suitable tenant firms, in providing business and managerial advices to these firms, and in creating links to investors and the wider business community. An experienced service team in BioTianfu Incubator can well provide services on research, technology and commercialization to satisfy the variable needs of startups.

Join the BioTianfu bioscience and technology community and with fully furnished incubation units, advanced equipments, mentoring programs, BioTianfu Forum and Tianfu Star Project, etc, Startups will have the maximum opportunity to success in the intelligence gathered environment.

Startups Profile

Sichuan Primed is a biopharmaceutical outsourcing company. Primed focuses on the disease model establishment and preclinical validation of new drugs. Primed in vivo pharmacology services include metabolic diseases (DM and DM complications, dislipidemia), CNS (PD, AD), inflammation (RA, CD), oncology, antibiotics, antivirus (HBV, HCV) and other established animal models and procedures. Primed also made significant progress in reproductive toxicity evaluation in non-human primates. The pre-clinical validation data of over 10 new drugs have been approved by US FDA or China CFDA.

HC Pharmaceutical Co. Ltd. is an innovative drug discovery company founded by a group of scientists with global drug discovery experience and proving track record. By using its proprietary drug discovery platform, HC Pharma is focusing on cancer, diabetes and multiple sclerosis. Currently, we have a prostate cancer and multiple sclerosis program in pre-clinical stage with global IP protection.

ZepleTech is a biotechnology company engaged in the development of various pharmaceutical products with an emphasis on anti-cancer drugs. It specializes in high-speed medicinal chemistry to discover novel small molecule inhibitors of signaling pathways that are critical to proliferation. High-throughput synthesis and screening technology platforms are being established and applied to design, synthesize, and develop new drugs. Clinical development processes will be conducted by partnering with biotechnology and pharmaceutical companies following the efficient identification of the pre-clinical oncology candidates.

Celula(Chengdu) Medical Technology Co., Ltd. was founded in 2013, which is a subsidiary of Celula Inc. in US.Celula develops products for clinical diagnostics and biomedical research. The core technology is for single and rare cell isolation, identification and analysis.The technology includes proprietary instrument, reagents and bioinformatic analysis. Celula clinical products include non-invasive prenatal, cancer and infectious disease diagnostics.

CONTACT DETAILS

Tianfu Life Science Park, NO.88, South Keyuan Road, Hi-Tech Zone, Chengdu, P.R.China
Tel: +86-28-8597 5146
Fax: +86-28-8531 1575
Email: info@tianfulifesciencepark.com

NEW ENGLAND BioLabs® Inc.
enabling technologies in the life sciences

Make ends meet.

Gibson Assembly® Cloning Kit

New England Biolabs has revolutionized your laboratory's standard cloning methodology. The Gibson Assembly Cloning Kit combines the power of the Gibson Assembly Master Mix with NEB 5-alpha Competent *E. coli*, enabling fragment assembly and transformation in just under two hours. Save time, without sacrificing efficiency.

Making ends meet is now quicker and easier than ever before, with the Gibson Assembly Cloning Kit from NEB.

Gibson Assembly Cloning Kit provides robust transformation efficiencies

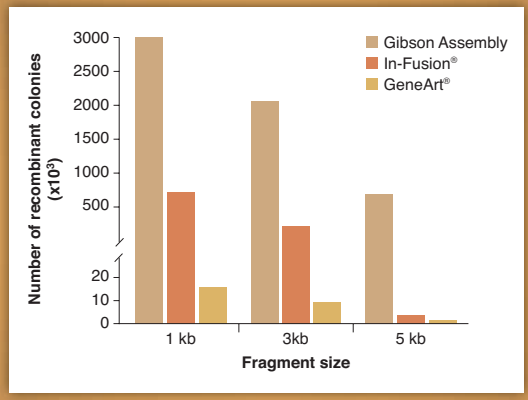

Assembly reactions containing 25 ng of linear pUC19 vector and 0.04 pmol of each fragment were performed following individual suppliers' recommended protocols and using the competent cells provided with the kit. The total number of recombinant colonies was calculated per 25 ng of linear pUC19 vector added to the assembly reaction.

NEBuilder™ for Gibson Assembly

Visit **NEBGibson.com** to view the latest tutorials and to try our primer design tool.

SGIDNA

Join Keystone Symposia for Two Unique Events

HIV/AIDS: Strategies for an Endgame

December 13, 2013 | 1:00–2:30 PM EST

Our first FREE, LIVE webcast.

This 90-minute event will aim to determine the optimal strategy to end the AIDS epidemic, with a particular focus on discussing the merits of pre-exposure prophylaxis versus vaccines.

Moderator: Bruce Walker
Panelists: Myron (Mike) Cohen, Betsy Herold, Julie McElrath and Gary Nabel

Visit **www.keystonesymposia.org/KSHIV** to register and to submit a question/topic that you would like addressed during the discussion.

Big Data in Biology

March 23–25, 2014 | San Francisco, California, USA

Our first SHORT, TWO-DAY symposium.

This conference will address the challenges of sharing, archiving, integrating and analyzing the vast amounts of biological data now being generated. The event will bring together various research specialties that rarely interact, including plant scientists, medical geneticists, genomicists, microscopists and neurobiologists, as well as computer scientists, computational biologists, mathematicians and technologists. Event sessions start at 8 AM on March 24.

Scientific Organizers: Lincoln D. Stein, Doreen Ware and Michael Schatz

Session Topics:

- **Databases and Clouds**
- **Panel on Big Data Challenges and Solutions: Control Access to Individual Genomes**
- **Personal Genomes**
- **Imaging/Pharmacogenomics**

Discounted Abstract Deadline: ***November 19, 2013***
Student/Postdoc Scholarship Application Deadline: ***November 19, 2013***
Abstract Deadline: ***December 18, 2013***
Discounted Registration Deadline: ***January 21, 2014***

For more information and to view the full program, visit **www.keystonesymposia.org/14F2**

CONFIRMED SPEAKERS
(as of November 4, 2013):

Laura Clarke, European Bioinformatics Institute
Mark Gerstein, Yale University
David Haussler*, UC Santa Cruz
Jill P. Mesirov, Broad Institute
John Overington, European Molecular Biology Laboratory
Ajay Royyuru, IBM T.J. Watson Research Center
Michael Schatz, Cold Spring Harbor Laboratory
Dan Stanzione, University of Texas at Austin
Lincoln D. Stein, Ontario Institute for Cancer Research
Susan Sunkin, Allen Institute for Brain Science
Jason Swedlow, University of Dundee
Matt Wood, Amazon Web Services, Inc.

**Keynote Speaker*

KEYSTONE SYMPOSIA™
on Molecular and Cellular Biology
Accelerating Life Science Discovery

www.keystonesymposia.org | 970.262.1230 | 800.253.0685

Call for 2013 Cozzarelli Prize Nominations

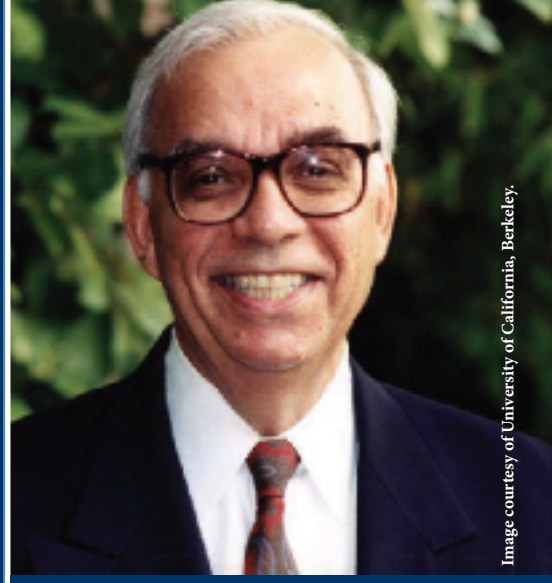

Image courtesy of University of California, Berkeley.

Nicholas R. Cozzarelli, former PNAS Editor-in-Chief

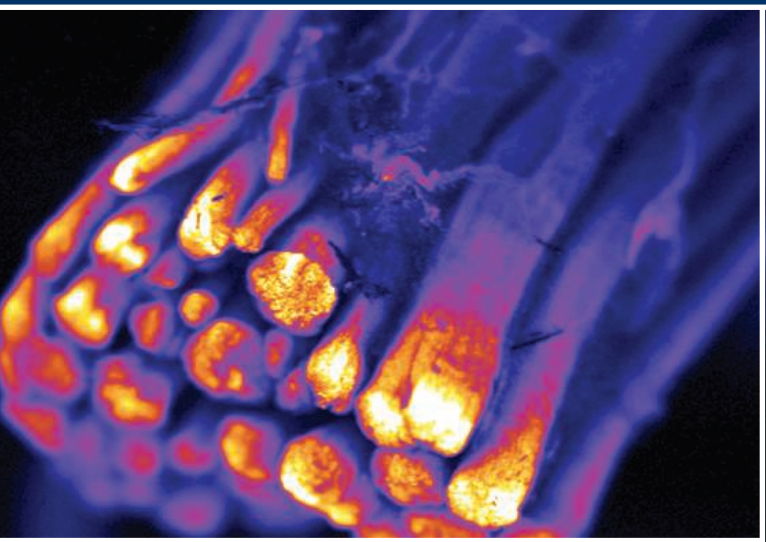

The PNAS Editorial Board is now accepting nominations through January 10, 2014 for the 2013 Cozzarelli Prize. This award recognizes scientific excellence and will be given to six papers published in PNAS during 2013.

Nominations should be sent to pnas@nas.edu and should include a citation and brief explanation of the merits of the work. The award recipients will be recognized during the PNAS Editorial Board Meeting and the NAS Annual Meeting Awards Ceremony on April 27, 2014 in Washington, DC.

PNAS
www.pnas.org

For more information and a list of previous winners visit www.pnas.org/cozzarelliprize.

eppendorf

PhysioCare concept

The New Legend

Eppendorf Reference® 2

»Reference« stands for extraordinary precision and accuracy, a long service life, and an ergonomic design. The new Reference 2 boasts these proven Premium characteristics and this operating philosophy with its innovative state-of-the-art technology; making it a reliable partner for you and your demanding work.

> Single-button operation enables ergonomic handling with reduced operating effort
> High precision and accuracy providing reliable pipetting results
> Quick and secure volume setting, incl. volume lock
> RFID chip contains all relevant data regarding the pipette

www.eppendorf.com/reference

GAS SORPTION ANALYZER

The Autosorb 6 iSA is designed to meet the needs of laboratories with high analytical throughput requiring rapid and accurate surface area and pore-size data. It provides the flexibility that allows up to six samples to run concurrently and completely independently. New enhancements provide protective dewar shields, which serve a dual purpose for both protecting the operator and the analyzer. Improved lighted displays clearly show the status of the instrument's operation. The Autosorb 6 iSA ASWin software has been updated to provide features to facilitate CFR 21 Part 11 compliance. This allows pharmaceutical laboratories to meet FDA regulations for electronic record keeping systems including features such as password controlled access, audit trail capabilities, and enhanced reporting features. In addition, the new software in both CFR and non-CFR modes provides enhanced import and export capabilities, flexible data storage, and full 64-bit compatibility to allow operation with current Windows operating systems.

Quantachrome Instruments
For info: 800-989-2476 | www.quantachrome.com

ANTIBODY PRODUCTION SERVICE

The MedixMAB by Design antibody production service is a completely customized service for the in vitro generation of high-performance monoclonal recombinant antibodies and Fab fragments. MedixMAB by Design presents an excellent foundation for superior IVD assays. With antibodies produced to the strictest international quality standards, the new service equips IVD manufacturers with a competitive advantage, helping to increase sales revenue without the need to invest in costly production facilities and expertise. The advanced production technology of the MedixMAB by Design service allows for the targeting of a broader range of antigens than possible in vivo, including poorly immunoreactive and toxic compounds, and recombinant MAB production is possible on a range of scales (mg to kg). As an alternative to producing full length MABs, Fab fragments can instead be generated in just three months, to greatly enhance specificity and sensitivity of an IVD assay in solid-phase applications.

Medix Biochemica
For info: +358-9-547-680 | www.medixbiochemica.com

GAS PRESSURE REACTORS

A new range of compact gas pressure reactors have been designed to be heated and stirred using standard hotplate stirrers with the unique DrySyn adapter that ensures excellent heat transfer. The base vessels are available from 50 mL to 500 mL and are rated up to 200 bar and 200°C enabling reactions including hydrogenation, carbonylation, and carboxylation at elevated temperatures and pressures to be routinely performed. With the added flexibility of standard and custom DrySyn inserts, Asynt gas pressure reactors provide chemists with a platform to undertake a single reaction from 100's of microliters, by itself or in parallel, up to a single reaction to the volume of the vessel. All vessels can be provided with a bursting disc, pressure gauge, pressure relief valve, PT100 temperature probe, thermowell for PT100, cooling coil, magnetic overhead stirrer with standard impeller (316 stainless steel), high-pressure burette assembly, and a range of glass or PTFE inserts and liners as well as PEEK internals if necessary.

Asynt
For info: +44-(0)-1638-781709 | www.asynt.com

TEMPERATURE CONTROL

Ideal for use by researchers and others performing metabolic studies, biodegradation assessments, forensic evaluations, compost research, toxicity screening studies, and other anaerobic or aerobic research, the Model 210 Heated Circulator and Model 5206M Recirculating Chiller provide temperature control over a range as broad as -10°C to +70°C (14°F to 158°F). Designed for use with anaerobic respirometers, the Model 210 Heated Circulator controls temperature from ambient to +70°C (158°F) with ±0.2°C (±0.4°F) stability. It has a 750 W heater and a single speed centrifugal pump that delivers up to 11.4 L/minute (3.0 gallons/minute) at 0.13 bar (2.0 PSI). The Model 5206M Chiller is recommended for use with aerobic respirometers. This ¼ HP chiller controls temperatures from -10°C to 70°C (14°F to 158°F) with ±0.1°C (±0.2°F) stability and a magnetic drive centrifugal pump that delivers up to 15.5 LPM (4.1 GPM) at 0.69 bar (10 PSI).

Polyscience
For info: 800-229-7569 | www.polyscience.com

COPY NUMBER VARIATION TOOL

The CNV detection tool of NextGENe version 2.3.4 forward includes a sophisticated new coverage-based algorithm developed for next generation sequencing (NGS) sequencing data from instruments such as Illumina, Roche, and Ion Torrent sequencing platforms. Applications include both whole exome as well targeted sequencing panels such as Ion Torrent AmpliSeq panels or the HaloPlex Target Enrichment System from Agilent Technologies. Copy number variations can now be detected in NGS data using dispersion measurements and a novel Hidden Markov Model (HMM) not found in other NGS analysis programs. With the new technology specified regions of a "sample" and a "control" are used to determine a coverage ratio measured in RPKM for every region (sample divided by sample plus control). CNV calls are made on the basis of changes in coverage, utilizing automatic measurement of noise (dispersion) and a novel HMM.

Soft Genetics
For info: 888-791-1270 | www.softgenetics.com

Electronically submit your new product description or product literature information! Go to **www.sciencemag.org/products/newproducts.dtl** for more information.

Newly offered instrumentation, apparatus, and laboratory materials of interest to researchers in all disciplines in academic, industrial, and governmental organizations are featured in this space. Emphasis is given to purpose, chief characteristics, and availability of products and materials. Endorsement by *Science* or AAAS of any products or materials mentioned is not implied. Additional information may be obtained from the manufacturer or supplier.

WEBINAR

Exome Sequencing in Today's Lab:

Shifting the Paradigm in Translational and Clinical Research

Wednesday, December 4, 2013

12 noon Eastern, 9 a.m. Pacific, 5 p.m. UK, 6 p.m. Central Europe

Next generation sequencing technologies have enabled a rapid expansion toward the understanding of inherited disorders, cancer biology, drug development, and treatment resistance. Exome sequencing has been increasingly and successfully applied in the clinical research setting for identifying common single nucleotide variants, copy number variations, and small insertions or deletions as well as rare de novo mutations that may explain Mendelian, complex, and rare genetic disorders. Recent advancement in rapid and low-cost exome sequencing make it an attractive alternative to traditional targeted gene panel sequencing for clinical research, while maintaining the possibility of discovering mutations in genes previously not associated with a disorder. Furthermore, the exome encompasses approximately 1% of the genome, yet contains approximately 85% of disease-causing mutations, making exome sequencing easier and cheaper than whole genome sequencing for identifying disease-causing variants in research.

Researchers are now applying proband-father-mother (trio) exome sequencing to uncover variants that potentially either cause or modify the condition under study. In this webinar, the audience will learn about the current applications of exome sequencing in clinical research and its impact on the future of health care.

Speakers

Christian Marshall, Ph.D.
The Hospital for Sick Children
Toronto, Canada

Christian Gilissen, Ph.D.
Radboud University Medical Centre
Nijmegen, The Netherlands

During the webinar, the speakers will:

- Detail their clinical research exome workflow from DNA to data analysis
- Compare exome sequencing to other variant screening approaches
- Shed light on the current paradigm shift to exome sequencing for clinical research
- Discuss how this shift may impact future clinical applications of exome sequencing
- Answer your questions live on air!

REGISTER NOW!
webinar.sciencemag.org

Webinar sponsored by

ion torrent
by life technologies™

Brought to you by the *Science*/AAAS Custom Publishing Office

Science
AAAS

Promega

FuGENE® HD
Illuminate Real Biology

Don't let old toxic transfection technology get in the way of your science. FuGENE® HD provides the power to transfect virtually any cell type while maintaining biologically relevant cell signaling responses.

Key applications:

- Cancer Biology
- Stem Cell Research
- Developmental Biology
- Neurobiology
- Immunobiology
- Lentivirus Production
- CHO Cell Protein Production

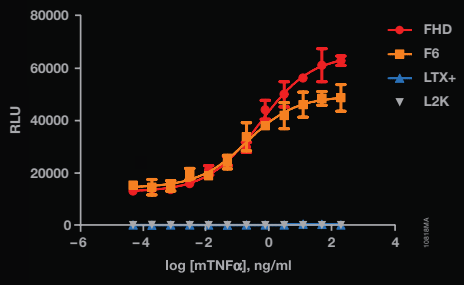

In this BaF3 cell model of NF-kB luciferase induction, only FuGENE® HD and FuGENE® 6 are able to create a usable assay.

To discover the power of FuGENE® HD for your biology, request a free sample at
www.promega.com/pathwaybiology

Looking to China for Scientific Careers

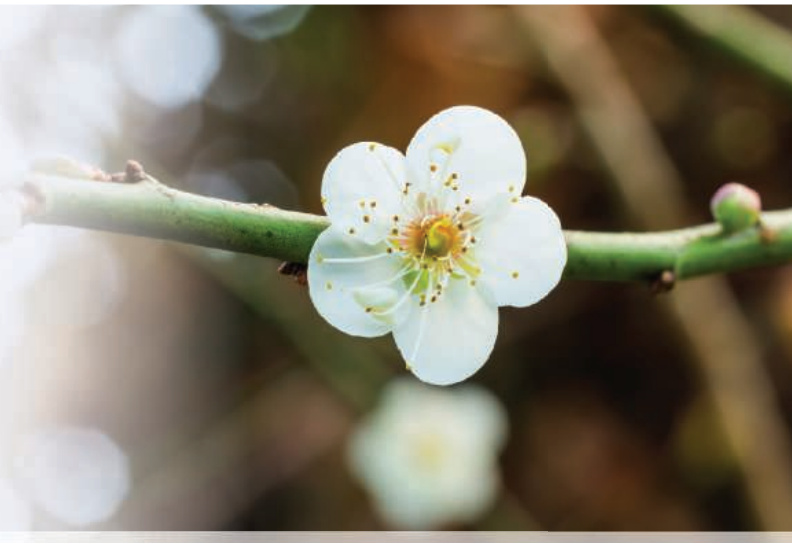

Plum Blossom in China

China's rise in the global marketplace has been accompanied by the government's increasing focus on boosting the quality and quantity of the country's scientific research. China's government and universities are stepping up incentives to retain Chinese scientists and entice foreign academics to build their careers in China, and some professors say funding for research is more readily available in China than in the West. As a result, scientists from all over the world are starting to choose China as a place to build their academic and research careers. **By Lenora Chu**

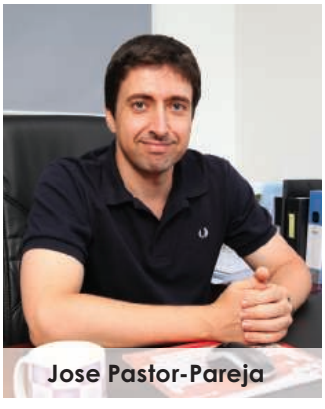

Jose Pastor-Pareja

Jose Pastor-Pareja was finishing up his postdoc in genetics at Yale University when his supervising professor, a Chinese national, began talking to him about science careers in China.

"Many friends and colleagues at Yale were Chinese as well," says Pastor-Pareja, "so I heard from people I trusted that this is a great time to do science in China in terms of funding and resources."

A Spanish national, Pastor-Pareja had academic job offers from universities in Spain, England, and China, but when Tsinghua University in Beijing came calling, Pastor-Pareja knew he'd found his home. He accepted an offer to become a principal investigator in Tsinghua's School of Life Sciences, equivalent to a tenure-track assistant professor position at a Western university.

"The level of science at Tsinghua and in Beijing is amazing," says Pastor-Pareja, who earned his Ph.D. at the Universidad Autónoma de Madrid. More than 30 *Drosophila* labs exist in Beijing, making the city's fruit fly resources comparable to Boston or New York. And Tsinghua is an international leader in cellular and developmental biology as well as structural biology and electron microscopy, explains Pastor-Pareja.

He was also drawn by the generous funding potentially available to him; indeed, after accepting Tsinghua's offer, Pastor-Pareja received an award from the government's Thousand Talents program, designed to encourage scientists and scholars working abroad to come to China. Altogether, he received funding totaling 2 million yuan (330,000 USD) on top of startup funds from Tsinghua totaling more than 6 million yuan (1 million USD), and the opportunity to start a 1,540 square foot fruit fly laboratory of his own. He describes his salary at Tsinghua as "roughly comparable to the United States—definitely better than Europe."

Despite being established in China less than a year ago, Pastor-Pareja's group is already proving productive and is nearly ready to publish a paper on the differences in extracellular matrix production in normal and tumoral tissue in the fruit fly. "At this stage, I'm benefitting from generous funding, better equipment than I had access to at Yale, and very smart and motivated students," Pastor-Pareja explains. He is also enjoying the energy of working with administrators and faculty who are as thrilled as he is to be at the university. continued>

"The level of science at Tsinghua and in Beijing is amazing."
—Jose Pastor-Pareja

Tsinghua University

Upcoming Features

Faculty Careers—February 7

Postdoc Careers—February 28

Cancer Research Careers—March 28

Faculty Positions at ShanghaiTech University (上海科技大学)

Officially endorsed to launch by Ministry of Education in China, ShanghaiTech University is jointly established by Shanghai Municipal Government and Chinese Academy of Sciences (CAS). The University currently consists of 4 schools: School of Physical Science and Technology (SPST), School of Information Science and Technology (SIST), School of Life Science and Technology (SLST) and School of Entrepreneurship and Management (SEM), as well as 2 institutes: Shanghai Institute for Advanced Immunochemical Studies (SIAIS) and iHuman Institute. The University offers programs for undergraduates, Master and Ph.D students, as well as professional students. In the short-term, ShanghaiTech aims to enroll 2,000 undergraduates and 4,000 postgraduates (including about 3,000 doctoral students). The first batch of graduate students was admitted in September of 2013, and undergraduate students will be admitted in 2014. ShanghaiTech plans to build a faculty of 1,000 members, with about half of them recruited internationally, and the other half coming from CAS. The faculty team now includes 3 Nobel Laureates and 23 Academicians of CAS. Located in CAS Pudong Science Park in Zhangjiang Hi-Tech Park, ShanghaiTech boasts of state of the art research infrastructure and forms a research and innovation network with neighboring national research institutions/facilities such as CAS Shanghai Advanced Research Institute, Shanghai Synchrotron Radiation Facility, National Facility for Protein Science, and Drug Discovery and Development Platforms. ShanghaiTech will create a dynamic hub where research, education, and innovation meet to provide a multi-disciplinary approach to learning and to solving problems facing society. We are committed to pursuing academic excellence and promoting open collaborations with those who share the same vision.

We are seeking applications and nominations for multiple tenure-track and tenured positions at all ranks.

Initial Research Support Package: University will provide internationally competitive start-up fund plus support of Research Associate and Post-Doctoral fellows. Laboratory space will be provided matching the research needs.

Compensation and Benefits: Salary is highly competitive and commensurate with experience and academic accomplishments. ShanghaiTech also offers a comprehensive benefit package including housing benefits.

1. School of Physical Science and Technology (SPST)

SPST is established to encourage interdisciplinary research particularly focused on Materials, Environment and Energy. The School is expected to have about 100 regular tenured and tenure-track faculty, 1,200 graduate and 750 undergraduate students.

Qualifications: Doctoral degree in Physical Science and Engineering as well as postdoctoral experience are required for applicants to junior level positions. They will be expected to establish an independent, internationally recognized research program, to supervise students and to teach two courses a year. The senior position applicant is expected be leading scientist in his/her research discipline. We particularly welcome those with research interests related to Energy, Materials and Environment Science and Engineering to apply.

2. School of Information Science and Technology (SIST)

SIST seeks first-class faculty candidates in all cutting edge areas of Information science and technology. Our recruitment focus includes, but is not limited to, the following special research areas: advanced computer architecture and technologies, nano-scale electronics, ultra-high speed and low power circuits, intelligent multimedia and integrated signal processing systems, next-generation computer systems, computational foundations, big data, data mining, visualization, computer vision, bio-computing, smart energy/power devices and systems, highly-scalable and multi-service heterogeneous networking, as well as various inter-disciplinary areas involving the foundation and applications of information science and technology.

Qualifications: Candidates must demonstrate: A strong interest in undergraduate and graduate education; Well-developed research plans and demonstrated record/strength/potentials; Ph.D. (Electrical Engineering, Computer Engineering, Computer Science, or closely related field); A minimum relevant research experience of 4 years.

3. School of Life Science and Technology (SLST)

SLST seeks first-class scientists in these five research areas: Protein science and biotechnology, Stem cell research and regenerative medicine, Systems biology and translational medicine, Physical biology and molecular imaging, Chemical biology and innovative pharmacology.

Qualifications: The successful candidates should have an exceptional track record of research in life sciences or a closely related discipline within the last five years. Besides maintaining an active research program, the recruited candidates will also be expected to contribute to the educational missions of undergraduate and graduate programs within SLST.

4. School of Entrepreneurship and Management (SEM)

SEM provides students with practical knowledge in strategic emerging industries where there is a high demand for commercialization of innovation that advances China's economic development. SEM programs focus on the applied fields of technology innovation management, entrepreneurship and MSE management, as well as venture capital management. SEM offers advanced studies through MBA, EMBA, and EDP programs.

Qualifications: An applicant should possess a doctoral degree in professional studies such as Economics, Finance, or Management. Industry experience is preferred but not necessary. Faculty responsibilities include teaching MBA or EMBA students and conducting applied research often working with companies. SEM especially welcomes applicants with interests related to Innovation, Entrepreneurship, and Venture Capital.

5. Shanghai Institute for Advanced Immunochemical Studies (SIAIS)

SIAIS focuses on elucidating the most fundamental problems in life science research, particularly in immunochemistry. We are seeking highly motivated and outstanding candidates with strong interests in antibody design and engineering, antibody assay method and platform technology, antibody therapeutics, ADC chemistry, structural biochemistry, cell biology and translational medical research.

Qualifications: Qualified candidates should possess a doctoral degree in physical or life science with successful track records in academia or pharmaceutical industry. SIAIS particularly welcomes those with research interests that emphasize innovation and transformation.

6. The iHuman Institute

The iHuman Institute is established to encourage interdisciplinary computational and experimental research focused on human cell signaling combining chemistry, biology, imaging, and structural biology. Academic basic sciences and applied sciences with industry will be integrated together providing all researchers with unique scientific opportunities.

Qualifications: Successful applicants should have a doctoral degree in Physical or Life Sciences as well as postdoctoral experience for junior level position. Applicants will be expected to establish an independent, internationally recognized research program and supervise students. The senior position applicants are expected be leading scientists in his/her research disciplinary. We particularly welcome those with research interests related to chemical biology and bioinformatics to apply.

Application Procedure: Submit a cover letter containing the description of the major research achievements, a 2-3 page statement of research interests, a CV and the names and addresses of three individuals who can serve as references to the email addresses given below:

SPST	**SPST@shanghaitech.edu.cn**
SIST	**SIST@shanghaitech.edu.cn**
SLST	**SLST@shanghaitech.edu.cn**
SEM	**SEM@shanghaitech.edu.cn**
SIAIS	**SIAIS@shanghaitech.edu.cn**
iHuman	**iHuman@shanghaitech.edu.cn**

ShanghaiTech University, Building 8, 319 Yueyang Road, Shanghai 200031, China
Review of applications will start immediately and will continue until positions are filled.
For more information, please visit our website: ***www.shanghaitech.edu.cn***

FULL TIME FACULTY POSITIONS AT
UNIVERSITY OF SCIENCE AND TECHNOLOGY OF CHINA (USTC)

The University of Science and Technology of China (USTC), is one of the most prestigious universities in China and the only university jointly endowed by both the Chinese Academy of Sciences (CAS) and the Ministry of Education of China (MOE). Widely recognized for its culture and tradition in talent focus and academic priority, USTC is a thriving institution with stimulating atmosphere for ground-breaking research and innovation. USTC scholars enjoy enormous freedom in realizing their own research aspirations and gaining international visibility, and USTC students are reputed in their deep fond of science and independent thinking. Numerous USTC alumni have become world-renowned scientists and entrepreneurs.

POSITIONS

Government Supported Recruitment Programs

POSITION	QUALIFICATIONS
1000 Talents Program (1000Plan) Professorship for Young Scholars	•<40 yrs old •Overseas PhD degree + no less than 3 consecutive years of overseas postdoc research experience Or Chinese domestic PhD degree + no less than 5 consecutive years of overseas postdoc research experience •Demonstrated excellence in publication & experience in internationally visible research projects
100 Talents Program of Chinese Academy of Science (CAS 100Plan) Professorship	•<45 yrs old •PhD degree + No less than 4 consecutive years of postdoctoral overseas research experience •Demonstrated excellence in publication & experience in internationally visible research projects
Chang Jiang Scholars Program of Chinese Ministry of Education -Distinguished Professorship	•<45 yrs old •Currently an associate professor, or in an equivalent position, of a world renowned research institution •Proven excellence in research achievements

Tenured Positions

POSITION	QUALIFICATIONS
•Full Professor •Associate Professor	•Demonstrated excellence in publication, funding or patent record •Strong experience in establishing research programs •Academic rank will be commensurate with experience

Contract Positions

POSITION	QUALIFICATIONS
•Research Professor •Research Associate Professor •Postdoctoral Researcher	•Upon specific needs of each research group (Please visit USTC website at http://en.ustc.edu.cn, and explore the hiring information of each school)

SUPPORT, SALARY AND BENEFITS

USTC is featured with and proud of its highly collegial, interactive, and supportive environment for researchers. Besides, it offers competitive start-up package among all the "C9 League" universities of China. The benefits include spacious housing, subsidized faculty dining, premium medical services, etc. Professors hired through the recruitment programs will receive supplementary remuneration, as well as assistance on the establishment of a dedicated research team. The start-up package includes adequate start-up funds, newly renovated office, ample laboratory space, and plenty of research assistants. Please visit the USTC Talent Recruitment and Services website for more details: http://employment.ustc.edu.cn.

ACADEMIC DISCIPLINES

USTC has a broad range of academic disciplines, covering natural sciences, engineering, management, and some emerging interdisciplinary fields. All disciplines have open for employment opportunities, with particular emphasis on enhancing and broadening USTC's strengths and representation in engineering and high tech areas, such as nuclear science & engineering, future internet, advanced manufacturing, etc.. The University embraces applicants of all ranks, from internationally recognized investigators who would establish their own research groups and platforms, to junior scholars who may complement our existing research programs.

CONTACT US

Qualified applicants are invited to send a job intention letter and a curriculum vitae to: job@ustc.edu.cn.

Mailing Address:
Talents Recruitment & Services Office
University of Science and Technology of China
96 Jinzhai Road, Hefei, 230026, P.R. China
Telephone: +86-551-63607709
Fax: +86-551-63637049

Certainly, he says, there are challenges to living in China: It's difficult to find his favorite Western foods, and it's hard to ignore the pollution in Beijing. Then there's the language barrier: "Everybody will tell you learning Chinese is a daunting task."


Fudan University

KNOWLEDGE SHARING

For **Ming Li,** who grew up in China's former capital city of Nanjing, the incentive to pursue his career in China amounted to a combination of both personal and professional reasons.

Li had been a star student at the University of Southern California's (USC) Viterbi School of Engineering, while researching signal processing and speech recognition. But when the time came for him to survey the job market, Li felt the pull home to China to be closer to his family. He was initially concerned that research support for young faculty members wouldn't be adequate at many traditional Chinese universities, but luckily found that wasn't the case, particularly for those that collaborate with partner institutions in the West. Such alliances help Chinese universities attract a higher caliber of student, maintain higher standards for research, and encourage faculty independence, Li says.

Li received job offers from two prestigious global partnerships in science and engineering: the Shanghai Jiao Tong University-the University of Michigan Joint Institute and Sun Yat-sen University-Carnegie Mellon University (SYSU-CMU) Joint Institute of Engineering. Shanghai Jiao Tong University and Sun Yat-sen University are ranked 3rd and 7th, respectively, among all universities in China, according to the 2013 list compiled by the Chinese University Alumni Association. Li ultimately accepted a tenure-track position at the SYSU-CMU Joint Institute of Engineering (JIE), located in Guangdong Province in southern China. Under the collaboration model, he'll be teaching and performing research for the 2013–14 academic year at Carnegie Mellon in Pittsburgh as a visiting professor, and then will head to China the following year to continue teaching and also start up his research lab.

"Teaching at SYSU-CMU-JIE is the same in style and quality as at Carnegie Mellon, and the research is also very promising," says Li. By accepting a position at a joint institute, Li gets the best of both worlds. He is able to work with CMU faculty to jointly supervise graduate students but is also eligible for Chinese government funding.

He describes his salary as "very close to" what he would be earning at an American university and competitive compared with other academic positions in China, leaving him with no financial worries, Li explains. And as an added bonus, he and his wife—both only children—will be closer to their parents back home once he completes his visiting year at CMU and relocates to China.

Professor **Junfeng Wang** also appreciates being near his family, but cites China's prominence in nuclear magnetic resonance research as the primary reason for his return. Indeed, China has hosted the last three major nuclear magnetic resonance-related conferences. He completed his postdoctoral training at Harvard University in 2009 and accepted a position as director of the magnetic resonance program at the Chinese Academy of Sciences' High Magnetic Field Laboratory (CHMFL)—one of only five high magnetic field labs in the world. Accessing funding in China is easier than in the West due to the increasing support from central and local governments, Wang says; indeed Wang's lab itself was sprung from a 2008 government initiative.

MAKING AN IMPACT

David Waxman was researching population theory at the University of Sussex when an academic colleague—who had split time between China and the United Kingdom for years—urged him to consider doing research in China. Waxman visited his colleague in Shanghai several times and found the city to be an exciting place to live and work. He also made a surprising discovery: He was drawn to the rare opportunity to impact students' education in a way that wasn't possible in the United Kingdom.

Chinese culture doesn't necessarily encourage students to question teachers, Waxman says. "I want students to question me, argue with me, and formulate ideas with me."

His colleague in China promptly assisted with Waxman's application for a Thousand Talents central government grant to fund Waxman's time and research in China. Waxman was awarded a five-year contract as a professor of biology at Fudan University in Shanghai, one of China's top universities. He has few teaching duties compared with the commitments required for a standard faculty position back in the United Kingdom, he says, which often involves administrative- and teaching-related duties that can be at least 50% of a faculty member's time.

"I have an enormous amount of freedom and resources to do my research," explains Waxman. "I have a very generous startup package which means that at the present time I am not pressed to get grants in China, though I expect to apply in the future. It's a very big thing for scientists not to have to apply for grants all the time; continued>

"Teaching at SYSU-CMU-JIE is the same in style and quality as at Carnegie Mellon, and the research is also very promising."
—Ming Li

CREDITS: (BOTTOM) PHOTO COURTESY OF MING LI

中国科学院大连化学物理研究所
Dalian In statute of Chemical Physics, Chinese Academy of Sciences

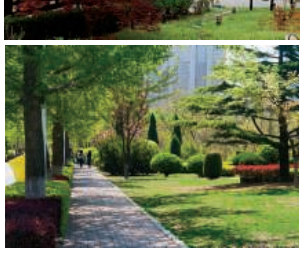

Welcome Talents to Joining Dalian Institute of Chemical Physics, Chinese Academy of Sciences

Dalian Institute of Chemical Physics

Founded in 1949, Dalian Institute of Chemical Physics (DICP), Chinese Academy of Sciences (CAS), is located in the beautiful port city of Dalian in Northeast china. In the past half century, research here has closely reflected the economic and scientific needs of China. The Institute has an important series of achievements, principally in the fields of catalytic chemistry, chemical engineering, chemical laser and molecular reaction dynamics, organic synthesis, and chromatography for modern analytic chemistry and biotechnology. These achievements have contributed greatly to the economic and technological development of China.

Dalian National Laboratory for Clean Energy

Dalian National Laboratory for Clean Energy (DNL)is China's first National Laboratory in the field of energy research, and integrates laboratories across DICP and other institutions. Research at DNL is focused on the efficient conversion and optimal utilization of fossil energy, clean energy conversion technologies and the economically viable use of solar and biomass energy. The research activities will benefit from the existing strong background of the DICP in chemistry, physics, chemical engineering, biology, and materials science, in addition to our extensive network of national and international collaborations. DNL is integrated on the DICP campus and would be taken as a main research platform to develop both fundamental and applied researches in DICP.

Development Strategy

DICP focuses on sustainable energy research and coordinates the development of environment optimization, biotechnology and advanced material in a multidisciplinary atmosphere by strengthening technological integration and innovation. DICP aims to play indispensable roles in national economy and security, and to become a leading research institute in the world.

Research Fields

Physical Chemistry, Catalytic Chemistry, Industrial Catalysis, Petrochemical Engineering, Solar Energy, Photoelectrocatalysis, Biomass Conversion, Low-carbon Chemistry, Fuel Cell Technology, Energy Storage Technology, Materials Chemistry, Advanced Materials, Energy Materials, Organic Chemistry, Biotechnology, Bioinformatics, Structural Biology, Synthetic Biology, Translational Medicine, Metabonomics, Systems Biology, Cell Biology, Analytical Chemistry, Combustion Chemistry, Energy Strategy

Recruitment Programs

National Thousand Talents Program (Full-time & Part-time)
National Thousand Talents Program for Foreign Experts (Full-time)
National Thousand Talents Program for Young Scientists (Full-time)
CAS Hundred Talents Program (Full-time)
DICP Hundred Talents Program (Full-time)
DICP Outstanding Postdoctoral Scholarship Program

Support, salary and benefits

Generous start-up package, competitive salary and benefits will be provided based on different recruitment programs. The start-up package includes adequate start-up funds, newly renovated office, ample laboratory space, and plenty of research assistants. The benefits include medical insurance, retirement and house subsidy. For leading professors and outstanding post doctors, salary at a level of international counterparts would be offered.

Contact us

Please send applications, inquires and nominations to talents@dicp.ac.cn. All applications should include a CV and a list of detailed publications. Those interested in cluster hiring should send CVs and publications as a group. Visit DICP website for more details:http://www.talent.dicp.ac.cn.

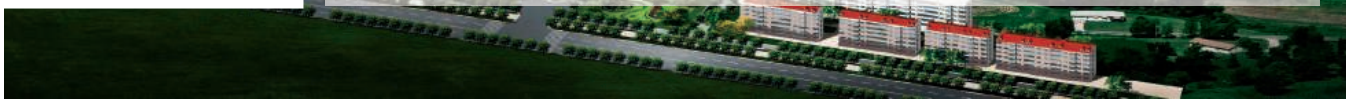

Featured Participants

Center for China and Globalization
en.ccg.org.cn/_d1479.htm

Fudan University
www.fudan.edu.cn/english-new

High Magnetic Field Laboratory, Chinese Academy of Sciences
english.hf.cas.cn/r/Research-Divisions/HFML

Joint Institute of Engineering, Sun Yat-sen University-Carnegie Mellon University
jie.sysu.edu.cn

Key Laboratory of Green Process and Engineering, Chinese Academy of Sciences
research.nvidia.com/content/IPE-CAS-ccoe-summary

Shanghai Jiao Tong University-the University of Michigan Joint Institute
umji.sjtu.edu.cn

Tsinghua University
www.tsinghua.edu.cn/publish/th/index.html


David Waxman

meanwhile, grants in Britain and America are increasingly hard to get."

He works with several Ph.D. students and has enjoyed the opportunity to train them "in the way that I know," says Waxman. "By the end of their schooling, I'd like them to be independent researchers." Waxman is realistic about the impact he might make, but hopes he can "drop a stone into a pond and cause a ripple effect by training the next generation of leaders."

The potential to make a huge impact in a country that is undergoing rapid change draws many other researchers to China. Chemical Engineer **Chuanfang Yang,** for example, says he saw an opportunity to make a big difference with the country's pressing concerns over clean air and water. "Sustainable growth is much needed in China, but it's mostly taken for granted in Western countries," said Yang, who left an R&D job at an environmental company in the United States to become a professor at the Chinese Academy of Sciences' Key Laboratory of Green Process and Engineering. Not so in China, where outdoor air pollution contributed to nearly 1.2 million premature deaths in 2010, according to reports analyzed by the Health Effects Institute, a U.S.-based nonprofit that studies the health impact of air pollution.

INCENTIVES TO COME

Over the past decade, the Chinese government has been steadily introducing incentive programs to lure scientists from other countries as well as keep homegrown talent in China.

The most high-profile program within the last few years is the central government's Thousand Talents program, which aims to draw experts in science, technology, and entrepreneurship to the country (and is the program supporting the research of both Tsinghua's Pastor-Pareja and Fudan's Waxman). The application process is long and multilayered, but the benefits are generous for those who succeed: a salary plus benefits, a lump-sum of 1 million yuan (about 160,000 USD), and research subsidies ranging from 3 to 5 million yuan (490,000 USD to nearly 820,000 USD) over a three-year period.

The Chinese Academy of Sciences (CAS) also sponsors an incentive program called the 100 Talent Plan, which grants 2 million yuan (325,000 USD) or more to promising young academic leaders. The initiative has successfully drawn more than 1,000 foreign and expatriate Chinese scientists to work at one of the 100 or so institutes at CAS.

> **"It's a very big thing for scientists not to have to apply for grants all the time; meanwhile, grants in Britain and America are increasingly hard to get."**
> **—David Waxman**

The Ministry of Education (MOE) sponsors the Yangtze River Scholar Scheme program, which aims to bring 200 visiting science professors and chairs to Chinese universities annually. Awardees work in China for three- to five-year terms, and are eligible for bonuses up to 200,000 yuan annually (32,000 USD) or 30,000 yuan monthly (5,000 USD), depending on the level of award granted.

The MOE also has a joint initiative with the Li Ka Shing Foundation called the Chang Jiang Scholars program, which awards research grants and a three-year position at a Chinese university to professors of all disciplines, including science, economics, and social science, from both China and abroad. And the National Natural Science Foundation of China administers a fund to lure overseas scholars to China to conduct basic scientific research.

Provincial and municipal governments in China are also launching programs to attract and retain scientific talent; for example, the governments of Shanghai and Beijing each sponsor a Thousand Talents program distinct from that of the central government.

These incentives are certainly helping. To date, the central government's Thousand Talents program has drawn more than 3,000 global experts to China, and the provincial governments' parallel programs have brought more than 20,000 over the past five years, according to **Huiyao Wang,** director general of the Center for China and Globalization, a think tank in Beijing. Among many high-profile Thousand Talents awardees is Jeff Lehman, the former continued>

Collaborative Innovation Center for Cancer Medicine

Sun Yat-sen University Cancer Center

Postdoctoral Positions

Sun Yat-sen University, Fudan University, Peking Union Medical College and the National Institute of Biological Sciences are partnering to set up a new "Collaborative Innovation Center for Cancer Medicine" following a national initiative to develop medical science and technologies for cancer care in China. The purpose is to establish a leading international center for innovation capable of conducting large-scale outstanding research with an interdisciplinary team of oncology experts competitive on an international scale, providing a model in China for talent training, in order to be at the forefront of cancer prevention and treatment and build a world-class center.

The center's main missions are to raise the level of cancer care and prevention in China according with international standards, increase the rate of early detection and treatment, develop anti-cancer therapy with higher efficacy, and finally protect national health.

This collaborative innovation center's major research directions are genomics, cancer genesis and epigenetic, origin and regulation of tumor stem cell, cancer metabolism, cancer immunology, tumor heterogeneity and precise treatment. The research team should work together to achieve a certain amount of basic science breakthroughs and key technological advances, with their associated intellectual property.

Several post-doctoral positions are open in the Collaborative Innovation Center for Cancer Medicine.

(1) Required qualifications for the post-doctoral position
- PhD Degree, Biological or Biomedical major
- At least 1 publication as first author in journals of impact factor above 5.0 or mainstream journals like JBC
- The candidate will go through an expert committee interview

(2) Job Compensation and additional information
- 3 months probation
- No fixed years of working
- Contract to be renewed every year
- Annual salary: 200,000 RMB

Please send your CV with job title to **zhongjunx@sysucc.org.cn**
Contact person: Mr. Zhong and Mrs. Yang,
Phone: 86-20-87343810/3129
Website: **www.sysucc.org.cn**

Sun Yat-sen University Cancer Center

Senior Overseas Scientist Job Openings

Sun Yat-sen University Cancer Center was founded in 1964 by the regroupment of the cancer hospital and the cancer research institute of Sun Yat-sen University. After nearly 50 years of constant evolution, Sun Yat-sen University Cancer Center grew to become one of the largest integrated centers in China for cancer care, education, research and prevention. Based on its comprehensive strengths, Sun Yat-sen University Cancer Center plays a critical role across China, especially in the Guangdong province, in the latest advances for tumor prevention and treatment.

SYSUCC was awarded many prestigious titles, such as, national key disciplines (Oncology), State Key Laboratory (SKL) of Oncology in South China, National Key Laboratory (Ministry of Education), Provincial Key Laboratory (Guangdong Province), Biotherapy Center in South China, and National Center for Clinical Trials of Anti-cancer Drugs, Doctoral Degree Granting Institution, Post-doctoral Research Station, and Guangdong Anti-cancer Association Partnering Institution.

The Chinese Journal of Cancer (CJC) was named the authoritative journal of clinical medicine in 2011. In 2012, the number of new scientific projects and their associated amount of financial support increased significantly with a governmental provisional budget for scientific research exceeding 100 Million RMB for the first time. 2012 was also a record year for the number of scientific projects obtained from the National Natural Science Foundation of China, with in total 55 projects for an amount of about 35 Millions RMB in funding. Accordingly, the number of SCI publications reached 253 for a total cumulated impact factor of 892.

Sun Yat-sen University Cancer Center is very active in its international exchanges and has developed numerous substantial collaborations with leading overseas medical institutions over the years. M.D. Anderson Cancer Center (USA) and Karolinska Institute (Sweden) both are our long-term partners, with a long history of academic exchange, focusing on joint-research programs.

Being a major actor in cancer care in China, SYSUCC is also recognized on an international scale and has many opportunities to interact with international partners. Actively promoting international exchanges and cooperation have enabled SYSUCC to become one of important Bases and windows in China in the areas of tumor pathogenesis and targeted therapy for international cooperation and Academic Exchanges.

Sun Yat-sen University Cancer Center is highly selective in its recruitment and currently employs about 2,200 staffs, including 315 senior staffs, 2 academicians, 61 PhD supervisors, 92 Master supervisors. Recently 6 professors have been enrolled from the "thousand talents" program" (a national initiative to recruit leading experts in their field).

Senior scientist's positions for overseas experts are now available in Sun Yat-sen University Cancer Center for the following fields: bioinformatics, cancer immunology, molecular medicine, animal models, gene therapy, translational medicine, diagnostic technology and medical physics.

To apply, please contact:

Mr. Zhong and Mrs. Wen
Phone: 86-20-87343810/3129
Email: zhongjunx@sysucc.org.cn
Website: **www.sysucc.org.cn**

"I feel really lucky to have gotten this opportunity, and I highly recommend that everyone moves out of their comfort zone at least once in their life."

—Melody Toosky

president of Cornell University who launched Peking University's Transnational Law School and now serves as vice chancellor and chief executive officer of New York University Shanghai.

Wang, who researches issues surrounding the global migration of talent, notes that many of the academics he talks to are acutely aware that opportunities in the West are saturated, while China is pouring resources into narrowing the gap on the science and technology front.

And China has become a more attractive place for foreigners to live, compared with just 10 years ago. "In the old days, foreigners would feel isolated and be the only person traveling with an interpreter," says Wang. "Now much of China is cosmopolitan and universities are more open; it's much more convenient to live here."

Not surprisingly, China draws more scientists from other Asian countries than anywhere else, with Europe and the United States coming in second and third, respectively. As for the foreign student population, South Korea supplies the highest number of scholars, followed by the United States and Japan, according to the China Association for International Education.

Meanwhile, the number of Chinese living overseas is increasing; however, more and more are now coming back. In 2009, the number of Chinese overseas students who came back to China exceeded the 100,000 mark and has continued to increase each year at increments ranging from 20 to 40 percent annually, according to the State Administration of Foreign Experts Affairs.

CURRENT CHALLENGES

Certainly, China still has challenges to overcome while advancing toward being a world-class scientific research hub. **Fei Li ,** who earned his Bachelor's from Peking University and his Ph.D. from the University of Washington, says the Chinese respect products that have a scientific basis, which makes working as a nutrition scientist in the country much more rewarding. He was drawn to the opportunity to help participate in developing China's science and technology sector at its early stages, and has found plenty of opportunities in different research areas.

Yet he has observed that China is still working toward becoming a more hypothesis-driven scientific culture, moving away from a model that has historically been driven by studies of empirical observations. He also feels that the country's science is heavily focused toward applied and translational science rather than basic science. The funding is geared more toward results-oriented projects that "can rapidly contribute to GDP growth, [rather] than basic research that may have more fundamental effects in the long run," says Li, who is currently supporting an American nutrition company's R&D business in the Asia Pacific region, including China, from one of its offices in Singapore.

Further, while many institutes and universities in Beijing and Shanghai are world-class, the atmosphere and opportunities for international academic exchanges and collaboration can still be lacking at institutions in smaller cities, says CAS' Wang. It would help, Wang says, if funding programs provided more coherent and strategic support for institutes and universities in these cities. Scientists in smaller cities might also need to pay special attention to seeking out their own opportunities for advancement and exchange.

But scientists do feel China's academic environment is moving in a positive direction. Researchers in China are publishing more papers in elite journals year over year, and certainly, in a country where most of the top leaders are scientists and engineers, the focus on these important fields is sure to continue.

Melody Toosky has found her time in China "priceless." A Ph.D. in microbiology and immunology, she had offers to work at startup pharmaceutical companies and in academic laboratories in California. But she wanted to do research on infectious diseases and was drawn to a laboratory at Tsinghua University to research adaptive mistranslation of mycobacteria. So she accepted a contract to pursue her postdoctoral studies there, and says her time in China has allowed her to "break through the veil of my own ideologies, culture, and mentality and gain a deeper appreciation for the universal pursuit of scientific methodology."

Toosky works mostly with Chinese Ph.D. students, and describes the work the group is doing as "cutting edge." They are in the process of publishing results just 18 months after she arrived. "I feel really lucky to have gotten this opportunity, and I highly recommend that everyone moves out of their comfort zone at least once in their life," she says.

Peking University

CREDITS: (FROM TOP) PHOTO COURTESY OF MELODY TOOSKY; © ISTOCKPHOTO.COM/WINHORSE

Lenora Chu is a writer based in Shanghai, China.

DOI: 10.1126/science.opms.r1300138

東南大學
SOUTHEAST UNIVERSITY

Faculty Positions Available in Southeast University, China

Established in 1902, located in Nanjing, formerly known as Nanjing Institute of Technology in 1952, Southeast University is one of the top research-oriented universities in China, focusing on fundamental cutting edge research and high-level education, covering such diverse fields as science, engineering, technology, humanities, economics, management and law. SEU is one of the first universities funded by China's "211" and "985" programs. It has over 20 national or provincial research institutes, with a number of key research bases. **(www.seu.edu.cn)**

Requirements & Qualifications

Southeast University invites applications from outstanding scientists for tenure track positions, and positions of chair professors and visiting professors. The University also provides distinguished candidates with very strong continuing support to apply for programs such as "1000 Plan Professorship for Young Talent" and "Chang Jiang Scholars Program".

1000 Plan Professorship for Young Talent

Candidates should be under the age of 40; in engineering or natural sciences major; with Ph.D. or M.D./Ph.D. degree from a world-renowned university with at least 3 years of research experience, or with PhD degree from Mainland China with at least 5 years of research and teaching experience abroad. Applicants should have a position in a well-known university or other corresponding institutions overseas.

Chang Jiang Scholars Program(Distinguished Professors/Chair Professors)

Distinguished Professors:

Applicants should hold at least associate professor or other equivalent positions in well-known universities. Besides, applicants should be below 45 years old if in a field of natural sciences, and below 55 in a field of humanities and social sciences. Successful applicants should work full-time in the university. The employment contract is for 3 years.

Chair Professors:

Applicants should have a strong research background as well as teaching experience, and should currently hold professorship or other corresponding positions in well-known universities abroad. Successful applicants should work in the university for at least 2 months per year. The employment contract is for 3 years.

Salary, Benefits and Support

Successful applicant will be offered highly competitive salary and benefits, research space, extensive opportunities for collaboration both within the University and with neighboring institutions. The support includes sufficient laboratory space, startup funding, relocation fee and competitive salary commensurate with experience, and other employee benefits.

Contact Us

The application period is not limited.

Qualified applicants for "1000 Plan Professorship for Young Talent" and "Chang Jiang Scholars Program" are invited to send the job intention letter and CV to: ymsun@seu.edu.cn. Applicants for tenure track positions or visiting professors are invited to send the job intention letter and CV with "Faculty Application" as title to: rsk@seu.edu.cn. For further information, please search Human Resource Department, Southeast University, 2 Sipailou Rd, Nanjing, China, 210096 (http://rsc.seu.edu.cn/) or reach us at 86-25-83792621.

Equal Opportunity Employer for Minorities/Females/Persons with Disabilities/Veterans

Faculty Positions
Jiangsu University (Zhenjiang, Jiangsu, China)

Jiangsu University (UJS), with a history of 110 years, is a comprehensive university especially reputed for its strength in engineering. The research fields cover 10 primary academic categories including engineering, nature science, medicine, management, economics, law, literature, philosophy, pedagogy, and art. Currently, UJS holds in total 8 post-doctoral research stations, 9 primary academic categories with a variety of disciplines for doctoral degrees that offer 42 Ph.D. programs. In addition, UJS holds two national key academic disciplines and one additional discipline as a candidate under cultivation, as well as 3 province leading disciplines. We intend to recruit outstanding talents to join UJS.

Recruitment position contains: 1. discipline leader in Basic Medical Science, whose research field includes: medical biochemistry, molecular diagnosis, hematology, etiology, immunology etc; 2. discipline leader in Chemical Engineering, whose research field includes: environmental monitoring, nanophase materials, catalytic chemistry, green chemistry technology, advanced separation technology, new functional materials etc. The candidates of discipline leaders are expected to have long been engaged in the research in the above field, and have got good academic achievement and academic influence. UJS will supply generous benefits and key support to the discipline leaders. In addition, UJS invites applications and nominations for tenured and tenure-track faculty members in the following fields: Material Science and Engineering, Electrical Engineering, Information and Communication Engineering, Computer Science and Technology, Control Science and Engineering, Civil Engineering, Mechanics, Vehicle Engineering, Traffic and Transportation Engineering, Basic Medical Science, Clinic, Applied Economics, Mathematics, Biology, Optical Engineering, Chemical Engineering and Technology and Pharmacology.

The positions are available for Distinguished Professor, Leading Professor, Full Professor, Associate Professor, and Assistant Professor, which can also be the candidate for the talent programs such as Global Experts program, Changjiang Scholar Program, Distinguished Professor of Jiangsu Province, High-level Innovation Talents and Innovation Team Leader of Jiangsu Province. A successful candidate should hold a Ph.D. degree and an international recognized research record.

The University offers competitive salaries, fringe benefits including medical/dental insurance, retirement and housing subsidy. The positions are available now. Reviewing of application materials will begin on the 15th November 2013 and will be continue until positions are filled.

To know more about the related disciplines and positions, please visit:
http://ww.ujs.edu.cn/pub/xiaonei/rczp.
Contact: Phone: Mr. Cai +86-511-88789658 or Mr. Shao +86-511-88789659 .E-mail: hr@ujs.edu.cn.

Faculty Positions Available in Beihang University, China

Established in 1952, located in Haidian District, Beijing, Beihang University is one of the top research-oriented universities in China, focusing on fundamental cutting edge research and high-level education, covering such diverse fields as science, engineering, technology, humanities, economics, management and law. One of the first universities funded by China's "211" and "985" programs, it has seven national key laboratories and twenty-five provincial and ministerial key laboratories. At present, the university has a total area of two million square meters, and over 3800 faculty and staff.

Beihang University is on a clear path to become a world-class university in many engineering and science disciplines. As part of Beihang's further pursuit for excellence in research and education, we have expanded our global search for the best research talent to join our International Research Institute for Multidisciplinary Science (IRIMS). Five independent international research centers (IRC) were established recently under the name of IRIMS. As the core part of IRIMS, IRCs are devoted to establish a world-class, advanced and multidisciplinary research platform.

Beihang University invites applications for full-time Professors, Associate Professors and excellent scientists. Preference will be given to candidates whose research emphasis demonstrates the potential to complement and advance the IRIMS existing research strengths. Successful candidates will be provided competitive salaries and start-up funds.

Positions Available

- Position offered by the Recruitment Program of Global Experts (1000 Plan Professorship)
- Position offered by the Chang Jiang Scholars Program
- Position offered by the Recruitment Program of Global Young Experts (1000 Plan Professorship for Young Talents)
- Position offered by Beihang University's Zhuoyue Program of Professors
- Position offered by Beihang University's Zhuoyue Program of Associate Professors.

Interested individuals should send curriculum vitae by email to **rscrcb@buaa.edu.cn**, with "Faculty Application from *Science*" in the title. For more information, please visit the university's Human Resource Department website **http://rsc.buaa.edu.cn/**, or contact us by email **rscrcb@buaa.edu.cn** or by telephone **86-010-82317779**.

深圳大学

2013 Shenzhen University Oversea Recruitment

Shenzhen University (SZU) was founded as a public university in 1983 with the accreditation of the State Council of the People's Republic of China.
There are many famous scholars in SZU. Currently, there are 1,500 teachers on campus and about 60% of them have gotten Phd. Now, SZU has 2 Academicians of Chinese Academy of Sciences, 3 Academicians of Chinese Academy of Engineering, 2 members of "1000-Talents Scheme", 6 scholars who have won awards from the National Science Foundation for Distinguished Young Scholars, 4 scholars who have won awards from the "Chang Jiang Scholars Program", 3 members of New Century Millions of Talents Project at national level and 3 chief scientists in the National 973 Academic Program.

SZU, thirsty for talents, warmly welcomes numerous outstanding elites to join us as distinguished professors, associated professors or lecturers.

A. Distinguished professor
1) Eligibility: Candidates of the national "1000-Talents Scheme", "1000-Young-Talents Scheme", "Outstanding Youth", "Chang Jiang Scholars Program" and "100-Talents Scheme" of the CAS, professors or associated professors from overseas famous universities and outstanding scholars having fundamental academic influence.
2) Remuneration: It is yearly payroll for a distinguished professor, about RMB500,000-1,200,000. SZU will provide support in scientific research expenses and laboratory construction fee for a distinguished professor as well as in constructing his academic research team. Especially, Shenzhen local government will give scientific research expenses of RMB2,000,000 – 5,000,000 to a candidate who study such subjects as science, engineering and medicine and are eligible for the Peacock Program or Shenzhen High-Level Talent Program.

B. Professor, associated professor, lecturer and Liyuan Scholar Plan
(1) Professor, associated professor and lecturer
SZU warmly welcome oversea scholars who have achieved a Phd degree or have experiences of post-doctoral research and are competent for our positions of professor, associated professor and lecturer. Excellent candidates will be engaged as professors or associated professors directly by SZU according to their academic achievements.

Remuneration: the minimum annual salary is RMB310,000 for a professor, RMB250,000 for an associated professor and RMB180,000 for a lecturer.
Any professor, associated professor and lecturer could apply for Liyuan Scholar Plan, Peacock Program or Shenzhen High-Level Talents Program. If any person achieved any of the above plans, he could apply to Shenzhen Government for different subsidies by relevant plan.

(2) Liyuan Scholar Plan
Any teacher could apply for this plan. There are three levels for this plan, such as "Liyuan Leading Scholar", "Liyuan Outstanding Scholar" and "Liyuan Excellent Youth" respectively.
1) Three-level scholars: Liyuan leading scholar will be awarded to full-time teachers as a top-leader in his academic area. Liyuan outstanding scholar will be awarded to full-time teachers, aged under 45 and having 3 years' working experiences. Liyuan excellent youth will be awarded to young scholars aged under 35 who had gotten Phd and had one year's academic research experience in relevant research institutions.
2) Award standards: SZU will provide a living allowance for Liyuan leading scholars in 5 years, including two levels, RMB500,000 per year At the first level and RMB150,000 per year at the second. SZU will give a living allowance to Liyuan outstanding scholars in 3 years, RMB100,000 per year. SZU will give a living allowance to Liyuan excellent youth in 9 years at the most, RMB100,000 per year.

C. Shenzhen Oversea High Level Talents Policy
1) Candidates: oversea experts or oversea scholars. There are three levels for this plan, Level A , B and C respectively
2) Remuneration: candidates will receive an award of RMB500,000-1,500,000. Candidates whose research program is in such subjects as science, engineering and medicine respectively could enjoy scientific research expenses from RMB200,000 to 5,000,000. Talents at Level A could apply for scientific research expenses of more than RMB5,000,000.

Contact Us
For more information, please visit **http://www.szu.edu.cn**. If you're interested, please send your CV and relevant materials to any of the following email addresses:
Miss Liyun liyun@szu.edu.cn, 0086-755-26536111
Miss Gaoying gaoying@szu.edu.cn, 0086-755-26535295
Mr. Renqiang szursc@sina.cn , 0086-755-26535295

IDG/McGOVERN INSTITUTE
FOR BRAIN RESEARCH AT TSINGHUA

Faculty Positions

IDG/McGovern Institute
for Brain Research at Tsinghua University

Who we are?

The IDG/McGovern Institute for Brain Research at Tsinghua University (IMIBR-THU) is seeking for neuroscience researchers to fill full time faculty positions at the assistant or associate professor level. This institute was founded in April, 2011, based on generous support from the McGoverns with International Data Group (IDG). It is accomodated in an affiliated building of School of Medicine, right on campus of Tsinghua, which stands as the leading university of China. With focus on neuroscience, especially on cell, molecular, system and computational neuroscience, IMIBR-THU aims to build, within next five to ten years, a top brain research center marked as a genetically based and new-tech development-driven research program. Scores of outstanding scientists, among whom several enjoy international reputation, are making an increasingly dynamic neuroscience community in IMIBR-THU.

What you will be greeted with?

In this emerging area of neuroscience, researches on brain have drawn great attention universally. The Chinese government demonstrates growing enthusiasm for support of these researches as well. In such context, IMIBR-THU has suggested starting from interdisciplinary studies to inspire innovative ideas. Its research goals are described as: 1. To reconstruct the biochemical processes of memory formation; 2. To gain insights into organization of memory at neural circuits and system levels; 3. To gain insights into molecular basis of pathogenesis for human cognitive disorders. It is believed an era boasting great opportunities will be ushered in the near future. Working at IMIBR-THU, a principal investigator will be supported jointly by the IDG fund and Tsinghua University.

What is expected from you?

A successful candidate will have an earned Ph. D degree in neuroscience and be capable of leading an independent research team. Preference will be given to those with distinguished records of research productivity, and professional involvement with well-recognized societies in this domain. It is highly desirable if the candidate can complement IMIBR-THU's current faculty. Applicants should submit materials including a cover letter, a CV, at least three recommendation letters, and a brief description of future research plan to:
Dr. Yi Zhong, Director
E-mail: mcgovern@biomed.tsinghua.edu.cn.
Qualified applicants will be invited to have on-site interviews at Tsinghua. Further information about IMIBR-THU could be obtained from http://mcgovern.med.tsinghua.edu.cn/.

Inspite of impressive scientific progress mankind has achieved up to now, brain disorders remain formidable challenge for healthcare and are afflicting numerous worldwide. We are hopeful that outstanding and promising scientists as you are would join our efforts to seek breakthroughs in brain researches and contribute to the improvement of human life.

Faculty and Post-doctoral Positions at Collaborative Innovation Center for Genetics and Development, China

Ministry of Education of China has launched the new "2011 Collaborative Innovation Centers (CIC)" initiative. Among these is Collaborative Innovation Center for Genetics and Development (CICGD, http://cicgd.fudan.edu.cn) established jointly in September 2012 by Fudan University, Shanghai Jiao Tong University, Nanjing University, Shanghai Institutes for Biological Sciences and Institute of Genetics and Developmental Biology, Chinese Academy of Sciences, Yunnan University and Xizang University, as well as partnering with Yale University, Baylor Medical School, and Penn State University.

The CICGD focuses on the understanding of genetic mutations and homologous recombination and their impact on human health and development, and conducts collaborative research on: (1) the molecular mechanism of gene mutation and evolution, (2) the molecular basis of homologous recombination, (3) the genetic basis of major human diseases, (4) the regulation of animal and plant development. The CICGD aims to create a collaboration and innovation platform both diverse and integrated, both dynamic and sustained, to provide an excellent environment for original and creative collaboration by leading scientists, who in turn will build a world-class institute at the frontier of genetic studies. To achieve these goals, the CICGD is now recruiting full-time faculty members who will lead research teams, as well as visiting scholars, post-doctoral fellows and doctoral students. The requirements are as follows:

1, Principal investigators (PIs) and visiting scholars

Applicants for full-time positions should have research experience in life science areas including: genetics, biochemistry, structural biology, cell biology, physiology, developmental biology, bioinformatics and genomics, and synthetic biology, and have completed two or more years of postdoctoral training with substantial academic achievements. Researchers with independent experience as group leaders or laboratory directors are welcome. The rank and compensation levels will depend on experience and scholarship, and comparable to international standards, with generous start-up support. Faculty members will also teach and contribute to other student training activities. For more detailed information regarding positions, responsibilities and research directions, please contact the administration office of the CICGD.

Part-time Visiting Scholars are also appointed at one of three ranks, according to experience and accomplishments. The CICGD provides internationally competitive package for the visiting scholars, including living cost allowance. Applicants also need to identify a CICGD PI as a collaborator. Please contact the administration office of the CICGD for further details.

2, Post-doctoral fellows

Researchers who have recently obtained a Ph.D. degree in one of the areas stated above are welcome to submit a CV and a cover letter for a post-doctoral position. The applicants should have published high quality articles in life science journals; the successful applicant will be supported according to international standards and carry out collaborative research projects under the supervision of at least two PIs.

3, Ph.D. students

Students strongly interested in genetics and development and having obtained a bachelor's or master's degree in a well-known research and educational institution are welcome to apply for doctoral training under the supervision of at least two PIs. The CICGD provides an excellent collaborative environment and academic training for doctoral students, and has high expectation of the students, who will be supported by a generous and competitive stipend.

The CICGD warmly welcomes scientists and students throughout the world to apply. Applicants should send resume and inquire to the following address, and labeled with "Application for CICGD PI (or post-doctoral fellows, or doctoral students)."

Contact information:

Ms. Xiaohua Liang
Administration office,
Collaborative Innovation Center for Genetics and Development,
Tel: 86-21-65642800
E-mail: genetics2011@fudan.edu.cn

Address:

School of Life Sciences,
Fudan University,
Room 220, Liren Biology Building,
220 Handan Road, Yangpu District (Postal Code: 200433),
Shanghai, the People's Republic of China

Faculty Positions in School of Life Sciences Tianjin University

Tianjin University, established in 1895 named Peiyang University, is the first university in China. Tianjin University is among the first 16 prestigious National Universities designated by the government in 1959, and is also among the first group of universities in "211" and "985" Projects, which are invested by the nation for developing world class universities.

School of Life Sciences, Tianjin University, sets an ambitious goal to rank top among international peers. With this international faculty recruitment, we invite talents from the world to build a competitive team. We expect scientists with excellence in modern biology and medicine for research and teaching. Appointments will be made at the Instructor, Associate or Full Professor level. Tianjin University offers excellent resources to support new faculties, including competitive salary, start-up packages, and state-of-the-art research facility. Some outstanding candidates would be considered to join Peiyang Scholar Plan of Tianjin University with an annual salary ranging from 400 to 600 thousand RMB before tax.

Areas of special interest include human health, immunology, structural biology, microbiology, oncology, and biomedicine. Applicants must have a strong record of research accomplishments, as documented by publications in leading peer-reviewed journals. A commitment to excellence in teaching is essential. Candidates should have a PhD, MD or MD/PhD with two or more years of postdoctoral training.

Applicants should submit a cover letter, curriculum vitae, statement of research and teaching interests, and three letters of reference to Ms. Bu Fanxu at **bufanxu@tju.edu.cn**. Positions are available immediately and applications will be considered until positions are all filled.

For further information, please visit **http://www.tju.edu.cn/** or contact us at **bufanxu@tju.edu.cn** or telephone: **+86-22-27403902**.

School of Life Sciences, Tianjin University
No.92 Weijin Road, Nankai District, Tianjin, P.R.China, 300072

Faculty Positions in the School of Pharmacy

The School of Pharmacy at Shanghai Jiao Tong University invites applications for full-time faculty positions at all academic ranks. Major research interests include, but are not limited to, drug metabolism and pharmacokinetics, drug target identification, high throughput screening, biotech drug delivery, pharmacogenomics, metabolomics, TCM and natural compounds, cell engineering and antibody drugs, and pharmaceutical analysis. Candidates with experience in pharmaceutical administration and clinical pharmacy are also welcome to apply.

Qualified candidates must have an earned Ph.D. degree or equivalent in life sciences, postdoctoral training experience and work experience in related research areas. Applicants for Distinguished Professors should have an established research program with funding history, independent research and teaching experience in a major research institution, and an excellent publication record. Qualified applicants are also welcome to apply for Special Research Scientists positions and other entry-level faculty positions.

Established in 1896, Shanghai Jiao Tong University (SJTU) is one of the major research universities in China. The School of Pharmacy was established in 2000 and has been fully accredited to offer bachelor, master and doctoral degrees in pharmaceutical sciences. For more information about the School, visit **http://pharm.sjtu.edu.cn**

Applicants should email their curriculum vitae and a brief description of their research interests to the Search Committee at **qianxp@sjtu.edu.cn.** Applicants should provide contact information for three individuals who can write letters of recommendation. Applications will be reviewed on a rolling basis until the positions at the respective ranks are filled.

Early Independent Scientists in the NIH Intramural Research Program

The National Institutes of Health, the nation's premier agency for biomedical and behavioral research, is recruiting for Early Independent Scientists in the NIH Intramural Research Program (IRP). We are looking for new Ph.D., M.D., D.D.S., or equivalent doctoral researchers who have the creativity, intellect, and maturity to flourish in an independent research position.

The IRP is home to more than 1,000 tenured and tenure-track investigators and 5,000 trainees. We provide an environment that encourages and supports innovative, high-impact research. To enhance the development and early-stage careers of exceptional investigators, the IRP is participating in the NIH Common Fund's "NIH Director's Early Independence Award" program, http://commonfund.nih.gov/earlyindependence. The NIH has developed this program to support recent doctoral graduates in independent positions without the need to perform a postdoctoral career fellowship.

Thus, the graduate can immediately start an independent career after graduation. Successful Early Independence Award candidates will be provided the resources to establish an independent research program, including salary and benefits, support for lab personnel, lab space, supplies, and start-up equipment. At the time of application, candidates must be within 12 months of completing their Ph.D., M.D., or D.D.S. degree; or for clinician-scientists, within twelve months of completing their core clinical residency program.

Complete applications must be received by December 13, 2013. Candidates should submit electronically a cover letter, curriculum vitae, and a 2- to 3-page statement of research interests and future plans, and arrange to have 3 letters of reference sent to: Charles Dearolf, Ph.D.; Assistant Director for Intramural Research; National Institutes of Health; dearolfc@od.nih.gov. The NIH will notify selected candidates shortly thereafter, and work with the candidates to submit an application to the NIH Common Fund program by January 31, 2014.

Candidates must meet eligibility requirements of the Common Fund program, as described http://grants.nih.gov/grants/guide/rfa-files/RFA-RM-13-009.html.

The NIH recognizes a unique and compelling need to promote diversity in the biomedical, behavioral, clinical, and social sciences research workforce. The NIH expects its efforts to diversify the workforce to lead to the recruitment of the most talented researchers from all groups. We encourage applications from talented researchers from diverse backgrounds underrepresented in biomedical research, including underrepresented racial and ethnic groups, persons with disabilities, and women for participation in all NIH-funded research opportunities.

Boston, MA

Northeastern

Asst/Assoc/Full Professor Resilient and Sustainable Energy Systems

Requisition Number: FTFR000417

Division/College: College of Engineering

FT/PT: Full Time

POSITION SUMMARY:
The Department of Electrical and Computer Engineering at Northeastern University invites applications for open positions at all levels, with a preference toward senior levels. We seek exceptional candidates addressing problems in resilient and sustainable energy systems, with expertise broadly in one or more of the following areas:

- Utility power systems
- Power electronics and machine drives
- Renewable energy and sustainable systems
- Networks and cyber-physical systems
- Large scale system monitoring and control

The successful senior candidate should be an established researcher with a sustained record of funding, peer reviewed publications, and strong technical leadership. Outstanding candidates at the assistant professor level will also be considered. Successful candidates will be expected to develop strong independent research programs and to excel in teaching in both our undergraduate and graduate programs.

QUALIFICATIONS:
A Ph.D. in Electrical and Computer Engineering or a closely related field by the start date is required.

ADDITIONAL INFORMATION:
Northeastern's ECE department has 47 faculty with established areas of excellence in sensing and imaging (with an NSF ERC), communications and digital signal processing, power and control systems, power electronics, RF/microwave magnetic materials and device technologies. The Department is a member of the NSF Engineering Research Center for Ultra-wide-area Resilient Electric Energy Transmission Networks.

Northeastern University is ideally located in the heart of Boston and is in close proximity to a number of major academic institutions and innovative technology companies and installations. Northeastern's departments and research centers maintain strong collaborative interactions with many of these institutions, and the University is also home to a number of NSF-, DHS-, NIST- and NIH-supported core research centers. At the core of the Northeastern engineering education experience is our top ranked cooperative education program.

Applications should include a complete curriculum vitae, a statement of current and future research interests, a statement of teaching interests, and contact information for at least four references. For more information, contact Professor Ali Abur (abur@ece.neu.edu). Review of applications will begin immediately and will proceed until the position is filled.

To be considered for this position please visit our web site and apply on line at the following link: **http://apptrkr.com/407474**

Northeastern University is an Equal Opportunity, Affirmative Action Educational Institution and Employer, Title IX University. Northeastern University particularly welcomes applications from minorities, women and persons with disabilities. Northeastern University is an E-Verify Employer.

Royal Society Research Professorship

The Royal Society's most prestigious funding scheme is now open for applications. The Royal Society Research Professorships provide long term support to world-class scientists, releasing them from teaching and administration to enable them to focus on research.

The scheme provides a substantial contribution to salary, which can be supplemented at the discretion of the host organisation; a one-off start-up grant of up to £35,000; and research expenses of up to £16,000 per academic year. Funding is available for five years, with the opportunity for renewal for a further five years.

These posts enable individuals of proven ability and achievement to undertake independent, original research at a UK institution. Former Research Professors include Presidents of the Royal Society and Nobel Laureates.

Several Royal Society Research Professorships are available. The number of awards made will be determined by the quality of applications received. The Professorships may be awarded in any field across the natural sciences but the following are restricted to specific areas:

- The Royal Society Wolfson Research Professorship in Physics or Chemistry at the interface with Biology
- The Royal Society GSK Research Professorship in Molecular aspects of Medicine
- The Royal Society Napier Research Professorship to ascertain the cause of cancer, including any corresponding allied disease and the means of prevention, cure and alleviation

Scientists of any nationality can apply and applications are particularly welcomed from scientists currently resident outside the UK.

Closing date: 13 March 2014

Host universities are encouraged to use the long lead time to identify and attract the best candidates. Fast-track applications will be considered during this period for truly exceptional overseas candidates.

To find out more visit
royalsociety.org/grants/schemes
or email **seniorfellowships@royalsociety.org**

THE ROYAL SOCIETY

Registered Charity No 207043

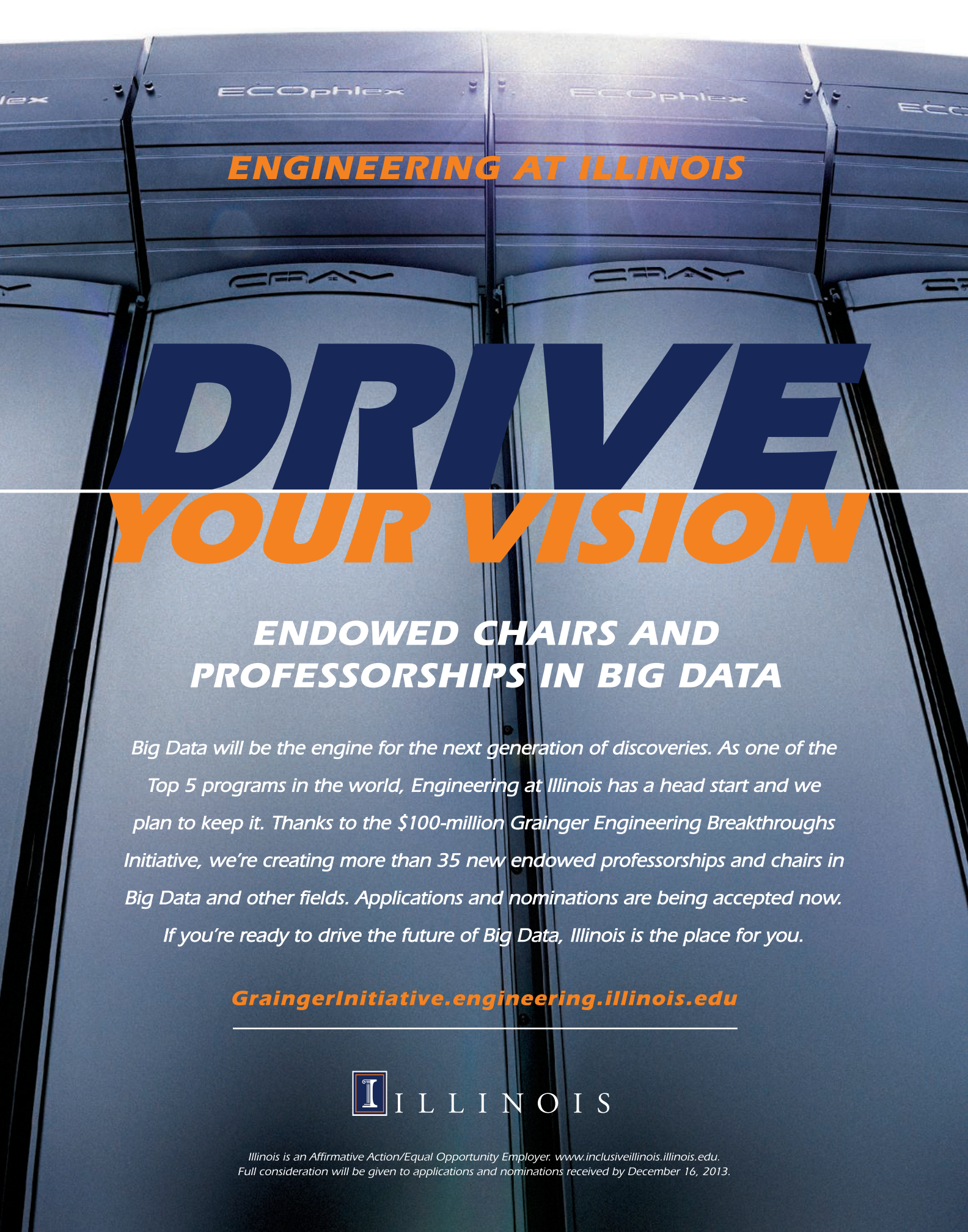

ENGINEERING AT ILLINOIS

DRIVE YOUR VISION

ENDOWED CHAIRS AND PROFESSORSHIPS IN BIG DATA

Big Data will be the engine for the next generation of discoveries. As one of the Top 5 programs in the world, Engineering at Illinois has a head start and we plan to keep it. Thanks to the $100-million Grainger Engineering Breakthroughs Initiative, we're creating more than 35 new endowed professorships and chairs in Big Data and other fields. Applications and nominations are being accepted now. If you're ready to drive the future of Big Data, Illinois is the place for you.

GraingerInitiative.engineering.illinois.edu

ILLINOIS

Illinois is an Affirmative Action/Equal Opportunity Employer. www.inclusiveillinois.illinois.edu.
Full consideration will be given to applications and nominations received by December 16, 2013.

Gastrointestinal Microbiologist Assistant or Associate Professor

The University of Nebraska–Lincoln is seeking applicants for a 9-month, tenure-leading faculty position in the Department of Food Science and Technology at the rank of Assistant or Associate Professor. The successful candidate will develop and lead an internationally recognized research program focused on understanding the impact of the gut microbiota on human health and disease by utilizing genome-based and molecular approaches to study interactions of microbial GI communities with the epithelium, pathogens, probiotics, prebiotics, or bioactive food components.

We anticipate the candidate will contribute to existing graduate and undergraduate microbiology courses and develop/teach (in part or in whole) a new graduate/undergraduate course in gastrointestinal biology, microbiology, or ecology. Collaborations with other scientists and faculty are expected. The department is located in a modern, well-equipped facility that houses resources for anaerobic microbiology, genomics, and immunology research. The new, state-of-the-art UNL Gnotobiotic Mouse Facility offers opportunities for innovative research employing conventional and germ free animal models. The incumbent will be joining a well-established interdisciplinary team of researchers focused on understanding the relationships among the gut ecosystem, host genetics, dietary interventions, and host health. Information about the gut health program can be found at **www.gfi.unl.edu**. Requires a Ph.D. in Microbiology, Immunology or a closely related field and relevant postdoctoral experience. Must have demonstrated potential to conduct independent research.

Lincoln, Nebraska, a community of nearly 300,000, offers the ambiance of a friendly small town while offering attractions and entertainment opportunities of a metropolitan area. Lincoln has a thriving entertainment district with many fine restaurants and shops, galleries and other artistic treasures, a well-known live music scene, and numerous parks, golf courses, and bike trails. The capital city of Nebraska, Lincoln is home to state government and the flagship campus of the University of Nebraska system. Lincoln has a stable economy, affordable housing, and in 2013, was ranked by *Forbes Magazine* as the 4th best city in the U.S. for business and careers.

For full position details and to apply, visit **http://employment.unl.edu**, requisition number **F_130219**. Complete the application form and attach as three separate documents a curriculum vitae, a two-page description of a proposed research program, and a brief statement of teaching philosophy. Applicants should also arrange to have three letters of reference sent directly to: **Dr. Robert Hutkins, University of Nebraska-Lincoln, 143 Filley Hall, Lincoln, NE 68583-0919**. Application review will begin on **January 15, 2014** and will continue until the position is filled.

The University of Nebraska has an active National Science Foundation ADVANCE gender equity program, and is committed to a pluralistic campus community through Affirmative Action, Equal Opportunity, work-life balance, and dual careers.

Two Assistant Professor positions, Biological Sciences/Medical Education

The University of Idaho seeks to expand our expertise in host-microbe interactions by hiring two Assistant Professors in the Department of Biological Sciences that have expertise in infectious diseases or immunology. These two talented researchers will join a vibrant research community and contribute to teaching in the WWAMI regional medical education program, a partnership between the University of Washington School of Medicine (UWSOM) and the states of Washington, Wyoming, Alaska, Montana and Idaho. The University has a strong commitment to interdisciplinary studies, and has invested in high-level genomics, computing, imaging, and mass spectrometry facilities to support research in these areas.

Each successful candidate will establish an extramurally funded research program, teach one course in the department of Biological Sciences, and share responsibility for classroom instruction of first year medical students.

One of the positions will involve WWAMI Medical Education Program teaching in the Pathogenic Microbiology course; the other position will involve teaching in the Immunology course. Review of applications begins 12/01/13.

For a full description and application materials, visit **http://apptrkr.com/404267**

Assistant/Associate Professor Chemical Biology • Medicinal Chemistry Drug Delivery • Pharmacology

The University of Southern California (USC) Department of Pharmacology & Pharmaceutical Sciences (www.usc.edu/schools/pharmacy/departments) invites applications for an Assistant/Associate Professor position, tenure-track or tenured, with research interests in chemical biology, medicinal chemistry, pharmacology, drug delivery and/or drug discovery. Of particular interest are candidates with research interests at the chemistry/biology interface and with the capability of working in a multidisciplinary department with chemists and biologists. Candidates should have a doctoral degree and postdoctoral experience in chemistry, pharmaceutical sciences, pharmacology, biochemistry, or a related discipline. The successful candidate is expected to develop an internationally recognized and externally-funded research program. Special attention will be given to candidates with research programs complementing and expanding existing departmental strengths in chemical biology, drug design and discovery, drug delivery, molecular signaling, neuroscience, and imaging, leading to therapeutic translational opportunities in drug discovery/development. Successful candidates are also expected to participate in teaching at the graduate and professional levels.

USC offers cutting-edge opportunities for multidisciplinary, interdisciplinary, and translational research collaborations, including an NIH-sponsored Clinical and Translational Science Institute, an NCI-designated Comprehensive Cancer Center, an NIH-sponsored Liver and GI Diseases Center, the Broad Center for Regenerative Medicine and Stem Cell Research, the Diabetes & Obesity Research Institute, and the Zilkha Neurogenetics Institute. The USC Provost's Initiative provides core infrastructure support in several areas including Biomedical Imaging Sciences, Biomedical Nanoscience, and Neurosciences. USC also offers access to one of the widest varieties of affiliated private and public hospitals in the United States (**http://www.lacusc.org/**).

For consideration, please apply online at **Jobs@USC**, Requisition **ID#021864** (**https://jobs.usc.edu/applicants/Central?quickFind=72733**). Applications should include a cover letter, curriculum vitae, the names of three references, and a summary of research accomplishments, future research, and educational goals. Review of applications begins immediately and will continue until the position is filled. Applicants may send inquiries to: **Julio Camarero, PhD, Associate Professor, Chair, Pharmacology and Pharmaceutical Sciences Search Committee, University of Southern California School of Pharmacy, 1985 Zonal Avenue, Los Angeles CA 90089-9121; Email: jcamarer@usc.edu**.

The University of Southern California values diversity and is committed to equal opportunity in employment. Women and men, and members of all racial and ethnic groups, are encouraged to apply.

AAAS is here – helping scientists achieve career sucess.

Every month, over 400,000 students and scientists visit ScienceCareers.org in search of the information, advice, and opportunities they need to take the next step in their careers.

A complete career resource, free to the public, *Science* Careers offers hundreds of career development articles, webinars and downloadable booklets filled with practical advice, a community forum providing answers to career questions, and thousands of job listings in academia, government, and industry. As a AAAS member, your dues help AAAS make this service available to the scientific community. If you're not a member, join us. Together we can make a difference.

To learn more, visit
aaas.org/plusyou/sciencecareers

AAAS + U = Δ

wellcome trust sanger institute

Faculty Positions

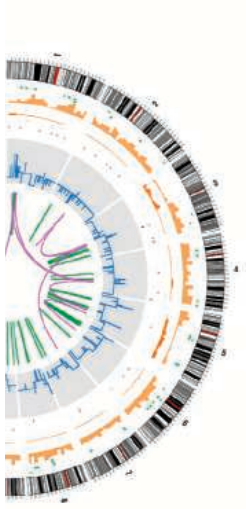

The Wellcome Trust Sanger Institute (http://www.sanger.ac.uk/) is seeking talented scientists to join its Faculty to contribute to and develop its scientific portfolio.

The Institute is an internationally renowned genomic research centre, based south of Cambridge. Our mission is to use genome sequences to advance understanding of the biology of humans and pathogens in order to improve human health. By using high-throughput approaches and state-of-the-art platforms in sequencing, model organisms and cell genetics, we free our researchers to concentrate on biological questions in a way that is only possible in a few institutions around the world. As a result, we have built an exceptional record in publishing leading research, delivering first-class resources and training the next generation. We also play an important role in many national and international consortia. The result is a unique, vibrant and interactive research environment with synergies and cross-fertilisation of ideas across and between programmes.

The Institute is co-located on the 100-acre Genome Campus with the European Bioinformatics Institute (EMBL-EBI), the Wellcome Trust Conference Centre and its associated advanced courses and conferences programme. We share a broader vision to develop the Campus as a hub of science, business, advanced scientific training and cultural activities in the area of genetics and genomics.

We are seeking outstanding scientists at different career stages – from first independent position to senior PIs—with interests across our scientific portfolio:

- **Human Genetics**
- **Cancer Genetics & Genomics**
- **Pathogen Variation — in particular Parasites and Host and Virus Genetics of Infection**
- **Malaria — Population genomics and high-throughput experimental genetics**
- **Mouse & Zebrafish Genetics**
- **Computational Genomics**
- **Cellular Genetics**

Positions carry a significant core package of salaries and support backed by competitive employment terms including excellent benefits and relocation support.

Applications from women, who are under-represented in our Faculty, are particularly encouraged, although we welcome approaches from any scientists with relevant research interests. We seek to provide a supportive family-friendly environment to enable scientists at all levels to balance their professional and home lives. This includes options for flexible and part-time working, an on-site nursery and childcare voucher scheme.

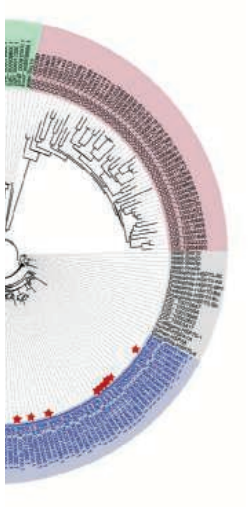

Further information on all aspects of being a Faculty member at the Sanger Institute can be found at http://q.sanger.ac.uk/newfac13. General enquiries should be directed to facultysearch@sanger.ac.uk. For informal discussion, contact Helen Atkinson in the first instance (ha4@sanger.ac.uk, (+44) 01223 496979).

Please apply through http://q.sanger.ac.uk/newfac13. You will need also to provide:

- a Curriculum vitae, complete list of publications and details of three referees
- a two-page description summarising scientific achievements to date
- a three-page outline of future research plans indicating how these fit with, contribute to and make use of Sanger Institute programmes and infrastructure.

Closing date for applications: 15th December 2013

California State Polytechnic University, Pomona, Biological Sciences Department

TENURE-TRACK FACULTY POSITION MICROBIOLOGIST

The Biological Sciences Department at California State Polytechnic University, Pomona (Cal Poly Pomona) invites applications for a tenure-track, ASSISTANT PROFESSOR, position in Microbiology, beginning September 2014. The area of specialty is open, but candidates who study environmental microbiology are encouraged to apply. A Ph.D. in microbiology or a related field is required. Post-doctoral experience and previous teaching experience are preferred. The successful candidate will have the potential for excellence in undergraduate teaching, and for developing an externally-funded research program that will involve undergraduate and Master's students. Teaching responsibilities will include microbial ecology, general microbiology, microbial physiology and specialty courses in the candidate's area of expertise, and may involve participation in introductory biology and other courses in microbiology. Cal Poly Pomona is a comprehensive Master's university with a diverse student body. The successful candidate will have demonstrated an ability to be responsive to the educational equity goals of the university and its increasing ethnic diversity and international character.

Applicants should forward: (1) a cover letter that briefly describes the candidate's training, experience, and teaching and research interests; (2) *curriculum vitae*; (3) statement of teaching philosophy; (4) proposed plan of research; (5) representative publication reprints; and (6) the names and contact information of three (minimum) to five (preferred) references to: **Chair, Microbiologist Search Committee, Biological Sciences Department, California State Polytechnic University, 3801 West Temple Avenue, Pomona, CA 91768**. Electronic submission of application materials as a single PDF file is preferred (**microbiol_search@csupomona.edu**). Review of applications begins on **January 6, 2014**. Official transcripts and three letters of reference will be required of all finalists. For further information, visit the Department web site at: **http://www.csupomona.edu/~biology**.

California State Polytechnic University, Pomona is an Equal Opportunity, Affirmative Action Employer.

XJTU–HKUST
Joint School of Sustainable Development
under planning

西安交通大學 XI'AN JIAOTONG UNIVERSITY

香港科技大學 THE HONG KONG UNIVERSITY OF SCIENCE AND TECHNOLOGY

Founding Dean

With a vision to advance education and research in sustainable development, The Hong Kong University of Science and Technology (HKUST), in partnership with Xi'an Jiaotong University (XJTU), is establishing the XJTU-HKUST Joint School of Sustainable Development (JSSD). Located in Xi'an of PR China and in close collaboration with HKUST's core operation in Hong Kong, the School will focus on educating a new generation of graduates who are capable of contributing to sustainable development, and on undertaking interdisciplinary high-impact research in energy conservation, resource management and environmental protection. English will be the School's language of instruction and other official conduct.

HKUST is a world-class leading research university and has been ranked overall No. 1 university in Asia for the last two years by QS Asian University Rankings®. XJTU, established in 1896, is in the C9 League, which consists of the top nine prestigious universities in China. The JSSD will have three departments: Sustainable Energy; Sustainable Materials; and Sustainable Systems. Within the next five years, the School is expected to have up to 60 faculty members and an enrollment of more than 1,000 undergraduate and postgraduate students in the three departments.

We are searching for a leading scholar with the vision and capability to be the founding Dean of JSSD. The successful candidate will be a senior academic administrator of HKUST appointed with tenure for posting to the JSSD in Xi'an. The appointee will assume full responsibility for all substantive academic and administrative matters of JSSD, including strategic planning and implementation, organization development, budget planning and control, external publicity, and maintaining relations and linkages with alumni and all relevant parties including governments, institutions and industries. Candidates must meet the high academic and professional standards of the HKUST senior faculty and should possess relevant experience in university administration at the senior level. Proficiency in both English and Chinese is mandatory. Understanding and knowledge of the higher education sector in Hong Kong and the Mainland is essential.

Concurrent with a tenured professorial appointment, the appointment as Dean of JSSD will be for an initial term of five years which is renewable. Remuneration is highly competitive with generous benefits.

Applications/nominations together with a curriculum vitae, a vision statement of the development of the School, and the contacts of at least three referees should be sent to the Chairman of the Search Committee for Dean of JSSD, c/o Human Resources Office, The Hong Kong University of Science and Technology, Clear Water Bay, Hong Kong [email: jssddsrch@ust.hk]. Review of applications/nominations will begin in December 2013 and will continue until the position is filled. For further information about HKUST, XJTU and JSSD, please visit the following websites: HKUST - http://www.ust.hk; XJTU - http://www.xjtu.edu.cn/en/index.html; JSSD - http://www.jssd.ust.hk/en/home.htm

(Information provided by applicants will be used for recruitment and other employment-related purposes.)

Director

The Board of Trustees of the National Synchrotron Radiation Research Center (NSRRC) is seeking a Director to lead and develop the facilities, including Taiwan Light Source (TLS), Taiwan Photon Source (TPS) and Center's experimental facilities abroad, plus scientific programs. The candidate should be a scientific thought leader with extensive senior executive experience and ready to provide strategic vision and to secure the funding. The candidates should have outstanding scientific accomplishments with strong written and verbal communication skills in both English and Chinese. For details of the opening, please visit NSRRC website, **http://www.nsrrc.org.tw/english/index.aspx** and select the recruitment Ad.

TPS is a 3rd generation 3-GeV light source, scheduled to be commissioned in 2014. NSRRC is a government funded national research laboratory with its first accelerator TLS made available to researchers since 1993. The facilities serve over 2000 users annually.

The required documents can be forwarded via e-mail to **Ms. Grace Lin, grace@nsrrc.org.tw** or by registered mail to **Director Search Committee, NSRRC, 101 Hsin-Ann Rd., Hsinchu Science Park, Hsinchu 30076, Taiwan**, post dated before **Dec. 31, 2013**.

UNIVERSITY OF CAMBRIDGE

www.jobs.cam.ac.uk

Tenure-Track Faculty Position - University Lecturer

Department of Physiology, Development and Neuroscience

Salary: £37,382-£47,314

Applications are invited for a research-oriented, tenure-track University Lectureships. The post is available from 1 April 2014 or as soon as possible thereafter. We are searching for an outstanding scientist, with an excellent publication record, who does cutting edge and fundable work in a field which complements our broad, existing programme of research in the Department of Physiology, Development and Neuroscience (http://www.pdn.cam.ac.uk/research/). Applicants should also have an aptitude and enthusiasm for teaching and be willing to contribute effectively to our undergraduate programme (http://www.pdn.cam.ac.uk/teaching).

Appointment will be for a probationary period of five years with appointment to the retiring age thereafter, subject to satisfactory performance.

The pensionable salary scale starts at £37,382 to £47,314 per annum.

Further particulars are available from http://www.pdn.cam.ac.uk/jobs. Applications, including a curriculum vitae and a completed CHRIS/6 form (Parts 1 and 3 only, available at http://www.admin.cam.ac.uk/offices/hr/forms/chris6) should be sent to hodsec@pdn.cam.ac.uk

Informal enquiries may be made to Professor Bill Harris, Head of Department, email: wah20@cam.ac.uk or tel: 01223 766137/333772.

Please quote reference PM02005 on your application and in any correspondence about this vacancy.

Closing date: 3 January 2014

The University values diversity and is committed to equality of opportunity.

The University has a responsibility to ensure that all employees are eligible to live and work in the UK.

DEPARTMENT OF BIOLOGY
THE UNIVERSITY OF UTAH

Cellular Biology at the University of Utah

The Department of Biology at the University of Utah invites applications for a tenure-track faculty position at the assistant professor level in cellular biology. Applicants should be addressing fundamental questions in any aspect of eukaryotic cellular biology including, but not limited to, gene expression, signaling, trafficking, development, evolution or neurobiology, and in plants, animals, fungi or protists. In addition to developing a vigorous independent research program, the successful candidate will be expected to contribute enthusiastically to the Department's increasingly interdisciplinary teaching mission at the undergraduate and graduate levels. Please visit **http://www.biology.utah.edu/** for an overview of the Department and the University, which provides exceptional opportunities for collaboration in research, education and outreach across many departments in several colleges.

Review of applications will begin immediately and continue until the position is filled, but to ensure full consideration, applications should be complete by **January 15, 2014**. We are especially interested in hiring a candidate who will contribute to the diversity of our faculty. Applications for this position can be made at: **http://utah.peopleadmin.com/postings/28018**

The University of Utah is an Equal Opportunity/Affirmative Action employer and educator. Minorities, women, and persons with disabilities are strongly encouraged to apply. Veteran's preference. Reasonable accommodations provided. For additional information: http://www.regulations.utah.edu/humanResources/5-106.html. The University of Utah values candidates who have experience working in settings with students from diverse backgrounds, and who possess a strong commitment to improving access to higher education for historically underrepresented students.

CHEMISTRY FACULTY POSITION: Drug Discovery Department

Moffitt Cancer Center, an NCI-designated Comprehensive Cancer Center, is seeking applications from Assistant, Associate and Full Professor level individuals to participate in the Drug Discovery Department. Bioorganic, synthetic and/or medicinal chemists looking for strong biological collaborators and outstanding core facilities are encouraged to apply. Experience in the design of protein-protein interaction disruptors and/or targeting long non-coding RNA is highly desirable but not required.

Moffitt has extensive core laboratory facilities available such as: NMR and mass spectroscopy, synthetic and parallel chemistry, structural biology, molecular modeling, high throughput screening, proteomics and microarray.

Candidates for the rank of Assistant Professor/Member must have a Ph.D. in synthetic organic chemistry or related areas and at least two years postdoctoral experience. Candidates for the rank of Associate or Full Professor/Member must have a proven track record of independent federal funding and research and at least five years experience in rank. Moffitt is affiliated with the University of South Florida. Primary and secondary University appointments are available. Candidates from industry are also encouraged to apply and must demonstrate an exemplary track record in drug discovery.

Please send curriculum vitae, statement of research interests and the names and addresses of three or more references in electronic (PDF) format to Said Sebti, Professor and Chair, Drug Discovery Department, at **Said.Sebti@Moffitt.org**. In addition, please complete an application at http://www.moffitt.org/careers/employment-opportunities/job-search; enter requisition #11928 in the keyword search box. The selection committee will begin reviewing applications on Dec. 20, 2013, and continue until the position is filled.

12902 MAGNOLIA DRIVE, TAMPA, FL 33612 | 1-888-MOFFITT | MOFFITT.ORG

Moffitt Cancer Center provides a tobacco-free work environment. We are an equal opportunity, affirmative action employer and a drug-free workplace.

Massachusetts Institute of Technology

Come work with us!

Faculty Positions

Department of Earth, Atmospheric and Planetary Sciences

The MIT Department of Earth, Atmospheric and Planetary Sciences has been undergoing a major expansion of its activities in climate science. Positions have recently been filled in the areas of atmospheric chemistry, paleoclimate and ocean biogeochemical cycles. We seek applicants for further appointments in climate-related fields, especially as they pertain to observations, models and theory in atmospheric dynamics and physical oceanography. Preference will be given to junior appointments at the assistant professor level, but a more senior appointment can be considered for an individual with exceptional qualifications.

The successful candidates will have a strong record of accomplishment in their discipline, a strong commitment to teaching and student advising, and a keen interest in relating their work to complementary research in the Department and/or in the MIT/Woods Hole Joint Program in Oceanography. Joint appointments with other MIT departments can be negotiated as appropriate.

Applicants should submit a curriculum vitae, one-page descriptions of research and teaching plans, and the names, email addresses, and phone numbers of three professional referees. Please do not ask your referees to upload letters at the time of application; letters will be requested directly by MIT. Questions may be addressed to Prof. John Marshall, Search Committee Chair, at jmarsh@mit.edu. Applications are being accepted at Academic Jobs Online at https://academicjobsonline.org/ajo/jobs/3556. To receive consideration, a complete application must be received by May 31, 2014.

We especially encourage minorities and women to apply because of MIT's strong commitment to diversity in engineering education, research and practice.

MIT is an Equal Opportunity/ Affirmative Action employer.

http://web.mit.edu

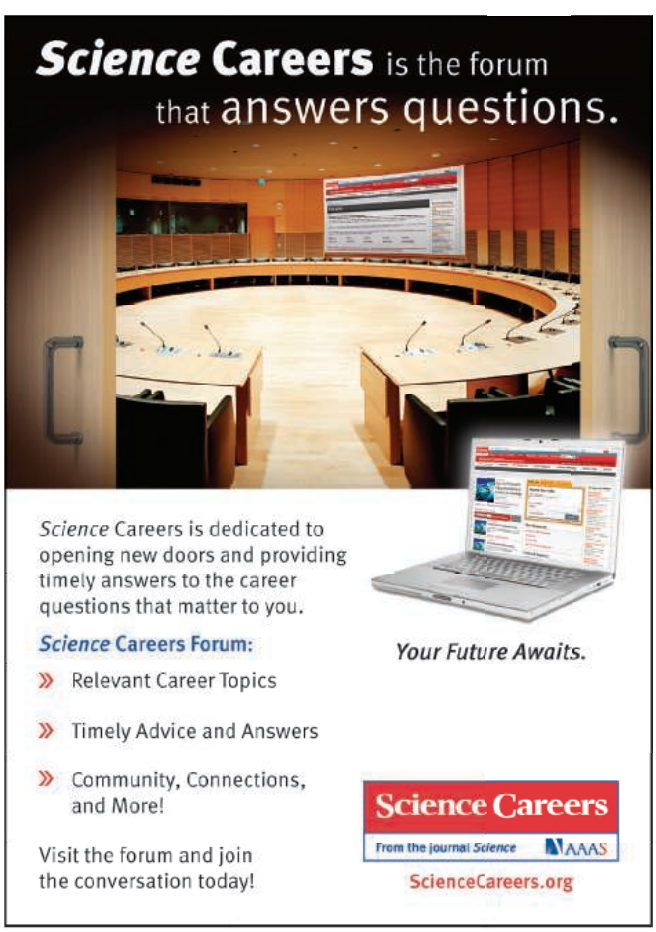

DANA-FARBER
CANCER INSTITUTE

Assistant/Associate Professor Opportunities

Precision (Personalized) Oncology Medicine

Assistant/Associate Professor, Clinical Computational Biology

The Department of Medical Oncology and the newly-formed Center for Cancer Precision Medicine at Dana-Farber Cancer Institute (DFCI) and Brigham and Women's Hospital (BWH) invite applications for a full-time appointment as an Assistant Professor or Associate Professor of Medicine to establish a research program in cancer genomics and clinically-oriented computational biology. The successful candidate will have a proven track record of innovative methodological research in computational biology, clinical genomic/molecular data interpretation, and collaborative translational cancer research relevant to the use of genomic data to guide medical management. This individual will join the Center for Cancer Precision Medicine and conduct an independent computational research program that also collaborates closely with disease-oriented investigators at the DFCI and BWH. Candidates with prior experience in the development of algorithms that facilitate cancer precision medicine genomic data interpretation are especially encouraged to apply. Candidates must have an MD and/or a PhD.

Assistant/Associate Professor, Translational Research (Solid Tumors)

The Department of Medical Oncology at the Dana-Farber Cancer Institute (DFCI) and the Department of Medicine, Harvard Medical School invite applications for an individual to develop an independent, laboratory-based translational research program focused on the application of precision medicine within solid tumors. The successful candidate will join the newly-formed Center for Cancer Precision Medicine and the Division of Molecular and Cellular Oncology. The research program will also interface closely with translational research efforts within the Departments of Pathology, Radiology, and Surgery at the Brigham and Women's Hospital. Candidates with an interest in the genomic/molecular basis of exceptional clinical responses and therapeutic resistance are especially encouraged to apply. A proven track record of outstanding laboratory research is required and prior experience in leading team-based cancer precision medicine projects is a plus. Candidates must have an MD and/or a PhD and should be board-certified or board-eligible in Internal Medicine and Medical Oncology.

These positions will be housed principally at the Dana-Farber Cancer Institute (an NCI-designated Comprehensive Cancer Center) and the Brigham and Women's Hospital, while also collaborating closely with the Broad Institute of Harvard and MIT. Academic appointments will be at the Assistant/Associate Professor level and salary and benefits will be competitive with other institutions.

Interested candidates must submit a curriculum vitae, a research plan, and three letters of reference to: Levi A. Garraway, MD, PhD, Director, Center for Cancer Precision Medicine, Dana-Farber Cancer Institute, 450 Brookline Avenue, Boston, MA 02215. Please send submissions via email to: ccpmsearch@partners.org.

HARVARD MEDICAL SCHOOL

BRIGHAM AND WOMEN'S HOSPITAL

Dana-Farber Cancer Institute/Brigham and Women's Hospital/ Harvard Medical School are Equal Opportunity/Affirmative Action Employers actively committed to increasing the diversity of our faculty: people with disabilities, veterans, women and members of underrepresented minority groups are therefore strongly encouraged to apply.

Weill Cornell Medical College in Qatar

FACULTY POSITION

In a pioneering international initiative, Cornell University and Weill Cornell Medical College established the Weill Cornell Medical College in Qatar (WCMC-Q) through a unique partnership with the Qatar Foundation for Education, Science and Community Development. In operation since 2002 in Doha, Qatar, WCMC-Q seeks candidates for a faculty position to teach in the field of:

BIOLOGY

We are seeking a biologist who will have primary responsibility for the teaching of a two-semester foundation-level Biology sequence (including laboratories) to a select group of highly motivated undergraduate pre-medical students. The successful candidate will also contribute to the teaching of more advanced courses in the biological and biomedical sciences, as appropriate. In addition to the principal teaching obligation, the successful candidate will be expected to participate in student academic advising, committee work, research, and the broader academic life of WCMC-Q.

Eligible candidates will hold a Ph.D. degree in Biology or Biological Sciences or a closely related discipline. Preference will be given to candidates who demonstrate a record of excellence in and commitment to teaching and scholarship. Experience of teaching at the professorial level in the North American higher education system will be highly valued.

A comprehensive and highly competitive salary and foreign-service benefits package, including fully furnished housing and other supplementary benefits, is provided. The appointment will be on a non-tenure track and is normally for three years in the first instance, renewable by mutual agreement.

Qualified applicants are invited to submit a letter of application outlining their interest in the position and how their skills and experience match WCMC-Q's requirements, along with a full curriculum vitae, at:

http://job.qatar-weill.cornell.edu

Please note that due to the high volume of applications, only short-listed candidates will be contacted. The Search Committee will begin reviewing applications immediately and will continue until the position is filled. Short-listed candidates will be asked to provide names of three references.

Cornell University is an equal opportunity, affirmative action educator and employer.

POSITIONS OPEN

UT SOUTHWESTERN MEDICAL CENTER

DIRECTOR OF THE CENTER for Human Nutrition

The University of Texas Southwestern (UTSW) Medical Center has initiated a search for a new Director of the Center for Human Nutrition. UT Southwestern is a premier academic institution with an exceptionally strong tradition of accomplishment in metabolism, genetic, and clinical research.

The Center for Human Nutrition has excelled under the leadership of the current director, **Scott M. Grundy,** M.D., who will step down after leading the internationally acclaimed Center for over 30 years. The Center is supported by a large endowment.

Candidates should have an outstanding record of achievement in metabolism and a vision for growing and directing programs of excellence in scientific, clinical, and translational research, as well as community engagement and education. Appointment to the UT Southwestern faculty will be at the rank of **ASSOCIATE** or **FULL PROFESSOR** with tenure.

Interested candidates should send curriculum vitae to **e-mail: nutrition.search@utsouthwestern.edu.**

UTSW is an Affirmative Action/Equal Opportunity Employer. Women, minorities, veterans, and individuals with disabilities are encouraged to apply.

REGULAR FELLOW WITH CDC/NIOSH

The National Institute for Occupational Safety and Health (NIOSH) invites applications for a Regular Fellow position to join its Toxicology and Molecular Biology Branch (TMBB), in the Health Effects Laboratory Division. The NIOSH Health Effects Lab is studying the impact of occupational exposure to new and known fibrotic agents as it relates to health effects and risk evaluation. Training opportunities are available to conduct research in conjunction with goals related to the National Occupational Research Agenda (NORA). Current studies include: (1) Signaling pathways leading to pulmonary fibrotic pathology; (2) biomarkers of exposure and toxicity; and (3) receptor-mediated toxicity and pharmacology. The successful candidate should have a Master's or Ph.D. degree in Toxicology, Pharmacology, or in a related biomedical field. Experience is needed in molecular, cellular, and small animal techniques. Salary is dependent upon academic degree and experience. Send curriculum vitae and contact information of three references to: **Dr. Qiang Ma CDC/NIOSH/HELD/TMBB, 1095 Willowdale Road, M.S. 3014, Morgantown, WV 26505; e-mail: qam1@cdc.gov.** *NIOSH is an Affirmative Action/Equal Opportunity Employer.*

ASSISTANT PROFESSOR of Biochemistry & Computational Medicine and Bioinformatics

The University of Michigan Medical School seeks a tenure-track Assistant Professor for a dual appointment in the Departments of Biological Chemistry and Computational Medicine and Bioinformatics. The successful candidate will have demonstrated highly productive computational approaches to biochemical and/or global molecular processes, such as gene expression, metabolic network analysis, biochemical signaling, and protein structure. Applications should be submitted by e-mail to **Ms. Amanda Howard** (**e-mail: amanhowa@med.umich.edu**) and should include a cover letter, curriculum vitae, a brief summary of recent research, a two-page summary future research plans, and names and contact information for at least three references. To ensure full consideration, all materials should be received by December 20, 2013.

Women and underrepresented minorities are encouraged to apply. The University of Michigan is supportive of the needs of dual career couples and is an Equal Opportunity/Affirmative Action Employer.

POSITIONS OPEN

MULTIPLE FACULTY POSITIONS College of the Environment and Ecology (CEE)

A top research university in a best living coastal city, Xiamen University is known for its academic excellence. The newly established CEE focuses its research programs on costal and wetland environment, ecosystem and management. CEE is seeking excellent scientists with expertise in global ecosystem, climate change, molecular/genomic ecology, remote sensing/modeling, watershed environment, and pollution treatment science and engineering etc. Qualified candidates will be nominated for national/provincial talent plans with excellent startup package and compensation. Applications are reviewed year round. For full consideration, submit before December 20. Details at **website: http://cee.xmu.edu.cn. E-mail: ceezp@xmu.edu.cn.**

PHYSIOLOGIST/NEUROBIOLOGIST

The Biology Department of Franklin & Marshall College invites applications for a **VISITING ASSISTANT PROFESSOR** position in animal physiology, beginning July 2014 (pending administrative approval). Position is renewable for up to three years on evidence of good teaching and/or continued administrative approval. Candidates should have a Ph.D., demonstrated strengths in teaching and research, and broad interests in animal physiology. Annual teaching responsibilities include two sections (each with lecture and laboratory) of a team-taught sophomore-level course in plant and animal physiology and development, and an advanced laboratory elective in the candidate's area of specialization. We encourage applications from candidates with expertise in neurobiology. The successful candidate will have the opportunity to engage undergraduates in research, and opportunities to participate in our interdisciplinary programs: Biochemistry and Molecular Biology, Bioinformatics, Animal Behavior, Neuroscience, and Public Health. Franklin & Marshall is a small (enrollment 2,400), highly selective coeducational liberal arts college with a tradition of excellence in science and student research. In 2007, the Biology Department moved into a 100,000 sq. ft. state-of-the-art interdisciplinary teaching and research facility, which includes a research-grade plant growth facility, aquatic rooms, and a vivarium.

Applicants should submit a cover letter, curriculum vitae, teaching evaluations (if available), graduate transcripts, a statement of teaching philosophy, and a statement of plans to actively engage undergraduates in research. In addition, please provide names and e-mail addresses of three individuals who will provide letters of reference. Electronic applications will not be accepted. Priority will be given to applications received by January 10, 2014. Send applications to: **Dr. Peter Fields, Department of Biology, Franklin & Marshall College, P.O. Box 3003, Lancaster, PA, 17604. Telephone: 717-291-4118; e-mail: janice.kaufman@fandm.edu; website: http://www.fandm.edu/biology.** *Franklin & Marshall College is committed to having an inclusive campus community, and as an Equal Opportunity Employer, does not discriminate in its hiring or employment practices on the basis of gender, race or ethnicity, color, national origin, religion, age, disability, family or marital status, or sexual orientation.*

MICROBIOLOGIST

The Department of Biology, California State University (CSU) Bakersfield invites applicants for an **ASSISTANT PROFESSOR** tenure-track position in Microbiology. Candidates must have a Ph.D. in biological sciences and will be expected to teach non-majors and majors courses in microbiology and cell biology, and are also required to conduct research in their area of specialization. Available September 1, 2014. Application deadline is December 15, 2013. See **website: http://www.csub.edu/biology** for full description and application instructions, or contact the **Department of Biology, California State University, Bakersfield, telephone: 661-654-3089.** *CSU Bakersfield is an Affirmative Action/Equal Opportunity Employer.*

POSITIONS OPEN

ASSISTANT PROFESSOR in Ecology and Evolution of Microbiomes Iowa State University (Ames, Iowa)

Iowa State University has launched the Presidential High Impact Hires Initiative to support targeted faculty hiring in areas of strategic importance. A cluster hire of eight faculty in four colleges within the strategically important area of Translational Health is included among the 29 high-impact hires targeted in this Presidential Initiative.

As part of this initiative, the Department of Ecology, Evolution & Organismal Biology (EEOB) at Iowa State University invites applications for a tenure-track position at the Assistant Professor level in the Ecology and Evolution of Microbiomes to begin fall 2014. We seek a creative individual investigating key questions in the systems biology of microbiomes related to health. Possible research areas may include: ecology and evolution of microbial communities; interactions of microbiomes with host phenotypes, and their change over time; mechanisms underlying the evolution and dynamics of microbiomes; and meta- and functional genomics, metabolomics, or metagenome evolution of microbial communities. Successful candidates will join a dynamic department embedded in a highly integrative and collaborative campus. Applicants must have a Ph.D., are expected to establish a nationally recognized, externally funded research program, and will contribute skillfully to undergraduate and graduate education.

A full description and application instructions can be found at **website: http://www.iastatejobs.com/applicants/Central?quickFind=84626.** Applicants should submit a cover letter, curriculum vitae, a research/vision statement that includes how their research program addresses unresolved problems in the field, a teaching statement, and up to three reprints. Consideration of applications will begin December 1, 2013. Submission of three confidential letters of recommendation should be arranged as per instructions in the on-line application system. Please address questions about the position to **e-mail: microbiomes@iastate.edu.**

Iowa State University values diversity and is an Affirmative Action/Equal Employment Opportunity Employer with an NSF ADVANCE program.

ASSISTANT PROFESSOR

The Rutgers University-Camden Campus seeks a broadly trained scientist in Systems Biology (including Synthetic Biology) for a tenure-track Assistant Professor position beginning in fall 2014. The ideal candidate will have both experimental and theoretical interests in modeling and investigating biological systems. The successful candidate will become a member of the recently formed Center for Computational and Integrative Biology (CCIB), with an appointment in the most suitable of the following departments: Biology, Chemistry, Computer Science, Mathematics, or Physics. (See detailed ad at **website: http://fas.camden.rutgers.edu/faculty-research/fas-job-searches/.**) Ph.D. and postdoctoral training are required. Arrange for electronic copies of curriculum vitae, statements of teaching and research interests, and three letters of recommendation to be sent to **e-mail: fazzino@camden.rutgers.edu.** *Rutgers is an Equal Opportunity/Affirmative Action Employer. Women and minorities are encouraged to apply.*

MARKETPLACE